

NASA CR-112119-2

**EVALUATION OF COATED COLUMBIUM ALLOY
HEAT SHIELDS FOR SPACE SHUTTLE
THERMAL PROTECTION SYSTEM APPLICATION**

Vol I.

VOLUME II

PHASE II ♦ SUBSIZE HEAT SHIELD AND SMALL SIZE TPS EVALUATION

August 1973

By
W. E. Black et al

1172-309418

Prepared Under
Contract NAS1-9793

Prepared by
CONVAIR AEROSPACE DIVISION OF GENERAL DYNAMICS
San Diego, California

for
National Aeronautics and Space Administration
LANGLEY RESEARCH CENTER
Hampton, Virginia

1

PRECEDING PAGE BLANK NOT FILMED
FOREWORD

This report was prepared by Convair Aerospace Division of General Dynamics — San Diego Operation under Contract NAS1-9793 for the National Aeronautics and Space Administration, Langley Research Center, Hampton, Virginia. It was administered under the direction of the Materials Division, Materials Application Branch, Metals Section with Mr. D. R. Rummler acting as the Technical Representative of the Contracting Officer. The Convair program manager was W. E. Black. Other Convair Aerospace personnel who participated in this program were J. W. Baer (process development and deputy program manager), T. J. DeLacy (nondestructive evaluation), A. F. Fujimoto (design), R. S. Wilson (structural analysis), G. A. Howell (thermodynamics analysis), G. L. Getline (acoustic fatigue analysis), H. G. Brittain, G. E. Copeland, and J. R. Kerr (environmental testing), O. H. Moore (acoustic testing).

In addition, the subcontract and support assistance is acknowledged for: L. J. Korb (Rockwell International Space Division - RI program coordination), A. J. Richardson (Rockwell International Space Division - micrometeoroid impact testing), E. L. Whiffen (Rockwell International Space Division - subsize heat shield welding), B. G. Calfin (Northrop Corporation Aircraft Division - small size heat shield brazing), L. Sama and B. Reznik (HiTemCo - coating application and field repair techniques), J. D. Culp (McDonnell Douglas Astronautics Company - field repair techniques), S. J. Gerardi (Vac-Hyd Processing Corporation - coating application), R. J. Maraia, B. G. Cour-Palais (NASA JSC) and R. Thomson (LaRC) [micrometeoroid impact testing], T. Chen and J. D. Robb (Lightning and Transients Research Institute - lightning strike testing), L. J. Robles (Electron Beam Welding, Inc. - small size TPS component welding), and W. G. Burnett (Burnett Industries - small size TPS component machining).

This report covers the Phase II performance period from February 1971 to July 1973.

PRECEDING PAGE BLANK NOT FILMED
CONTENTS

	Page
FOREWORD	iii
1 SUMMARY	1
2 INTRODUCTION	3
3 HEAT SHIELD CONFIGURATION STUDY	5
4 SUBSIZE PANEL FABRICATION	21
5 SUBSIZE PANEL TEST.	31
5.1 Test Plan	31
5.2 Test Profile	31
5.3 Test Equipment	33
5.3.1 Environmental simulation	33
5.3.2 Loading apparatus	40
5.3.3 Deflection measurements	43
5.4 Test Procedure	44
5.5 Test Results and Discussion	44
5.5.1 Group 1, C-129Y/R-512E, corrugated	45
5.5.2 Group 2, C-129Y/R-512E, tee stiffened	55
5.5.3 Group 3, Cb-752/R-512E, corrugated	61
5.5.4 Group 4, Cb-752/R-512E, tee stiffened	72
5.6 Test Analysis	83
5.6.1 General	83
5.6.2 Cyclic creep	89
5.7 Metallographic Examination	98
5.7.1 As-coated panels	100
5.7.2 Group 1, C-129Y/R-512E, corrugated	105
5.7.3 Group 2, C-129Y/R-512E, tee stiffened	108
5.7.4 Group 3, Cb-752/R-512E, corrugated	108
5.7.5 Group 4, Cb-752/R-512E, tee stiffened	116
5.7.6 Metallography summary	127
5.8 Nondestructive Evaluation	128
5.8.1 Summary	128
5.8.2 NDT techniques employed during Phase II	129
5.8.3 Discussion of test results	131
6 DESIGN AND ANALYSES OF SMALL-SIZE TPS	143
6.1 Design Conditions	143
6.1.1 Vehicle selection and flight environment	143
6.1.2 TPS design criteria	148
6.1.3 Material properties	151

	Page
6.2 Small Size TPS Design	160
6.2.1 Preliminary design	160
6.2.2 Final design	161
6.3 Small-Size TPS Thermal Analysis	167
6.3.1 Summary	167
6.3.2 Environmental conditions	167
6.3.3 Material properties	168
6.3.4 Methods of analysis	172
6.3.5 Insulation sizing	172
6.3.6 Tee-stiffened panel	173
6.3.7 Corrugated panel	185
6.3.8 Panel support structure	195
6.4 Small-Size TPS Structural Analysis	202
6.4.1 Summary	202
6.4.2 Method of analysis	203
6.4.3 Tee-stiffened panel assembly.	204
6.4.4 Corrugated panel assembly	219
6.4.5 Panel flutter	249
6.4.6 Acoustic fatigue analysis	269
6.4.7 Creep	275
7 FABRICATION OF TPS HARDWARE	279
7.1 Configurations	279
7.2 Materials	286
7.2.1 Metals	286
7.2.2 Coatings	291
7.2.3 Insulation	292
7.3 Fabrication Sequence	292
7.3.1 Welding	292
7.3.2 Heat treatment	296
7.3.3 Brazing	296
7.4 System Weights	303
7.5 System Costs	309
8 SMALL SIZE FULL SCALE ENVIRONMENTAL TESTING	313
8.1 Hot Gas Flow Tests	313
8.1.1 Test equipment and procedure	313
8.1.2 Test observations and results	320
8.1.3 Test summary	337
8.2 Radiant Heat Tests	337
8.2.1 Test equipment and procedure	337
8.2.2 Test observation and results	342
8.2.3 Test summary.	355

	Page
8.3 Acoustic Tests	355
8.3.1 Test equipment and procedure	355
8.3.2 Test observations and results	362
8.3.3 Test summary.	367
9 LIGHTNING STRIKE TESTS	377
9.1 Mechanism of Lightning Discharge	377
9.2 Test Specimen Fabrication	381
9.3 Lightning Strike Testing	385
10 MICROMETEOROID IMPACT TESTS	393
10.1 Introduction	393
10.2 Test Specimens	393
10.3 Impact Testing	393
10.3.1 Erosion tests	393
10.3.2 Cratering test	396
10.3.3 Perforation tests	401
11 CONCLUDING REMARKS	409
APPENDIX A: CONVERSION OF U.S. CUSTOMARY UNITS TO SI UNITS . .	413
APPENDIX B: NONDESTRUCTIVE EVALUATION	417
APPENDIX C: ACOUSTIC FATIGUE ANALYSIS PROGRAM (P5454) . . .	437
APPENDIX D: BRAZE SYSTEM QUALIFICATION	449
APPENDIX E: ACOUSTIC TEST DATA	465
REFERENCES	515

FIGURES

3-1 Honeycomb Sandwich Heat Shield Concept (Preliminary)	7
3-2 Bead Stiffened Heat Shield Concept (Preliminary)	8
3-3 Rib and Tee Stiffened Heat Shield Concepts (Preliminary)	9
3-4 Isogrid Stiffened Heat Shield Concept (Preliminary)	10
3-5 Vee-Flat Corrugation Stiffened Heat Shield Concept (Preliminary) . .	11
3-6 Open Corrugation Heat Shield Concept (Preliminary)	12
3-7 Cruciform/Tubular Post Support Structure Concept (Preliminary) . .	13
3-8 Hat Section/Cantilevered Channel Support Structure Concept (Preliminary)	14
3-9 Hinged Heat Shield Concept (Preliminary)	15
4-1 As-Coated Unexposed Subsize Corrugated Panel	24
4-2 As-Coated Unexposed Subsize Tee-Stiffened Panel	24
4-3 Corrugated Panel Fabrication Sequence	25
4-4 Tee-Stiffened Panel Fabrication Sequence	25

	Page
4-5 Subsize Tee-Stiffened Panel Fabrication Sequence	27
4-6 Cb-752/R-512E Electron Beam Weld on Subsize Tee-Stiffened Panel .	28
4-7 Microstructure of Unexposed Cb-752/R-512E	29
4-8 Microstructure of Unexposed C-129Y/R-512E	30
4-9 Cb-752/R-512E Cap Edge from Subsize Tee-Stiffened Panel	30
5-1 Design and Test Profile	32
5-2 Flight Simulation Facility	34
5-3 Quartz Lamp Furnace Chamber	35
5-4 Flight Simulation Test Panel Mounted in Test Fixture	36
5-5 Temperature Distribution on Corrugated Subsize Panel at Constant Power Settings	37
5-6 Force Cylinders for Load Application	38
5-7 Load Link and Portable Strain Indicator	39
5-8 Bristol Pressure Programmer	39
5-9 Subsize Panel Loading Apparatus	41
5-10 Front View of Panel YSC-3 After 20 Flight Simulation Cycles . . .	47
5-11 Rear View of Panel YSC-3 After 20 Flight Simulation Cycles . . .	48
5-12 Front View of Panel YSC-3 After 100 Flight Simulation Cycles . . .	49
5-13 Rear View of Panel YSC-3 After 100 Flight Simulation Cycles . . .	50
5-14 Front View of Panel YSC-2 After 100 Flight Simulation Cycles . . .	51
5-15 Rear View of Panel YSC-2 After 100 Flight Simulation Cycles . . .	52
5-16 Permanent Deformation Along Longitudinal Center Axis of Panel YST-3 After 100 Flight Simulation Cycles	53
5-17 Permanent Deformation of Flange Along the Line of Mounting Holes of Panel YSC-3 After 100 Flight Simulation Cycles	53
5-18 Permanent Deformation Along Longitudinal Center Axis of Panel YST-2 After 100 Flight Simulation Cycles	54
5-19 Permanent Deformation of Flange Along the Line of Mounting Holes of Panel YSC-2 After 100 Flight Simulation Cycles	54
5-20 Movement of Lower End of Panel YSC-3 With Respect to Stiffener Bar After 100 Flight Simulation Cycles	55
5-21 Beginning of Edge Attack and Increased Surface Spall on Panel YST-3 After 59 Flight Simulation Cycles	56
5-22 Skin Failure Extending Through Panel YST-3 After 83 Flight Simulation Cycles	58
5-23 Front View of Panel YSC-3 After 100 Flight Simulation Cycles . . .	59
5-24 Rear View of Panel YST-3 After 100 Flight Simulation Cycles . . .	60
5-25 Extent of Permanent Creep Deflection of Panel YST-3 After 100 Flight Simulation Cycles	61
5-26 Front View of Panel YST-4 After 64 Flight Simulation Cycles . . .	62

	Page
5-27 Rear View of Panel YST-4 After 64 Flight Simulation Cycles . . .	63
5-28 Close-up View of Damaged Areas of Panel YST-4 After 64 Flight Simulation Cycles	64
5-29 Front View of Panel BSC-1 After Nine Flight Simulation Cycles . . .	65
5-30 Rear View of Panel BSC-1 After Nine Flight Simulation Cycles . . .	66
5-31 Front View of Panel BSC-1 After 100 Flight Simulation Cycles . . .	67
5-32 Rear View of Panel BSC-1 After 100 Flight Simulation Cycles . . .	68
5-33 Front View of Panel BSC-2 After 100 Flight Simulation Cycles . . .	69
5-34 Rear View of Panel BSC-2 After 100 Flight Simulation Cycles . . .	70
5-35 Permanent Creep Deflection Along Longitudinal Central Axis of Panel BSC-1 After 100 Flight Simulation Cycles	71
5-36 Permanent Creep Deflection Along Longitudinal Central Axis of Panel BSC-2 After 100 Flight Simulation Cycles	71
5-37 Front View of Panel BST-4 After 20 Flight Simulation Cycles . . .	73
5-38 Front View of Panel BST-3 After 100 Flight Simulation Cycles . . .	74
5-39 Rear View of Panel BST-3 After 100 Flight Simulation Cycles . . .	75
5-40 Front View of Panel BST-4 After 100 Flight Simulation Cycles . . .	76
5-41 Rear View of Panel BST-4 After 100 Flight Simulation Cycles . . .	77
5-42 Bending About Transverse Axis of Panel BST-3 After 100 Flight Simulation Cycles	78
5-43 Bending About Transverse Axis of Panel BST-4 After 100 Flight Simulation Cycles	78
5-44 Coating Damage and Erosion of Panel BST-3 After 100 Flight Simulation Cycles	79
5-45 Front View of Panel BST-1 After 100 Flight Simulation Cycles . . .	81
5-46 Rear View of Panel BST-1 After 100 Flight Simulation Cycles . . .	82
5-47 Bending of Panel BST-1 After 100 Flight Simulation Cycles . . .	83
5-48 Panel BST-2 Oxidation Site at 66 Flight Simulation Cycles Before Coating Repair	84
5-49 Panel BST-2 at 66 Flight Simulation Cycles After Coating Repair . . .	85
5-50 Front View of Panel BST-2 After 100 Flight Simulation Cycles — 34 Cycles After Coating Repair	86
5-51 Rear View of Panel BST-2 After 100 Flight Simulation Cycles — 34 Cycles After Coating Repair	87
5-52 Close-up View of Panel BST-2 After Coating Repair Before Further Flight Simulation Cycling	88
5-53 Close-up View of Panel BST-2 After Coating Repair and Further Cycling to 100 Flight Simulation Cycles	88
5-54 Location of Deflection Measurements	90
5-55 Spanwise Deflection Versus Span for Specimen BSC-1	91

	Page
5-56 Creep Deflection Versus Cycles for Specimen BSC-1	92
5-57 Creep Deflection Versus Cycles for Specimen BSC-2	92
5-58 Comparison of Specimen BSC-1 Cross Section Profiles Before and After Exposure	93
5-59 Initial and Final Dimensions Derived From Contour Gauge Measure- ments (in Test Fixture)	94
5-60 Temperature Distribution Over Corrugation Section at Time of Maxi- mum Temperature	95
5-61 Test Load and Temperature Profile	96
5-62 Predicted Creep Deflection Along Semi-Span of Corrugated Panel . .	97
5-63 Location of Sections for Metallographic Examination of Corrugated Panels	100
5-64 Location of Sections for Metallographic Examination of Tee- Stiffened Panels	100
5-65 Microstructure of Unexposed Cb-752/R-512E Corrugated Panel . .	101
5-66 Microstructure of Unexposed Cb-752/R-512E Corrugated Panel . .	102
5-67 Microstructure of Unexposed Cb-752/R-512E Corrugated Panel . .	102
5-68 Microstructure of Unexposed Cb-752/R-512E Tee-Stiffened Panel . .	103
5-69 Microstructure of Unexposed Cb-752/R-512E Tee-Stiffened Panel . .	103
5-70 Microstructure of Unexposed Cb-752/R-512E Tee-Stiffened Panel . .	104
5-71 Microstructure of Unexposed Cb-752/R-512E Tee-Stiffened Panel . .	104
5-72 Microstructure of Exposed C-129Y/R-512E Corrugated Panel . . .	105
5-73 Microstructure of Exposed C-129Y/R-512E Corrugated Panel . . .	106
5-74 Microstructure of Exposed C-129Y/R-512E Corrugated Panel . . .	106
5-75 Microstructure of Exposed C-129Y/R-512E Corrugated Panel . . .	107
5-76 Microstructure of Exposed C-129Y/R-512E Corrugated Panel . . .	107
5-77 Microstructure of Exposed C-129Y/R-512E Tee-Stiffened Panel . .	109
5-78 Microstructure of Exposed C-129Y/R-512E Tee-Stiffened Panel . .	109
5-79 Microstructure of Exposed C-129Y/R-512E Tee-Stiffened Panel . .	110
5-80 Microstructure of Exposed C-129Y/R-512E Tee-Stiffened Panel . .	110
5-81 Microstructure of Exposed C-129Y/R-512E Tee-Stiffened Panel . .	111
5-82 Microstructure of Exposed C-129Y/R-512E Tee-Stiffened Panel . .	111
5-83 Microstructures of Exposed C-129Y/R-512E Tee-Stiffened Panel . .	112
5-84 Microstructure of Exposed C-129Y/R-512E Tee-Stiffened Panel . .	113
5-85 Microstructure of Exposed C-129Y/R-512E Tee-Stiffened Panel . .	113
5-86 Microstructure of Exposed C-129Y/R-512E Tee-Stiffened Panel . .	114
5-87 Microstructure of Exposed C-129Y/R-512E Tee-Stiffened Panel . .	114
5-88 Microstructure of Exposed Cb-752/R-512E Corrugated Panel . . .	115
5-89 Microstructure of Exposed Cb-752/R-512E Corrugated Panel . . .	115
5-90 Microstructure of Exposed Cb-752/R-512E Corrugated Panel . . .	116

	Page
5-91 Microstructure of Exposed Cb-752/R-512E Corrugated Panel . . .	117
5-92 Microstructure of Exposed Cb-752/R-512E Corrugated Panel . . .	117
5-93 Microstructure of Exposed Cb-752/R-512E Corrugated Panel . . .	118
5-94 Microstructure of Exposed Cb-752/R-512E Tee-Stiffened Panel . . .	118
5-95 Microstructure of Exposed Cb-752/R-512E Tee-Stiffened Panel . . .	119
5-96 Microstructure of Exposed Cb-752/R-512E Tee-Stiffened Panel . . .	120
5-97 Microstructure of Exposed Cb-752/R-512E Tee-Stiffened Panel . . .	120
5-98 Microstructure of Exposed Cb-752/R-512E Tee-Stiffened Panel . . .	121
5-99 Microstructure of Exposed Cb-752/R-512E Tee-Stiffened Panel . . .	121
5-100 Microstructure of Exposed Cb-752/R-512E Tee-Stiffened Panel . . .	122
5-101 Microstructure of Exposed Cb-752/R-512E Tee-Stiffened Panel . . .	123
5-102 Microstructure of Exposed Cb-752/R-512E Tee-Stiffened Panel . . .	123
5-103 Microstructure of Exposed Cb-752/R-512E Tee-Stiffened Panel . . .	124
5-104 Microstructure of Exposed Cb-752/R-512E Tee-Stiffened Panel . . .	124
5-105 Microstructure of Exposed Cb-752/R-512E Tee-Stiffened Panel . . .	125
5-106 Microstructure of Exposed Cb-752/R-512E Tee-Stiffened Panel with "Laboratory" Repair	125
5-107 Microstructure of Exposed Cb-752/R-512E Tee-Stiffened Panel with "Laboratory" Repair	126
5-108 Microstructure of Exposed Cb-752/R-512E Tee-Stiffened Panel with "Field" Repair	126
5-109 Ultrasonic C-scan Recording Showing Lack of Braze	130
5-110 Thermoelectric Testing of Small Size Panels	133
5-111 Autoradiograph of Tagged Coating	135
5-112 Results of R-512E/Cb-752 Alloy Limited Oxidation Test	135
5-113 Autoradiograph Versus Oxidation Damage During R-512E/Cb-752 Alloy Screening Test	136
5-114 Container and Equipment for Applying Radioactive Coating	137
5-115 Autoradiograph of Green Coating Showing Lack of Wetting	139
5-116 Autoradiographic Signatures of Coated Heat Shields	140
6-1 Orbiter Lower Surface Area of Investigation	143
6-2 Selected Boost History - Lower Surface X/L = 0.025	144
6-3 Boost External Noise Time History	146
6-4 Heat Shield Panel Acoustic Environment	146
6-5 Boost Engine Vibration Spectrum at Heat Shield Attach Points	147
6-6 Orbiter Lower Fuselage Pressure Distribution for Mated (Orbiter/ Booster) Configuration (SSV 134C)	147
6-7 Selected Entry History - Lower Surface X/L = 0.025	149
6-8 Preliminary Design Tensile Properties Versus Temperature for Cb-752/R-512E Based on Net As-Coated Section	152
6-9 Coefficient of Thermal Expansion Versus Temperature for Cb-752 . .	152

	Page
6-10 Thermal Conductivity Versus Temperature of Cb-752	153
6-11 Specific Heat Versus Temperature for Cb-752	153
6-12 Preliminary Design Allowable Stress on Cb-752 for 1% Creep Strain Based on Net As-Coated Section	153
6-13 Preliminary Design Tensile Properties Versus Temperature for C-129Y/R-512E Based on Net As-Coated Section.	154
6-14 Coefficient of Thermal Expansion Versus Temperature for C-129Y .	154
6-15 Thermal Conductivity Versus Temperature for C-129Y	154
6-16 Specific Heat Versus Temperature for C-129Y	155
6-17 Preliminary Design Allowable Stress on C-129Y for 1% Creep Strain Based on Net As-Coated Section	155
6-18 Thermal Conductivity of TD NiCr	155
6-19 Specific Heat of TD NiCr	156
6-20 Thermal Conductivity of Titanium (Ti-6Al-4V) . .	156
6-21 Specific Heat of Titanium (Ti-6Al-4V)	156
6-22 Thermal Conductivity of Dyna-Flex Insulation	157
6-23 Specific Heat of Dyna-Flex Insulation	157
6-24 Total Normal Emittance Versus Exposure Cycles for R-512E Coated Cb-752 and C-129Y	160
6-25 Preliminary Design of Tee-Stiffened Heat Shield Test Assembly . .	162
6-26 Preliminary Design of Corrugated Heat Shield Test Panel Assembly .	164
6-27 Final Design of Tee-Stiffened Heat Shield Test Assembly	165
6-28 Final Design of Corrugated Heat Shield Test Assembly.	166
6-29 Boost Heating Rate History (Lower Fuselage, X/L = 0.025)	168
6-30 Boost Surface Pressure Profile Lower Surface (X/L = 0.025) . . .	169
6-31 Entry Heating Rate History (Lower Fuselage, X/L = 0.025)	170
6-32 Entry Surface Pressure Profile (Lower Fuselage, X/L = 0.025) . .	171
6-33 Insulation Thickness Selection	173
6-34 Predicted Backup Structure and Insulation Surface Temperature History	174
6-35 Predicted Tee-Stiffened Panel Temperatures During Ascent	175
6-36 Predicted Tee-Stiffened Panel Ascent Temperature Distribution, Time = 180 Seconds	176
6-37 Predicted Tee-Stiffened Panel Ascent Temperature Distribution, Time = 440 Seconds	177
6-38 Predicted Tee-Stiffened Panel Temperatures During Entry	179
6-39 Predicted Tee-Stiffened Panel Entry Temperature Distribution, Time = 140 Seconds	180
6-40 Predicted Tee-Stiffened Panel Edge Structure Temperature Distribution	181

	Page
6-41 Predicted Tee-Stiffened Panel Temperature Distribution for Several Sections Near the Joint	182
6-42 Predicted Tee-Stiffened Panel Overlapped Edge Temperature Distribution	183
6-43 Predicted Tee-Stiffened Panel Temperature Distribution Along the 12-Inch (30.48 cm) Length Between Tees	184
6-44 Predicted Corrugated Panel Temperature During Entry, Axial Flow .	186
6-45 Predicted Corrugated Panel Entry Temperature Distribution, Axial Flow, Time = 450 Seconds	187
6-46 Cross Flow Heat Transfer Correction Factor	188
6-47 Predicted Corrugated Panel Temperatures During Entry, Cross Flow.	189
6-48 Predicted Corrugated Panel Entry Temperature Distribution, Cross Flow, Time = 450 Seconds	190
6-49 Predicted Corrugated Panel Temperatures During Entry, Axial Flow (Final Design)	191
6-50 Predicted Corrugated Panel Entry Temperature Distribution, Axial Flow, Time = 450 Seconds (Final Design)	192
6-51 Predicted Corrugated Panel Edge Structure Temperature Distribution	193
6-52 Predicted Corrugated Panel Temperature Distribution	194
6-53 Predicted Corrugated Panel Edge Structure Temperature Distribution Assuming Infinite Contact Conductance at Interface	196
6-54 Predicted Corrugated Panel Overlapped Edge Structure Temperature Distribution	197
6-55 Predicted Corrugated Panel Temperature Distribution	198
6-56 Predicted Corrugated Panel Overlapped Edge Structure Temperature Distribution Assuming Infinite Contact Conductance at Interface . .	199
6-57 Panel Support-Post Schematic	200
6-58 Predicted Panel Support-Post and Primary Structure Temperature Histories	201
6-59 Predicted Support-Post Temperature Distribution	202
6-60 Beam Model and Typical Cross Section	223
6-61 Equivalent Airspeed Versus Mach Number During Boost Phase . . .	250
6-62 Post Model	253
6-63 $R=0.1$ and Random S-N Curves for Coated Cb-752	256
6-64 $R=0.15$ and Random S-N Curves for TD NiCr	257
6-65 Response Acceleration (G_{rms}) Versus Panel Weight	258
6-66 Inner Post Wall Thickness Versus Panel Weight	258
6-67 Ultimate and Limit Bending Moment Distributions for a 2.75- Pound (12.49 kg) Panel	259

	Page
6-68 Mated Vehicle Configuration (on Pad)	270
6-69 Constant Life Fatigue Diagram for Coated Cb-752	276
7-1 Open-Corrugated TPS Exploded Assembly	280
7-2 Exterior View of Brazed Cb-752 Open Corrugation Heat Shield . . .	281
7-3 Interior View of Brazed Cb-752 Open Corrugation Heat Shield . . .	282
7-4 Tee-Stiffened TPS Exploded Assembly	283
7-5 Tee-Stiffened Cb-752 Heat Shield Panel – Skin Side Ready Coating	284
7-6 Tee-Stiffened Cb-752 Heat Shield Panel – Interior Side Ready for Coating	285
7-7 Tee-Stiffened Cb-752 Heat Shield Panel – Interior Side Prior to Final Weld	287
7-8 Details of Closure Welds – Welded Panel to Beam – Tee-Stiffened Cb-752 Heat Shield Panel	288
7-9 Detail of Closure Welds – Welded Panel to Beam – Ready for Welding, Tee-Stiffened Cb-752 Heat Shield Panel	289
7-10 Coating Application Test Specimen	293
7-11 Tee-Stiffened Heat Shield Panel Fabrication Sequence	294
7-12 Open Corrugation Heat Shield Panel Fabrication Sequence	295
7-13 Electron Beam Weld Qualification and Tool Development	297
7-14 Sample Weld Joint Configurations	298
7-15 Final Weld Qualification Panel	299
7-16 Braze Process Development Program	301
7-17 Braze Qualification Program for Columbium Alloy Cb-752	302
7-18 Open Corrugation TPS Components Prior to Testing	304
7-19 Open Corrugation TPS Component Prior to Testing	305
7-20 Tee-Stiffened TPS Component Prior to Testing	306
7-21 Tee-Stiffened TPS Components Prior to Testing	307
7-22 Columbium Alloy TPS Cumulative Average Cost	312
8-1 SEAR Test Facility.	314
8-2 Hot Gas Flow Test Profile	315
8-3 SEAR Facility Control, Programming, and Data Acquisition Center .	317
8-4 Thermocouple Locations for Open Corrugation TPS	318
8-5 Thermocouple Locations for Tee-Stiffened TPS	319
8-6 Open Corrugation TPS Specimen Installed in SEAR Facility Prior to Testing	321
8-7 Open Corrugation TPS Specimen After 10 Hot Gas Flow Cycles . . .	322
8-8 Panel Separation and Edge Damage of Open Corrugation TPS Specimen After 10 Hot Gas Flow Cycles	323
8-9 Open Corrugation TPS Specimen with Main Heat Shield Removed After 10 Hot Gas Flow Cycles	324

	Page
8-10 Open Corrugation TPS Specimen After 20 Hot Gas Flow Cycles . . .	326
8-11 Predicted Structure and Insulation Surface Temperature History . .	328
8-12 Predicted Panel Support Post and Primary Structure Temperature Histories	329
8-13 Predicted Support Post Temperature Distribution	330
8-14 Hot Gas Flow Test Composite Temperature Distribution - Open Corrugation TPS	332
8-15 Unexposed Tee-Stiffened TPS Specimen - Side View	333
8-16 Tee-Stiffened TPS Specimen After 20 Hot Gas Flow Cycles - Side View	334
8-17 Unexposed Tee-Stiffened TPS Specimen - End View	335
8-18 Tee-Stiffened TPS Specimen After 20 Hot Gas Flow Cycles - End View	336
8-19 Hot Gas Flow Test Composite Temperature Distribution - Tee- Stiffened TPS	339
8-20 Cryotherm/Radiant Heat Lamp Facility	340
8-21 Cryotherm Heat Chamber	341
8-22 Cryotherm/Radiant Heat Chamber System Schematic	343
8-23 Open Corrugation TPS Specimen After 50 Radiant Heat/Pressure/Load Cycles - View Looking Downstream	345
8-24 Open Corrugation TPS Specimen After 50 Radiant Heat/Pressure/Load Cycles - Side View	346
8-25 Radiant Heat Test Composite Temperature Distribution - Open Corrugation TPS	348
8-26 Radiant Heat Test Composite Temperature Distribution - Tee- Stiffened TPS	350
8-27 Tee-Stiffened TPS Specimen Before Thermal Cycling - Side View . .	351
8-28 Tee-Stiffened TPS Specimen After 50 Radiant Heat/Pressure/Load Cycles - Side View	352
8-29 Tee-Stiffened TPS Specimen Before Thermal Cycling - View Looking Upstream	353
8-30 Tee-Stiffened TPS Specimen After 50 Radiant Heat/Pressure/Load Cycles - View Looking Upstream	354
8-31 TPS Specimen Mounting Technique for Acoustic Testing	356
8-32 Tee-Stiffened TPS Specimen Mounted in Reverberation Chamber Wall .	357
8-33 1/3 Octave and Octave Band Center Frequencies - 152 dB OASPL (Pre-thermal Tests)	358
8-34 1/3 Octave and Octave Band Center Frequencies - 155 dB OASPL (Pre-thermal Tests)	359
8-35 1/3 Octave and Octave Band Center Frequencies - 152 dB OASPL (Post-thermal Tests)	360

	Page
8-36 1/3 Octave and Octave Band Center Frequencies - 155 dB OASPL (Post-thermal Tests)	361
8-37 Tee-Stiffened Heat Shield after 25 Acoustic Cycles	363
8-38 Tee-Stiffened TPS Support Posts and Insulation after 25 Acoustic Cycles	364
8-39 Partially Disassembled Tee-Stiffened TPS After 20 Hot Gas Flow Thermal Cycles and 100 Acoustic Cycles	365
8-40 Tee-Stiffened Heat Shield (Exterior Side) and Attachments After 20 Hot Gas Flow Thermal Cycles and 100 Acoustic Cycles	366
8-41 Open Corrugation Heat Shield after 25 Acoustic Cycles	368
8-42 Open Corrugation TPS Support Posts and Insulation after 25 Acoustic Cycles	369
8-43 Open Corrugation Heat Shield (Exterior Side) and Attachments After 20 Hot Gas Flow Cycles and 100 Acoustic Cycles	370
8-44 Open Corrugation Heat Shield (Interior Side) and Attachments After 20 Hot Gas Flow Cycles and 100 Acoustic Cycles	371
8-45 Partially Disassembled Open Corrugation TPS After 50 Radiant Heat Thermal Cycles and 100 Acoustic Cycles	372
8-46 Open Corrugation Heat Shield (Exterior Side) and Attachments After 50 Radiant Heat Thermal Cycles and 100 Acoustic Cycles	373
8-47 Open Corrugation Heat Shield (Interior Side) and Attachments After 50 Radiant Heat Thermal Cycles and 100 Acoustic Cycles	374
8-48 Open Corrugation Heat Shield Showing Forward Beam Disbond After 20 Thermal Cycles and 100 Acoustic Cycles	375
9-1 Mechanism of Lightning Step Leader Approach and Passage Through an Aerospace Vehicle	377
9-2 Streamering from Model in Laboratory Illustrates Induced Streamer- ing from Approaching Natural Lightning Discharge That Guides Stroke into Vehicle	378
9-3 Stroke Off Nose is Swept Back Over Undersurface of Vehicle to Produce Pit Marks and a Few Holes in Undersurface	379
9-4 Composite Current Waveform of Natural Lightning Discharge Showing Three Main Phases: High Current, Intermediate Current, and Low Current Long Duration	380
9-5 Illustration of Spacecraft Contact Mechanism and Movement Through Lightning Channel	381
9-6 Mechanism of Stroke Hang-on	382
9-7 Cb-752/R-512E Lightning Strike Specimen Components Prior to Assembly	383
9-8 Electrical Resistance Measurements of Lightning Strike Specimens .	384

	Page
9-9 Test Arrangement for High Rate of Rise Test	386
9-10 Test Arrangement for the Intermediate Current Test	387
9-11 Oscillograms of Lightning Waveforms Used in Test of Columbium Heat Shield Panels	388
9-12 As-Coated Cb-752 Test Specimen After Lightning Strike Test Sequence	389
9-13 Pre-Oxidized Cb-752 Test Specimen After Lightning	390
9-14 Cb-752/R-512E Heat Shield Following Lightning Strike Tests and Thermal Exposure	392
10-1 Columbium Alloy Coupons After 50 Thermal Cycles Prior to Bombardment	397
10-2 Columbium Alloy Coupons After Bombardment	400
10-3 Hypervelocity Particle Penetration Into Unexposed C-129Y/R-512E Coupons	401
10-4 Hypervelocity Particle Penetration Into C-129Y/R-512E Coupons After Exposure to 50 Cycles to 2400° F (1589°K)	402
10-5 Hypervelocity Particle Penetration Into Cb-752/R-512E Coupons After Exposure to 50 Cycles to 2400° F (1589°K)	402
10-6 Columbium Alloy Coupons After Bombardment and Thermal Exposure	403
10-7 Columbium Alloy Coupons After Bombardment and Thermal Exposure	404
10-8 Columbium Alloy Coupons After Bombardment, Repair and Thermal Cycling	408

TABLES

3-1 Heat Shield Configuration Evaluation	6
3-2 Small Size Heat Shield Structural Summary	16
3-3 Heat Shield Manufacturing, Inspection and Refurbishment Summary . .	17
3-4 Columbium Alloy Heat Shield Configuration Selection	19
4-1 Average Room Temperature Properties of As-Received Sheet Alloy .	21
4-2 Ingot Chemistries of Phase II Subsize Panel Columbium Sheet Material	22
4-3 Typical Chemical Analysis of TD NiCr for Phase II Fasteners for Subsize Panels	23
5-1 Measurements for Determination of Panel Deflection	43
5-2 Flight Simulation Test Results	45
5-3 Summary of Derived Test Deflections	92
5-4 Subsize Panel Load Profile	95

	Page
5-5 Metallographic Examination of Subsize Panels	99
5-6 Nuclear Activation Analysis of Coated Panel (YST-1)	141
5-7 Correlation of Nuclear Activation Test Data	142
6-1 Summary of Specifications and Material Properties	158
6-2 Total Normal Emittance for Cb-752/R-512E	159
6-3 Total Normal Emittance for C-129Y/R-512E	159
7-1 Chemical Analysis of Small Size TPS Columbium Alloy Cb-752	290
7-2 Typical Chemical Analysis of Small Size TPS TD NiCr	291
7-3 TPS Components Weight Breakdown	308
7-4 TPS Fabrication Cost Breakdown	310
7-5 Columbium Alloy TPS Cost Projection	311
8-1 Open Corrugation TPS Hot Gas Flow Test Thermal Summary	331
8-2 Tee-Stiffened TPS Hot Gas Flow Test Thermal Summary	338
8-3 Open Corrugation TPS Radiant Heat Test Thermal Summary	347
8-4 Tee-Stiffened TPS Radiant Heat Test Thermal Summary	349
10-1 Columbium Alloy Room Temperature Properties	394
10-2 Tensile Test Results for Bombarded Specimens After 50 Thermal Cycles	395
10-3 Average Tensile Properties for Diffusion Bonded Specimens	395
10-4 Cratering Data for Unexposed C-129Y/R-512E	398
10-5 Cratering Data for Exposed C-129Y/R-512E	399
10-6 Cratering Data for Exposed Cb-752/R-512E	399
10-7 Perforation Test Results	404

SYMBOLS

A	area, spacing
B	modulus of elastic foundation, compressibility parameter
BARZ	distance of a section centroid from surface of skin
BM	bending moment
BS	body station
b	span, spacing
C	couple arm
C_p	specific heat
D	bending rigidity, diameter
D_2	plate bending stiffness in Y direction
d	diameter
dB	decibel
dim	dimension
E	modulus of elasticity in tension
E_c	modulus of elasticity in compression
E_T	tangent modulus
EIXX	bending rigidity
F	strength, stress
f	stress, frequency
f()	function of
G	acceleration

SYMBOLS (continued)

h	height
I	moment of inertia
K	constant
K_D	deflectional stiffness
K_T	stress concentration factor
k	thermal conductivity
k_d	support stiffness
L	length
M	mach number, moment
M.S.	margin of safety
m	mass
max	maximum
min	minimum
N	number
OA	overall
P	axial load
p	pressure
Q	lateral load
q	dynamic pressure
R	correction factor, radius, reaction load
REF	reference

SYMBOLS (continued)

S	shear, standard deviation
S_F	scatter factor
S_N	amplitude
SPL	sound pressure level
T	temperature
THD	thread
TIG	tungsten inert gas
TYP	typical
t	time, thickness
ULT	ultimate
V	velocity
W	weight
WX	beam curvature due to pressure loading
WXP	beam curvature due to temperature gradient
w	running load
X, Y, Z	rectangular coordinates
y	distance from neutral axis
α	angle of attack, coefficient of thermal expansion
Δ	differential
δ	deflection
ϵ	strain, emittance

SYMBOLS (continued)

ζ	damping ratio
η	plasticity factor
θ	included angle
λ	damping factor, flutter parameter
ν	Poisson's ratio
ρ	density
σ	stress

Subscripts

A	section location
all	allowable
B	section location
b	bending
c	coating, compression
cr	critical
cy	compressive yield
E	equivalent
e, eff	effective
F	flight
M	moment
max	maximum
min	minumum

SYMBOLS (continued)

rms	root mean square
s	skin, stress
t	thermal, tension
tu	tensile ultimate
ty	tensile yield
ult	ultimate
w	web
y	yield

EVALUATION OF COATED COLUMBIUM ALLOY
HEAT SHIELDS FOR SPACE SHUTTLE THERMAL
PROTECTION SYSTEM APPLICATION

VOLUME II

Phase II

Subsize Heat Shield and Small Size TPS Evaluation

By W. E. Black et al.
Convair Aerospace Division of General Dynamics

1 SUMMARY

This is the second phase of a three part program to evaluate columbium alloy thermal protection systems (TPS) for the Space Shuttle. Phase I was directed toward establishing design parameters and investigating material characteristics applicable to a predicted environment for heat shields. Phase II was directed toward selecting one material system and one structural configuration after exposure to simulated flight conditions.

Initially a trade study was conducted of seven heat shield configurations. These were evaluated for structural reliability, fabricability, weight, inspectability, and refurbishability. Two concepts, a tee-stiffened and an open corrugation, were selected as offering the most potential for system success. Fourteen subsize heat shields of a full scale section were fabricated from C-129Y and Cb-752 and silicide coated with R-512E. These subsize panels were subjected to a simulated flight profile representing temperature, local surface pressures, and applied pressure differential loads. All corrugated panels of both alloys sustained 100 cycles without structural or coating failure. Two C-129Y/R-512E tee-stiffened panels experienced coating breakdown and substrate erosion. Although these specimens were subjected up to 41 cycles after substrate erosion was observed, no structural failures (i.e., structural collapse) occurred. All Cb-752/R-512E panels performed well with one panel being successfully repaired after 66 cycles and completing 100 cycles. As a result of this evaluating the Cb-752/R-512E system was selected for hardware application during the subsequent phases.

Four small size, full scale TPS specimens were fabricated from Cb-752 in the tee-stiffened and open corrugation configurations. The fabrication processes employed included machining, sheet metal forming, electrical discharge machining, chemical milling, electron beam welding, vacuum brazing, heat treating, and creep flattening. All were accomplished without difficulty and resulted in high quality components.

Each of the four small size specimens was subjected to intermittent acoustic excitation and thermal testing. No detrimental effects were found from the 100 simulated mission acoustic exposure series. Two types of thermal testing were conducted. The first was a one atmosphere, oxidizing, convective, subsonic hot gas flow simulating a reentry thermal profile for 20 cycles. These 20 cycles conducted at one atmosphere are the equivalent of 80 to 100 cycles at reduced pressures. The second test was a 50 cycle exposure of reduced pressure, pressure differential loading, radiant heat testing through a simulated boost and reentry profile. All specimens survived the tests with no evidence of coating breakdown or substrate erosion. Distortion or deformation due to thermal or mechanical loading was within specified limits. System thermal response also was excellent. Neither tee-stiffened TPS specimen experienced mechanical failure. One of the two open corrugation TPS specimens experienced brazing disbond while the second survived without failure. All components were readily disassembled, both in the interim and following the test series.

The effect of lightning strikes on the oxidized and unoxidized coated columbium alloy heat shields was examined. Three types of tests were conducted: 1) a high current rise discharge, 2) a maximum energy discharge, and 3) a high current discharge. It was observed that conditions (1) and (2) would result in some coating damage but would not jeopardize the mission. The maximum current strike (3) would result in severe damage to a panel. However, since the condition exemplifies a pre-launch mode, identification of the damaged panel would be made and the panel replaced.

Simulated micrometeoroid impact tests were also conducted on coated columbium alloy specimens. Three types of tests were conducted: 1) erosion, 2) cratering, and 3) perforation. Neither the erosion or cratering conditions resulted in coating damage to the specimens. Field and laboratory repairs were made on the perforated specimens and all were successfully cycled 50 times through a simulated entry temperature profile.

Several conventional NDE methods were used throughout the program to determine the quality of the applied coating. In addition, a new technique of radioactive labeling was used to analyze the coating process. It is believed that the radionuclide tag (^{147}Pm), for the first time, showed the wetability of edges and limitations of the coating that require special consideration. The degree of difficulty encountered when dipping as well as the sensitivity of the unfired (green state) coating to handling and abrasion was shown.

Phase II concluded with the selection of the tee-stiffened TPS configuration for further development and application in Phase III. This selection was based on an overall assessment of relative weight, cost, and structural performance of the tee-stiffened and open corrugation TPS.

The units used for physical quantities delineated in this report are given in both the U.S. Customary Units (USCU) and in the International System of Units (SI). The USCU were used as primary units throughout this report with the SI conversions parenthesized. Conversion factors pertinent to the present investigation are presented in Appendix A.

2 INTRODUCTION

The economical development of manned systems for outer space depends on the development of low-cost, lightweight, reliable systems employed on reusable reentry spacecraft. The NASA approach to this development is to provide vehicles capable of earth landings and possessing the aerodynamic maneuvering characteristics of aircraft and yet able to withstand spacecraft reentry temperatures. This system has been designated the Space Shuttle.

The key element in the success of these vehicles is the thermal protection system (TPS). It must be capable of withstanding the structural static and dynamic loads as well as dissipating the frictional heat in aerodynamically slowing down the vehicle. One promising concept from a reliability, inspectability, cost, and resuability standpoint is that of metallic radiative heat shields. It is toward columbium alloys as applied to heat shields operating in the temperature range of 2000 to 2400 °F (1366 to 1589 °K) that this study has been directed.

The principal objective is to evaluate coated columbium alloy thermal protection systems by a logical sequence of analytical and experimental investigations involving simulated mission and environmental conditions. These efforts were directed toward the selection, characterization, and design of one material system (i.e., one columbium alloy with one coating), one heat shield configuration, and one support system with insulation. Reported herein are the results of Phase II of this study.

Phase I was initiated by selecting a model vehicle with an associated total environment from prelaunch to landing. This vehicle and environment would be the basis for the design conditions, design criteria, and test conditions used throughout the program. This selection was followed by an experimental and analytical evaluation of the properties of the material systems as applied to heat shields. Phase I culminated with the selection of two material systems (Cb-752/R-512E and C-129Y/R-512E) for further application and evaluation in Phase II.

This phase, which was partially concurrent with Phase I, consisted of two parts involving two types of panels. Part 1 involved the analytical investigation of several heat shield configurations. The two most promising concepts were to be selected for subsize panel fabrication and testing. From this was to be selected the better performing of the two material systems for further, larger scale evaluation. A complete TPS (i.e., heat shields, support structure, and insulation) was then fabricated for each of the two configurations for testing under hot gas flow and radiant heat with applied loads at reduced pressures with supplemental acoustic testing. Also investigated were the forming, machining, and joining methods to be used for the fabrication of complete thermal protection systems. Based on the total performance of the two TPS configurations, one concept was to be selected for full-scale, full-size system evaluation in Phase III.

Two types of TPS will be designed, fabricated, and tested during Phase III. One will be designed for testing in the NASA Langley Research Center Thermal Protection System Facility (TPSTF). This specimen is intended to study the effects of hot gas flow on parallel and transverse heat shield joints. The second specimen will be a full-scale, nine-panel configuration representative of an orbiter vehicle lower surface. This specimen will be exposed to simulated mission duty cycles consisting of combined thermal, load, acoustic testing to verify structural adequacy. Phase III will demonstrate the structural and thermal adequacy and the manufacturability of full-sized, coated columbium alloy thermal protection systems and provide data necessary to project the performance and cost of these systems for Space Shuttle vehicles.

3 HEAT SHIELD CONFIGURATION STUDY

This program has been directed toward developing a metallic radiative TPS with maximum concern for structural reliability. Since columbium alloys require a coating to resist oxidation and to maintain structural integrity, fabrication methods with consideration for coating application are extremely important. To assure adequate coverage of the components, the details must be inspectable with reasonable ease between missions within the given turn-around time. Components that are questionable for an additional mission must be easily removed for repair or replacement. All of these factors can affect the system weight. However, the weight of the TPS cannot be permitted to jeopardize the mission payload. With these factors apparent, a configuration study was undertaken to evaluate several candidate heat shield configuration.

The study illustrates the interaction of the various disciplines involved. An evaluation was made by applying weighting factors to specific variables for candidate heat shield concepts. Ranking and net worth of each of the five variables shown in Table 3-1 (reliability, weight, fabricability, inspectability, and refurbishability) considered to be most important were determined by experienced personnel from each of the involved disciplines; i.e., design, structural analysis, weight analysis, fabrication and process development, cost analysis, and nondestructive evaluation.

Preliminary designs of seven basic heat shield configurations, three methods of support, and two alloys were submitted for trade studies. These configurations are shown in Figures 3-1 through 3-9. The original concepts were: honeycomb sandwich, bead-stiffened, rib and tee-stiffened, grid-stiffened, vee-flat corrugation stiffened, and open corrugation. Tubular support posts, clips, and cantilevered channels were considered but not analyzed as an integral part of the preliminary study. A hinged panel concept was also proposed. This would have offered a system that was readily inspectable; however, assembly difficulties and corner gaps rendered this design impractical.

The trade study was based on heat shields of the general size 12 by 16 inches (30.5 by 40.6 cm) and a design profile shown in Figure 5-1. The critical loading occurred during launch at $t = 170$ seconds when the pressure differential load was 3.0 psi (20.7 kN/m²) and the temperature was 340°F (444°K). In the structural analyses the panels were considered to have simply supported edge conditions with joints that permit free thermal expansion. Five configurations had ribs or corrugations (in the direction of flow) that behave essentially as simply supported beams under normal pressure loading. The remaining two configurations were treated as plates. The short span, 12 inches (30.5 cm), minimum gages, and stiffener spacing, in general, dictated the section geometry. The analysis was composed of:

- (1) Ultimate static strength

Table 3-1. Heat Shield Configuration Evaluation

Parameter	Basis	Weighting Factor
Reliability	Ability to go 100 flights	0.35
Weight	Pounds of system	0.25
Inspectability	a. Time to initially inspect b. Time to inspect within given turn-around	0.20
Fabrication	Time and material	0.10
Refurbishment	Time to replace or repair within given turnaround	<u>0.10</u> 1.00

(2) Maximum creep strain

(3) Maximum total deflection (pressure loading and permanent creep)

In addition each panel was designed to be unbuckled at limit load, since it is considered that local bending deformation associated with buckling would enhance cracks in the coating and possibly initiate failure. No change in material properties due to the effects of accumulative exposure to elevated temperature was made for the parametric study. However, the effective material thickness was assumed to be progressively reduced by 0.0001 inch (0.0025 mm) per side per flight. A linear rate of diffusion was assumed between the coating and substrate. To account for the effective thickness in the creep strain analysis, the design life of 100 missions was simulated in groups of 10 flights with the increment of creep strain and coating diffusion in each time interval factored by 10. Redistribution of internal stress due to accumulated creep strains was included in the analysis.

All configurations were found to be critical for skin buckling or ultimate static strength during launch except for the bead stiffened heat shield for the C-129Y material, which was deflection critical. The panel configurations and dimensions are given in Table 3-2.

Following the preliminary structural configurations, the heat shields were examined for fabricability and inspectability as shown in Table 3-3. Consideration was given to the number of elements and complexity of the parts required to make up a panel. Three methods of joining were considered: brazing, diffusion bonding, and welding. Since the

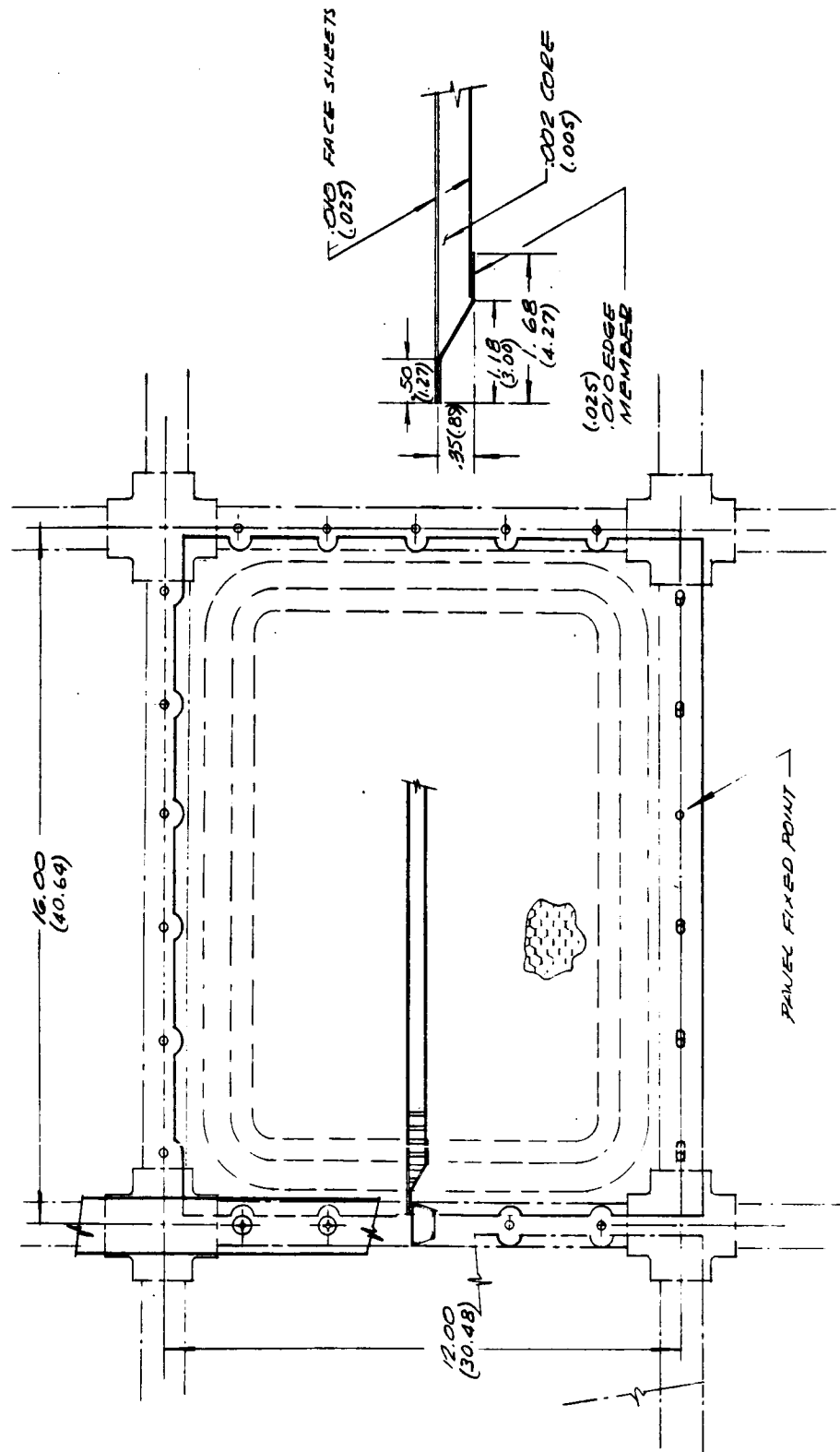


Figure 3-1. Honeycomb Sandwich Heat Shield Concept (Preliminary)

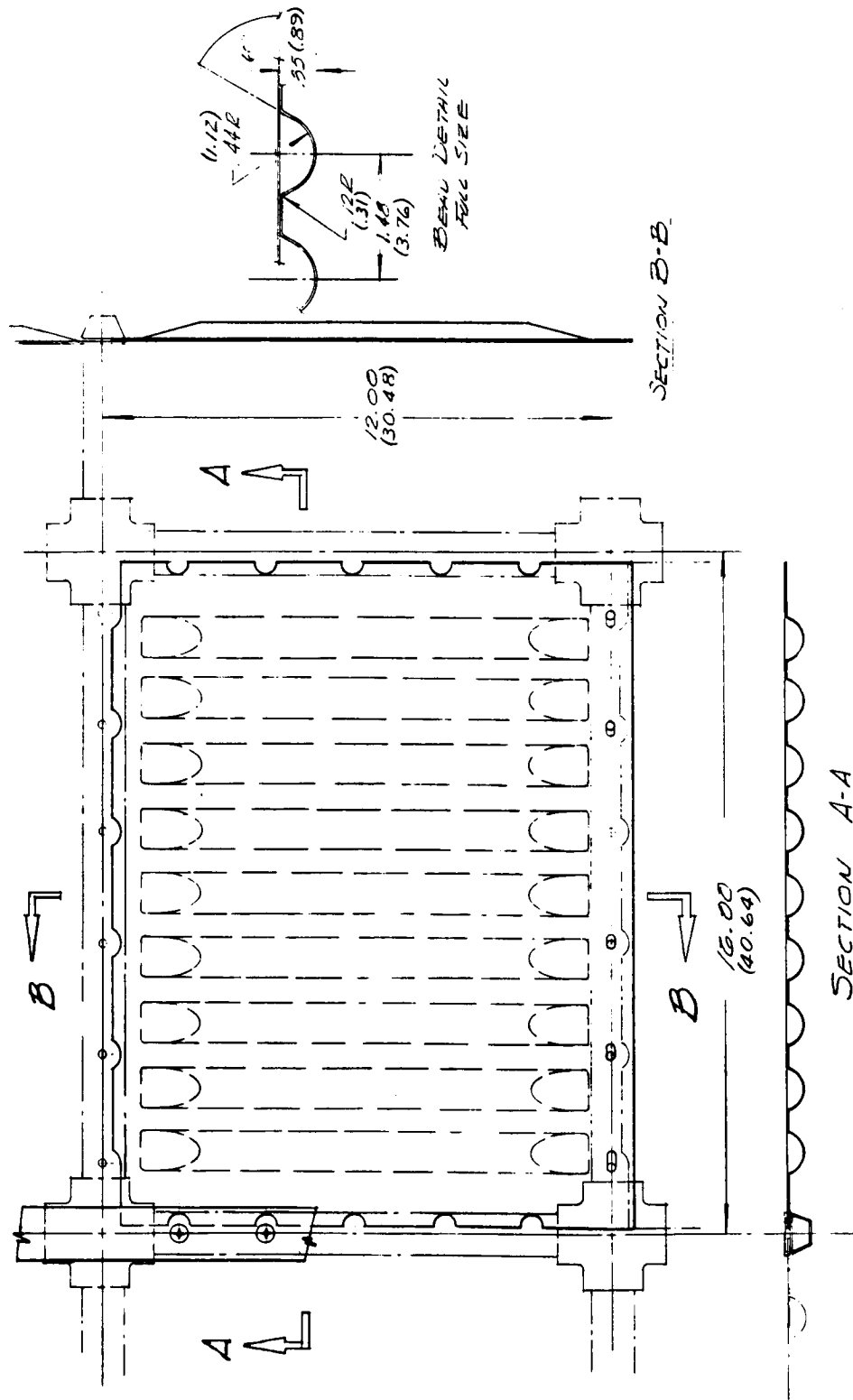


Figure 3-2. Bead Stiffened Heat Shield Concept (Preliminary)

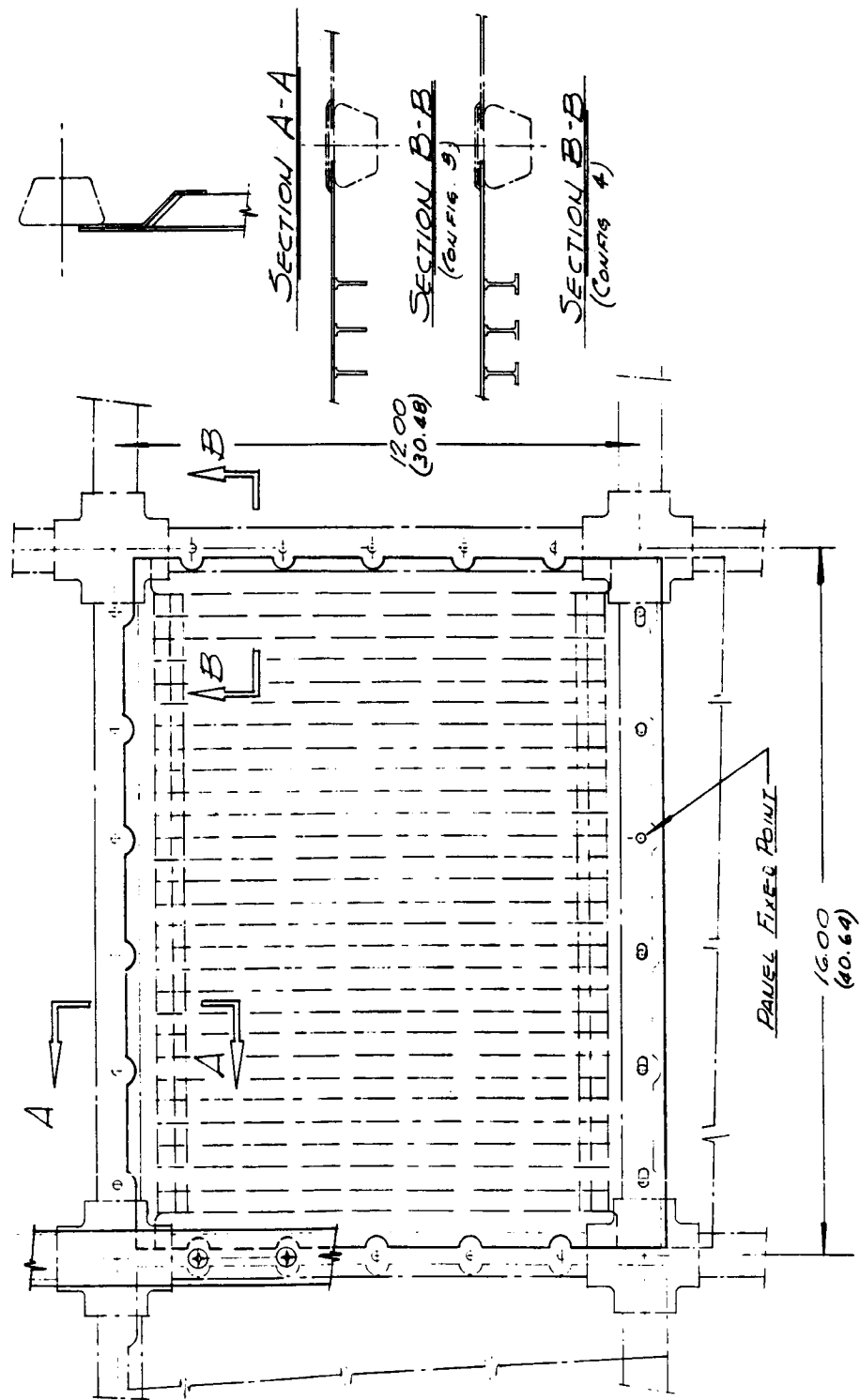


Figure 3-3. Rib and Tee Stiffened Heat Shield Concepts (Preliminary)

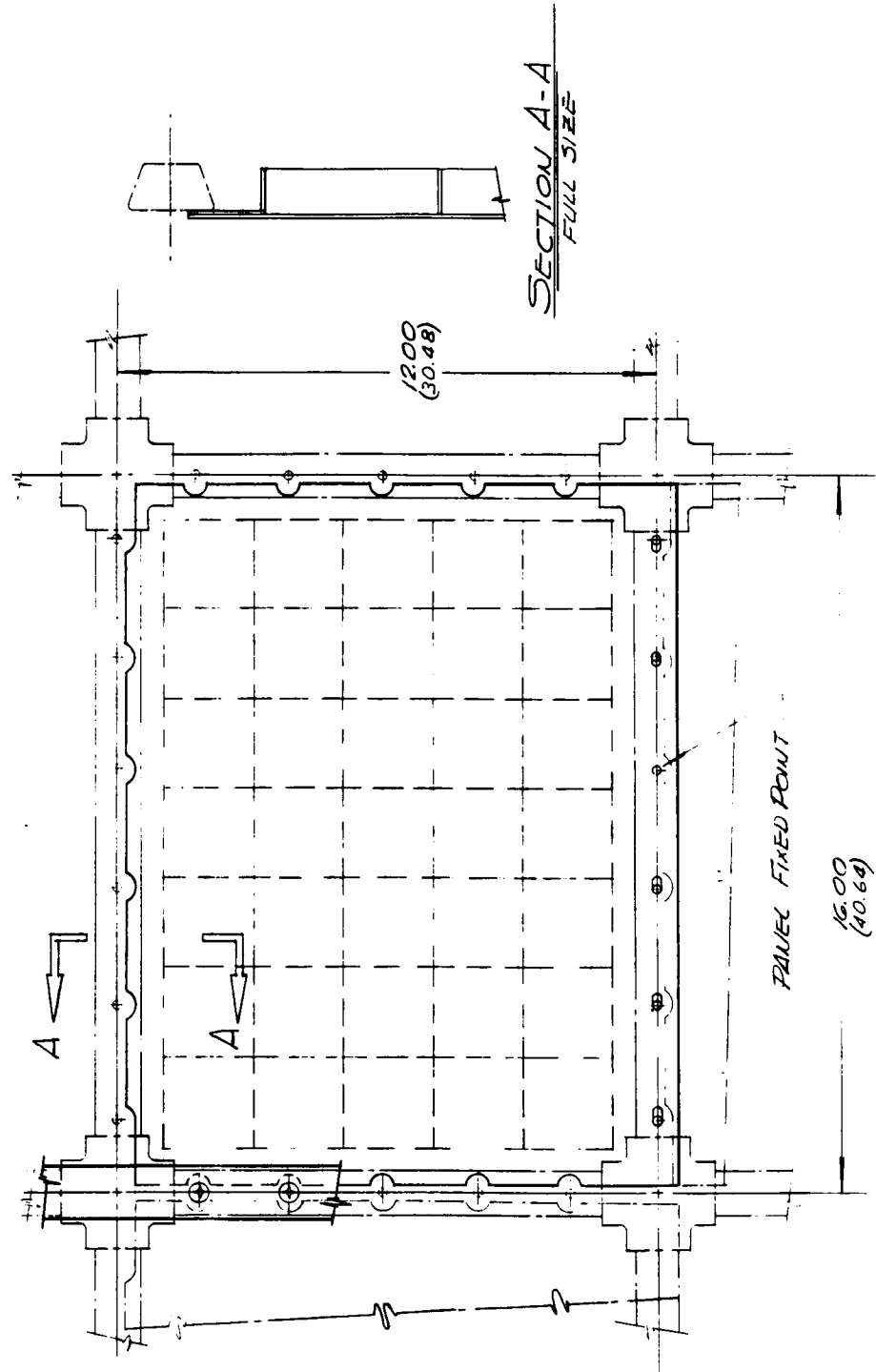


Figure 3-4. Isogrid Stiffened Heat Shield Concept (Preliminary)

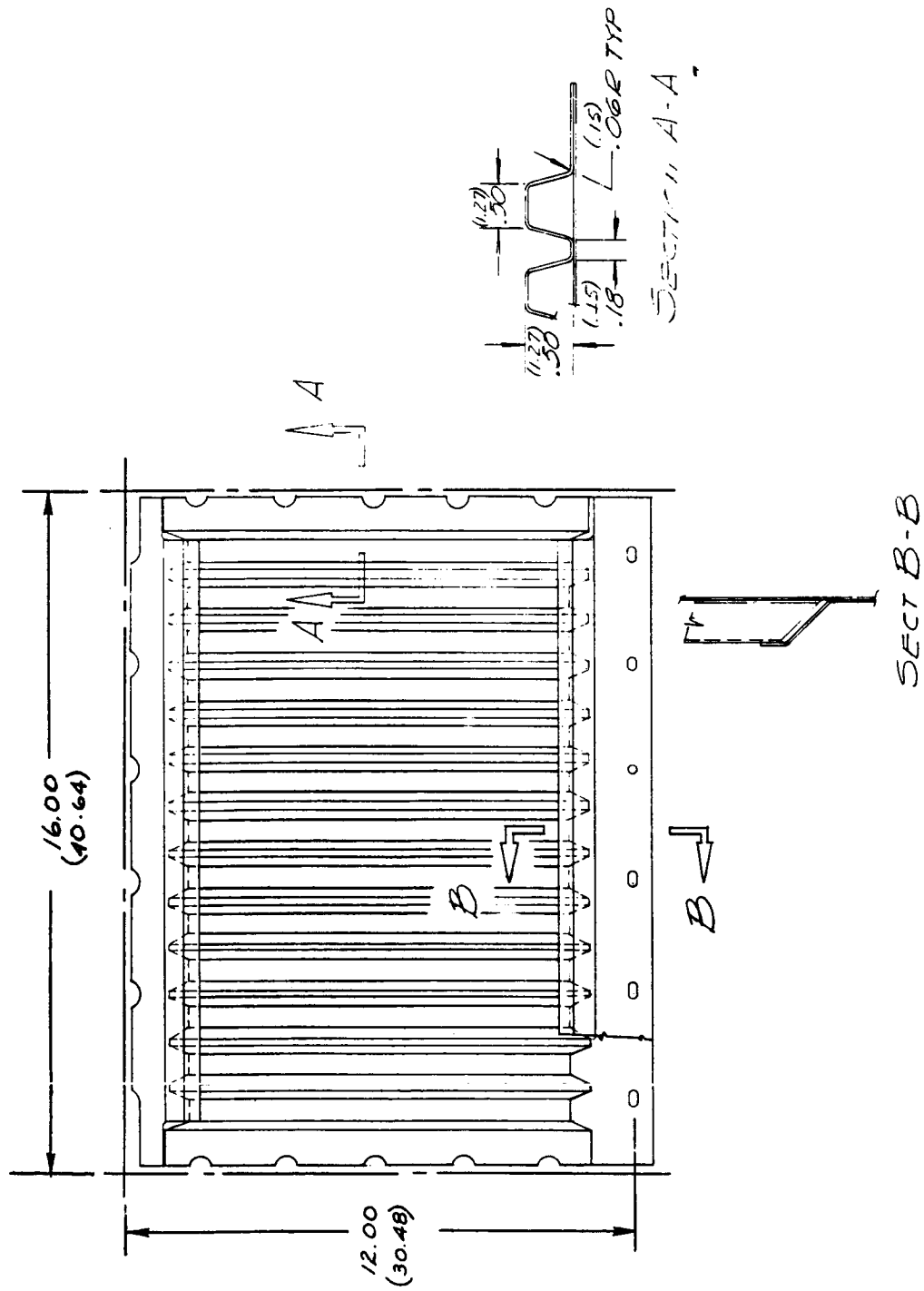


Figure 3-5. Vee-Flat Corrugation Stiffened Heat Shield Concept (Preliminary)

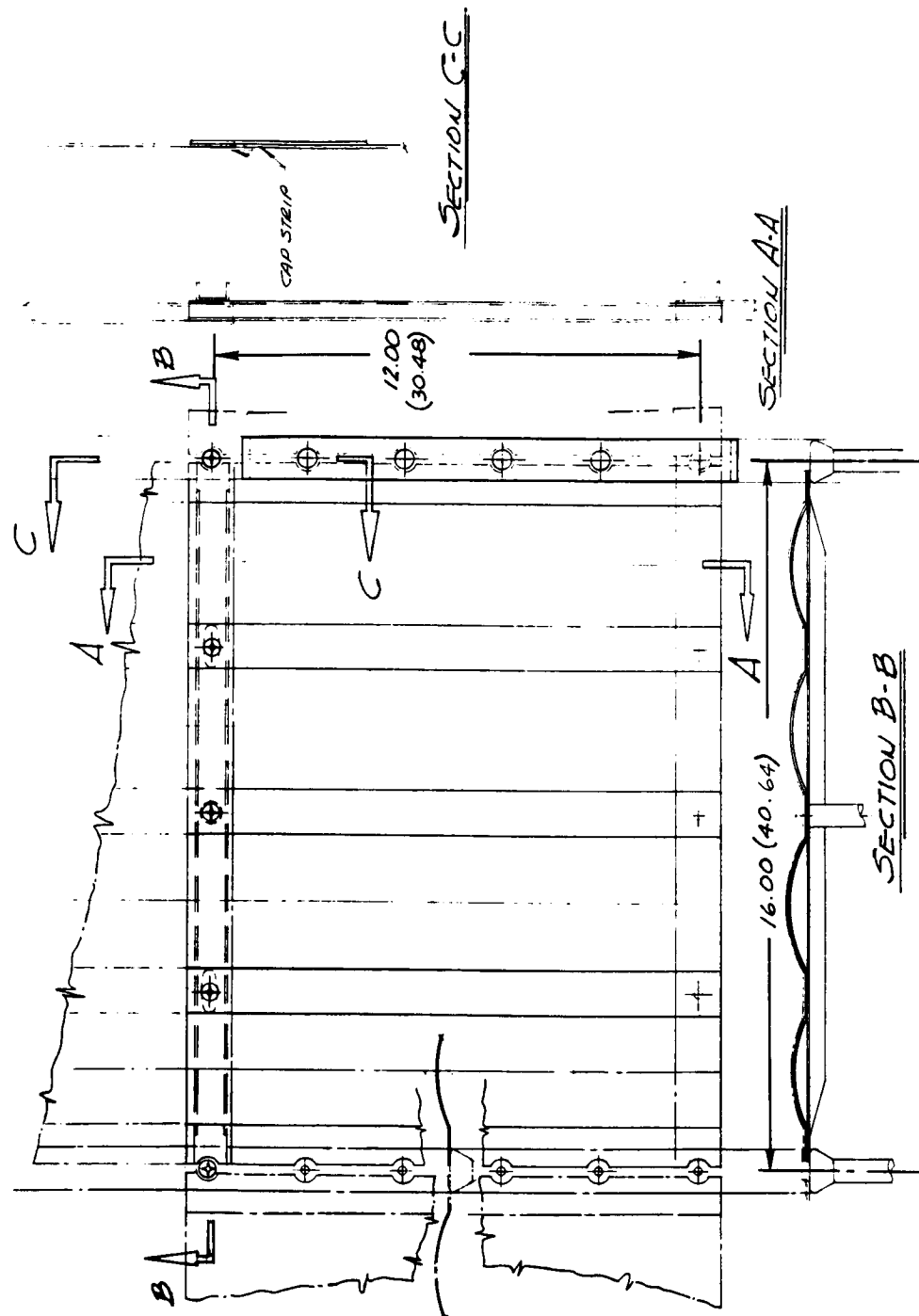


Figure 3-6. Open Corrugation Heat Shield Concept (Preliminary)

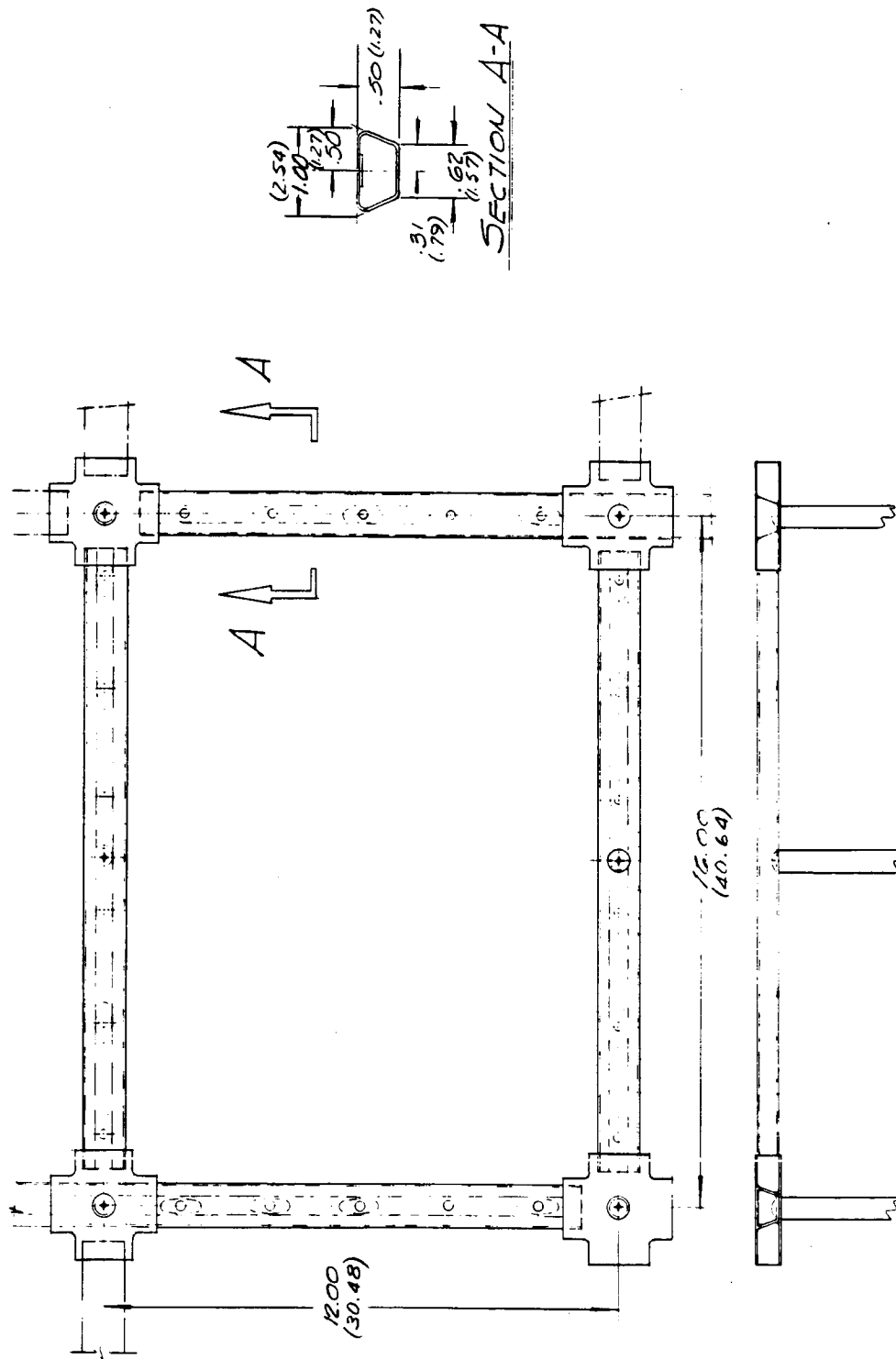


Figure 3-7. Cruciform/Tubular Post Support Structure Concept (Preliminary)

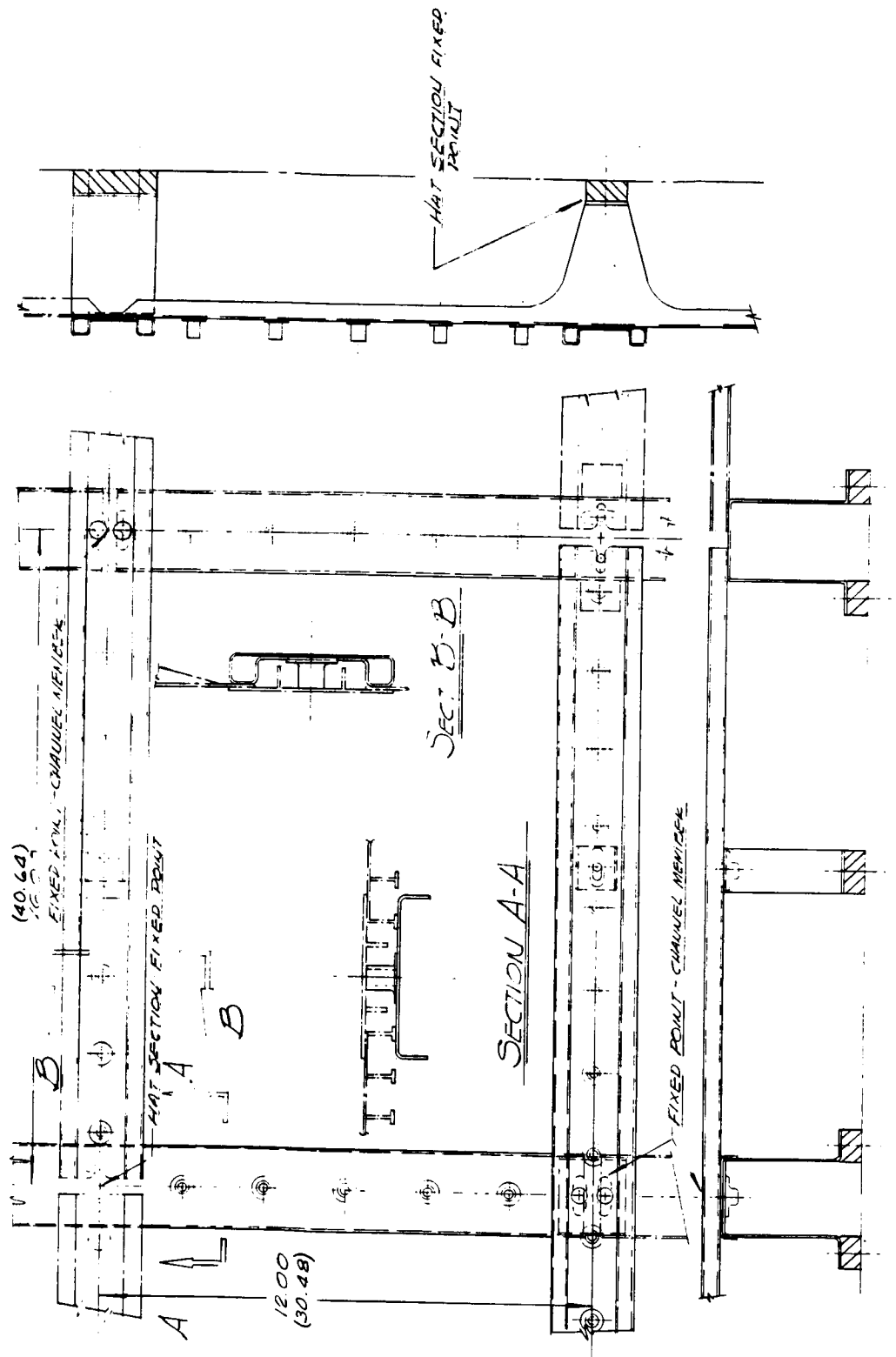


Figure 3-8. Hat Section/Cantilevered Channel Support Structure Concept (Preliminary)

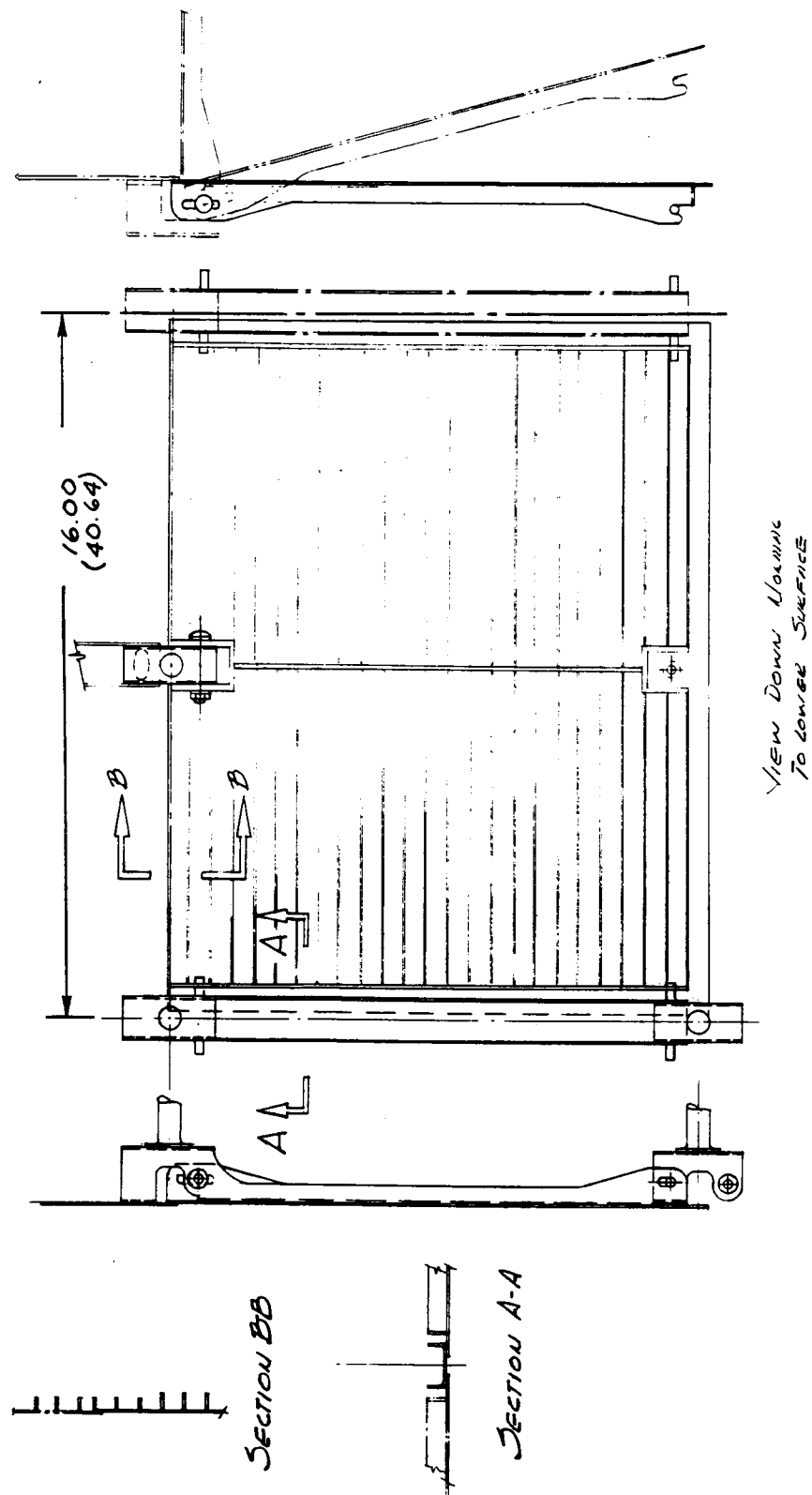
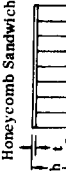
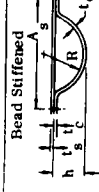
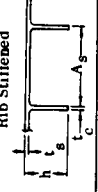
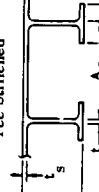
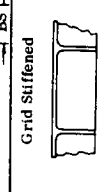
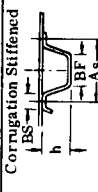
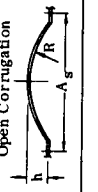


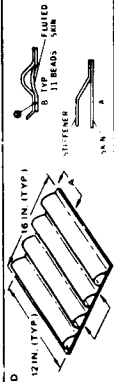
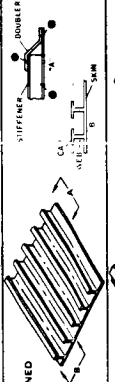
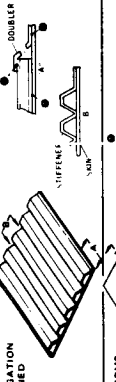
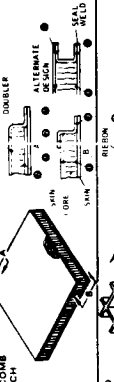
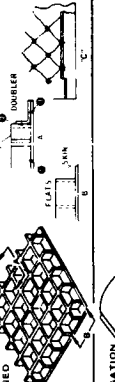
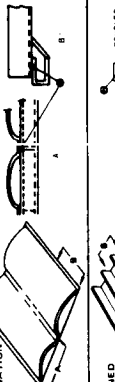
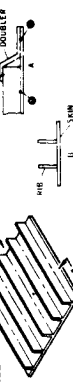
Figure 3-9. Hinged Heat Shield Concept (Preliminary)

Table 3-2. Small Size Heat Shield Structural Summary

Configuration	Material	A _s		H		R		B _s		B _f		t _s [*]		t _c [*]		t _{c1}		Deflection [†]		Creep Strain ^{**}		M.S. [‡]		Weight	
		in.	mm	in.	mm	in.	mm	in.	mm	in.	mm	in.	mm	in.	mm	in.	mm	in.	mm	in/in	mm/mm			lb/ft ²	kg/m ²
Honeycomb Sandwich 	Cb-752	—	—	0.35	8.89	—	—	—	—	—	—	0.010	0.254	—	—	—	—	0.032	0.813	—	—	+5.88	—	2.29	0.097
	C-129Y	—	—	0.35	8.89	—	—	—	—	—	—	0.010	0.254	—	—	—	—	0.031	0.787	—	—	+6.10	—	2.40	0.101
Bead Stiffened 	Cb-752	1.48	37.59	0.35	8.89	0.44	11.18	—	—	—	—	0.014	0.356	0.014	0.356	0.010	0.254	0.173	4.394	0.0021	0.0533	—	—	—	—
	C-129Y	1.48	37.59	0.35	8.89	0.44	11.18	—	—	—	—	0.014	0.356	0.014	0.356	0.010	0.254	0.213	5.410	0.0036	0.0914	+0.03	—	—	—
Rib Stiffened 	Cb-752	1.00	25.40	0.96	24.38	—	—	—	—	—	—	0.012	0.305	0.016	0.406	—	—	0.058	1.473	0.0062	0.0157	+2.79	—	1.52	0.060
	C-129Y	1.00	25.40	0.92	23.37	—	—	—	—	—	—	0.012	0.305	0.016	0.406	—	—	0.072	1.829	0.0026	0.0320	+2.06	—	1.58	0.063
Tee Stiffened 	Cb-752	1.50	38.10	0.69	17.53	—	—	0.20	5.08	—	—	0.012	0.305	0.012	0.305	0.020	0.508	0.048	1.219	0.00051	0.0129	+3.58	—	1.39	0.059
	C-129Y	1.50	38.10	0.67	17.02	—	—	0.20	5.08	—	—	0.012	0.305	0.012	0.305	0.020	0.508	0.059	1.499	0.00103	0.0262	+2.73	—	1.46	0.062
Grid Stiffened 	Cb-752	1.15	29.21	0.69	17.53	—	—	—	—	—	—	0.012	0.305	0.012	0.305	—	—	0.014	0.356	—	—	+14.71	—	1.53	0.065
	C-129Y	1.15	29.21	0.67	17.02	—	—	—	—	—	—	0.012	0.305	0.012	0.305	—	—	0.015	0.381	—	—	+13.67	—	1.60	0.068
Corrugation Stiffened 	Cb-752	1.00	25.40	0.51	12.95	—	—	0.18	4.46	0.50	12.70	0.010	0.254	0.010	0.254	—	—	0.038	0.965	0.00010	0.0025	+4.79	—	1.59	0.067
	C-129Y	1.00	25.40	0.49	12.45	—	—	0.18	4.46	0.50	12.70	0.010	0.254	0.010	0.254	—	—	0.042	1.067	0.00018	0.0046	+4.24	—	1.62	0.069
Open Corrugation 	Cb-752	4.00	101.6	0.50	12.70	3.00	76.20	—	—	—	—	0.018	0.457	—	—	—	—	0.080	2.032	0.00043	0.0109	+1.75	—	1.12	0.047
	C-129Y	4.00	101.6	0.50	12.70	3.00	76.20	—	—	—	—	0.017	0.432	—	—	—	—	0.096	2.438	0.00087	0.0221	+1.29	—	1.14	0.048

* Effective thickness after 100 flights assuming a uniform diffusion rate of coating into substrate of 0.0001 inch (0.0025 mm) per side per simulated flight.
† Due to maximum pressure differential load after 100 flights.
** After 100 flights.
‡ Based on critical buckling stress due to maximum pressure differential load after 100 flights.

Table 3-3. Heat Shield Manufacturing, Inspection and Refurbishment Summary

TPS PANEL CONCEPT	ELEMENTS	Joining (▲ Indicates Preferred Process)												Coating		Mfg. Complexity	System Refurbishment
		Skin/Stiffener Joint ①				Beam-Doubler/Stiffener Joint ②				Beam-Doubler/Skin Joint ③				Application	Inspection		
		Braze	Diff. Bond	Fusion Weld		Braze	Diff. Bond	Fusion Weld		Braze	Diff. Bond	Fusion Weld					
	1 SKIN 1 BEADED STIFFENER 2	Δ	▲	—		—	—	—	—	—	—	—	—	7	5	1	3
	1 SKIN 12 RIBS & CAPS 2 BEAM DBLR. 15 (MFG. WITH 2 SKINS)	Δ	Δ	▲		Δ	—	▲		Δ	▲	—		4	4	4	2
	1 SKIN 1 STIFFENER 2 BEAM DBLR. 4	Δ	▲	—		Δ	▲	—		Δ	▲	—		6	6	5	4
	2 SKINS 1 CORE 4 BEAM DBLR. 7	Δ	▲	—		Δ	▲	—		Δ	▲	—		1	1	7	5
	1 SKIN 14 RIBBONS 4 BEAM DBLR. 19	Δ	▲	Δ		Δ	Δ	▲		Δ	Δ	—		5	7	6	5
	1 SKIN 2 BEAM DBLR. 3	—				—				—				2	2	2	1
	1 SKIN 12 RIBS 2 DOUBLERS 15	Δ	Δ	▲		Δ	—	▲		Δ	▲	—		3	3	3	2

panels were to be silicide coated, each concept was assessed for the ease of coating application and degree of inspectability.

The examination of manufacturing complexity considered tooling, number of parts, assembly procedures and sequence, number of available processing options, state-of-the-art or developmental needs, risk factors and confidence levels.

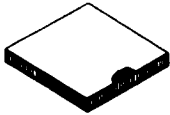
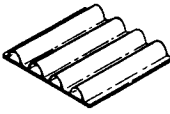
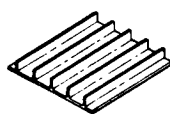
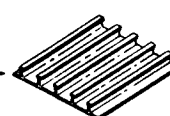

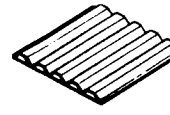

The coatability aspect considered the cleaning and ease of application for dipping, spraying and edge overcoating. The ability to inspect the joints and coating is of sufficient importance as to impact the panel design, therefore, each configuration was evaluated for its ability or complexity to be inspected by visual means as well as by radiography, electron-emission, thermoelectric, and ultrasonics.

Each configuration was graded for structural performance, reliability, weight, ease of fabrication, refurbishability, and inspectability. Ultimately each configuration was evaluated on the basis of an idealized structure having a value of 10. An idealized columbium alloy configuration was assumed that would best satisfy the following criteria: allow all surfaces to be coated, minimize faying surfaces before coating, maximize edge and corner radii and minimize coating strains, be fully inspectable, minimize use of coated fasteners, minimize sliding load-carrying surfaces, avoid contact with incompatible materials, and have minimum weight and cost (Reference 1). Every effort was made to make the study objective. Hence, a method was used for applying weighting factors that indicated the relative importance of each parameter. Factored ratings were then totalled as shown in Table 3-4. The two concepts were the highest percentage of the "ideal" configuration were selected for further study and development.

It was determined by the overall evaluation (Table 3-4) that the two most favorable heat shield configurations were the open corrugation and the tee-stiffened. The open corrugation had the obvious advantage of being relatively simple to form, coat, and inspect. As originally conceived (Figure 3-6) it had fewer fasteners and joints than the other concepts. It does, however, usually present structural problems at the support and edges. The tee-stiffened panel (Figure 3-3) is also relatively easy to fabricate although it has a relatively large number of components. The preferred method of joining the webs and beams to the skin and caps is by electron beam fusion welding with which considerable experience and confidence has been achieved. Coating the structure can be considered as intermediately difficult since all regions are accessible during dip processing, but it contains blind areas (on the interior side of the cap and beams). While not presenting a problem for coating other than requiring overcoating of the edges, inspection of the blind areas by sophisticated techniques is difficult.

This type of configuration trade study, dealing primarily with the heat shield, is not an end in itself. More appropriately, as was determined during the design and analysis phase, it should include more attention to various substructure, support systems, and

Table 3-4. Columbium Alloy Heat Shield Configuration Selection

Concept	Reliability (0.35)		Weight (0.25)		Inspect- ability (0.20)		Fabric- ability (0.10)		Refurbish- ability (0.10)		Weight- ing Factor Total	Rank
	5	1.75	5	1.25	9	1.80	3	0.30	5	0.50	5.60	4
	5	1.75	6	1.50	5	1.00	6	0.60	3	0.30	5.15	5
	6	2.10	6	1.50	7	1.40	6	0.60	6	0.60	6.20	3
→ 	6	2.10	8	2.00	6	1.20	5	0.50	6	0.60	6.40	2
	3	1.05	7	1.75	5	1.00	5	0.50	5	0.50	4.80	7
	4	1.40	6	1.50	5	1.00	7	0.70	4	0.40	5.00	6
→ 	8	2.80	9	2.25	9	1.80	9	0.90	9	0.90	8.65	1
<div>↑ Factored Rating</div> <div>↑ Concept rated on basis of 10</div>												

closeouts. This was particularly true with the corrugation design, which became increasingly complex when attempting to make the panel self-sustaining and adhering to the requirement of minimizing surface fasteners. However, the deficiencies of the various candidate configurations were exposed by the study. Thus, more stringent attention to detail could be given to the most promising configurations where specific problems could be examined.

4 SUBSIZE PANEL FABRICATION

The materials used for fabrication of the subsize test specimens in Part I of Phase II were: (1) coated columbium alloys for the test panels and load members, and (2) a dispersion strengthened nickel alloy, TD NiCr, for the threaded fasteners. Columbium alloy threaded fasteners were manufactured and coated for use, but were abandoned in favor of TD NiCr fasteners due to problems associated with the removal of coated fasteners after thermal exposure. Thermocouple temperature surveys of the panel, conducted during calibration for flight simulation testing, indicated that fastener temperatures were sufficiently low to permit the substitution of TD NiCr fasteners for the coated columbium. These substitute fasteners performed satisfactorily throughout the simulation testing program.

The columbium alloys selected in Phase I and used for fabrication in Part I, Phase II were Cb-752 (Cb-10W-2.5 Zr) and C-129Y (Cb-10Hf-10W-0.1Y), both furnished by Wah Chang Albany Corporation, Albany, Oregon, in compliance with Convair Aerospace Specification 0-00947 (Reference 2). Both alloys were supplied in the fully recrystallized condition. Typical material properties from certifications are presented in Table 4-1. The ingot chemistries for the two heats each for both alloys are presented in Table 4-2.

A thoria dispersion strengthened nickel alloy, TD NiCr, was utilized for fasteners. This material was provided by NASA-Lewis Research Center and was produced by Fansteel, Incorporated under Contract NAS 3-13490. A typical chemistry for this material is presented in Table 4-3.

Table 4-1. Average Room Temperature Properties
of As-Received Sheet Alloys

Property	C-129Y		Cb-752	
	Heat 57209	Heat 57240	Heat 70035	Heat 70036
F_{ty} @ 2% offset, ksi (MN/m ²)	71.3 (491.6)	71.9 (495.8)	63.4 (437.1)	63.2 (435.8)
F_{tu} , ksi (MN/m ²)	86.4 (595.7)	87.2 (601.2)	81.4 (561.3)	80.7 (556.4)
Elongation, %	25.5	24.5	30.7	30.9
Hardness in BHN (avg.)	205	202	186	179
ASTM grain size	9.5	9.0	9.5	9.0
Nominal density, lb/in ³ (g/cm ³)	0.343 (9.49)		0.326 (9.02)	

**Table 4-2. Ingot Chemistries of Phase II Subsize
Panel Columbium Sheet Material**

Element	C-129Y		Cb-752	
	Heat 57209	Heat 57240	Heat 70035	Heat 70036
Composition in percent by mass				
Y	0.09/0.11	0.13/0.13		
Hf	9.6/10.3	9.2/10.0		
W	9.9/10.3	9.8/10.0	9.7/9.8	9.1/9.6
Zr			2.4/2.8	2.6/2.6
Cb	Balance	Balance	Balance	Balance
Impurities content in ppm				
Al	< 20	< 20		
B	< 5	< 5		
C	100/120	90/120	70/80	30/30
Cd	< 5	< 5		
Co	< 10	< 10		
Cr	< 20	< 20		
Cu	< 40	< 40		
Fe	< 50	< 50		< 50
H	2.7/2.8	3.5/3.9	2.5/2.8	1.3/1.8
Hf			550/550	500/530
Mg	< 20	< 20		
Mn	< 20	< 20		
Mo	< 20	20		
N	30/35	40/50	15/63	47/66
Ni	< 20	< 20		
O	110/130	< 50	< 50/90	90/140
Pb	< 20	< 20		
Si	< 50	< 50		
Sn	< 10	< 10		
Ta	1800/1900	820/870	2700/3000	2750/2950
Ti	< 40	< 40		
V	< 20	< 20		
Y			140/170	100/160
Zr	2900/2600	3200/3700		

Table 4-3. Typical Chemical Analysis of TD NiCr for
Phase II Fasteners for Subsize Panels

Alloy:	Ni-20Cr — 2ThO ₂
Heat Treat Condition:	Stress Relieved
Form:	Rod
Heat Number:	3817
Chemical Analysis in Percent by Mass	
Carbon:	0.0152
Sulphur:	0.0025
Chromium:	19.73
Thoria (ThO ₂):	1.65
Nickel:	Balance

Subsize heat shield panels of a single-skin, unstiffened corrugation and a tee-stiffened configuration were fabricated for Phase II, Part I from each of the two alloys (Cb-752 and C-129Y) selected in Phase I. These panels were 4.75 inches (12.07 cm) wide by 7.57 inches (19.23 cm) long and 0.5 inch (1.27 cm) to 0.7 inch (1.78 cm) deep.

A corrugated panel is shown in Figure 4-1. The specimen panel consists of a formed, single corrugation and two straps that bolt across the lower surface of the specimen at one end and at the center. These straps (not shown in Figure 4-1) serve to offer side constraint during testing in a manner similar to that afforded by adjacent corrugations in a full panel. The sheet material for the panel is 0.025 inch (0.064 cm) thick with both straps 0.080 inch (0.203 cm) thick.

The tee-stiffened panel shown in Figure 4-2 consists primarily of a full face sheet or panel skin and three tee-shaped ribs. Each end of the panel has an angle-shaped load member that distributes the input loads into all of the ribs and the skin during testing and also serves to stabilize the ribs. These angle members are welded to the panel skin and to the rib ends and are continuous extensions of the rib caps or flanges. All material used in the fabrication of these tee-stiffened panels was a nominal 0.020 inch (0.051 cm) thick prior to coating.

The fabrication sequence for a corrugated panel is shown in Figure 4-3 and that of a tee-stiffened panel in Figure 4-4. Both Cb-752 and C-129Y used in the fabrication of the panels possess nearly equal fabricability; therefore, no differentiation will be made between them in subsequent fabrication discussions. Likewise, both alloys are equally as coatable with R-512E silicide coating and require identical preparation for coating.

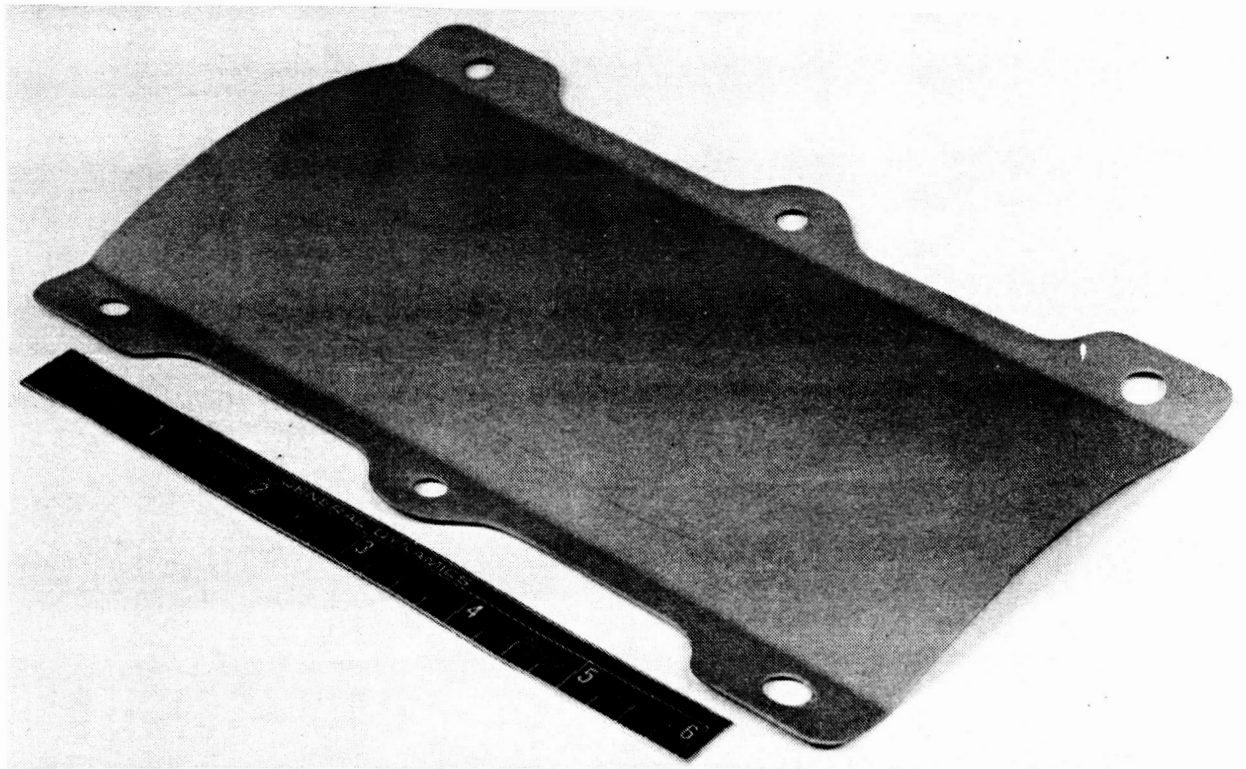


Figure 4-1. As-Coated Unexposed Subsize Corrugated Panel (Photo 123474B)

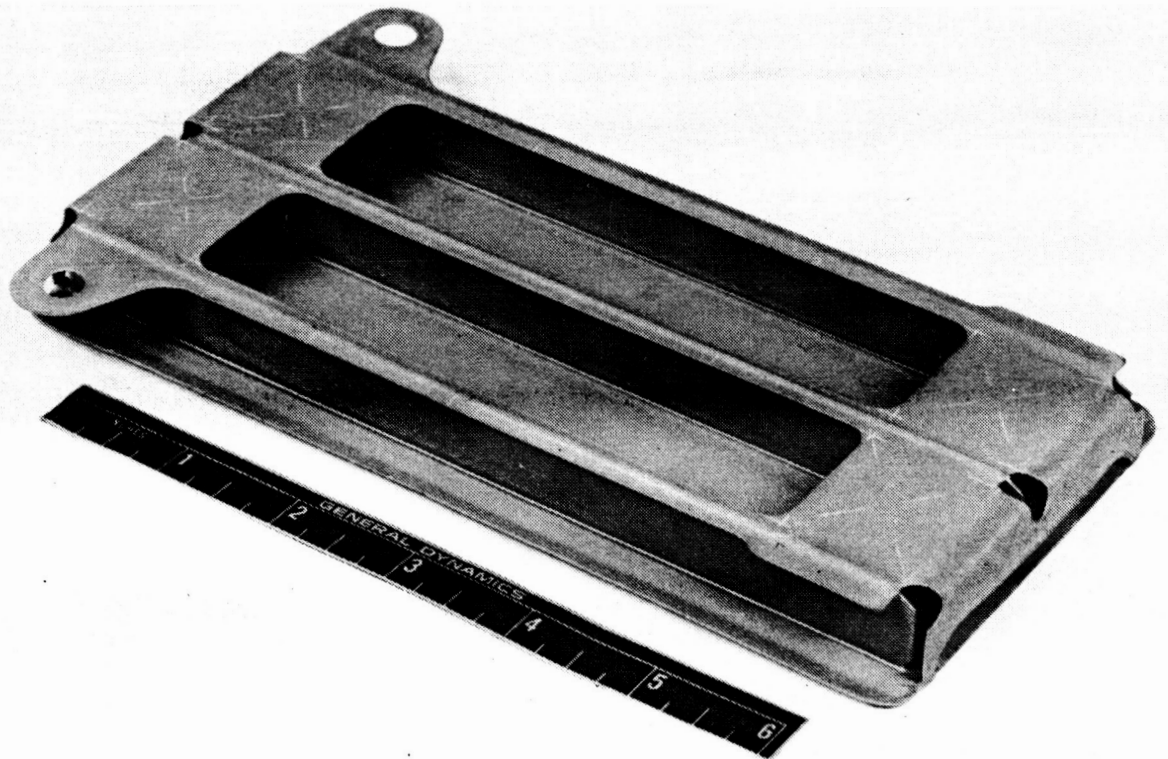


Figure 4-2. As-Coated Unexposed Subsize Tee-Stiffened Panel (Photo 123471B)

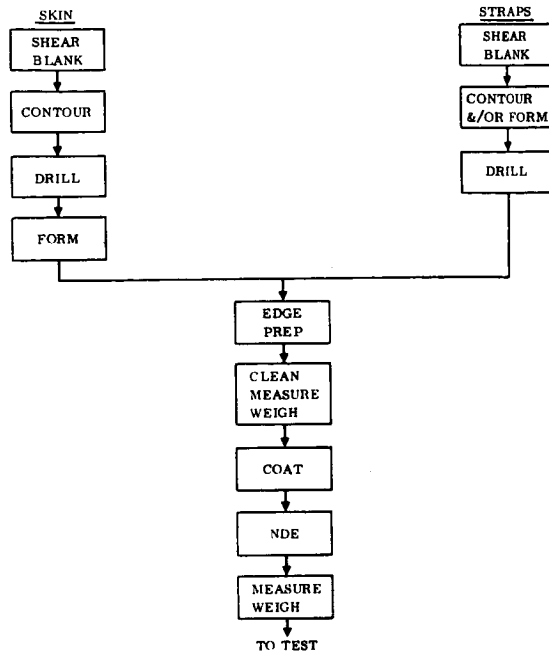


Figure 4-3. Corrugated Panel Fabrication Sequence

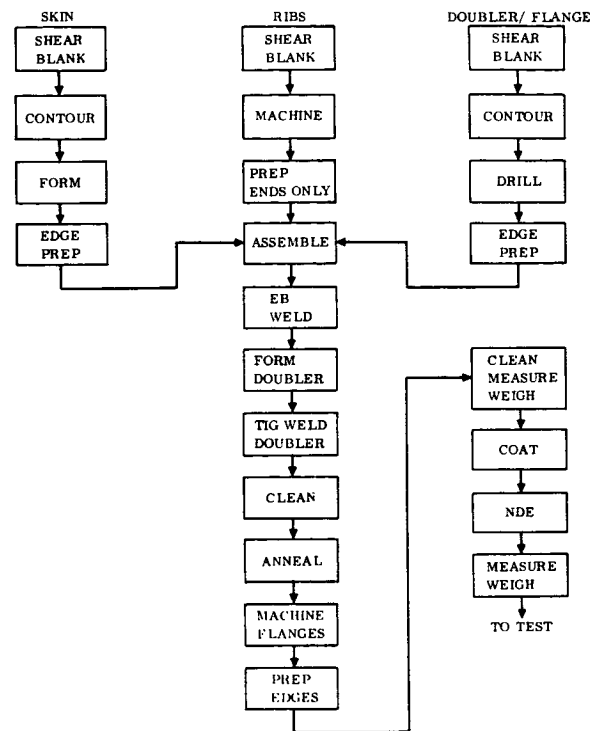


Figure 4-4. Tee-Stiffened Panel Fabrication Sequence

It can be seen from the photograph of the corrugated panel Figure 4-1 and from the sequence diagram Figure 4-3 that the fabrication of the corrugated panel is quite simple and involves only a few normal sheet metal practices and processes. The only exception is the edge and corner preparation operation, which involves a rounding or radiusing of the surfaces manually, by vibrating finishing, or by a combination of both. This prepares the edges and corners with the best condition for the application of the silicide coating.

The tee-stiffened panel (Figures 4-2 and 4-4) is a welded sheet metal structure that requires several more manufacturing operations than does the corrugated panel. However, the structure employs reasonably normal sheet metal fabrication. Only the edge and corner preparation and the use of electron beam welding differentiates this structure from other common sheet metal structures. The requirements for edge and corner preparation for coating are the same as for the corrugated panel, although there are many more surfaces to be prepared on this panel. The edge preparation noted in Figure 4-4 is sequenced to be done when the operation can be the most readily performed during assembly (i.e., in detail or at some stage of assembly).

Figure 4-5 graphically portrays the assembly, welding, and final forming operations for the tee-stiffened panel. It can be seen that the primary electron beam welding was done with the doublers in a flat and unformed position. This permitted access to the interior of the panel from either end for removal of internal weld tooling, for the inspection of the penetration side of the welds, and/or for the repair of the welds. After completion of the electron beam welding, the doublers were formed down, creating the panel end angles that were then tungsten inert gas (TIG) welded to the ends of the skin.

The electron beam welds were specified to be burn-through welds with 100% penetration, 100% root fusion of the flange, and fillets on each side of the vertical web or rib. The TIG welds were required to have 100% fusion with no unfused regions permitted at the juncture of the doubler tabs and the skin. Figure 4-6 shows a cross-section of a typical electron beam weld taken from a Cb-752 tee-stiffened panel. Coated welds such as this have repeatedly been tested successfully through 100 simulated entry missions involving temperatures to 2400°F (1589°K) flight environments and loads. The R-512E coating is readily visible on the outer surfaces of the metal.

The tooling philosophy for electron beam welding of the tee-stiffened panels was 100% solid, hard tooling (aluminum and chrome-plated copper). This required that all elements of the panel be assembled and located in the tooling before electron beam welds were made and all welds be accomplished without removing the panel from the tooling. Upon completion of the welds, the tooling was removed — permitting inspection of both sides of all welds. When rewelding or repair welding was necessary, the tooling was reassembled on the part before welding. A limited number of interior repair welds were made without the aid of internal tooling. The TIG welds were performed without weld tooling and were made manually in a controlled atmosphere chamber.

Visual and penetrant inspection techniques were employed to determine the quality of the welds. The defects associated with electron beam welds were of a minor nature and generally were located at or near the ends of welds. They included incomplete penetration and root fusion, minimal fillets, pits and porosity, laps and possible cracks. A number of these were found to be surface defects and were removed, or were of such a minor nature as to be ignored. Furthermore, during subsequent flight simulation testing of coated tee-stiffened panels, there was found to be no correlation between coating life or failure and the presence of known weld defects in or near electron beam welds.

Final annealing of the welded panels was done at 2400°F (1589°K) in a vacuum heat-treating furnace. Pressures less than 5×10^{-5} torr (6.67 mN/m²) were maintained. For protection from possible contamination during heat treatment, the panels were individually wrapped in tantalum foil.

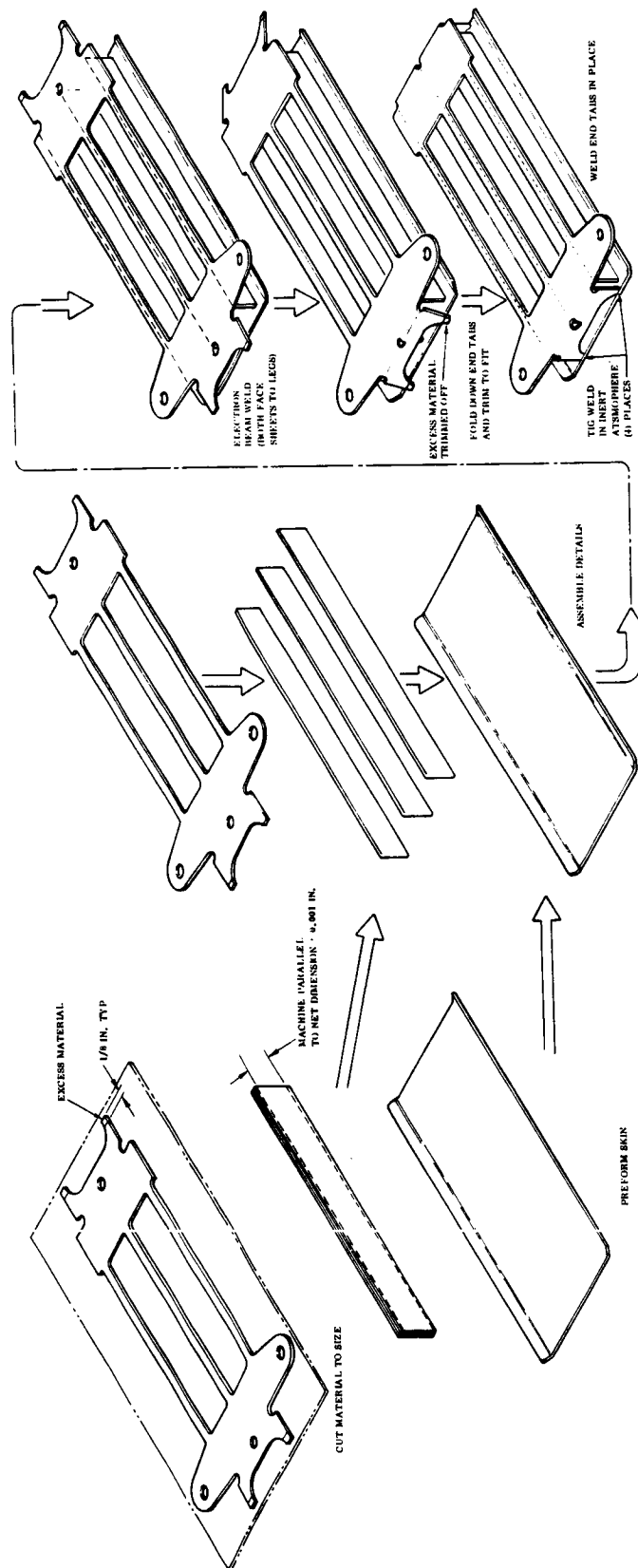


Figure 4-5. Subsize Tee-Stiffened Panel Fabrication Sequence

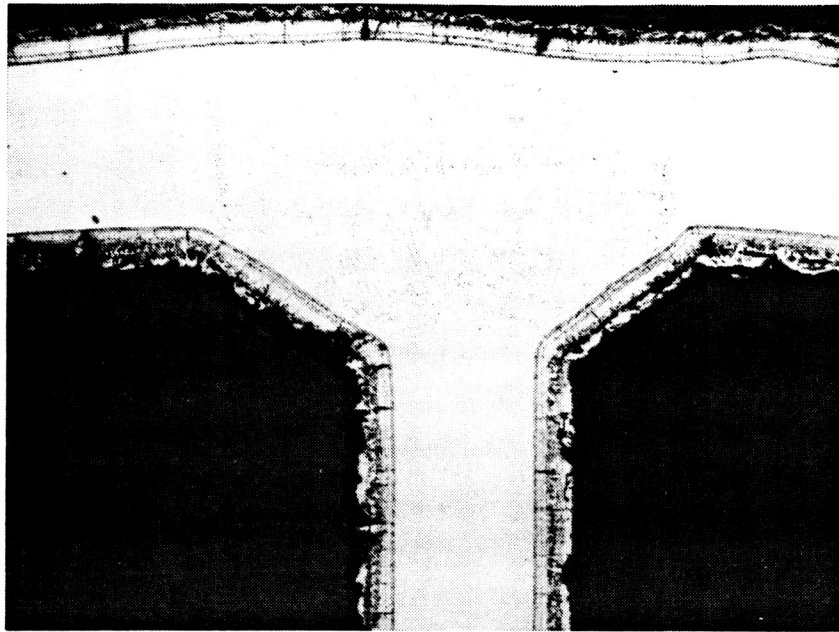


Figure 4-6. Cb-752/R-512E Electron Beam Weld on Sub-size Tee-Stiffened Panel (Photo D2741)

In general, both local and overall panel distortion from welding was small. The amount of tee-flange distortion depended upon the amount and the type of repair and rewelding that had been performed.

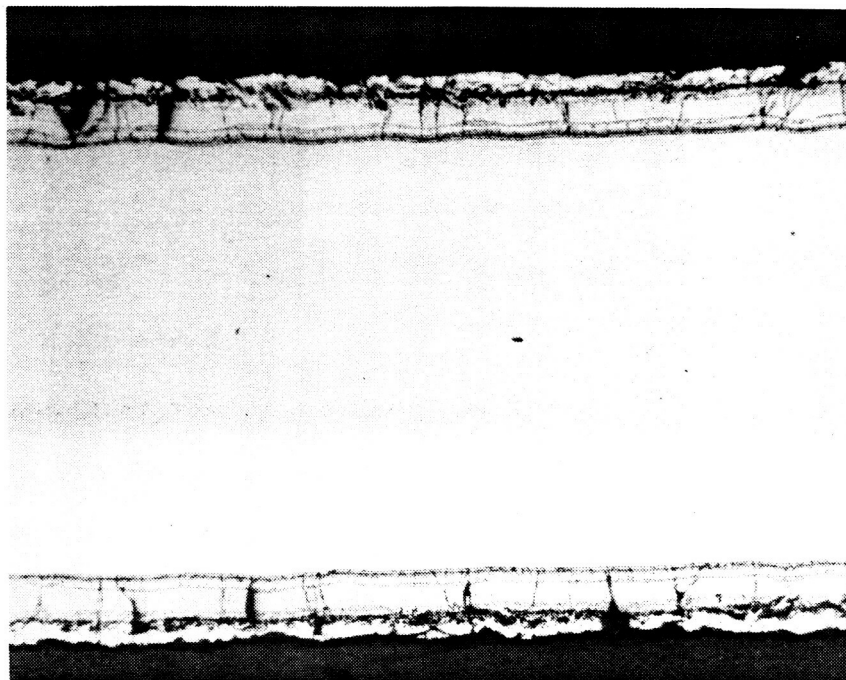
The tee-stiffened panels made of C-129Y had fewer weld defects, lower distortion, and more uniformity of weld filleting than the panels made from Cb-752. This difference, however, may possibly be attributed to the improvement in fabrication skills with practice since the C-129Y panels were fabricated after the Cb-752 panels.

Phase I also selected one oxidation resistant coating for application to the columbium alloy hardware for Phase II. This was R-512E, a silicon — 20% chromium — 20% iron, fused silicide coating furnished by HiTemCo of Hicksville, New York (formerly Sylvania High Temperature Composites Laboratory). This coating was applied to the columbium alloy hardware following chemical or mechanical cleaning. Chemical cleaning was accomplished in a HNO_3 -HF acid solution, and mechanical cleaning was by grit blasting with iron particles. The coating slurry was applied by dipping and spraying with all edges overcoated or beaded using a miniature striping roller. Spray overcoating was employed on edges when the geometry of a part prevented using the striping roller.

After coating application, the parts were air dried at room temperature, followed by insertion into a high temperature vacuum furnace where they were baked at a low temperature, 400 to 600°F (478 to 589°K) to remove the coating binder and other volatiles. The furnace temperature was then increased to 2600°F (1700°K) where the coating fused and flowed evenly over all surfaces of the parts. This temperature was held for 60 minutes under a vacuum of less than one micron (133 mN/m^2) and the parts were then cooled to room temperature.

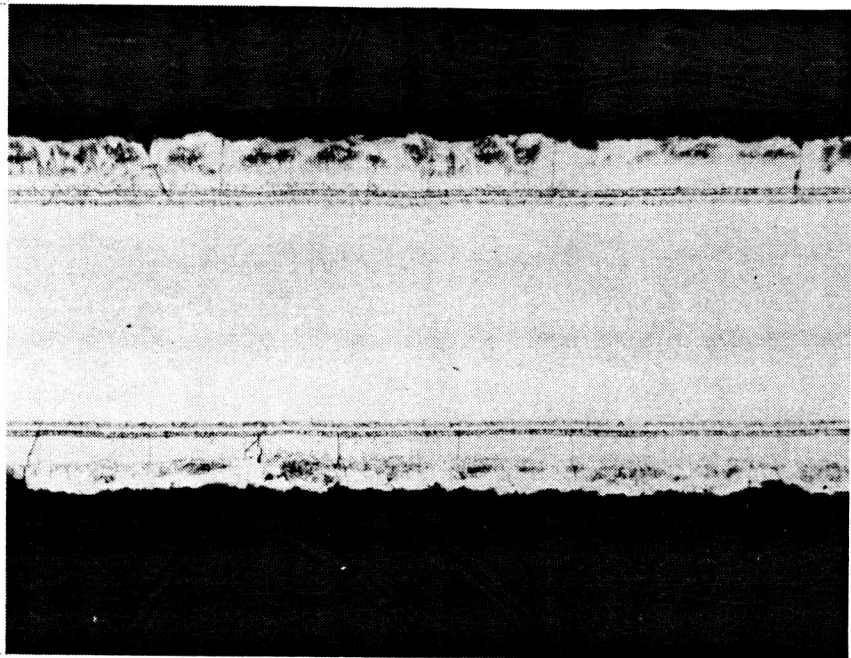
The thickness of the unfired or "green" coating was specified to be 20 to 25 mg/cm^2 , which resulted in a fused coating thickness of 0.003 inch (0.076 mm) to 0.004 inch (0.102 mm).

Figures 4-7 and 4-8 show R-512E fused silicide coating on columbium alloys Cb-752 and C-129Y respectively. These coatings are in the "as coated" condition (no thermal cycling) and illustrate a thickness of 0.003 inch (0.076 mm) on a 0.020 inch (0.508 mm) thick substrate. Figure 4-9 is a typical coated edge from a Cb-752 test panel. This edge was overcoated by beading with a striping roller. It can be seen that the coating thickness at the edge is uniform and free from the characteristic coating edge cracks that can result from inadequate edge preparation or radiusing.



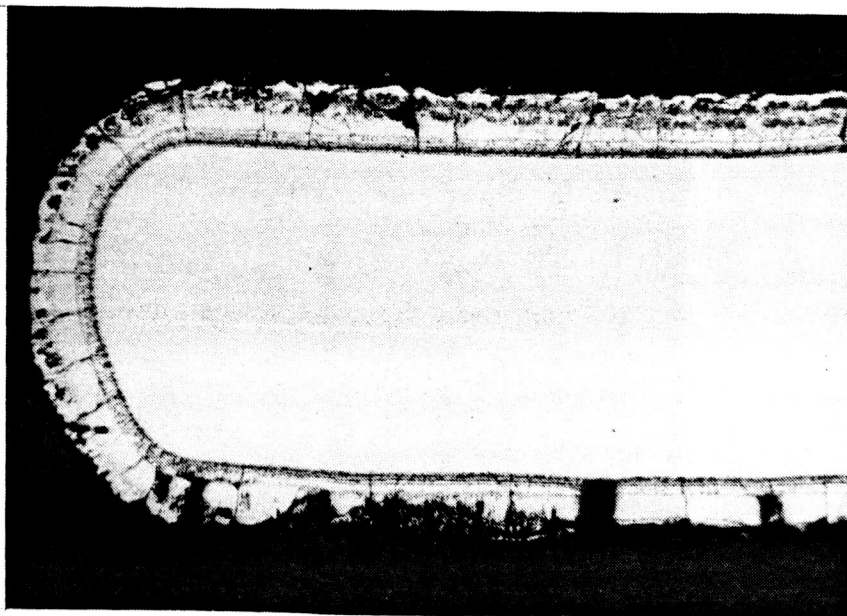
100X

Figure 4-7. Microstructure of Unexposed Cb-752/R-512E (Photo D2752)



100X

Figure 4-8. Microstructure of Unexposed
C-129Y/R-512E (Photo D1133)



100X

Figure 4-9. Microstructure of Unexposed Cb-752/R-512E
Cap Edge from Subsize Tee-Stiffened Panel
(Photo D2746)

5 SUBSIZE PANEL TEST

5.1 Test Plan

As in Phase I, flight simulation testing was the primary part of an experimental investigation of material characteristics and panel configurations for heat shield applications.

Two panel configurations, each fabricated from two different columbium alloys and coated with the same silicide coating, were to be evaluated. From the results one coating/substrate combination was to be selected for further study in Part 2 of Phase II of the overall program. The panel configurations included corrugated and tee stiffened; the columbium alloys selected were Cb-752 and C-129Y, and the coating was the R-512E applied by HiTemCo. The coating on two of the panels contained a radionuclide tag element for NDE studies of coating behavior. The test plan called for three specimens each of the four types of panels (two alloys, two configurations) to be subjected to 100 flight simulation cycles. During the simulation testing (at approximately 10-cycle intervals), measurements of panel deflection were made for the purpose of determining cyclic creep. In addition, NDE, visual observations, and photographs were made. For one of the panels, field and laboratory coating repair techniques were evaluated. Following flight simulation cycling, extensive metallographic examinations were made of representative panels from each of the four groups.

5.2 Test Profile

The elemental test profile (Figure 5-1) used for the flight simulation testing closely follows the predicted boost and entry trajectory histories shown in Figures 6-2 and 6-7. The total test time per cycle was 3600 seconds. All essential parameters could be simulated within this time period, and it was consistent with equipment operating time. A ramp function temperature profile was selected to more easily analyze and correlate test results. The peak temperature during the simulated boost phase was 960° F (789° K), which was maintained for 220 seconds before returning to room temperature. The simulated entry temperature profile exhibited a peak temperature of 2400° F (1589° K) in 300 seconds and was held for 600 seconds. The temperature was decreased in 1000 seconds to 1600° F (1144° K) and was held for 400 seconds before returning to room temperature. The maximum simulated entry temperature of 2400° F (1589° K) was selected rather than the predicted temperature of 2300° F (1533° K). The maximum test temperature is believed to be a realistic maximum nominal temperature for coated columbium alloys.

The variation of the chamber pressure (which simulates the local surface pressure) during the simulated boost results from the rapid but non-controllable operation of the roughing and diffusion pumps. The chamber pressure is decreased from one atmosphere

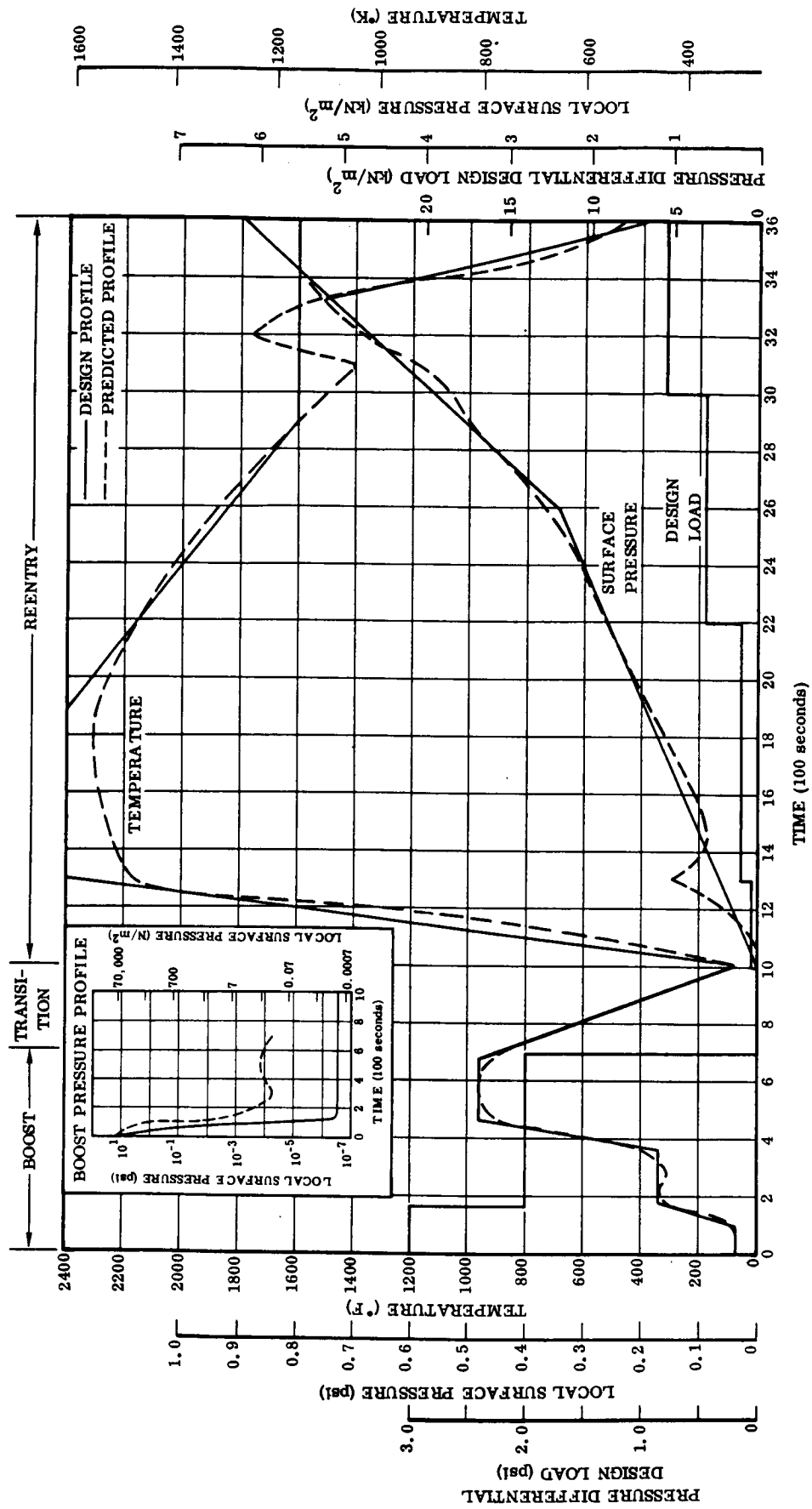


Figure 5-1. Design and Test Profile

to the 10^{-6} to 10^{-7} psi (7 to 70 mN/m²) range in approximately 160 seconds. Since the temperature during this period did not exceed 300° F (422° K), the difference in the effect of the oxygen present was considered to be inconsequential. The chamber pressure during the entry portion closely followed the predicted heat shield external surface pressure. The chamber pressure at the end of each test was 0.9 psi (6 kN/m²).

The test load profile shown in Figure 6-8 represents the loads due to pressure differentials associated with the flight. (It was assumed that the uniform circumferential heating during testing would result in no significant temperature differentials; therefore, thermal loads were ignored.) Up to 3 psi (20.7 kN/m²) might be experienced during the boost launch phase ($t = 0$ to 170 seconds) when the booster/orbiter interference effects might be present. This load represents a nominal stress level in the tee-stiffened panel of 13,287 psi (91.6 MN/m²) and 19,359 psi (133.5 MN/m²) in the corrugated panel. Up to 2 psi (13.8 kN/m²) might be experienced during the orbiter launch phase. This load represents a nominal stress level of 8858 psi (61.1 MN/m²) in the tee-stiffened panel skin and 12,906 psi (89.0 MN/m²) in the corrugated panel skin. The pressure differential loadings vary with entry time and were raised slightly during the last step to account for maneuvers expected during the cruise phase. The equivalent pressure differentials for the reentry portion of the test profile were 0.15, 0.45, and 0.85 psi (1.03, 3.10, and 5.86 kN/m²). The corresponding nominal stresses were 664, 1993, and 3765 psi (4.6, 13.7, and 26.0 MN/m²) for the tee-stiffened panel and 968, 2904, and 5485 psi (6.7, 20.0, and 37.8 MN/m²) for the corrugated panel.

The applied load was based on a net base metal cross section at the end of 100 cycles. A nominal coating thickness of 0.003 inch (0.008 cm) per side was to be applied to each specimen. The assumption was made that the base metal thickness was initially reduced by 0.001 inch (0.003 cm) per side due to the coating diffusion. Although this diffusion zone is, in effect, capable of carrying load, it was considered to be non-structural for the determination of test loads. An assumption was also made that the effective base metal thickness would be reduced at a rate of 0.000005 inch (0.000015 cm) per side per cycle. That is, at the end of 100 thermal cycles the total specimen thickness would be reduced by 0.001 inch (0.0025 cm) from the net as-coated thickness.

5.3 Test Equipment

5.3.1 Environmental simulation. - Simulation testing was performed in Convair Aerospace's Flight Simulation Facility. The unit consists of (1) a supporting stand, (2) quartz lamp heated test chambers, (3) a common vacuum manifold, (4) a vacuum pumping station, (5) specimen mounting fixtures through which tensile or bending loads can be applied, and (6) the associated control, regulation, and programming devices. Figure 5-2 shows the overall system; Figures 5-3, 5-4, 5-6, 5-7, and 5-8 are close-ups of some of the components.

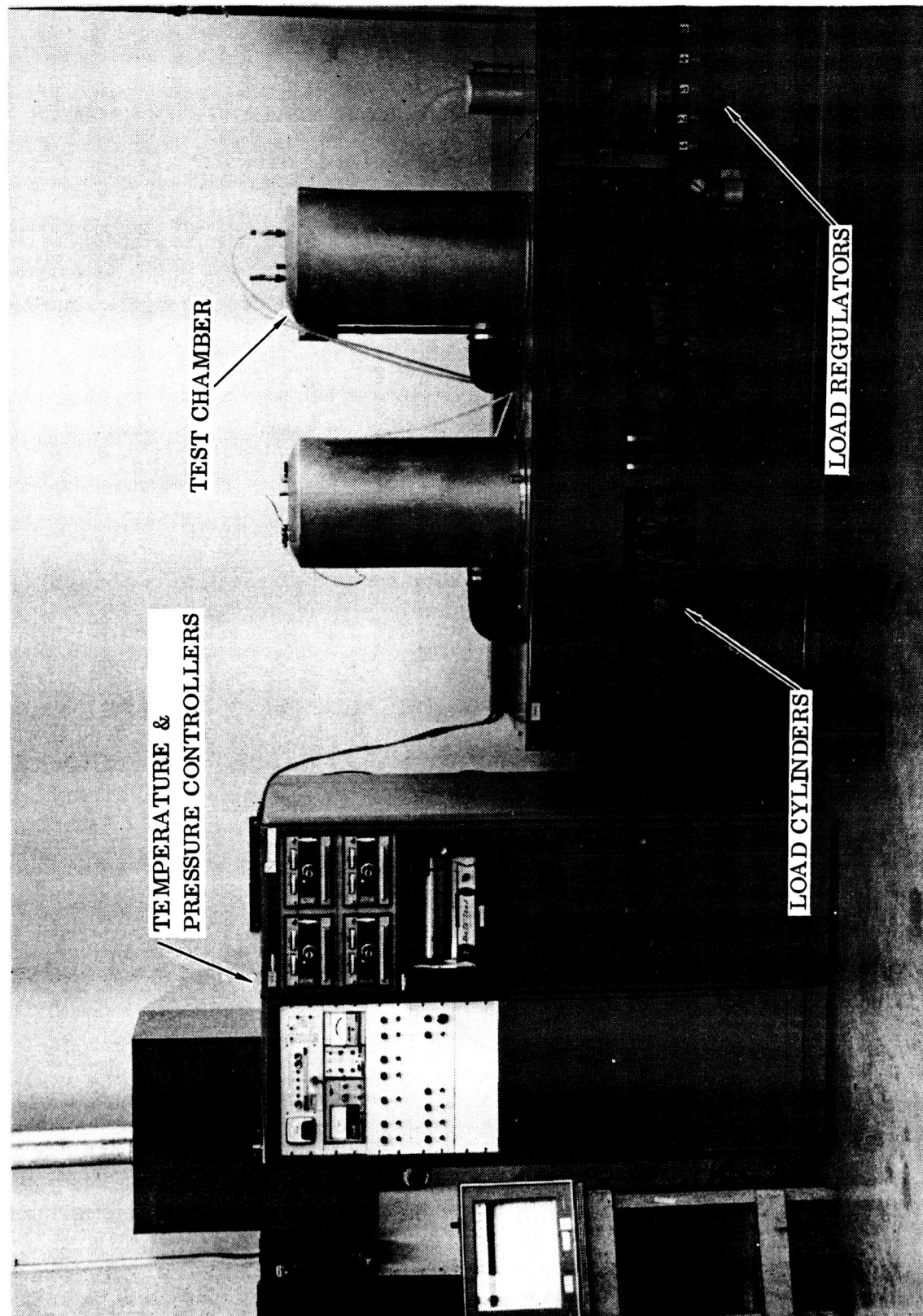


Figure 5-2. Flight Simulation Facility (Photo 126229B)

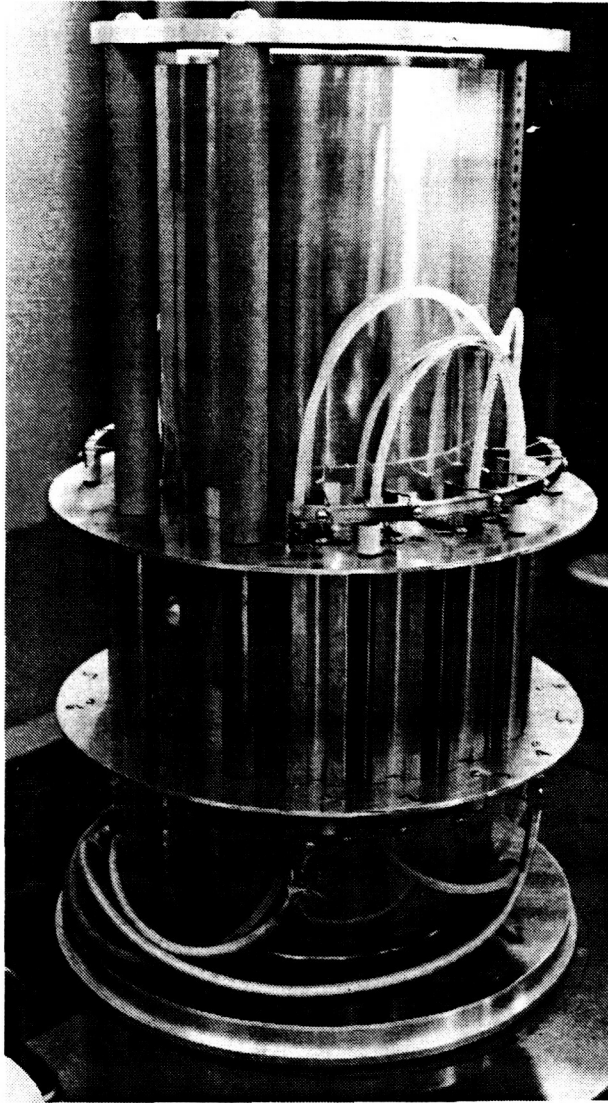


Figure 5-3. Quartz Lamp Furnace Chamber
(Photo 122031B)

The four small test chambers used in Phase I for elemental test specimens were replaced by two larger chambers for the subsize panel tests. One of these large furnace chambers with the outer cover removed is shown in Figure 5-3. Each chamber is made up of a rigid support containing a 200-mm-diameter quartz tube, vacuum sealed at both ends with O-rings. The panels (Figure 5-4), held in four point bend fixtures, are each heated with twelve 1200-watt quartz lamps (partially visible in Figure 5-3) mounted in elliptical aluminum reflectors around the periphery of the quartz tube. To increase the radiant heating efficiency, the quartz tube is enclosed by an Alzak electrobrightened aluminum reflector slotted to accept the 12 quartz lamps. The end supports and the lamp reflectors are water cooled. Additional cooling is provided by a blower that forces air at a high flow rate into the lower end support plate and outer cover, past the lamps, reflectors, and quartz tube and out the top between the upper end plate and the outer cover.

Because of the large mass of the subsize panels with their associated loading apparatus, it was necessary to provide top and bottom water-cooled reflectors within the chambers. These reflectors (shown in Figure 5-4) are connected to the upper end plate by tubes that serve as water conductors. Cooling water for the end reflectors is provided by means of flexible lines with quick disconnects that attach to the upper end plate (as shown in Figure 5-2).

The furnaces are controlled by Research Inc. Thermac temperature controllers and Phaser proportional power regulators. A single analog function generator (Data-track programmer) is utilized to provide the desired thermal profile for the chambers. The Thermac temperature controllers employ a closed-loop servo technique to control the temperature of the panels during exposure testing. A Pt/Pt + 13 percent Rh thermocouple mounted on each panel provides a feedback voltage proportional to specimen temperature. This voltage

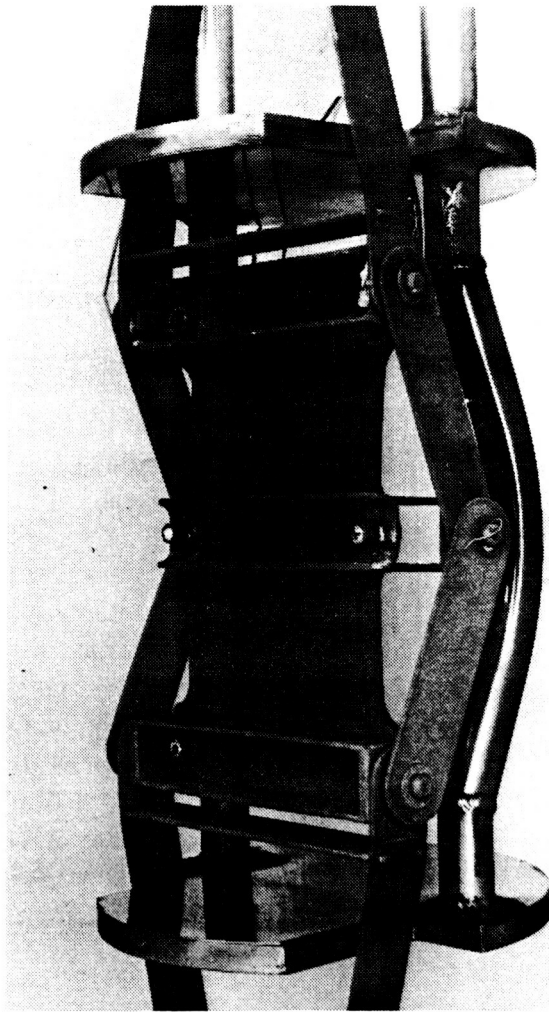


Figure 5-4. Flight Simulation Test Panel Mounted in Test Fixture (Photo 120936B)

is compared at the Thermac input to a command signal generated by an analog function generator. The command signal may be varied as a function of time according to a pre-plotted program chart mounted in the Data-trak.

During exposure testing, temperature was continuously monitored by a strip-chart recorder connected to the control thermocouples through a selector switch. Special care was taken in attaching the thermocouples to ensure the measurement of true specimen temperature. To prevent radiation of the quartz lamps directly onto the thermocouple, and to eliminate errors in measurement as a result of differences in emittance between thermocouples and panels, the following technique was used. The thermocouples were enclosed in Irish Refrasil sleeving and attached, one to each specimen with Irish Refrasil cord. Irish Refrasil, produced by HITCO, was chosen because of its ability to retain soft, flexible characteristics during high-temperature exposures and its compatibility with the silicide coatings. With the thermocouples shielded in this manner, errors in temperature measurement were minimized, while response to temperature change was rapid.

To fully define the test conditions as well as to assist in the analysis of corrugated panel deflection, the temperature distribution was determined for several power settings of the quartz lamp furnace. Because of space limitations for thermocouple feedthroughs only four thermocouples could be used at one time. For this reason the temperature distribution was obtained in one quadrant of the panel with a few additional measurements to check the symmetry about the vertical and horizontal centerlines. With the exception of the lower one inch (2.54 cm) of panel the temperature distributions in the four quadrants were within $\pm 5^{\circ}\text{F}$ (3°K) of each other. The lower one inch (2.54 cm) of the panel is shadowed on the back side by a stiffening strap of rather large mass. Temperatures in this region were 50 to 70°F (28 to 39°K) lower than in the upper one inch (2.54 cm) of panel. The steady-state temperature distributions for the four power settings are shown in Figure 5-5. The highest temperatures on the panels were found about 0.6 inch (1.52 cm)

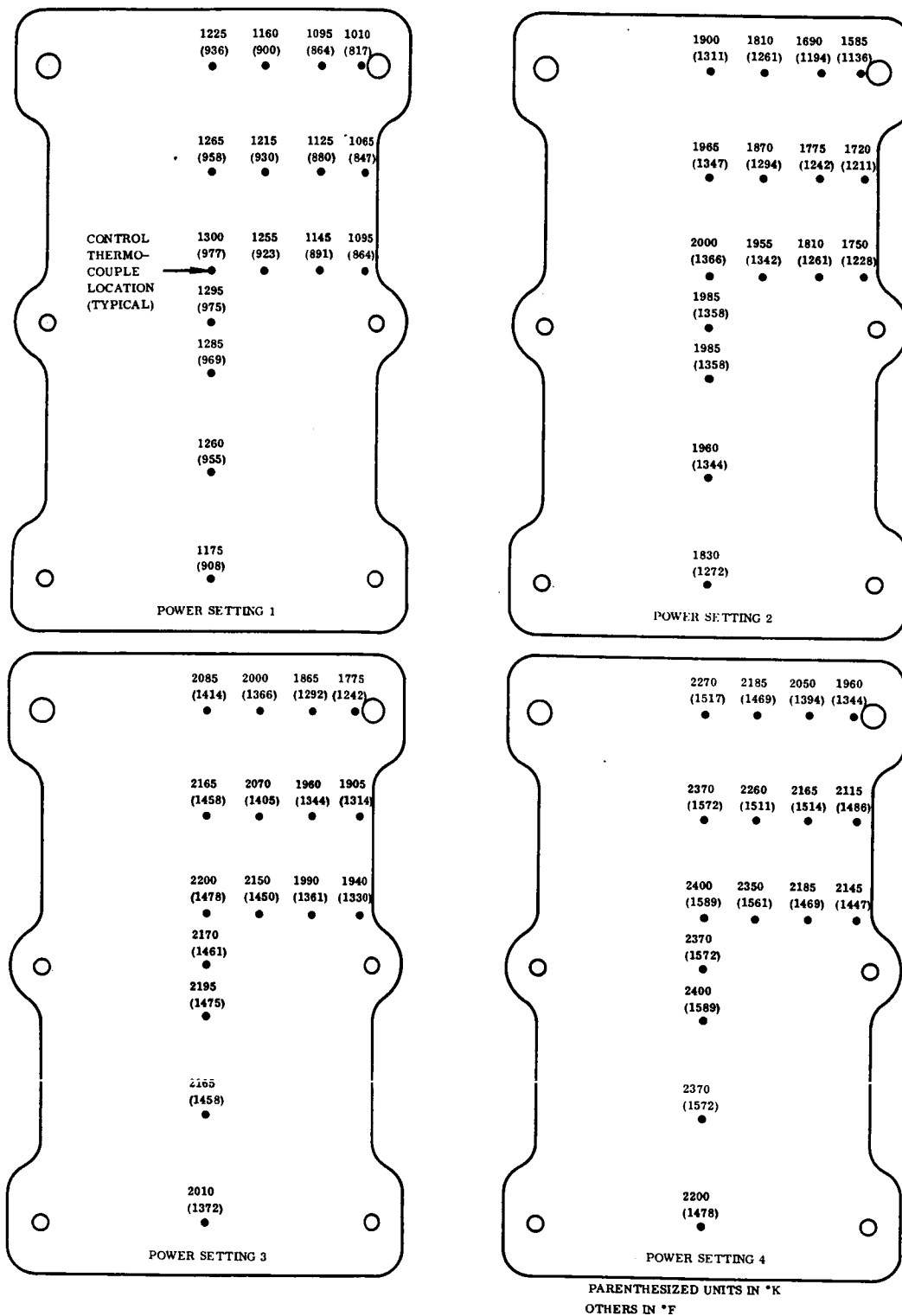


Figure 5-5. Temperature Distribution on Corrugated Subsize Panel at Constant Power Settings

above and below the center. It was here that the control thermocouple was located for both the temperature checks and the flight simulation exposures. Again a portion of the loading fixture shadows the central one inch (2.54 cm) of panel and causes the slightly lower temperatures. All temperature measurements performed during these calibration procedures were made after the specimens had reached equilibrium. With the furnace chambers plus the mass of the specimen and loading fixture used in this program a steady-state condition could be reached in a minute or less.

During simulation testing, temperature control was very good, with variations from the desired levels normally held to less than $\pm 10^{\circ}\text{F}$ ($\pm 6^{\circ}\text{K}$).

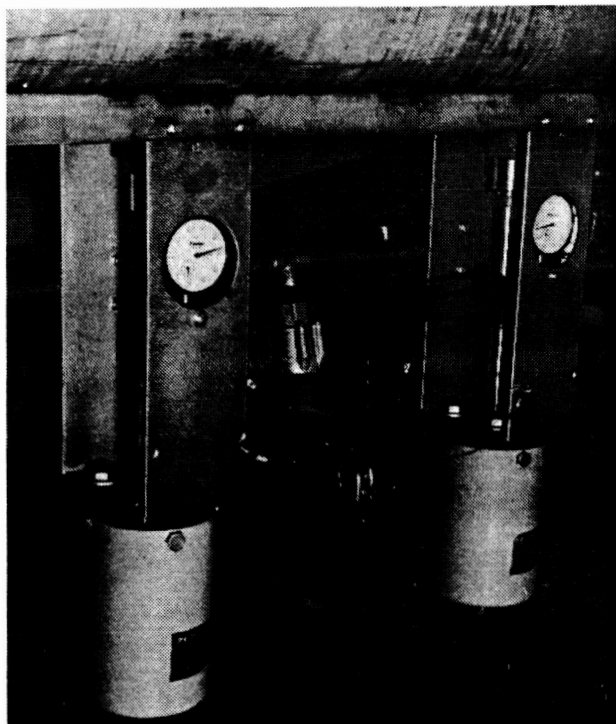


Figure 5-6. Force Cylinders for Load Application (Photo 111304B)

Load application was accomplished by pneumatic force cylinders located immediately below each chamber (Figure 5-6). The cylinders, manufactured by Bellofram, were a low-friction diaphragm type. The lower pullrods on the specimens pass through the common vacuum manifold, through low-friction rubber vacuum seals, and were pinned to the force cylinders as shown in Figure 5-6. Loads were applied by activating any of a series of solenoid operated valves connected to preset pressure regulators. The cylinders were connected in parallel so that both panels are loaded equally. Six independent pressure regulators were utilized — thus allowing the selection of six different load levels during a flight simulation cycle. Each cylinder can operate in the range from 0 to 500 pounds (0 to 2220 N).

Programming of the load profile was accomplished with the same Data-trak used for temperature. Load levels were preset with the six numbered regulators, which can be programmed to operate at any time during an exposure cycle. The loads can be applied for any desired duration, in any order, and as often as desired. The programmer uses a binary code system with three photodiodes operating a series of logic relays. The photodiodes are activated or deactivated by light or dark tapes placed on the Data-trak chart.

The following technique was used to preset the desired load levels for the simulation cycle. A calibrated load link was mounted in the system in the same position as a test

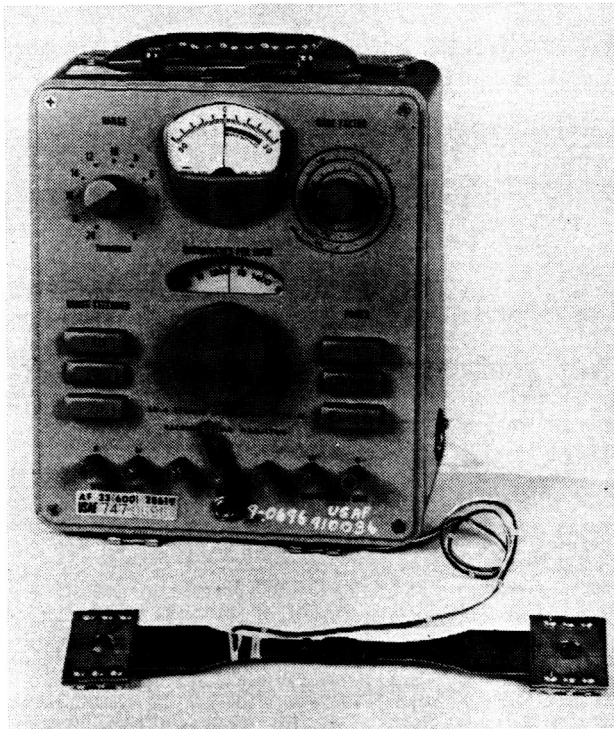


Figure 5-7. Load Link and Portable Strain Indicator (Photo 34174B)



Figure 5-8. Bristol Pressure Programmer (Photo 117206B)

specimen. The load link, shown in Figure 5-7, was made by attaching four strain gages to a dummy specimen of 0.026 inch (0.066 cm) thick, extra-full-hard type 301 stainless steel. Calibration of the load link was by deadweight loading in the range 0 to 20 pounds (0 to 89 N) and with a Baldwin-Energy SR-4 testing machine for higher loads. After mounting in the simulator, the system was evacuated and the six regulators adjusted to give the proper readout on the SR-4 portable strain indicator (Figure 5-7). This calibration procedure was repeated frequently during the test program, and loads were readjusted as necessary. Deviations from the required loads from chamber to chamber and from week to week were generally less than one pound (4.4 N) for loads less than 30 pounds (130 N) and less than five pounds (22 N) for loads greater than 30 pounds (130 N).

The environmental simulator is capable of operation in the pressure range from ambient to 2×10^{-7} psi (1.4 mN/m^2). The chambers are connected through a common manifold to a vacuum pumping station consisting of a Welch mechanical pump and a CVC oil diffusion pump. Chamber pressure can be controlled to ± 0.025 psi ($\pm 340 \text{ N/m}^2$) in the region from 0 to 7.4 psi (0 to 51 kN/m^2) by means of a solenoid operated leak valve operating against an independent pressure recovery pump. The leak valve is operated by a Bristol pressure controller (Figure 5-8). A precut cam on the Bristol unit was used to program the desired pressure profile.

During the reentry portion of the flight simulation cycle, the Bristol unit was used, as described above, for

obtaining the desired pressure profile (Figure 5-1). A different technique was necessary for obtaining the boost profile because of the wide pressure range required. During boost, the system was pumped down to its ultimate pressure as fast as possible and held constant until the beginning of reentry. The difference between the predicted and test pressure profiles (Figure 5-1) was small, and because of the relatively low temperatures during boost, this difference was believed to be of no consequence.

5.3.2 Loading apparatus. - Figure 5-9 illustrates the general arrangement of the loading apparatus. For discussion purposes the apparatus may be considered as consisting of three components: the yoke, the load shoes, and the connecting links. The yoke was made from two straps and served to transfer tensile loads from a single point to the outer load shoes. Removable spreader bars were installed between the yoke straps adjacent to the specimen to react the compressive loads at this point and thus reduce friction at the outer load shoe pivot.

There were three load shoe weld assemblies. Each shoe consisted of four parts - two straps and two machined end fittings. Each fitting had an integrally machined pin that picked up the yoke and connecting links. The load shoe was assembled by welding the straps to the end fittings. When the specimen was installed in the test apparatus, the shoes were positioned so that the straps presented a minimum shadow on the specimen.

The end load shoes were joined to the center shoe by four links, two on each side. The attachment of the yoke and links to the load shoes was secured by TD NiCr retainer pins. The yoke assembly, links, and load shoes were fabricated from columbium alloys. A tension load applied to the ends of the yoke induces bending in the test specimen in such a manner that its upper surface was in compression. It should be noted that the center shoe imparted load to the specimen by means of two straps joining its end fittings. Thus, the specimen experienced a maximum moment over about one inch (2.54 cm) at the center of the panel. The relative location of the shoes was chosen to simulate the end reactions and maximum bending moments expected during the large panel test program. Except for fasteners (bolts, nuts, and washers) all columbium alloy load fixture components were coated with R-512E to a nominal coating thickness of 6 mils (0.15 mm).

Both types of test specimens may be tested in this apparatus. The test specimen and shoe interface was the same at the outer shoe locations for both panel configurations. The center shoe, however, must accommodate both the corrugated and the tee-stiffened panels. This had been accomplished by designing one side of the shoe for the corrugated configuration and the other side of the shoe for the tee-stiffened configuration. Thus by rotating the center shoe 180 degrees either panel may be installed in the apparatus.

5.3.3 Deflection measurements. - Several types of creep deflection measurements were attempted during the course of the flight simulation exposures. The first technique was similar to that used in the Phase I tests. The procedure was to (1) suitably mark the panels and fixtures using hard (6H) pencil lines, (2) expose for about 10 flight cycles, (3) remove from the simulator and measure separation of the fiducial marks with a Gaertner cathetometer, and (4) repeat measurements after approximately every 10 cycles. For panels YSC-2 and YSC-3 one set of readings was taken in the center of each corrugated panel using a 1.25 cm gage length. Within the accuracy of the measurements (± 0.005 cm) no linear creep occurred in the central portion of the panel during 100 flight simulation cycles. Additional overall extension measurements were also made on the test fixture using a gage length of about 20 cm. Because of the small amount of panel deflection, movement of the panel within the test fixture, and coating failures in the fixture side straps, the overall extension measurements were inconclusive.

The cathetometer measurements of extension were discontinued, and another technique was pursued during the testing of two Cb-752/R-512E corrugated panels (BSC-1 and BSC-2). Table 5-1 lists the types of measurements that were included. Prior to mounting the panels in the loading fixtures they were weighed and thickness, width, and contour measurements performed. These were repeated at the completion of 100 cycles after removal from the test fixture. An additional set of measurements was made with the specimen attached to the test fixture. Panel height and width were measured before and after 100 flight cycles. Contour measurements, both line and point-to-point, were obtained at 0, 10, 20, 30, 40, 60, 80, and 100 cycles. A standard wire-type contour gage was used for the line measurements. For the point-to-point measurements, a rigid jig with 18 adjustable machine screws was mounted on the test fixture. The screws were adjusted to the contour of the panel, and after removal from the fixture their relative heights were measured with a 0.0001 inch (0.0025 mm) dial gage.

Table 5-1. Measurements for Determination of Panel Deflection

	Type of Measurement	Number of Locations	Measurement Made After the Following Number of Cycles
Unmounted	Weight	-	0, 100
	Thickness	9	0, 100
	Panel Width	3	0, 100
	Contour Gage (Line)	3	0, 100
Mounted in Fixture	Panel Width	3	0, 100
	Panel Height	9	0, 100
	Contour Gage (Line)	2	0, 10, 20, 30, 40, 60, 80, 100
	Contour Jig (Point)	18	0, 10, 20, 30, 40, 60, 80, 100

5.4 Test Procedure

The following is a step-by-step description of the procedure used to perform the flight simulation exposures and concurrent cyclic deflection measurements.

- (1) Perform preliminary measurements, i.e., thickness, weight, contour, width, and height.
- (2) Mount in loading apparatus and perform initial length and contour measurements.
- (3) Attach lower pullrod, tie on two Pt/Pt + 13 Rh thermocouples, and load panel assembly into simulator.
- (4) Pin lower pullrods to pneumatic force cylinders.
- (5) Initiate flight cycle by starting Data-trak and pump down system. High-vacuum valve to diffusion pump will automatically open when chamber pressure reaches 50 microns (6.7 N/m^2).
- (6) At completion of boost portion of cycle, manually close high-vacuum valve and initiate reentry rise by activating Bristol programmer.
- (7) During exposure, rotate thermocouple selector switch through its two positions at each temperature plateau to record the temperatures of the two panels.
- (8) At the end of the cycle, open the system to atmospheric pressure, reset the Data-trak and Bristol programmers, and begin next cycle.
- (9) At 10-cycle intervals, remove specimen and loading fixture from simulator and visually examine panels for evidence of coating spallation or failure, and any subsequent substrate attack. Measure loading fixture extension, panel contour, and submit to NDE laboratory for examination and photography.
- (10) At the completion of 100 cycles, remove panels from loading apparatus and perform final measurements and photography.

5.5 Test Results and Discussion

A total of 10 subsize panels (two alloys, one coating, two configurations, and two replicates, plus two radionuclide tagged panels) was exposure tested in the flight simulation portion of Part 1, Phase II of the test program. The results are summarized in Table 5-2. These panels received 964 total cycles with all but one completing 100 cycles.

Table 5-2. Flight Simulation Test Results

Alloy†	Configuration	Specimen No.	Cycles	Remarks
C-129Y	Corrugated	YSC-2	100	No erosion
C-129Y	Corrugated	YSC-3	100	No erosion
C-129Y	Tee Stiffened	YST-3	100	Surface erosion
C-129Y	Tee Stiffened	YST-4	64**	Surface erosion
Cb-752	Corrugated	BSC-1	100	No erosion
Cb-752	Corrugated	BSC-2	100	No erosion
Cb-752	Tee Stiffened	BST-1*	100	Edge erosion
Cb-752	Tee Stiffened	BST-2*	100	Edge erosion (repaired and recycled)
Cb-752	Tee Stiffened	BST-3	100	Oxidation at closeout welds and attachment holes
Cb-752	Tee Stiffened	BST-4	100	No erosion

† Coated with R-512E

** Withdrawn from test - see text.

* Tagged with radionuclide ^{147}Pm .

Testing was terminated on this particular panel (YST-4) after 64 cycles because of the similarity in coating failure and substrate attack to that experienced in a similar panel (YST-3). Although panel YST-3 suffered considerable damage from substrate erosion of the skin and stiffener cap beginning at approximately cycle 59, it completed 100 cycles without sustaining structural failure.

During exposure testing the specimens were removed from the simulator at 10- to 15-cycle intervals for visual examination, and, in addition, photographs were taken to retain a permanent record of any coating changes. The following is a description of the simulation results based on these visual observations for each group of panels (alloy/coating/configuration). Typical photographs (black and white) showing the changes in coating appearance with cycling are also included. Finally, color photographs of the panels at the completion of 100 cycles were taken to document typical post-cycling coloration. These color photographs are on file at NASA LaRC.

5.5.1 Group 1, C-129Y/R-512E, corrugated. - The two open-corrugation panels of this group both completed 100 flight simulation cycles with no evidence of coating failure or substrate erosion. Some permanent creep deflection occurred, but there was no structural failure. The general appearance of the panels at the completion of 100 cycles was excellent.

During the first 10 cycles, the color of the specimens changed from the original metallic grey to a dark grey-brown in the central regions with somewhat lighter shades at the edges where slight coating spall had occurred. Color changes were the same on both sides of the panels. During the remaining 90 cycles the light coating spall continued, but little overall color change took place. The principal change during exposure

was the appearance (on both sides) of oval-shaped areas about 1 inch (2.5 cm) wide by 1/2 inch (1.3 cm) high in the centers of the panels. Circular areas similar to these but less distinct appeared about 2 inches (5.1 cm) above and below the center of the panels. These regions, first noticeable after 20 cycles, were somewhat lighter in color and rougher in texture than the surrounding regions. After 50 cycles a slight yellow tint was visible. This yellow coloration became more distinct as cycling progressed, particularly in the central regions. One other observation was the appearance of a grey-white semicircular region about 4 inches (10.2 cm) in diameter on the concave side of the upper half of panel YSC-3. None of these regions appeared to be detrimental. The yellow tinted areas were probably the result of the conversion of columbium silicides to columbium oxide in the outer layer of the coating. The larger grey-white region could not be accounted for but, again, it was not considered detrimental. While experience has shown that considerable color variations over a specimen are normal, some of the distinction described herein can be attributed to the temperature distribution over the panels (see Figure 5-5).

Figures 5-10 and 5-11 are front and rear views of Panel YSC-3 after 20 flight simulation cycles. The photographs were taken with the panel mounted in the loading fixture and also show the upper and lower reflectors. The darkening of the coating, degree of coating spall around the edges, and appearance of a yellow region in the center and a grey-white region on the rear side were noted. The same panel at the completion of 100 flight cycles and removed from the test fixture is shown in Figures 5-12 and 5-13. The change in appearance from cycle 20 to cycle 100 is not very great. The other panel of this group, YSC-2, is shown after the completion of 100 flight cycles in Figures 5-14 and 5-15. The close similarity in behavior of these two panels during the exposure cycling is evident from an examination of these last four photographs.

Figures 5-16 to 5-19 show the degree of permanent deformation along the longitudinal center axis of the panels and of the flange along the line of the mounting holes. For both panels, the distortion along the flange is greater than that along the centerline of the specimen. These photos also show that the amount of deflection is greater in panel YSC-2 than in YSC-3. This increase was caused by a malfunction of one of the load regulators during cycling. The most critical load, that at 2400° F (1589° K), was found at the end of the ninetieth cycle to be approximately three times its desired value. Examination of extension data indicated that the overload probably first occurred between the fortieth and fiftieth cycles and continued until the ninetieth. Additional deformation, not noticeable in the figures, occurred at the ends of the panels. This was a flattening of the corrugation arch transverse to the longitudinal axis of the specimen. Only a portion of this deflection can be attributed to creep, however, with the balance resulting from movement of the panel with respect to the fixture. Figure 5-20 shows the amount of movement of the lower end of the panel with respect to the stiffener bar. (See Figure 5-11 for location of this stiffener.) At the completion of 100 flight cycles the two pieces were sufficiently bonded together to make this photograph. The reason

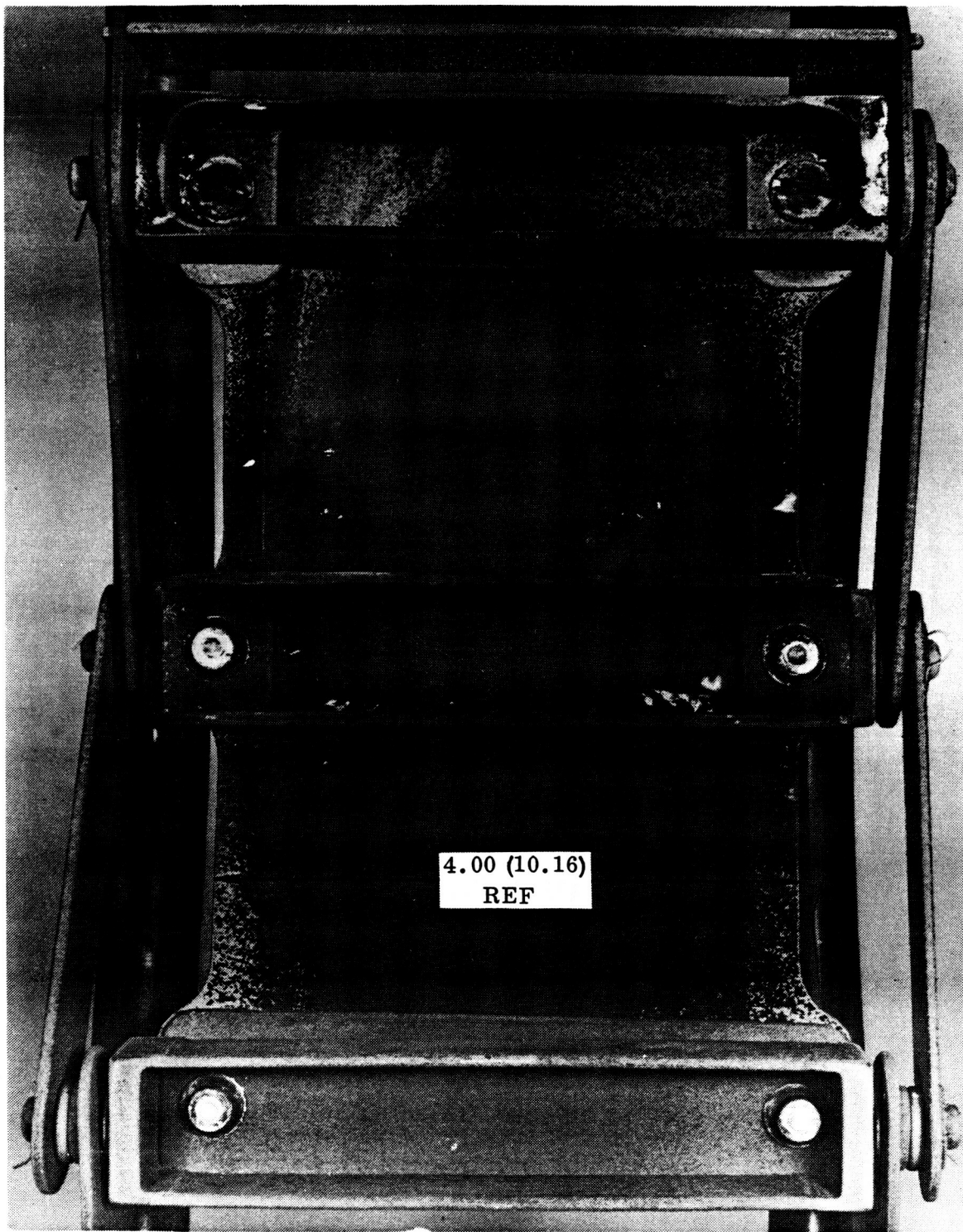


Figure 5-10. Front View of Panel YSC-3 After 20 Flight Simulation Cycles (Photo 121504B)

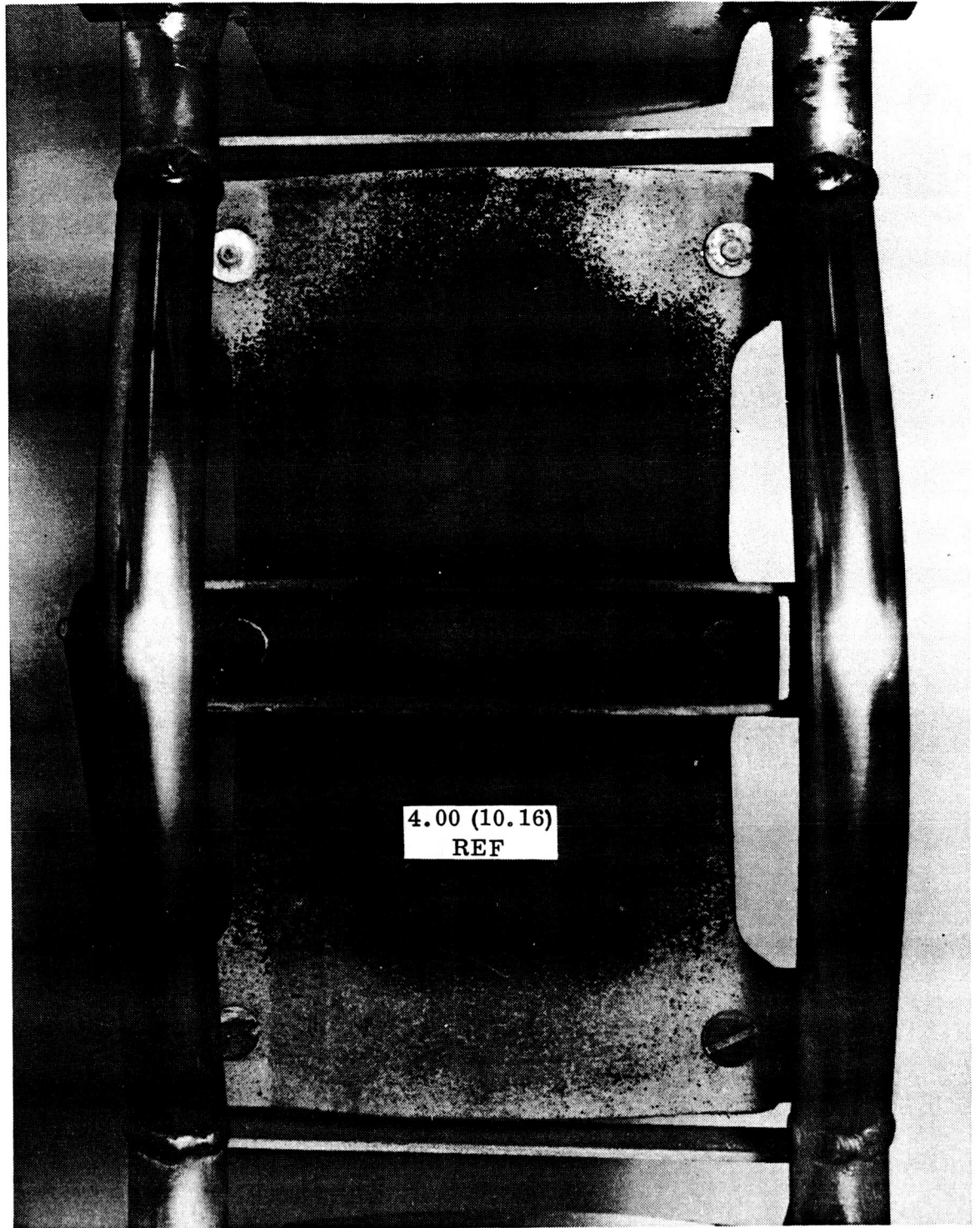


Figure 5-11. Rear View of Panel YSC-3 After 20 Flight Simulation Cycles (Photo 121505B)

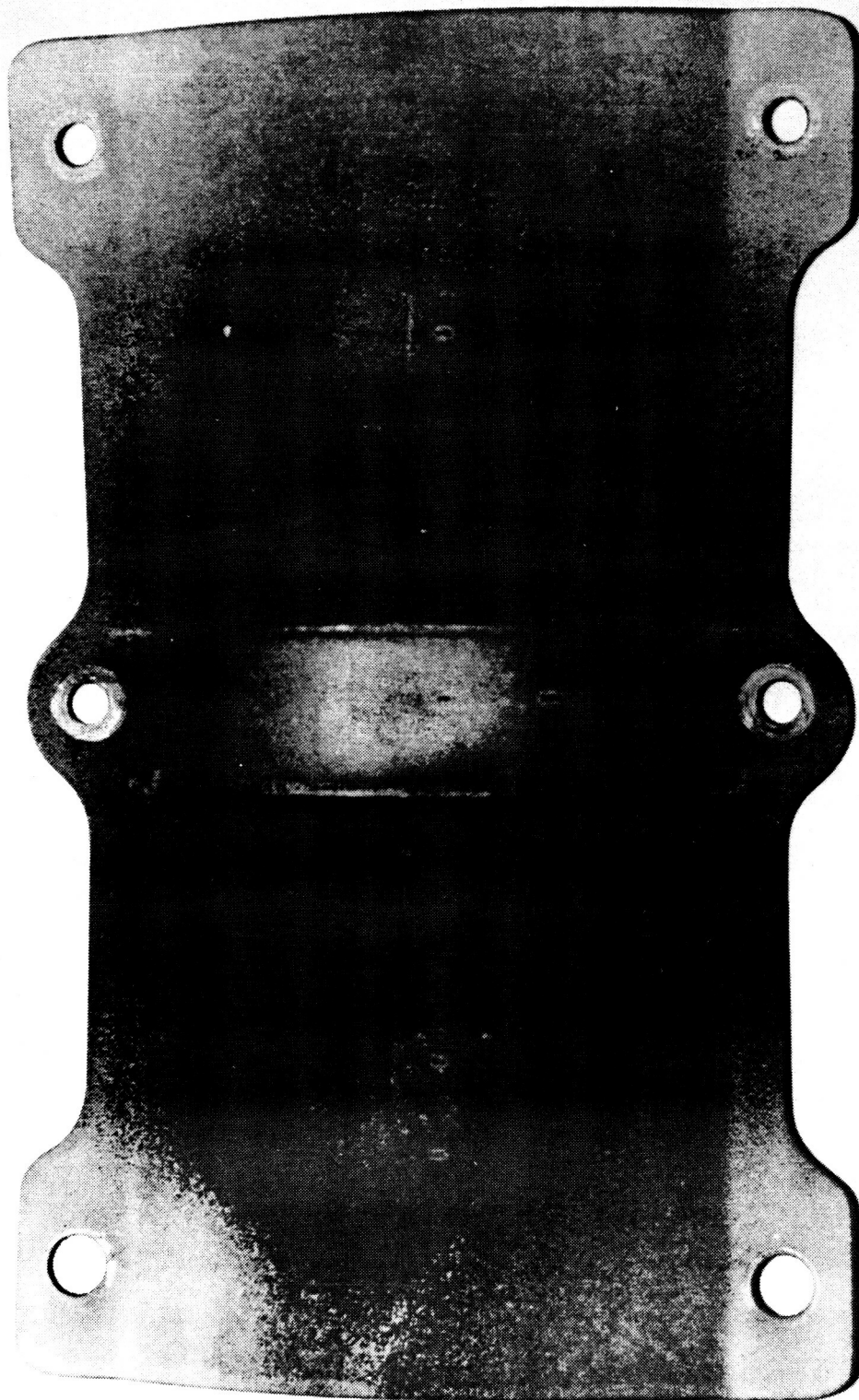


Figure 5-12. Front View of Panel YSC-3 After 100 Flight Simulation Cycles (Photo 122101B)

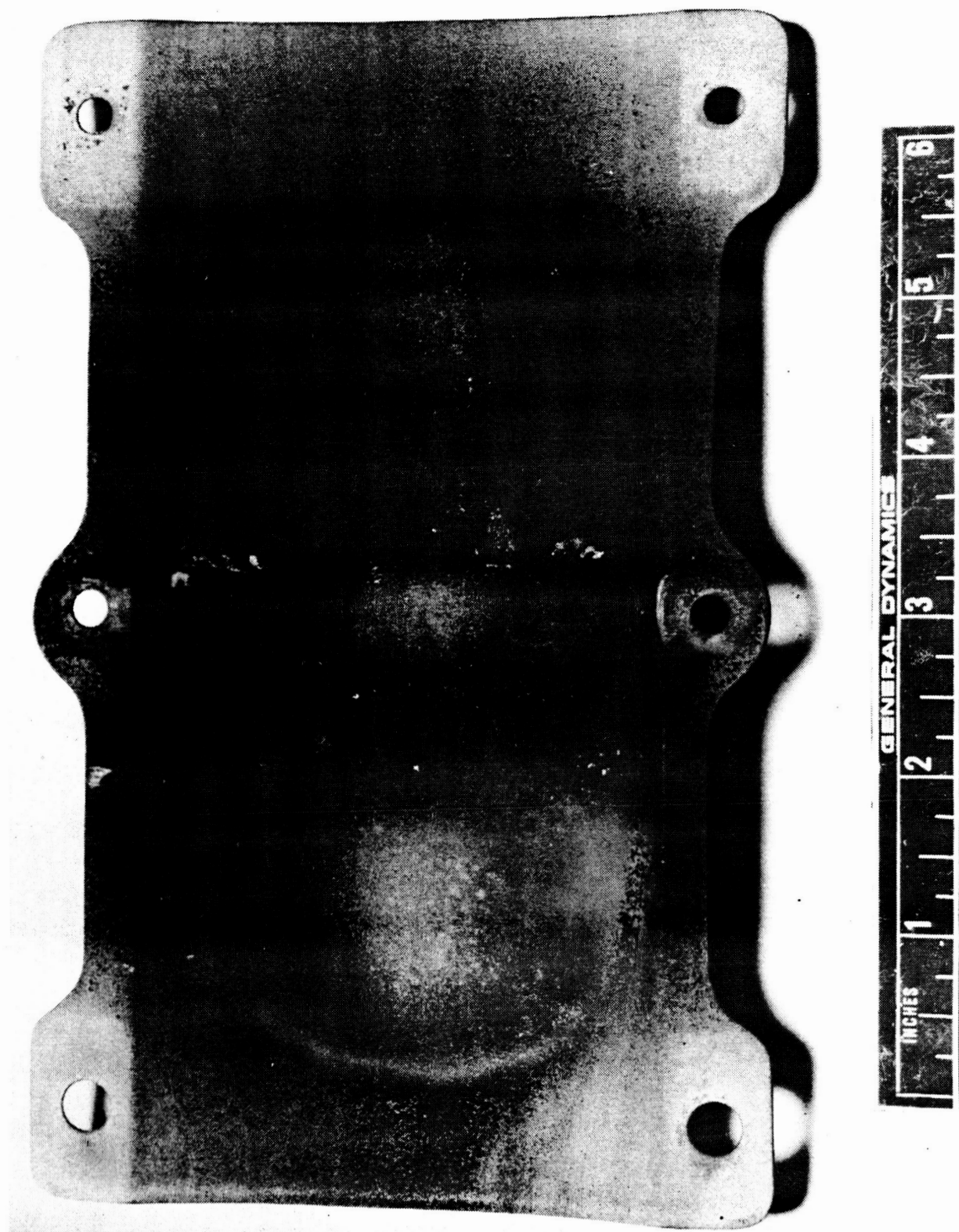


Figure 5-13. Rear View of Panel YSC-3 After 100 Flight Simulation Cycles (Photo 122098B)

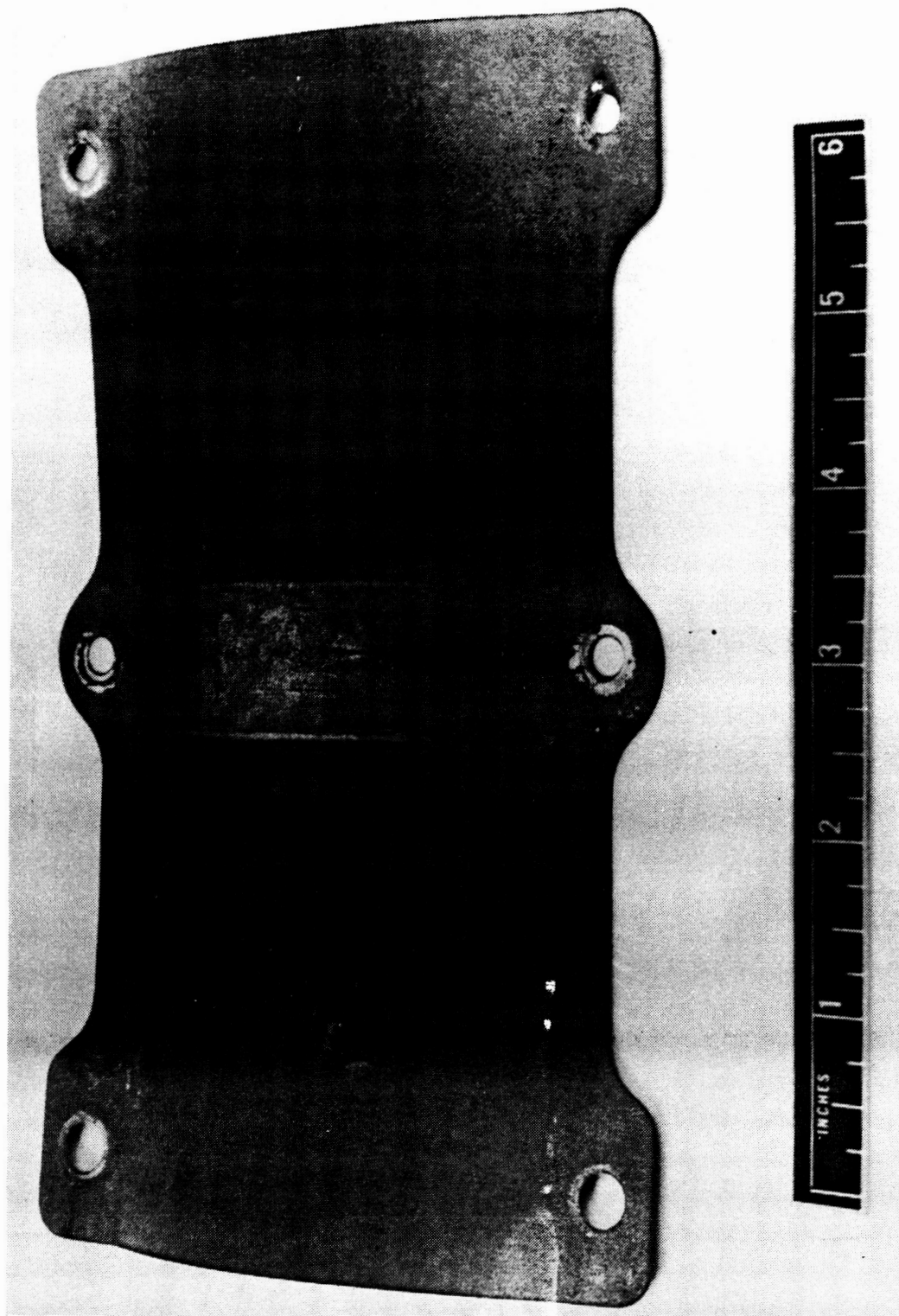


Figure 5-14. Front View of Panel YSC-2 After 100 Flight Simulation Cycles (Photo 121492B)

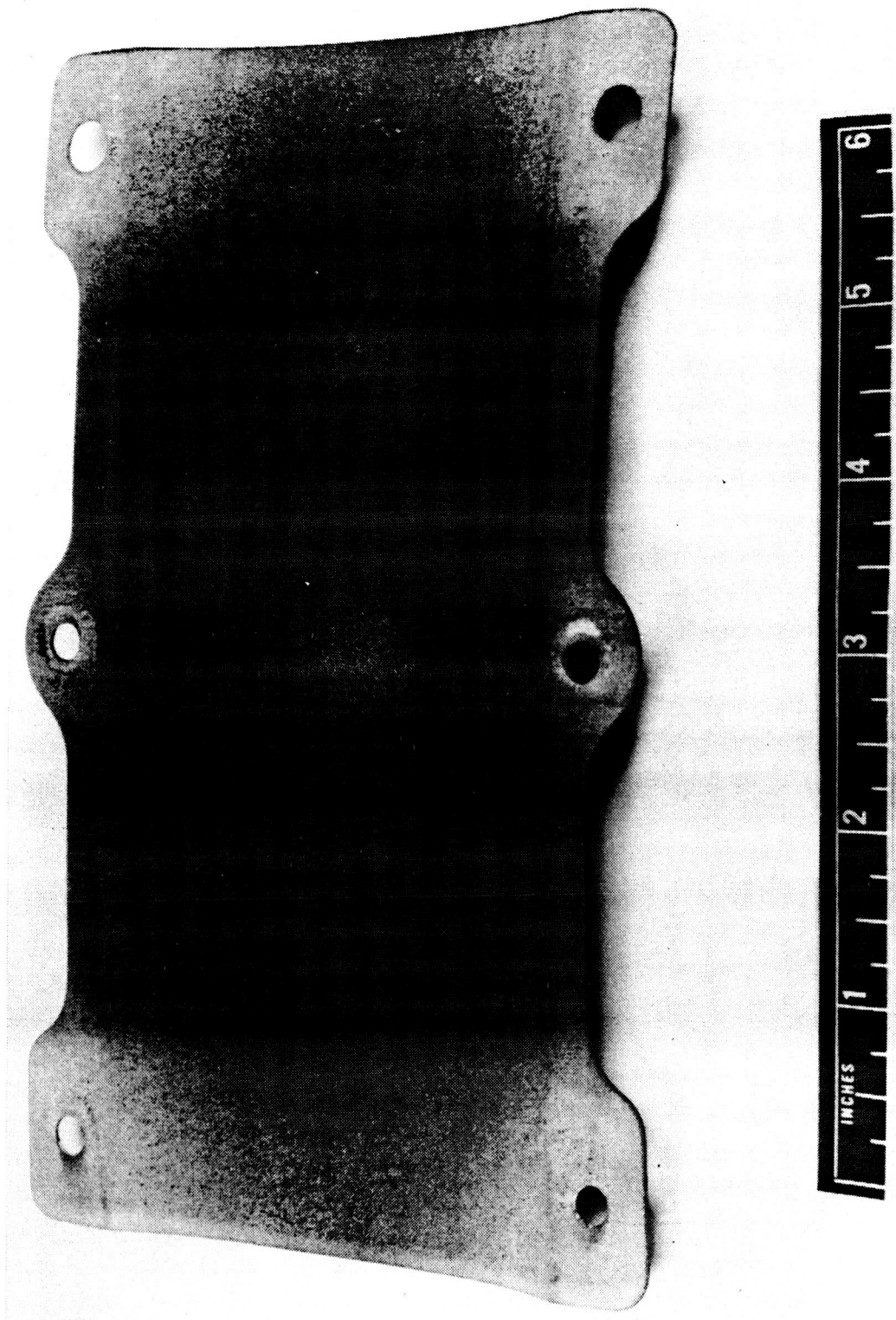


Figure 5-15. Rear View of Panel YSC-2 After 100 Flight Simulation Cycles (Photo 121493B)

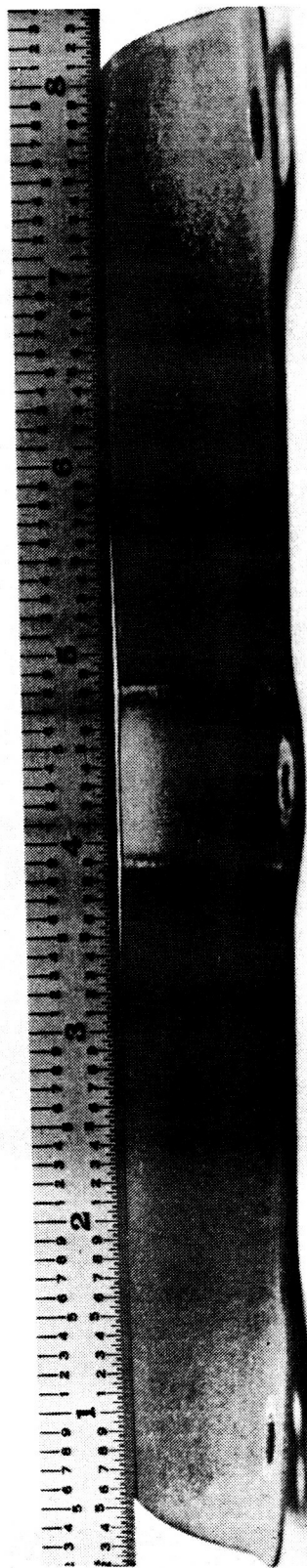


Figure 5-16. Permanent Deformation Along Longitudinal Center Axis of Panel YSC-3 After 100 Flight Simulation Cycles (Photo 122099B)

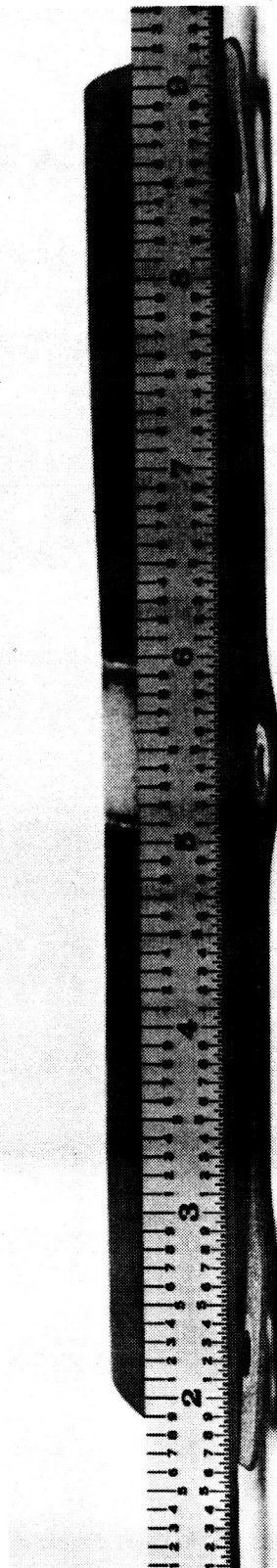


Figure 5-17. Permanent Deformation of Flange Along the Line of Mounting Holes of Panel YSC-3 After 100 Flight Simulation Cycles (Photo 122100B)

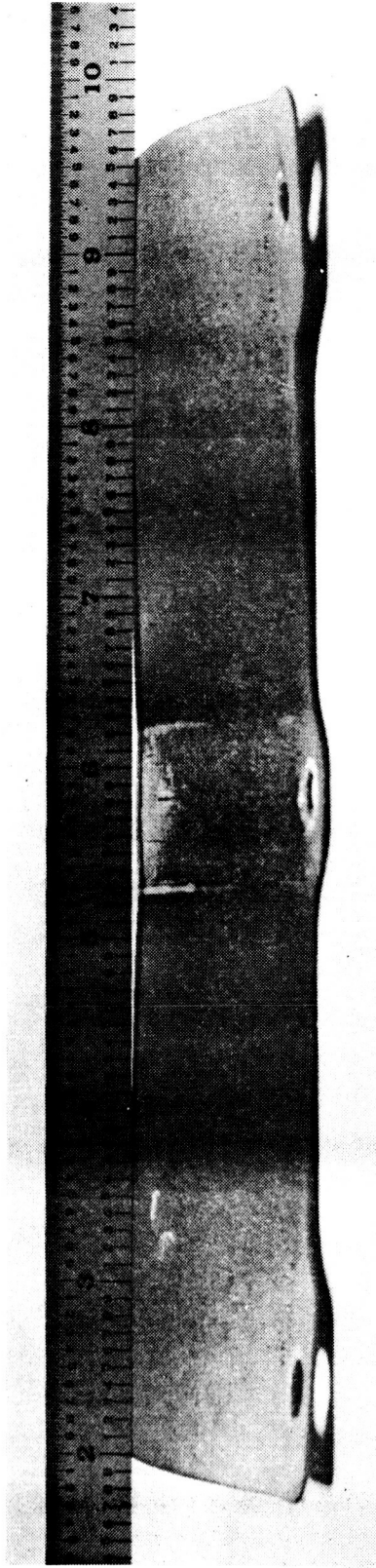


Figure 5-18. Permanent Deformation Along Longitudinal Center Axis of Panel YSC-2 After 100 Flight Simulation Cycles (Photo 121494B)

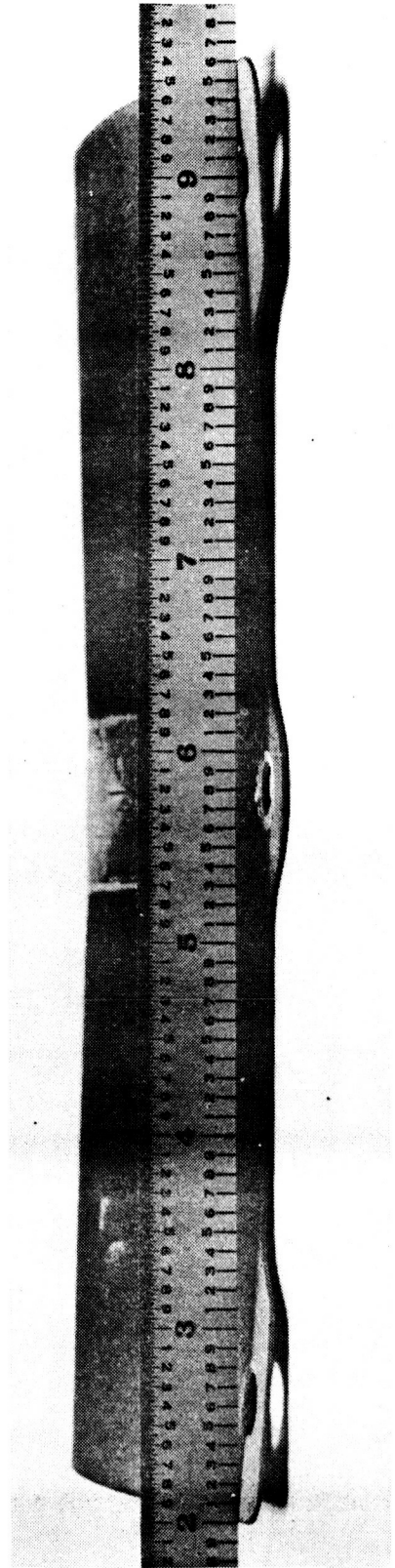


Figure 5-19. Permanent Deformation of Flange Along the Line of Mounting Holes of Panel YSC-2 After 100 Flight Simulation Cycles (Photo 121495B)

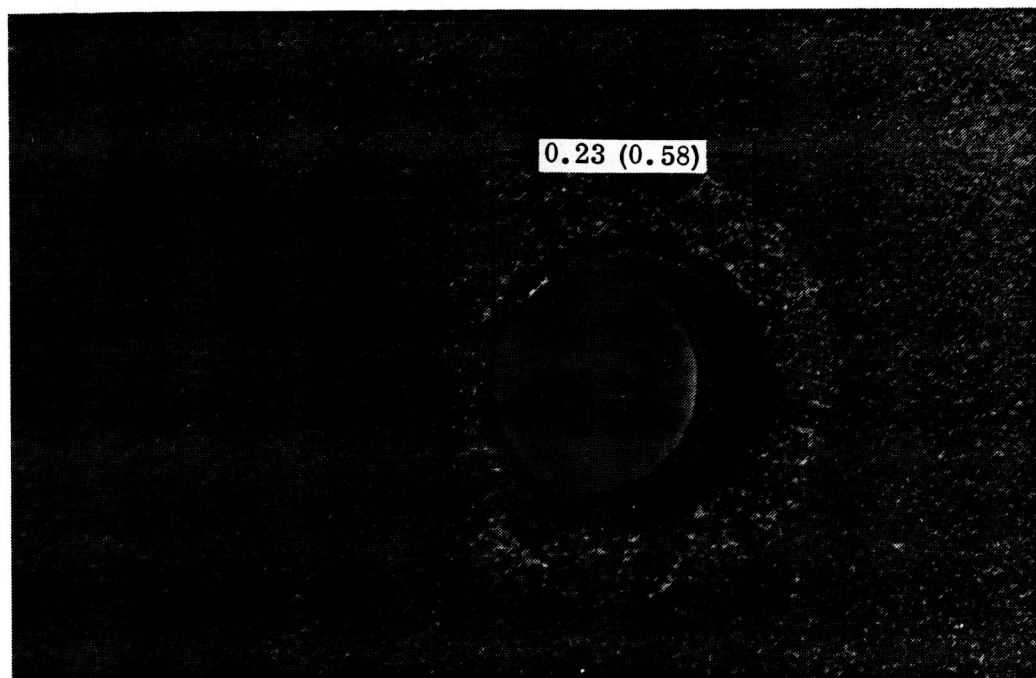


Figure 5-20. Movement of Lower End of Panel YSC-3 with Respect to Stiffener Bar After 100 Flight Simulation Cycles (Photo 121994B)

for the slippage was the difference in diameter of the holes and the mounting screws. In later testing of the Cb-752 corrugated panels this mismatch was overcome by inserting TD NiCr sleeves in the holes.

5.5.2 Group 2, C-129Y/R-512E, tee stiffened. – In contrast to the excellent performance of the corrugated panels, the tee-stiffened panels of the C-129Y/R-512E system suffered extensive coating spallation and substrate erosion. Structural damage, i. e., permanent creep deflection, was slight, however.

During the first 10 cycles the panels changed to a dark-grey color with a small amount of edge spall. These specimens were darker and more uniformly colored from top to bottom than the corrugated panels of Group 1. The first panel, YST-3, showed only light spall during the first 35 cycles. After 46 cycles, two sites of severe spallation were observed, one on the bottom end of the center web and the second on the outer edge of the skin about 0.8 inch (2 cm) from the bottom. Coating spall, which had been light up to this point, was beginning to increase on the webs. Two coating failures on the edge of the center flange were observed after 59 cycles. The failures were near the center of the panel about 0.4 inch (1 cm) apart and had the appearance of edge delamination. Heavy spall was visible on the center flange and on the skin (back side) on either side of the flange. Figure 5-21 shows the beginning of the edge attack and the increased surface spall. By 72 cycles the center flange was severely attacked with considerable substrate erosion on both edges. This attack extended over the center 1 inch (2.5 cm) and for about 1 inch (2.5 cm) below this. Two coating failures were visible in the skin on either side of the center web in the center of the panel. The

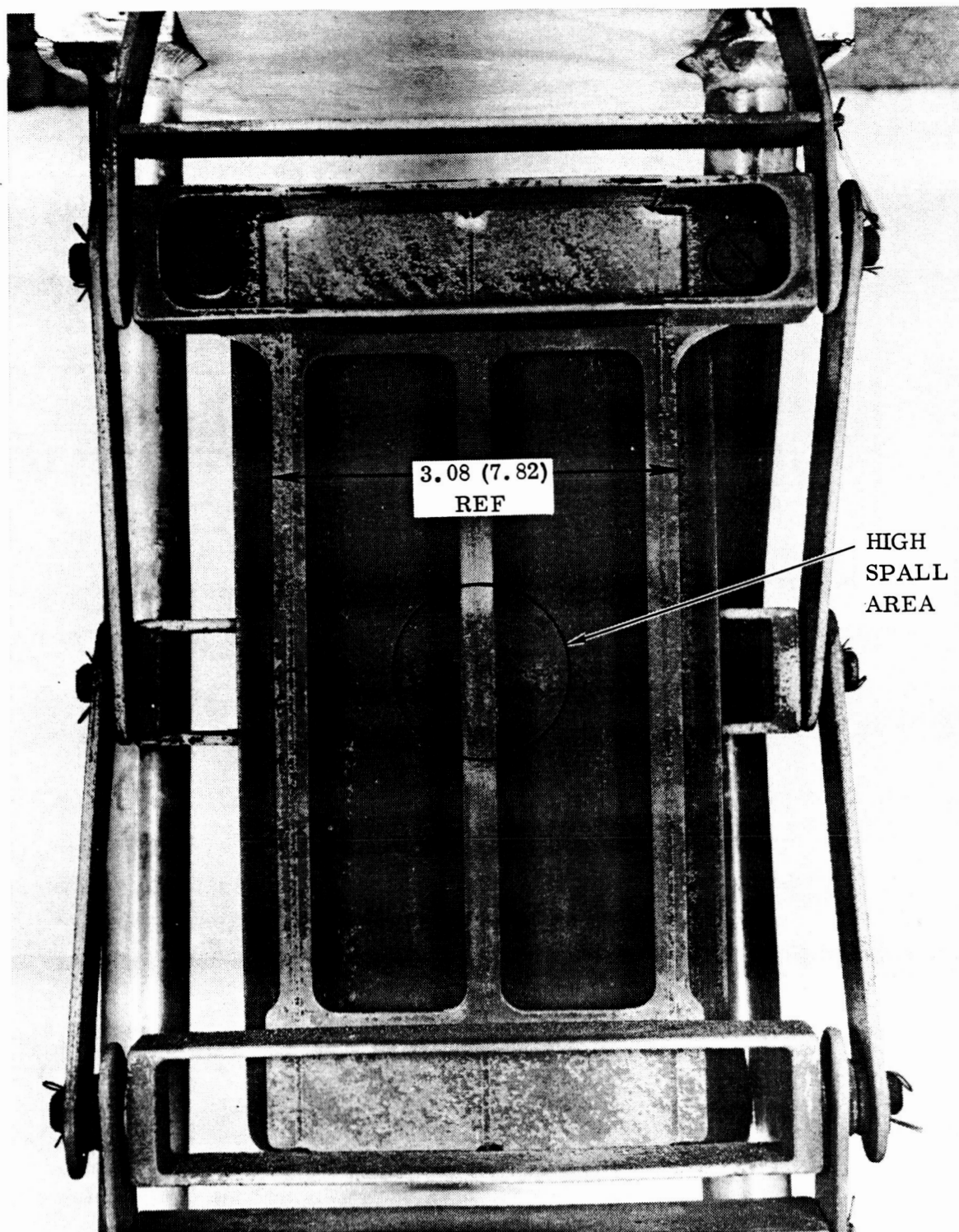


Figure 5-21. Beginning of Edge Attack and Increased Surface Spall on Panel YST-3 After 59 Flight Simulation Cycles (Photo 122944B)

surface of the skin was severely spalled with a blistered appearance. Figure 5-22 shows the panel after 83 cycles, at which time one of the skin failures had extended completely through the panel. Attack on the center flange was such that portions were almost entirely eroded away. Testing was continued to study the effects of the failure of a main structural member. After 100 cycles both surface failures had generated holes in the panel. The center flange and portions of the web were entirely eroded away for a length of about 2 inches (5 cm). Loss of the flange on the center web resulted in web distortion. Figures 5-23 and 5-24 are front and back views of the panel after 100 cycles. The severe substrate erosion, surface spall, and blistered appearance are clearly visible.

The buckling condition of the web was not associated with the restraining effects of the loading fixture. Therefore, it can be assumed that the local area would have performed in a similar manner if the cap had eroded away during a series of missions. This condition, had it gone unnoticed, would not have jeopardized the vehicle entry performance. However, since the potential failure region was clearly identifiable, a heat shield exhibiting this condition would have been repaired or replaced during normal vehicle turnaround inspection and maintenance. (Repair techniques are discussed in Sections 5.5.4 and 10.3.3.) This specimen and also YST-4 were allowed to erode in order to study the structural effects of the material system breakdown.

Figure 5-25 shows the extent of permanent creep deflection, which surprisingly is quite small considering the extent of panel damage. In addition to the bending of the panel about the transverse axis, several small buckles were observed in the skin during the 100 cycles. Some bending of the outer edges of the skin also occurred. This bending, barely visible in Figures 5-23 and 5-25, was observed about 1 inch (2.5 cm) above and below the horizontal centerline of the panel in the regions where the Refrasil cord was wrapped to attach the thermocouples. All of the the-stiffened panels exhibited this bending of the edges, with the effect much more pronounced in the Cb-752 panels.

The second C-129Y/R-512E tee-stiffened panel, YST-4, exhibited coating breakdown after 64 cycles in a manner almost identical to YST-3. Erosion on the edges of both sides of the flange of the center web and in the adjacent skin area were observed. In addition, several coating failures occurred on either side of the web about 0.12 inch (0.34 cm) from the skin. Because of the similarity with the previous specimen, this panel was withdrawn from testing at the completion of 64 cycles. Photographs of the panel removed from the test fixture after 64 cycles are shown in Figures 5-26 and 5-27. A close-up view of the damaged areas is presented in Figure 5-28.

With only 64 flight cycles completed, the degree of skin buckling was almost negligible and very little bending about the transverse axis was evident. Bending of the outer edges of the skin was about the same as that noted on Panel YST-3, however.

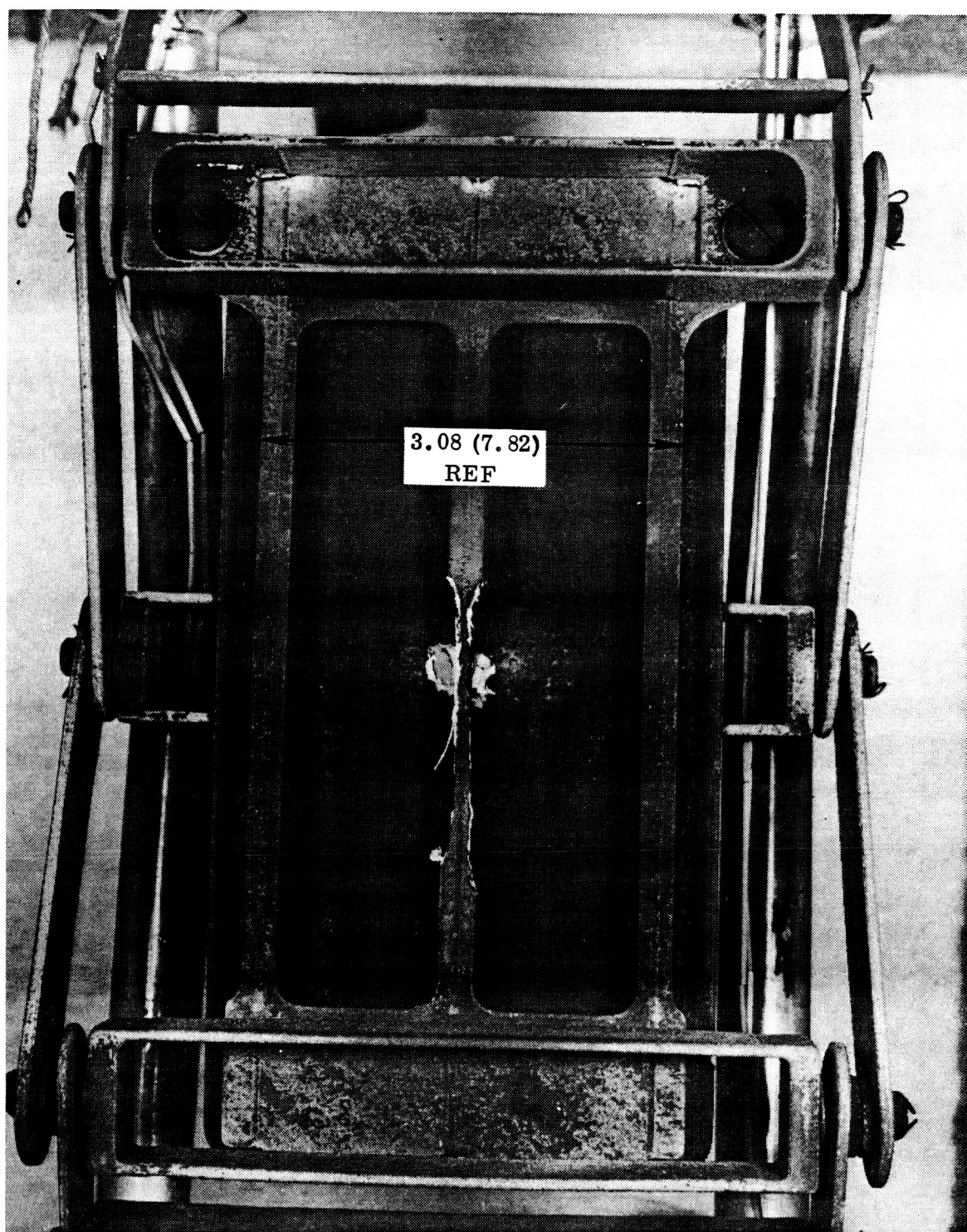


Figure 5-22. Skin Failure Extending Through Panel YST-3 After 83 Flight Simulation Cycles (Photo 123003B)

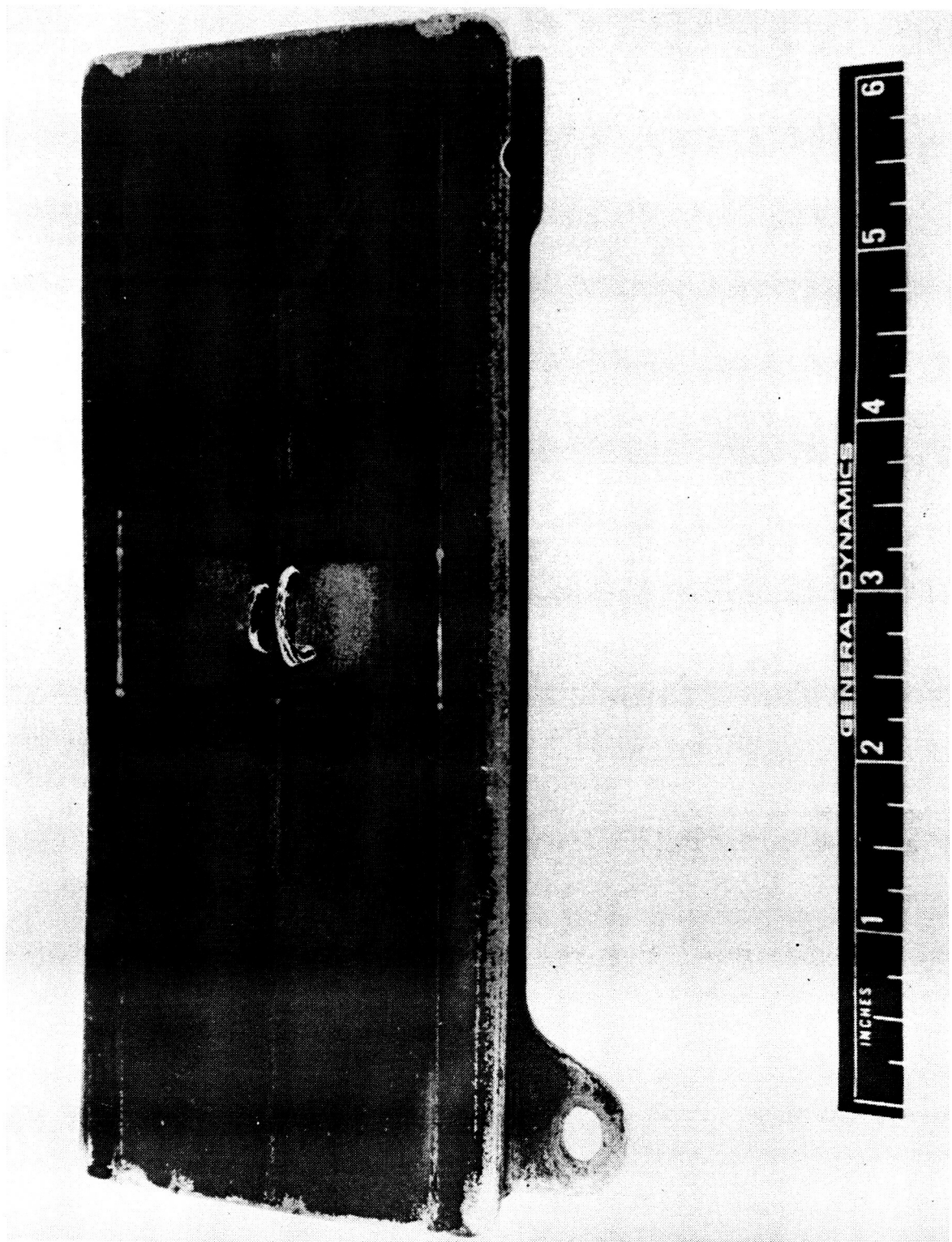


Figure 5-23. Front View of Panel YSC-3 After 100 Flight Simulation Cycles (Photo 123217B)

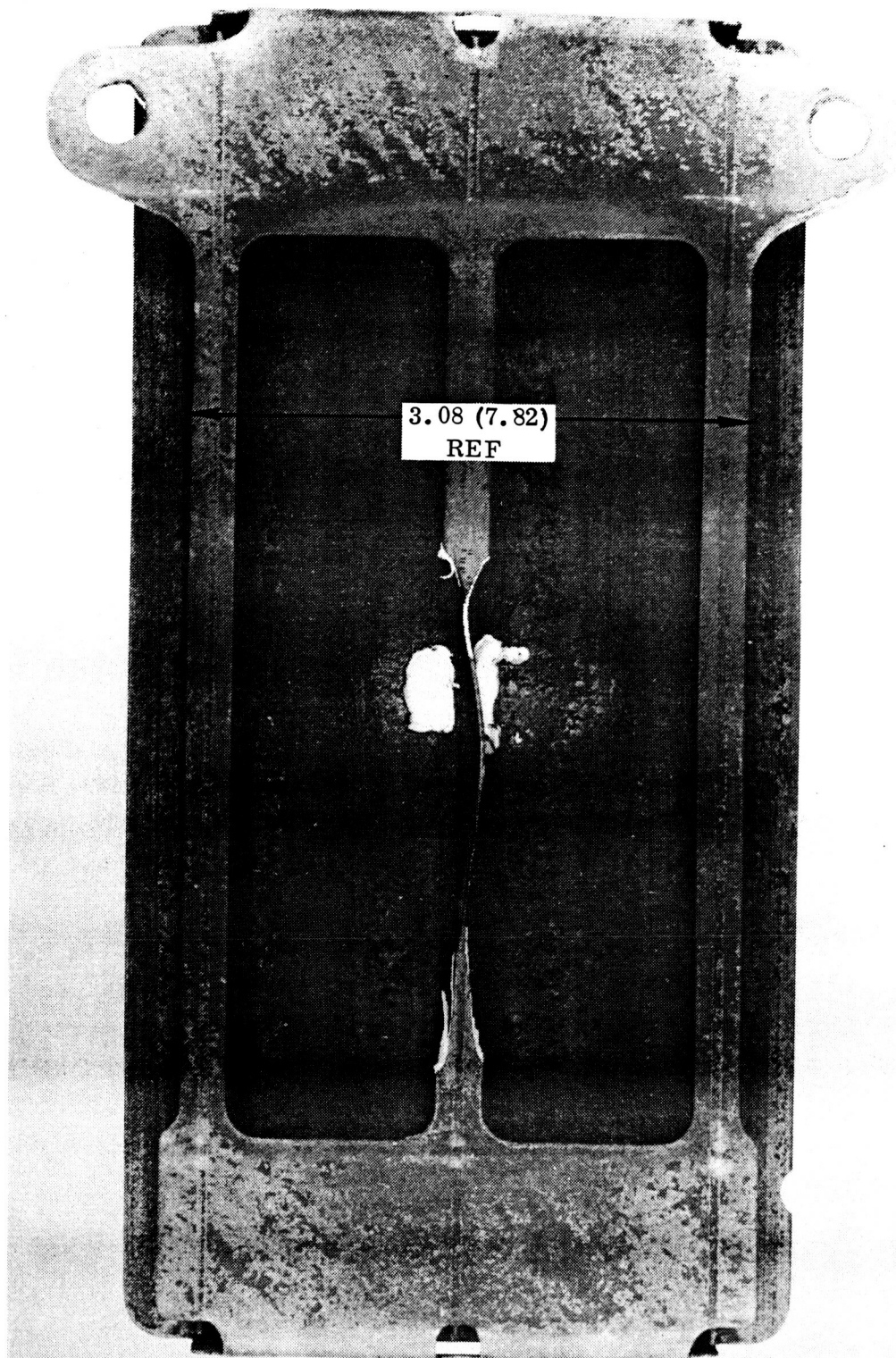


Figure 5-24. Rear View of Panel YST-3 After 100 Flight Simulation Cycles (Photo 123213B)

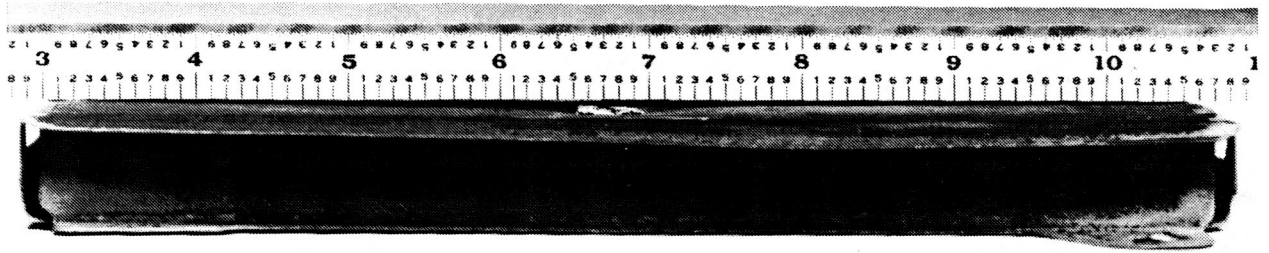


Figure 5-25. Extent of Permanent Creep Deflection of Panel YST-3
After 100 Flight Simulation Cycles (Photo 123219B)

One final point of interest on the exposure cycling of the tee-stiffened panels was the occurrence of a powdery white substance on the panels during the early stages of cycling. This material was found primarily at the inside corners where the webs joined the skin. Some of this white substance can be seen in Figure 5-27. It occurred on all of the tee-stiffened panels, both C-129Y and Cb-752, but only on the stiffener sides. A spectrographic analysis of the powder taken from one of the Cb-752 panels revealed the presence of only Si, Fe, Cr, Cb, W, and Zr. The first three elements are in the coating and the last three in the alloy. An explanation for the source of the powder was not found.

5.5.3 Group 3, Cb-752/R-512E, corrugated. — The two panels of this group completed 100 flight simulation cycles in excellent condition. Neither panel showed evidence of either structural failure or localized coating failure. The changes in appearance during cycling were nearly identical for the two panels. During the initial exposure cycles the panels changed in color from a metallic grey to a dark brown-grey with some lighter grey areas at the edges where slight coating spall had occurred (Figures 5-29 and 5-30). After 20 cycles, circular regions appeared in the central portion of the panels. These areas, about 1 to 2 inches (2.5 to 5 cm) in diameter can be seen in Figures 5-31 and 5-32. They were somewhat lighter in color, had a rougher texture, and exhibited more coating spall. As cycling progressed these regions took on a distinct yellow coloration. Surface roughness increased with cycling as did the amount of coating spall. After 80 cycles the yellow coloration on one of the panels, BSC-2, was less pronounced as a result of coating spall. The two panels are shown at the completion of 100 flight cycles in Figures 5-31 to 5-34. The principal difference between the panels is in the appearance of these circular regions. Much more of the yellow oxide (probably columbium oxide) has spalled away from panel BSC-2. No unusual deformation or deflection was visible in these regions on either panel. The degree of permanent creep deflection in the panels can be seen in Figures 5-35 and 5-36. Again the two panels are quite similar.

Several coating failure sites at the attachment holes of the panels are visible in Figures 5-31 to 5-34. These were the result of mechanical stresses during mounting or bearing stresses during loading and are not considered to be a significant result of the flight simulation exposures.

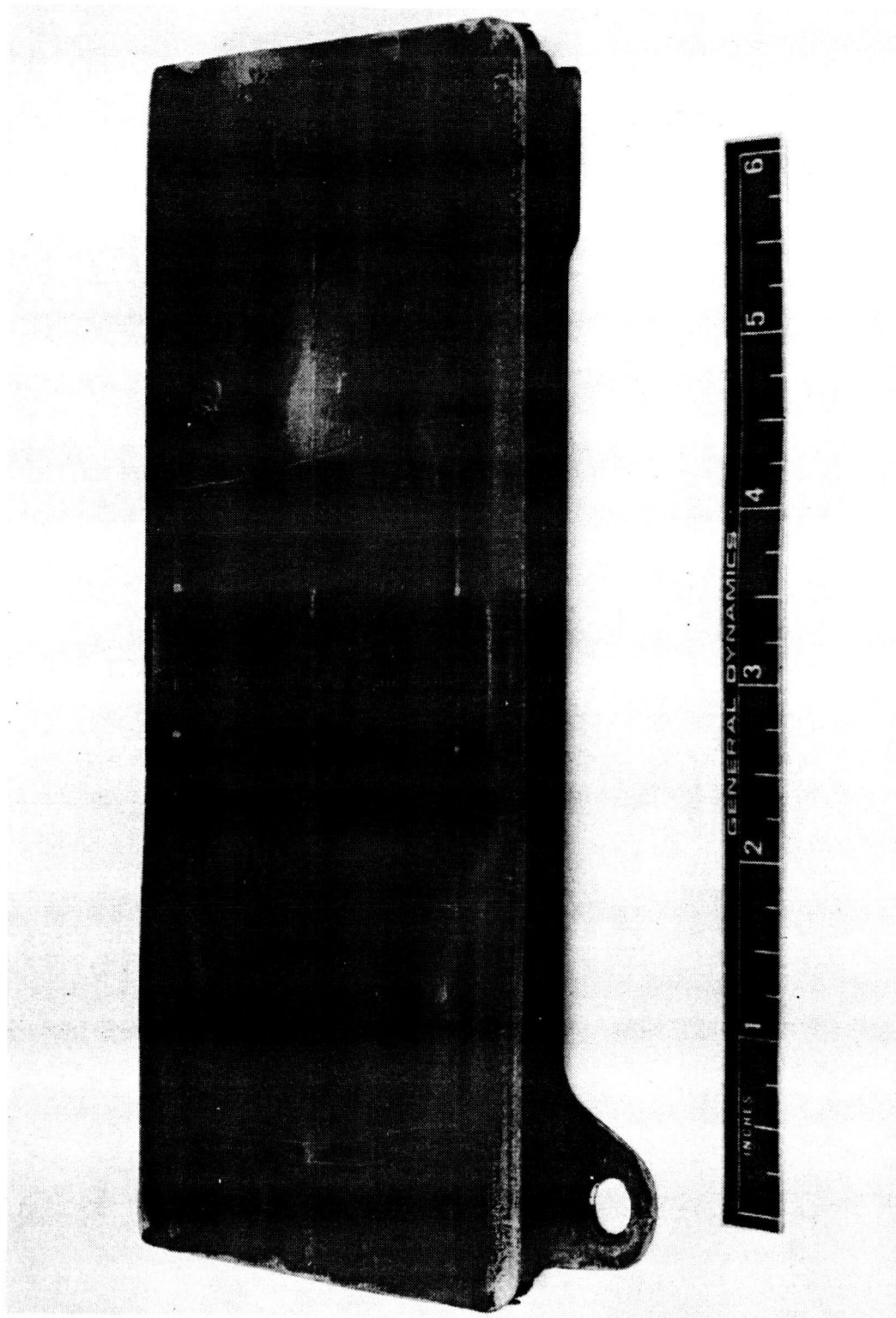


Figure 5-26. Front View of Panel YST-4 After 64 Flight Simulation Cycles (Photo 123475B)

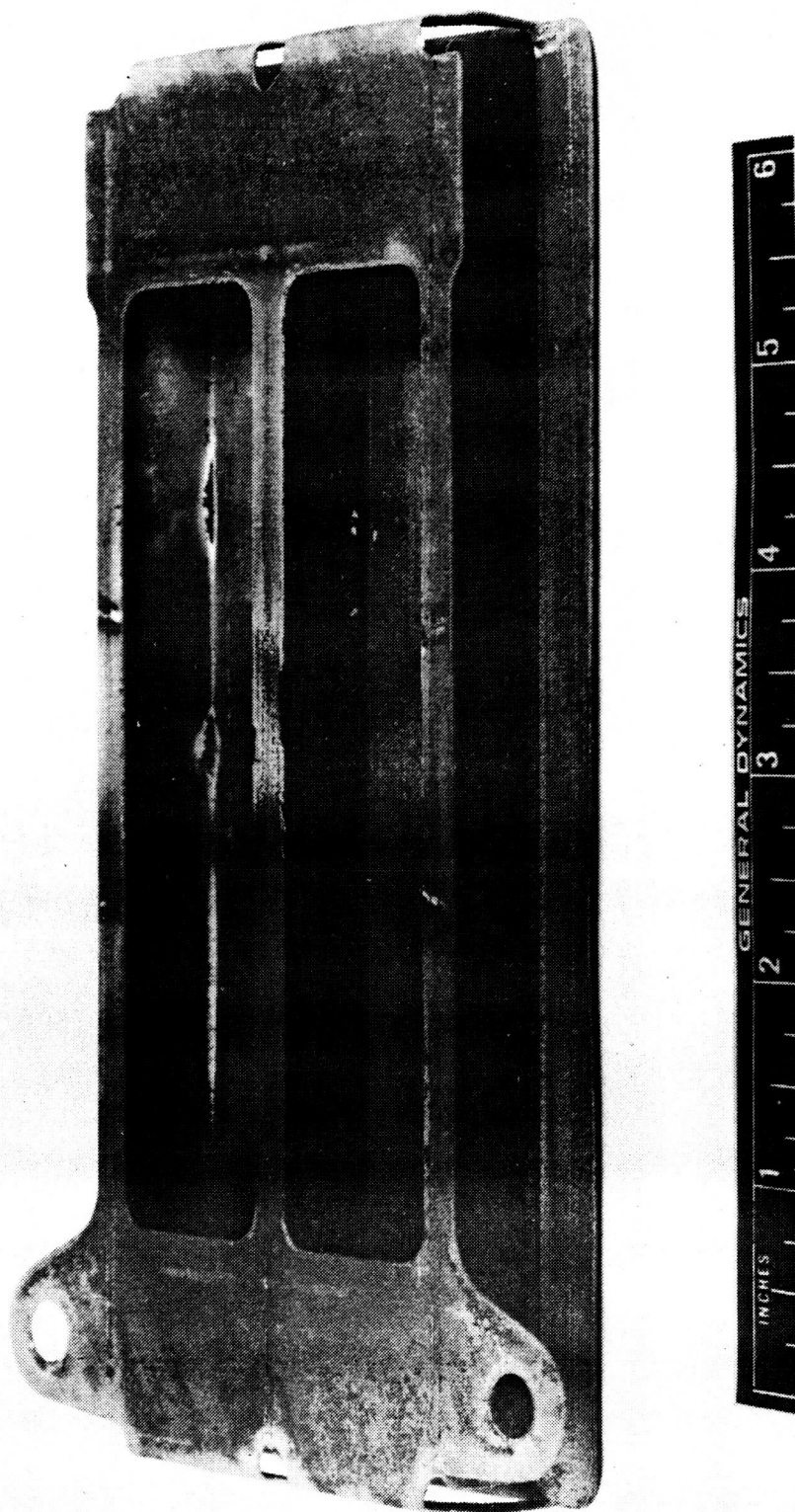


Figure 5-27. Rear View of Panel YST-4 After 64 Flight Simulation Cycles (Photo 123476B)

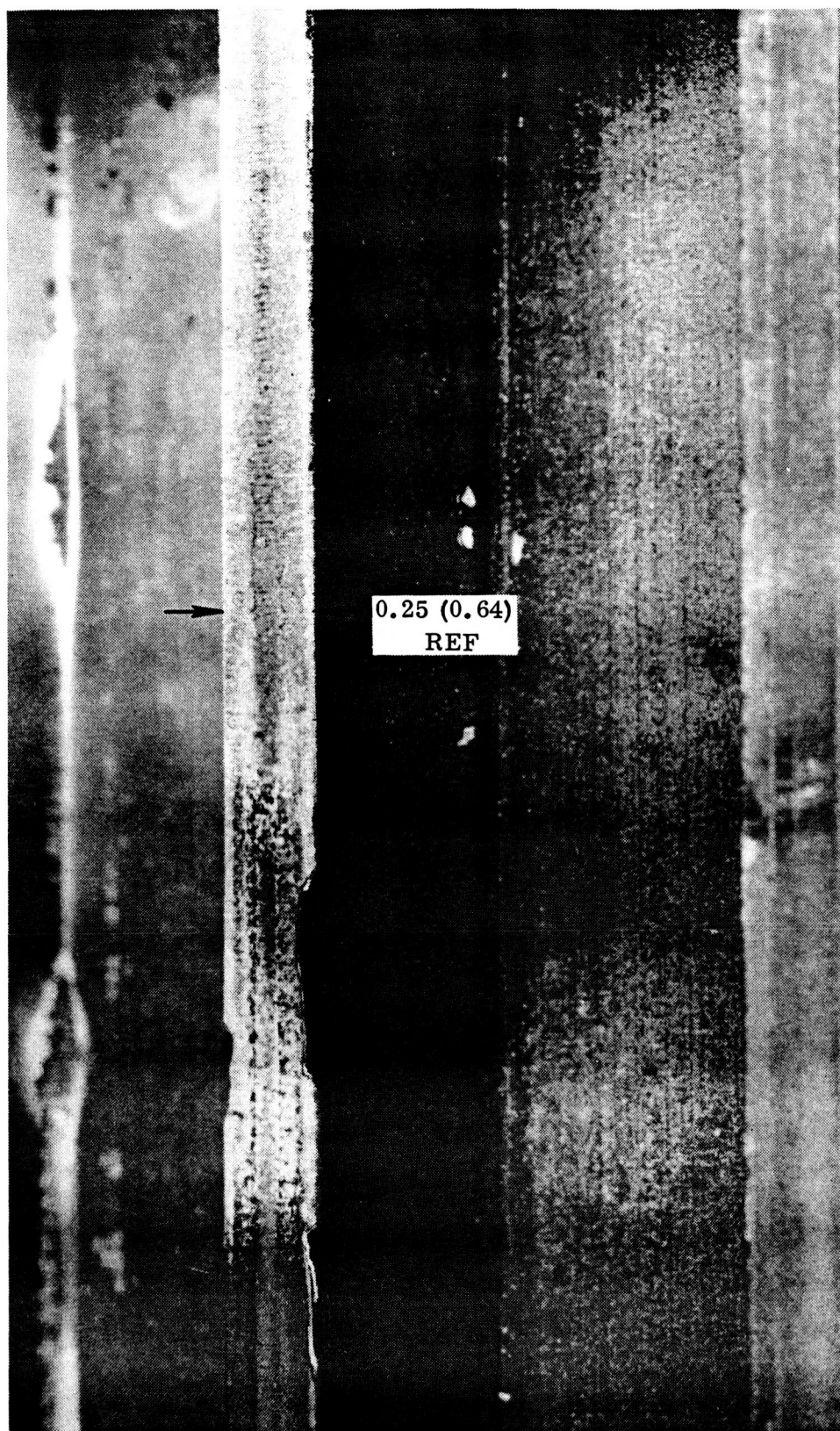


Figure 5-28. Close-up View of Damaged Areas of Panel YST-4
After 64 Flight Simulation Cycles (Photo 123477B)

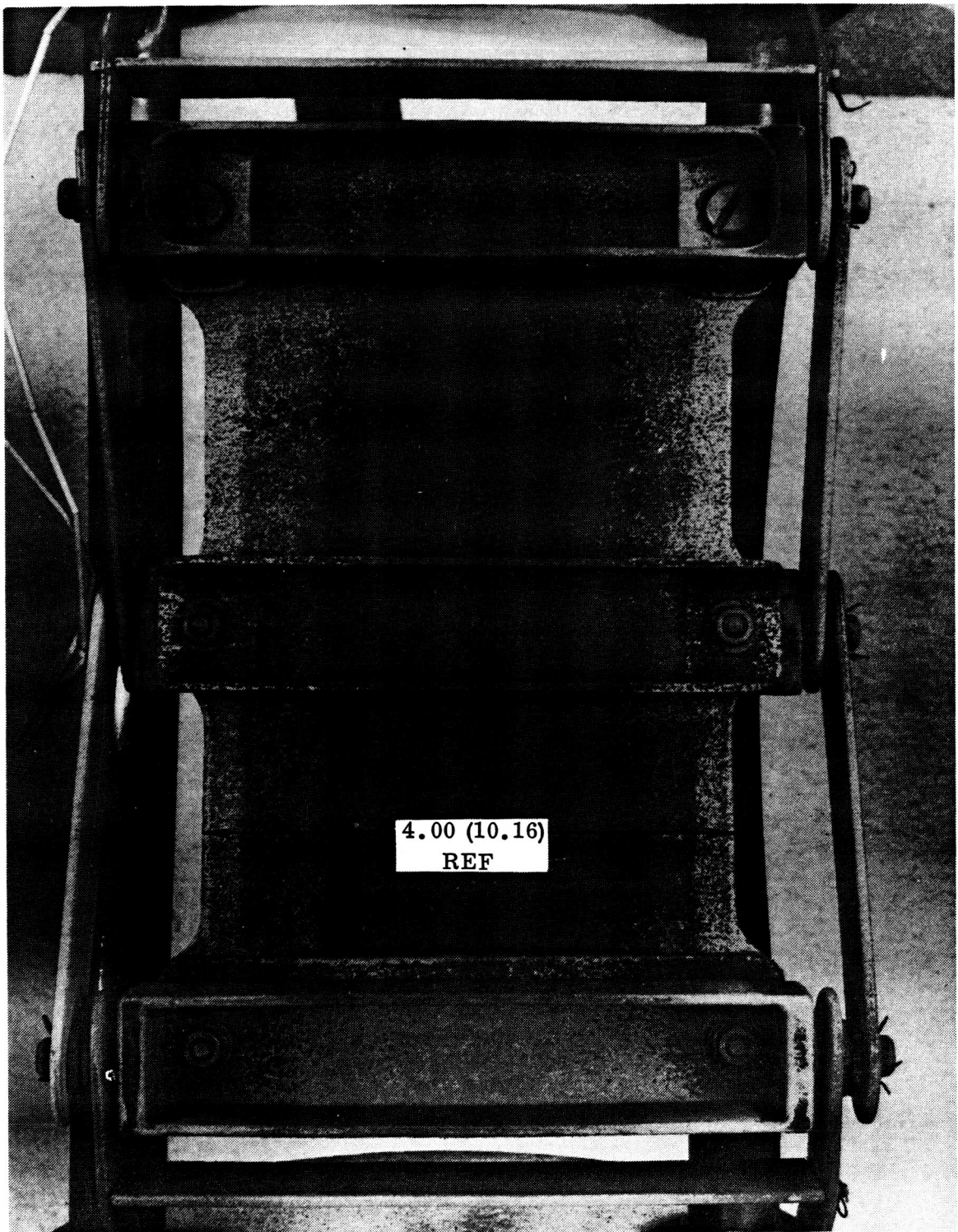


Figure 5-29. Front View of Panel BSC-1 After Nine Flight Simulation Cycles (Photo 124718B)

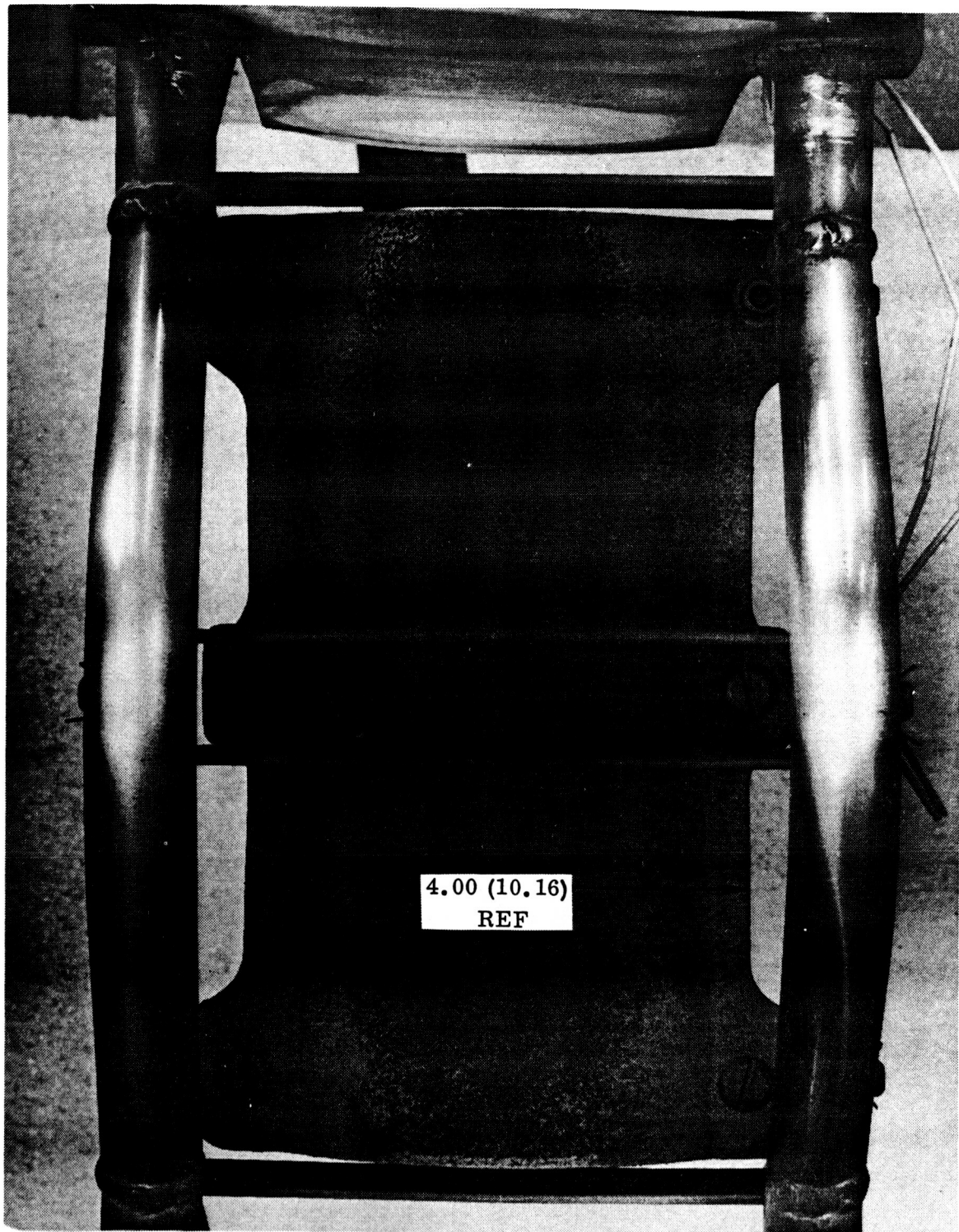


Figure 5-30. Rear View of Panel BSC-1 After Nine Flight Simulation Cycles (Photo 124720B)

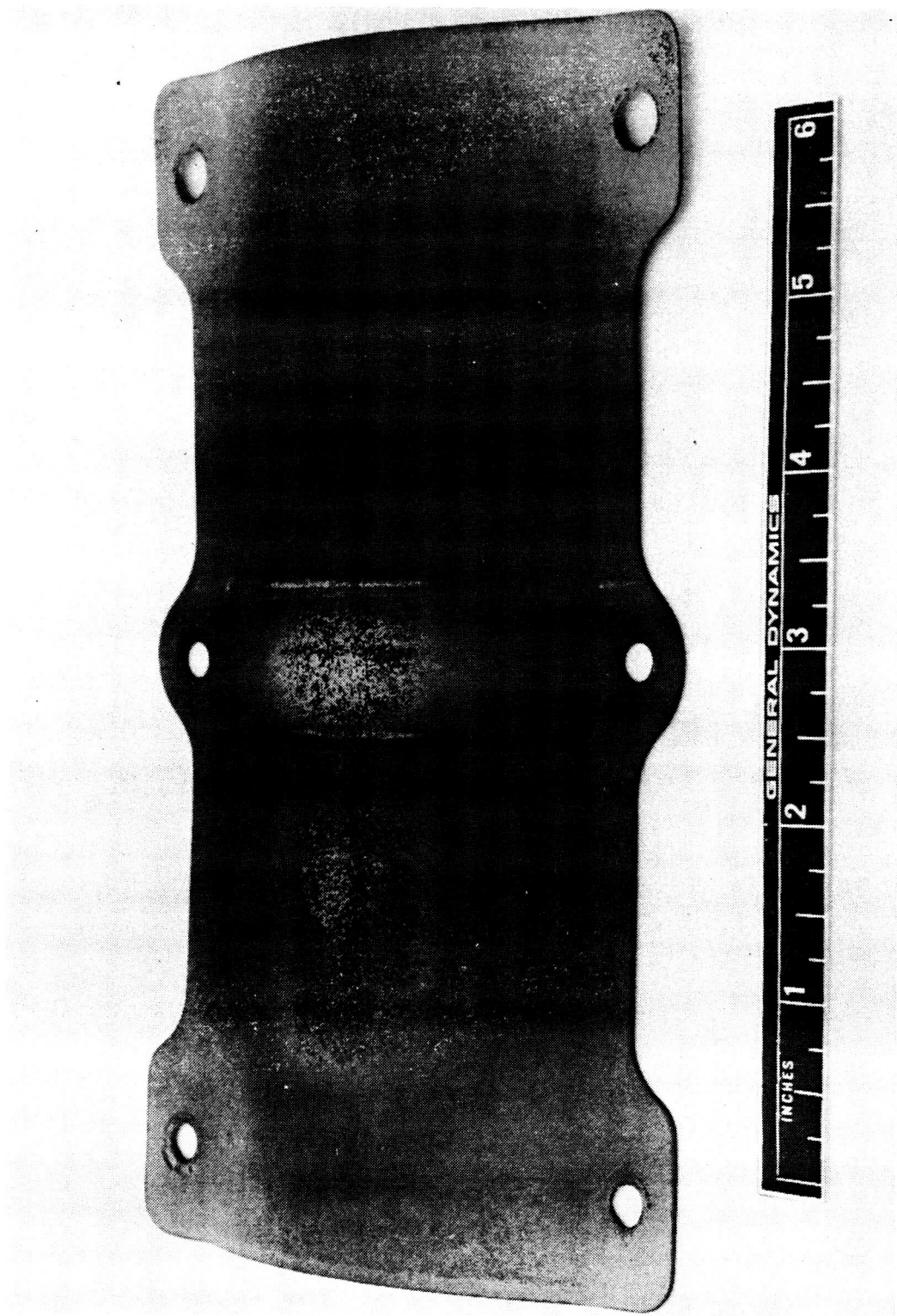


Figure 5-31. Front View of Panel BSC-1 After 100 Flight Simulation Cycles (Photo 125707B)

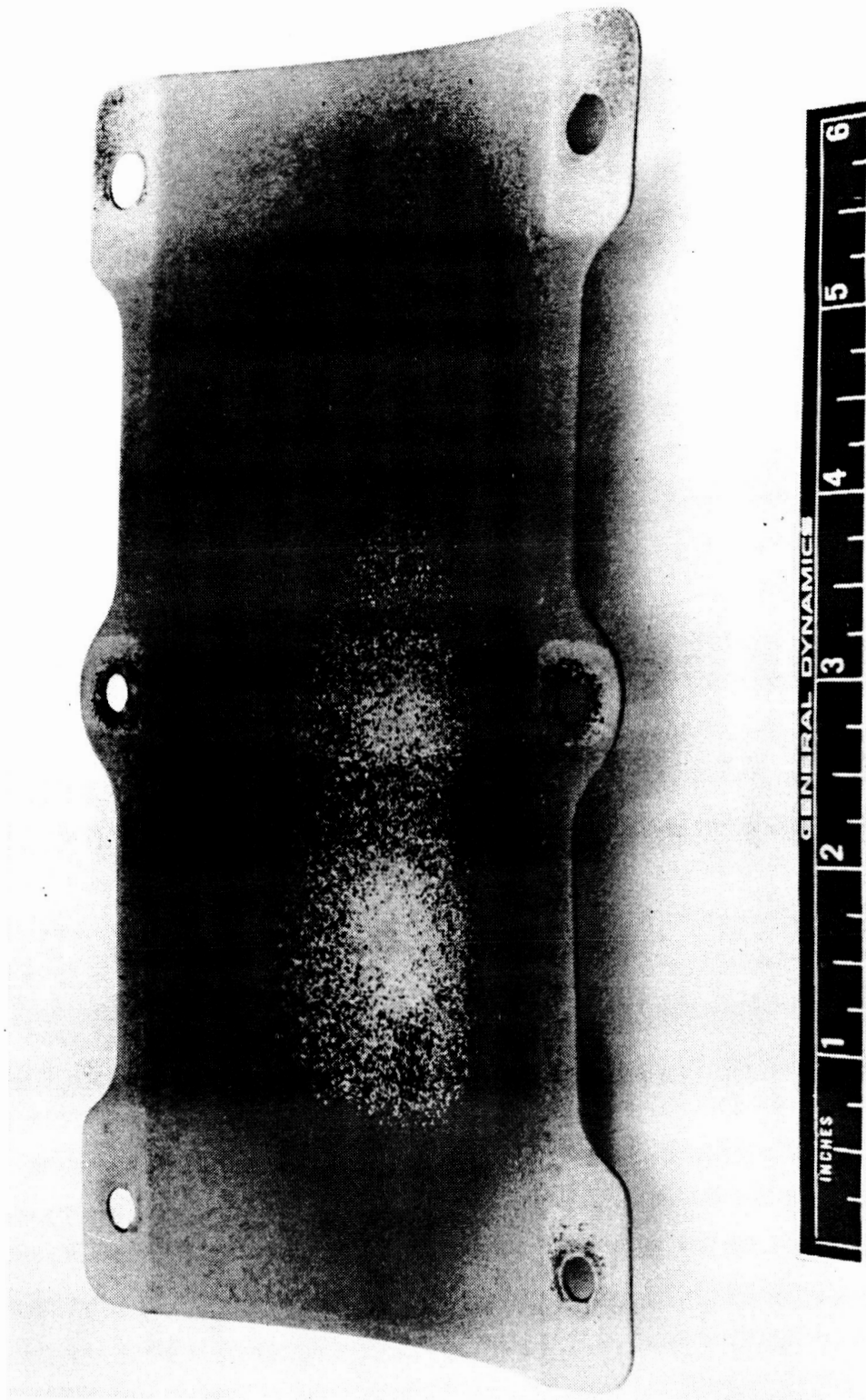


Figure 5-32. Rear View of Panel BSC-1 After 100 Flight Simulation Cycles (Photo 125708B)

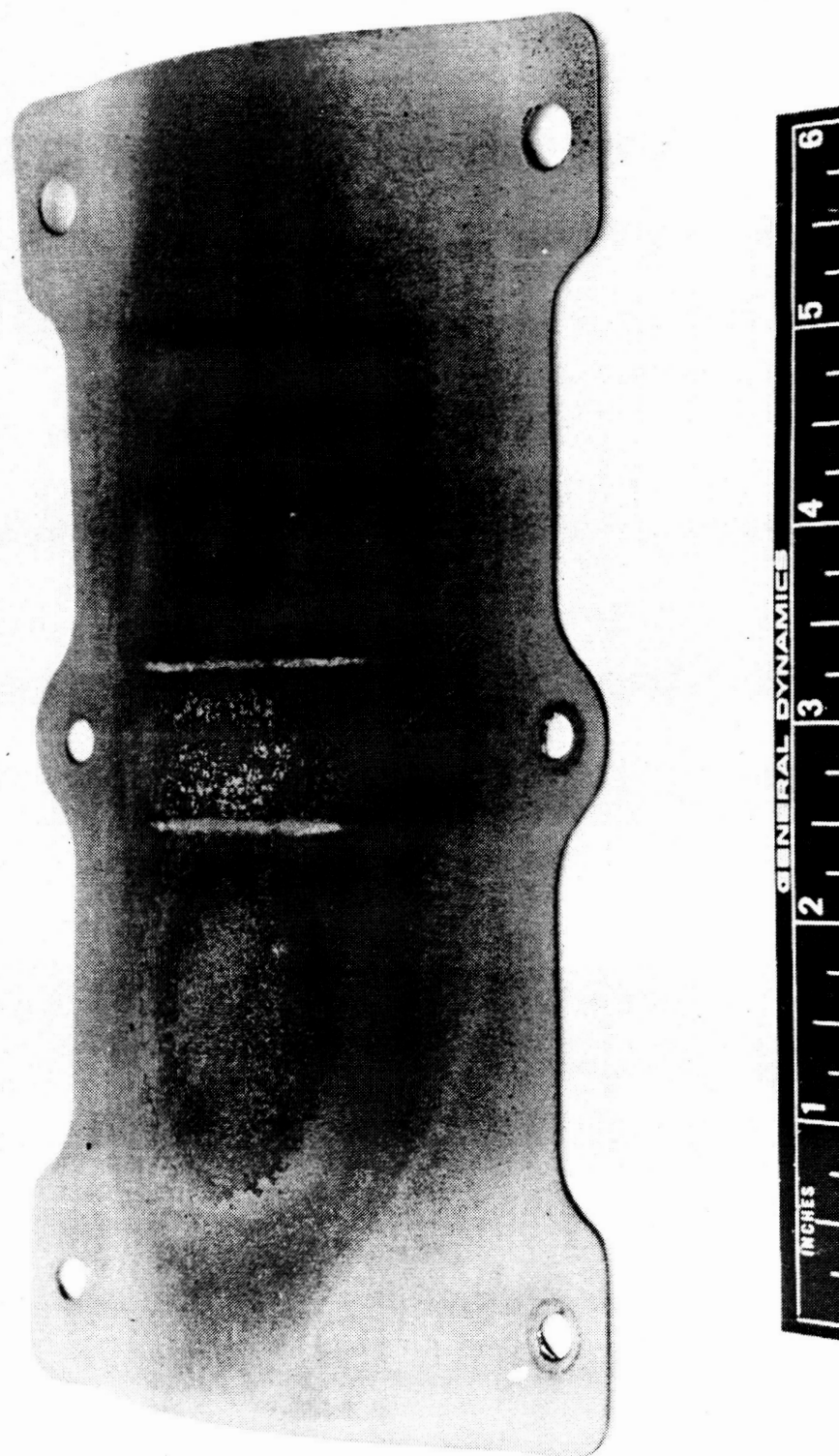


Figure 5-33. Front View of Panel BSC-2 After 100 Flight Simulation Cycles (Photo 125709B)

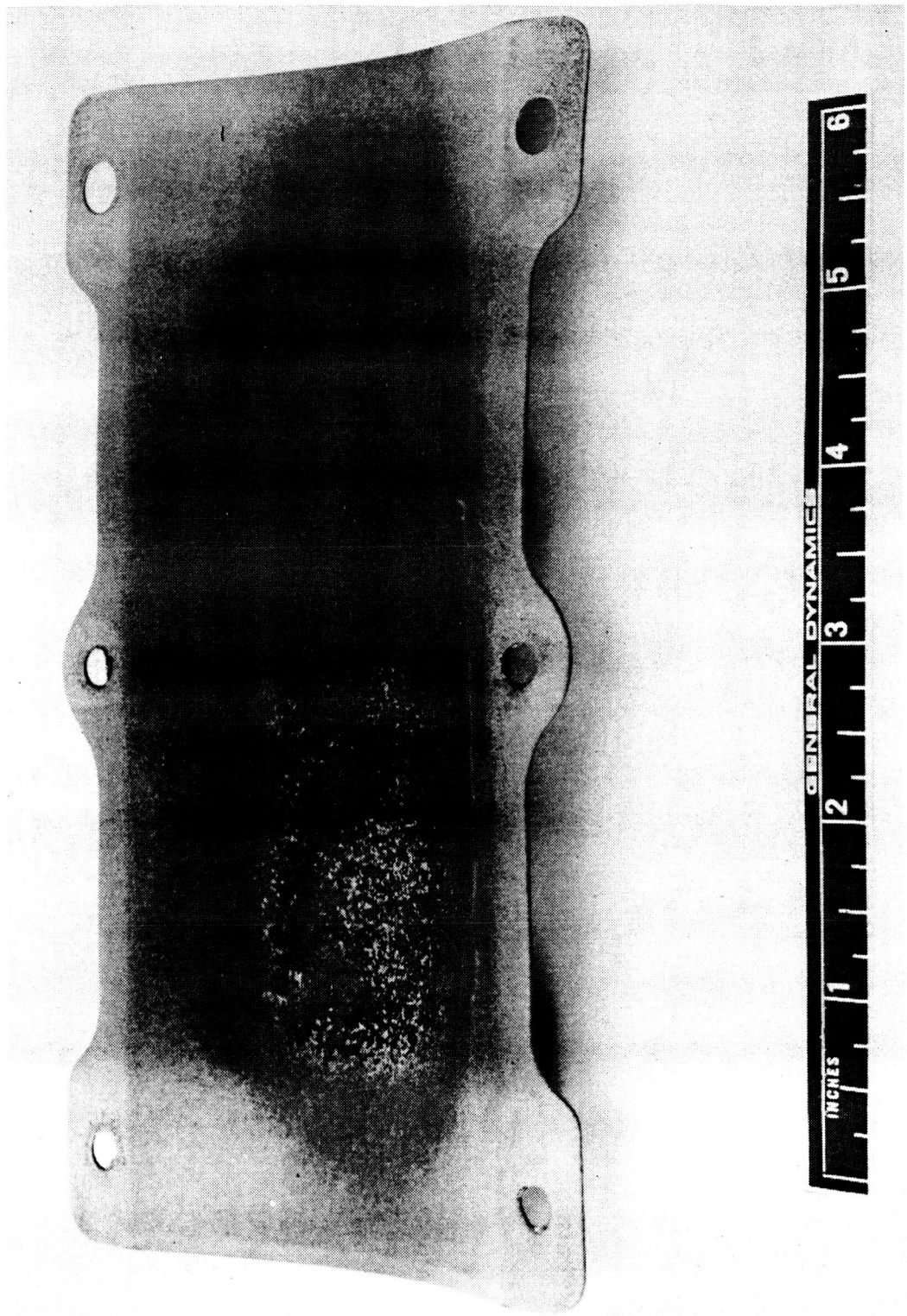


Figure 5-34. Rear View of Panel BSC-2 After 100 Flight Simulation Cycles (Photo 125706B)

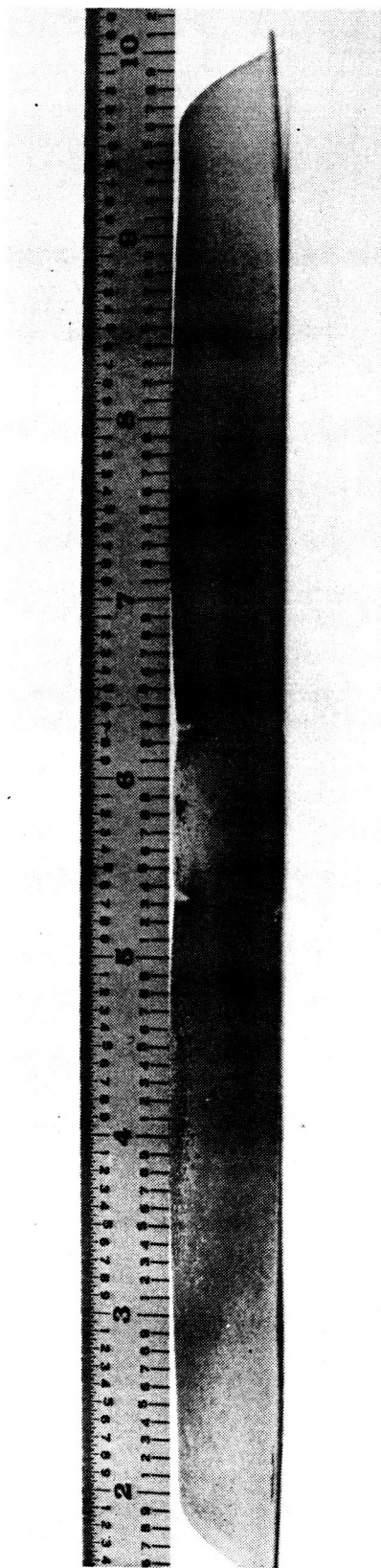


Figure 5-35. Permanent Creep Deflection Along Longitudinal Central Axis of
Panel BSC-1 After 100 Flight Simulation Cycles (Photo 125712B)

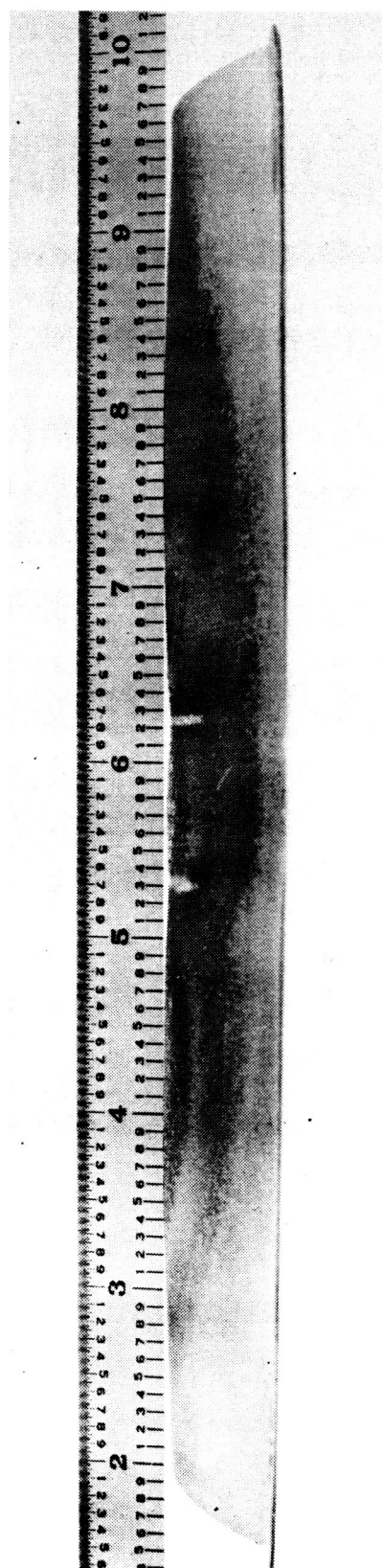


Figure 5-36. Permanent Creep Deflection Along Longitudinal Central Axis of
Panel BSC-2 After 100 Flight Simulation Cycles (Photo 125710B)

5.5.4 Group 4, Cb-752/R-512E, tee stiffened. - Four panels were tested in this group, two of which had been coated with the standard R-512E coating and two of which had been coated with a modified R-512E containing a dispersed radionuclide (^{147}Pm). Because of differences in the behavior of these two types of coated panels during flight simulation testing, they will be discussed separately.

The two panels with the standard R-512E coating, BST-3 and BST-4, each completed 100 flight cycles without structural failure or localized coating failure within the central test region. One panel, BST-4, had no coating failures while the other, BST-3, experienced some localized coating failure outside the central test region. These sites were found predominantly at or near the tungsten inert gas (TIG) welds and attachment holes (see Figure 4-5) in the end straps. These areas were not prepared for coating in the same careful manner as the central test section and consequently were not typical of a section of flight hardware.

Color changes after 100 cycles were the same for both panels, a rather uniform dark grey-brown except for a lighter color at the edges. Initially, thin coating spall was quite extensive, particularly on the stiffener sides. The spall revealed a light grey color that gradually darkened as cycling progressed. Figure 5-37 shows a panel early in the cycling. Front and rear views of the two panels at the completion of 100 cycles are shown in Figures 5-38 to 5-41. This gradual darkening can be seen by comparing Figure 5-37 with Figure 5-41. In addition to the overall color changes, several mildly yellow areas were visible on the back side of the skin of the panels at the completion of 100 cycles. These areas, Figure 5-39, were quite similar to the oval areas found on the C-129Y and Cb-752 corrugated panels.

Several regions of heavier spall, some with a slightly blistered appearance, were observed on both panels after 100 flight cycles. These included (1) front side between fixture center load pad, (2) back side on skin and center web along electron beam weld, and (3) back side on skin in several of the yellowish areas. The blistered appearance was found primarily on the back side of the skin on either side of the center web. The effect extended almost the entire length of the panel and was most pronounced in the vicinity of the electron beam weld.

As with the C-129Y panels, the degree of bending about the transverse axis was quite small. This can be seen in Figures 5-42 and 5-43 for the two Cb-752 panels.

The localized coating failure sites described earlier for panel BST-3 were first observed after cycle 41. Two areas of substrate erosion were noted near the junction of the skin and the upper end strap. These sites, one in the skin and one in the end

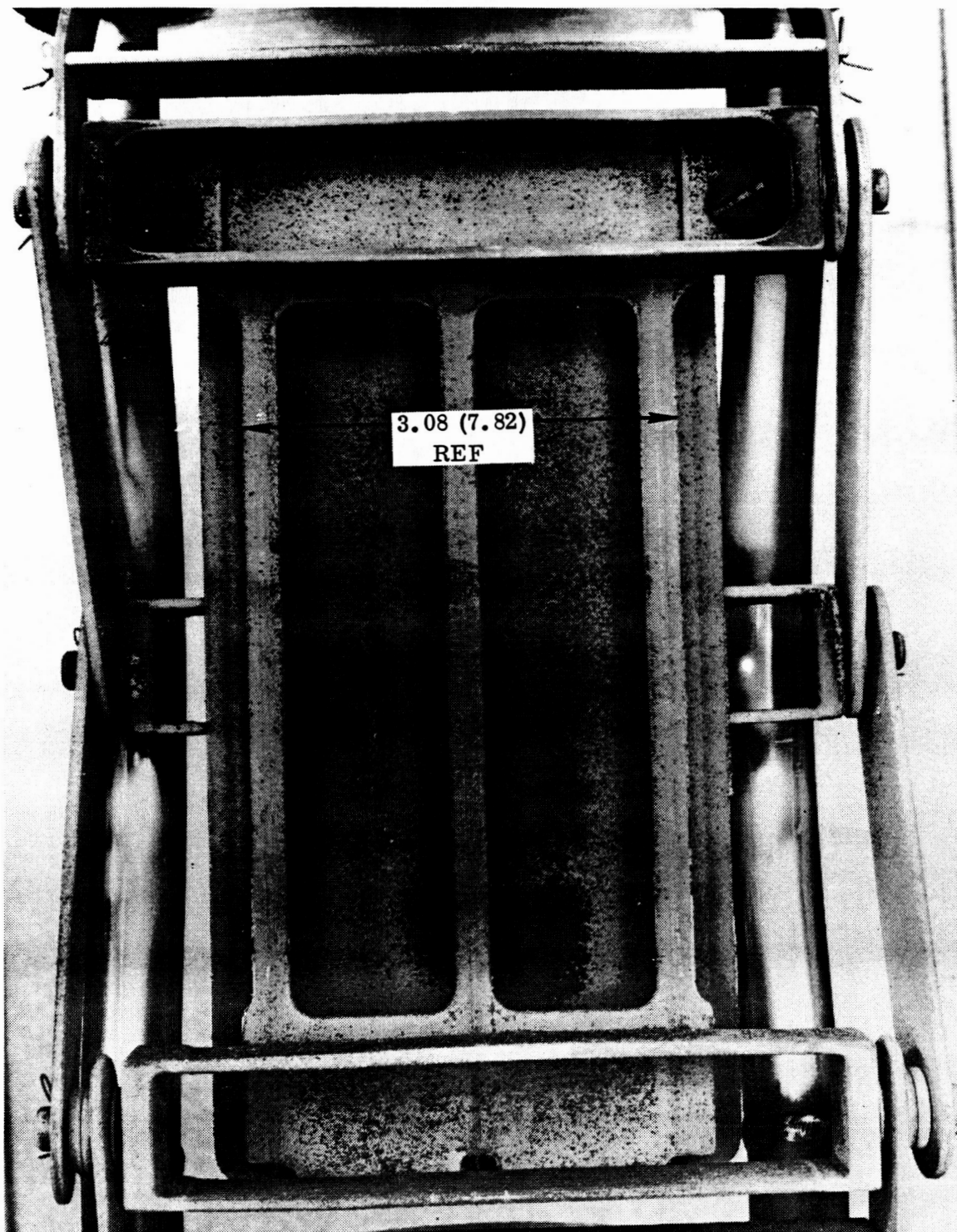


Figure 5-37. Front View of Panel BST-4 After 20 Flight Simulation Cycles (Photo 122485B)

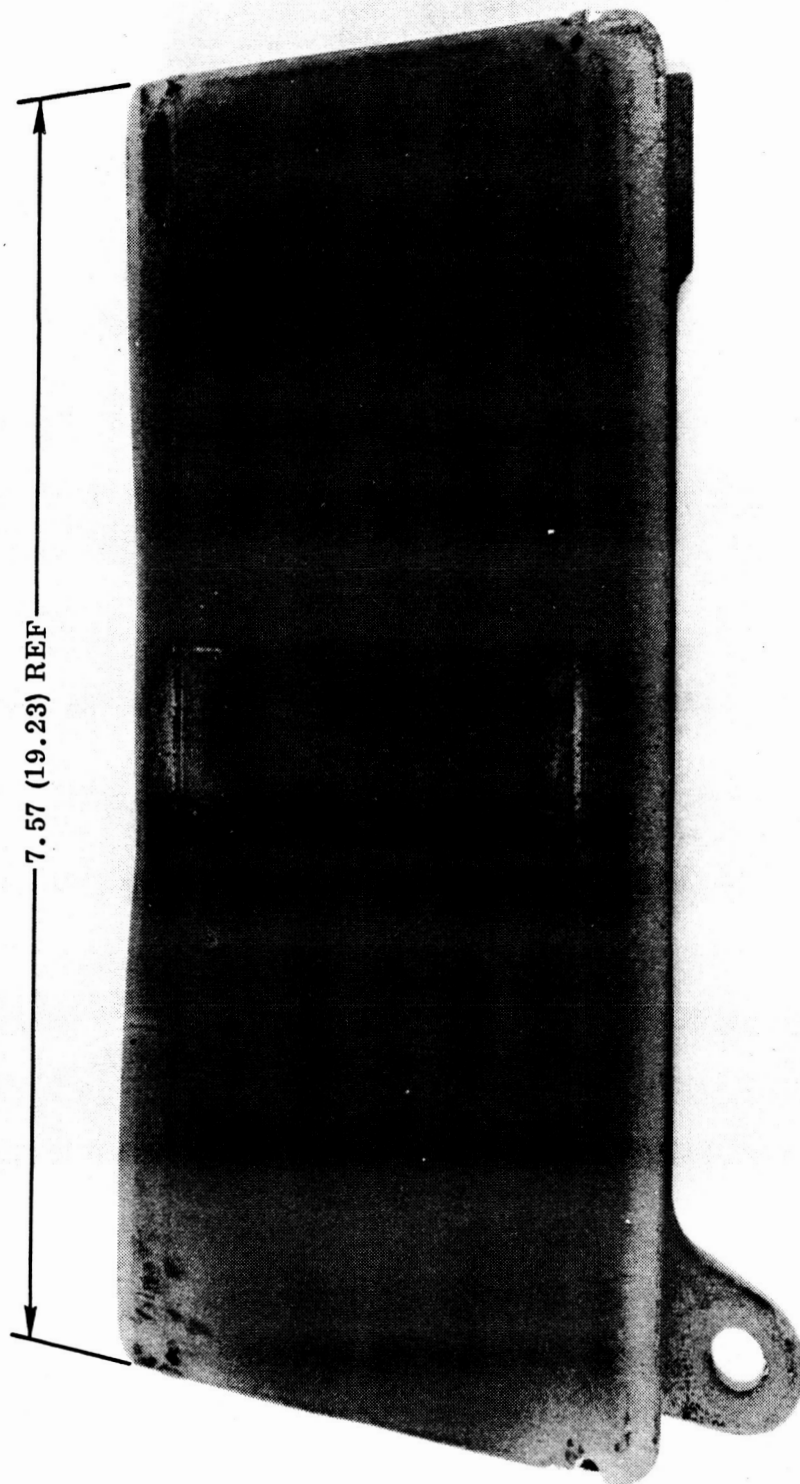


Figure 5-38. Front View of Panel BST-3 After 100 Flight Simulation Cycles (Photo 122530B)

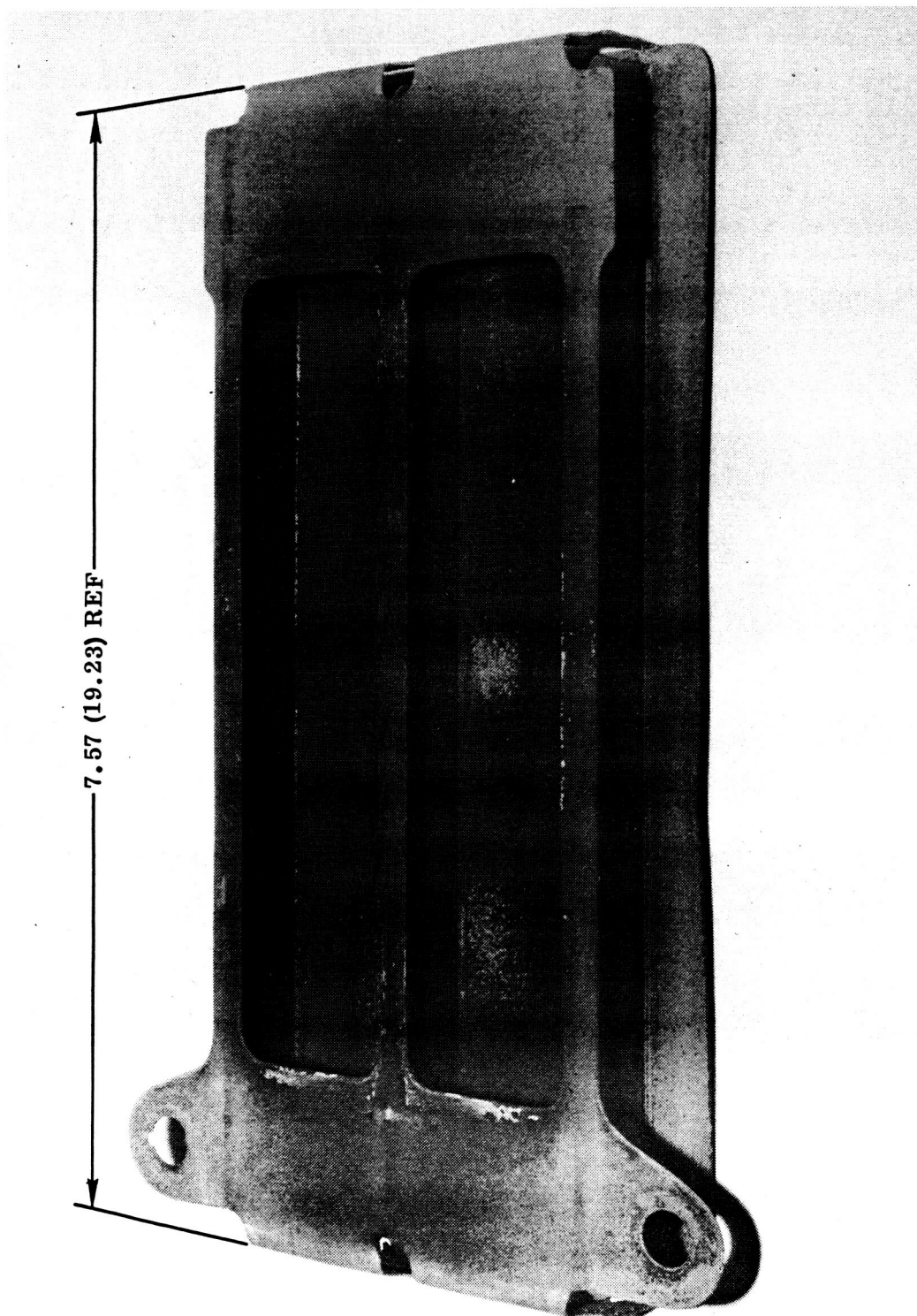


Figure 5-39. Rear View of Panel BST-3 After 100 Flight Simulation Cycles (Photo 122529B)

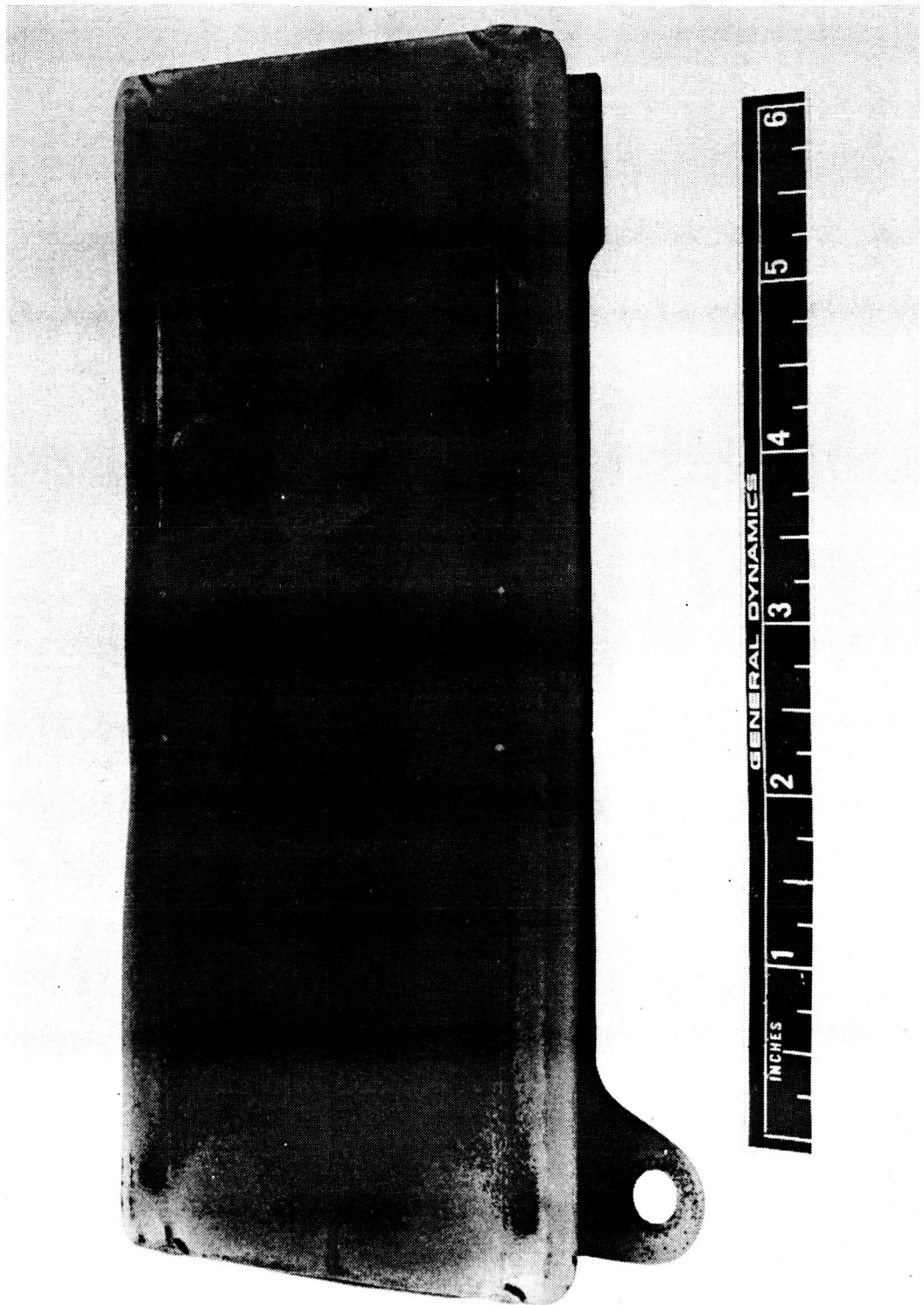


Figure 5-40. Front View of Panel BST-4 After 100 Flight Simulation Cycles (Photo 122817B)

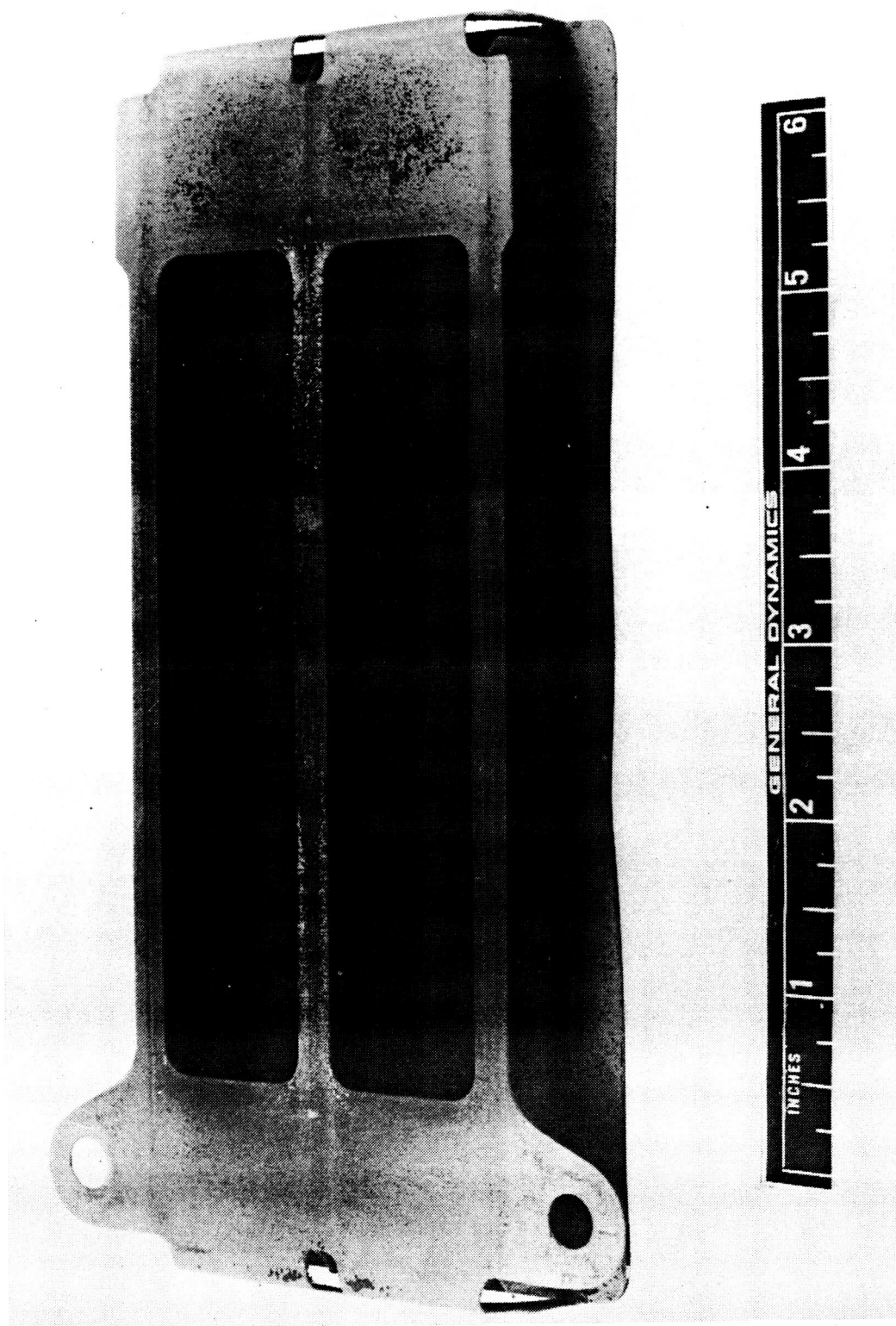


Figure 5-41. Rear View of Panel BST-4 After 100 Flight Simulation Cycles (Photo 122818B)

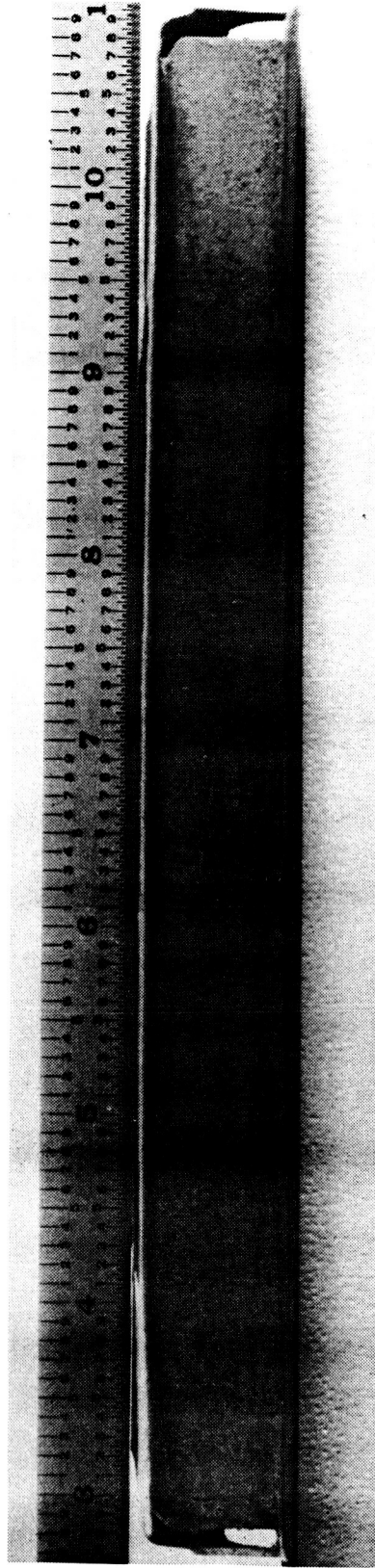


Figure 5-42. Bending About Transverse Axis of Panel BST-3 After
100 Flight Simulation Cycles (Photo 122531B)

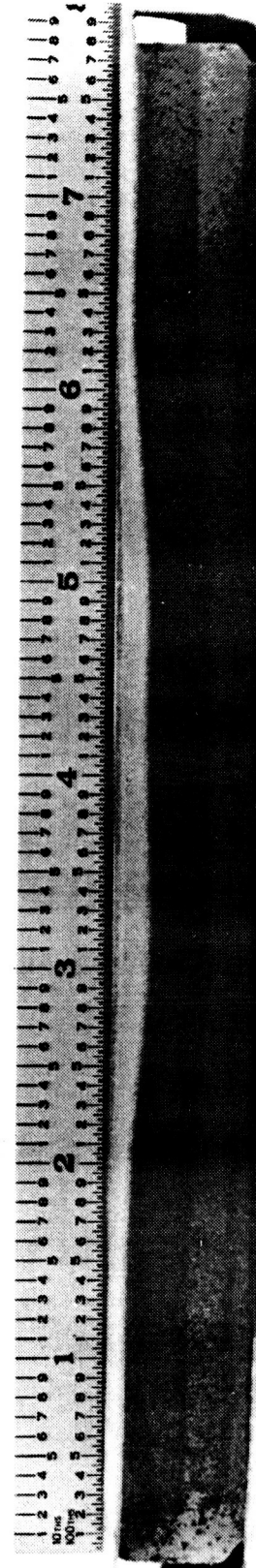


Figure 5-43. Bending About Transverse Axis of Panel BST-4 After
100 Flight Simulation Cycles (Photo 122815B)

strap, were either in or adjacent to one of the TIG welds joining the end strap to the skin. Similar erosion was observed at the junction of the skin and the lower end strap after 68 cycles, again in the TIG weld area. Also at 68 cycles a site was visible at the end of the rib near the electron beam weld joining the strap to the center rib. This site can be seen in Figure 5-39. At 79 cycles the first two coating damage sites had joined and completely consumed the connection between the skin and end strap. No structural failure occurred, however. This area is shown in Figure 5-44 along with coating erosion at one of the mounting holes.

The other two panels of this group, BST-1 and BST-2, were tagged with a radionuclide, ^{147}Pm , for NDE studies of coating processing and performance. While these panels completed 100 flight cycles with no structural failure, the performance of the coating was different than the standard R-512E applied to panels BST-3 and BST-4. It should be pointed out, however, that the panels containing the radionuclide were coated separately from the other panels, with different processing, a different operator, and independent furnace treatment (see Section 5.8).

The first tagged panel, BST-1, showed a localized coating failure after 64 cycles in the TIG weld area at the junction of the center web and the upper end of the stiffener. This was typical of previous oxidation sites observed on panel BST-3 with the standard coating. From 96 cycles on, however, attack occurred at several sites on the flange of the center web. These were edge-type failures and were located in the center of

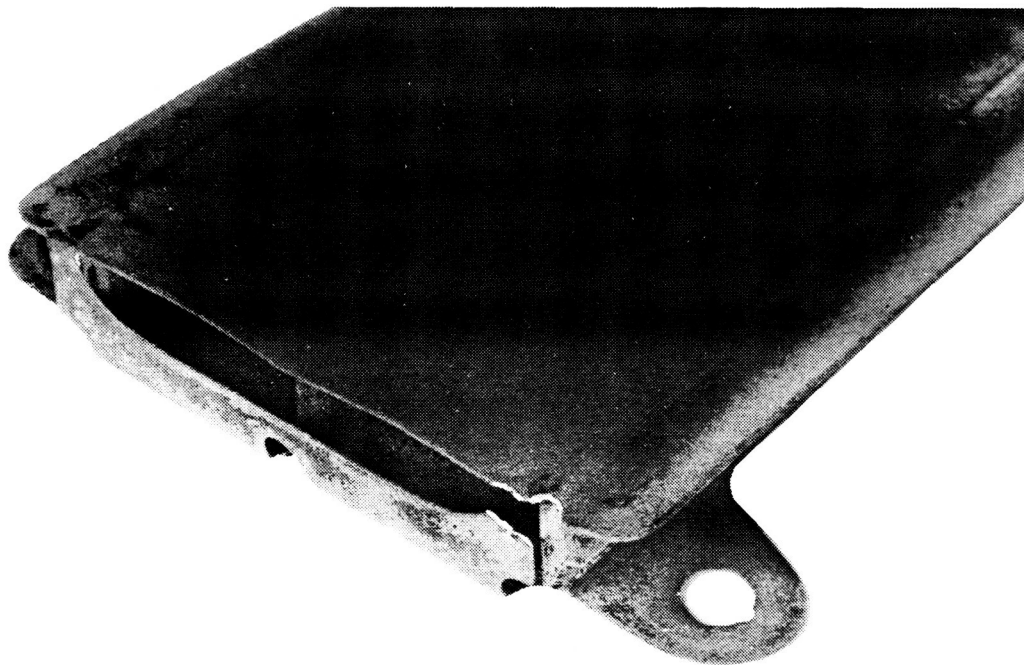


Figure 5-44. Coating Damage and Erosion of Panel BST-3 After 100 Flight Simulation Cycles (Photo 122527B)

the panel within the test region. Front and rear views of panel BST-1 after 100 flight cycles are shown in Figures 5-45 and 5-46. Several areas of substrate erosion are visible in Figure 5-45. The color change of this panel was much more uniform, particularly on the back side, than BST-3 and BST-4. The panel also showed much less surface spall on the back side, and the blistered appearance was not as evident. Figure 5-47 shows the slight amount of bending that occurred during the 100 cycles. Again the bending of the outer edges of the skin can be seen.

The second tagged panel, BST-2, was removed from test when an oxidation site was observed in the central test area after 66 cycles. The panel was sent to HiTemCo for a laboratory coating repair. The procedure was similar to that for application of the original coating. After repair, flight simulation testing of the panel was resumed. During the first 66 cycles color changes similar to those on the other tagged panel, BST-1, were obtained. One coating oxidation site was observed at 31 cycles but was located out of the central test area. The site was at the bottom of the skin at a TIG weld joining the end stiffener. At 66 cycles two additional oxidation sites were observed. One was located in the top end stiffener on the back side near the junction with the left side web. The second was at the edge of one of the outer flanges about 0.4 inch (1 cm) below the center of the panel, and it was for this that the test was halted in order to allow a coating repair. The oxidation site is shown before and after repair in Figures 5-48 and 5-49.

Upon resumption of cycling after the coating repair, little change occurred in the panel until about cycle 80. At this time, and continuing for the final 20 cycles, numerous small localized oxidation sites were observed. At the end of 100 cycles approximately 30 of these sites were visible. Two of them were surface-type failures and were the only ones found on the six Cb-752 panels tested. One was located on the front side of the skin at the electron beam weld joining an outer web to the face of the panel. The second was located on the back side of the skin approximately 0.4 inch (1 cm) from the center of the panel. Neither had completely penetrated the skin at the end of the 100 cycles.

At the end of 83 and 93 cycles on panel BST-2, "field" repairs were made to the localized failure sites using a modification of a technique developed by McDonnell Douglas Astronautics Company - East. The procedure was to remove the yellow oxide and cover the exposed area with a slurry composed of 60 weight percent Pyrex frit, 30 weight percent alumina, and 10 weight percent boron mixed with Microbrazing binder. For expediency, the repair coating was not given the normal firing at 2100° F (1422° K) but was used "as applied" with the flight simulation cycle providing the necessary firing conditions. These repairs were about 50% effective in preventing further substrate oxidation during the remaining cycles. The effectiveness could be greatly increased, however, with better preparation of the failure site (e. g., grit blasting) to remove all

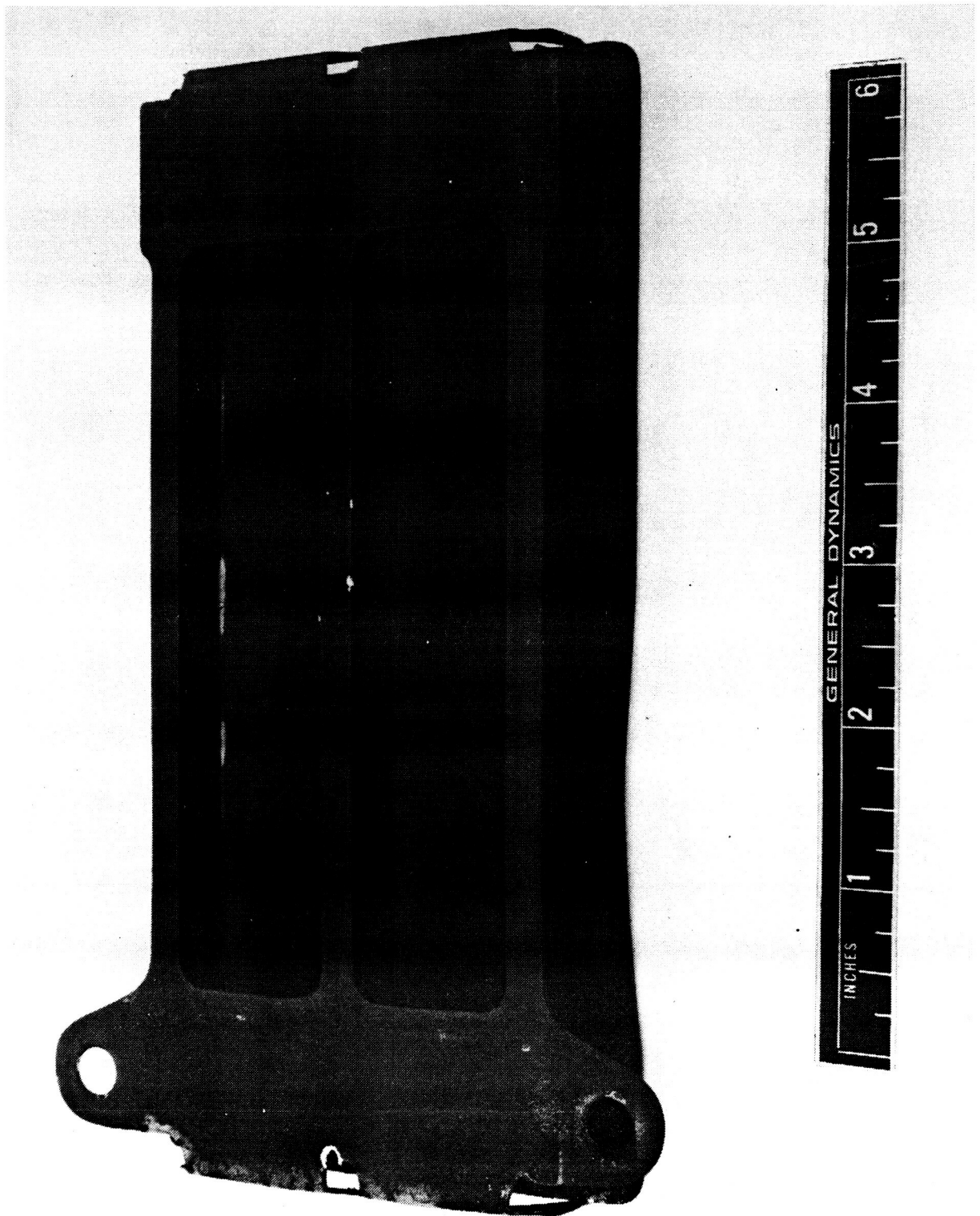


Figure 5-45. Front View of Panel BST-1 After 100 Flight Simulation Cycles (Photo 123799B)

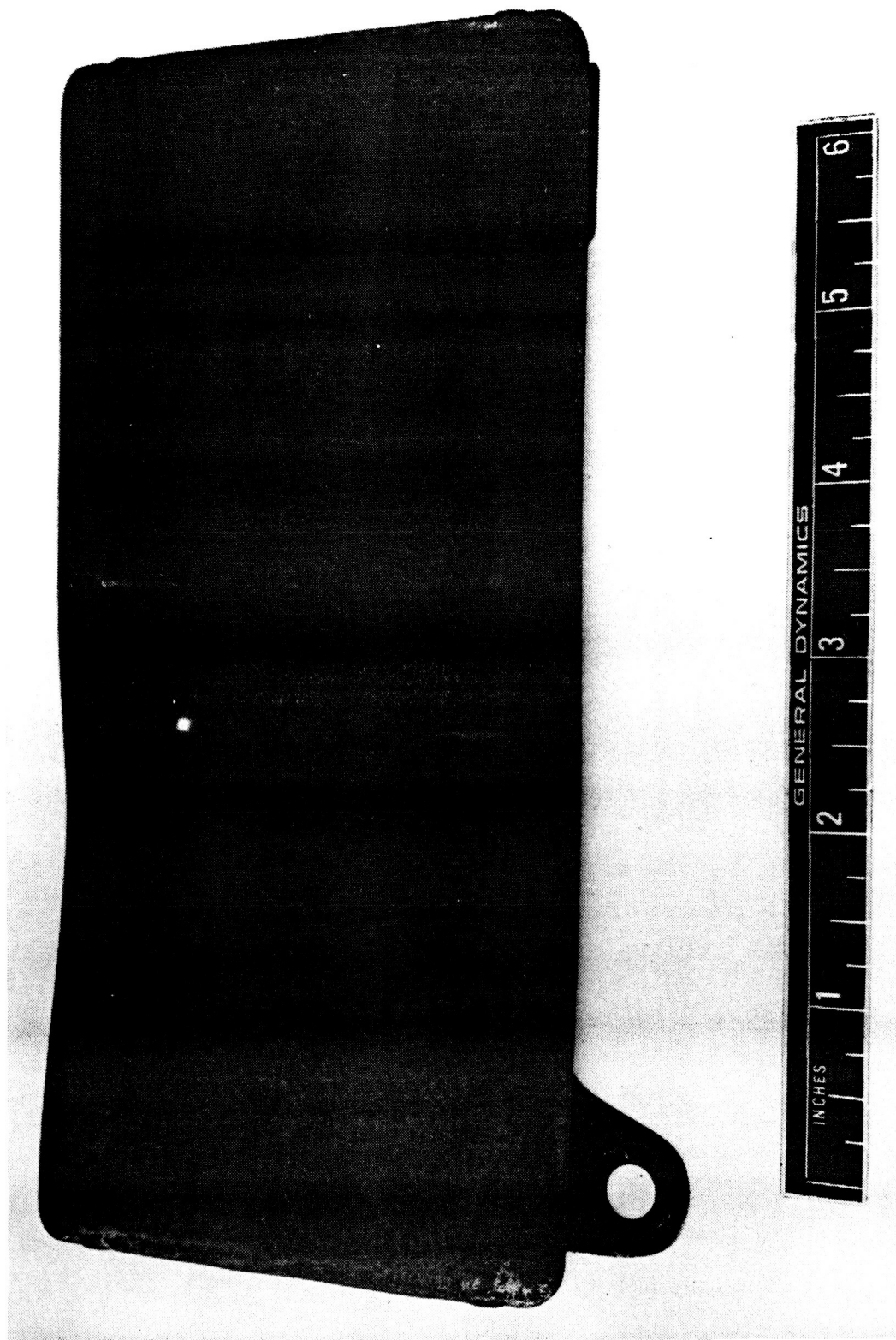


Figure 5-46. Rear View of Panel BST-1 After 100 Flight Simulation Cycles (Photo 123798B)

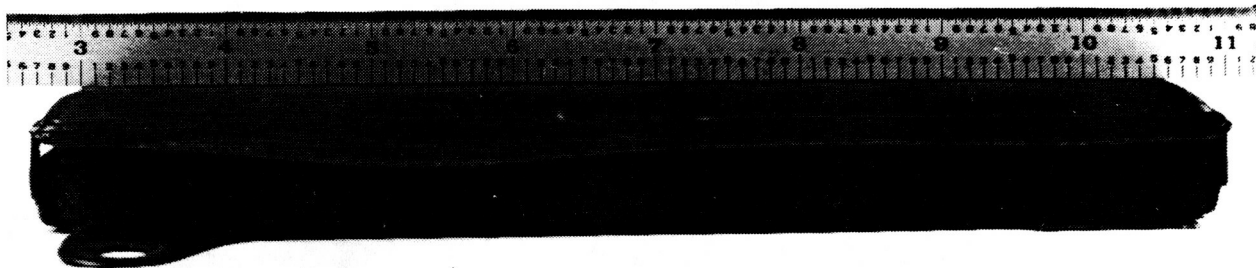


Figure 5-47. Bending of Panel BST-1 After 100 Flight Simulation Cycles (Photo 123802B)

traces of oxide and by using the recommended firing procedure. The laboratory repair performed by HiTemCo showed no evidence of renewed substrate oxidation at the end of 100 flight cycles.

Figures 5-50 and 5-51 show the panel at the completion of 100 flight cycles. Similar to the other tagged panel, BST-1, the color changes were more uniform; there was less surface spall and blistering, and the degree of skin buckling was less than that observed on the two untagged Cb-752 tee-stiffened panels. Also the circular or oval yellow areas that were found on most of the previously discussed panels were not observed on the two tagged panels. Figures 5-50 and 5-51 also show many of the localized coating failure sites including those at which a field repair was attempted. A close-up view of the HiTemCo repair is shown prior to cycling in Figure 5-52 and after 100 cycles (34 cycles after repair) in Figure 5-53. The effectiveness of the repair is readily apparent in these photographs.

5.6 Test Analysis

5.6.1 General. — The results of the flight simulation exposure testing (Table 5-2 and the preceding discussion) clearly demonstrated the capability of the Cb-752/R-512E material system to sustain the required 100 cycles in both corrugated and tee-stiffened panel configurations. At the completion of the 100 flight cycles, creep deformation was slight and, with the exception of the tagged panels, no coating breakdown or substrate erosion occurred in the central test regions. Typical of both alloys, oxidation sites were evident outside the main test area and were located primarily in the immediate vicinity of the TIG welds connecting the return tabs to the skin of the tee-stiffened panels. This region was very difficult to properly radius edges and to subsequently coat. The excellent performance of the Cb-752/R-512E during the subsized panel tests complemented its previous performance (no coating failures) during the Phase I evaluations (Reference 3). Therefore, the Cb-752/R-512E combination was selected as the only system to be used in the small size [12 by 16 inches (30.48 by 40.64 cm)] TPS.

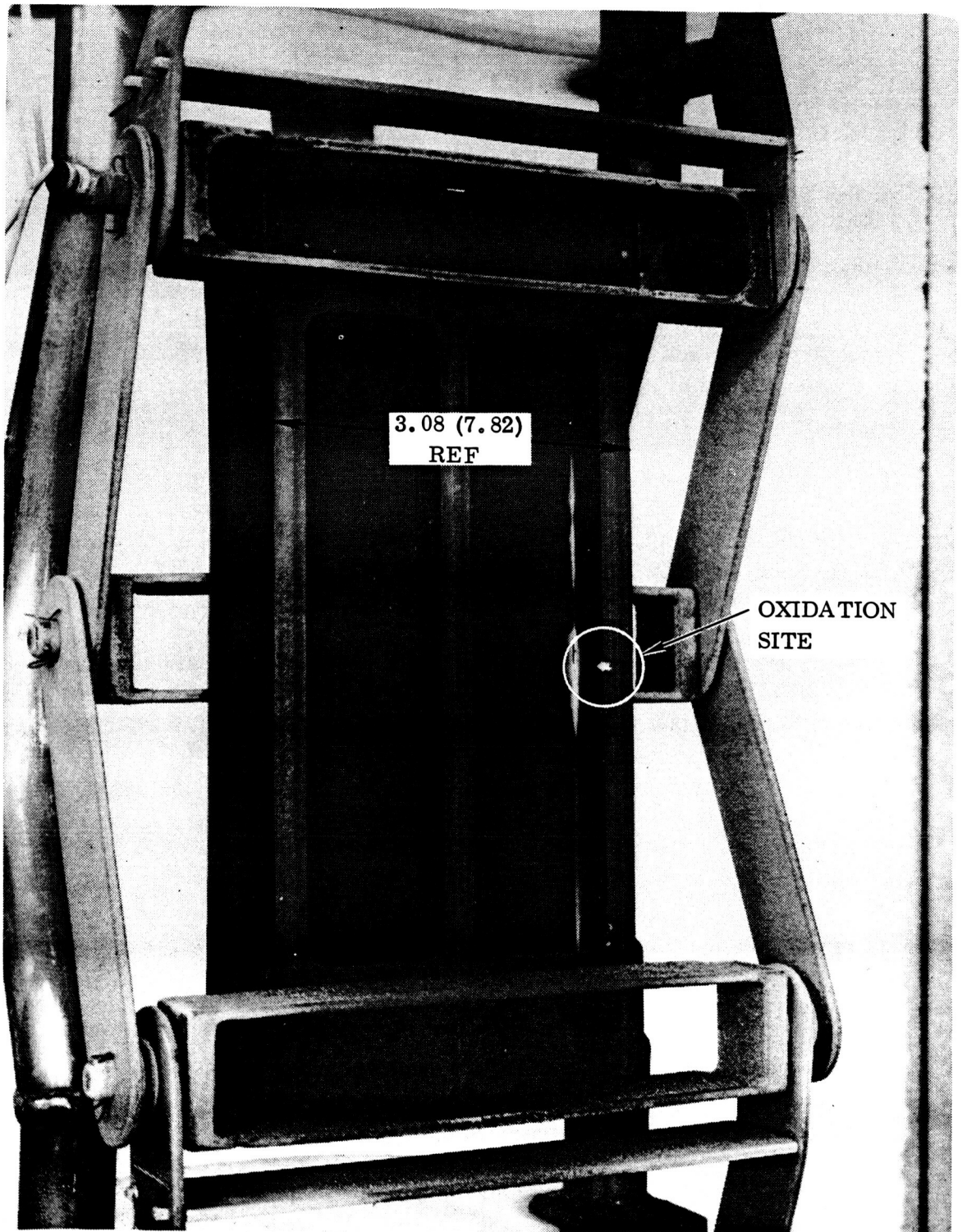


Figure 5-48. Panel BST-2 Oxidation Site at 66 Flight Simulation Cycles Before Coating Repair (Photo 121540B)

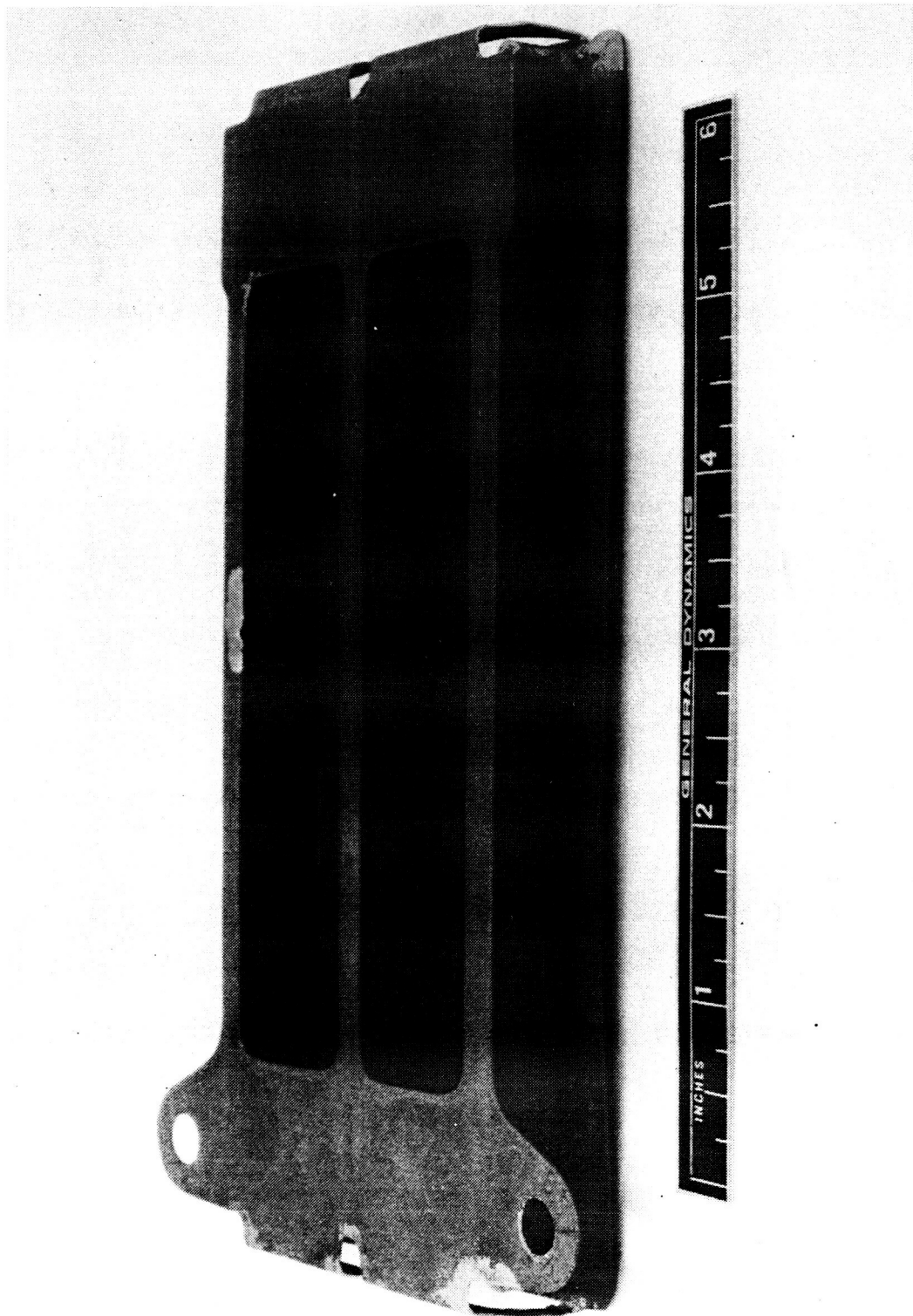


Figure 5-49. Panel BST-2 at 66 Flight Simulation Cycles
After Coating Repair (Photo 125205B)

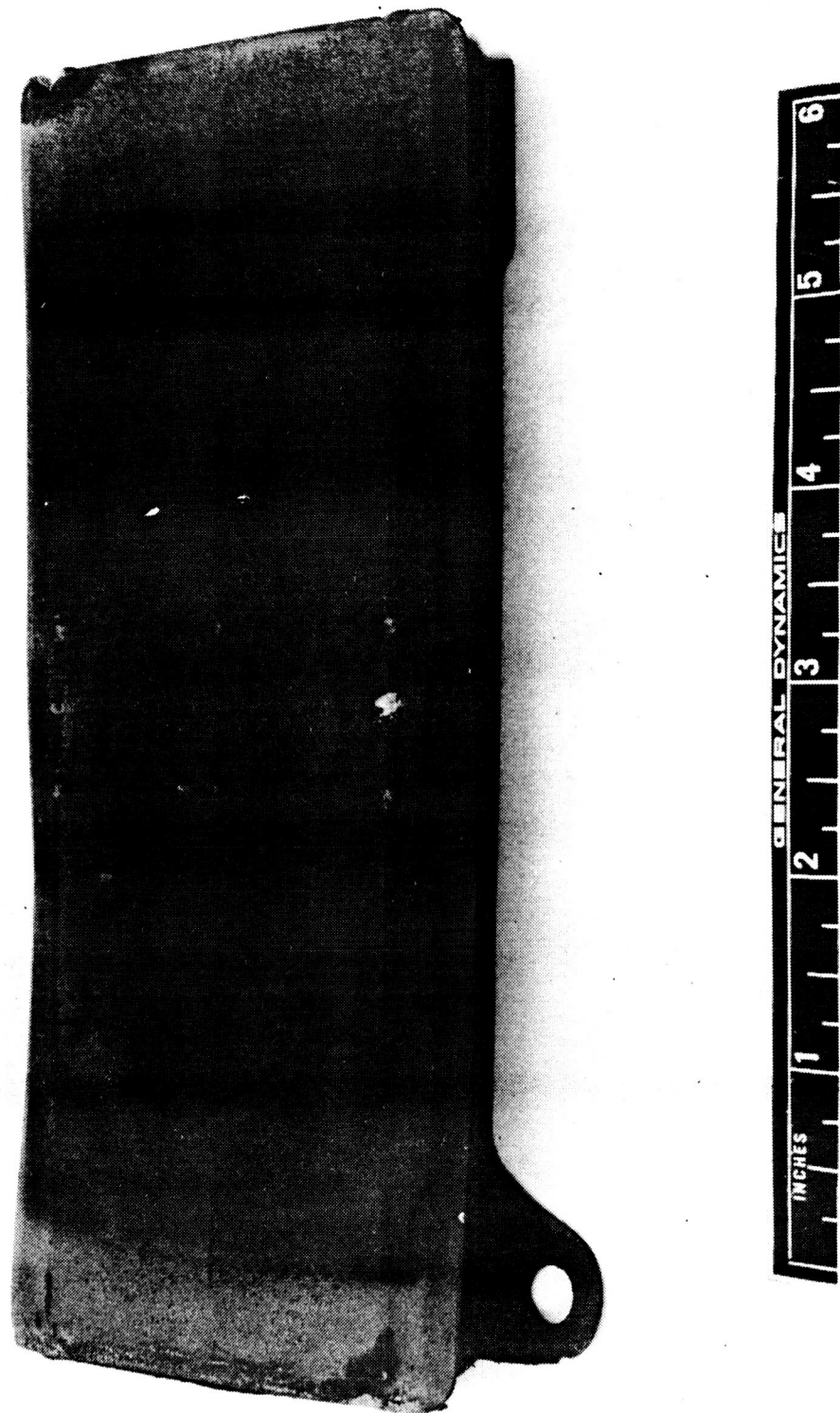


Figure 5-50. Front View of Panel BST-2 After 100 Flight Simulation Cycles -
34 Cycles After Coating Repair (Photo 125705B)

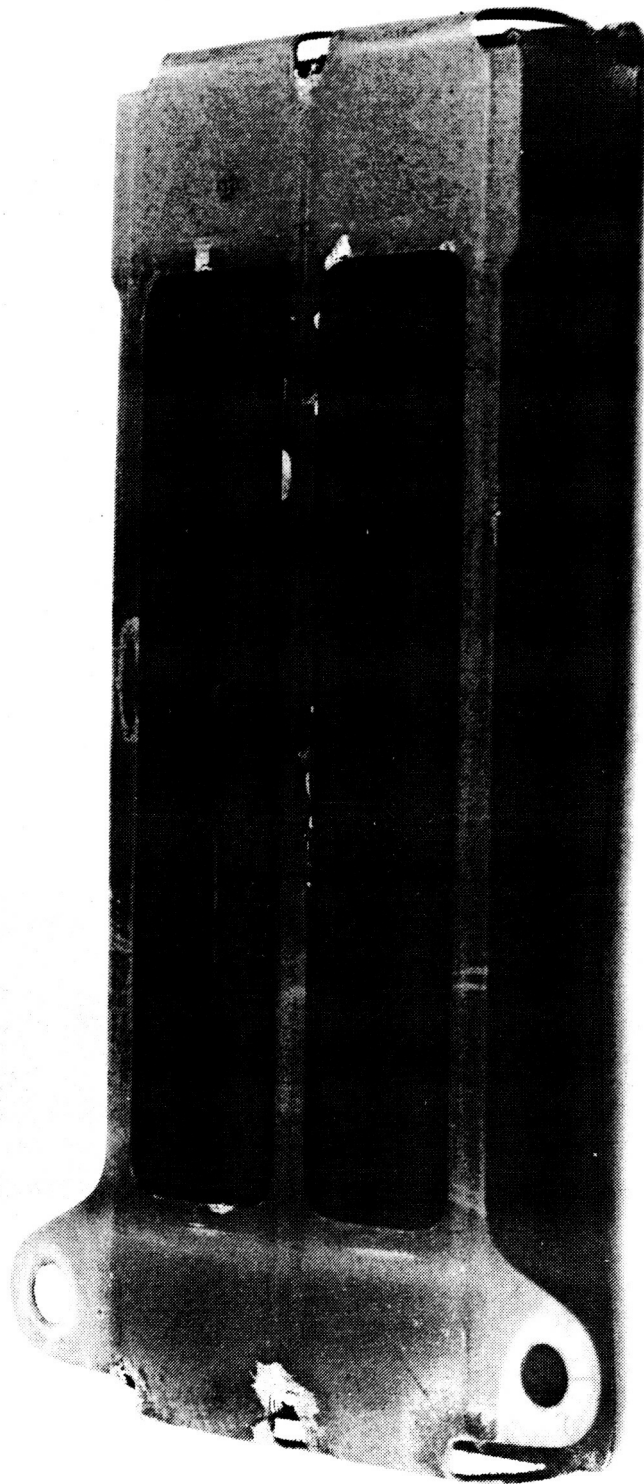


Figure 5-51. Rear View of Panel BST-2 After 100 Flight Simulation Cycles -
34 Cycles After Coating Repair (Photo 125704B)

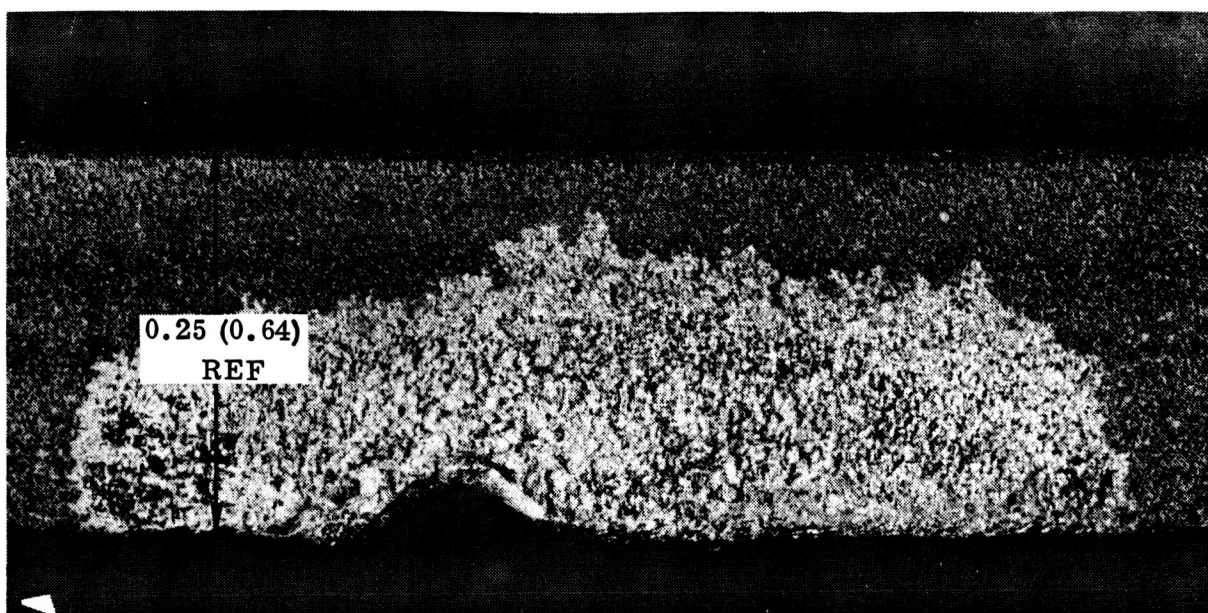


Figure 5-52. Close-up View of Panel BST-2 After Coating Repair Before Further Flight Simulation Cycling (Photo 125207B)



Figure 5-53. Close-up View of Panel BST-2 After Coating Repair and Further Cycling to 100 Flight Simulation Cycles (Photo 125713B)

The performance of the second material system, C-129Y/R-512E, also substantiated the observations and conclusions of the Phase I elemental tests. In those Phase I tests, 12 of 18 C-129Y/R-512E specimens sustained various degrees of edge erosion during the 100 flight simulation cycles. Also, the two tee-stiffened C-129Y panels both experienced coating damage and substrate oxidation at approximately 60 cycles. One C-129Y panel was continued in testing to 100 cycles with considerable attack of the substrate. The amount of deformation was surprisingly small, however, in view of the extensive material loss. The second C-129Y panel, experiencing similar attack, was removed from testing after 64 cycles. Edge attack was the dominant failure mode for both of the C-129Y/R-512E tee-stiffened panels. The two C-129Y corrugated panels, on the other hand, both survived 100 flight cycles with no coating breakdown or substrate contamination. Because of the temperature gradients in the simulator, edge temperatures of the corrugated panels were at least 250° F (394° K) lower than the control temperature at the center. Creep deflection of these panels consisted of a small amount of longitudinal bending and a slight flattening of the corrugation arch.

Two of the Cb-752 tee-stiffened panels were coated with the R-512E slurry modified with a radionuclide tagging agent for NDT studies. Both panels sustained numerous small oxidation sites during their 100 cycle exposure. The reason for the difference in performance between the untagged and tagged panels was not clearly established but was believed to have been related to the coating application process rather than the presence of the tag material (see Section 5.8). These small oxidation sites did, however, allow an attempt to evaluate the applicability of coating repairs, both field and laboratory, and to provide experience in the event that coating repairs are necessary in later stages of the program. The laboratory repair was completely successful, surviving 34 cycles with no further substrate erosion. While the field repairs were less effective due to improper surface preparation, the results were encouraging. The technique is an extremely simple one and with proper preparation of the defect site (i. e., complete removal of oxide) prior to slurry application it should prove to be very effective.

5.6.2 Cyclic creep. - The subsize tee-stiffened panels survived 100 flight simulation cycles with negligible permanent creep deflection while the corrugated panels had relatively large permanent deflection. Hence, the test results for the corrugated panel were selected for a post-test evaluation. Results for two specimens, BSC-1 and BSC-2, (Cb-752/R-512E) for which normal displacement and contour gage measurements were made at frequent intervals throughout the test are considered. It was not possible to measure true deflection of the specimens directly without removal from load apparatus at each inspection period. To compensate for this, normal offsets were measured at a number of locations along the span and the mid-span deflection determined from a faired curve drawn through a plot of these offsets versus span station. A creep deflection analysis was made using the creep data and analysis method given in Reference 3, Appendix C.

5.6.2.1 Deflection measurements: The normal displacements of two corrugated specimens (BSC-1 and BSC-2), measured from a reference surface, were taken at the specimen locations shown in Figure 5-54. Offsets were measured prior to exposure and at intervals of approximately 10 flight cycles for the first 40 cycles and at intervals of 20 cycles thereafter. Additional checks for overall distortion of the specimen cross sections were made using a contour gage at the same time intervals. The sections checked were at the forward support points and at mid-span.

A summary of the displacement measurements is shown in Table 5-3. Plots of normal displacement versus span are presented in Figure 5-55 for specimen BSC-1. Since in general the specimen was not parallel to the reference surface, the average of values at symmetrical points is plotted rather than the raw data. The maximum creep deflection (the deflection at mid-span relative to the support points) at each time is determined from faired curves drawn through the plotted points. Plots of creep deflection versus cycles are given in Figures 5-56 and 5-57. The final deflections (100 cycles) are 0.078 inch (0.198 cm) and 0.072 inch (0.183 cm) for BSC-1 and BSC-2 respectively.

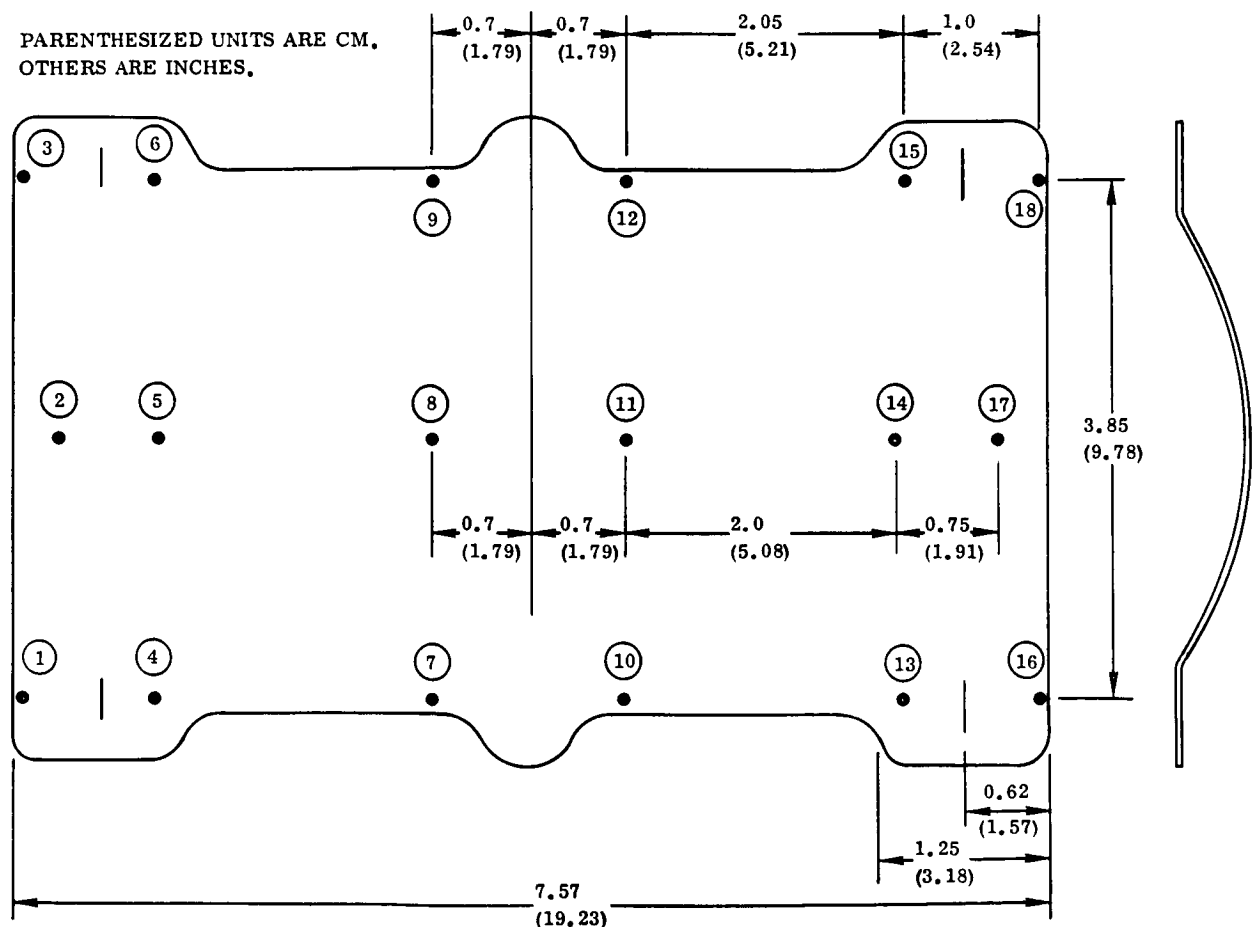


Figure 5-54. Location of Deflection Measurements

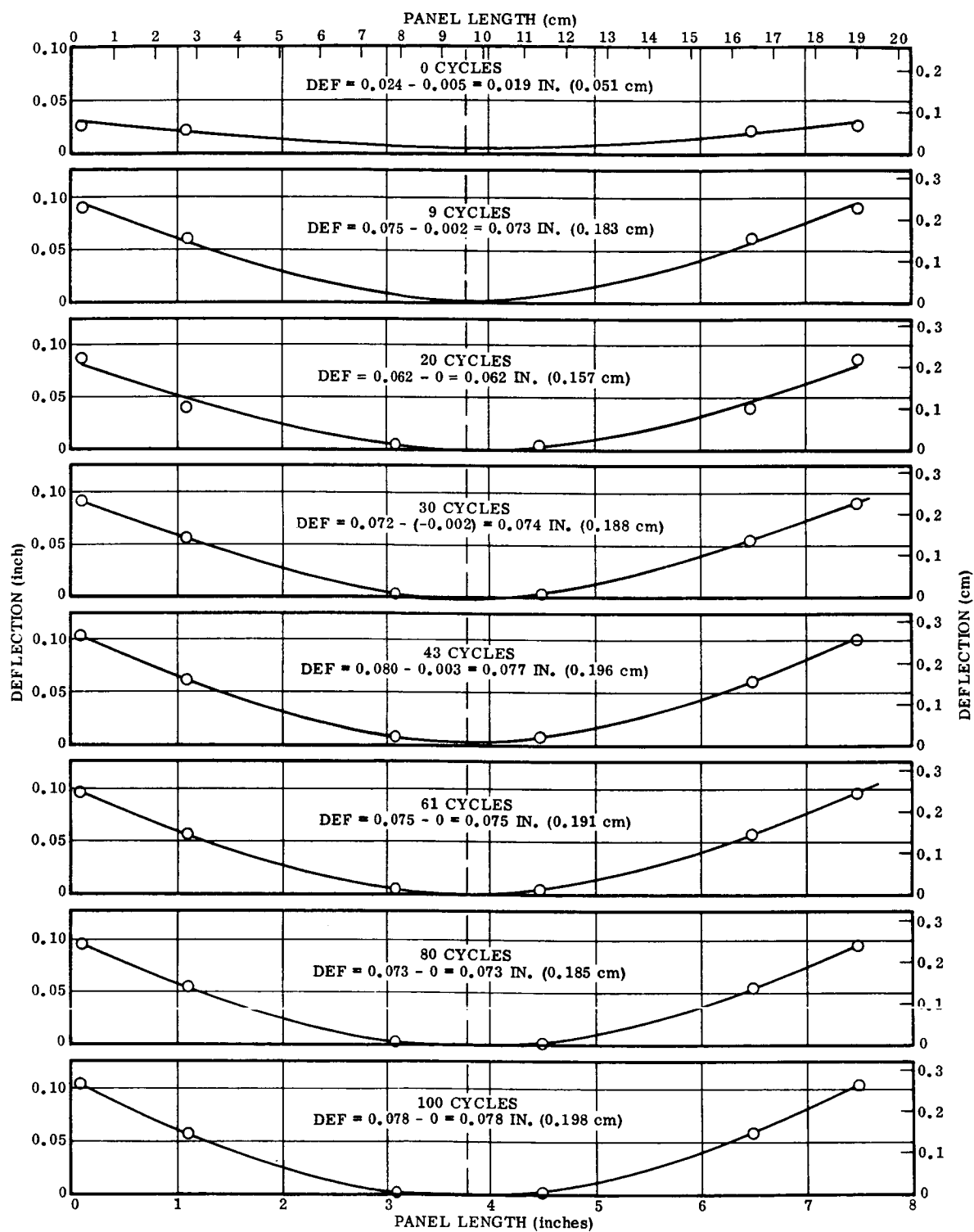


Figure 5-55. Spanwise Deflection Versus Span for Specimen BSC-1

Table 5-3. Summary of Derived Test Deflections

Specimen BSC-1			Specimen BSC-2		
Cycles	inch	mm	Cycles	inch	mm
0	0.019	0.483	0	-0.032	-0.813
9	0.073	1.854	10	0.069	1.753
20	0.062	1.575	20	0.060	1.524
30	0.074	1.880	30	0.069	1.753
43	0.077	1.956	40	0.062	1.575
61	0.075	1.905	60	0.064	1.626
80	0.073	1.854	80	0.069	1.753
100	0.078	1.981	100	0.072	1.829

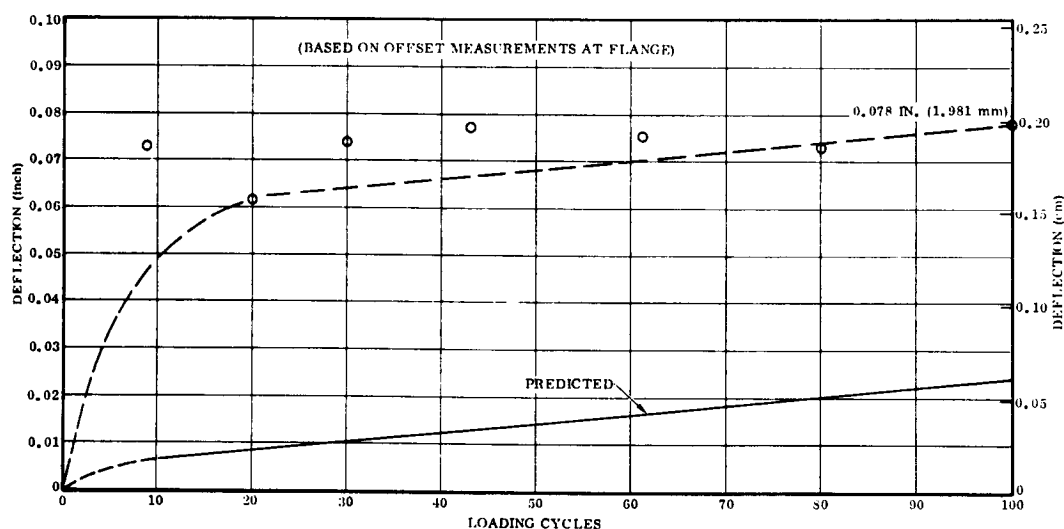


Figure 5-56. Creep Deflection Versus Cycles for Specimen BSC-1

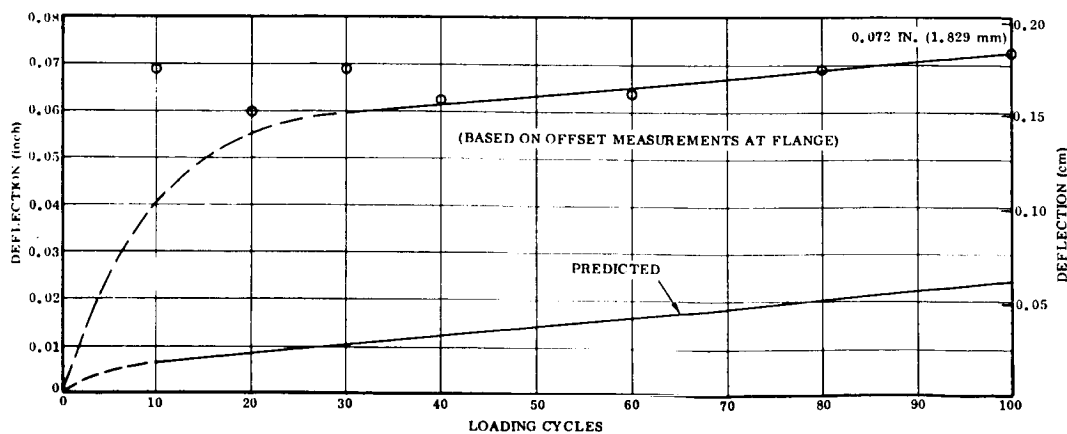


Figure 5-57. Creep Deflection Versus Cycles for Specimen BSC-2

5.6.2.2 Contour gage measurements: An initial visual inspection of the specimens gave the impression that the end cross sections had flattened by lateral spreading at the supports. However, the contour gage profiles indicate negligible distortion at the ends while the mid-span section had increased in depth by approximately 0.1 inch (0.25 cm). In addition, the contour gage profiles indicate that the initial (0 cycles) overall depth of cross section was less than the design of 0.5 inch (1.27 cm) at all locations. Tracings of the initial and final contours at the upper end and at mid-span of specimen BSC-1 are shown in Figure 5-58. The nominal design cross section and dimensions derived from the contour gage profiles are shown in Figure 5-59.

MEASURED USING CONTOUR GAUGE WITH
SPECIMEN MOUNTED IN FIXTURE

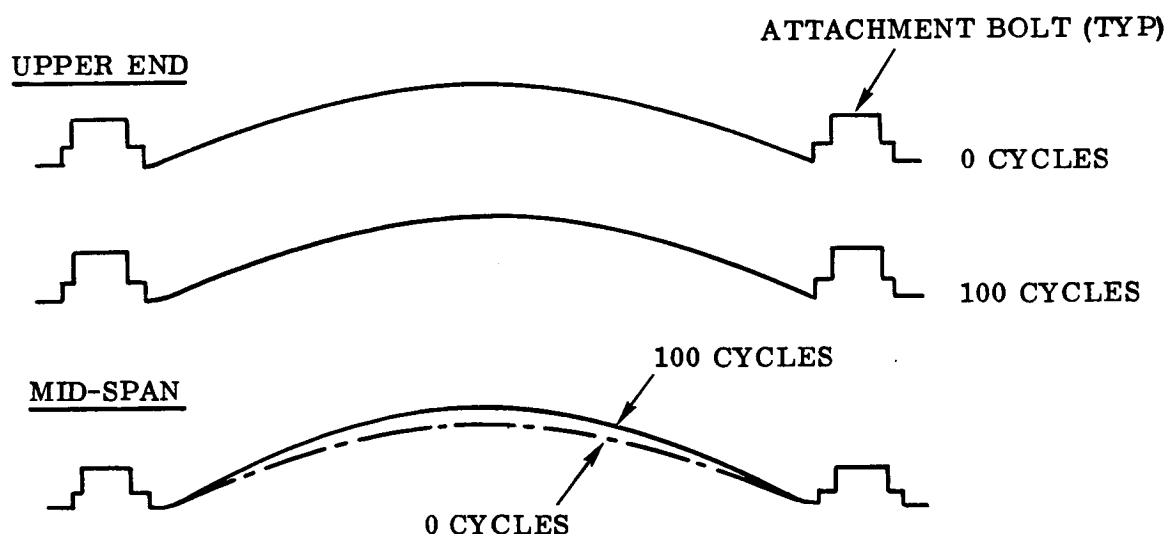
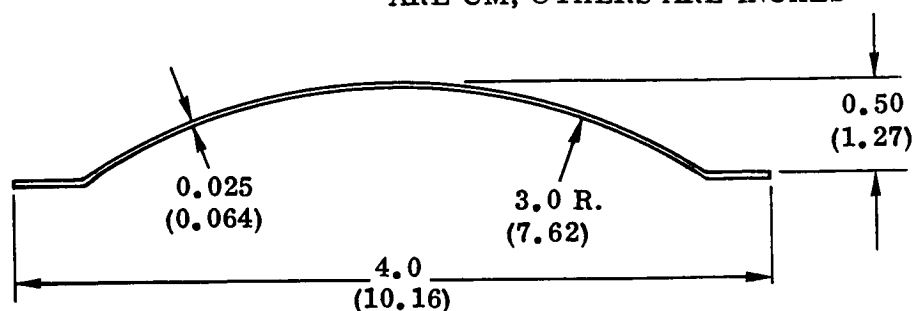


Figure 5-58. Comparison of Specimen BSC-1 Cross Section Profiles Before and After Exposure

5.6.2.3 Creep deflection analysis: A creep deflection analysis was made for the corrugated Cb-752/R-512E test specimen. The analysis utilized the Larson-Miller parameter plot for 1% creep strain and the correction factor for cyclic creep $[R = 9.289 - 0.00158(\sigma) + 2S]$ given in Reference 3. An initial substrate consumption during coating equal to one-half of this nominal coating thickness [0.003 inch (0.076 mm)] was assumed. Substrate consumption during cycling is based on the curve for Cb-752/R-512E given in Reference 3, Figure C-1.

The temperature distribution over the specimen cross section was based on data obtained from a temperature survey made during calibration. A plot of temperature versus specimen half-width at the time of maximum temperature is shown in Figure 5-60. The applied test loads schedule used in the analysis is given in Table 5-4. The analysis is based on the nominal design corrugation section. Internal stresses due to

CORRUGATED TEST PANEL — DIMENSIONS IN PARENTHESIS
ARE CM; OTHERS ARE INCHES



SECTION GEOMETRY

SPECIMEN NO.	CYCLES	APPROXIMATE RAD. (R)			HEIGHT (h)		
		TOP	MIDSPAN	BOTTOM	TOP	MIDSPAN	BOTTOM
BSC-1	0	3.80 (9.65)	3.64 (9.25)	3.70 (9.40)	0.42 (1.07)	0.44 (1.12)	0.42 (1.07)
	100	3.56 (9.04)	2.91 (7.39)	3.56 (9.04)	0.45 (1.14)	0.53 (1.35)	0.44 (1.12)
BSC-2	0	3.65 (9.27)	4.23 (10.74)	3.62 (9.19)	0.42 (1.07)	0.38 (0.97)	0.44 (1.12)
	100	3.38 (8.59)	2.92 (7.42)	3.24 (8.23)	0.46 (1.17)	0.54 (1.37)	0.48 (1.22)

Figure 5-59. Initial and Final Dimensions Derived From Contour
Gauge Measurements (in Test Fixture)

mechanical bending loads, temperature gradients, and accumulated creep strain were considered. The effect of shear was neglected (see Section 5.6.2.4).

Internal stresses and creep rates were computed at each time indicated on the simulated flight profile shown on Figure 5-61. Two analyses were made. In the first analysis 100 loading cycles were simulated by 10 analysis cycles with the increment of creep strain in each time increment factored by 10. In the second analysis a total of 10 loading cycles was simulated on a cycle-by-cycle basis. The computed deflections for 10 loading cycles are in good agreement [0.0062 inch (0.157 mm) and 0.00615 inch (0.156 mm) respectively]. A plot of predicted creep deflection versus semi-span is presented in Figure 5-62.

Table 5-4. Subsize Panel Load Profile

Test Cycle Time seconds	Pressure		Temperature Range		Applied Load	
	psi	(kN/m ²)	° F	(° K)	pounds	(kg)
0 to 170	3.0	20.7	70-340	294-444	170.3	77.3
170 to 700	2.0	13.8	340-960	444-789	113.1	51.3
700 to 1000	0.0	0.0	960-70	789-294	0.0	0.0
1000 to 1300	0.15	1.0	70-2400	294-1587	8.4	3.8
1300 to 2200	0.15	1.0	2400-2160	1587-1455	8.4	3.8
2200 to 3000	0.45	3.1	2160-1600	1455-1144	25.3	11.5
3000 to 3600	0.85	5.9	1600-400	1144-478	47.9	21.7

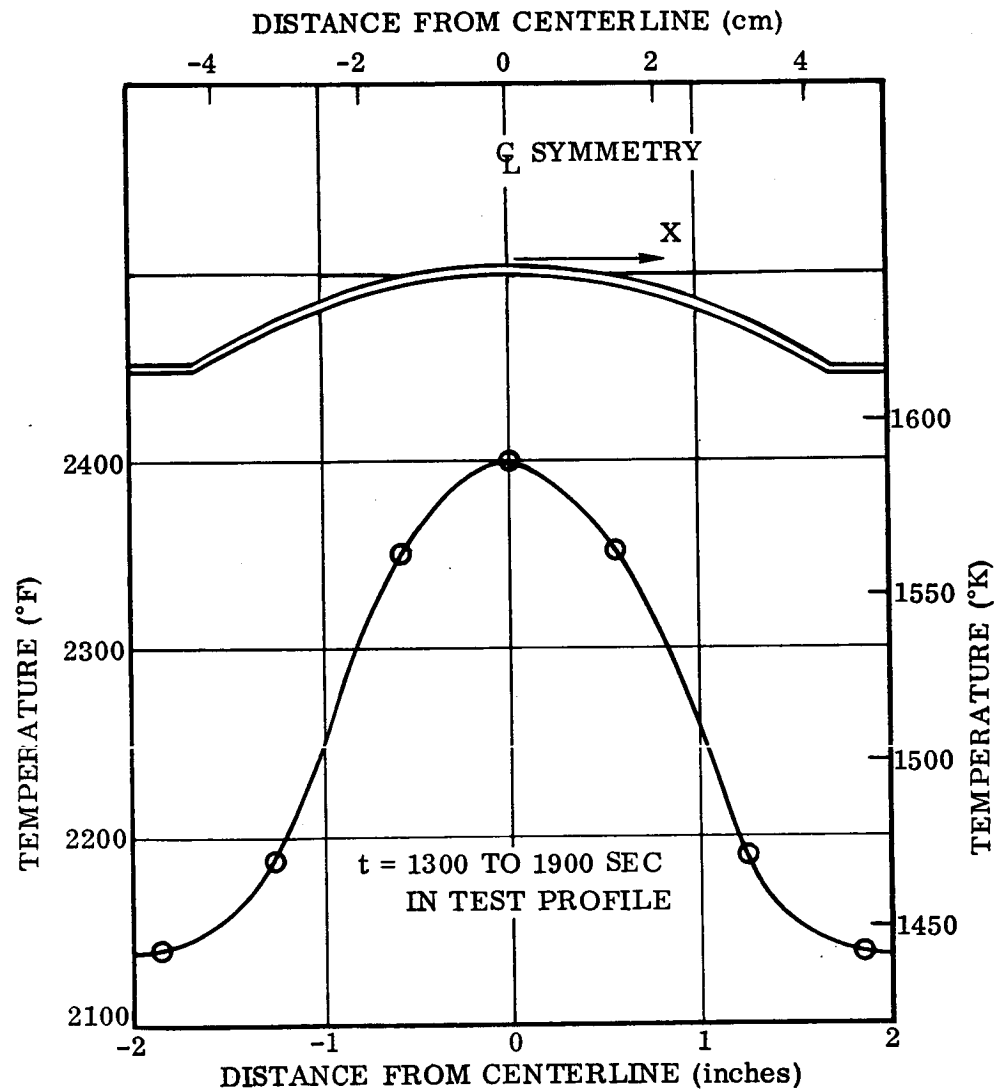


Figure 5-60. Temperature Distribution Over Corrugation Section at Time of Maximum Temperature

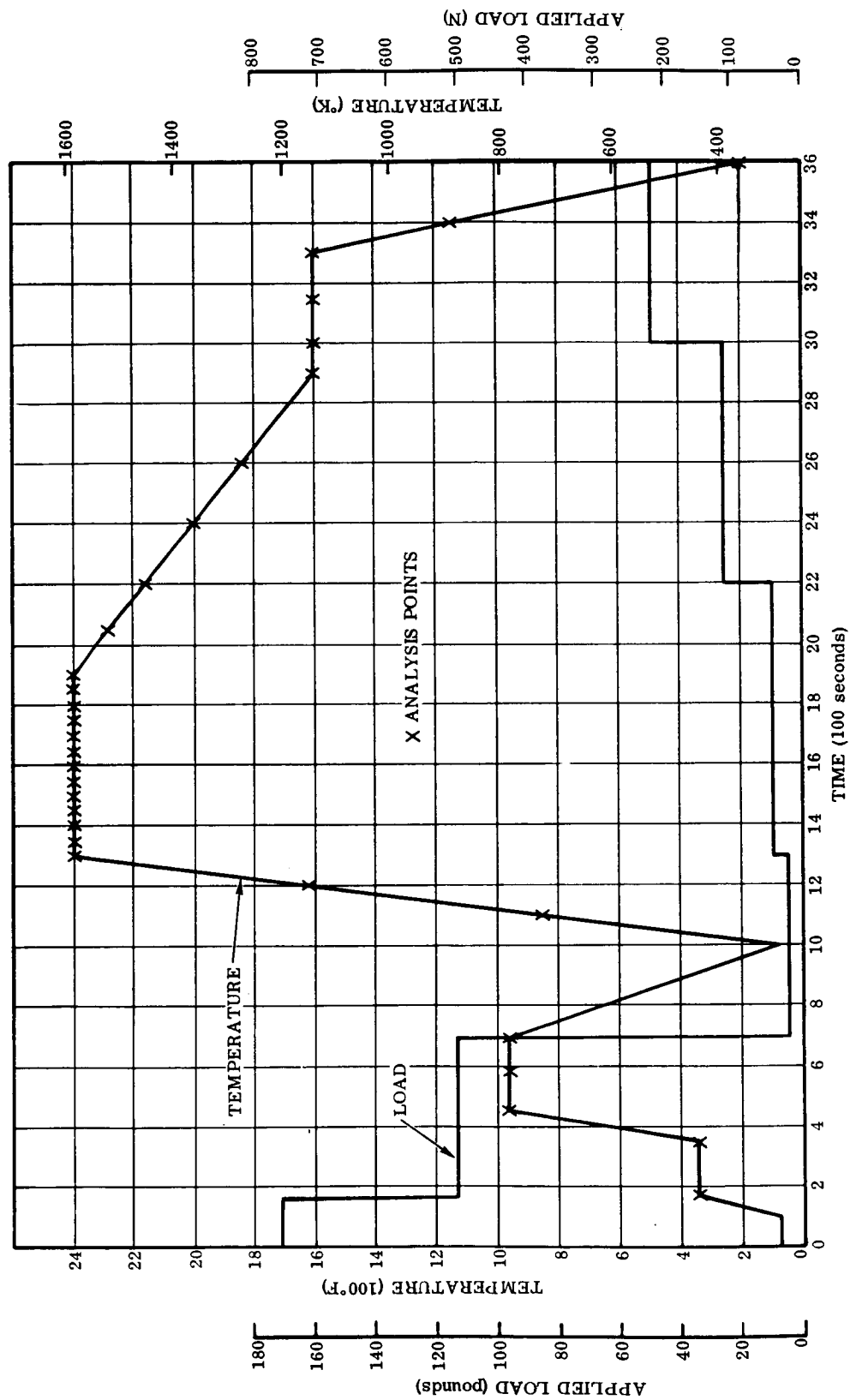


Figure 5-61. Test Load and Temperature Profile

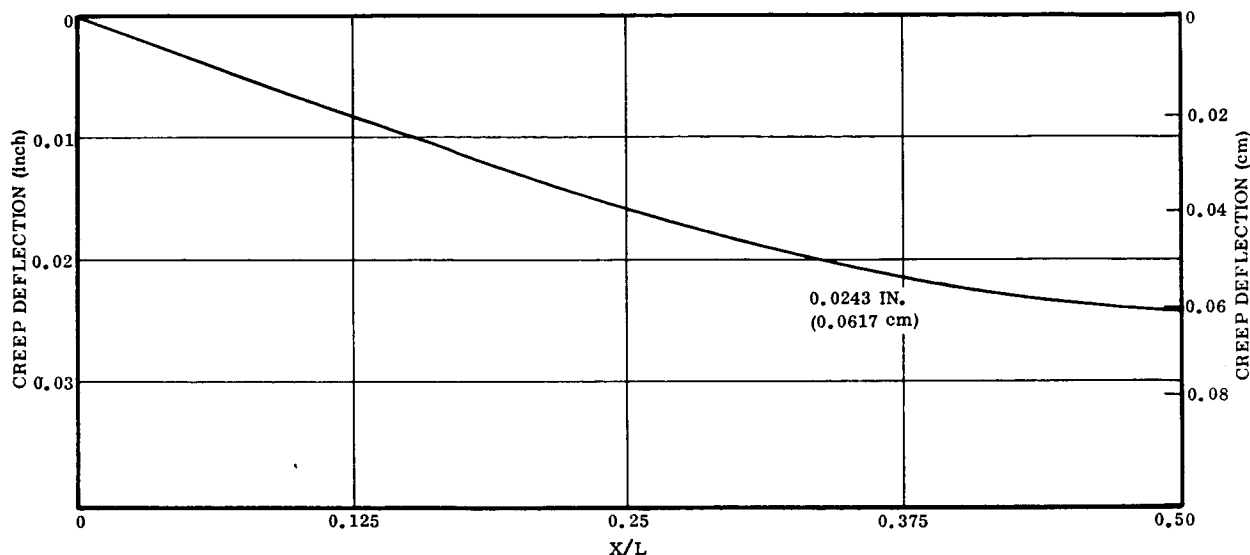


Figure 5-62. Predicted Creep Deflection Along Semi-Span of Corrugated Panel (100 Cycles)

5.6.2.4 Summary of creep analysis: Due to the distortion of the cross section, the true creep deflection of the specimen cannot be defined with any assurance. Values of 0.078 inch (1.98 mm) and 0.072 inch (1.83 mm) were found at the flanges for specimens BSC-1 and BSC-2 respectively. However, the deflections measured at the crown of the corrugations are essentially zero, apart from local deformation at the load points (see Figures 5-16 through 5-19). Assuming the deflection measured at the flanges is the true deflection, this value is approximately three times the predicted value of 0.024 inch (0.619 mm). Factors that would contribute to this discrepancy are:

- (1) Increased stress levels due to the reduced overall depth of the specimens.
- (2) An increased effective stress due to the interaction of shear and bending stress.

The following comparison illustrates the fact that in the short subsize panels the effect of shear is exaggerated. That is, the maximum shear is greater than in the corresponding uniformly loaded beam having the same maximum bending moment. In addition the maximum value exists over a greater part of the span. Hence, it is considered that creep deformation due to shear may be significant and since the peak shear and bending stresses interact, a further increase in creep rate could result. However, as previously stated, the true deflection of the specimen cannot be accurately determined. Therefore, the additional analysis required to predict the magnitude of the additional deflection due to shear for comparison purposes was not warranted. A comparison of the shear distributions for a 12.0 inch (30.48 cm) uniformly loaded beam and test beam is shown below.

Condition: Normal pressure = 3.0 psi (20.7 kN/m²)

$$R_1 = 55.34 \text{ lb (246.15 N)}$$

$$R_2 = 81.46 \text{ lb (362.33 N)}$$

Maximum shear at R_2

$$= 81.46 - (11.4)(1.55)$$

$$= 63.76 \text{ lb (283.60 N)}$$

Sub-Scale Test Panel

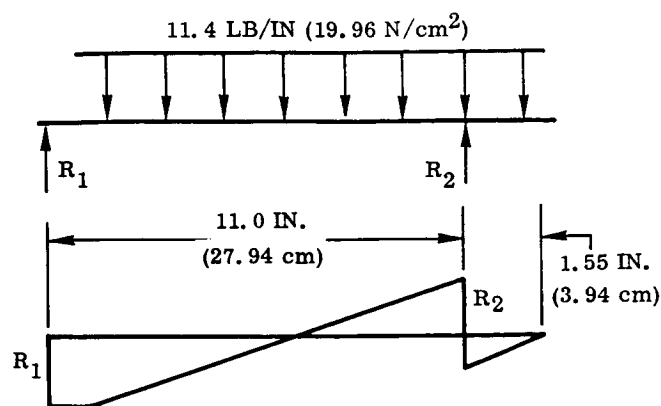
$$P = \frac{3.158 R}{1.462 - \delta_e}$$

$$R = \frac{P(1.462 - \delta_e)}{3.158}$$

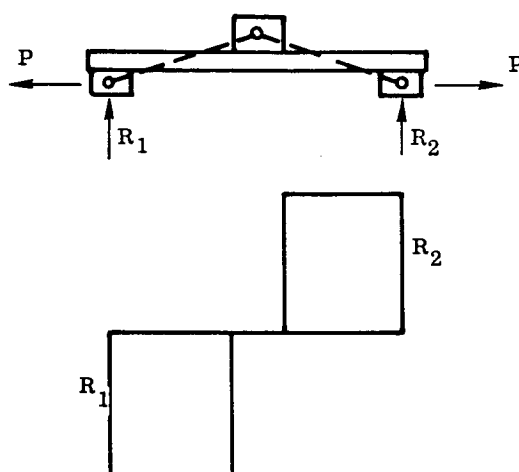
$$\delta_e = 0.017 \text{ in. (0.043 cm)}$$

$$\therefore R = \frac{170.3(1.462 - 0.017)}{3.158}$$

$$= 77.92 \text{ lb (346.59 N)}$$



SHEAR DISTRIBUTION



5.7 Metallographic Examination

Results of the flight simulation metallographic study are presented in five sections, one for unexposed panels and one each for the four alloy/configuration groups. The two as-coated, unexposed and seven exposed panels that were examined are listed in Table 5-5. Also included in the table are the number and locations of the sections that were mounted and polished and a brief comment on the condition of each panel. The section locations can be found by referring to Figures 5-63 and 5-64, which show how the panels were sectioned. For section locations 1, 2, 3, and 4 on the tee-stiffened panels the entire cross section through the thickness of the panel was included, i.e., the flange, web, and a portion of the skin.

The normal procedure for preparing the metallographic specimens was to use a very light etch (HF - HNO₃ - H₂O) to bring out the details in the coating and diffusion zone. Several of the mounts were later re-etched for a longer period of time to show the grain structure of the substrate and details of the electron beam weld joints.

Table 5-5. Metallographic Examination of Subsize Panels

Alloy	Configuration	Specimen No.	Number of Mounts	Section Location	Condition of Panel
C-129Y	Corrugated	YSC-3	4	7, 9, 10, 13	100 cycles, no coating failures
	Tee-stiffened	YST-3	2	2, 3	100 cycles, severe coating breakdown and substrate erosion in central test area
		YST-4	5	1, 2, 3, 5, 6	64 cycles, severe coating breakdown and substrate erosion in central test area
Cb-752	Corrugated	BSC-5	2	7, 9	As-coated
		BSC-1	7	7, 8, 9, 10, 11, 12, 13	100 cycles, no coating failures
	Tee-stiffened	BST-5	3	1, 2, 4	As-coated
		BST-3	5	1, 2, 3, 5, 6	100 cycles, no coating failures in central test area
		BST-1	1	1	100 cycles, tagged panel, several coating breakdown and substrate erosion sites in central test area
		BST-2	2	1, 3	100 cycles, tagged panel, several coating breakdown and substrate erosion sites in central test area, coating repairs made during the course of testing

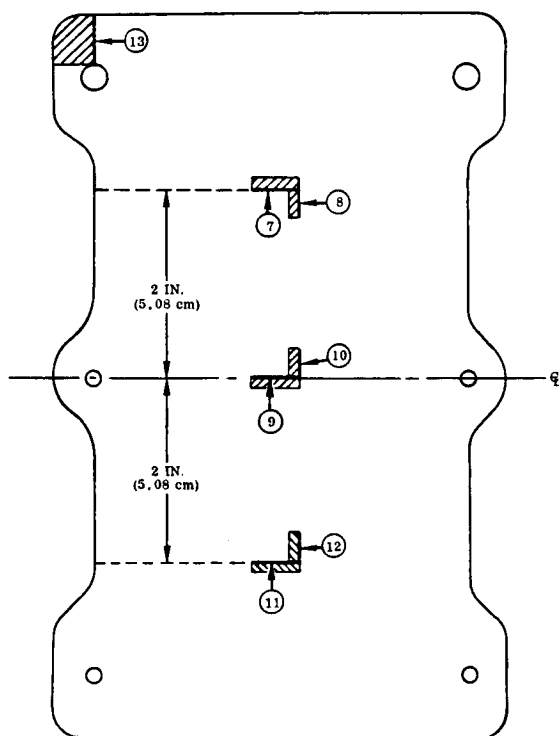


Figure 5-63. Location of Sections for Metallographic Examination of Corrugated Panels

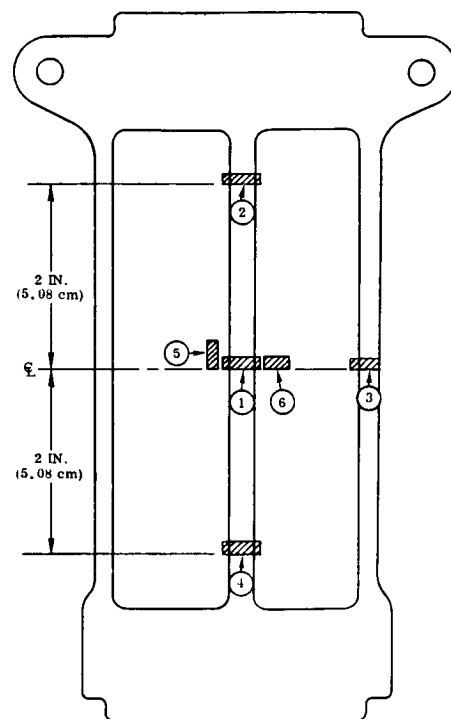


Figure 5-64. Location of Sections for Metallographic Examination of Tee-Stiffened Panels

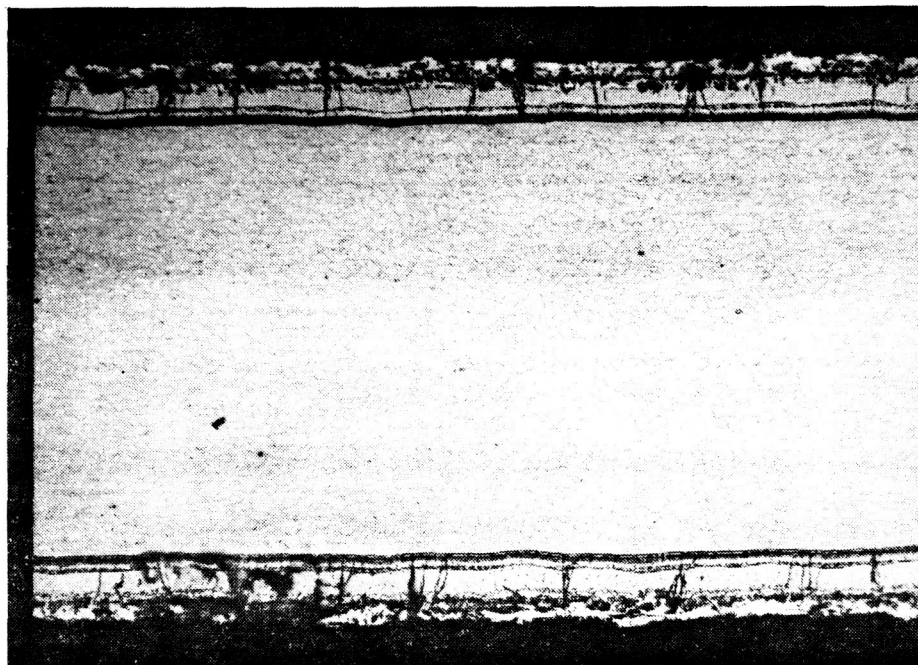
Several of the specimens were also etched by an electrolytic technique similar to anodizing. This method was particularly useful for revealing areas of oxygen contamination. Photomicrographs of these specimens were taken in color to more clearly illustrate the regions of contamination.

5.7.1 As-coated panels. — Two panels, one corrugated and one tee-stiffened, were examined in the as-coated condition for use as a baseline for comparison with the exposed panels and to determine coating uniformity. Both panels were of the Cb-752 alloy as this was the alloy selected for the Phase III effort. Photomicrographs of the unexposed panels are shown in Figures 5-65 to 5-67 for the corrugated panel and 5-68 to 5-71 for the tee-stiffened panel. The light etch used in Figures 5-65 and 5-66 reveals the various coating layers and numerous fine cracks typical of a silicide coating. These cracks, which are always present in silicide coatings, arise either during the coating process as a result of residual compressive stresses because of the large difference in specific volume of the substrate and the coating, or during cooldown after coating because of tensile stresses generated by thermal expansion mismatch between coating and substrate. Higher magnification views of the coating/substrate interface are shown in Figures 5-66 and 5-71. The absence of subsurface cracks parallel to the coating/substrate interface as well as voids or porosity is an indication of good coating

adherence. No evidence of contamination or formation of second-phase particles is visible in the substrate at these magnifications. The coating is composed of layers or zones (as many as seven can be distinguished) of disilicides and subsilicides, primarily MSi_2 in the outer layer, and M_5Si_3 in the inner layers, where $\text{M} = (\text{Cb}, \text{Cr}, \text{Fe})$.

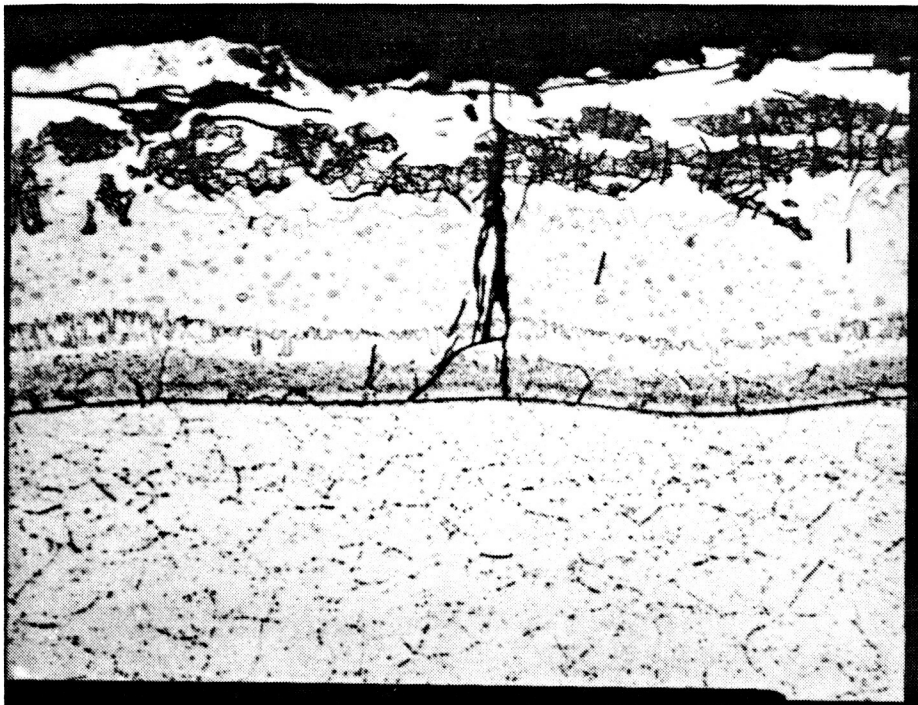
Figure 5-67 shows the more heavily etched microstructure. The longer etch tends to remove the detail of the coating and increase the crack size by chemical attack. The grain structure is generally equiax, although not particularly uniform, with the grain size about the same for the two panel configurations. The welds joining the web to the flange and the skin are clearly visible in Figures 5-68 and 5-69. They appear to be free of cracks, porosity, and gross contamination. Some undercutting (Figure 5-68) has occurred in the web/flange weld as a result of the multiple passes required in repair welding panel BST-5.

The photomicrograph shown in Figure 5-70 was taken at the edge of the flange at location 1 and again shows the good coating coverage typical of the HiTemCo process. It was at this edge that most of the test section coating failures occurred in Panels YST-3, YST-4, BST-1, and BST-2.



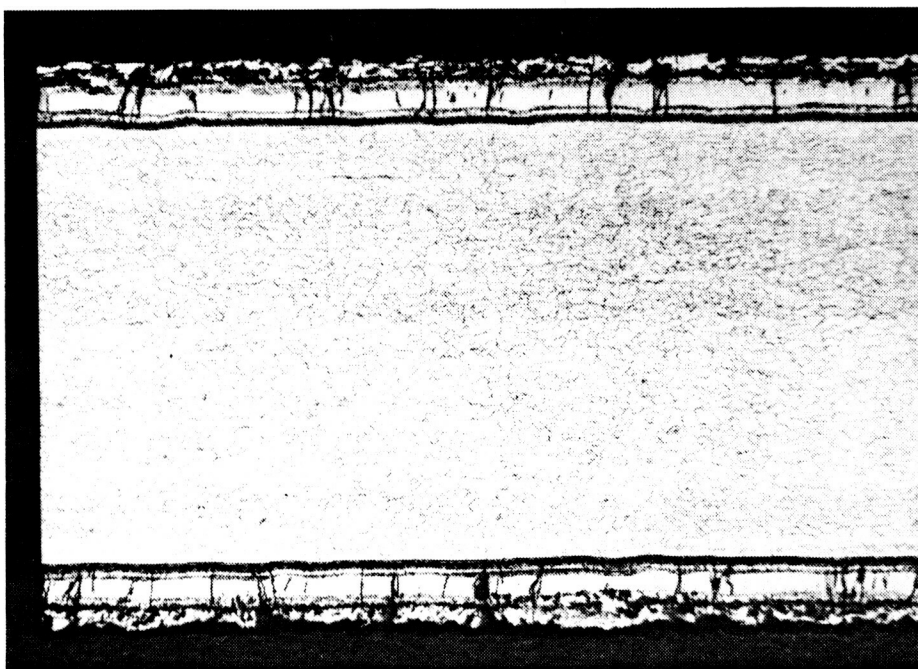
Magnification: 100X
Etch: Light
Panel No.: BSC-5
Flight Cycles: 0
Location: 9
Negative No.: D-2754
Mount No.: 467-P

Figure 5-65. Microstructure of Unexposed Cb-752/R-512E Corrugated Panel



Magnification: 500X
 Etch: Light
 Panel No.: BSC-5
 Flight Cycles: 0
 Location: 9
 Negative No.: D-2755
 Mount No.: 467-P

Figure 5-66. Microstructure of Unexposed Cb-752/R-512E Corrugated Panel



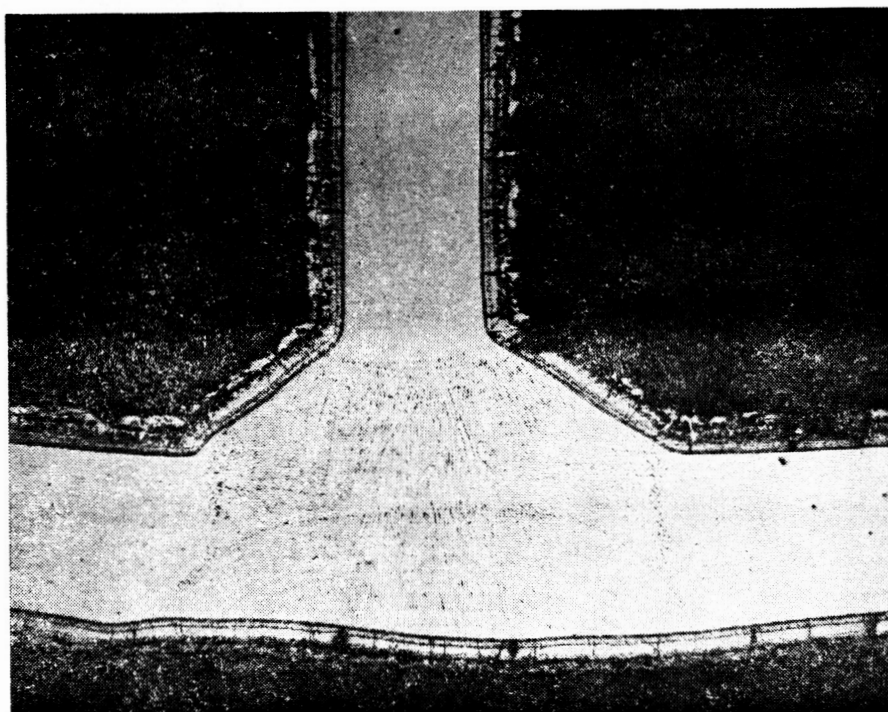
Magnification: 100X
 Etch: Heavy
 Panel No.: BSC-5
 Flight Cycles: 0
 Location: 9
 Negative No.: D-2937
 Mount No.: 467-P

Figure 5-67. Microstructure of Unexposed Cb-752/R-512E Corrugated Panel



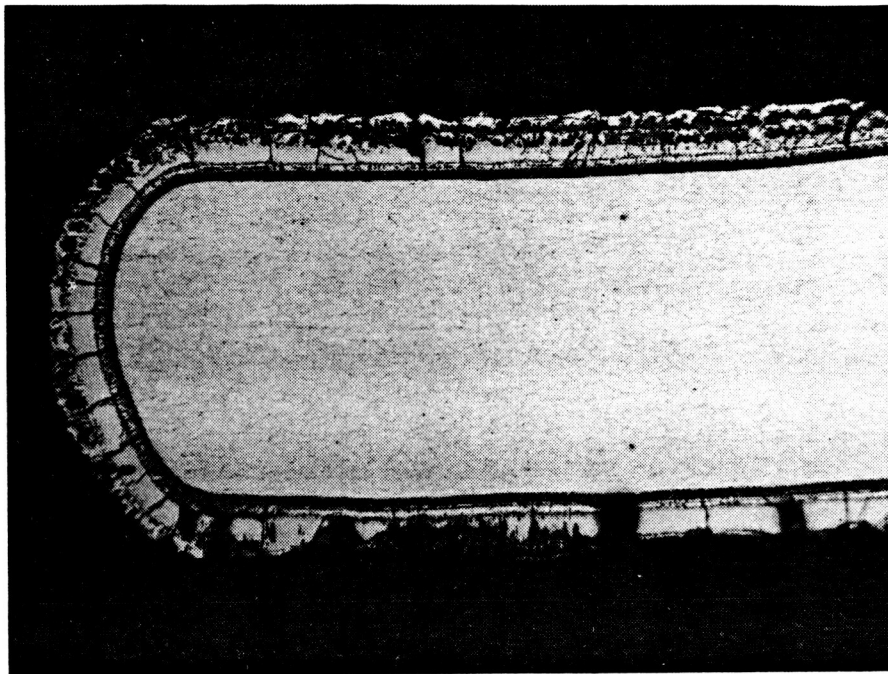
Magnification: 50X
 Etch: Light
 Panel No.: BST-5
 Flight Cycles: 0
 Location: 2
 Negative No.: D-2740
 Mount No.: 470-P

Figure 5-68. Microstructure of Unexposed Cb-752/R-512E Tee-Stiffened Panel (Flange-to-web joint)



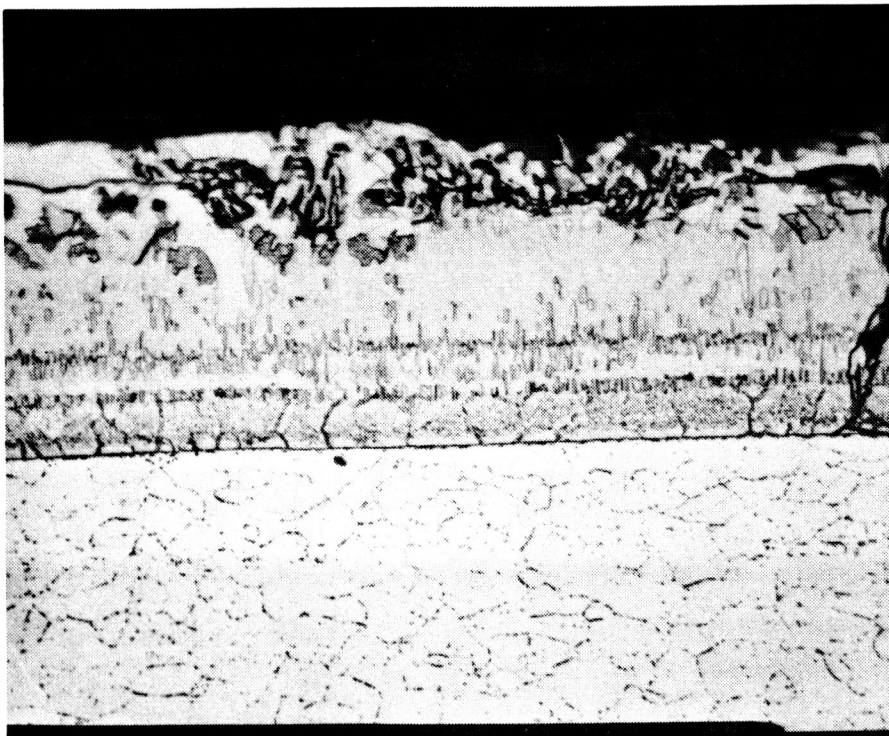
Magnification: 50X
 Etch: Light
 Panel No.: BST-5
 Flight Cycles: 0
 Location: 2
 Negative No.: D-2741
 Mount No.: 470-P

Figure 5-69. Microstructure of Unexposed Cb-752/R-512E Tee-Stiffened Panel (Skin-to-web joint)



Magnification: 100X
 Etch: Light
 Panel No.: BST-5
 Flight Cycles: 0
 Location: 1
 Negative No.: D-2746
 Mount No.: 469-P

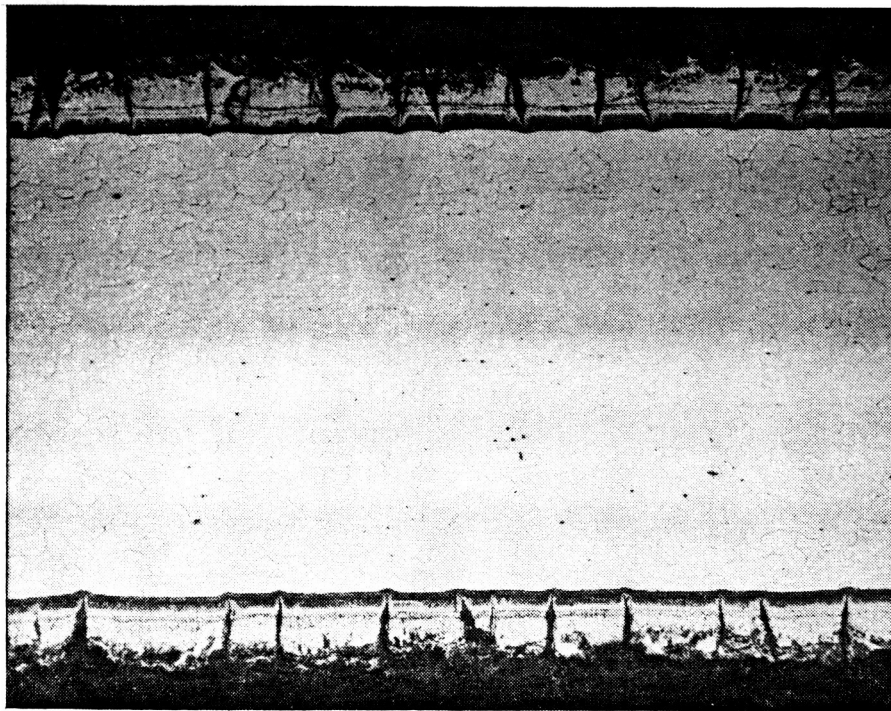
Figure 5-70. Microstructure of Unexposed Cb-752/R-512E Tee-Stiffened Panel



Magnification: 500X
 Etch: Light
 Panel No.: BST-5
 Flight Cycles: 0
 Location: 2
 Negative No.: D-2743
 Mount No.: 470-P

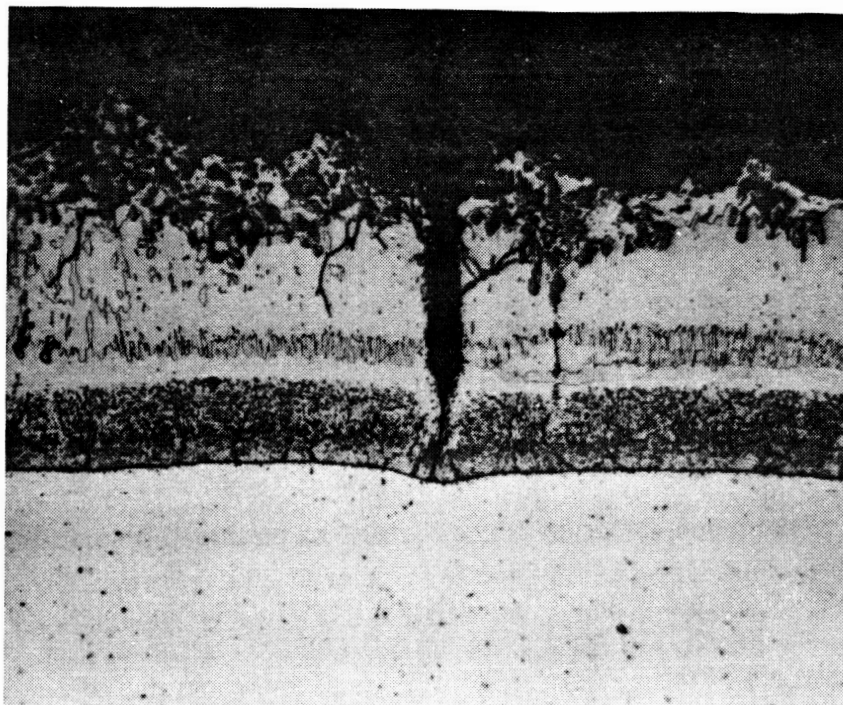
Figure 5-71. Microstructure of Unexposed Cb-752/R-512E Tee-Stiffened Panel

5.7.2 Group 1, C-129Y/R-512E, corrugated. - The two panels of this group completed 100 flight simulation cycles with no visible evidence of coating breakdown or substrate attack. These visual observations were confirmed by the metallographic examination of panel YSC-3. Neither substrate erosion nor oxygen contamination was observed in any of the examined regions. The effectiveness of the coating is clearly shown in Figures 5-72 to 5-74 which were taken from the center of the panel where the test temperature was maximum. After 100 cycles, the coating cracks have enlarged and filled with a grey oxide but have not penetrated through the diffusion zone into the alloy substrate. Some of the grey oxide is also visible on the outer surface of the coating. The anodizing etch used in Figure 5-74 is especially effective in showing the oxide-filled cracks in addition to its main purpose of indicating oxygen contamination. No oxygen contamination was found in this specimen. Figures 5-75 and 5-76 were taken from the corner of the panel (location 13). Because of the steep temperature gradient in the simulator, this area remained relatively cool during cycling and shows almost no effect from the 100 cycles. A thin oxide layer is visible at the outer edge but the coating cracks (see Figure 5-76) have not appreciably increased in size. From a comparison of thicknesses of the center section, Figure 5-72, and the corner section, Figure 5-75, a substrate consumption by diffusion zone growth of about 0.0005 inch (0.0013 cm) per side in 100 cycles was determined.



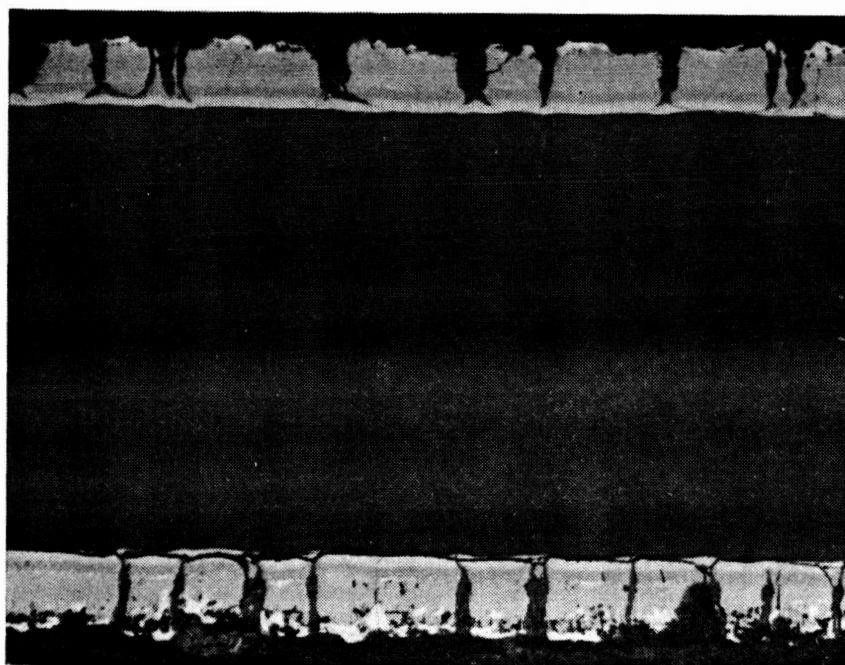
Magnification:	100X
Etch:	Light
Panel No.:	YSC 3
Flight Cycles:	100
Location:	9
Negative No.:	D-2837
Mount No.:	477-P

Figure 5-72. Microstructure of Exposed C-129Y/R-512E Corrugated Panel



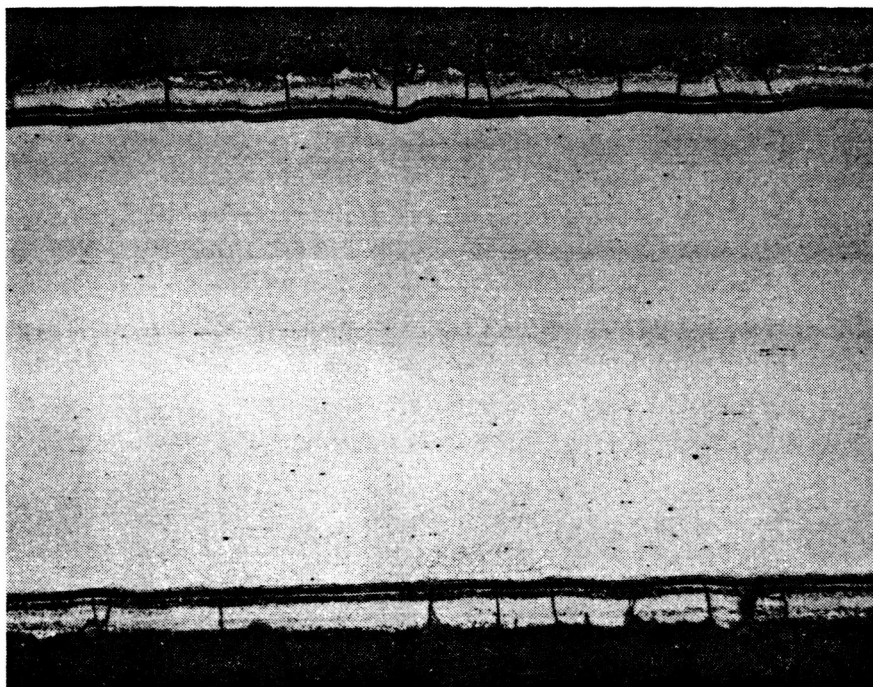
Magnification: 500X
 Etch: Light
 Panel No.: YSC-3
 Flight Cycles: 100
 Location: 9
 Negative No.: D-2842
 Mount No.: 477-P

Figure 5-73. Microstructure of Exposed C-129Y/R-512E Corrugated Panel



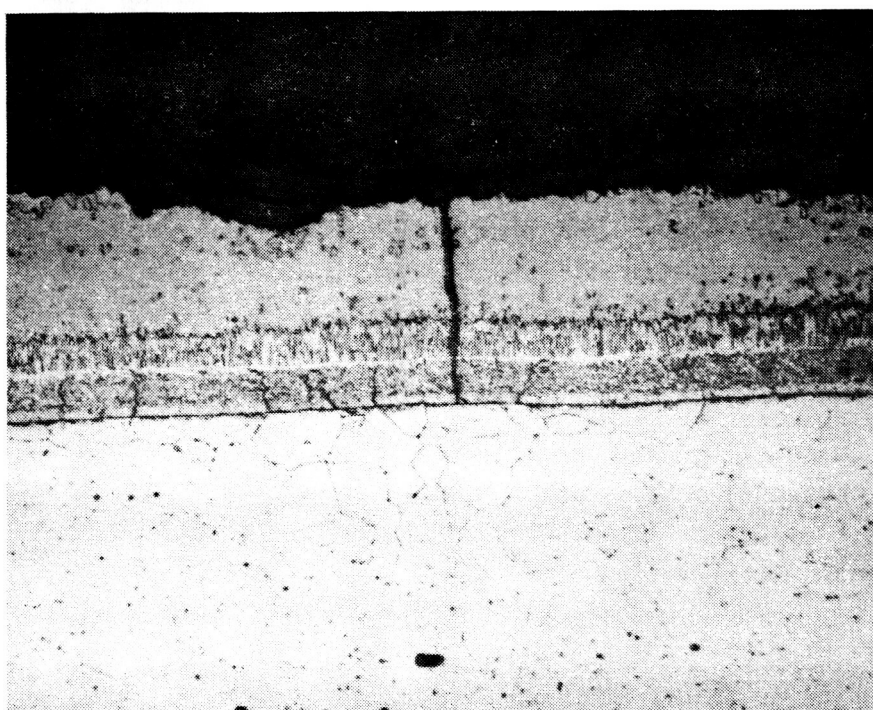
Magnification: 100X
 Etch: Anodized
 Panel No.: YSC-3
 Flight Cycles: 100
 Location: 10
 Negative No.: D-2971
 Mount No.: 477-P

Figure 5-74. Microstructure of Exposed C-129Y/R-512E Corrugated Panel



Magnification: 100X
 Etch: Light
 Panel No.: YSC-3
 Flight Cycles: 100
 Location: 13
 Negative No.: D-2843
 Mount No.: 479-P

Figure 5-75. Microstructure of Exposed C-129Y/R-512E Corrugated Panel



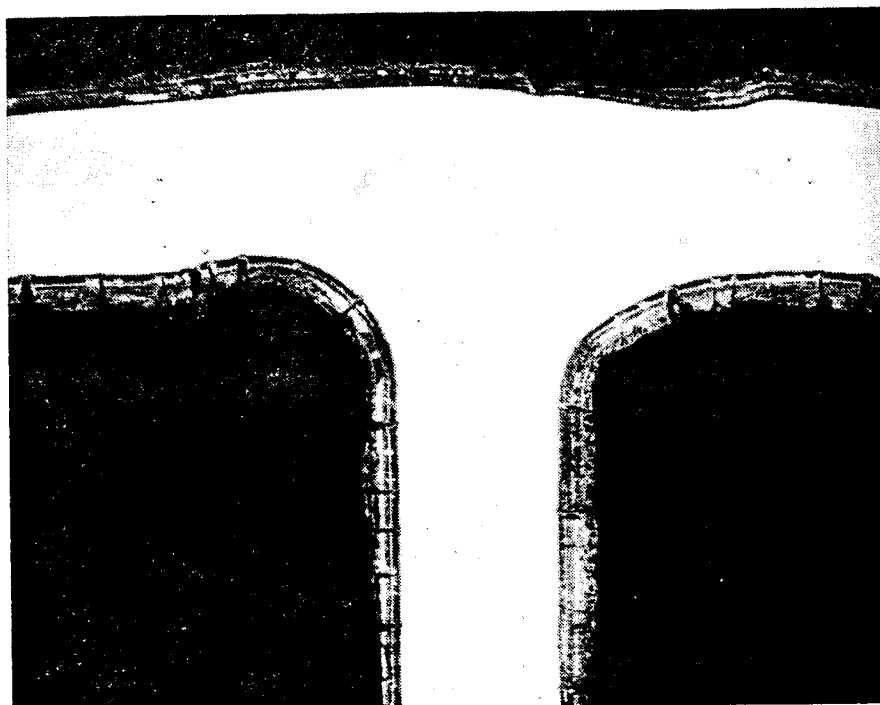
Magnification: 500X
 Etch: Light
 Panel No.: YSC-3
 Flight Cycles: 100
 Location: 13
 Negative No.: D-2844
 Mount No.: 479-P

Figure 5-76. Microstructure of Exposed C-129Y/R-512E Corrugated Panel

5.7.3 Group 2, C-129Y/R-512E, tee stiffened. - Photomicrographs for this group are presented in Figures 5-77 to 5-80 and 5-87 for panel YST-3 and Figures 5-81 to 5-86 for panel YST-4. The behavior of these panels during flight simulation testing was considerably different than that of the corrugated panels of the same material system. Both tee-stiffened panels experienced severe coating failure and substrate erosion while the corrugated panels exhibited no coating damage during the 100 cycles. The appearance of the coating microstructures was also quite different for the two types of panels. Figures 5-77 and 5-78 were taken from panel YST-3 in an area removed from the major coating failure region. While no contamination of the alloy is visible in this region, many of the coating cracks have penetrated very close to the substrate. The major difference between the two types of panels is the degree of oxidation of the coating itself. A much higher percentage of the coating has been consumed from the C-129Y/R-512E tee-stiffened panels after 100 cycles. This can be observed in the weld areas, the skin, web, and particularly the underside of the flange near the outer edges. There is also a difference in the structure of the coating in that a great deal of porosity is present in the outer layers. This is especially noticeable in panel YST-4 (Figures 5-81 to 5-86). This porous coating may in part explain the increased rate of oxidation observed in the C-129Y/R-512E panels. It can also be noted that since panel YST-4 was withdrawn from test after 64 cycles, the crack sizes are somewhat smaller than those of panel YST-3, which completed 100 cycles.

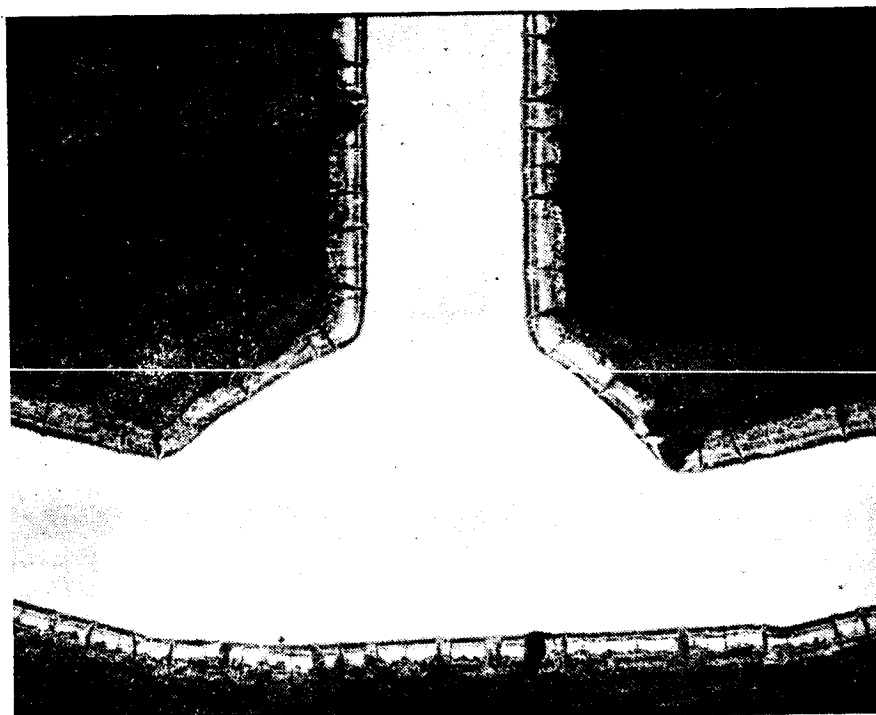
Sections from the welded center rib of panel YST-4 (Figures 5-81 and 5-82) do not appear to have been affected by the cyclic exposure. However, sections taken from the flange of the center rib adjacent to the weld show a localized coating failure and progressive contamination of the base metal (Figure 5-83). This coating failure initiated on the underside of the flange near the edge. This general area is shown for different locations on panels YST-4 and YST-3 in Figures 5-79, 5-83, and 5-87. In each case the amount of coating oxidation on the underside of the flange is greater than other regions of the panel. Many of the localized coating failure sites were located near these outer flange edges and may have been the result of this unusually high rate of coating oxidation. A post-examination review with HiTemCo personnel did not reveal any anomalies in the coating application procedures for the C-129Y/R-512E panels. Therefore, the reasons for the apparent coating porosity and the accelerated oxidation remain unknown.

5.7.4 Group 3, Cb-752/R-512E, corrugated. - Similarly to the C-129Y corrugated panels, those of the Cb-752 alloy also completed 100 flight simulation cycles with no evidence of coating or substrate attack; nor was any found during an extensive metallographic study of the group 3 panels. Seven sections of panel BSC-1 were examined - six from the central test region and one from a cooler end location. The six samples from the middle of the panel were very similar. Three sections are shown in Figures 5-88 to 5-90. All contain the typical oxide-filled coating cracks and a rather thin oxide layer at the outer region of the coating. The number and size of the coating



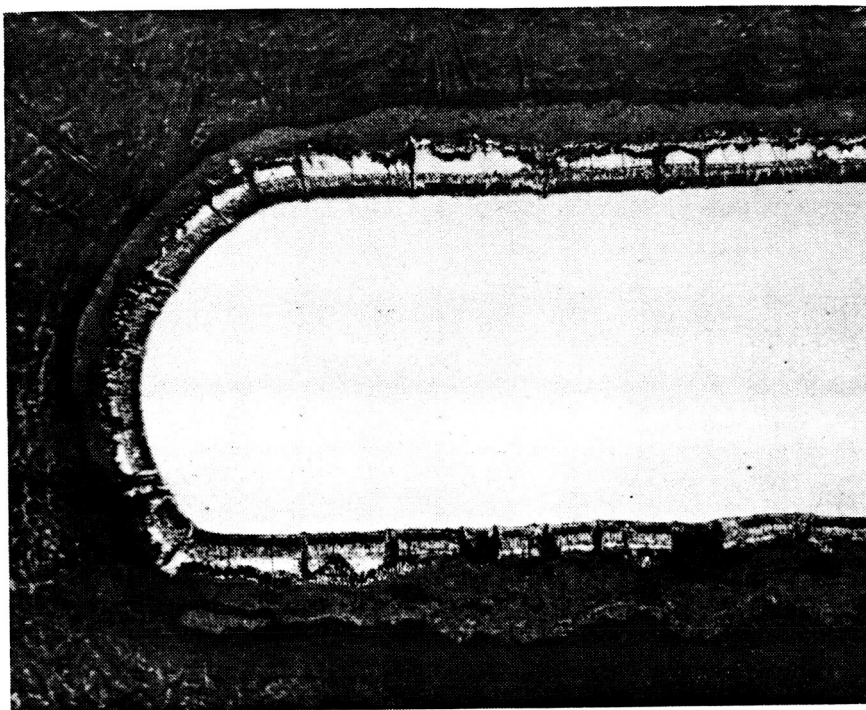
Magnification: 50X
 Etch: Light
 Panel No.: YST 3
 Flight Cycles: 100
 Location: 2
 Negative No.: D-2798
 Mount No.: 490-P

Figure 5-77. Microstructure of Exposed C-129Y/R-512E Tee-Stiffened Panel (Flange-to-web joint)



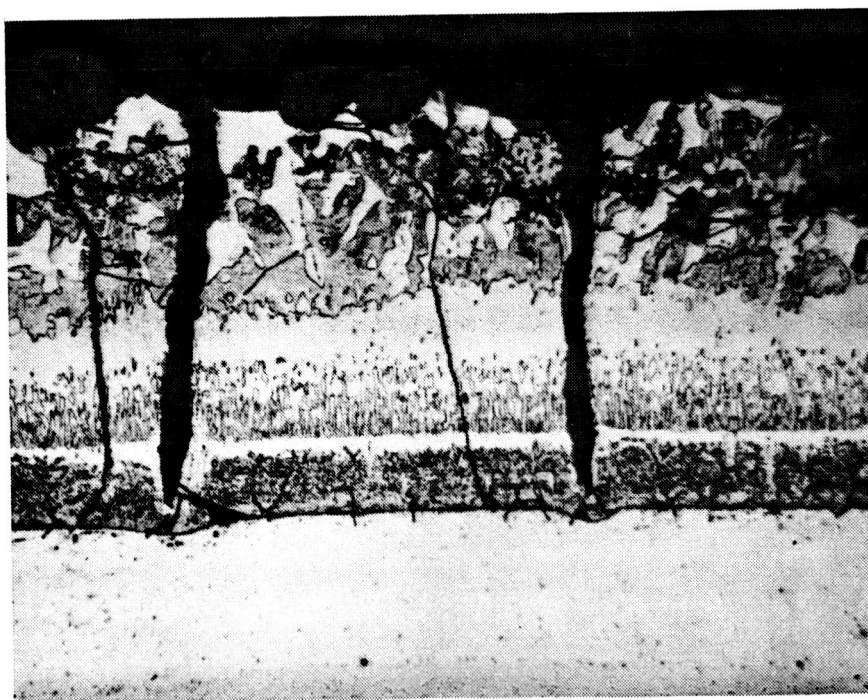
Magnification: 50X
 Etch: Light
 Panel No.: YST-3
 Flight Cycles: 100
 Location: 2
 Negative No.: D-2799
 Mount No.: 490-P

Figure 5-78. Microstructure of Exposed C-129Y/R-512E Tee-Stiffened Panel (Skin-to-web joint)



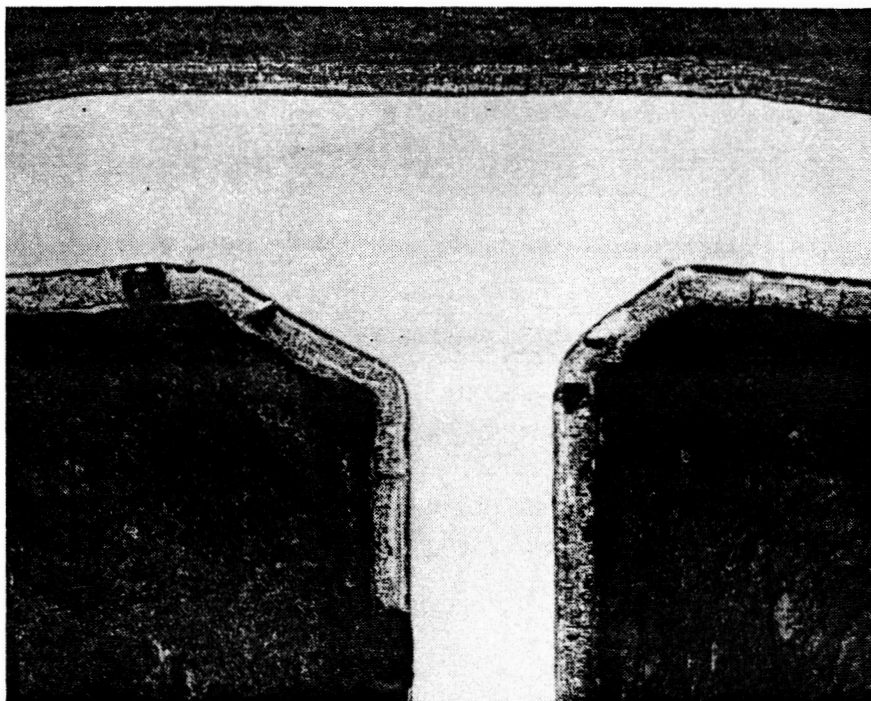
Magnification: 100X
 Etch: Light
 Panel No.: YST 3
 Flight Cycles: 100
 Location: 3
 Negative No.: D-2804
 Mount No.: 491-P

Figure 5-79. Microstructure of Exposed C-129Y/R-512E Tee-Stiffened Panel



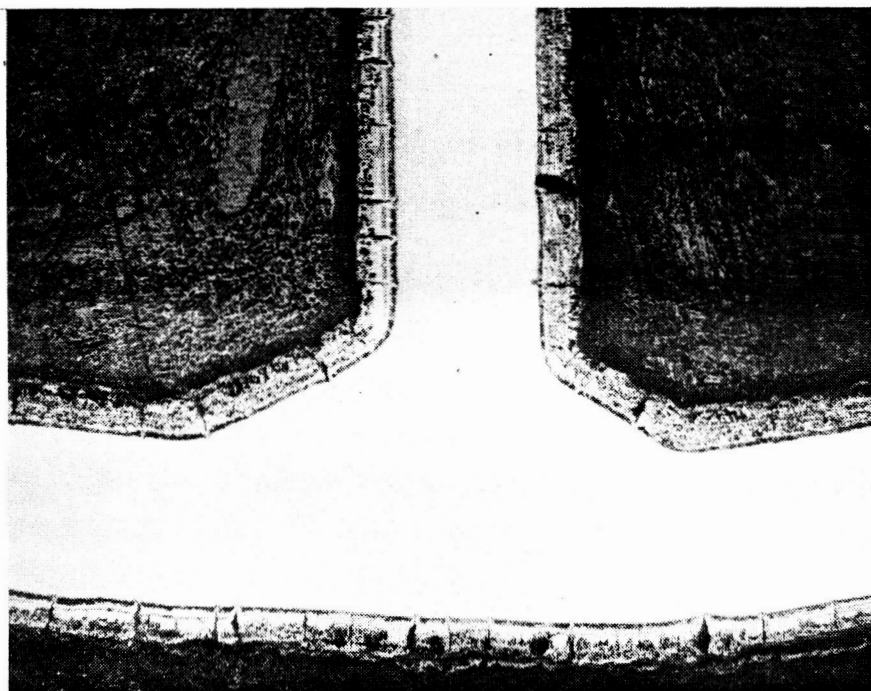
Magnification: 500X
 Etch: Light
 Panel No.: YST 3
 Flight Cycles: 100
 Location: 3
 Negative No.: D-2805
 Mount No.: 491-P

Figure 5-80. Microstructure of Exposed C-129Y/R-512E Tee-Stiffened Panel



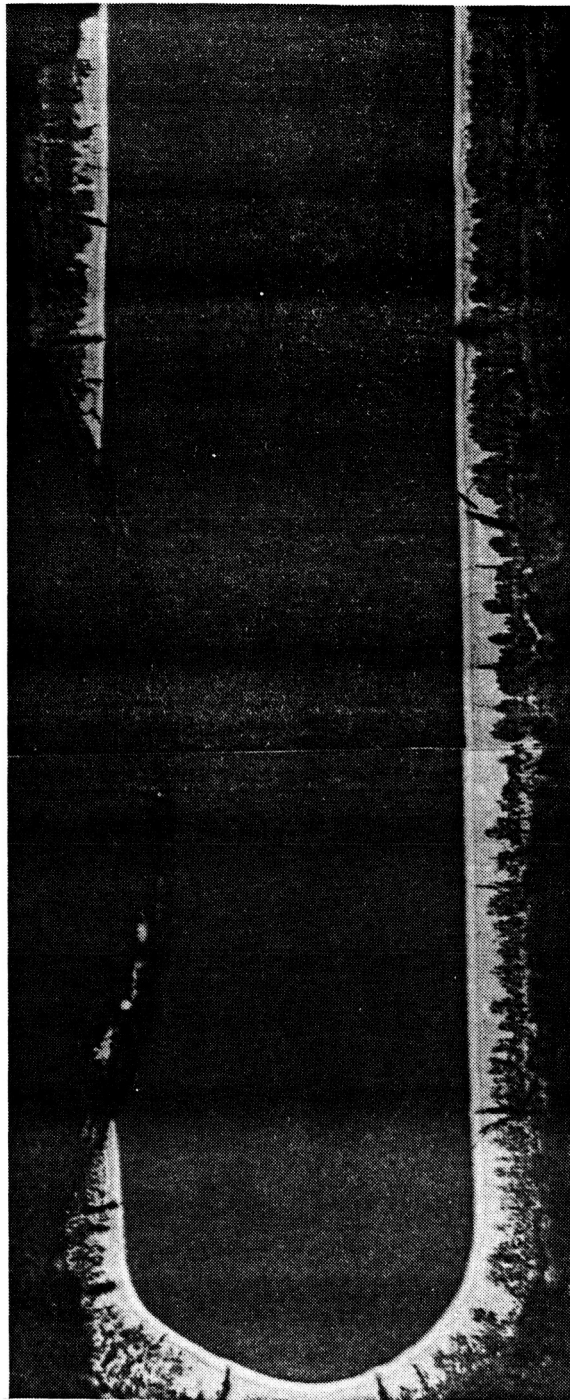
Magnification: 50X
 Etch: Light
 Panel No.: YST-4
 Flight Cycles: 64
 Location: 1
 Negative No.: D-2816
 Mount No.: 519-P

Figure 5-81. Microstructure of Exposed C-129Y/R-512E Tee-Stiffened Panel (Flange-to-web joint)



Magnification: 50X
 Etch: Light
 Panel No.: YST 4
 Flight Cycles: 64
 Location: 1
 Negative No.: D-2817
 Mount No.: 519-P

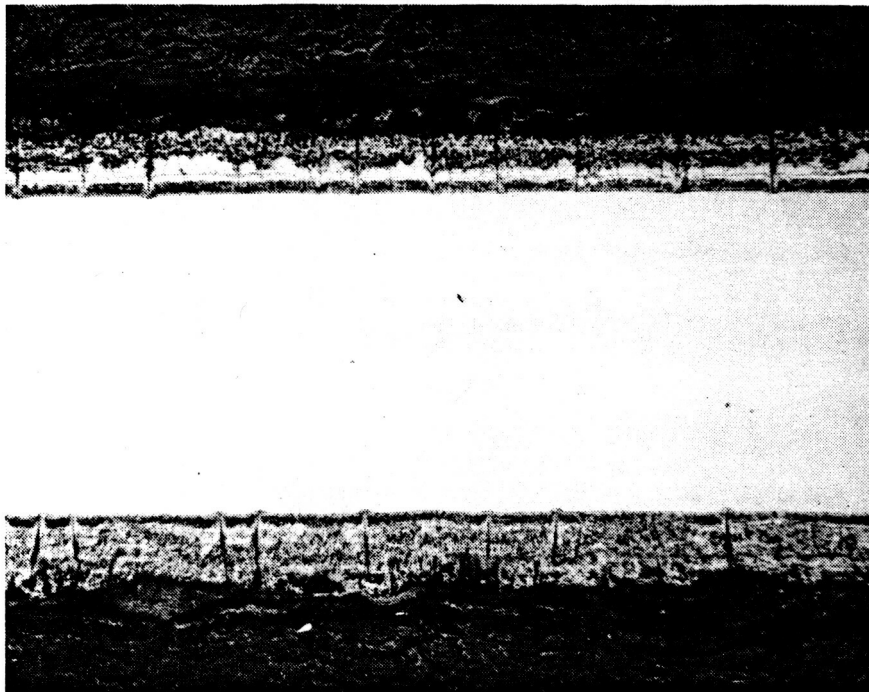
Figure 5-82. Microstructure of Exposed C-129Y/R-512E Tee-Stiffened Panel (Skin-to-web joint)



Magnification: 100X
 Etch: Anodized
 Panel No.: YST-4
 Flight Cycles: 64
 Location: 1
 Negative No.: D-2960
 Mount No.: 519-P

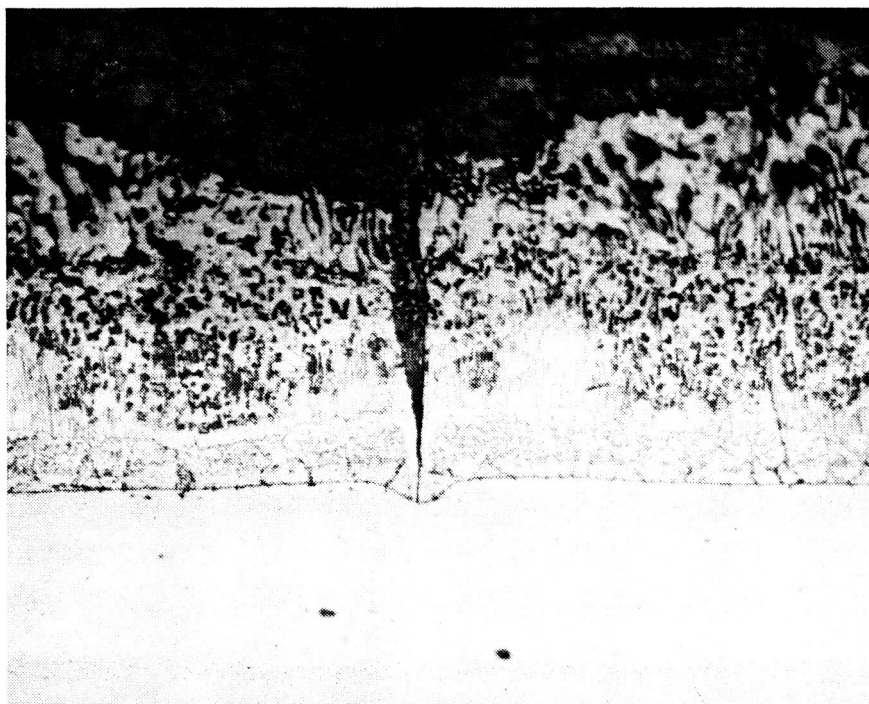
Magnification: 100X
 Etch: Anodized
 Panel No.: YST-4
 Flight Cycles: 64
 Location: 1
 Negative No.: D-2961
 Mount No.: 519-P

Figure 5-83. Microstructures of Exposed C-129Y/R-512E Tee-Stiffened Panel



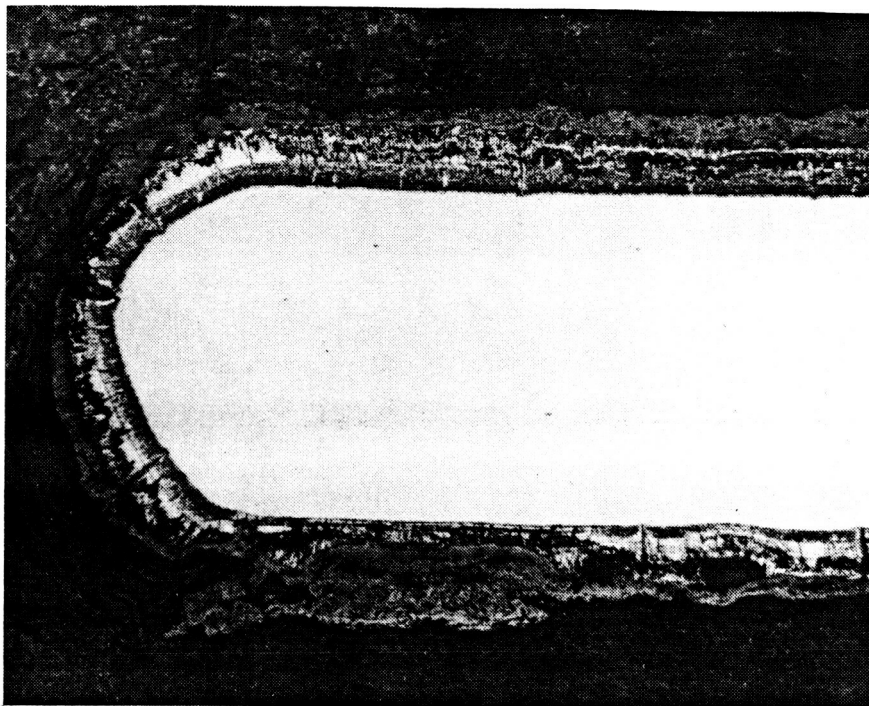
Magnification: 100X
 Etch: Light
 Panel No.: YST 4
 Flight Cycles: 64
 Location: 5
 Negative No.: D-2854
 Mount No.: 521-P

Figure 5-84. Microstructure of Exposed C-129Y/R-512E Tee-Stiffened Panel



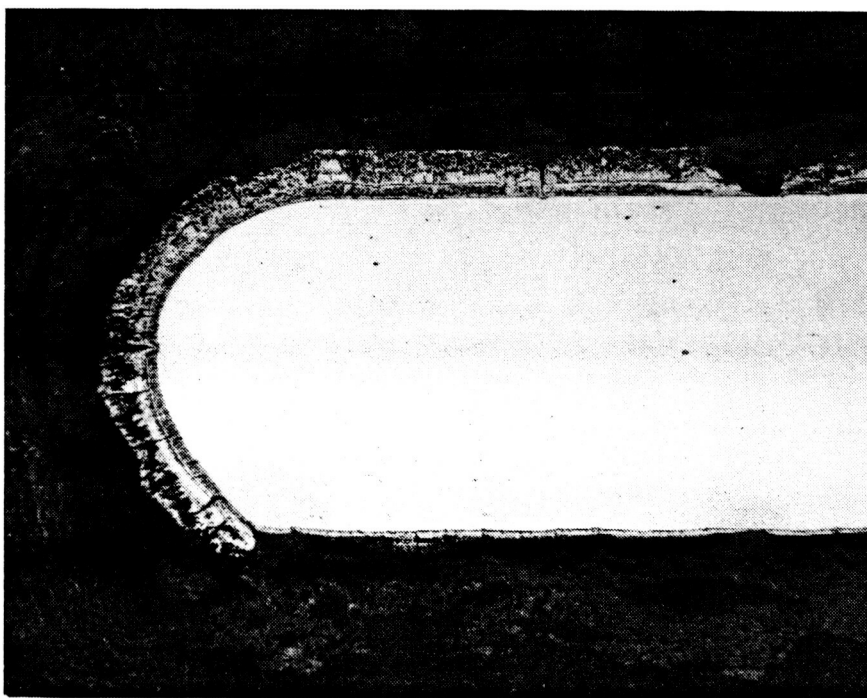
Magnification: 500X
 Etch: Light
 Panel No.: YST 4
 Flight Cycles: 64
 Location: 5
 Negative No.: D-2855
 Mount No.: 521-P

Figure 5-85. Microstructure of Exposed C-129Y/R-512E Tee-Stiffened Panel



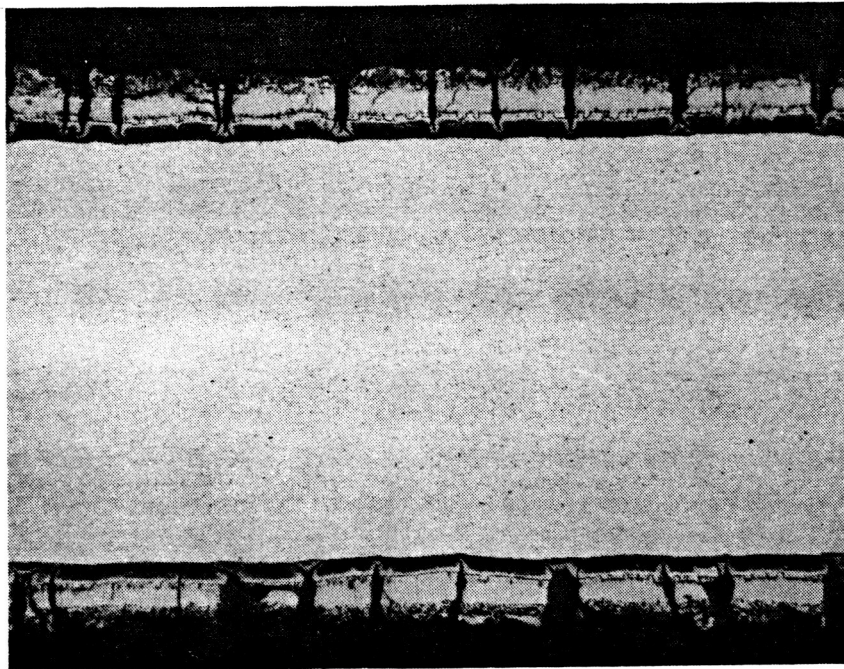
Magnification: 100X
 Etch: Light
 Panel No.: YST 4
 Flight Cycles: 64
 Location: 2
 Negative No.: D-2812
 Mount No.: 518-P

Figure 5-86. Microstructure of Exposed C-129Y/R-512E Tee-Stiffened Panel



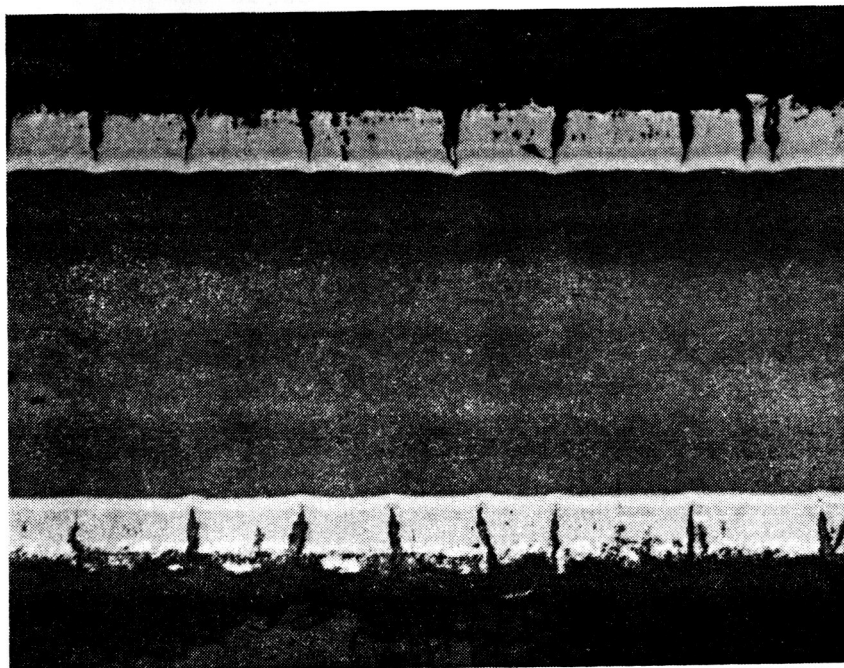
Magnification: 100X
 Etch: Light
 Panel No.: YST-3
 Flight Cycles: 100
 Location: 2
 Negative No.: D-2800
 Mount No.: 490-P

Figure 5-87. Microstructure of Exposed C-129Y/R-512E Tee-Stiffened Panel



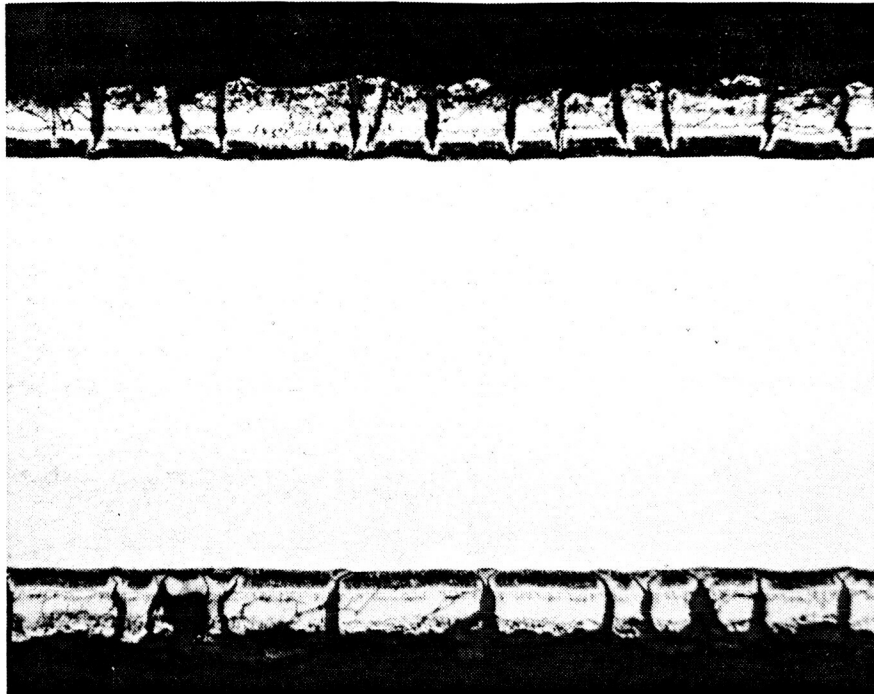
Magnification: 100X
 Etch: Light
 Panel No.: BSC-1
 Flight Cycles: 100
 Location: 8
 Negative No.: D-2759
 Mount No.: 492-P

Figure 5-88. Microstructure of Exposed Cb-752/R-512E Corrugated Panel



Magnification: 100X
 Etch: Anodized
 Panel No.: BSC-1
 Flight Cycles: 100
 Location: 10
 Negative No.: D-2972
 Mount No.: 494-P

Figure 5-89. Microstructure of Exposed Cb-752/R-512E Corrugated Panel



Magnification: 100X
 Etch: Light
 Panel No.: BSC-1
 Flight Cycles: 100
 Location: 12
 Negative No.: D-2781
 Mount No.: 495-P

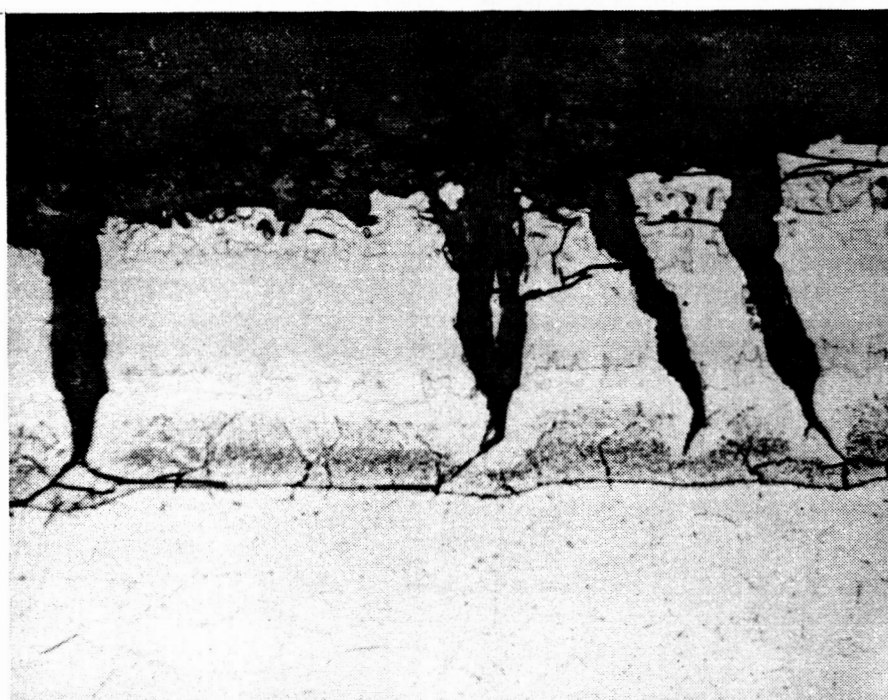
Figure 5-90. Microstructure of Exposed Cb-752/R-512E Corrugated Panel

cracks are very nearly the same in the three figures. An enlargement of the coating and coating/substrate interface is presented in Figure 5-91. One of the samples was then re-etched to bring out the grain structure. This is shown in Figure 5-92. A comparison of Figure 5-92 with Figure 5-67 from an unexposed panel shows that the grain size remained about the same during the 100 flight cycles.

The last photomicrograph from panel BSC-1, Figure 5-93, was taken from the relatively cool corner region for use in determining the amount of substrate consumption in 100 flight cycles. Comparison of this figure with Figure 5-90 gave a value of approximately 0.0005 inch (0.0013 cm) per side in 100 cycles for substrate consumption by diffusion zone growth. These values (both Cb-752 and C-129Y) agree quite well with measurements made on the coupon specimens used in Phase I (Reference 3).

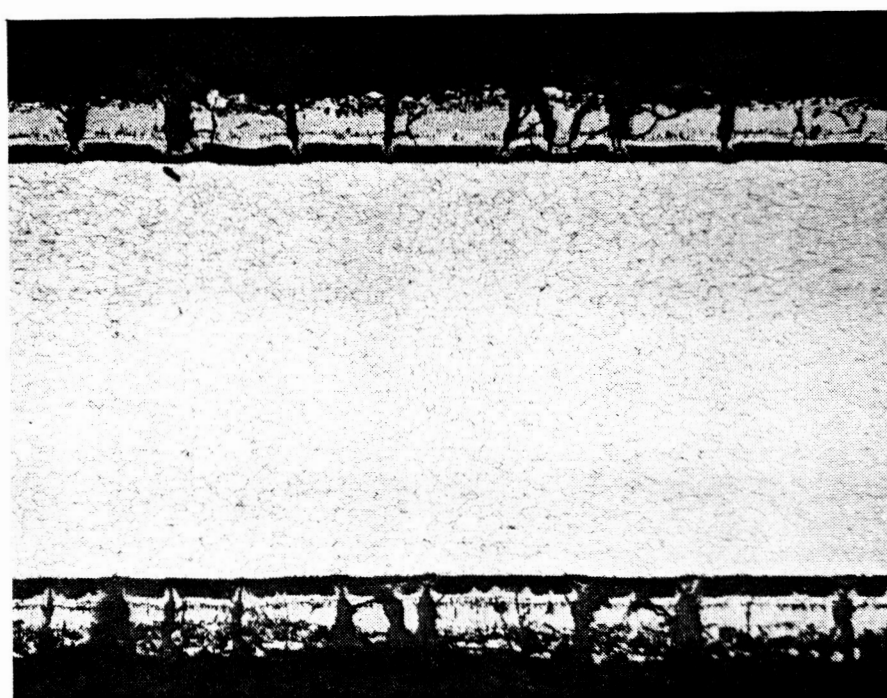
5.7.5 Group 4, Cb-752/R-512E, tee-stiffened. — Group 4 consists of two types of panels, tagged and untagged, which are more conveniently discussed in two sections.

The untagged panels performed exceedingly well with no evidence of coating breakdown or localized failure within the central test sections. Photomicrographs from one of these panels, BST-3, are presented in Figures 5-94 to 5-100. Figures 5-94 and 5-95, from the skin, are typical of the many areas examined. They show the usual oxide-filled coating cracks and the relatively thin oxide layer on the outer edges. With one



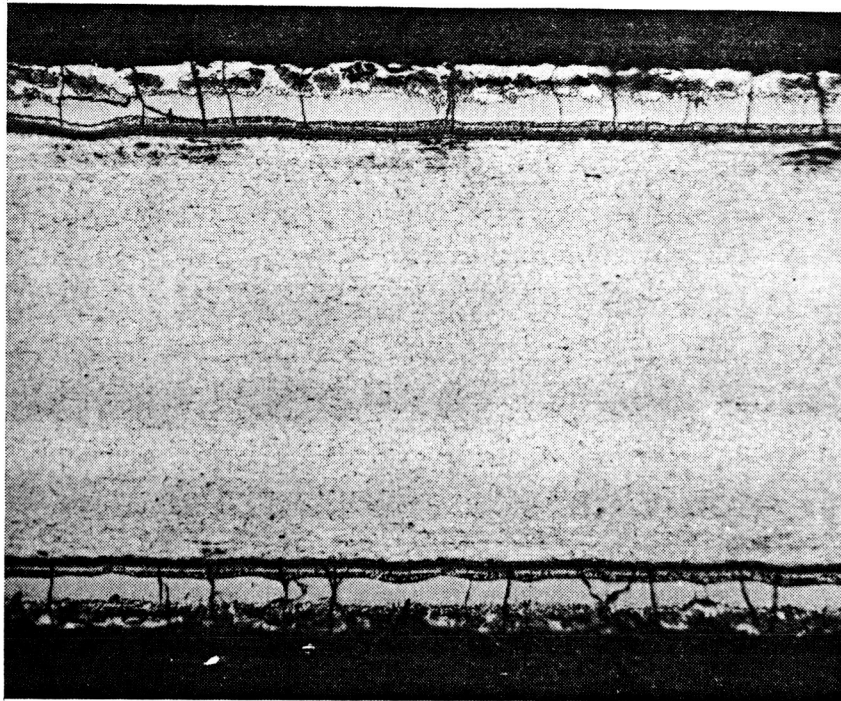
Magnification: 500X
 Etch: Light
 Panel No.: BSC-1
 Flight Cycles: 100
 Location: 10
 Negative No.: D-2778
 Mount No.: 494-P

Figure 5-91. Microstructure of Exposed Cb-752/R-512E Corrugated Panel



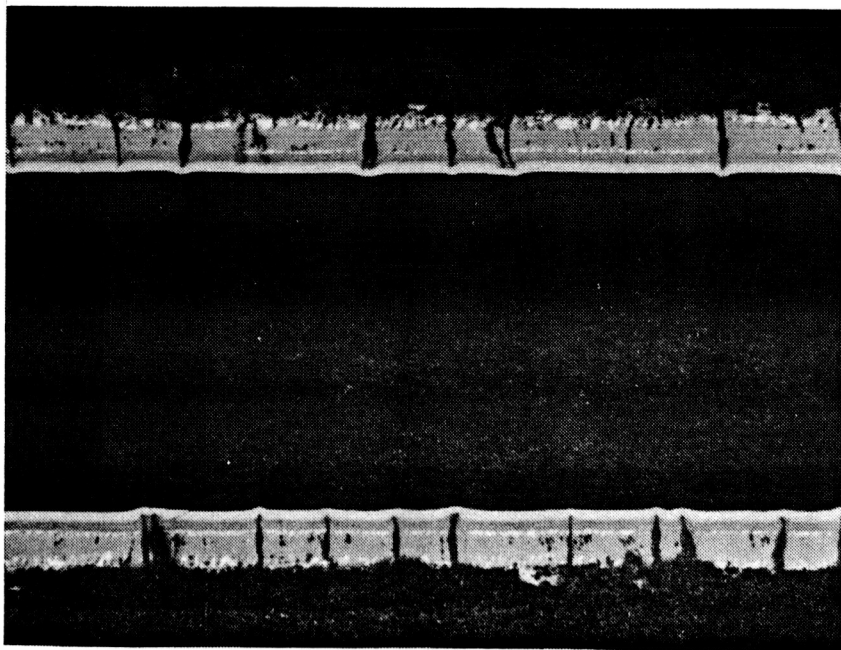
Magnification: 100X
 Etch: Heavy
 Panel No.: BSC-1
 Flight Cycles: 100
 Location: 10
 Negative No.: D-2941
 Mount No.: 494-P

Figure 5-92. Microstructure of Exposed Cb-752/R-512E Corrugated Panel



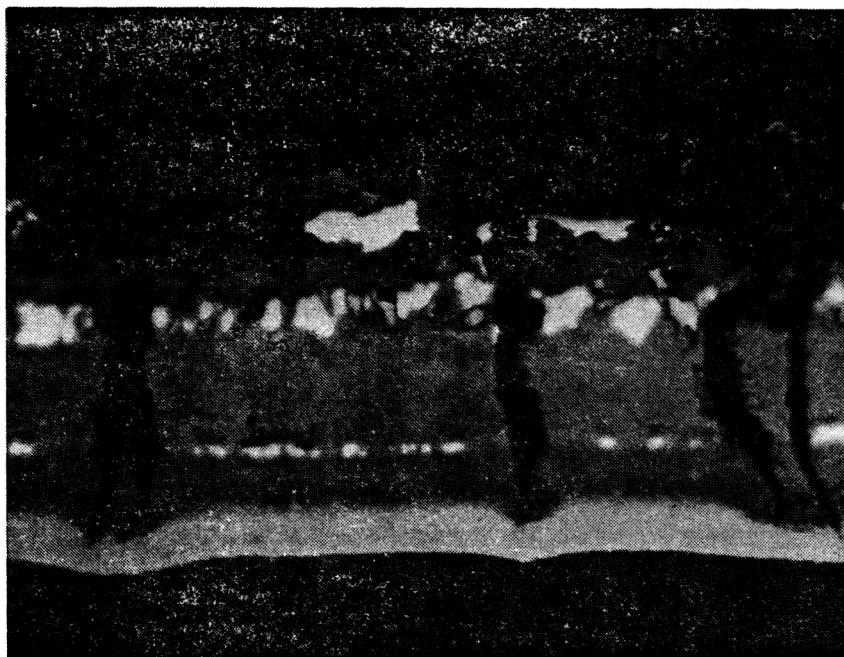
Magnification: 100X
 Etch: Light
 Panel No.: BSC-1
 Flight Cycles: 100
 Location: 13
 Negative No.: D-3298
 Mount No.: 493-P

Figure 5-93. Microstructure of Exposed Cb-752/R-512E Corrugated Panel



Magnification: 100X
 Etch: Anodized
 Panel No.: BST-3
 Flight Cycles: 100
 Location: 5
 Negative No.: D-3322
 Mount No.: 517-P

Figure 5-94. Microstructure of Exposed Cb-752/R-512E Tee-Stiffened Panel

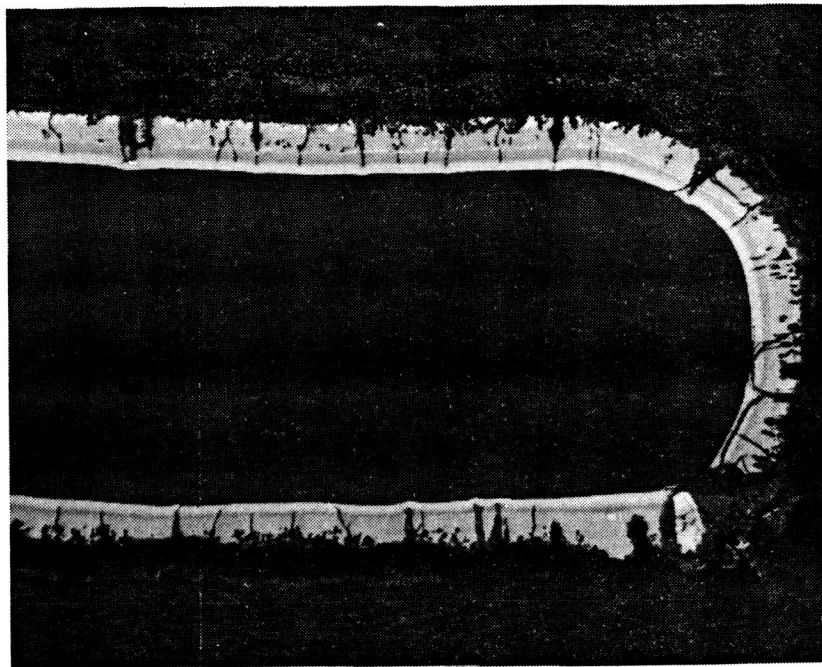


Magnification: 500X
 Etch: Anodized
 Panel No.: BST-3
 Flight Cycles: 100
 Location: 5
 Negative No.: D-3128
 Mount No.: 517-P

Figure 5-95. Microstructure of Exposed Cb-752/R-512E Tee-Stiffened Panel

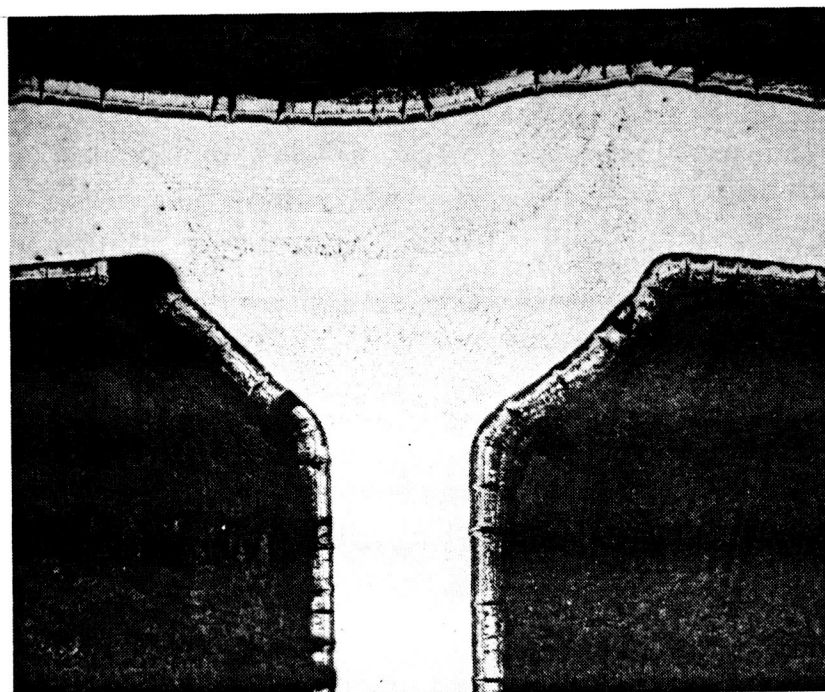
exception, no oxygen contamination of the substrate was observed in this panel. The one localized site of substrate contamination (Figure 5-96) was found at one of the outer flange edges in the center of the panel. As pointed out previously, these outer flange edges appear to be quite susceptible to localized coating failure. In the case of the untagged Cb-752 panels, however, the amount of damage was slight and does not appear to be a problem.

Figures 5-97 to 5-99 show the electron beam welds from the same center section as that from which Figure 5-96 was obtained. The welds appear to be unaffected by the flight simulation exposure with no evidence of contamination or adverse reactions with the coating. A comparison of the more heavily etched structure after 100 flight cycles, Figure 5-99, with a similar area prior to exposure, Figure 5-69, also indicates little change as a result of the flight simulation. The grain structure within the exposed weld is somewhat larger than in the unexposed welds, but with the limited number of joints examined it is not possible to determine whether this occurred during exposure or during the welding operation. In the region adjacent to that shown in Figure 5-96 on the inner side of the flange a site of heavy oxide buildup was found. Figure 5-100 shows the oxide to be approximately half as thick as the coating and diffusion zone. In addition to normal oxide penetration into a crack, a large pocket of oxide can be seen well within the coating zones. However, neither the oxide within the pocket nor the propagated cracks appear to have caused any reaction with the substrate after 100 cycles.



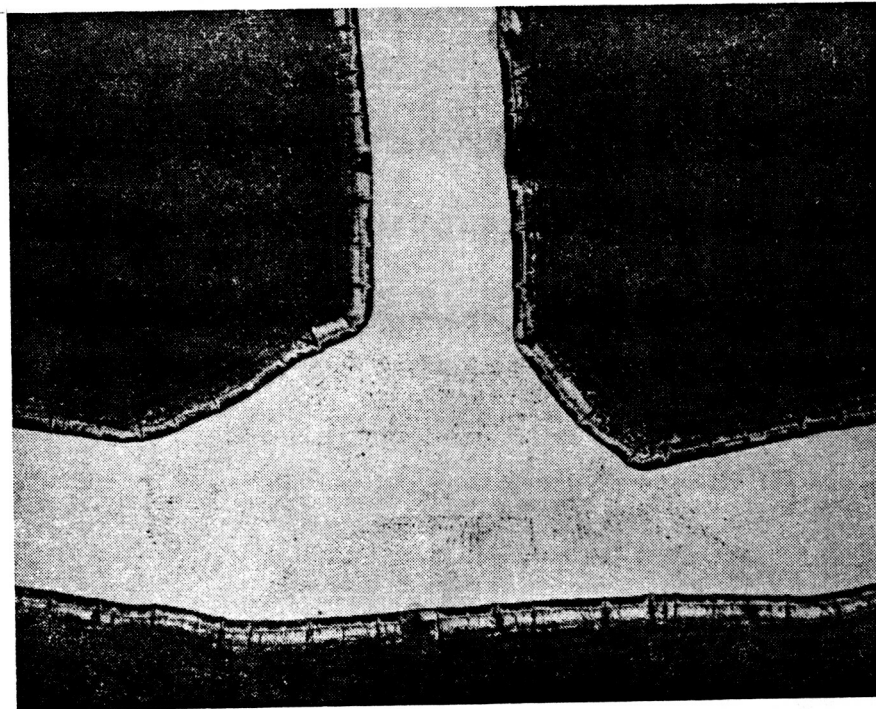
Magnification: 100X
 Etch: Anodized
 Panel No.: BST-3
 Flight Cycles: 100
 Location: 1
 Negative No.: D-2969
 Mount No.: 514-P

Figure 5-96. Microstructure of Exposed Cb-752/R-512E Tee-Stiffened Panel



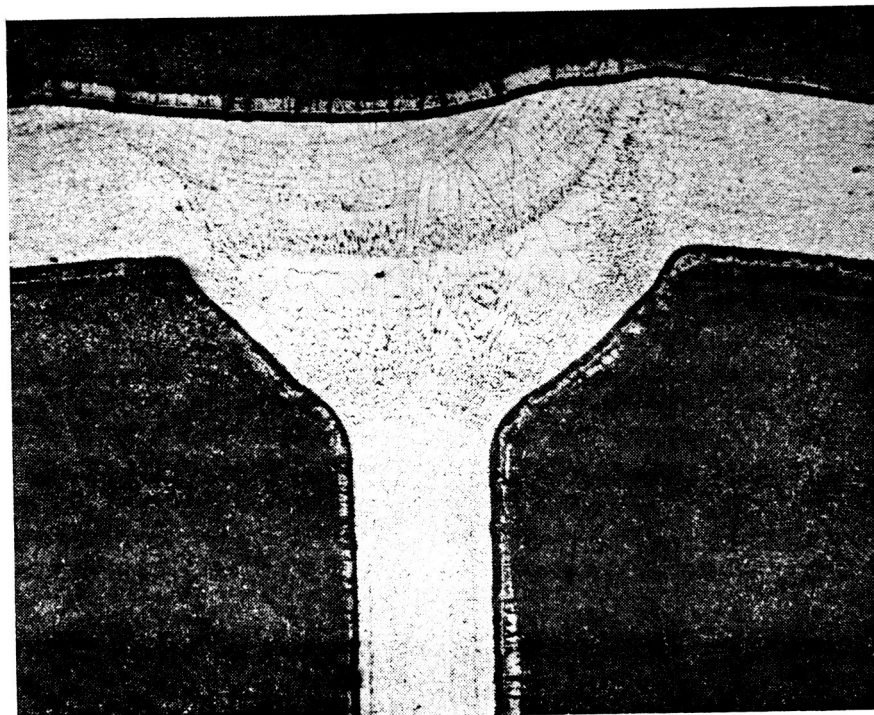
Magnification: 50X
 Etch: Light
 Panel No.: BST-3
 Flight Cycles: 100
 Location: 1
 Negative No.: D-2830
 Mount No.: 514-P

Figure 5-97. Microstructure of Exposed Cb-752/R-512E Tee-Stiffened Panel (Skin to web joint)



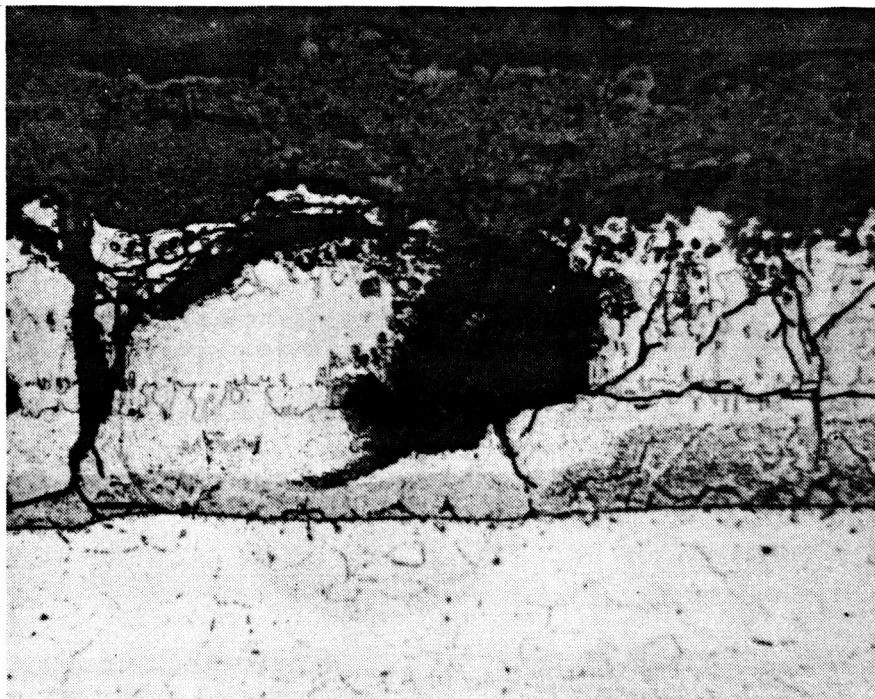
Magnification: 50X
 Etch: Light
 Panel No.: BST-3
 Flight Cycles: 100
 Location: 1
 Negative No.: D-2829
 Mount No.: 514-P

Figure 5-98. Microstructure of Exposed Cb-752/R-512E Tee-Stiffened Panel
 (Flange-to-web joint)



Magnification: 50X
 Etch: Heavy
 Panel No.: BST-3
 Flight Cycles: 100
 Location: 1
 Negative No.: D-2933
 Mount No.: 514-P

Figure 5-99. Microstructure of Exposed Cb-752/R-512E Tee-Stiffened Panel
 (Skin-to-web joint)

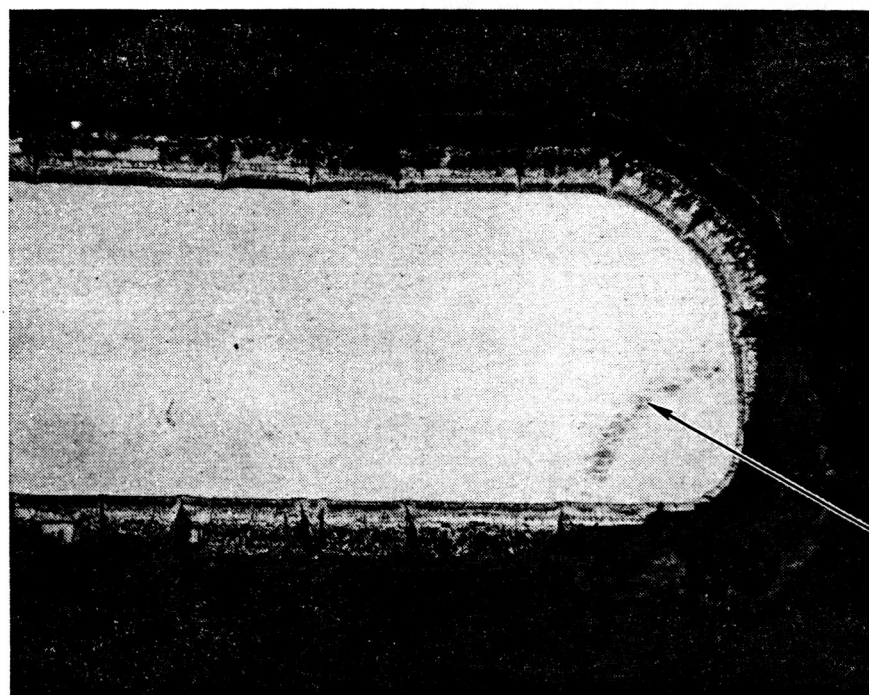


Magnification: 100X
 Etch: Light
 Panel No.: BST-3
 Flight Cycles: 100
 Location: 1
 Negative No.: D-2832
 Mount No.: 514-P

Figure 5-100. Microstructure of Exposed Cb-752/R-512E Tee-Stiffened Panel

In contrast to the excellent performance of the untagged panels, the two panels with the radionuclide tag added to the coating both experienced localized coating failure and substrate erosion within the central test region. The reason for this difference has not been established but is thought to have been the result of the processing treatment rather than the addition of the small amount of inert tag material (see Section 5.8). Examination of the exposed microstructure revealed nothing to account for the rather poor coating performance of the two tagged panels. A similar examination of a tagged panel prior to exposure might be useful, but no spares were available for sectioning.

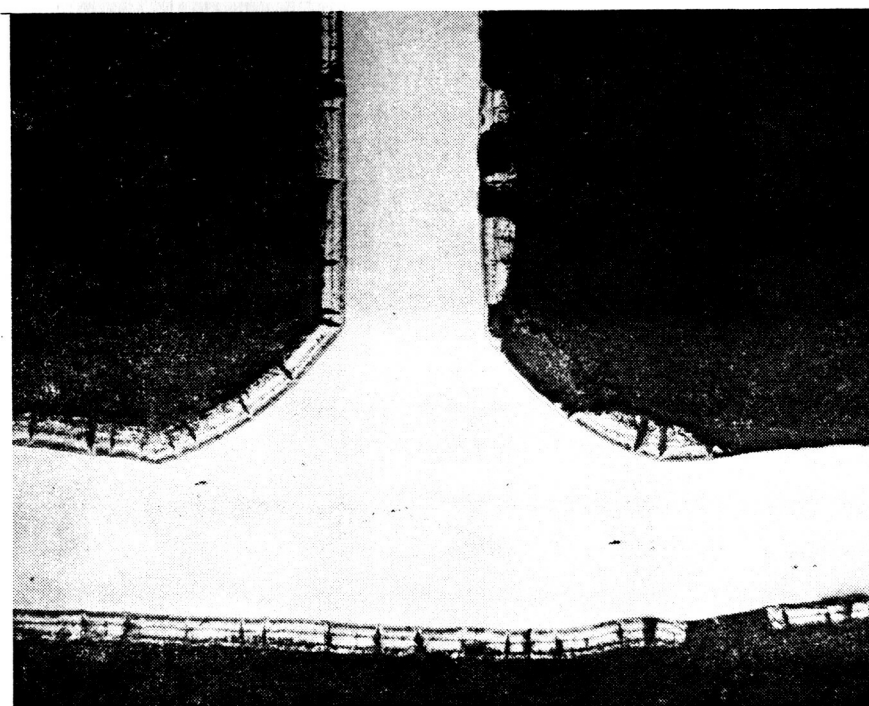
Photomicrographs from the two tagged panels are shown in Figures 5-101 to 5-108 for BST-1 and Figures 5-104 to 5-108 for BST-2. An end of the flange from the center of panel BST-1 is shown in Figure 5-101. This view shows substrate contamination in an area where the coating has been almost completely oxidized. Additional examples are shown in Figures 5-102 and 5-108. In each case much of the coating within a small region has been converted to an oxide. While the coating was still protective in these areas the remaining life was probably minimal. Similar areas were not found in panel BST-2, but rather a more uniform and somewhat thicker oxide layer throughout the microstructure was observed. This is shown in Figures 5-104 and 5-105. A comparison of these two photos with Figures 5-94 and 5-95 from BST-3 shows the great difference in the degree of oxidation of the coating on the tagged and untagged panels.



Magnification: 100X
 Etch: Light
 Panel No.: BST-1
 Flight Cycles: 100
 Location: 1
 Negative No.: D-2889
 Mount No.: 542-P

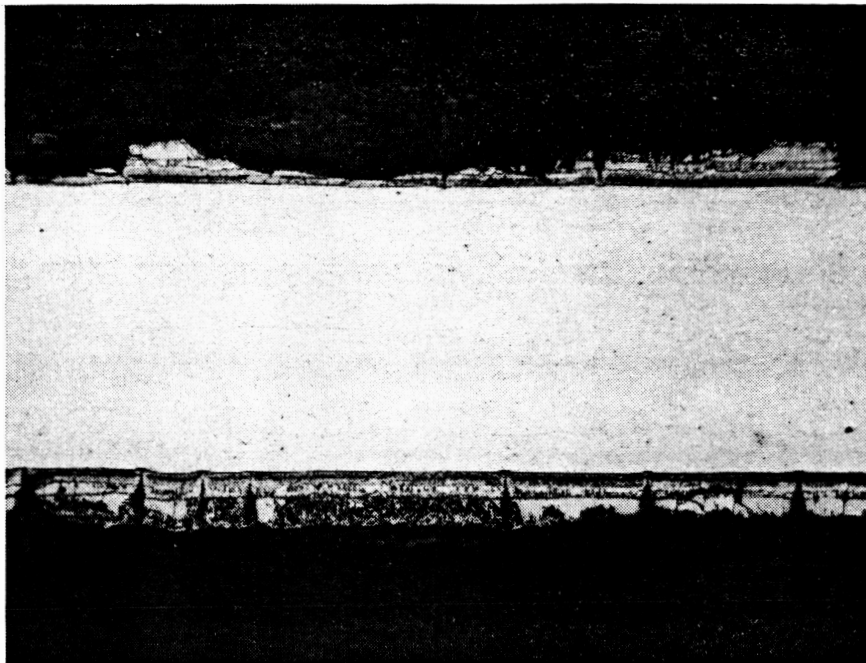
SUBSTRATE
 CONTAMINATION

Figure 5-101. Microstructure of Exposed Cb-752/R-512E Tee-Stiffened Panel



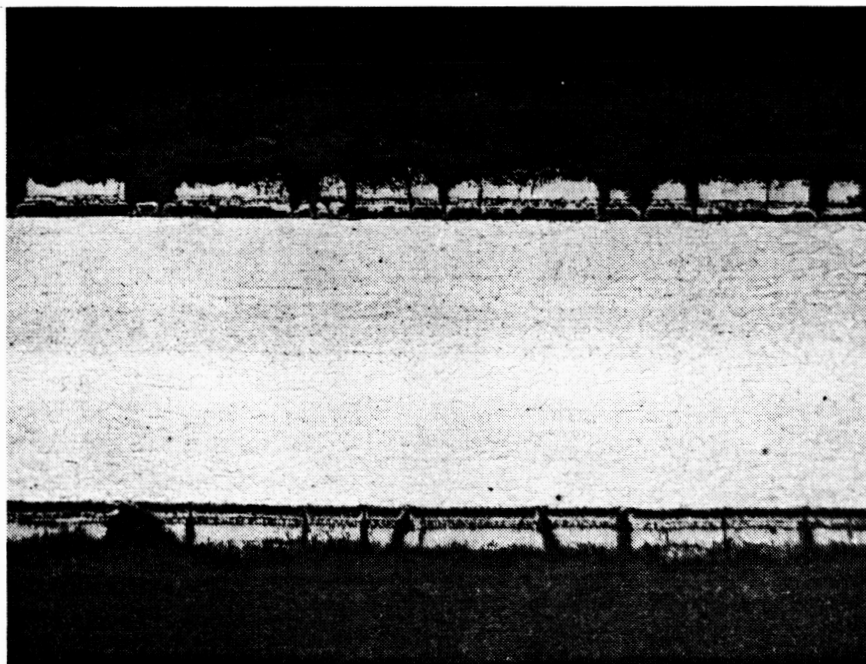
Magnification: 50X
 Etch: Light
 Panel No.: BST-1
 Flight Cycles: 100
 Location: 1
 Negative No.: D-2886
 Mount No.: 542-P

Figure 5-102. Microstructure of Exposed Cb-752/R-512E Tee-Stiffened Panel (Flange-to-web joint)



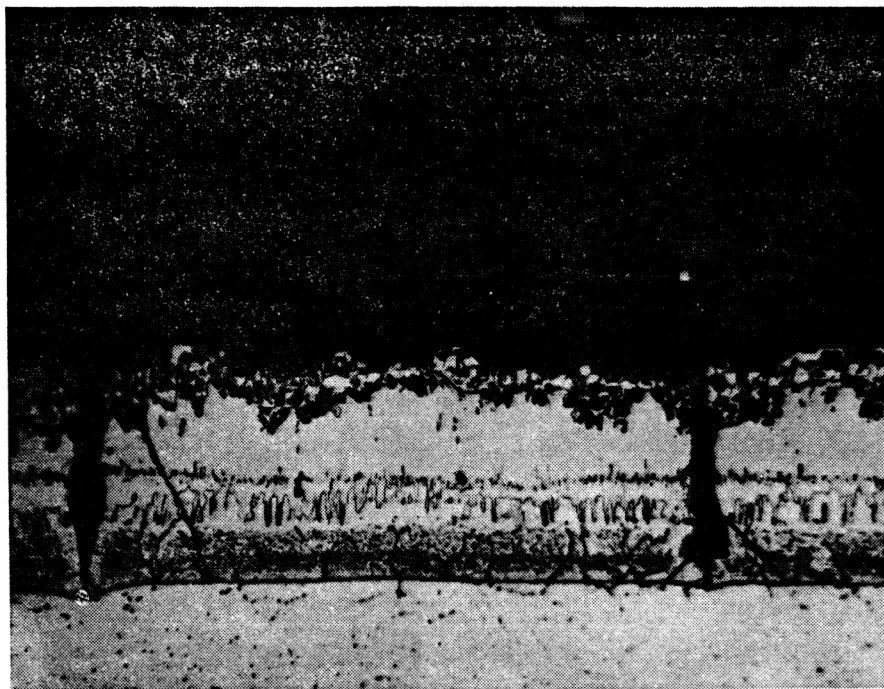
Magnification: 100X
 Etch: Light
 Panel No.: BST-1
 Flight Cycles: 100
 Location: 1
 Negative No.: D-2891
 Mount No.: 542-P

Figure 5-103. Microstructure of Exposed Cb-752/R-512E Tee-Stiffened Panel



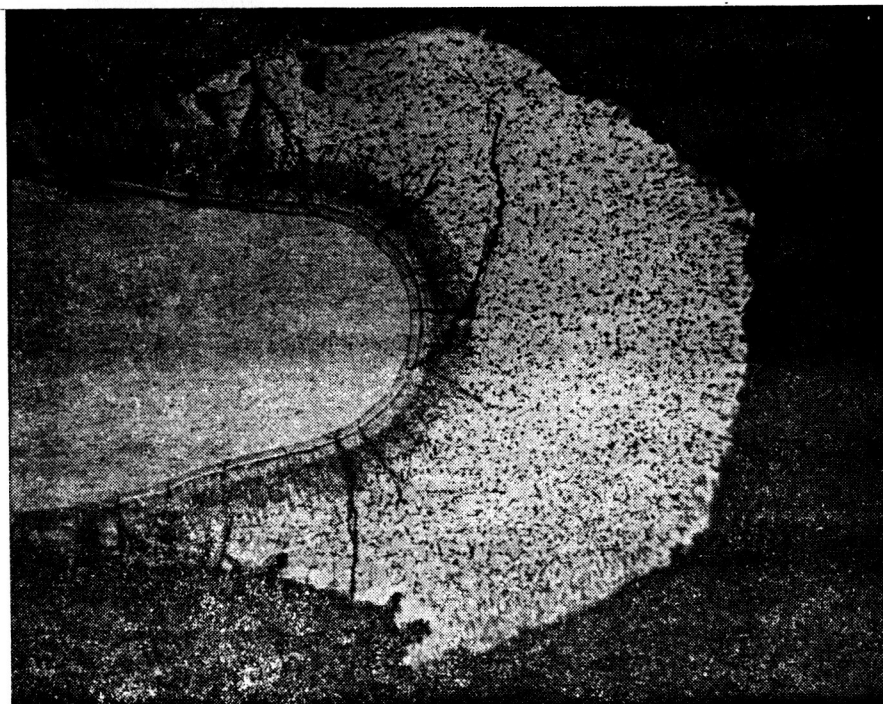
Magnification: 100X
 Etch: Light
 Panel No.: BST-2
 Flight Cycles: 100
 Location: 3
 Negative No.: D-3139
 Mount No.: 619-P

Figure 5-104. Microstructure of Exposed Cb-752/R-512E Tee-Stiffened Panel



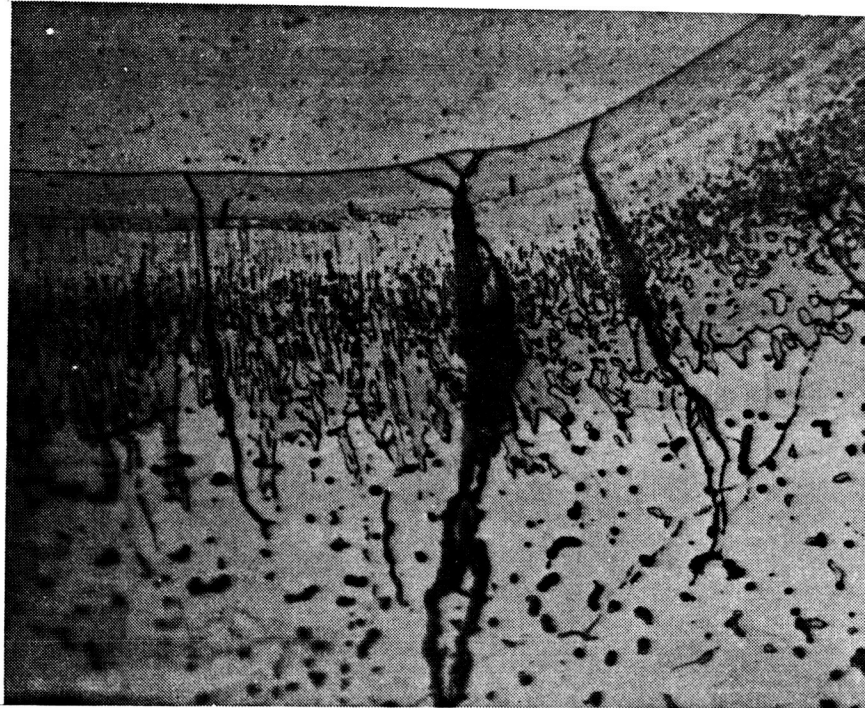
Magnification: 500X
 Etch: Light
 Panel No.: BST-2
 Flight Cycles: 100
 Location: 3
 Negative No.: D-3141
 Mount No.: 619-P

Figure 5-105. Microstructure of Exposed Cb-752/R-512E Tee-Stiffened Panel



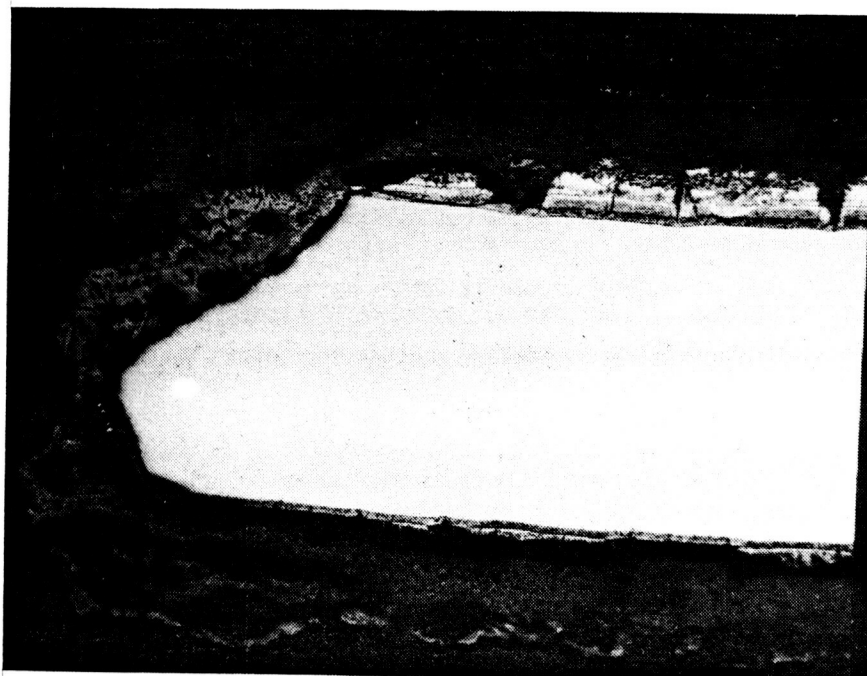
Magnification: 100X
 Etch: Light
 Panel No.: BST-2
 Flight Cycles: 100
 Location: 3
 Negative No.: D-3138
 Mount No.: 619-P

Figure 5-106. Microstructure of Exposed Cb-752/R-512E Tee-Stiffened Panel with "Laboratory" Repair



Magnification: 500X
 Etch: Light
 Panel No.: BST-2
 Flight Cycles: 100
 Location: 3
 Negative No.: D-3140
 Mount No.: 619-P

Figure 5-107. Microstructure of Exposed Cb-752/R-512E Tee-Stiffened Panel with "Laboratory" Repair



Magnification: 100X
 Etch: Light
 Panel No.: BST-2
 Flight Cycles: 100
 Location: 1
 Negative No.: D-3144
 Mount No.: 620-P

Figure 5-108. Microstructure of Exposed Cb-752/R-512E Tee-Stiffened Panel with "Field" Repair

While the amount of coating oxidation is quite different in these two panels the unoxidized coatings that remain are very similar in structure. A microprobe analysis of the tagged coating both before and after exposure might resolve the differences. This was, however, beyond the scope of the program.

As discussed in Section 5.5.1, panel BST-2 was used to evaluate two coating repair techniques during the flight simulation exposure. A section through the HiTemCo "laboratory" repair is shown in Figures 5-106 and 5-107. The structure of the coating is very similar to the original coating and appears to have been completely effective in preventing further oxidation. The large amount of the light colored constituent in the outer part of the coating was not identified but appears to be unreacted coating in an area of rather heavy application. A Convair "field" repair coating is shown in Figure 5-108. This particular repair was successful in arresting further substrate oxidation over a number of cycles. No interdiffusion of the coating and substrate can be seen. Lack of proper surface preparation, i. e., removal of all the oxide prior to application of the coating slurry undoubtedly is responsible, in part, for the poor bonding.

5.7.6 Metallography summary. - The metallographic results are consistent with the observations of Section 5.5, namely, (1) the Cb-752/R-512E material system exhibited better resistance to flight simulation exposure than did the C-129Y/R-512E system, and (2) the corrugated panel configuration, because of lower temperatures at the edges, probably was less susceptible to localized oxidation and substrate erosion than the tee-stiffened configuration. For the Cb-752/R-512E system, oxygen contamination of the substrate was found in only one location and that to a very limited extent. The C-129Y/R-512E system, however, showed contamination at several locations on both of the tee-stiffened panels. Also, a larger percentage of the coating thickness was oxidized on the C-129Y panels. This may be explained in part by the high degree of porosity observed in the coating after flight simulation exposure. In general, for both alloys the inside surfaces of the flanges on the tee-stiffened panels were more heavily oxidized than any other areas. It was in this region, near the outside edges, that most coating breakdown occurred. Substrate consumption during the 100 flight cycles was about 0.0005 inch (0.0013 cm) per side for both alloys. Resistance of the electron beam welds to flight simulation exposure was excellent for both systems. Coating uniformity was also excellent for the two systems.

Metallographic examinations of the tagged panels failed to determine the reason for their poorer performance during flight simulation testing. Considerable oxygen contamination of the substrate and heavy oxide layers were observed in both tagged panels. Sections through the "laboratory" and one of the "field" coating repairs on tagged panel BST-2 showed both repair techniques to be effective in halting further oxidation of the substrate. The laboratory repair was the more efficient, however, as it had formed a diffusion-type bond with the substrate.

It was readily apparent throughout the subsize test series that identification of troublesome areas could be made visually during normal inspection periods. It is expected of coated columbium alloy to exhibit a degree of spallation and a variety of surface colors ranging from gray to brown-yellow. These colorations have not been correlated to unusual behavior or failure. Excessive spallation relative to adjacent areas did result in nearly identical surface failures due to substrate erosion on two specimens. However, the most noticeable and identifiable denotation of substrate oxidation is a bright yellow protuberance.

5.8 Nondestructive Evaluation

5.8.1 Summary. — The value of nondestructive testing as a process control tool was demonstrated during Phase I by the performance of coatings which produced consistent NDE data, versus relative poor performance of coatings producing correspondingly inconsistent data. However, although nondestructive testing was performed intermittently during the flight simulation, NDE beyond initial inspection did not aid the detection of incipient coating failure.

During Phase II, NDT was performed following processing of the subsize panels to assure uniformity of the diffusion bonds and to qualify the thickness and uniformity of coatings which were screened to be within safe limits. It should be noted that defective coatings were not subjected to flight simulation thus biasing the data against the analysis and detectibility of significant defects.

The use of radioactive labeling (see Appendix B) to assist in the analysis of the coating and reaction kinetics associated with the manufacturing process showed that suspect areas, while experiencing attack, were not among those in which failure occurred during thermal cycling. However, areas which contained discontinuities reported by the labeling technique were not subjected to severe oxidation conditions, i.e., they were located outside regions of maximum stress and temperature. Based on the dispersion and resulting signature of the radioactive tag, it may be concluded that breakdown of the coatings was within the coating lifetimes for the particular alloys and heat shield configurations tested.

The radioactive labeling showed the C-129Y/R-512E coating system to be partially unreacted, i.e., the coating was refined in zones rich in high-melting-temperature material. It was thought that the apparent zone refining would adversely affect coating performance; early breakdown of the coating during flight simulation was predicted.

During simulation testing, the C-129Y alloy tee-stiffened panels did experience early oxidation damage whereas the Cb-752 alloy panels did not. A comparison of the autoradiography signatures of these panels clearly shows the Cb-752 alloy system to be uniform whereas the C-129Y alloy results in eutectic formation and refinement of coating

particles. During siliciding, the radioactive tag and carrier (promethium oxide/lanthanum oxide) concentrates at the solidification front, moving with the liquid pool as the coating slurry is alloyed and solidified. The direction of solidification as well as the effect of panel configuration on temperature distribution and coating flow, may be observed from the autoradiographs. These data are supported by the results of nuclear activation analyses performed on both tagged and untagged specimens removed from selected test panels.

Autoradiography of the green state coating also showed for the first time, the wet-ability of edges and limitations of the coating process which require special consideration. Examples presented in subsequent sections of this report show the difficulty of dipping with regard to edges as well as the sensitivity of the unfired, green state coating to handling and abrasion.

Although limited by the amount of inhouse funding (IRAD) which could be allocated for the study, the use of radioactive labeling represents a major contribution to the state-of-the-art. Further work in this area could lead to improvement in coating systems beyond the limits of current technology.

5.8.2 NDT techniques employed during Phase II. —Nondestructive testing applied during Phase II consisted of the following techniques (refer to Appendix B for theoretical discussion and background):

5.8.2.1 Ultrasonic C-scan testing: Ultrasonic testing was used to assist the analyses of brazed joints for the production of candidate heat shields. Reflection of sound at the interface of a disbond results in a change in the gated ultrasonic signal. A recording is produced showing the relative sound transmission over the area of the shield that may be related to the quality of the bond.

5.8.2.2 Stimulated electron emission radiography: This technique employs electrons which are emitted from the columbium alloy substrate as a result of X-ray bombardment. The relative intensity of electrons emerging from the coating may be attributed to the distribution of high-atomic number modifiers present and to coating thickness. Electron emission radiography was used during Phase II to observe general coating uniformity on panels and micrometeoroid specimens prior to flight simulation.

5.8.2.3 Thermoelectric testing: This technique employs a hot and cold junction between dissimilar elements (modifiers) in the coating to detect changes in coating composition and thickness. Thermoelectric testing was employed primarily to detect thinning along the edges of panels prior to flight simulation testing.

5.8.2.4 Radioactive labeling: Employing a weak beta-radiation emitting isotope (promethium-147), radioactive labeling provides inherent radiation emission properties

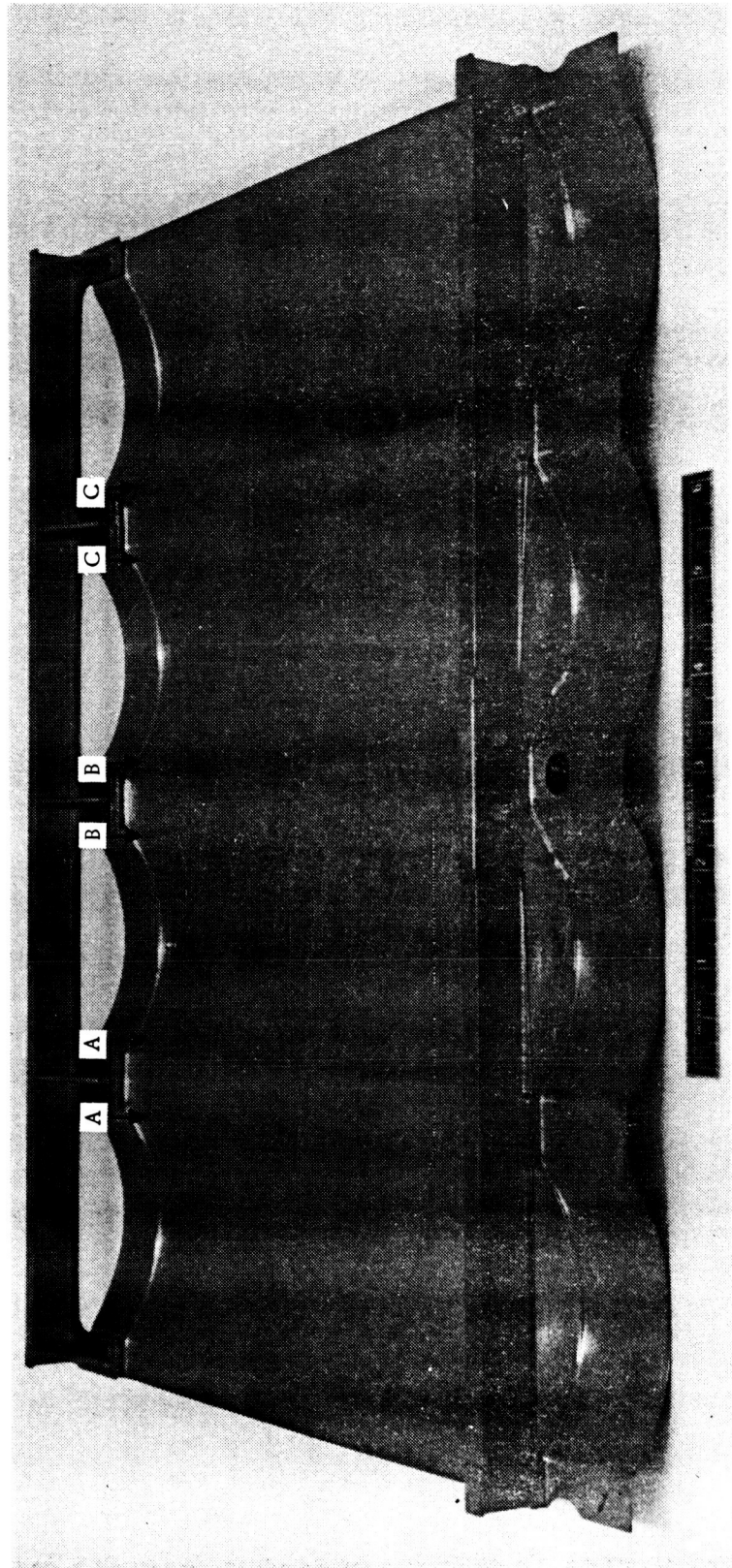
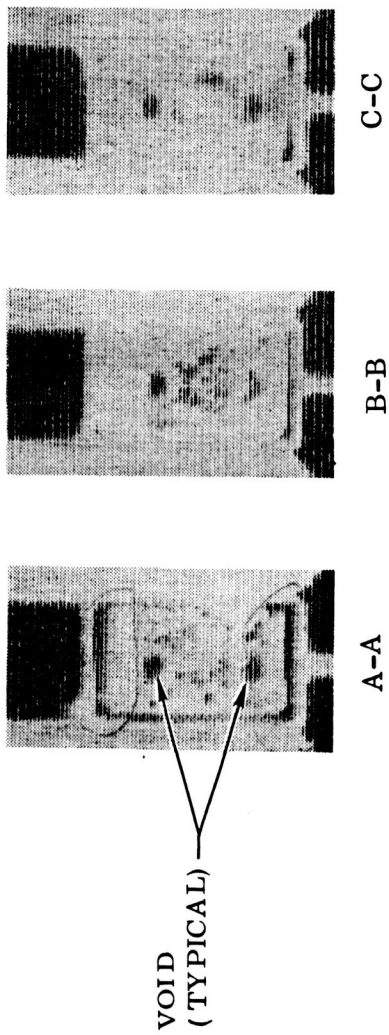


Figure 5-109. Ultrasonic C-scan Recording Showing Lack of Braze

to the coating in both the green and fired state. During Phase II, radioactive labeling was used to assist the analysis of the coating process and to provide inspection means for areas not readily accessible for alternate inspection.

5.8.3 Discussion of test results. —

5.8.3.1 Ultrasonics: The results of ultrasonics showed lack of setting of the braze alloy during initial attempts to fabricate panels employing stiffeners and load carrying attachment beams. Figure 5-109 is a C-scan recording showing the uniformity of selected joints between a transverse beam and corrugated panel evaluated early in Phase II. Ultrasonic data provided direction for improved fabrication techniques which reduced the presence of disbond. Panels showing lack of braze were not permitted to be coated but rather returned to the subcontractor for rework.

Panels were selected for flight simulation on the basis of ultrasonic data and visual examination of joint edges which gave no evidence of disbond. While failure of the aft joints of the hot gas flow test specimen occurred despite rework, the panel had been rejected initially as the result of ultrasonics and returned to the subcontractor for repair. A lack of noticeable columbium oxide in the joints following simulation testing suggests that the braze alloy may not have thoroughly interdiffused with the columbium resulting in a weak, brittle bond. Accordingly, failure of the aft joints along this transverse loaded beam could be attributable to bond strength which cannot be measured ultrasonically. It is possible that thermal stresses developed during the flight simulation could have exceeded the ductility limits of the braze joint considering the conditions of the test.

5.8.3.2 Electron emission radiography: Stimulated electron emission radiography was used for the initial screening of coated component and subsize heat shields. Non-destructive evaluation was not performed following flight simulation.

The results of electron emission radiography showed no major segregation of coating modifiers which should adversely affect shield performance. Based on general thickness and uniformity of the coatings, all panels were determined to be typical and within standard requirements. However, during flight simulation testing, the C-129Y tee-stiffened panels experienced breakdown of the coating, failing locally in the center of the panels. Based on the results of the initial nondestructive evaluation, it was assumed that this breakdown was within the average life time (60-80 cycles) of the shield for the particular alloy, coating and configuration involved.

5.8.3.3 Thermoelectric testing: Thermoelectric readings were made along the edges of all panels to assure coating uniformity and minimum thickness requirements. Again, despite local failure on the C-129Y tee-stiffened panels, the coatings as applied to all components subjected to flight simulation, were shown to be satisfactory. A comparison of typical data from the edges of tee-stiffened panels of each alloy, i.e., C-129Y and

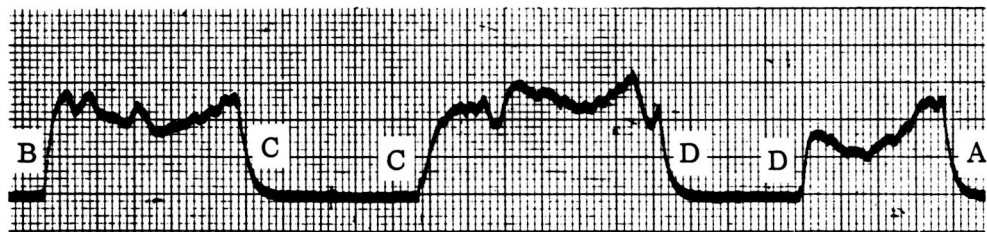
Cb-752 coated with R-512E is shown in Figure 5-110. It was noted that the thermoelectric response of both coated alloys indicated the coatings to be within safe thickness range [0.002-0.004 in. (0.051-0.101 mm)]. While local thinning was detected on various support hardware, such as bolts which were subsequently repaired, tests of major shield components gave no indication of significant defects.

The results of thermoelectric testing did not show differences between the C-129Y and Cb-752 alloy coatings on any of the heat shield components tested. It was also concluded from the NDT data that process control in producing these panels was exceptional. Unfortunately, the reliability of the thermoelectric test cannot be determined since defective shields were purposely not subjected to simulation testing. Panels undergoing flight simulation testing gave no evidence of early breakdown of the coating which may be attributable to edge defects.

The above conclusions appear contradictory to the general discussion of coating failure contained in Section 5.6. However, the edge attack initiated along the center ribs of the C-129Y tee-stiffened panels occurred late in the lives of the panels, i.e., after 60-80 reentry cycles. Similar attack did not occur on the Cb-752 alloy panels of the same configuration nor on other shield components of various coating systems and configurations subjected to identical test conditions. Accordingly, failures that occurred on the C-129Y tee-stiffened panels are probably within the average life-time of the coating system for this particular alloy, coating and shield configuration. A deeper look into this problem is contained in the following section.

5.8.3.4 Radioactive labeling: The results of Phase I showed that incipient coating breakdown may not be detected by conventional NDE methods. It was concluded from the coupon testing that general failure is apparently related to the mechanics of the coating process of which we have little knowledge. Earlier research (Reference 5) by Convair employing Mössbauer Spectroscopy was aimed at studying the basic mechanism of inter-diffusion of the coating and conditions under which general degradation or spallation of the coating may be expected. While these studies were not completed, it was hypothesized that general "coating wear" or progressive spallation, is attributable to a change in the chemical bond state of the coating as the result of oxidation. The size distribution of metallic particles (modifiers) in the slurry and the influence of the substrate on the formation and stability of the silicide has not been studied.

It was suggested for the current evaluation, that radioactive labeling be employed on a limited scale to assist the analysis of the coating process. Earlier studies employing a radionuclide (promethium-147) in a lanthanum oxide carrier was shown to provide two useful categories of nondestructive measurement: 1) autoradiography which provides a very detailed and high resolution picture showing coating distribution and integrity, and



Cb-752 (BST-3)



C-129Y (YST-2)

TYPICAL DATA

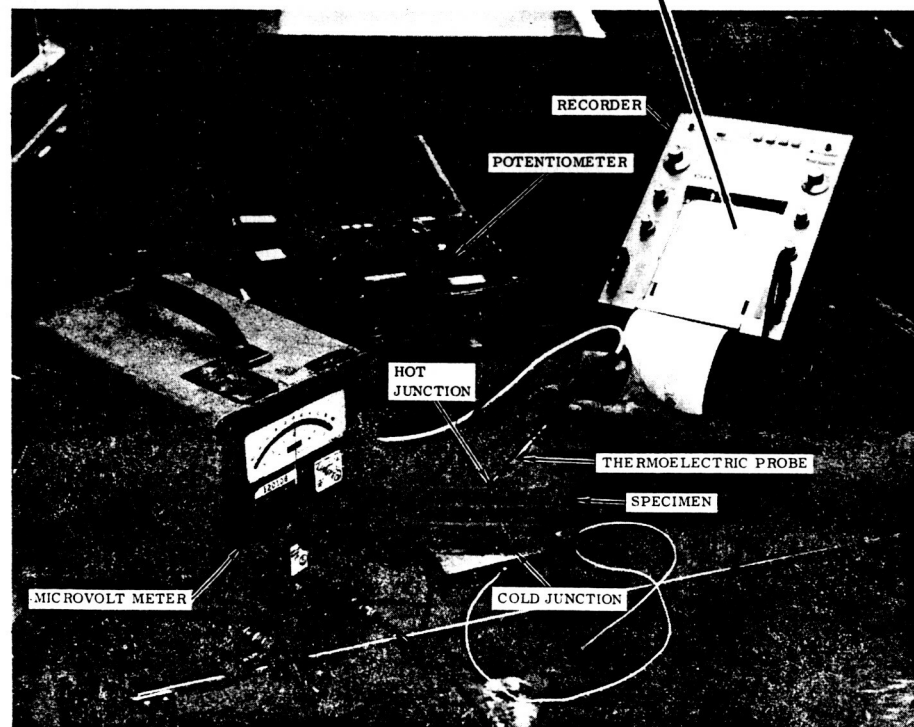


Figure 5-110. Thermoelectric Testing of Small Size Panels

2) direct radiation counting which provides a quantitative measure of the thickness of the coating. Calculations showed that a radioactive loading level of 0.02 microcuries per cm^2 ^{147}Pm would be sufficient for use with the HiTemCo coating. The required material addition (approximately 0.2 Wt%) was considered to be compatible with the coating. Pending satisfactory results of preliminary oxidation tests to evaluate the influence of the radionuclide and carrier on the performance of coated coupons, four of the twelve tee-stiffened panels were to be coated with a R-512E slurry modified with the radionuclide addition.

The weak ionization potential of the beta radiation emitted by promethium-147 cannot alter the properties of the coating. The coating, a conductive intermetallic compound, behaves more as a metal than as a semiconductor. Ionization produced by the beta radiation is without effect since any positive holes produced by ionization are rapidly refilled by electrons from the conductive band. Metallic radiation damage is primarily caused by atomic displacement which is non-existent with low energy electron bombardment.

The radiation emitted by ^{147}Pm has a peak energy of 0.224 MeV and an average energy of about 0.07 MeV. Since the average energy is below the approximate 100 KeV threshold for bremsstrahlung (X-ray emission associated with deflection of the beta particles by electrical interactions with the atoms of the coating), 99.9% of this energy is dissipated in the silicide via elastic and inelastic collisions. Elastic scattering particularly predominate when low energy beta particles interact with high atomic number substrates. Elastic scattering should produce no material damage.

Preparation for tagging: Early attempts to incorporate the radionuclide into the coating slurry involved the use of a rod mill to reduce the size and agglomeration of lanthanum oxide particles used to carry the promethium. While the average particle size was reduced to less than 10 microns, the binders of the coating were also broken down by the action of mechanical shear and by the temperature generated in the milling process. The resultant coating (slurry) lacked the viscosity and strength necessary for application; the slurry was discarded following attempts by HiTemCo to return these properties to the coating.

The technique for preparing the radionuclide tag involved ammonium hydroxide which was used to coprecipitate hydroxides of promethium and lanthanum. The precipitate was burned to ash to produce oxides of both rare earths. In a second attempt to combine the tag with the coating slurry, the ash was ground with a small quantity of the volatile vehicle (amyl acetate) of the coating using a mortar and pestle. Additional amyl acetate was added to the mixture and the fine particles suspended. The fines were removed with a pipette leaving residue (larger particles) at the bottom of the container. The process was repeated until all of the ash was suspended in amyl acetate. The solution was added to the green slurry and the ingredients mixed in a paint shaker for about 20 minutes.

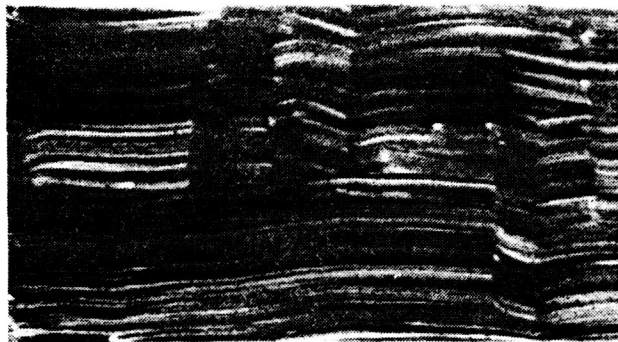


Figure 5-111. Autoradiograph of Tagged Coating (Light areas correspond to thinning attributable to brushing.)

Following preparation of the tagged slurry, a small quantity of the coating was applied by brush to a strip of plastic. An autoradiograph of the strip may be seen in Figure 5-111. As determined by enlargement of the autoradiograph, the average particle size of the radionuclide (carrier) was shown to be about 5 microns. Brush strokes showing variance in the thickness of the green coating can be seen in the figure.

Preliminary tests: Screening tests performed at HiTemCo showed no evidence of segregation or settling of coating constituents following shipment of the tagged

slurry between San Diego and New York. The viscosity of the coating was also shown to be within standard limits. Samples were prepared using Cb-752 coupons for oxidation tests. The specimens were tested together with untagged coatings in slow cycle oxidation using a maximum temperature profile of 2400°F (1589°K) and at one atmosphere. The 52 cycle test is equivalent to more than 200 reentry simulations.

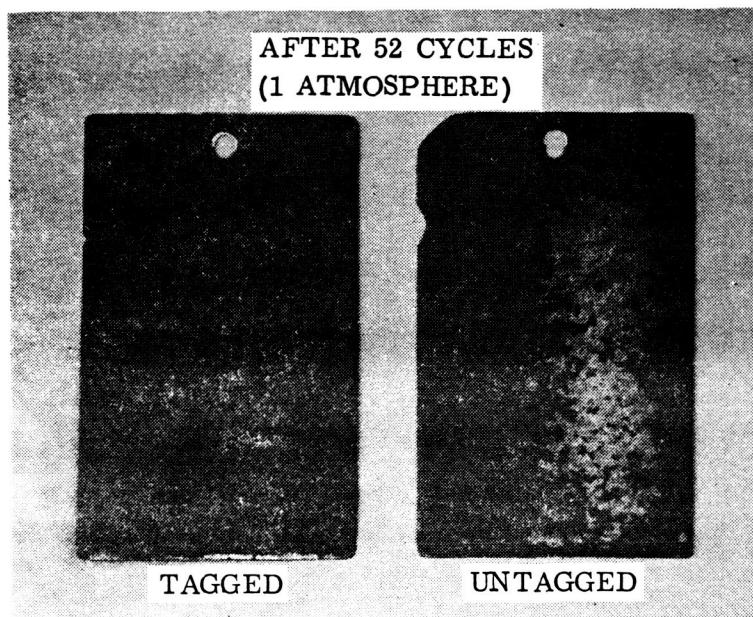


Figure 5-112. Results of R-512E/Cb-752 Alloy Limited Oxidization Test (This test showed the tagged coating to be more stable and more oxidation resistant than the untagged coating.)

The results of the oxidation tests showed the tagged coatings to be more stable and more oxidation resistant than the untagged coatings. While the number of specimens involved is statistically insignificant, i.e., the test lacked adequate sample size, the results did not indicate that the tag would adversely effect the performance of the coating. It was also noted from autoradiographs taken prior to oxidation testing, that segregation of the tag material evidenced in the autoradiograph corresponded to the oxidation pattern initiated in the coupons. A typical comparison of these data may be seen in Figures 5-112 and 5-113.

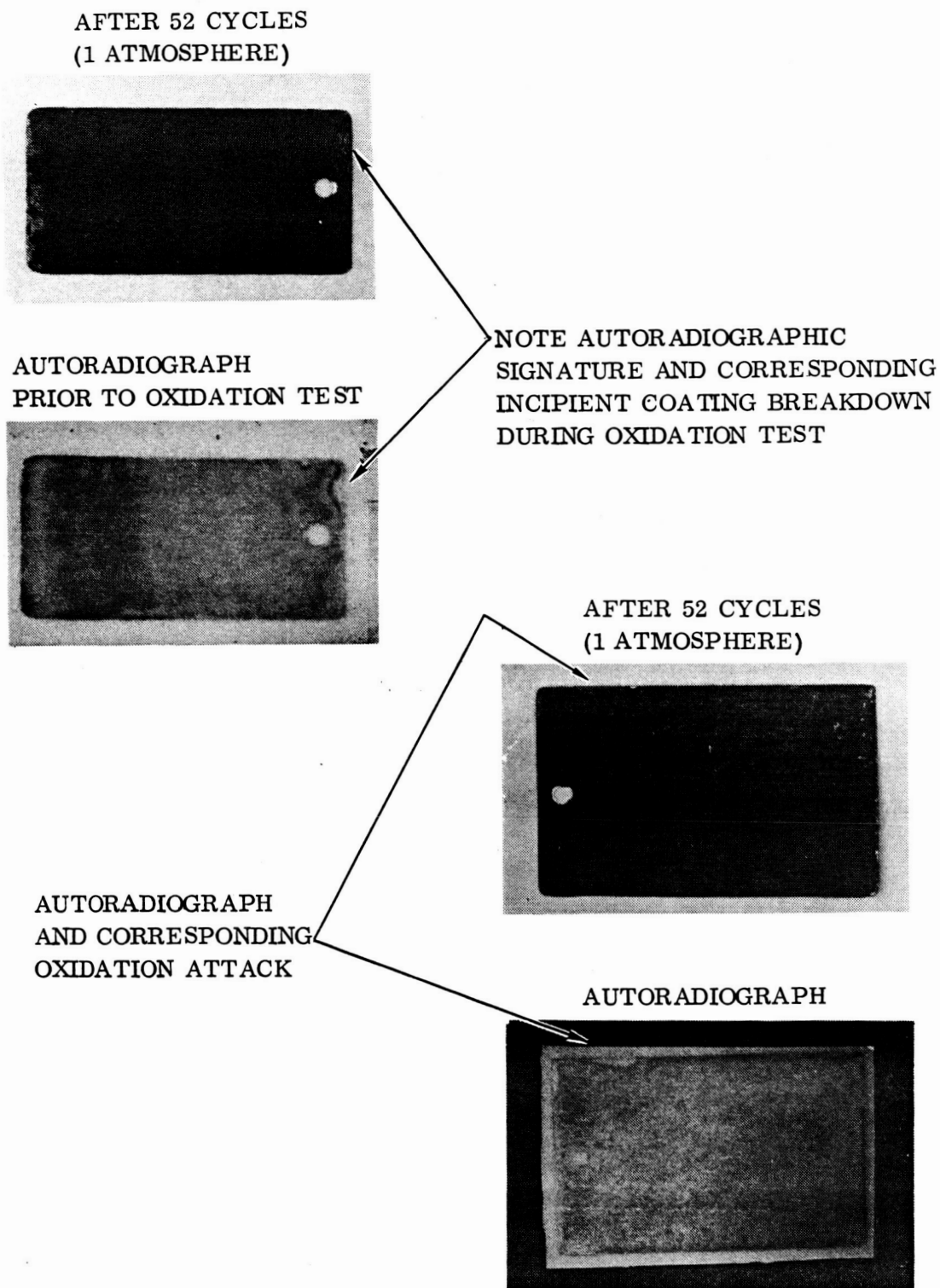


Figure 5-113. Autoradiograph Versus Oxidation Damage During R-512E/Cb-752 Alloy Screening Test

Earlier experiments with radioactive labeling had indicated that the radionuclide (carrier) would segregate in accordance with the movement or concentration of major modifiers or constituents in the coating required for oxidation protection. Accordingly, beginning oxidation damage may have been predicted from the autoradiographic signatures developed prior to the slow cycle oxidation tests.

Coating of tee-stiffened panels: Prior to applying the tagged coating to the tee-stiffened panels, the slurry was reblended and amyl acetate added to optimize the viscosity of the slurry for application by dipping. A withdrawal rate was established to obtain an average coating weight of 22 to 25 mg/cm². Autoradiography was again used to assure uniformity of the coating prior to any application to test hardware.

Safety considerations imposed restrictions upon the coating operation which could not be conducted without the use of a hood, remote handling equipment, and personnel monitoring. Spraying was not permitted in applying the radioactive slurry and a special container was required to prevent possible contamination due to accident (see Figure 5-114). During coating operations, the use of gloves and restrictive handling procedures made it difficult for the coating technician to establish conditions representative of production. While every effort was made to duplicate the conditions of the test, neither the technician nor the equipment used to coat the tagged panels was the same as used in preparing the untagged panels.

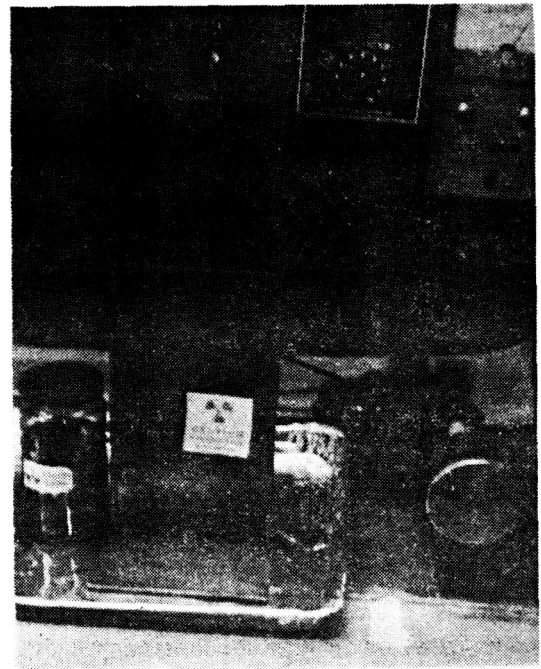
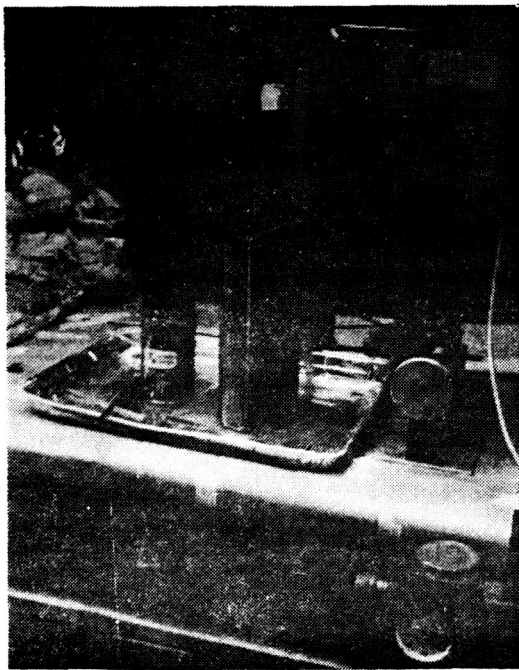


Figure 5-114. Container and Equipment for Applying Radioactive Coating

Following application to a tee-stiffened panel, the uniformity of the green coating was observed by contact autoradiography. The results of this test provided evidence of the wettability of the panel. For the first time, the difficulty of coating edges could be studied with the aid of autoradiography which provided insight into the relative thickness and distribution of the coating beyond the resolution of conventional techniques. The results of this test are shown in Figure 5-115.

As the result of the autoradiography, the edges of the tee-stiffened panels were re-coated using a striping tool. Areas of the panels showing evidence of thinning or buildup of the coating slurry were given special attention during the coating operation.

Application to test panels: Four tee-stiffened panels (two of each alloy) were coated with the tagged slurry. The autoradiographic signature was unique; signatures for the same alloy and configuration were mirror images of each other. The pattern of the image for the case of the Cb-752 coating showed the coating to be extremely uniform with no evidence of segregation. The direction of solidification of the liquid slurry was evident in the radiograph by the presence of radionuclide concentration at one end of the panel as shown in Figure 5-116. From these signatures, it is evident that the solidification order of the coating is dependent upon configuration despite temperature uniformity in the furnace.

In the case of the C-129Y tee-stiffened panels, the radionuclide was shown to be segregated throughout the panel. Consideration of the particle physics associated with the dispersion of the radionuclide and its probable behavior in the coating, suggested that the radionuclide was concentrating at the solidification front, moving with the liquid pool as the coating slurry alloyed and solidified. It appeared from the autoradiographic signatures that interdiffusion with the C-129Y substrate producing ternary eutectic formation and refinement of particles in the coating should adversely affect coating performance.

Nuclear activation analysis was performed of etchings from selected areas of a C-129Y tee-stiffened panel (YST-1) which was not subjected to reentry simulation. The etching was performed twice with dilute HNO_3/HF in each of four areas of the panel displaying absence, light, average and heavy concentrations of the radionuclide. The first etch in each area was shorter in duration than the second etch. Each etch solution was dried under a heat lamp which resulted in a hydrated nitrate with a small amount of fluoride; it may be assumed that the dried sample was approximately 25% metal.

The dried sample was analyzed for Fe, Cr, Hf, and W using comparative standards. It was noted that the etched areas were crazed subsequent to coating, which means that the acid did not penetrate uniformly. This suggests that the coating was not uniform. Boundary lines present in the coating were comparatively susceptible to etching. The experimental data are presented in Tables 5-6 and 5-7.

TYPICAL REGIONS OF
NON-WETTING INDICATED
BY ARROWS

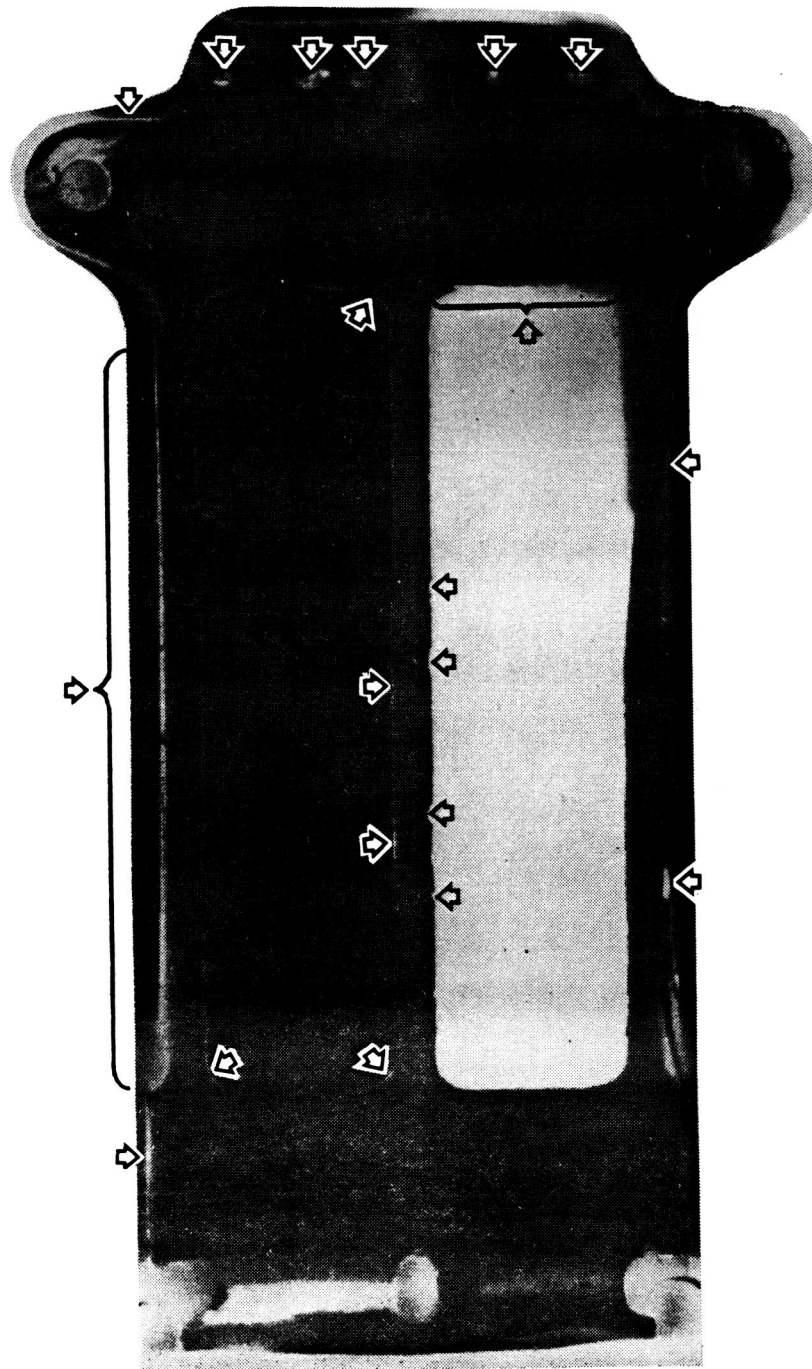
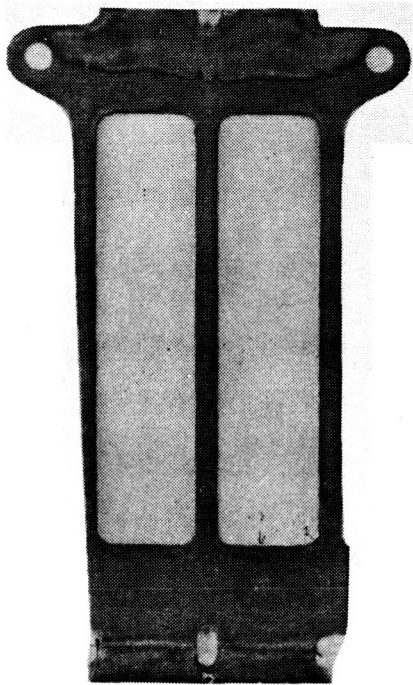


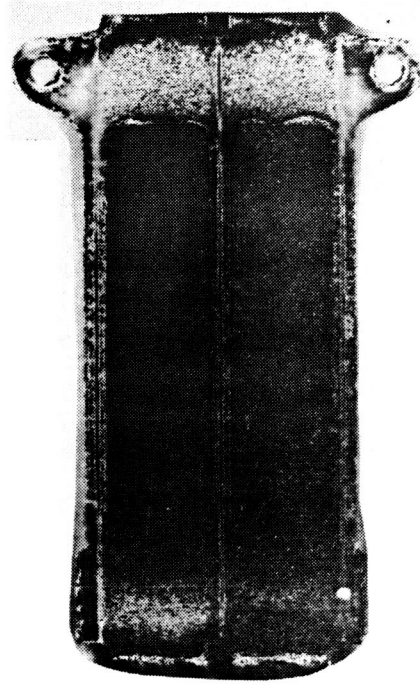
Figure 5-115. Autoradiograph of Green Coating Showing Typical Lack of Wetting

R-512E/Cb-752



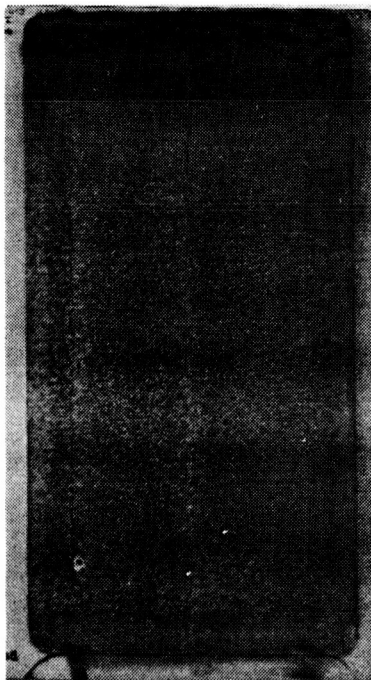
BACK

R-512E/C-129Y

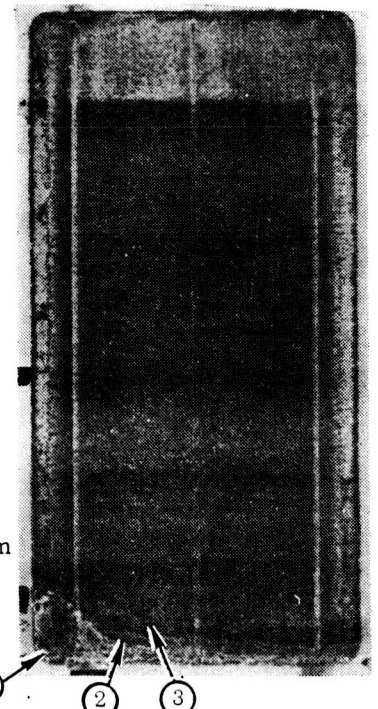


BACK

FRONT



FRONT



- ① LIGHT CONCENTRATION ^{147}Pm
- ② AVERAGE CONCENTRATION ^{147}Pm
- ③ HEAVY CONCENTRATION ^{147}Pm

Figure 5-116. Autoradiographic Signatures of Coated Heat Shields

Table 5-6. Nuclear Activation Analysis of Coated Panel (YST-1)

Characteristic of Dried Etch Solution	Panel Location						
	#1, (dark), ~0.05 cm ²		#2, (avg.), ~0.06 cm ²		#3 (light), ~0.08 cm ²		#4(white- no activity)
	1st	2nd	1st	2nd	1st	2nd	
	<u>Etch</u>	<u>Etch</u>	<u>Etch</u>	<u>Etch</u>	<u>Etch</u>	<u>Etch</u>	
Weight, mg	2.3	10.3	2.7	9.8	3.4	10.0	4.0
β counts/min/mg	30.8	11.7	26.1	6.4	10.4	4.2	20.3
Cr, % w	4.22	3.01	3.74	3.39	4.68	3.19	4.03
Fe, % w	3.29	4.17	1.79	3.13	2.47	3.90	3.28
W, % w	2.70	2.58	1.66	3.07	2.49	3.32	4.73
Hf, % w	1.24	2.45	1.56	2.32	1.23	2.97	2.16
<u>Etched Surface</u>							
Craze	Fine		Medium		Coarse		Coarse

It is clear from the preceding data that there is correlation between the amount of chromium present in the coating and the presence of tungsten. The distribution of these elements in the C-129Y tee-stiffened panels is not uniform which may account for the relatively poor oxidation resistance of the coating. The amount of tungsten present is significantly higher in areas showing low levels of radioactivity in the autoradiographs.

The iron to tungsten ratio in the first etch follows the progression of radioactivity while in the second etch the iron plus chromium to tungsten ratio, (Cr + Fe): W, follows this progression. This suggests that at depths the radioactivity attempts to follow both chromium and iron but is replaced by tungsten. At the surface of the coating the chromium does not correlate, possibly because of oxidation. (The radioactivity would tend to follow the closest oxide.) While the chromium can exist in three states (+2, +3 or +6), the iron exists only as +3.

Conclusion: It is important to note that the conditions of processing, i.e., handling and equipment, used to prepare the tagged panels were not the same as for the case of the untagged panels. While both operations were highly controlled, the tagged panels were subject to operator error due to the handling precautions of the materials involved and handling limitations of the facilities. It may be assumed that local oxidation along the edges of the tagged panels is attributable to process variables which can easily be corrected.

Table 5-7. Correlation of Nuclear Activation Test Data
(Based on data from Table 5-6)

A. Second Etch

X	Y	Pearson Product-Moment Correlation Coefficient, r^*	Regression Line	
			Slope	Intercept
W	Fe	-0.557	-0.299	+4.644
W	Cr	+0.957	+0.461	+1.826
W	Hf	-0.399	-0.15	+2.99
Fe	Cr	-0.730	-0.655	+5.777
Fe	Hf	+0.59	+0.42	+0.96
Cr	Hf	-0.622	-0.490	+4.15
Activity	Hf	-0.74	-0.0364	+0.286
Activity	Cr	+0.74	+0.046	+2.916
Activity	Fe	-0.228	-0.0158	+3.788
Activity	W	+0.701	+0.0903	+2.464

B. First Etch

W	Fe	+0.889	+1.353	+0.153
W	Cr	+0.818	+0.779	+2.85
W	Hf	-0.996	+0.787	-0.365
Fe	Cr	-0.464	+0.290	+3.483
Fe	Hf	+0.845	+0.438	-0.093
Cr	Hf	+0.866	+0.718	-2.015
Activity	Hf	-0.285	-0.010	+1.243
Activity	Cr	-0.726	-0.032	+4.93
Activity	Fe	+0.272	+0.019	+2.09
Activity	W	-0.199	-0.009	+1.95

Note: Elements as % wt. Activity as cpm/mg.

*Ref. Introduction to Statistical Analysis, Third Edition, Dixon and Massey.

The radioactivity signatures showing general differences between the two coating systems (R-512E/Cb-752 and R-512E/C-129Y) is representative of production processing. The uniformity of these coatings is highly dependent upon the choice of substrate and upon the particle size-range distribution of elements contained in the slurry.

Radioactive labeling should be considered for future studies to analyze the reaction kinetics associated with the coating process. The application of the technique may provide information necessary for improved coating technology well beyond the current state of the art.

6 DESIGN AND ANALYSES OF SMALL-SIZE TPS

6.1 Design Conditions

6.1.1 Vehicle selection and flight environment. – The model vehicle, the investigative region, the design environment, and the design criteria were established during Phase I of this program (Reference 3). In the interest of maintaining continuity within this report, several of the more pertinent sections are repeated herein.

The model vehicle and the region selected for investigation to serve as the basis for TPS design and test are shown in Figure 6-1. The region selected for study is located between stations $X/L = 0.025$ [53 inches (1.25 meters)] and 0.050 [106 inches (2.49 meters)] where $L = 2120$ inches (53.85 meters). The vehicle cross-section at $X/L = 0.025$ is 64 inches (1.63 meters) and at $X/L = 0.050$ is 90 inches (2.29 meters) in diameter. The maximum radiation equilibrium temperatures in the investigative region range from 2400°F (1589°K) to 2000°F (1366°K).

6.1.1.1 Boost: The boost parameters, dynamic pressure, heating rate, and temperatures are presented in Figure 6-2 for a vehicle location of $X/L = 0.025$. It assumes a zero-lift ascent to separation at 183.5 seconds followed by a coast of 2.5 seconds between stages. Optimum pitch-plane steering of the powered orbiter continues until 434 seconds when the orbiter reaches the insertion orbit of 50 by 100 n. mi. (9.26 by 18.52 km) at a 55° inclination. After the orbit is circularized at 100 n. mi. (18.52 km), an additional burn is made to place the orbiter into a 100 by 270 n. mi. (18.52 by 50 km) path that is subsequently circularized into a nominal 270 n. mi. (50 km) by 55° inclination orbit. The maximum acceleration of the 3,500,000-pound (1,589,000 kg) fixed-gross-weight configuration was limited to 3 g.

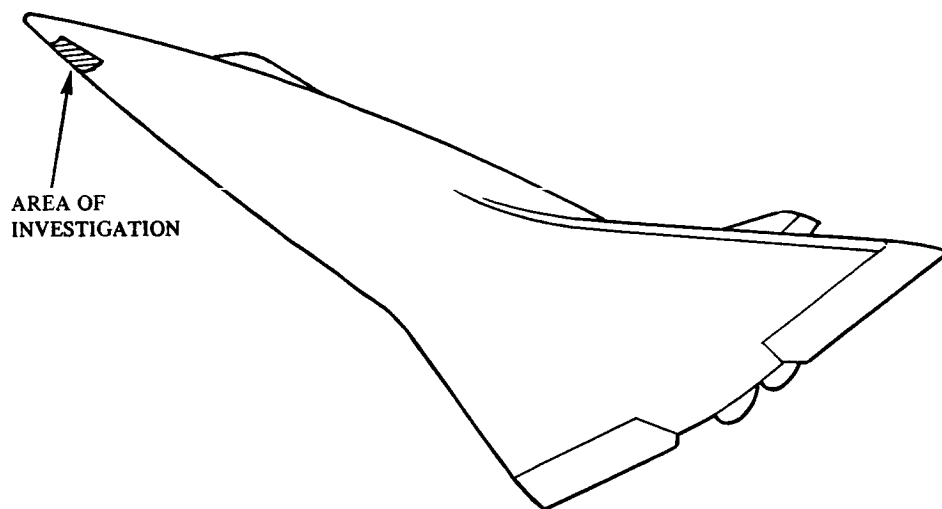


Figure 6-1. Orbiter Lower Surface Area of Investigation

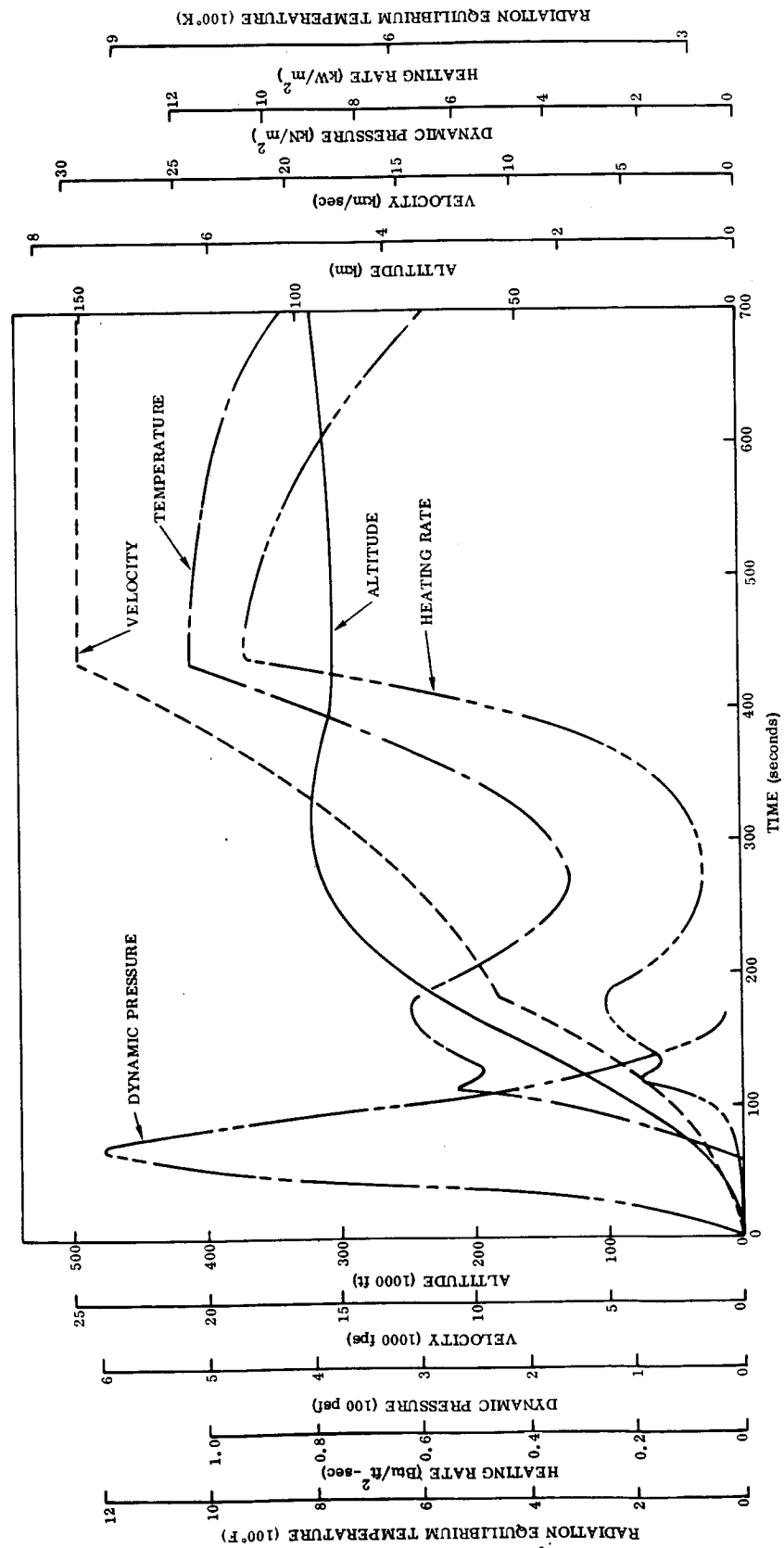


Figure 6-2. Selected Boost History - Lower Surface $X/L = 0.025$

The vibration response environment on the heat shield panels is the result of booster engine noise at ignition, aerodynamic noise during the transonic/maximum dynamic pressure period of boosted flight, and mechanical vibration of the orbiter boost engines. Booster engine liftoff noise levels were calculated on the basis of procedures contained in WADC TR 57-354 (Reference 5), and WADC TR 58-343, Volume II (Reference 6), modified by data from S&E ASTN/MSFC and published in Convair Report No. 76-549-4-151/AD-71-28 (Reference 7).

During the transonic period, aerodynamic shock waves will form at various locations and generally move aft. Turbulence in the boundary layer beneath these shocks will be amplified by their presence, providing significant vibratory excitation. In addition, shock waves from the booster will amplify the turbulence in the orbiter boundary layer, causing like effects. Also, separated flow will undoubtedly occur in the interference region between the booster and orbiter. The prediction procedures developed by Coe and Rechten (Reference 8), Ailman (Reference 9), and Robertson (Reference 10), have been used based on information furnished on the steady aerodynamic flow conditions. The environment transmitted to the heat shield support structure during orbiter boost phase will depend on the engine support structure, the orbiter primary structure, and the heat shield support structure configuration. Methods developed during the Apollo CSM and Saturn S-II programs have been employed to calculate the vibration environment at the heat shield attach points. Figure 6-3 presents a time history of the external acoustic environment that may be expected during liftoff and atmospheric boost flight. The liftoff acoustic noise environment shown in Figure 6-4 was developed by modifying Saturn V liftoff noise data with corrections for engine size, chamber pressure, and distance from the source. The maximum dynamic pressure aerodynamic noise environment shown in Figure 6-4 combines shock-boundary layer interaction effects (below 160 Hz) at $M = 1.4$ with estimates of unperturbed flow (References 11, 12, and 13).

The orbiter boost engine mechanically transmitted vibration environment is shown in Figure 6-5. It presents a vibration spectrum at the heat shield attach points and was derived from Saturn S-II/J-2 engine-induced vibration data.

Orbiter surface pressure histories for the booster trajectory in the mated configuration were derived from wind tunnel data and were available for discrete Mach numbers (References 14 and 15). Figure 6-6 shows the results of one such wind tunnel test at Mach number $M_\infty = 1.16$, which is close to the Mach number coinciding with maximum dynamic pressure. The data is plotted using the worst-case conditions of boost where the angle of attack may vary from a maximum of -6.7° for a headwind condition [$q_{\max} = 689$ psf (40 kN/m^2)] to $+3.0^\circ$ for a tailwind [$q_{\max} = 486$ psf (23.3 kN/m^2)]. A tolerance of ± 0.5 psi (3.5 kN/m^2) was added for the ability of the passive vent system to maintain static pressure. These data were the basis for the positive 3 psi (20.7 kN/m^2) heat shield differential pressure criteria presented in Section 6.1.2.

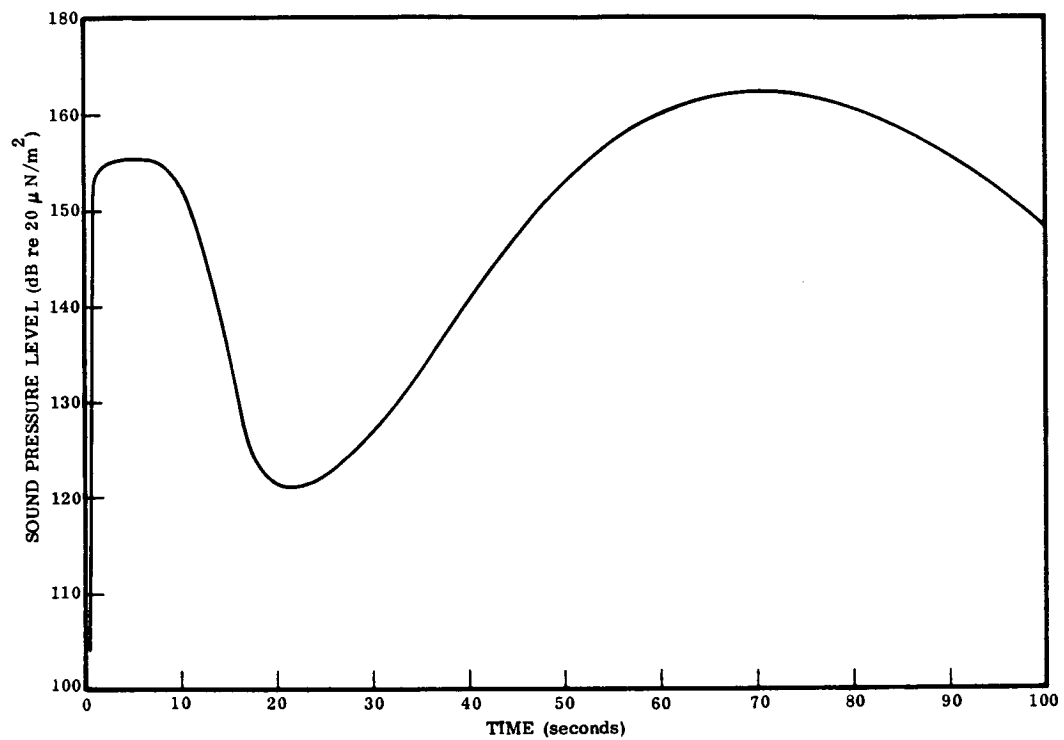


Figure 6-3. Boost External Noise Time History

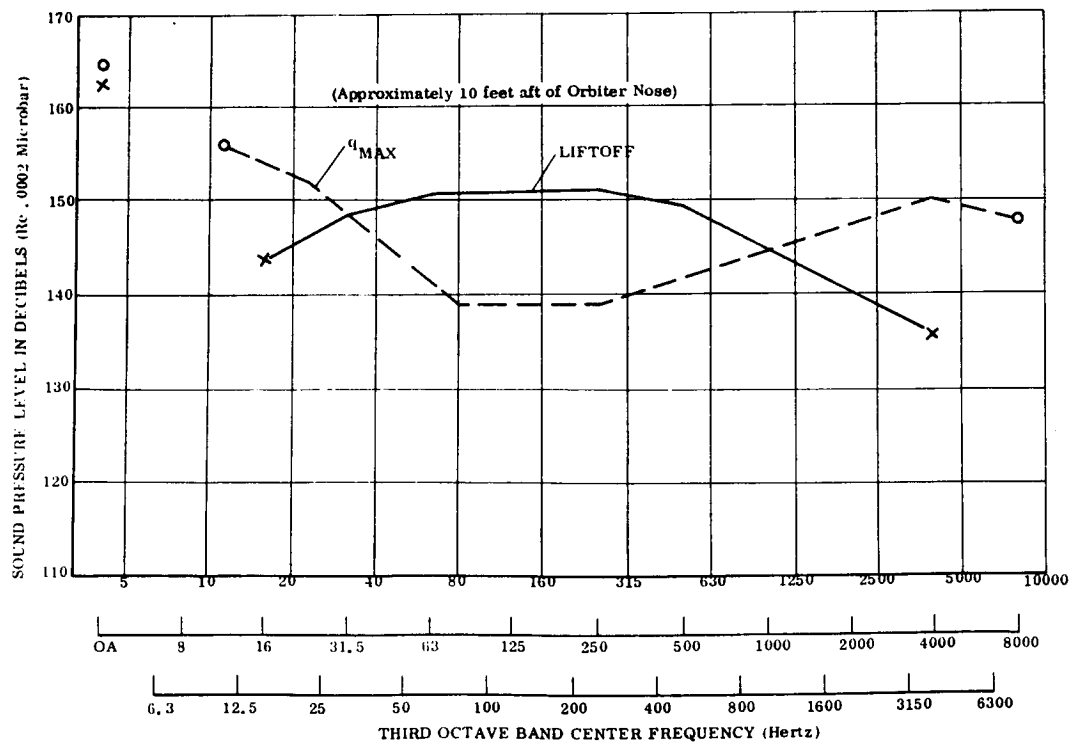


Figure 6-4. Heat Shield Panel Acoustic Environment

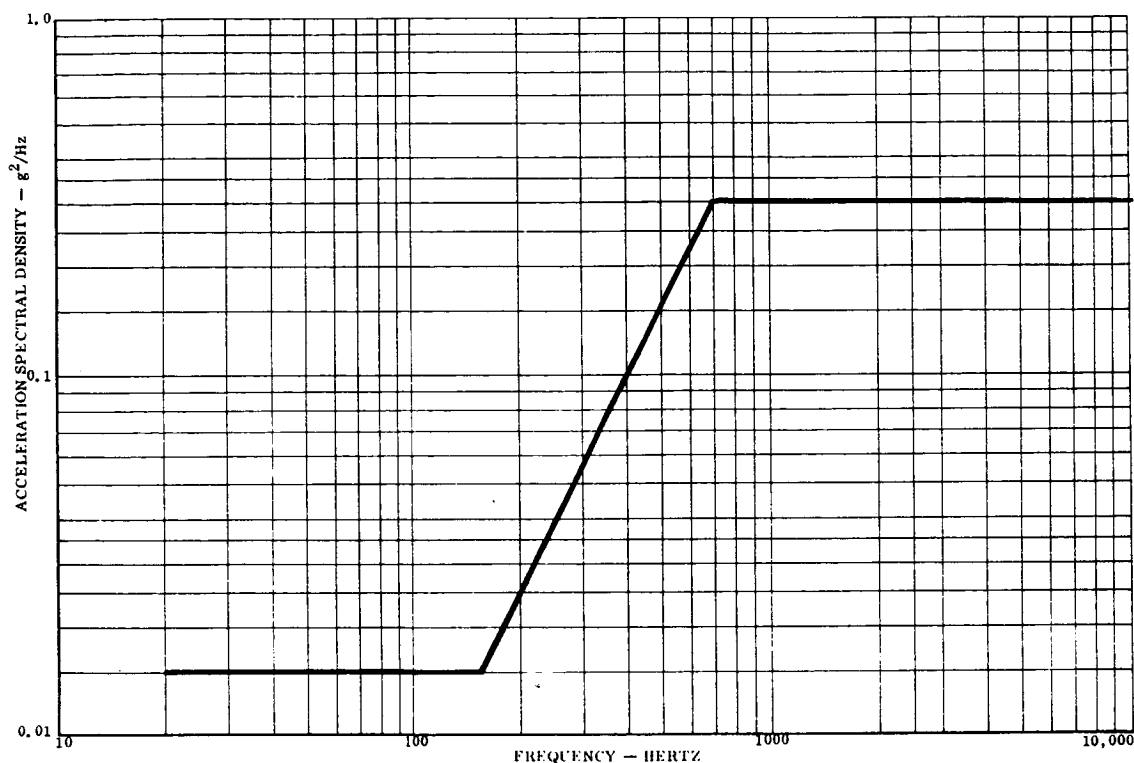


Figure 6-5. Boost Engine Vibration Spectrum at Heat Shield Attach Points

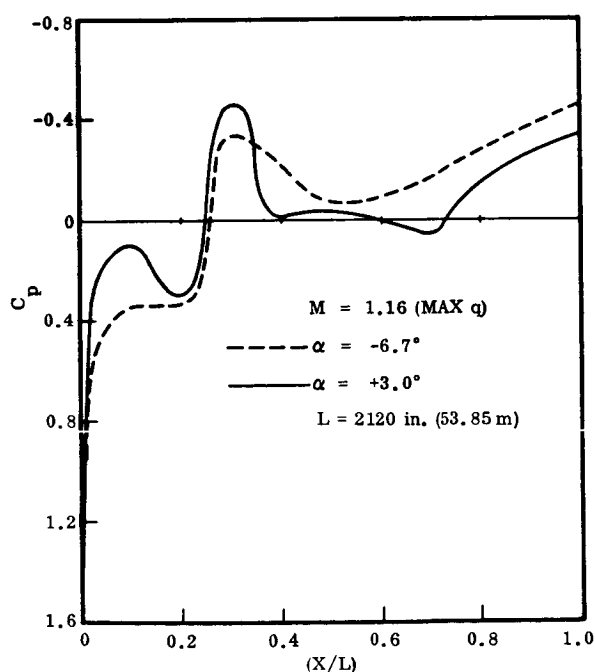


Figure 6-6. Orbiter Lower Fuselage Pressure Distribution for Mated (Orbiter/Booster) Configuration (SSV 134C)

6.1.1.2 Entry environment: The atmospheric heating environment definition for the Space Shuttle system covers the entire range of convective heating analysis. Because of the complicated vehicle configurations and flow fields, experimental data is relied on heavily, and is correlated and extrapolated using analytical techniques to predict the heating environment. Analysis of Apollo flight test data has demonstrated the validity of this approach. Typical entry environments are presented as examples of the environments that were used to establish test requirements.

The vehicle is represented as a point mass, i. e., translational equations of motion only are considered. Entry is assumed to begin at 400,000 feet (121.6 km) following a 435-fps

(132.6 m/sec) retro from a 270 n. mi. (50 km), 55° inclination orbit. The entry interface with a spherical rotating earth was at the ascending node. Roll maneuvers are performed about the velocity vector; therefore, the aerodynamics (i. e., heating distribution) remain symmetrical about the vehicle centerline. Figure 6-7 presents the entry histories. The apparent discontinuities in the heating and temperature curves may be correlated with the vehicle angle of attack changes. The spikes that initiate at approximately $t=2000$ seconds result from a laminar-to-turbulent boundary layer transition.

The surface pressure history presented in Figure 6-7 is based on the hypersonic Newtonian pressure coefficient and is considered to be accurate to approximately 2400 seconds in the entry trajectory. The pressure spike results from a pitchover maneuver. During entry, pressures are low. The maximum surface pressure (assuming no venting) would vary between approximately 0.2 psi (1.4 kN/m²) when the heat shield was at 2400° F (1589° K) to approximately 0.6 psi (4.1 kN/m²) when temperatures dropped below 1500° F (1089° K). Venting of the panel underside would reduce this differential. The maximum pressure differential across the panel in the entry phase would occur during a 2.5 g maneuver, which could be made at any time after 2500 seconds of entry. At this time a 1 psi (6.9 kN/m²) maximum pressure is experienced. For design purposes, an additional 1 psi (6.9 kN/m²) was added for venting tolerances. The maximum panel temperature after 2500 seconds of entry would be below 400° F (478° K).

The boost and reentry histories (Figures 6-2 and 6-7) have been modified and combined into the profile previously shown in Figure 5-1 for design and flight simulation testing.

6.1.2 TPS design criteria. - The main structural considerations are to design panels that: (1) have minimum weight and volume, (2) are reusable, (3) permit external removal from the vehicle, (4) permit inspection, and (5) accommodate thermal stress, deflections, and rotations. The critical design environments are established from the flight profile. Generally, the boost and entry environments design the outer heat shield panels, the boost environment sizes the heat shield and its supports, and the entry environment controls the materials. The entry environment generally causes the more severe thermal stresses. The outer heat shield panels are sized so that they sustain normal air loads, and are of sufficient stiffness to resist panel flutter. The standoffs are sized so that they transmit the panel air load to the structure, provide slip joints to accommodate thermal expansion, and minimize the number of thermal shorts. Initially, the panels and their components are sized to withstand the boost pressure loads that occur near maximum dynamic pressure and at low material temperatures. The panel size and gages are then checked for combined mechanical and thermal stresses at the maximum aerodynamic load condition and the maximum surface temperature condition, and the thermal distribution through the thermal protection and structural system is determined. In all cases, the panel size and the heat shield components are limited to a combined stress resulting from air load, inertia loads, and thermal loads that are below the selected material allowables for crippling, compressive yield, and

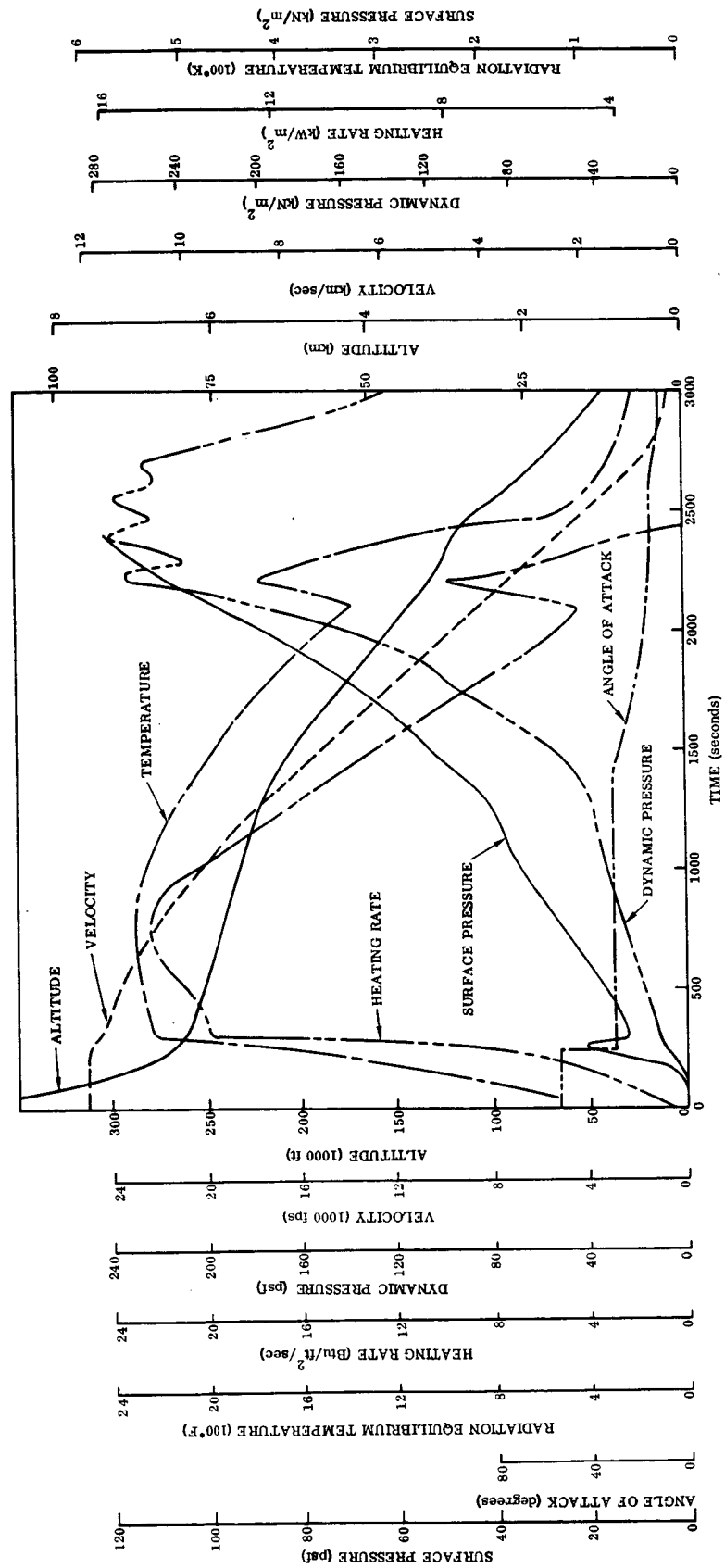


Figure 6-7. Selected Entry History - Lower Surface $X/L = 0.025$

tensile yield. Once the panel size has been established on a strength-stability-creep basis, the heat shield is examined to determine that no combinations of load (including dynamic load) and temperature produce deflections or rotations that would be structurally excessive (cause permanent set) or create hot spots resulting from perturbation heating effects.

The heat shield design criteria listed here consist of performance requirements (sometimes called failure modes or success criteria) and design goals.

6.1.2.1 Design goals: The goals are:

- (1) Have minimum weight
- (2) Be reusable for 100 missions
- (3) Permit external removal of heat shields
- (4) Permit coating inspection between flights

6.1.2.2 Performance requirements: Stress predictions will consider the actual effective structural material thickness and discount coating thickness. In materials where substrate thickness is a function of time, stress, temperature, and contact environment, it is necessary to consider the change of substrate thickness that is caused by these variables. The performance requirements are:

(1) Material rupture shall not be experienced during the service life of the vehicle. Material rupture shall be defined as a crack or hole that allows leakage of hot gases into the substructure and insulation. Rupture shall not occur even in an extreme flight maneuver or other circumstance where pressure and inertia loads are 1.5 times greater than the maximum predicted. In this case, however, it may be necessary to replace the panel before the next flight because of excessive plastic deformation.

(2) Material 0.2% offset yield shall not be exceeded during periods of flight when temperatures are below the range of significant creep.

(3) Out-of-plane deflections occur during the boost and entry phases due to differential pressure and thermal gradient loadings respectively. In addition, there are deflections that result from permanent creep deformations. The heat shields shall be designed to minimize aerodynamic drag and temperature increases by limiting inflight panel waviness. In the region of the vehicle to be examined, the maximum permissible waviness shall vary as a straight line whose function is defined by: $\delta = 0.1 + 0.04 L$ [(B.S.-12)/110], where L = the panel length (in inches) between supports and B.S. denotes the vehicle body station (Reference 16).

This deflection includes deflection of the supports, joints, and panels. It includes thermal and mechanical distortion as well as creep considerations. Creep effects shall be considered as accumulative over one service life (100 flights).

In the prediction of creep strain, consideration will be given restraining effects of adjacent material subjected to a different temperature/stress experience (e.g., plane sections remaining plane in beam cross-section). The residual stresses caused by these restraints will be evaluated and considered in progressive load cycles. For example, it would be expected that no significant residual stresses existed on the first flight and that considerable residual stresses were present on the next-to-last. This condition will materially affect the creep experienced in the second flight being different than that experienced in the last.

(4) Stability of structural components shall be assured. Compressive loads shall not cause instabilities even when the pressure and inertia source of these loads become 1.5 times the maximum predicted. Bowing of members due to accumulative creep effects shall be considered. Creep buckling and panel deflections shall be considered accounting for material property changes as a function of temperature.

(5) In no case shall flaws increase in size to a point that any of the performance requirements are not achieved, e.g., cracks shall not grow through the material so that a gas leak is allowed, cracks shall not grow so that structural instabilities result.

(6) Panel flutter shall be prevented in all modes, including first-vibration mode flutter, and in traveling-wave and standing-wave phenomena as defined by NASA SP-8004.

External surfaces shall be free of panel flutter at all dynamic pressures up to (1) 1.5 times the local dynamic pressure expected to be encountered at any Mach number in flight, and (2) the maximum dynamic pressure expected for dispersed abort trajectories.

(7) The panels shall have the capability to dissipate a lightning strike defined by MIL-B-5087 without loss of vehicle or mission capability.

6.1.3 Material properties. —

6.1.3.1 Mechanical and physical properties: The mechanical and physical properties (References 17 and 18) used in the analyses performed during this program are presented in the following section (Figures 6-8 through 6-23). It should be noted that the values presented here are slightly different than the recommended values presented in Appendix C of the contract Phase I final report (Reference 3). The values used in

the Phase II analyses are based on the "preliminary design curves." This was necessitated by the partial concurrency of the two phases and the fact that the recommended design values (Reference 3) were derived after the completion of the small size TPS analyses. The mechanical properties given are for the net base metal area after coating with HiTemCo R-512E allowing for a loss of 0.0015 inch (0.0381 mm) per side during the coating process with the application of 0.003 inch (0.076 mm) per side. No allowance was made for the subsequent coating/base metal diffusion as a result of cyclic exposure. However, the preliminary tensile properties are held to be conservative for 100 cycle exposure up to 2400° F (1589° K), see Appendix C, Reference 3 . The preliminary creep properties are also for the as-coated condition. It should be noted, however, that these are standard static creep data and, therefore, are probably unconservative when used for high-temperature cyclic exposure. See Sections 4.2.5.2, 4.5.4, Appendix B and Appendix C of Reference 3 . Table 6-1 presents a summary of the applicable material specifications and properties.

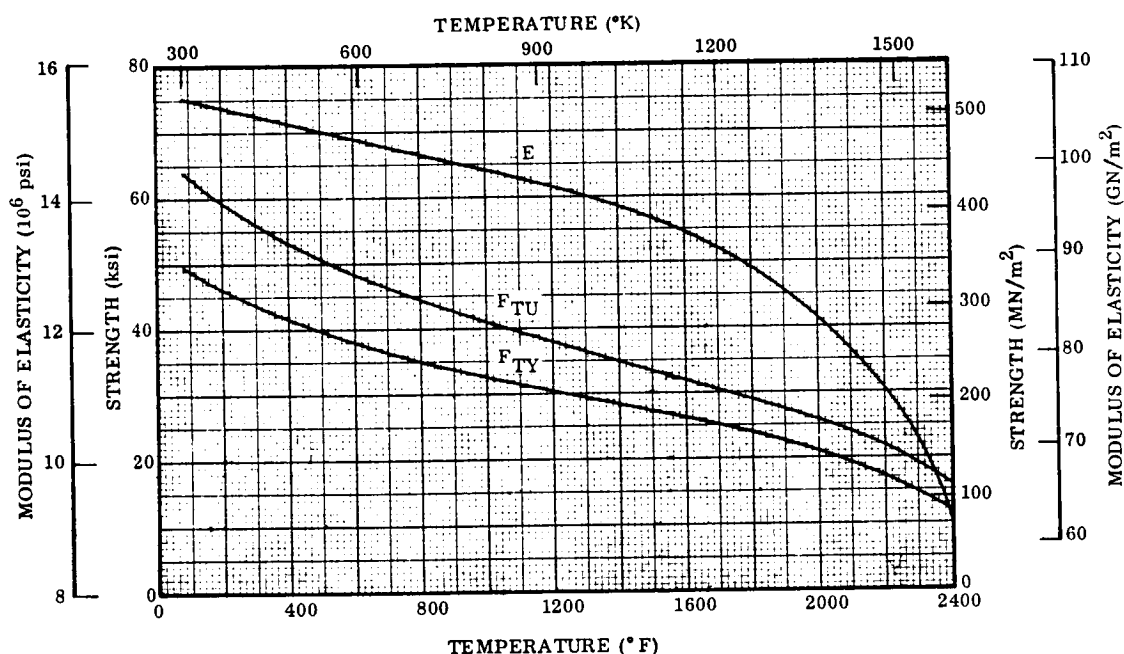


Figure 6-8. Preliminary Design Tensile Properties Versus Temperature for Cb-752/R-512E Based on Net As-Coated Section

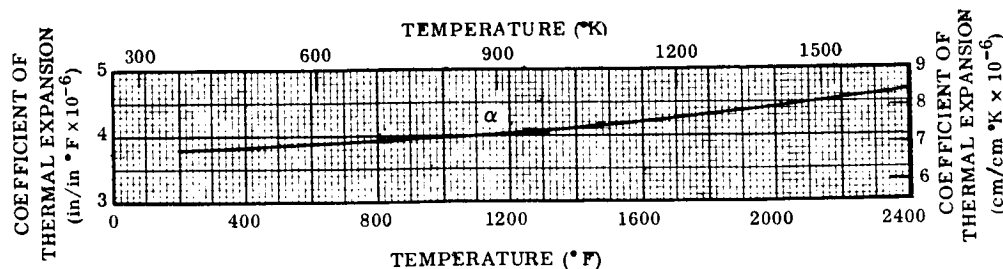


Figure 6-9. Coefficient of Thermal Expansion Versus Temperature for Cb-752

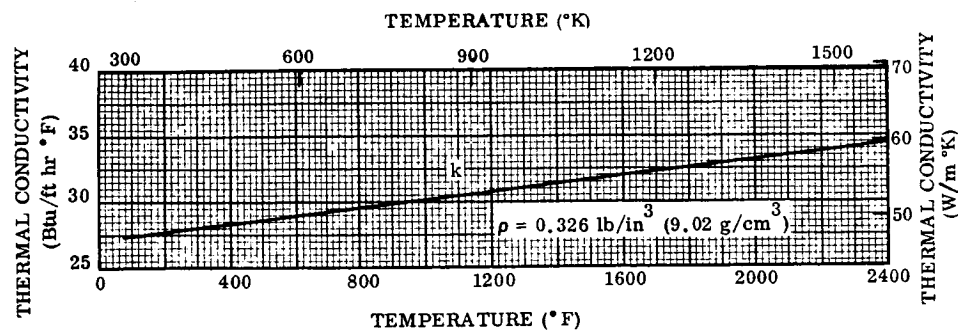


Figure 6-10. Thermal Conductivity Versus Temperature for Cb-752

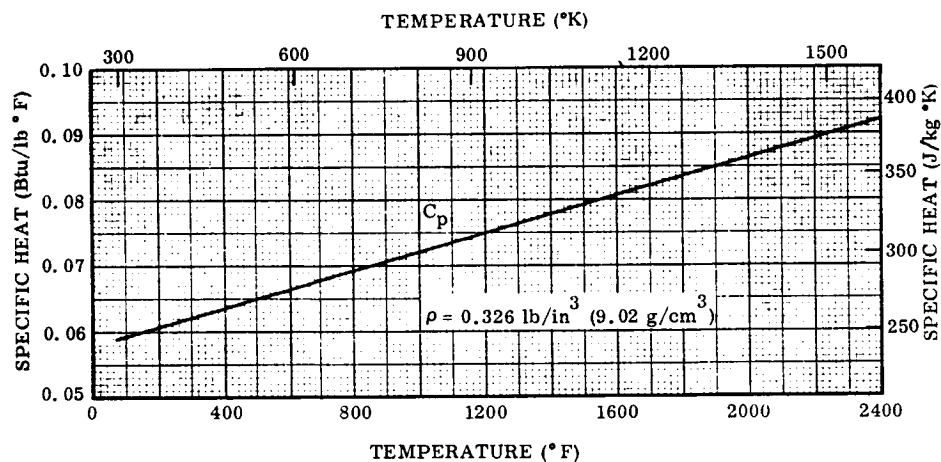


Figure 6-11. Specific Heat Versus Temperature for Cb-752

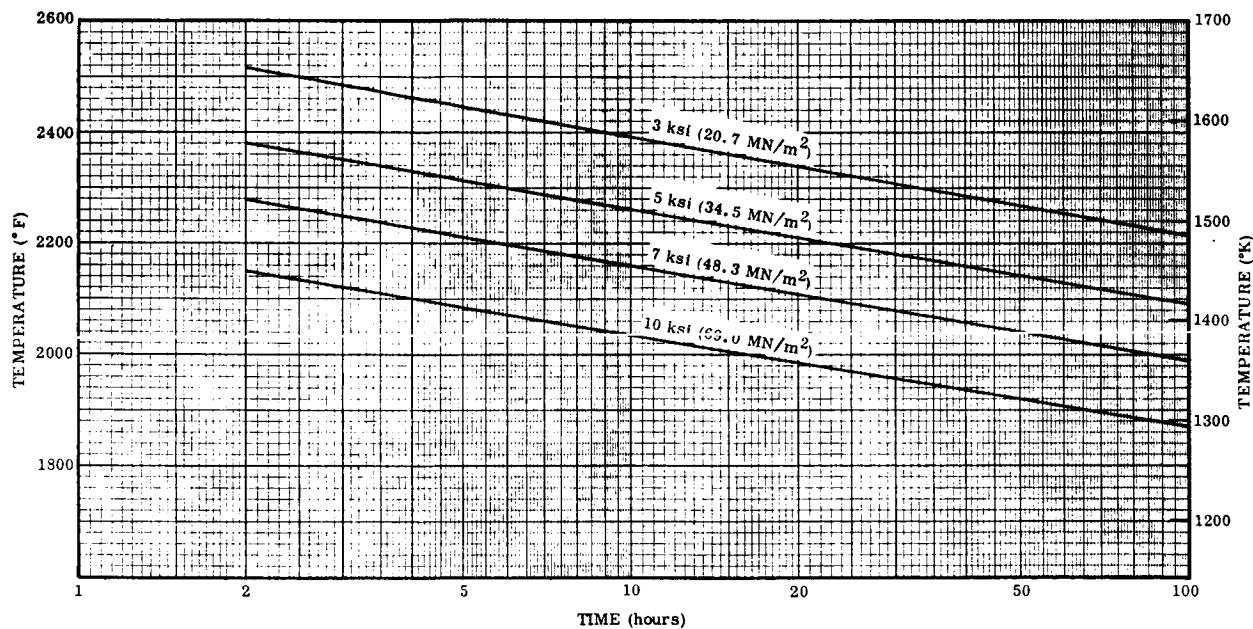


Figure 6-12. Preliminary Design Allowable Stress on Cb-752 for 1% Creep Strain Based on Net As-Coated Section

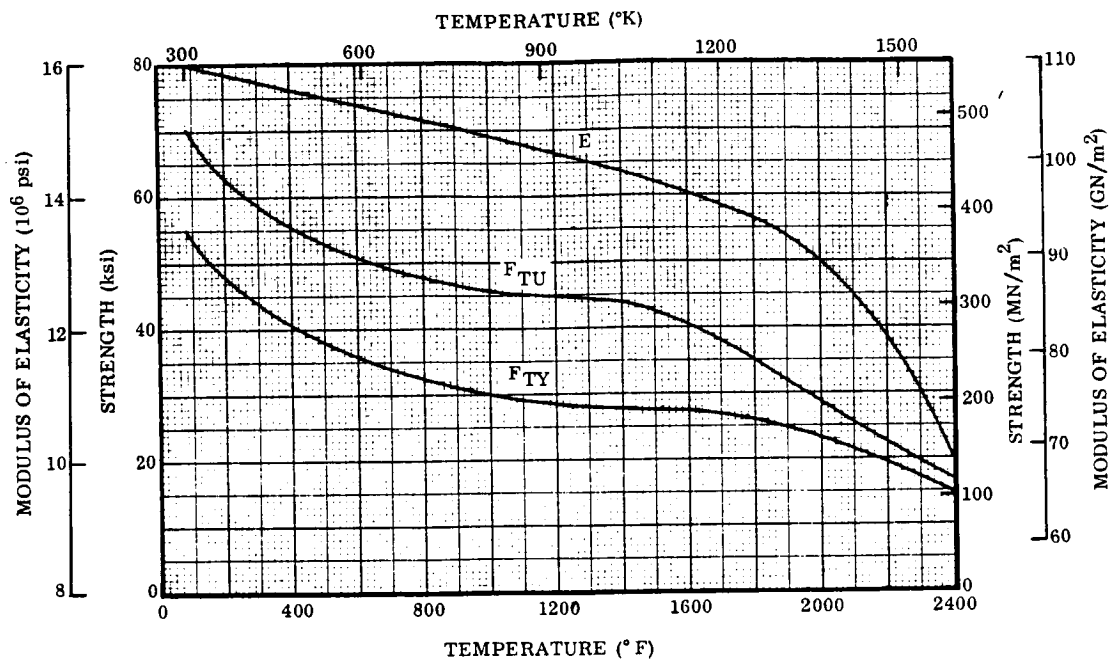


Figure 6-13. Preliminary Design Tensile Properties Versus Temperature for C-129Y/R-512E Based on Net As-Coated Section

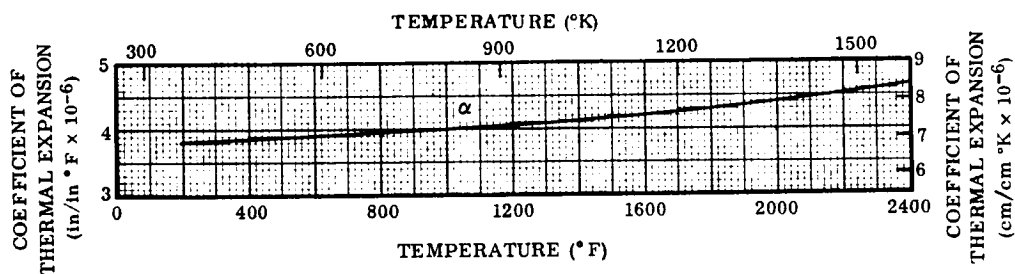


Figure 6-14. Coefficient of Thermal Expansion Versus Temperature for C-129Y

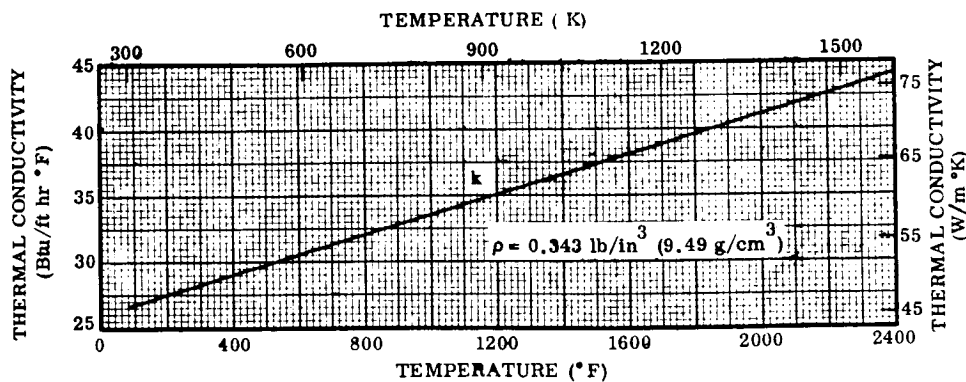


Figure 6-15. Thermal Conductivity Versus Temperature for C-129Y

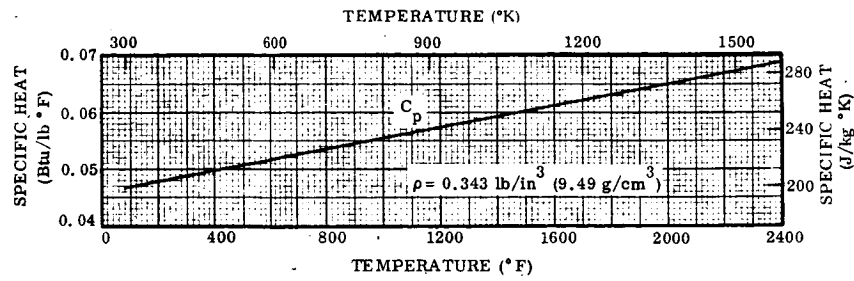


Figure 6-16. Specific Heat Versus Temperature for C-129Y

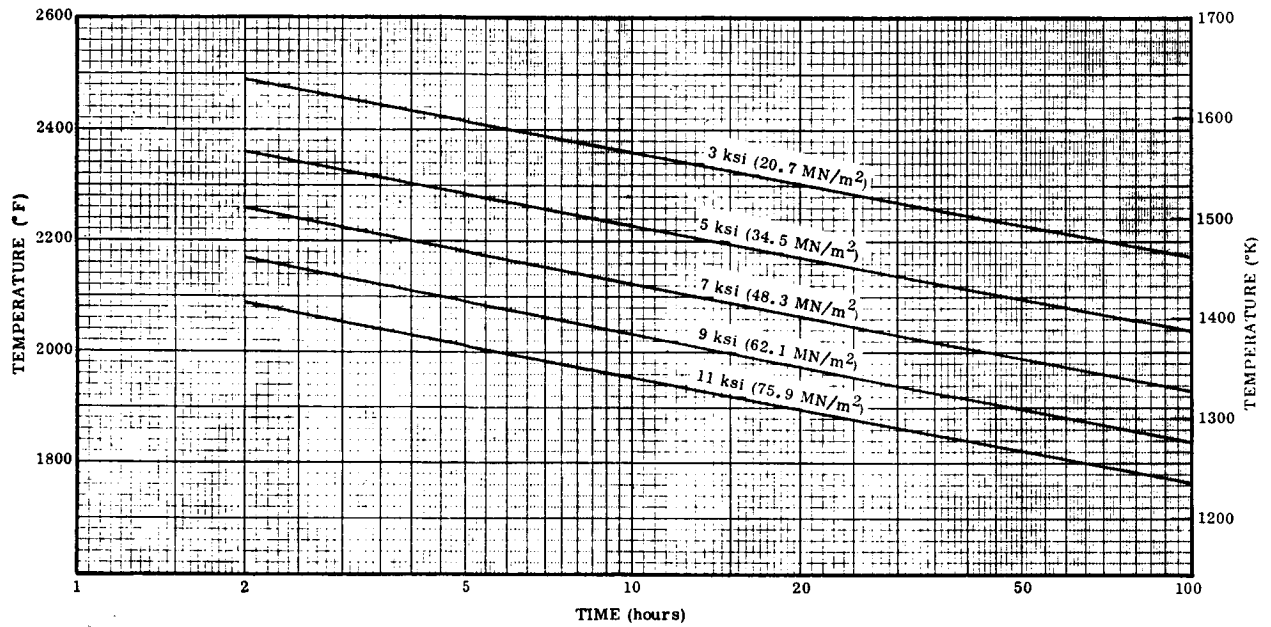


Figure 6-17. Preliminary Design Allowable Stress on C-129Y for 1% Creep Strain Based on Net As-Coated Section

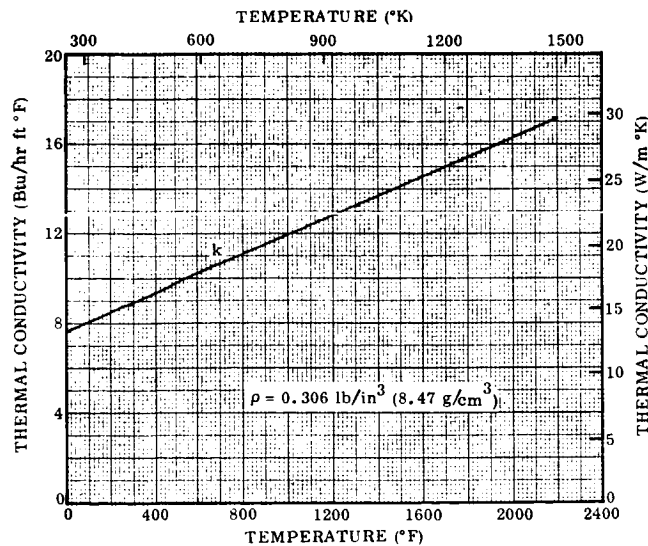


Figure 6-18. Thermal Conductivity of TD NiCr

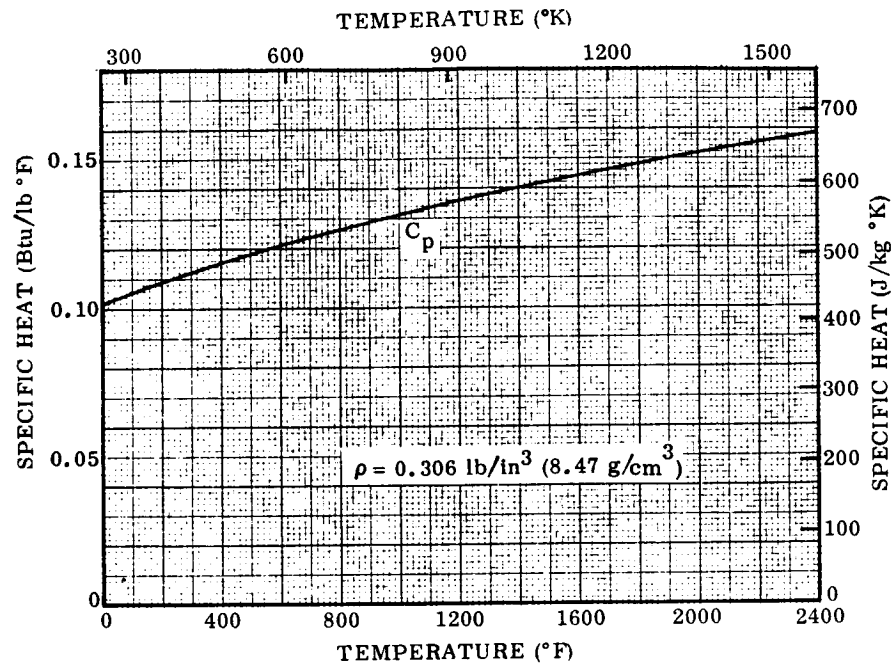


Figure 6-19. Specific Heat of TD NiCr

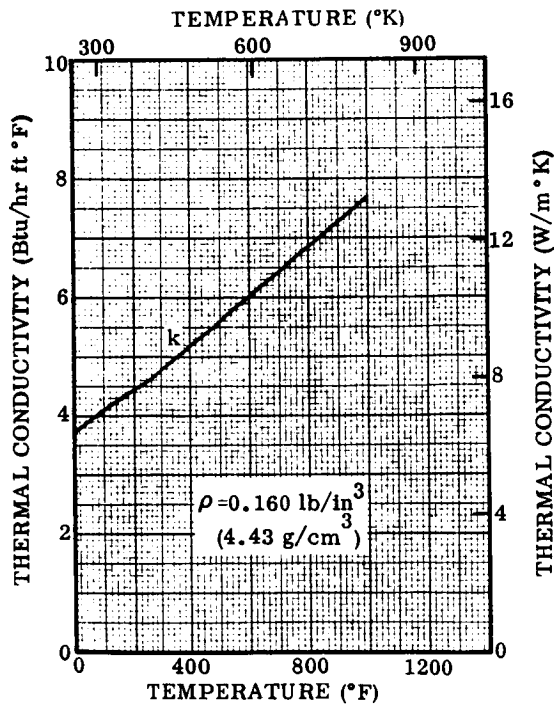


Figure 6-20. Thermal Conductivity of Titanium (Ti-6Al-4V)

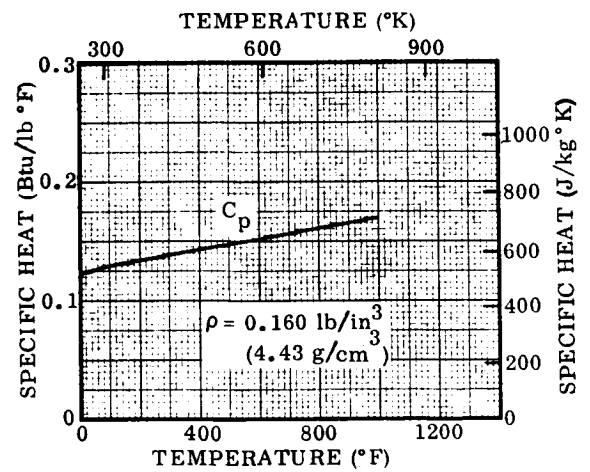


Figure 6-21. Specific Heat of Titanium (Ti-6Al-4V)

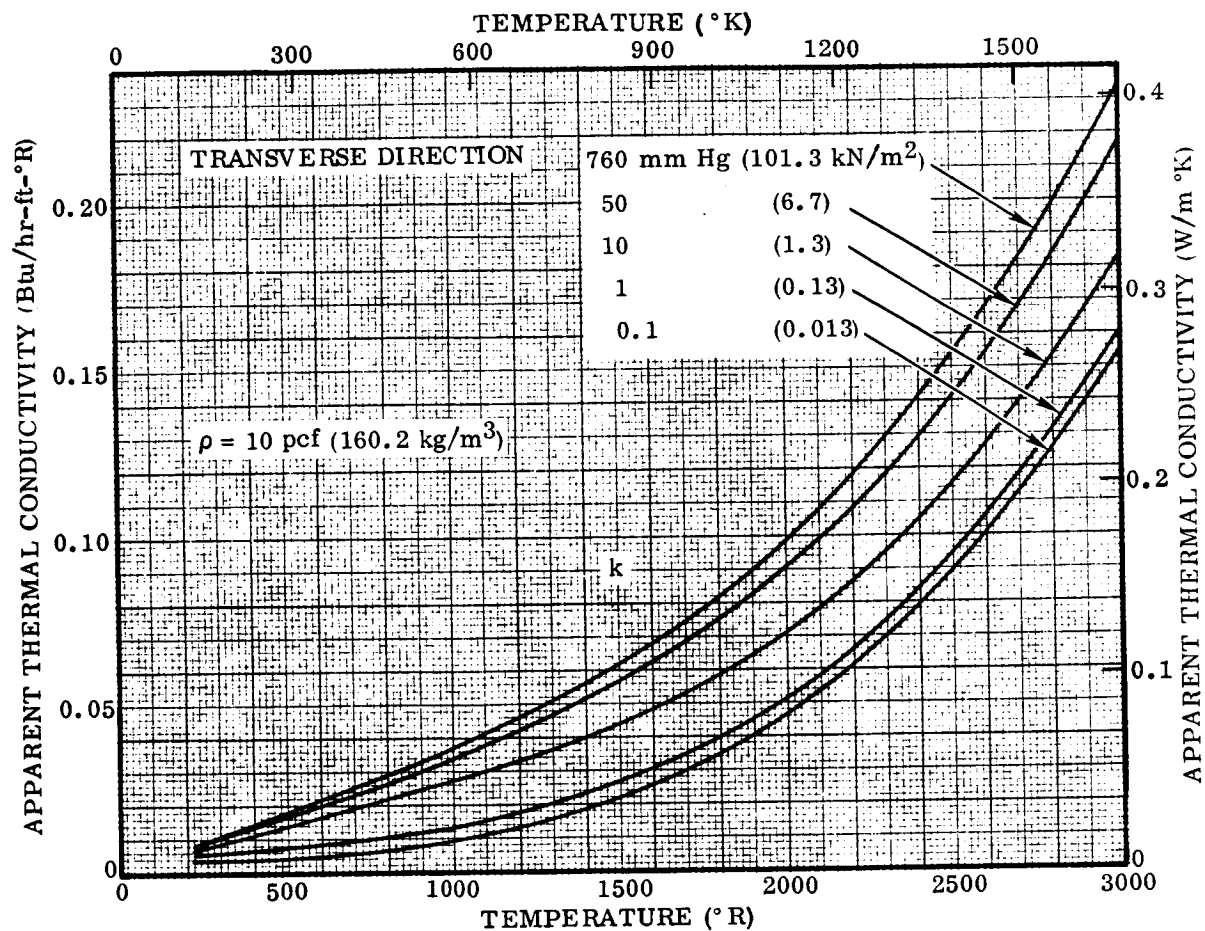


Figure 6-22. Thermal Conductivity of Dyna-Flex Insulation

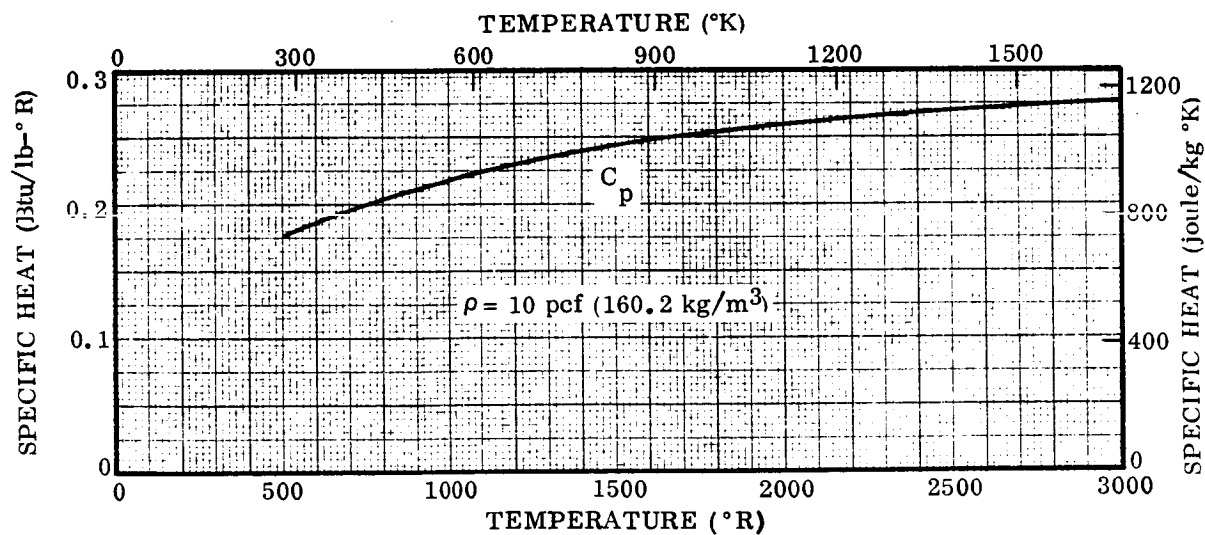


Figure 6-23. Specific Heat of Dyna-Flex Insulation

Table 6-1. Summary of Specifications and Material Properties

Alloy Specification	- GDCA Specification 0-00947	
Cleaning Specification	- GDCA Specification 0-73510	
Diffusion Coating Specification	- GDCA Specification 0-73511	
Alloy Condition	- Recrystallized	
Coated Room Temperature	Cb-752	C-129Y
<u>Mechanical Properties</u>		
F_{tu}	64 ksi (see Figure 6-8)	70 ksi (see Figure 6-13)
F_{ty}, F_{cy}	50 ksi (see Figure 6-8)	55 ksi (see Figure 6-13)
E	15.5×10^6 psi (see Figure 6-8)	16.0×10^6 psi (see Figure 6-13)
<u>Physical Properties</u>		
Density (Uncoated)	0.326 lb/in ³	0.343 lb/in ³
Emissance	See Table 6-2	See Table 6-3
Thermal Expansion	See Figure 6-9	See Figure 6-14
Thermal Conductivity	See Figure 6-10	See Figure 6-15
Specific Heat	See Figure 6-11	See Figure 6-16

6.1.3.2 Emissance: For design and analytical calculations to determine skin temperatures used in this program, the emissance values for R-512E coated Cb-752 and C-129Y are based on recent work of Reference 19. The average total normal emissance for three samples for each of the three nominal temperatures indicated are given in Tables 6-2 and 6-3. Emissances are shown for each data set during increasing and decreasing temperature portions of the profile.

Since most thermal calculations are based on one value for emissance rather than varying emissance with temperature, the data from Tables 6-2 and 6-3 were averaged for cycles and plotted in Figure 6-24. The trends for the two alloys are almost mirror images of each other. The average emissance over the 100 cycles for Cb-752/R-512E was 0.818 and for C-129Y/R-512E was 0.873. The standard deviation for the Cb-752 was 0.016 and for C-129Y was 0.029. Therefore, in order to be slightly conservative (i.e., give slightly higher radiation equilibrium temperature values), the recommended total normal emissance for Cb-752/R-512E is 0.80 and for C-129Y/R-512E is 0.84.

Table 6-2. Total Normal Emittance for Cb-752/R-512E

Temperature at which ϵ was Measured During Profile Exposure °F	(°K)	Number of Reentry Cycles				
		1	10	25	50	100
1600	1144	0.873	0.856	0.770	0.756	0.767
2000	1366	0.859	0.829	0.826	0.829	0.796
2400	1589	0.880	0.895	0.860	0.910	0.897
2000	1366	0.769	0.808	0.798	0.816	0.783
1600	1144	0.734	0.836	0.764	0.779	0.757
Average		0.823	0.845	0.804	0.816	0.800
Arithmetic mean		= 0.818				
Mean deviation		= 0.013				
Standard deviation		= 0.016				
Recommended emittance value		= 0.80				

Table 6-3. Total Normal Emittance for C-129Y/R-512E

Temperature at which ϵ was Measured During Profile Exposure °F	(°K)	Number of Reentry Cycles				
		1	10	25	50	100
1600	1144	0.984	0.859	0.883	0.803	0.826
2000	1366	0.958	0.885	0.905	0.824	0.853
2400	1589	0.954	0.927	0.910	0.916	0.931
2000	1366	0.871	0.824	0.884	0.840	0.852
1600	1144	0.850	0.831	0.826	0.805	0.815
Average		0.923	0.865	0.882	0.838	0.855
Arithmetic mean		= 0.873				
Mean deviation		= 0.024				
Standard deviation		= 0.029				
Recommended emittance value		= 0.84				

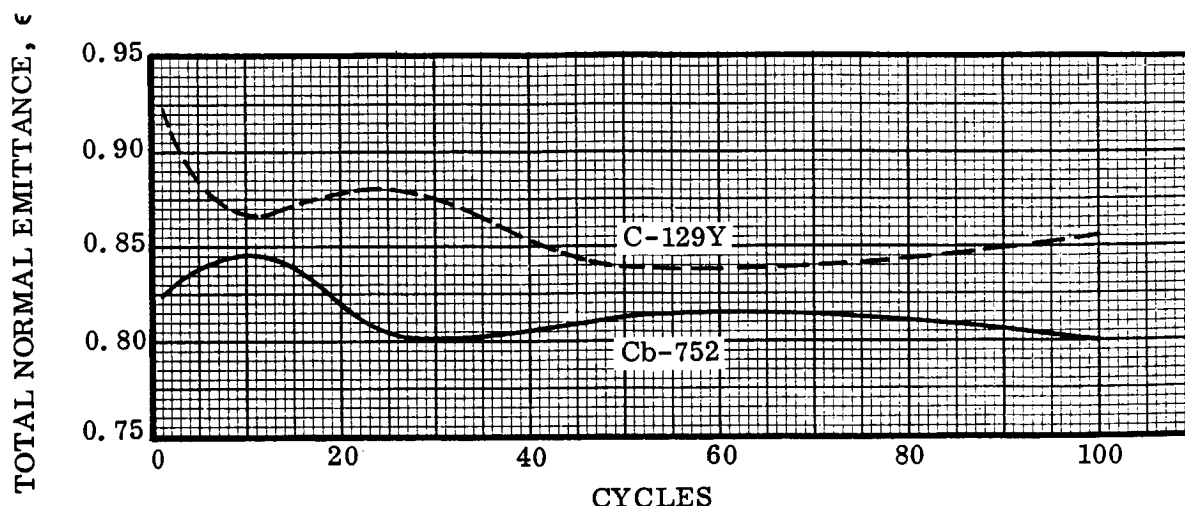


Figure 6-24. Total Normal Emittance Versus Exposure Cycles for R-512E Coated Cb-752 and C-129Y

6.2 Small Size TPS Design

This section encompasses two phases of the design task. The first is the preliminary design, which was submitted for sizing by thermal and structural analyses. The second phase is the redesign into the final configurations. The configuration restraint was imposed by the test fixture size and the test conditions. The test area was approximately 22 by 22 inches (55.88 by 55.88 cm). Therefore, a heat shield size of 12 by 16 inches (30.48 by 40.64 cm) was selected to provide for a region of unaffected edges.

6.2.1 Preliminary design. – A preliminary design of the integrated heat shield and support system design was made for the two selected heat shield configurations. The primary object of the design was to minimize the number of surface fasteners that would be required to be removed for panel replacement and substructure and insulation inspection while maintaining reduced surface leakage areas.

The tee-stiffened concept shown in Figure 6-25 incorporates these design requirements. The panel is oriented longitudinally by the longitudinal support beam and tee-section panel retainer by a single bolt. The panels are positioned in the transverse direction at the upper end by shear pins and a single recessed bolt in the plug at the center of the panel, while the lower panel edge is shingled by the succeeding panels.

The panel is installed by dropping it in position over the TPS supporting structure and sliding the panels forward to engage the shear pins into the slots provided in the panel support beam. The single recessed bolt is installed in the plug and maintains

the shear pin in position. The succeeding panels are sandwiched between the upper edge of the installed panel and the panel support beam. The center bolt provides the single fixed point for the panel. The panel is allowed to expand longitudinally and transversely about this point.

The panel pressure loadings, both internally and externally, are reacted to the supporting structure primarily by the two transverse channel beams. The beam is fixed about the center post and allowed to expand in either direction into the corner beam support fittings. The longitudinal support beam is fixed at one corner fitting and allowed to expand towards the other fitting. The beam is slotted at one end and pinned at the other end of the fitting.

All attachment bolts are recessed approximately 2 inches (5.08 cm) below the skin line. The bolts are installed in a recessed cup attached to the panel edge. The plug and bolt are attached through a 0.094 inch (0.238 cm) diameter hexagonal hole. The plug design differs from the other snap-in designs proposed in the past in that the plug is not subject to loss from vibration or loadings.

The corrugated panel concept shown in Figure 6-26 is similar to the tee-stiffened concept except that no allowance need be made for transverse panel expansion. The expansion is taken up by corrugation deflection. The longitudinal panel edges are restrained from vertical movement by tee-section retainers. A similar recessed cup design is shown for panel attachment at the upper edge with a shingled lower edge.

6.2.2 Final design. - Following initial thermal and structural analyses several shortcomings were apparent. The shear pin attachment method for the tee-stiffened panel was found to provide excessive bearing on a relatively thin coated edge. This would have been an area with a high probability of coating failure. In addition, the tolerance mismatch and the probable distortion of the heat shield as a result of thermal cycling would have made panel installation/refurbishment difficult. The redesign made the support beam integral with the panel and self sustaining.

Thermal analyses revealed an excessive heat short for the columbium alloy support posts. Therefore, bi-metal posts were designed such that a transition from columbium alloy to TD NiCr was made at a point where the temperatures were near 2000° F (1366° K). This also permitted the use of TD NiCr fasteners which are considerably less troublesome than coated refractory metal fasteners. With no other major changes made, the final design layout for the tee-stiffened TPS is shown in Figure 6-27.

Except for the same support-post modifications and some minor adjustments to facilitate fabrication, few changes were made to the open-corrugation heat shield. The final design layout for this system is shown in Figure 6-28.

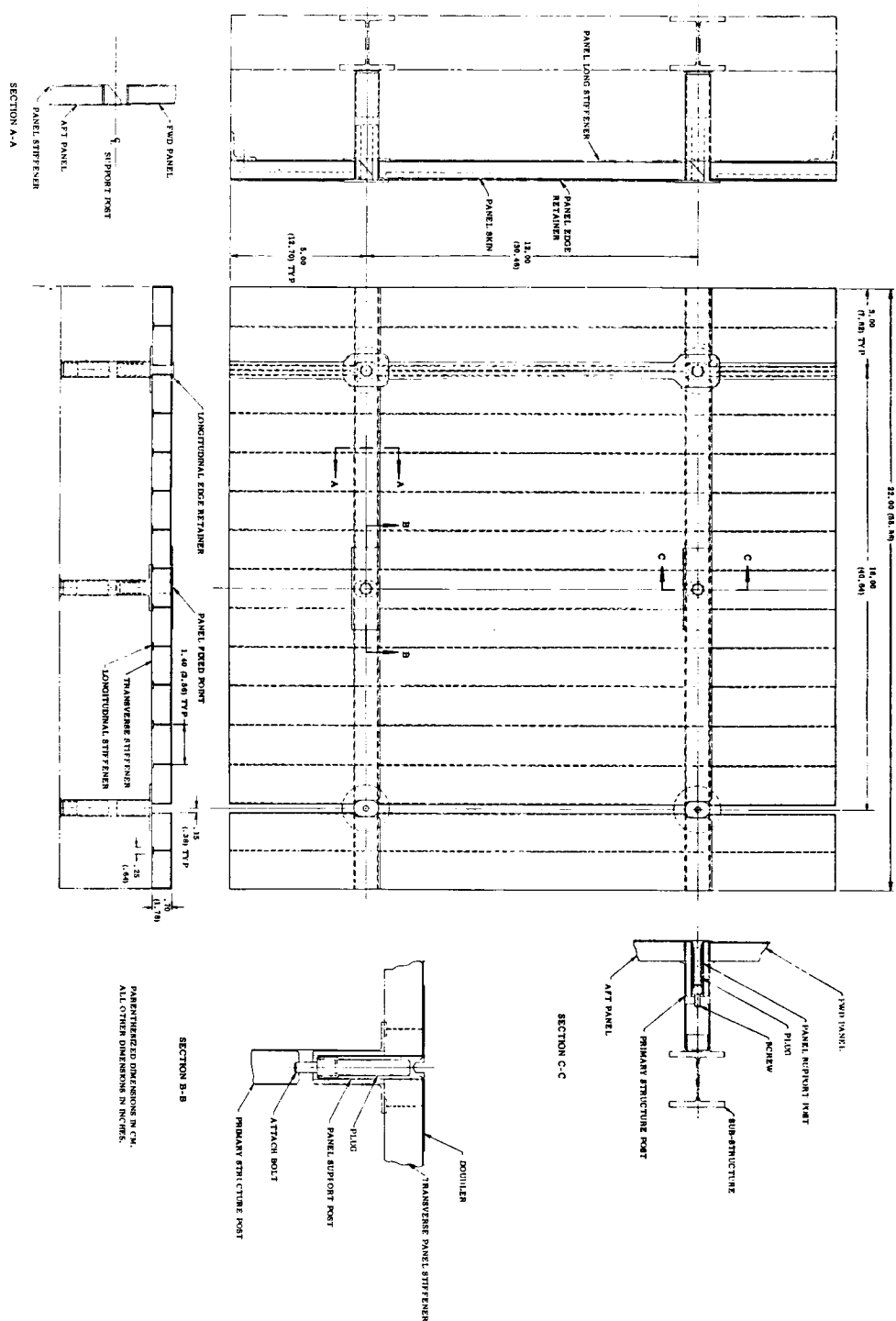


Figure 6-25. Preliminary Design of Tee-Stiffened Heat Shield Test Assembly (Sheet 1 of 2)



FIGURE 6-26

FIGURE 6-26

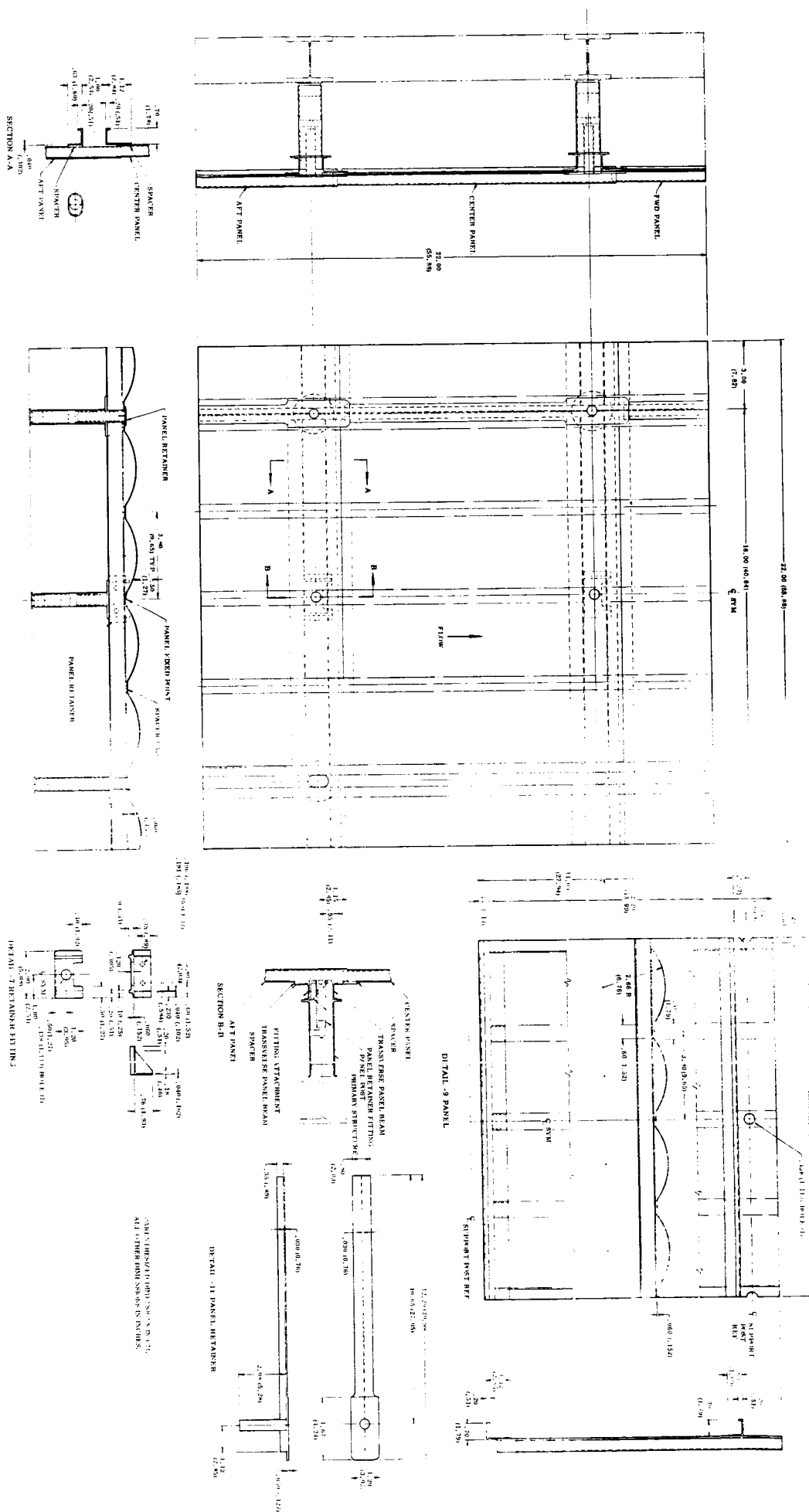


Figure 6-26. Preliminary Design of Corrugated Metal Shield Test Panel Assembly



156

6.3 Small-Size TPS Thermal Analysis

6.3.1 Summary. - The objective of this study was to conduct the necessary thermal analyses to determine the temperatures and temperature gradients expected in the small size coated columbium alloy tee-stiffened and corrugated heat shield designs. These small size panels [12 by 16 inches (30.48 by 40.64 cm)] were to be built and exposed to simulated flight conditions.

Insulation sizing and temperature predictions are presented for the two small-scale coated columbium alloy heat shield thermal protection systems. Mathematical thermal models were developed and employed to predict the thermal performance of the designs to be tested at the radiant heating test facility in the Convair Spacecraft Test Laboratory.

A total thickness of 3.7 inches (9.4 cm) of 10.0 pcf (160.2 kg/m^3) Dyna-Flex insulation is required to limit the backup structure to 650°F (616°K) where the insulation is not interrupted by panel support posts. Local areas at the base of the post experience peak temperatures of about 800°F (700°K) after vehicle landing.

Transient temperature predictions of the heat shield elements show that peak temperature gradients occur at about 140 seconds after the initiation of the entry maneuver. Temperature gradients in the tee-stiffened panel are more severe than those experienced by the corrugated panel in axial flow. An estimate of the influence of cross flow on corrugated panel temperatures shows large temperature gradients at high temperatures due to flow separation and reattachment effects. For the cross flow assumptions used, the 2760°F (1789°K) peak panel temperature obtained is considerably above the 2400°F (1589°K) nominal limit for the coated columbium.

Thermal analysis of the tee-beam edges and overlapped edges of the designs shows large thermal gradients during the initial portion of the entry trajectory due primarily to the concentration of mass at the edges.

6.3.2 Environmental conditions. - The aerodynamic heat transfer and local static pressure histories used in this analysis were taken from Figures 6-2 and 6-7. These illustrations are for a vehicle location of $X/L = 0.025$ where coated columbium alloy heat shields would be applicable. Figures 6-29 and 6-30 show the heat transfer rate and local static pressure during boost. Similar data for entry are presented in Figures 6-31 and 6-32. The peak heat transfer rate shown in Figure 6-31 [$22.4 \text{ Btu/ft}^2\text{-sec}$ (254.2 kW/m^2)] yields a maximum panel surface radiation equilibrium temperature of 2310°F (1539°K) at a surface emittance (ϵ) of 0.80. The maximum nominal temperature limit for coated columbium alloys is 2400°F (1589°K) which corresponds to a heat transfer rate of $25.5 \text{ Btu/ft}^2\text{-sec}$ (289.4 kW/m^2) for $\epsilon = 0.80$. Testing of heat shields under this program will be conducted to a maximum temperature of 2400°F (1589°K) and thus the peak heat transfer data (Figure 6-31) was arbitrarily modified to some

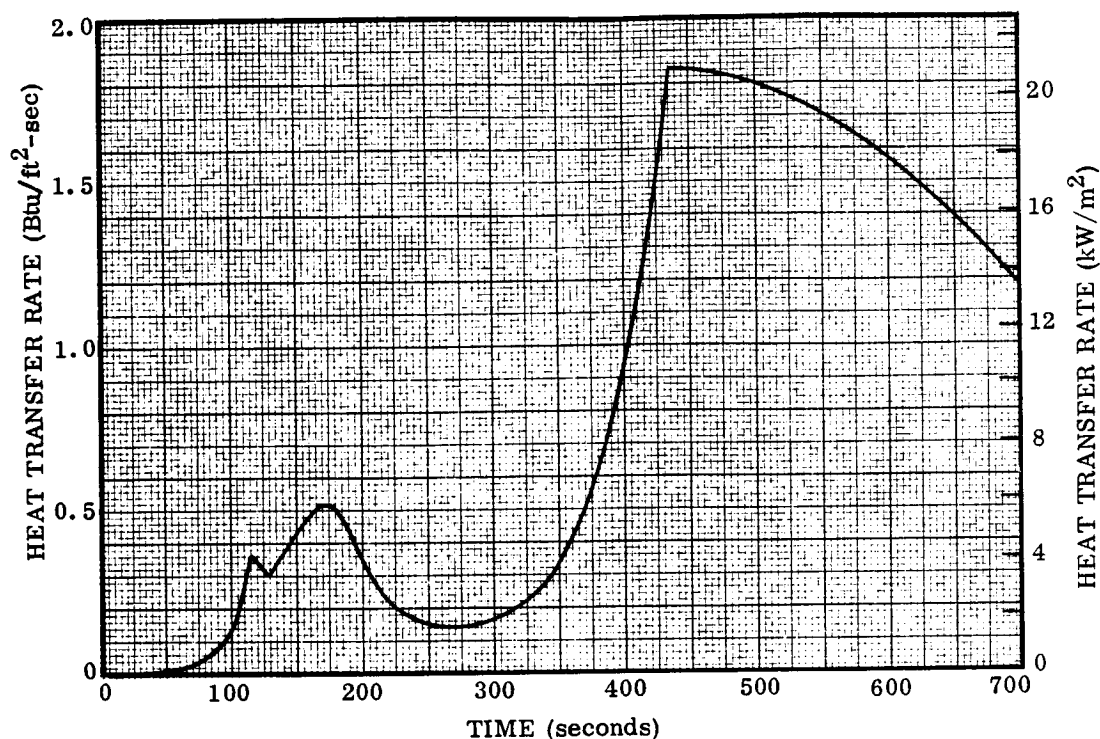


Figure 6-29. Boost Heating Rate History (Lower Fuselage, X/L=0.025)

extent to yield 2400°F (1589°K) temperatures. This modified heat transfer rate data was used in all thermal analysis results presented in the following sections.

6.3.3 Material properties. – The analysis of thermal protection systems is extremely dependent on the thermal properties of the materials used. The density, specific heat, and thermal conductivity data used in this analysis are presented in Section 6.1.3 and were obtained from several sources.

The test panels will be insulated with 10.0 pcf (160.2 kg/m³) Dyna-Flex insulation. The apparent thermal conductivity in the transverse direction shown in Figure 6-22 was obtained from tests at Convair Aerospace over a broad range of pressures (Reference 20). For the lateral direction, the data of Figure 6-22 is increased by 15% based on the results reported in Reference 21.

The thermal properties of columbium alloy Cb-752 were obtained from Reference 17. A surface thermal emittance of 0.80 was used.

The data for the density and conductivity of TD NiCr was obtained from Reference 22. The specific heat of TD NiCr was estimated from the data of Reference 23 using 80% nickel and 20% chromium. The thermal properties of titanium were obtained from Reference 24.

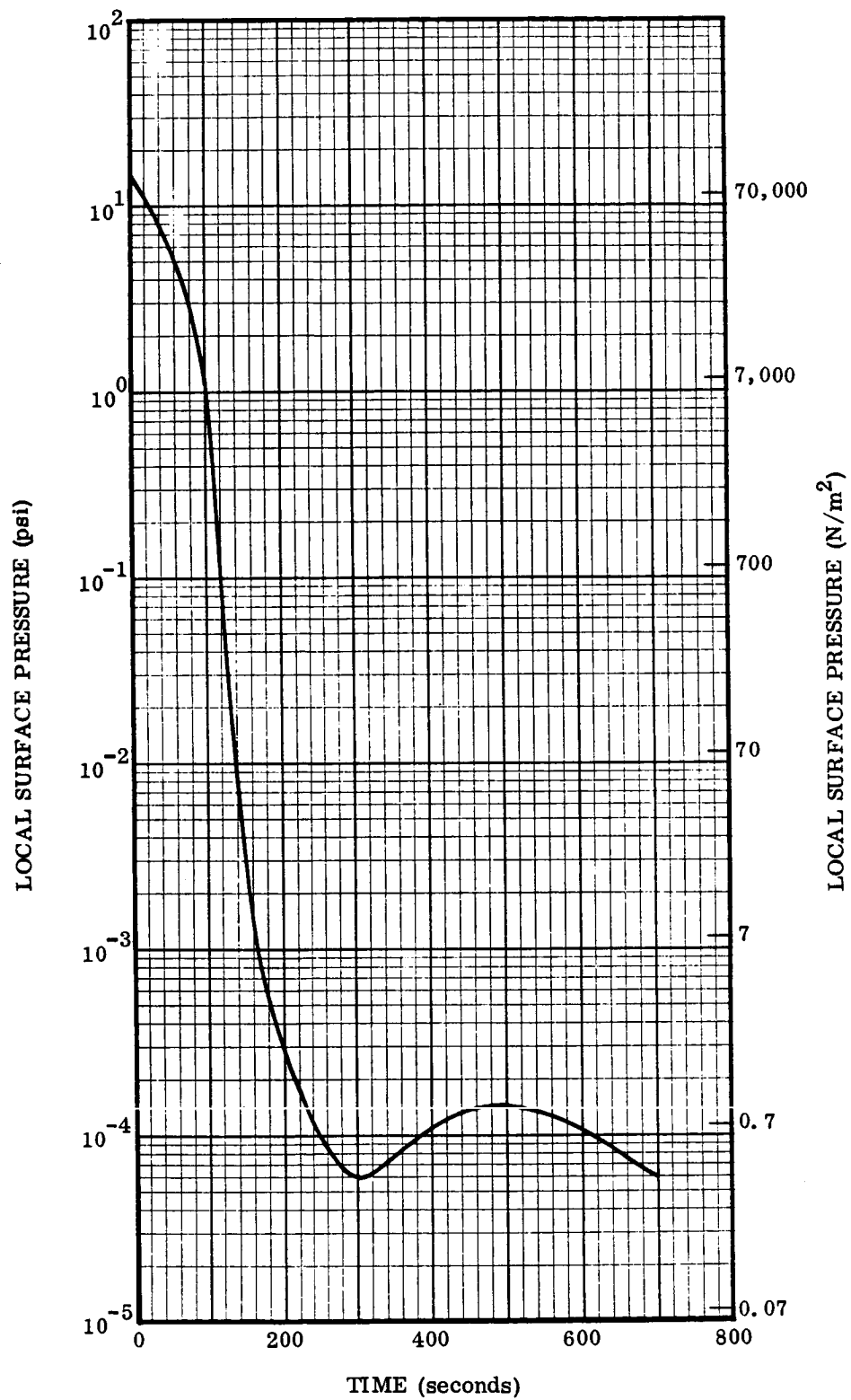


Figure 6-30. Boost Surface Pressure Profile Lower Surface ($X/L = 0.025$)

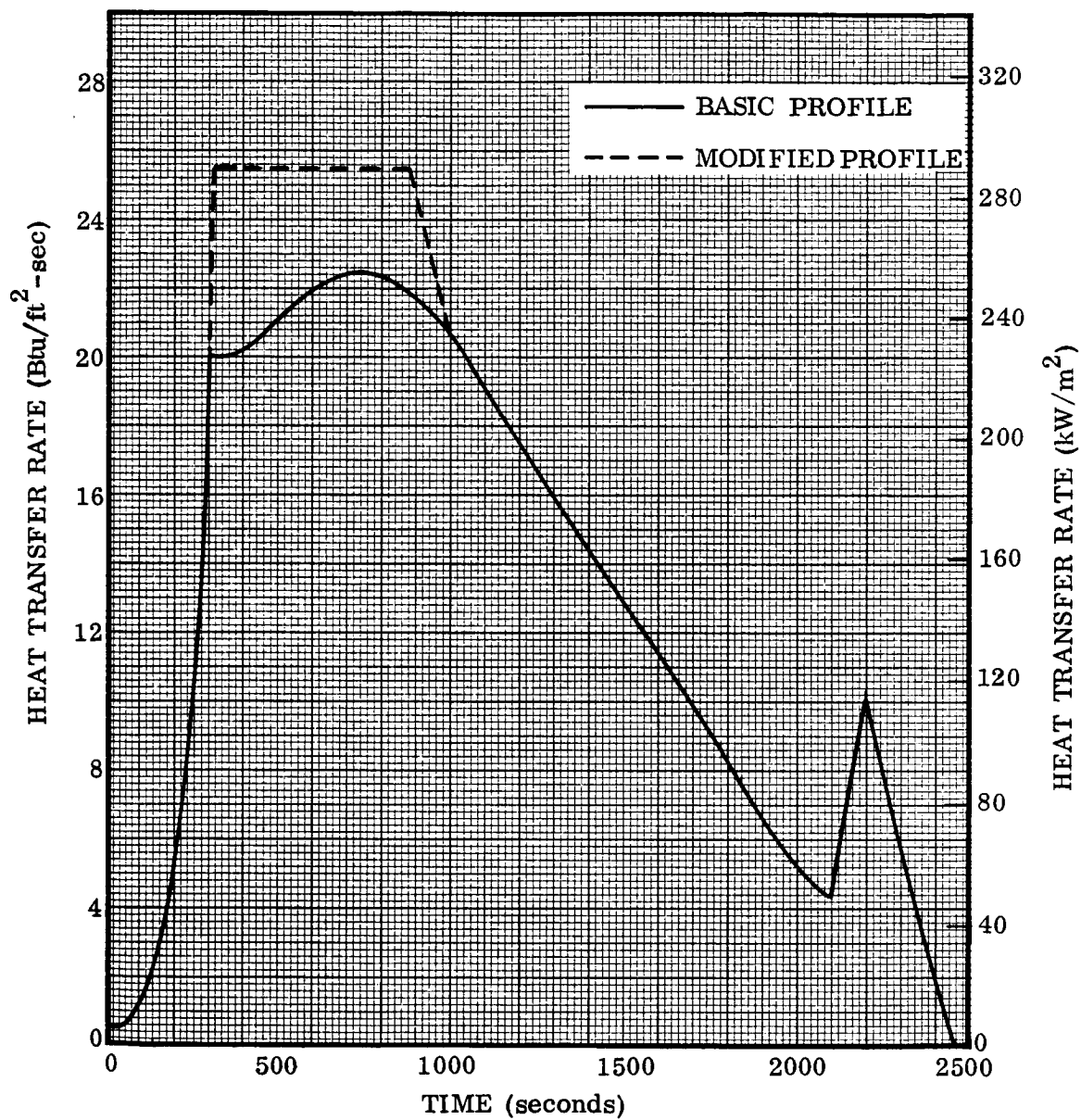


Figure 6-31. Entry Heating Rate History (Lower Fuselage, $X/L = 0.025$)

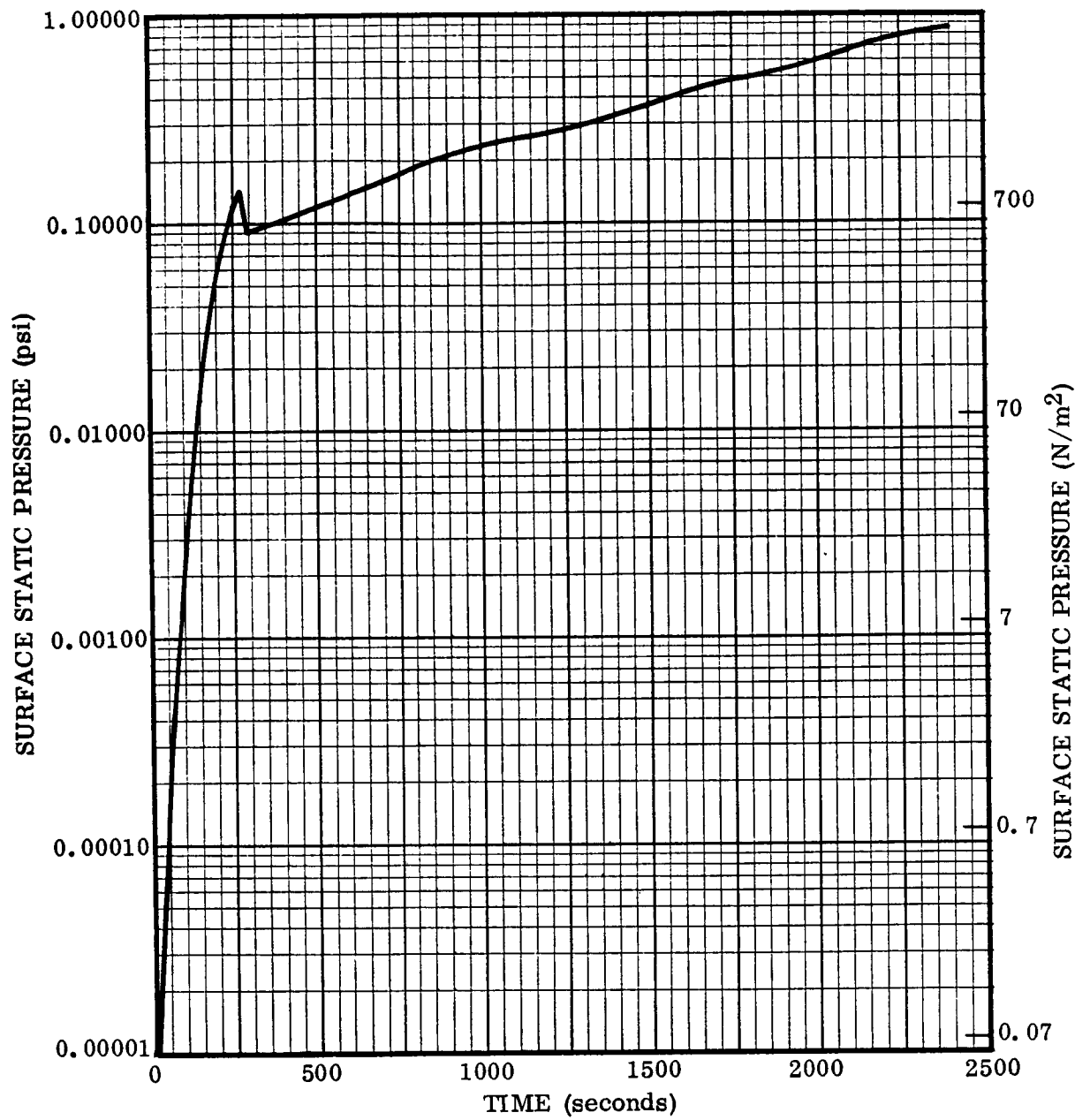


Figure 6-32. Entry Surface Pressure Profile (Lower Fuselage, $X/L = 0.025$)

6.3.4 Methods of analysis. — The thermal analyses presented in this study were conducted using the Convair Aerospace computer program 2772, Transient and/or Steady State Temperature Prediction Program. This heat transfer program accommodates a broad variety of engineering thermal analysis requirements. The program includes provisions for radiation interchange between elements of the model and radiation to deep space. Problems involving multiple materials with specific heat, conductivity, and emittance as a function of temperature, and with conductivity as a function of both temperature and pressure are analyzed.

Aerodynamic heating of panel surface elements is simulated as a heat flux that varies with time. The effect of wall temperature on heat flux can be included, but for entry heating this effect is small and was not included in the present analyses. View factors between elements of the thermal models were obtained by using the computer programs of References 25 and 26. The overall radiant interchange factors including multiple reflections for gray diffuse surfaces at constant emittance were obtained from the program of Reference 27. Where possible, symmetry was used to yield thermal models with a minimum number of elements.

Columbium alloy heat shields must be coated to retard oxidation at high temperatures. When coated, one-third of the coating thickness results from penetration of the base metal. Diffusion of the coating into the base metal continues as the material is cycled at high temperatures. A coating of 0.003 inch (0.008 cm) was applied to the panels manufactured under this program, and it was assumed that a diffusion of 0.00001 inch (0.00003 cm) per side would occur during each cycle. Thus, if the original panel thickness is 0.020 inch (0.051 cm), after coating the new base metal thickness is 0.018 inch (0.046 cm), and the total thickness is 0.024 inch (0.061 cm). After 100 cycles, the final base metal thickness is 0.016 inch (0.041 cm). Thermal properties of the coating material and diffusion zone are not known at present. In this study, panel temperatures and temperature gradients are based on (1) conduction using the base metal thickness after 100 cycles [0.016 inch (0.041 cm) in above example], and (2) thermal inertia using the total thickness [0.024 inch (0.061 cm) in above example] and the density and specific heat of Figures 6-10 and 6-11. The conduction heat transfer terms used for the coated columbium elements in the support post analysis, however, are based on the total thickness. These assumptions should yield the worst case panel gradients and the worst case with respect to heat transfer through the support post to the backup structure.

6.3.5 Insulation sizing. — Insulation sizing is based on a thermal model that includes effects of both temperature and pressure on insulation thermal conductivity. The local static surface pressure at $X/L = 0.025$ was employed. An 0.020 inch (0.051 cm) titanium adiabatic backup structure was used, and it was assumed that the insulation and backup structure were initially at $+100^{\circ}\text{F}$ (311°K) prior to entry.

Insulation sizing results based on 10.0 pcf (160.2 kg/m³) Dyna-Flex data of Figures 6-22 and 6-23 are presented in Figure 6-33. A thickness of approximately 3.7 inches (9.4 cm) is required to limit the backup structure to 650°F (616°K). The backup structure and insulation surface temperature histories are presented in Figure 6-34. An insulation surface emittance of 0.80 was assumed.

It is anticipated that the backup structure geometry (stiffeners, etc.) and the availability of auxiliary internal cooling of the backup structure on the flight vehicle after landing will have a significant effect on backup structure temperature and insulation sizing requirements.

6.3.6 Tee-stiffened panel. - Temperature predictions for the tee-stiffened panel during ascent are presented in Figure 6-35. Panel temperatures prior to liftoff were assumed uniform at +70°F (294°K). Peak temperature gradients across the panel (location A to location C in Figure 6-35) of about 80 and 160°F (300 and 344°K) occur at about 180 and 440 seconds after liftoff respectively. Detailed temperature distributions for these two cases are presented in Figures 6-36 and 6-37.

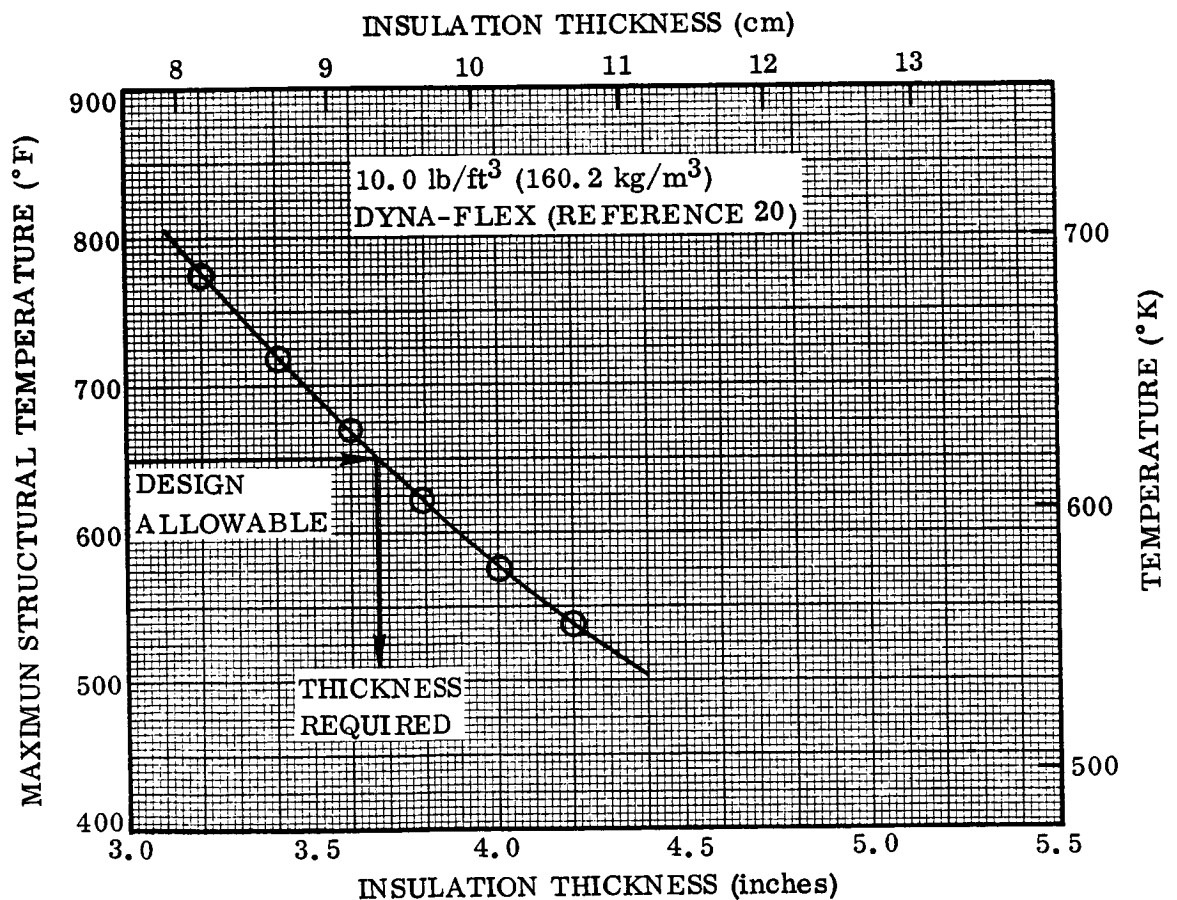


Figure 6-33. Insulation Thickness Selection

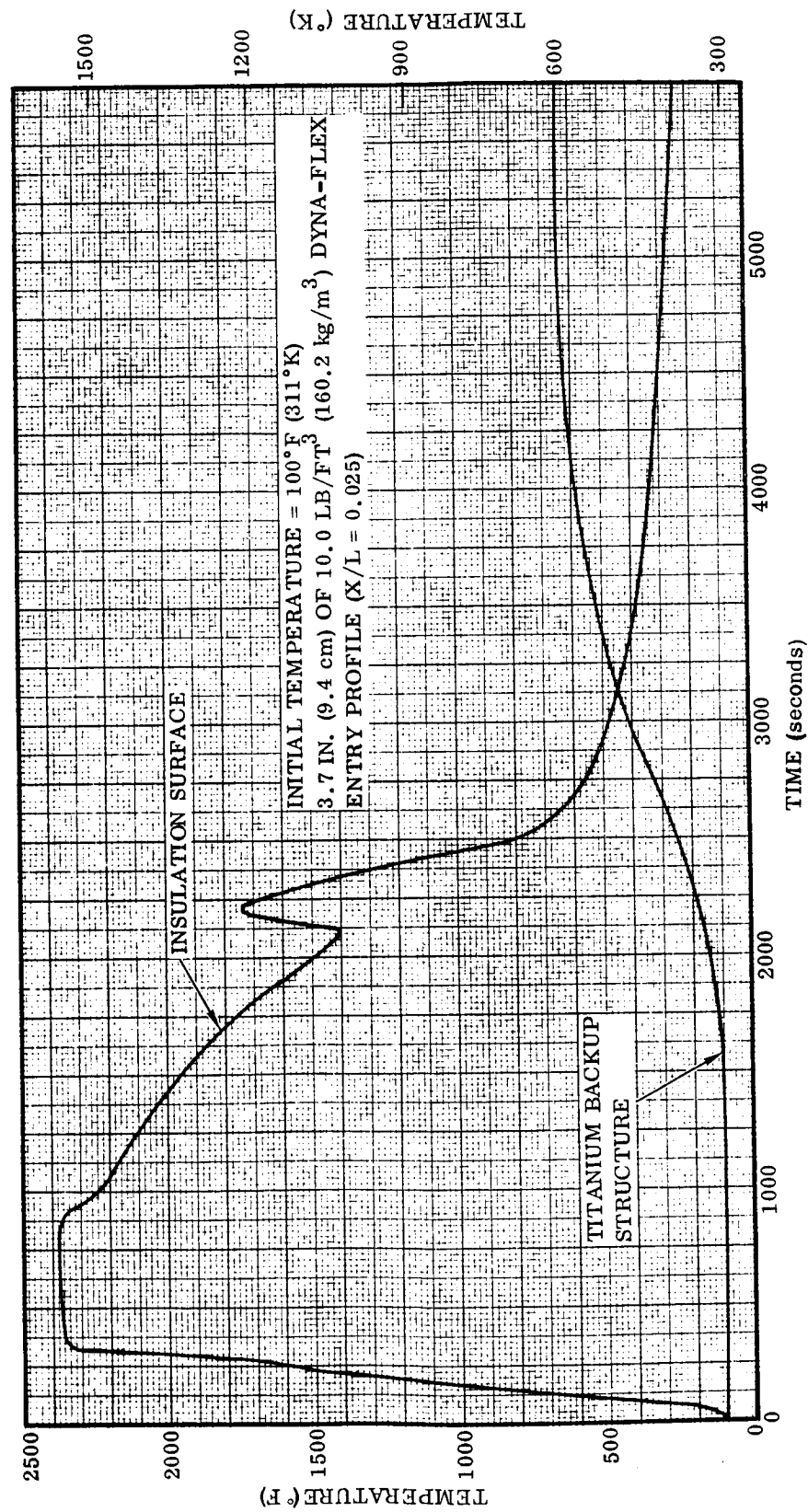


Figure 6-34. Predicted Backup Structure and Insulation Surface Temperature History

COATED COLUMBIUM Cb-752

OVERALL THICKNESS - 0.024 IN. (0.061 cm)

EFFECTIVE THICKNESS - 0.016 IN. (0.041 cm) (100 FLIGHTS)

$\epsilon = 0.80$

BOOST PROFILE ($X/L = 0.025$)

INITIAL TEMPERATURE = 70° F (294° K)

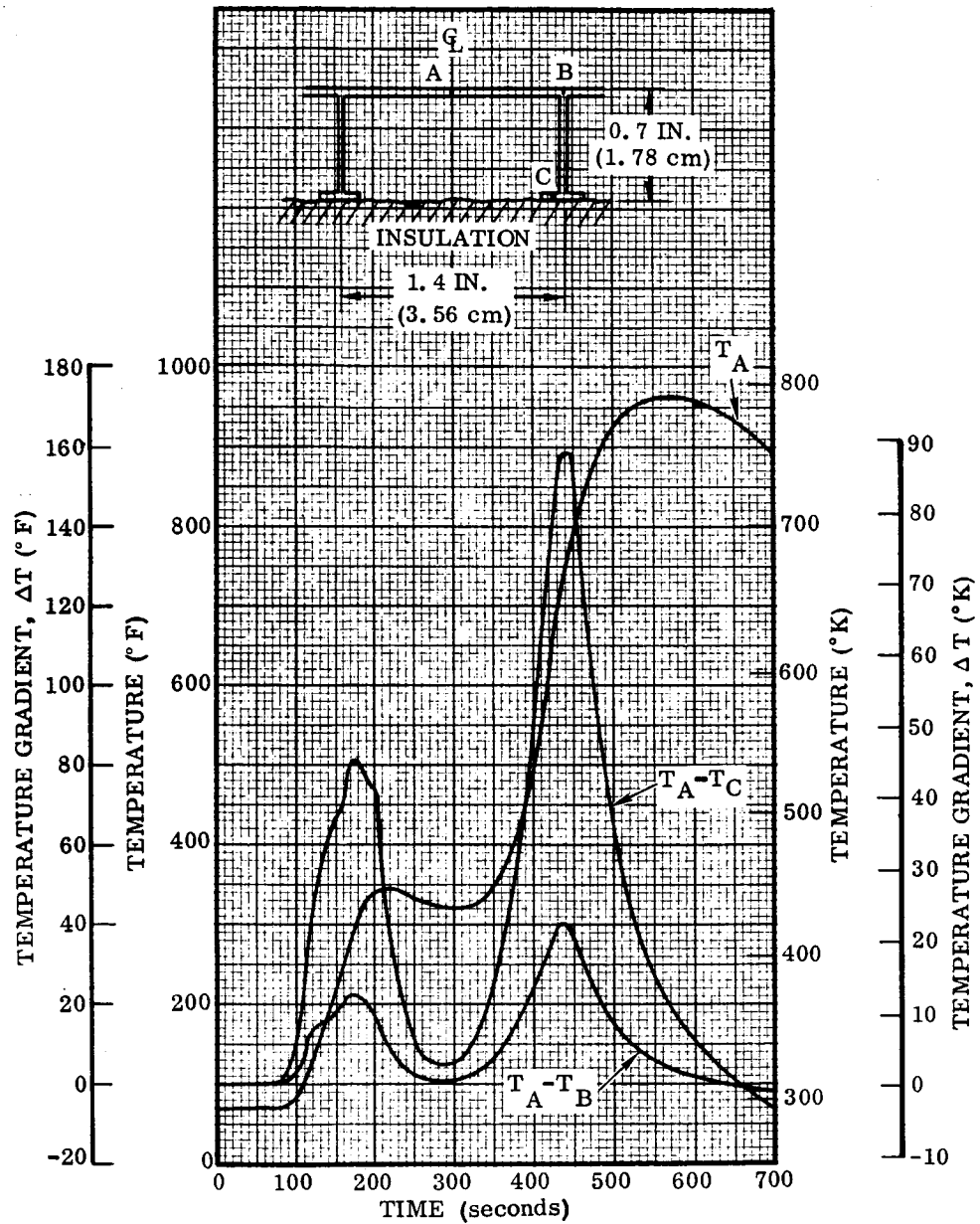


Figure 6-35. Predicted Tee-Stiffened Panel Temperatures During Ascent

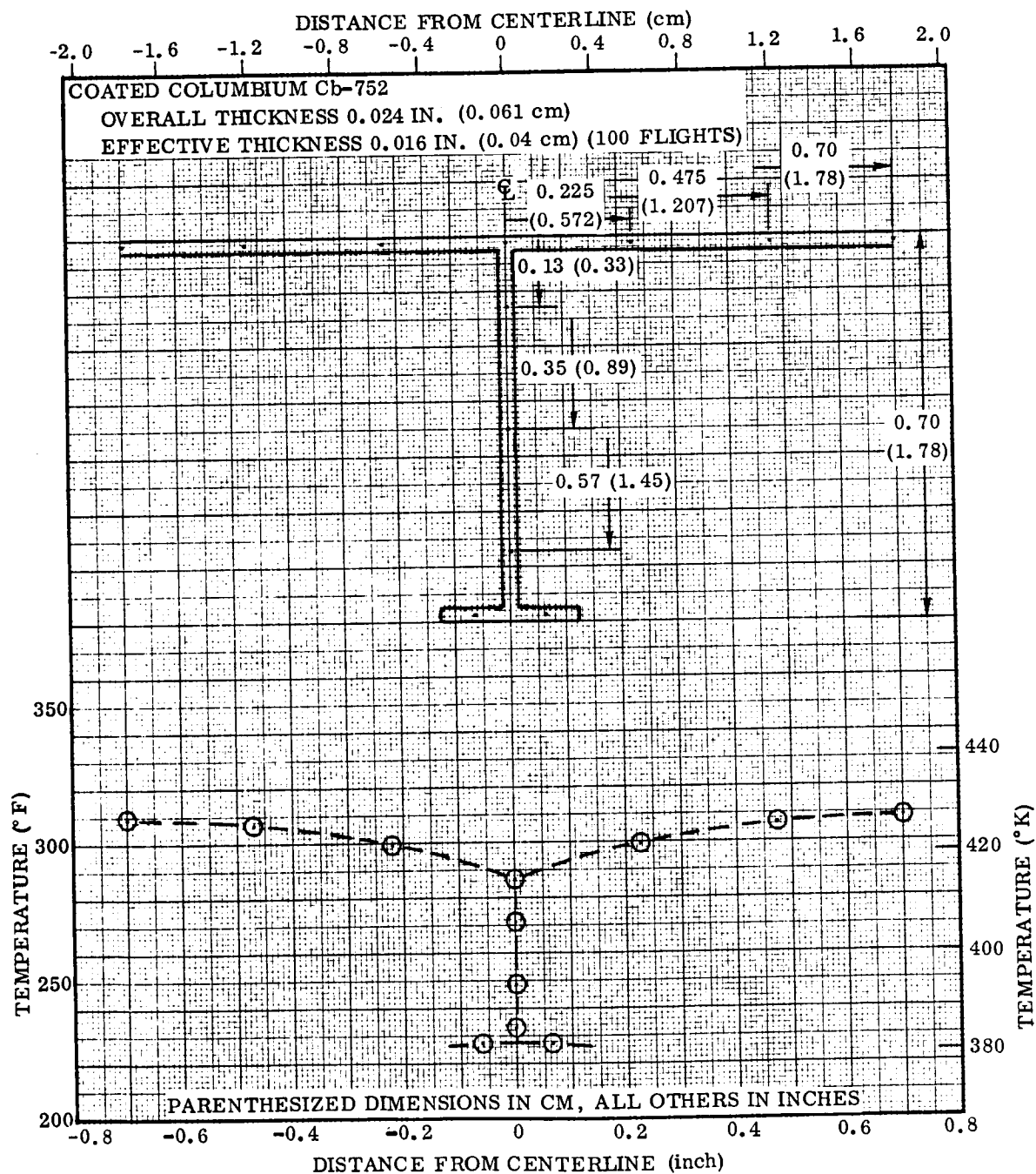


Figure 6-36. Predicted Tee-Stiffened Panel Ascent Temperature Distribution, Time = 180 Seconds

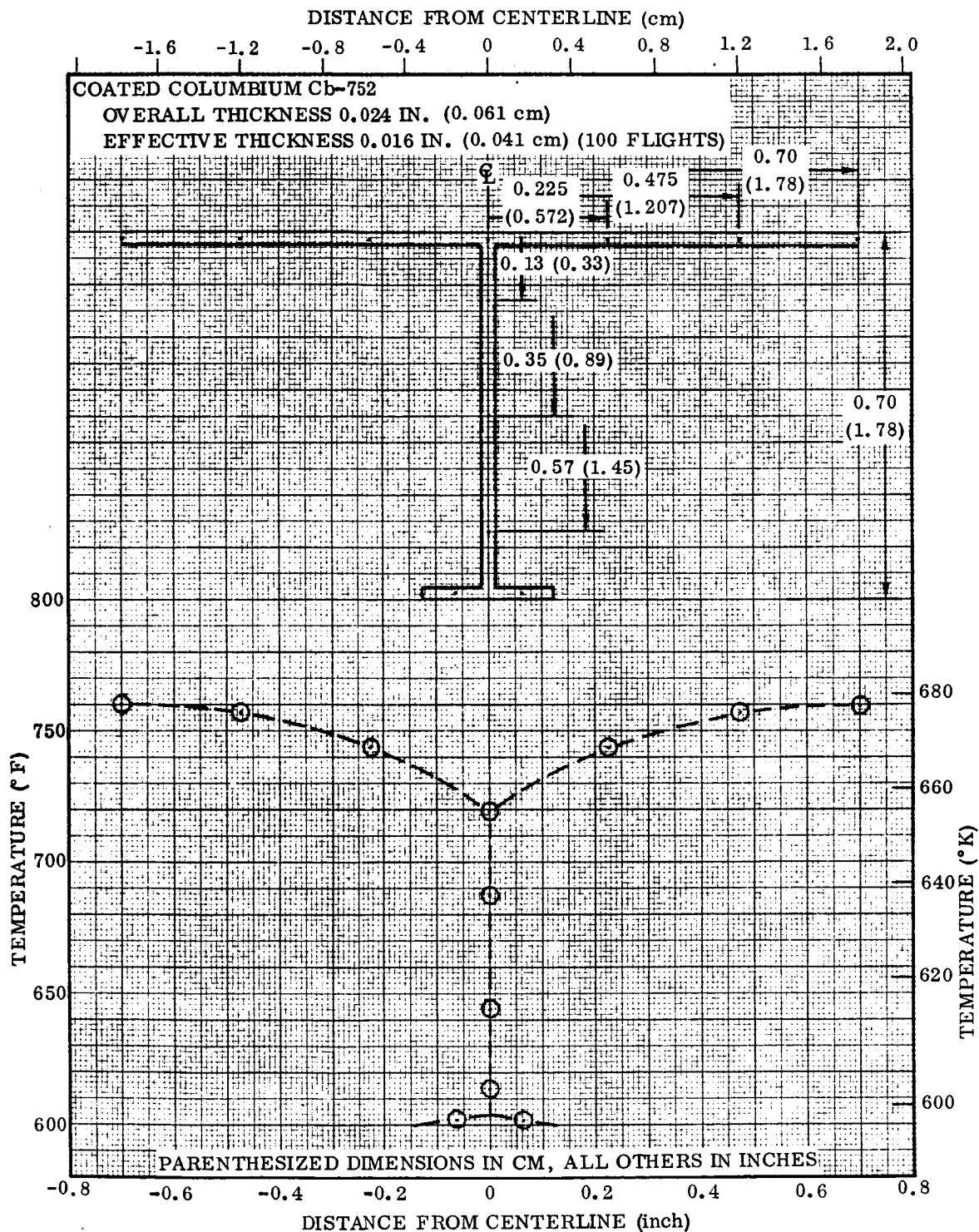


Figure 6-37. Predicted Tee-Stiffened Panel Ascent Temperature Distribution, Time = 440 Seconds

Predicted temperature histories during the 2400-second entry trajectory are presented in Figure 6-38. A uniform initial temperature of -190°F (150°K) was used here to determine maximum thermal gradients. This represents the minimum temperature expected for the case where the panel is exposed to deep space for a long period of time just prior to entry with no external solar, albedo, or earth thermal heating. A peak temperature gradient of 250°F (394°K) occurred at about 140 seconds after initiation of the entry maneuver, and the detailed temperature distribution for this case is presented in Figure 6-39.

Ascent maximum temperature gradients of Figures 6-36 and 6-37 occurred near peaks in heat flux rates, whereas the heating rate was still increasing (Figure 6-31) after the peak temperature gradient occurred during entry (Figure 6-39). It has been found that as the tee-stiffened panel temperatures increase to about 400 to 900°F (478 to 755°K), heat transfer via internal radiation increases rapidly to such an extent that even though the external heat flux is still rapidly increasing, the temperature gradients start to decrease and are quite small when maximum temperatures are reached.

Thermal models were developed to determine the temperature distributions at the edges of the tee-stiffened panel. A butted joint/tee-beam configuration is employed at the sides, and the forward and aft edges are overlapped. Peak temperature gradients at the edges occurred at about 140 seconds after initiation of entry.

The temperature distribution near the tee-beam joint and a schematic of the model are presented in Figure 6-40. It was assumed that physical contact between the tee-beam and the rib-stiffened panel edges was poor (infinite contact resistance) and thus heat transfer between the tee-beam and panel edges is only via radiation. It is apparent from Figure 6-40 that if a zero contact resistance (infinite contact conductance) were assumed, the results would not change much for this configuration since the temperature difference between the tee-beam and the panel at the contact point using just radiation is only about 40°F (277°K).

The rather large temperature gradient along the panel surface near the edge [200°F (366°K) temperature difference between locations on the surface at 0.16 inch (0.41 cm) and about 1.10 inches (2.79 cm) from the centerline in Figure 6-40] is caused by the concentration of mass and increased thermal inertia at the joint.

The predicted temperature distribution for several tee-sections adjacent to the joint is presented in Figure 6-41.

A schematic of the tee-stiffened panel overlapped edge configuration and the temperature distribution near the edges is presented in Figure 6-42. The worst case was assumed at the overlap since only radiation heat transfer was considered between the leading and trailing edges. The temperature distribution obtained along the length of

the 12 inch (30.48 cm) panel between tees is presented in Figure 6-43. The concentration of thermal mass at the overlapped edges of the panel causes relatively large temperature gradients between the edges and the center of the panel.

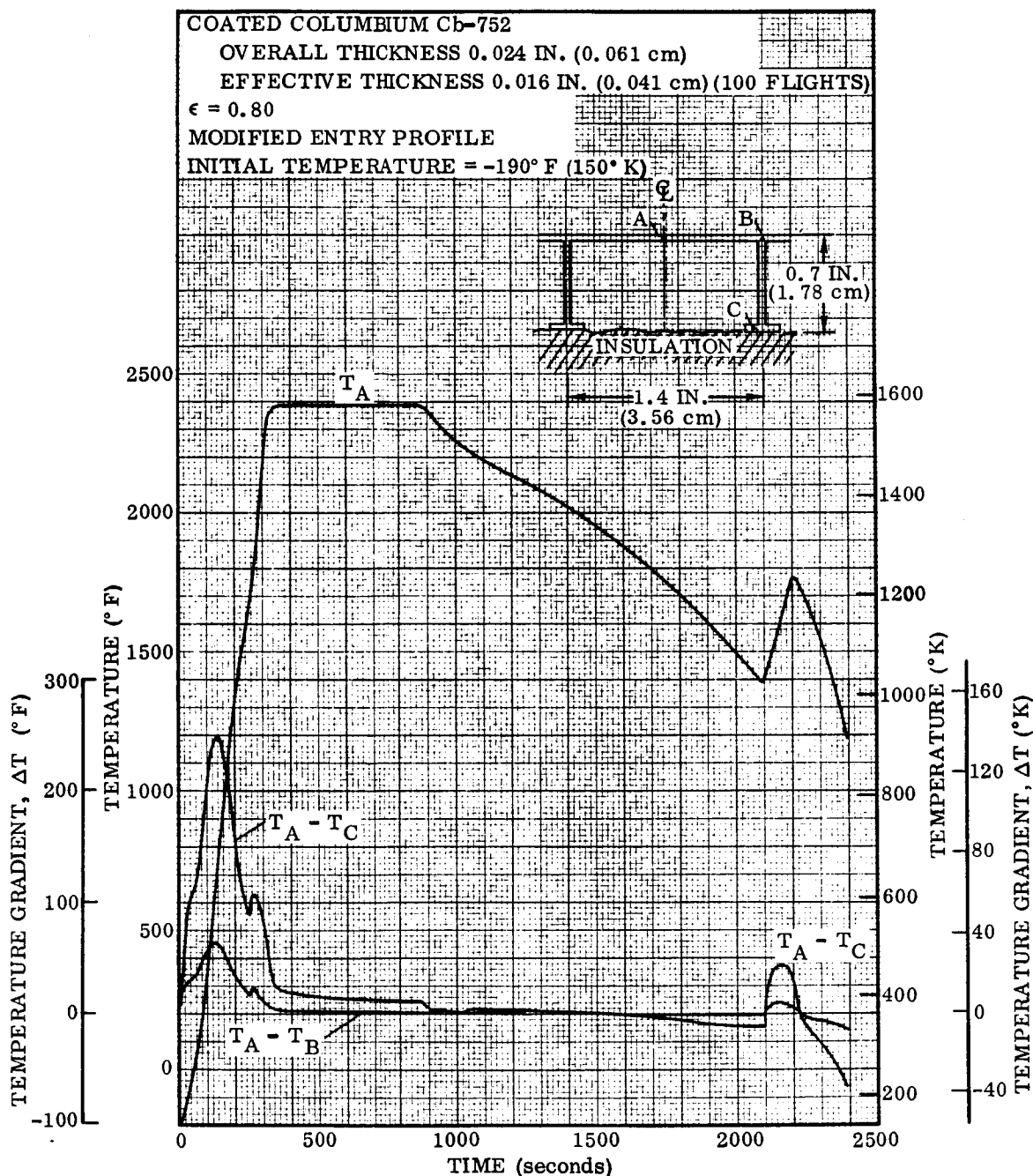


Figure 6-38. Predicted Tee-Stiffened Panel Temperatures During Entry

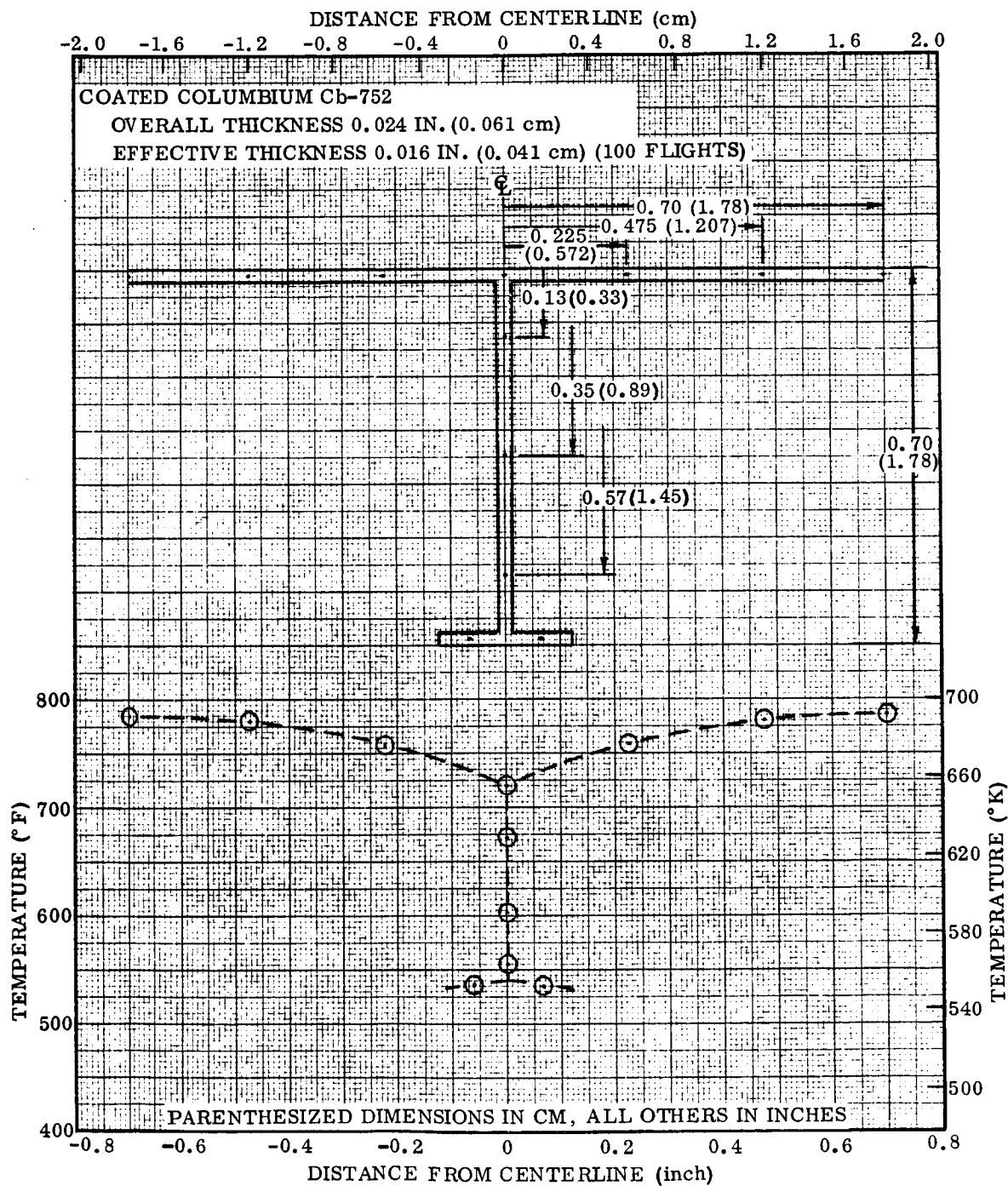


Figure 6-39. Predicted Tee-Stiffened Panel Entry Temperature Distribution, Time = 140 Seconds

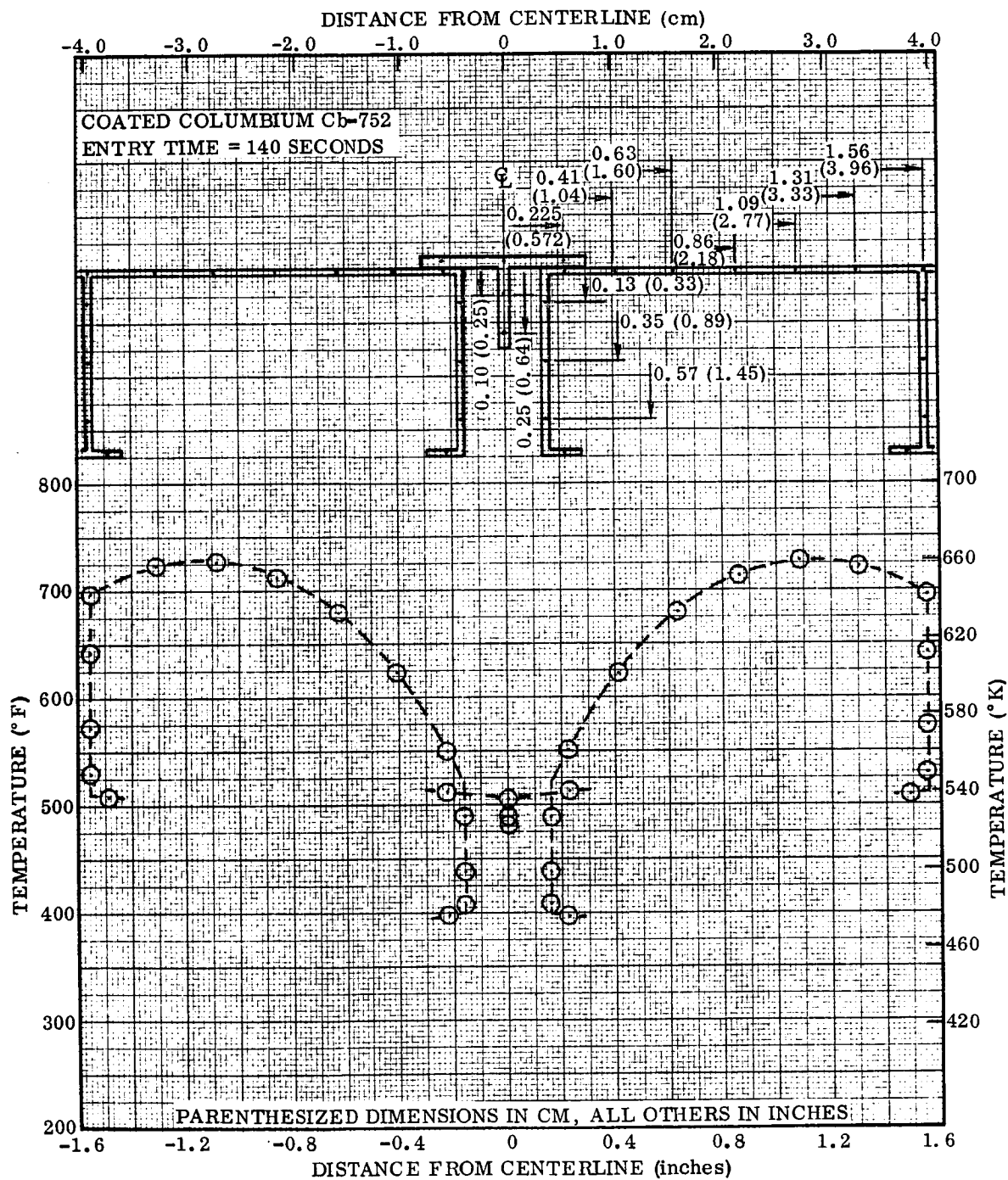


Figure 6-40. Predicted Tee-Stiffened Panel Edge Structure Temperature Distribution

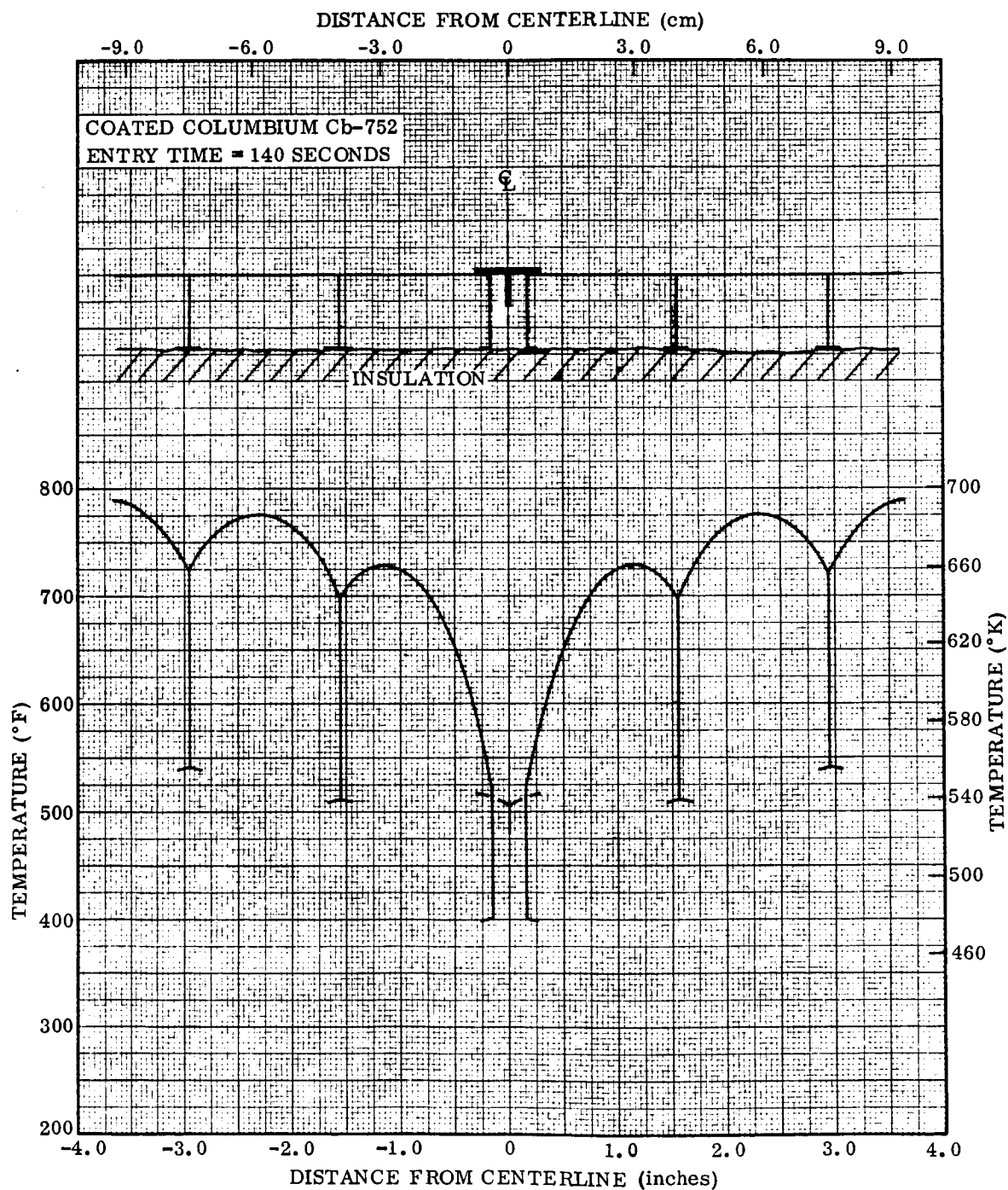


Figure 6-41. Predicted Tee-Stiffened Panel Temperature Distribution for Several Sections Near the Joint

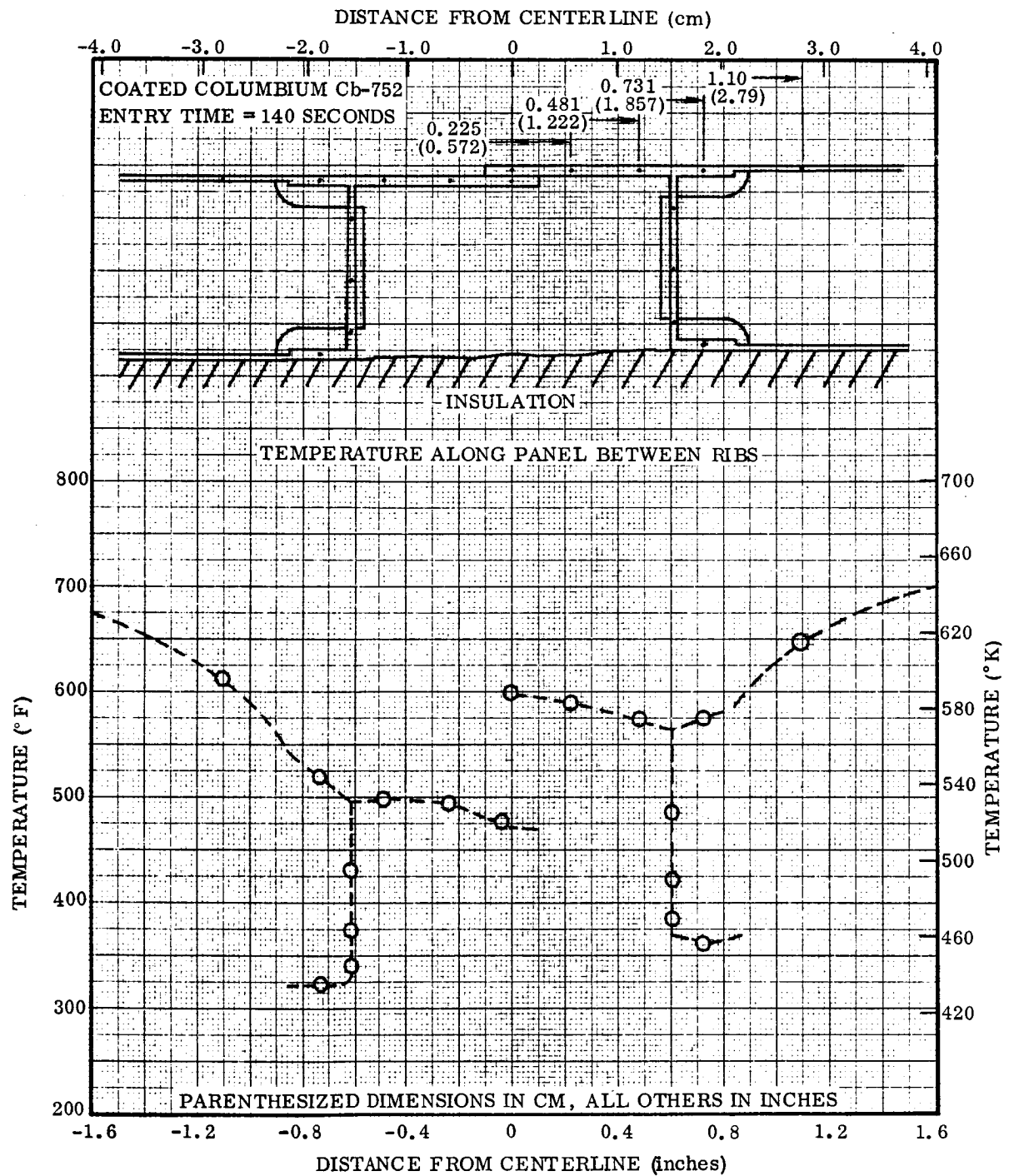


Figure 6-42. Predicted Tee-Stiffened Panel Overlapped Edge Temperature Distribution

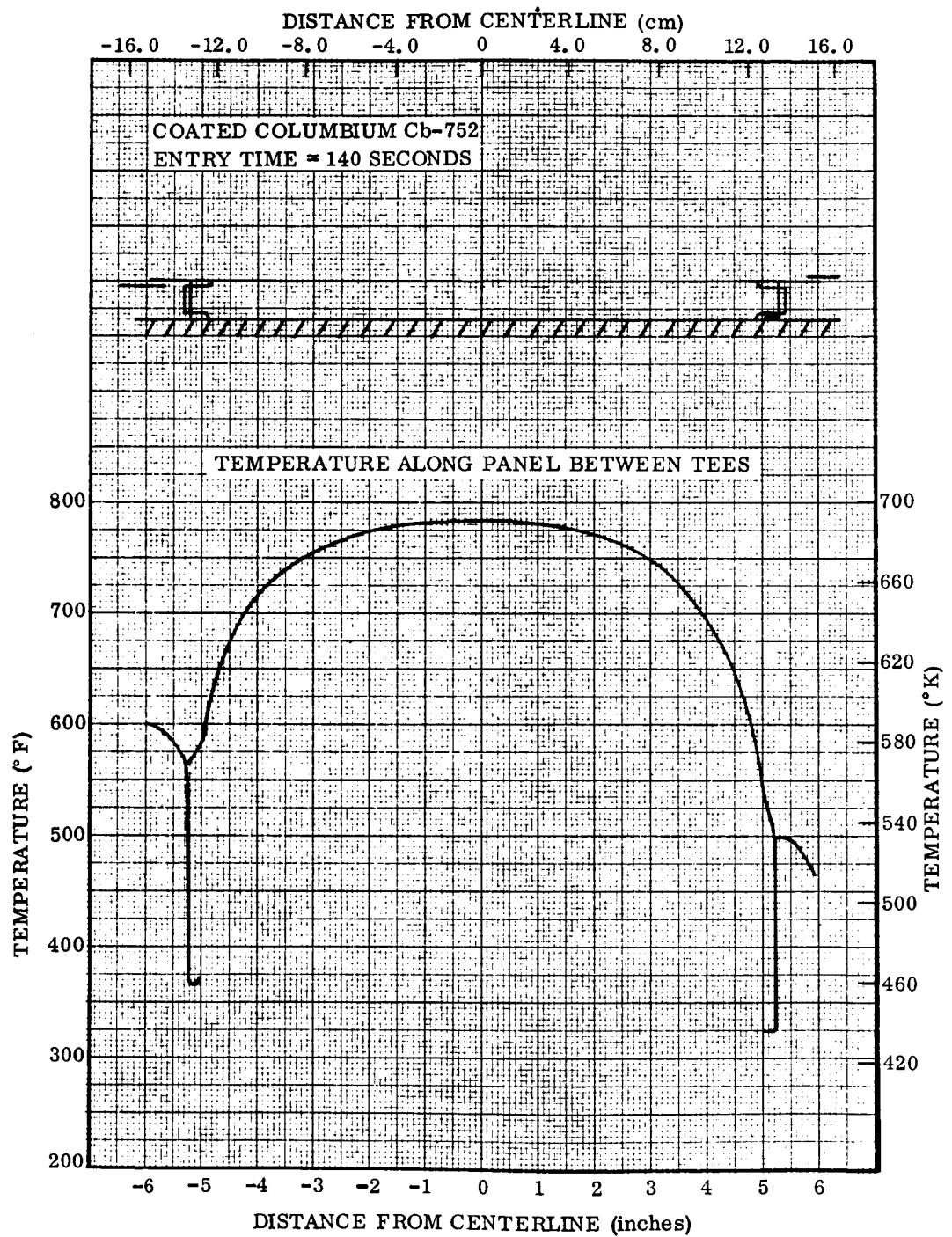


Figure 6-43. Predicted Tee-Stiffened Panel Temperature Distribution Along the 12-Inch (30.48 cm) Length Between Tees

6.3.7 Corrugated panel. - Temperature predictions for the corrugated panel are presented for the initial phases of the entry trajectory where maximum thermal gradients occur. For the corrugated panel, heating rates are dependent on the flow conditions and the orientation of the panel with respect to the flow. A study was conducted to determine what effect these variables have on the thermal performance.

Temperature predictions for the corrugated panel assuming axial flow are presented in Figure 6-44. The heating rates were the same as that used in Figure 6-38, but the predicted maximum panel temperature is somewhat higher [about 2430° F (1605° K) at location B in Figure 6-44 compared to about 2390° F (1583° K) at location A in Figure 6-38]. This higher temperature is due to the larger wetted area of the corrugated configuration and the decreased radiant heat transfer to space caused by self-shadowing. Maximum temperature gradients occur at the high heating rates, but the gradients are relatively small (Figure 6-44). The temperature distribution at 450 seconds after initiation of entry is presented in Figure 6-45.

The representative heat transfer correction factor presented in Figure 6-46 was used to illustrate the effect of cross flow on the corrugated panel configuration temperatures and temperature gradients. The results of this analysis are presented in Figures 6-47 and 6-48. A peak panel surface temperature of about 2760° F (1789° K) and relatively large temperature gradients (at high temperatures) along the surface were obtained. The data of Figure 6-46 is only representative in nature. Heating rates to corrugations in cross flow are complex functions of corrugation geometry and flow conditions including boundary layer thickness, run length, and condition of the boundary layer (laminar or turbulent). Detailed analysis of these variables is beyond the scope of this study. The simple comparison presented here, however, indicates that the corrugated panel must be aligned with the flow to avoid (1) large temperature gradients at high temperatures, and (2) local overheating.

The results discussed above were based on a preliminary 4.0 inch (10.17 cm) wide configuration with an overall thickness of 0.023 inch (0.058 cm). Temperature predictions for the final corrugated design [3.8 inch (9.65 cm)] width and [0.025 inch (0.064 cm)] overall thickness in axial flow are presented in Figure 6-49 and 6-50.

A schematic of the corrugated butted joint/tee-beam edge, and the temperature distribution within 1.5 inches (3.81 cm) of the joint at the 140 seconds entry time point (maximum gradient in corrugation next to joint) are presented in Figure 6-51. The temperature distribution out to the center of the panel [8.0 inches (20.4 cm) from the joint] is presented in Figure 6-52.

The results in Figures 6-51 and 6-52 are based on radiation heat transfer only across the area where the tee-beam and the panel make contact. This assumption plus the relatively thick tee-beam compared to the panel causes the large temperature

differential [about 170° F (350° K)] between the tee-beam and the panel edge shown in Figure 6-51. A peak temperature differential of about 230° F (383° K) actually occurred at about 110 seconds after entry, and the differential decreased rapidly to less than 20° F (266° K) after about 220 seconds as both the temperatures and the radiation heat transfer increased.

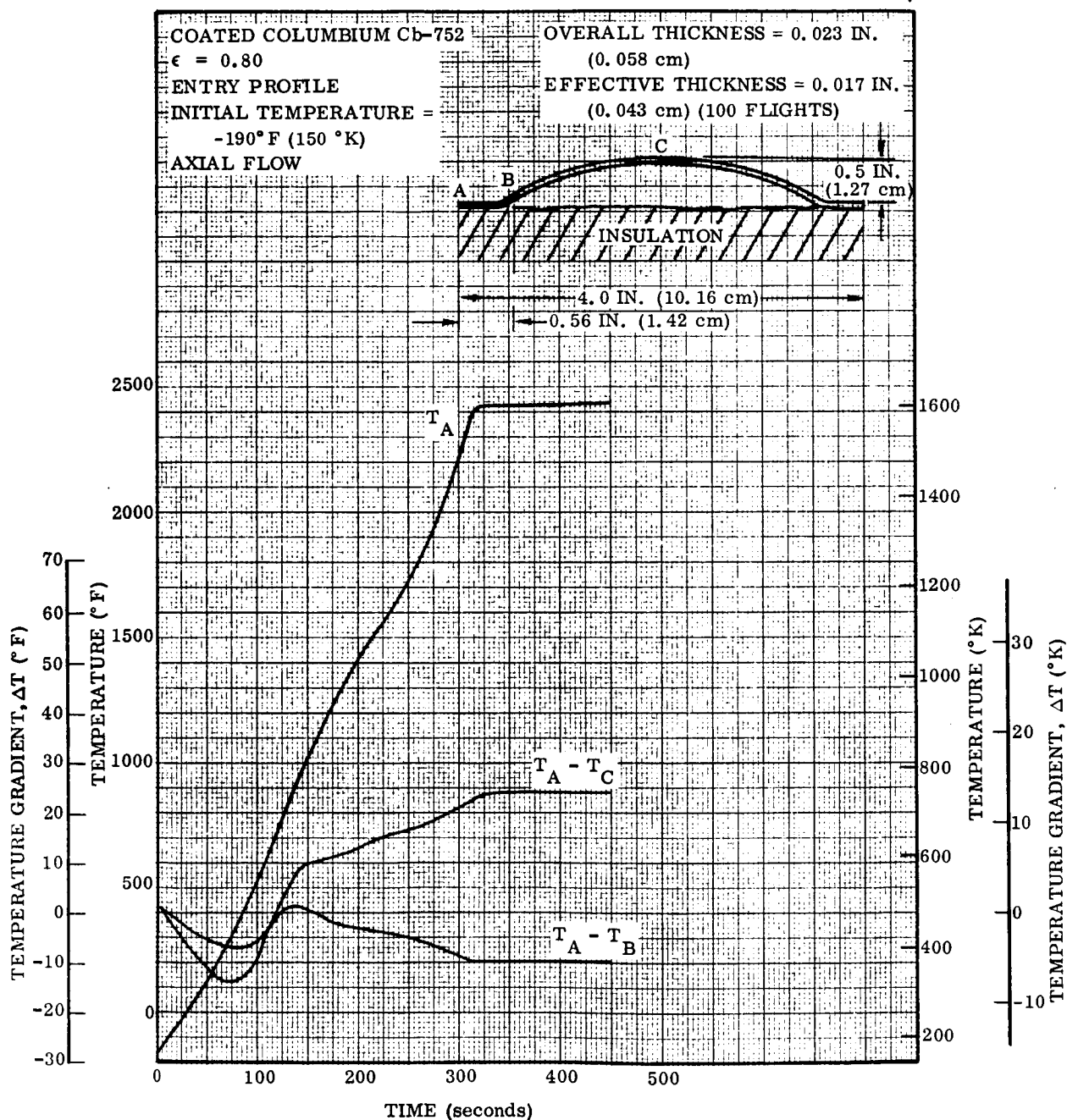


Figure 6-44. Predicted Corrugated Panel Temperature During Entry, Axial Flow

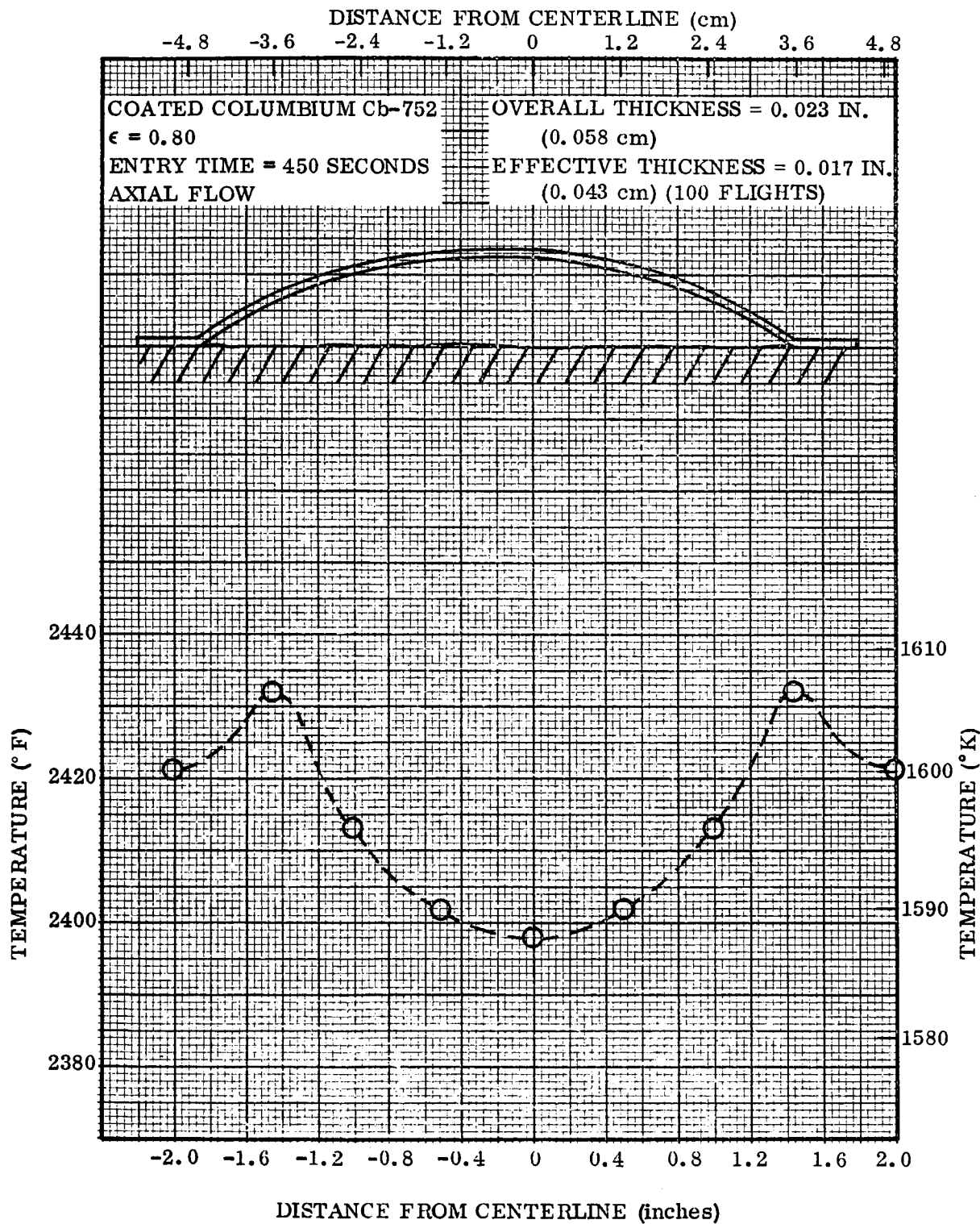


Figure 6-45. Predicted Corrugated Panel Entry Temperature Distribution, Axial Flow, Time = 450 Seconds

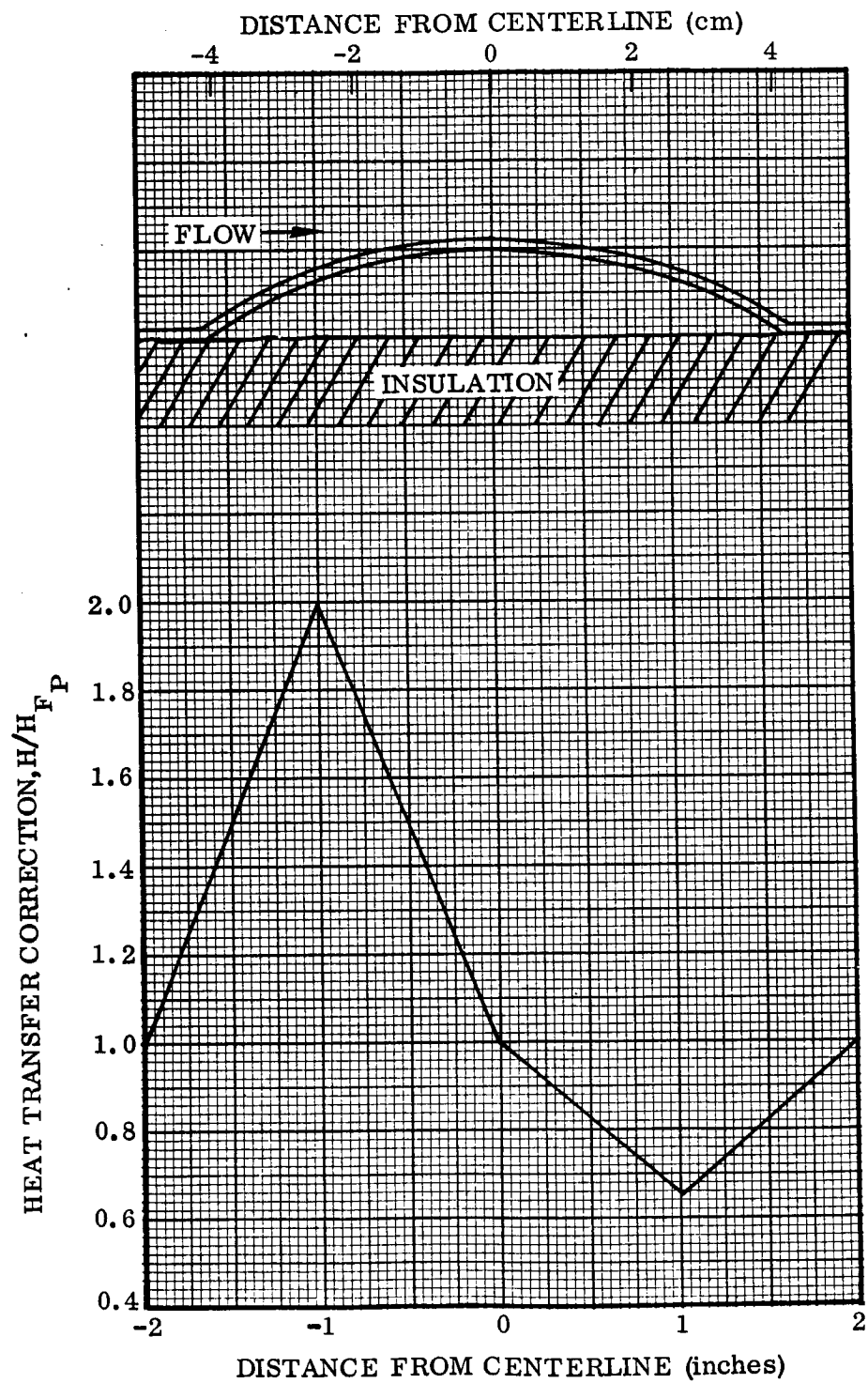


Figure 6-46. Cross Flow Heat Transfer Correction Factor

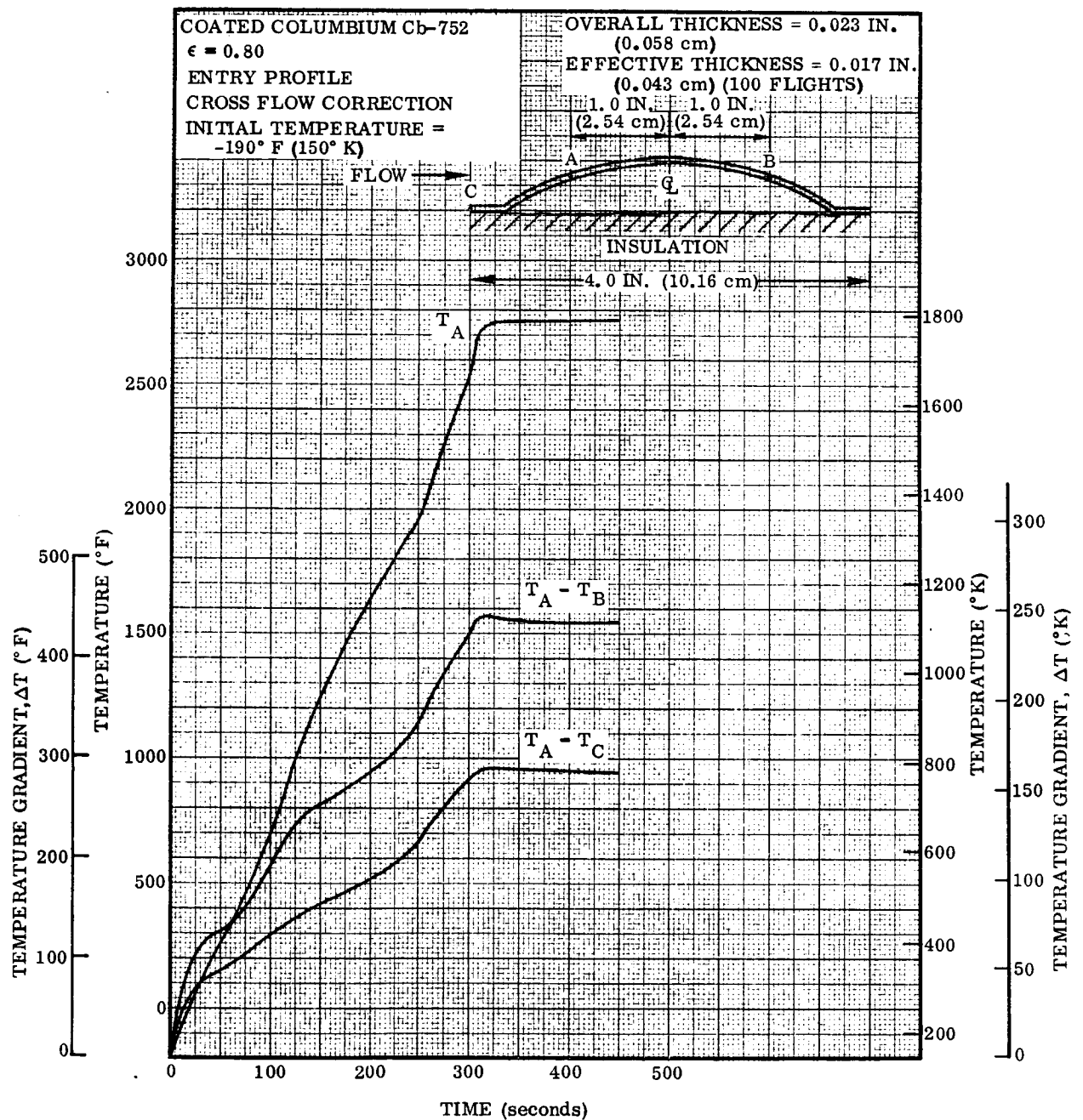


Figure 6-47. Predicted Corrugated Panel Temperatures During Entry, Cross Flow

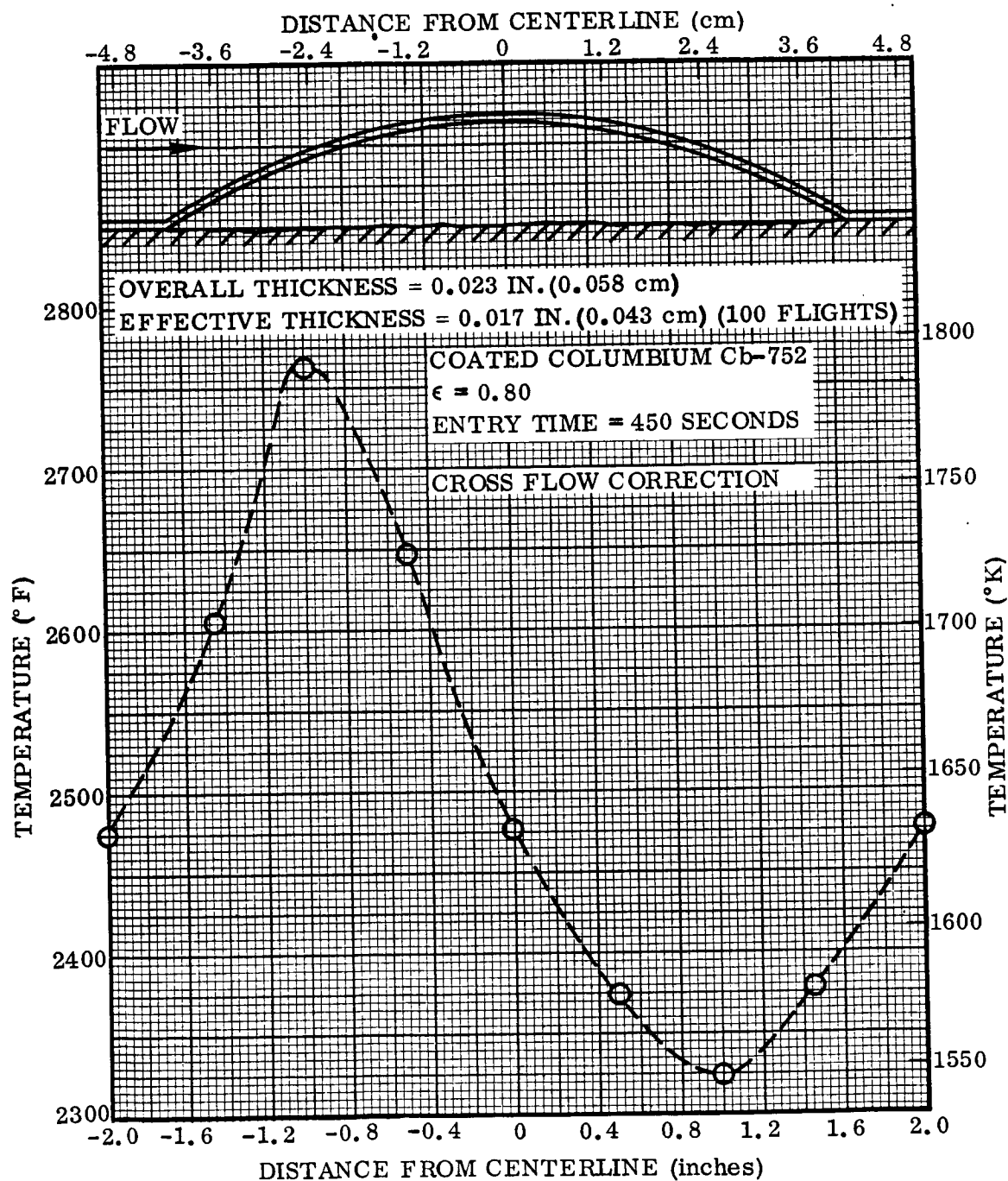


Figure 6-48. Predicted Corrugated Panel Entry Temperature Distribution, Cross Flow, Time = 450 Seconds

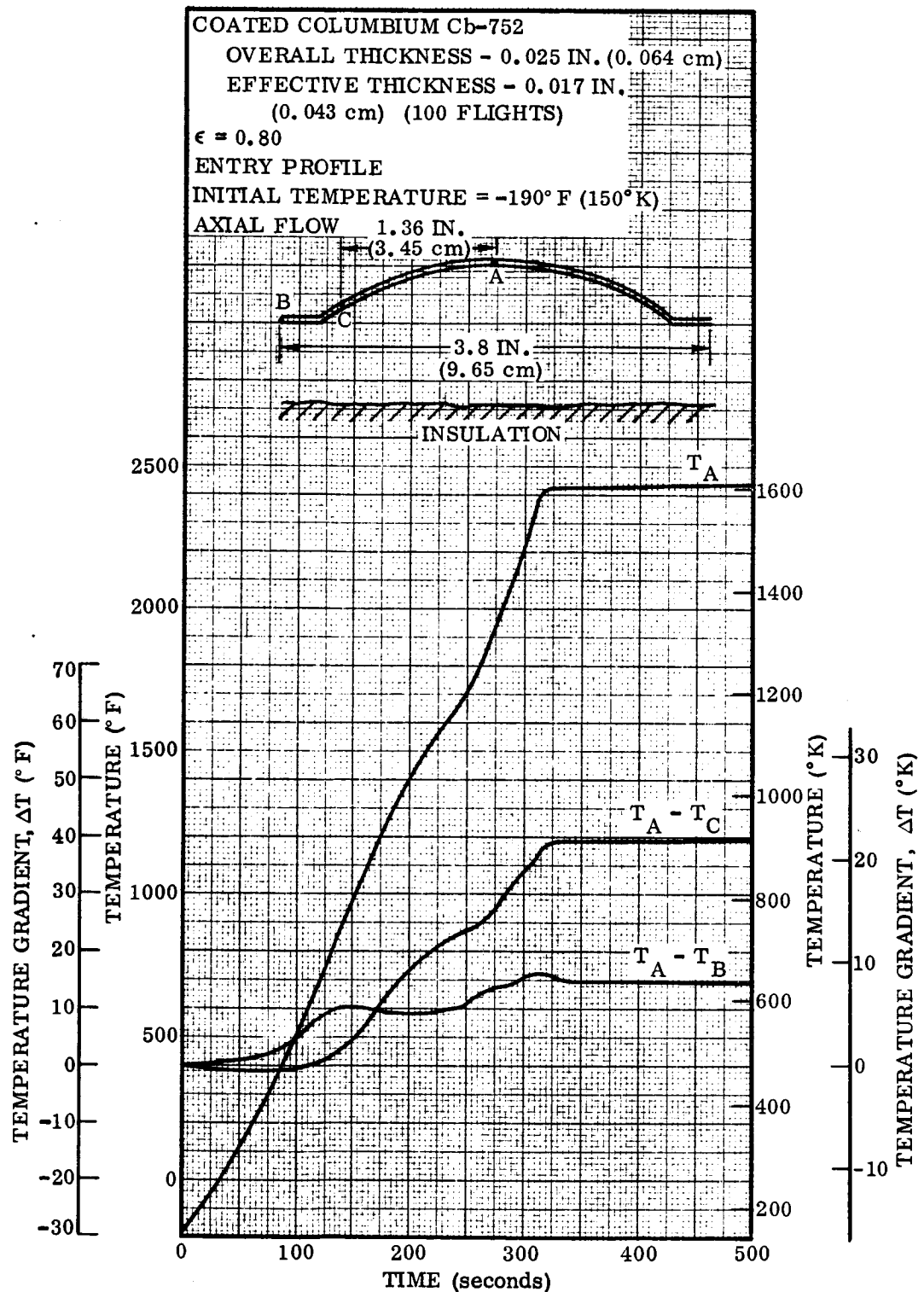


Figure 6-49. Predicted Corrugated Panel Temperatures During Entry, Axial Flow (Final Design)

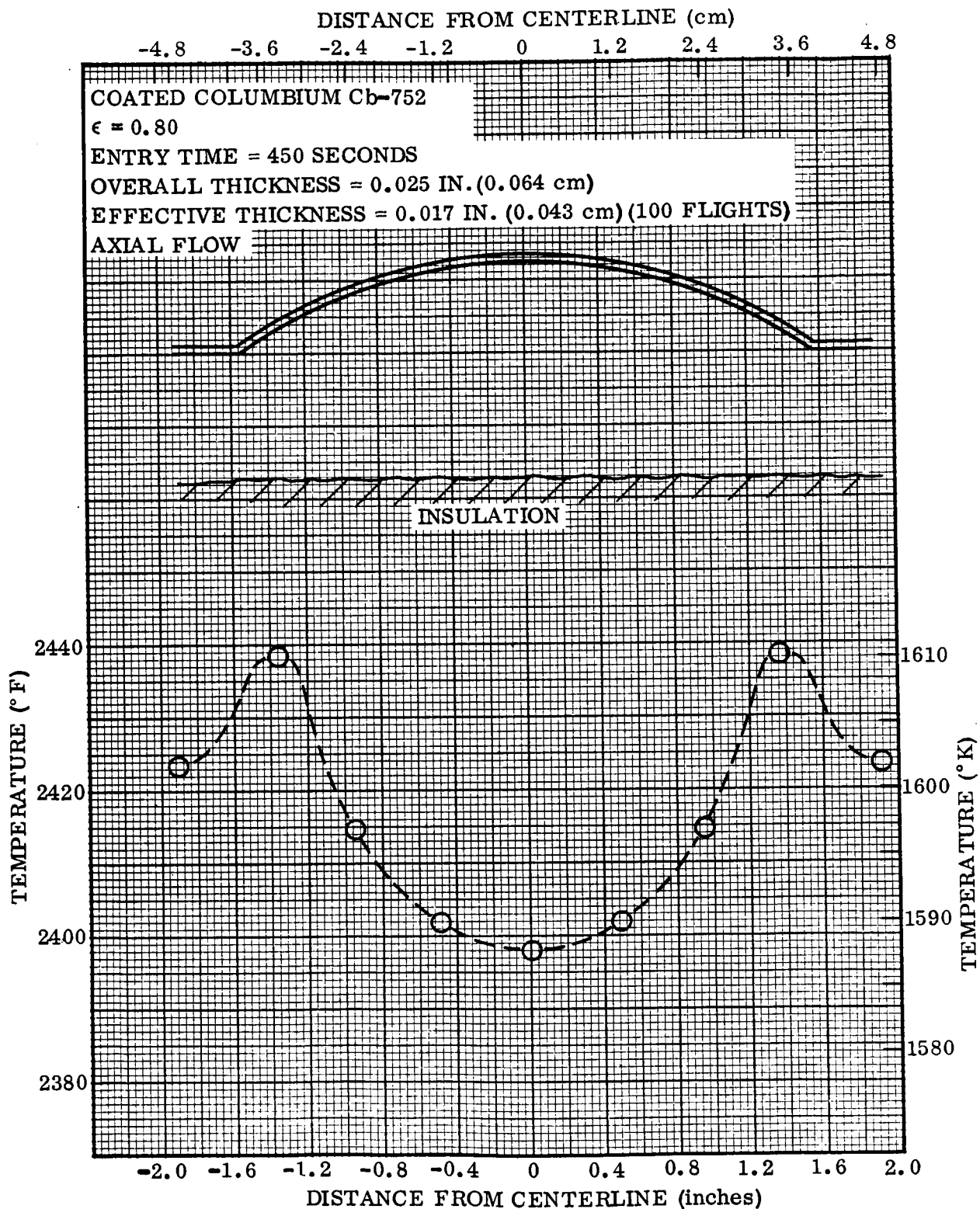


Figure 6-50. Predicted Corrugated Panel Entry Temperature Distribution, Axial Flow, Time = 450 Seconds (Final Design)

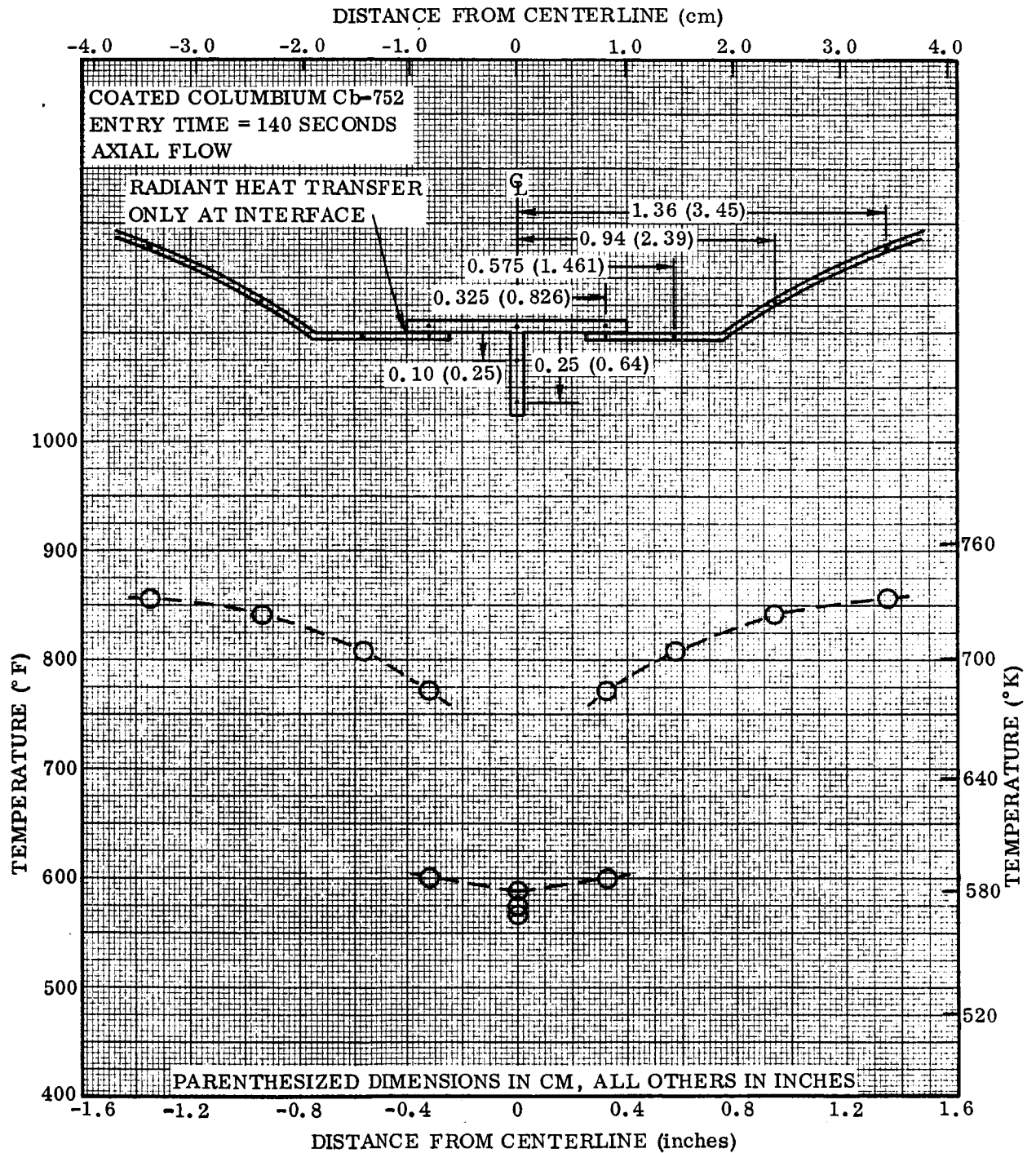


Figure 6-51. Predicted Corrugated Panel Edge Structure Temperature Distribution

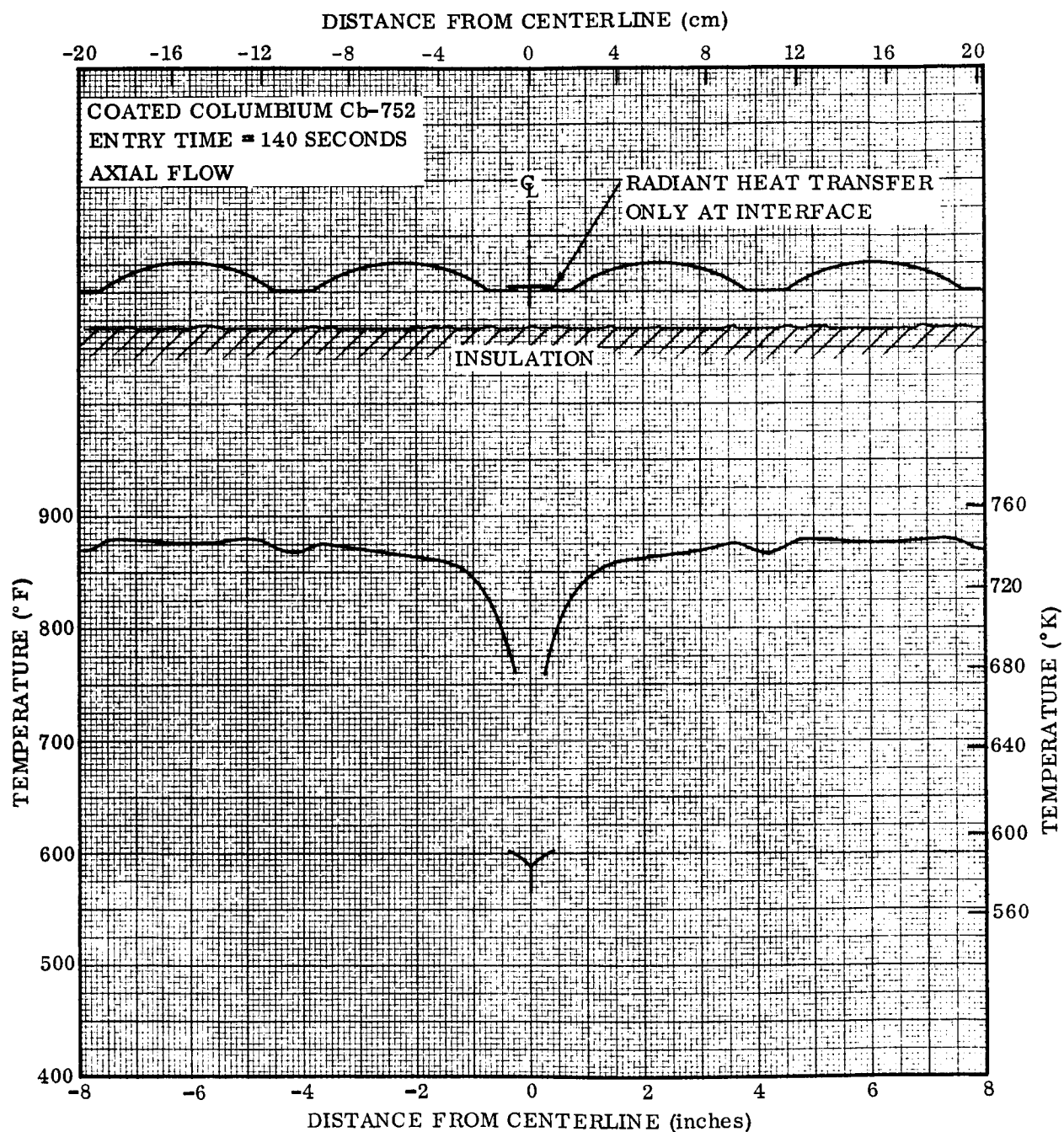


Figure 6-52. Predicted Corrugated Panel Temperature Distribution

The effect on the temperature distribution of assuming an infinite contact conductance at the tee-beam/panel interface is presented in Figure 6-53. For this case, the maximum temperature gradient in the corrugation adjacent to the tee-beam occurs at 110 seconds. The data at 140 seconds presented in Figure 6-53 is directly comparable to that shown in Figure 6-51, and these data represent the limiting cases with respect to the variation in heat transfer possible across the tee-beam/panel interface.

The forward and aft portions of the corrugated panels have thickened sections attached to beam stiffeners, and the edges are overlapped. These relatively massive beams and their associated thermal inertia cause large thermal gradients during the initial heat-up portion of the entry trajectory. The temperature distribution obtained near the joint and along the panel between corrugations, assuming radiant heat transfer only at the overlap, are presented in Figures 6-54 and 6-55. Using the radiant-heat-transfer-only assumption yields a 550° F (561° K) temperature difference between the two panels where they overlap. Results obtained by assuming infinite conduction at the overlap are presented in Figure 6-56.

These results should represent the limiting cases. Both cases show extremely large temperature gradients in the panels near the thickened sections where the panels are attached to the beams.

6.3.8 Panel support structure. - Both the tee-stiffened and corrugated panel designs have similar support-post configurations. The upper portion of the post is made of coated columbium alloy, which can withstand the 2400° F (1589° K) temperature to which the panel will be exposed. The lower portion of the post is made of TD NiCr, which has about a 2000° F (1366° K) maximum design temperature and has a significantly lower thermal conductivity than columbium alloys. The objective of this portion of the study is to determine the length of the TD NiCr portion of the post, and to determine the backup structure temperatures at the base of the post.

A schematic of the support-post configuration is presented in Figure 6-57. It was found that a 2.3 inch (5.85 cm) TD NiCr lower support post is required as shown. It was also determined that the TD NiCr post section must be filled with insulation prior to assembly to prevent heat transfer via radiation to the backup structure.

Predicted temperature histories at several support-post assembly locations are presented in Figure 6-58. Initial temperatures prior to entry were assumed uniform at 100° F (311° K), which represents a pre-entry orientation where the panel surface is exposed to solar heating. The upper portion of the TD NiCr attachment bolt reached a predicted peak temperature of 2030° F (1383° K) at about 950 seconds as shown. The backup structure at the base of the post reached a predicted peak temperature of 800° F (700° K) at about 2900 seconds. At primary structure locations away from the post, peak temperatures were less and occurred later, which is due to soak-back of the heat trapped

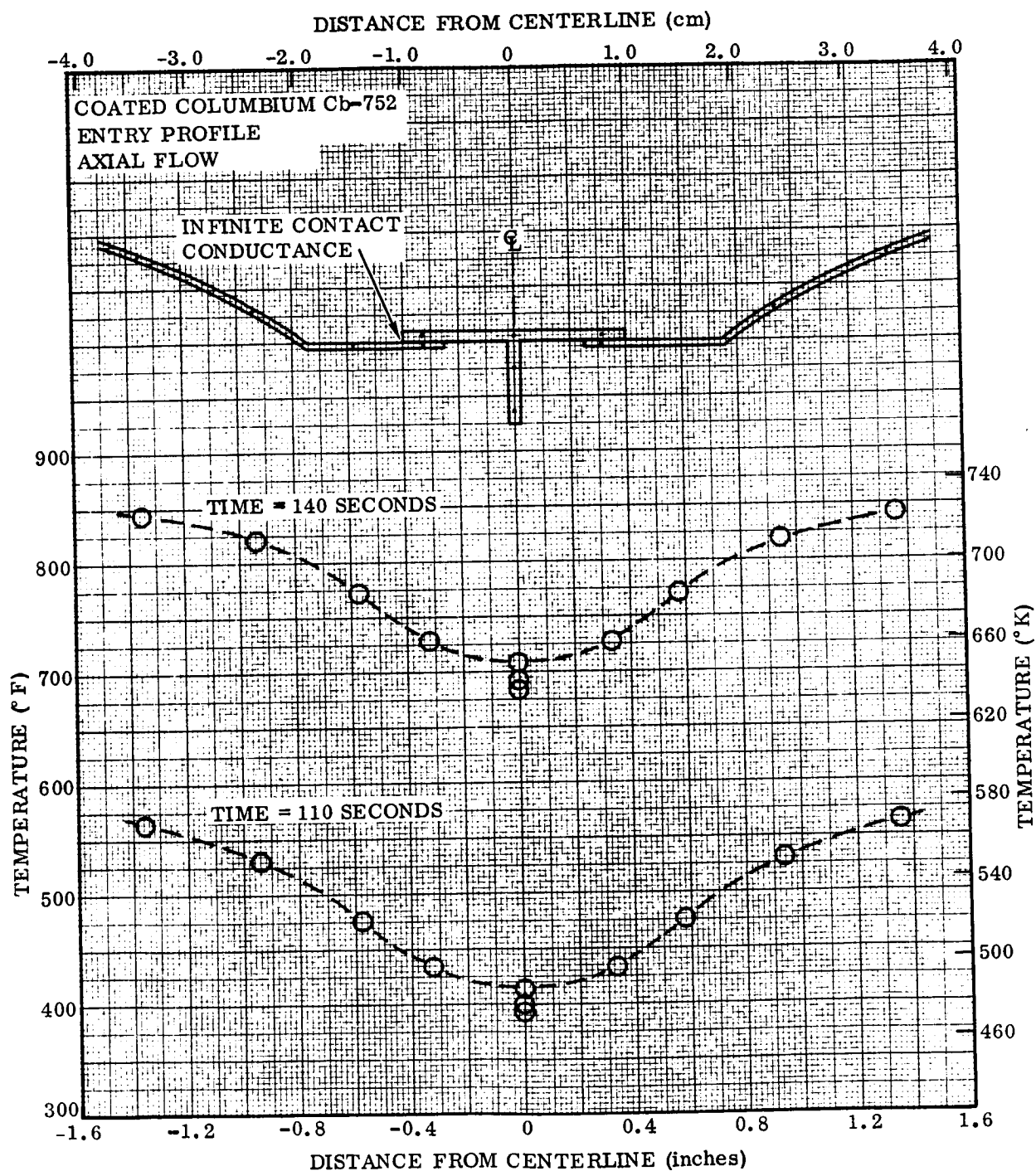


Figure 6-53. Predicted Corrugated Panel Edge Structure Temperature Distribution Assuming Infinite Contact Conductance at Interface

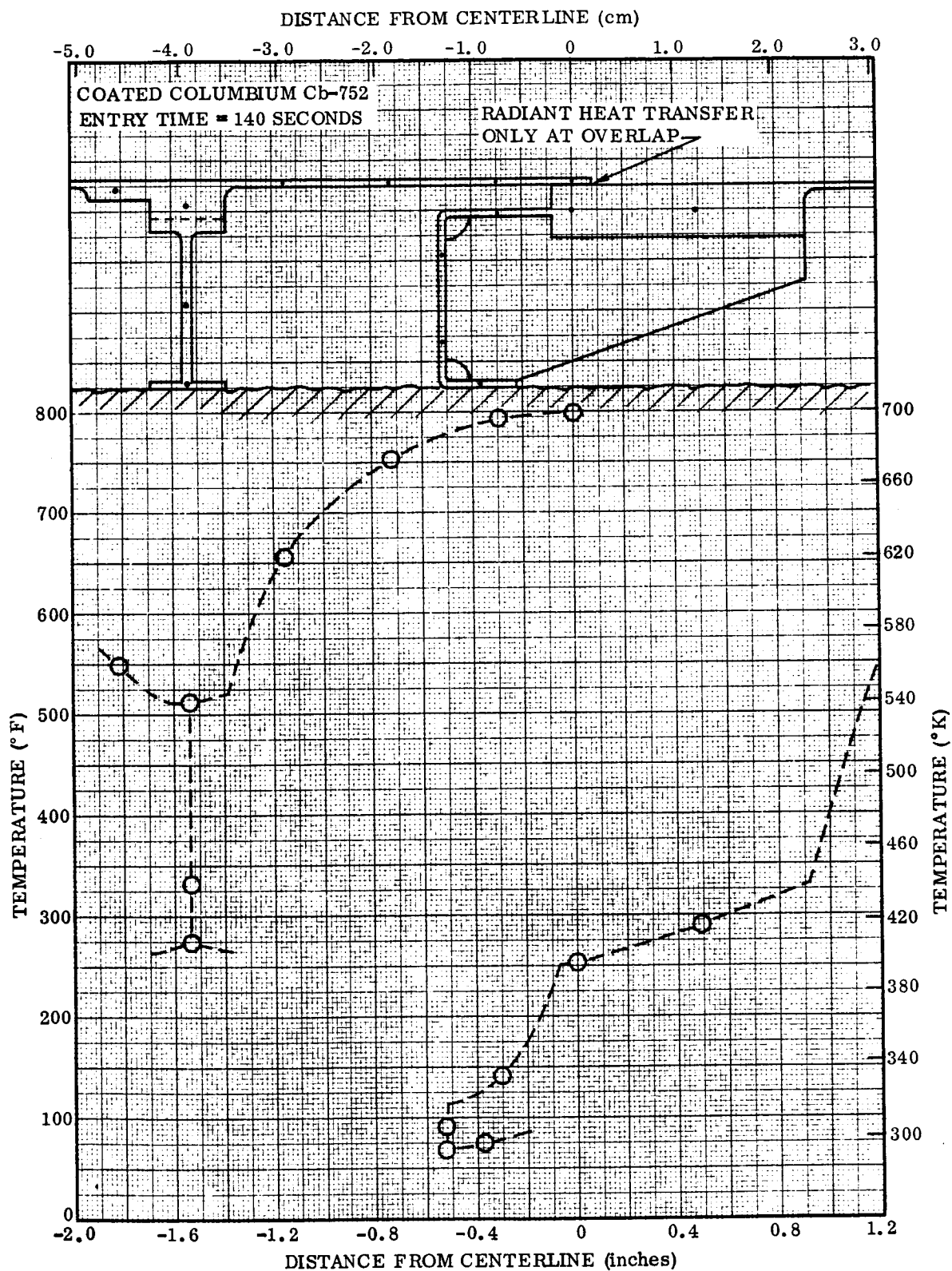


Figure 6-54. Predicted Corrugated Panel Overlapped Edge Structure Temperature Distribution

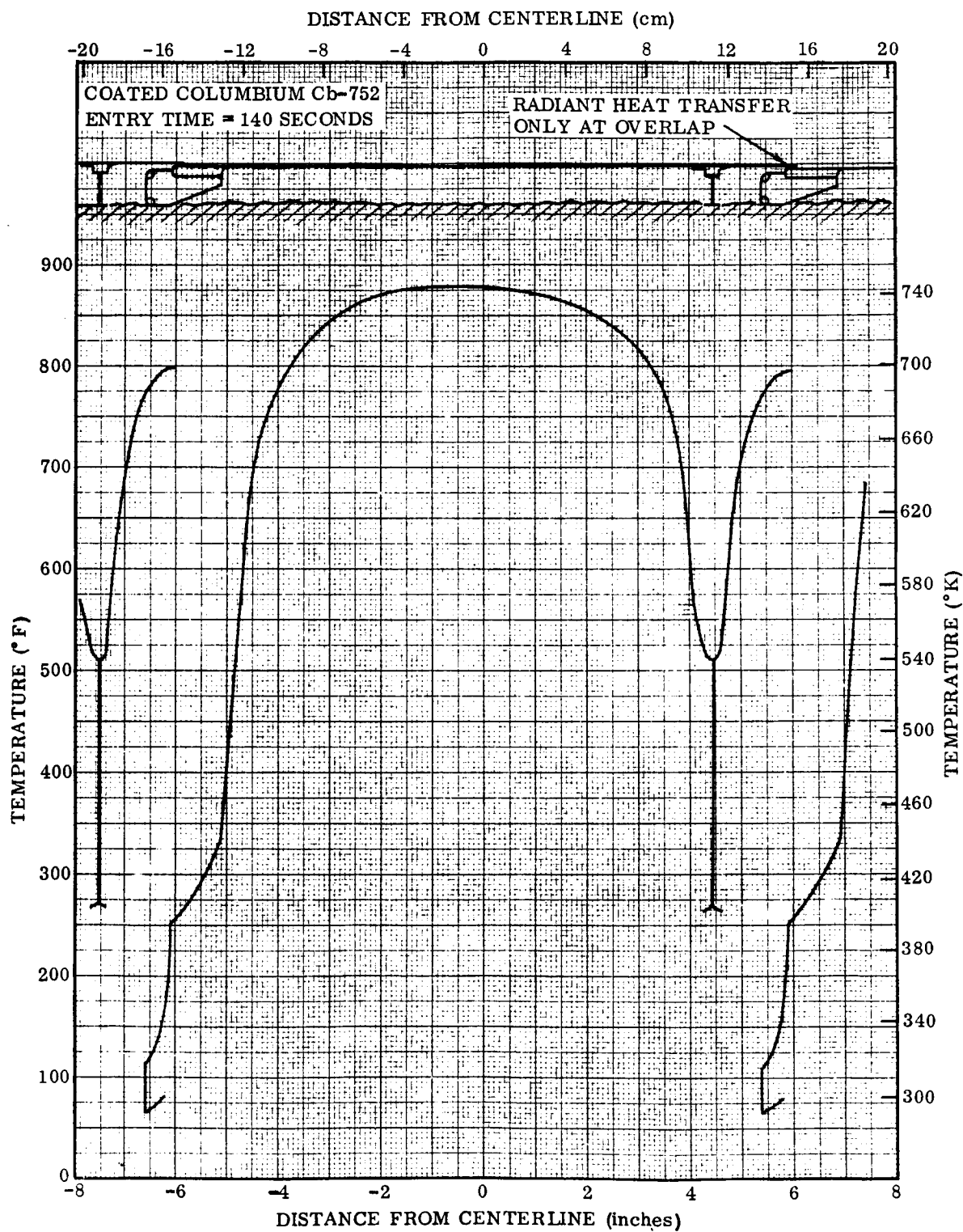


Figure 6-55. Predicted Corrugated Panel Temperature Distribution

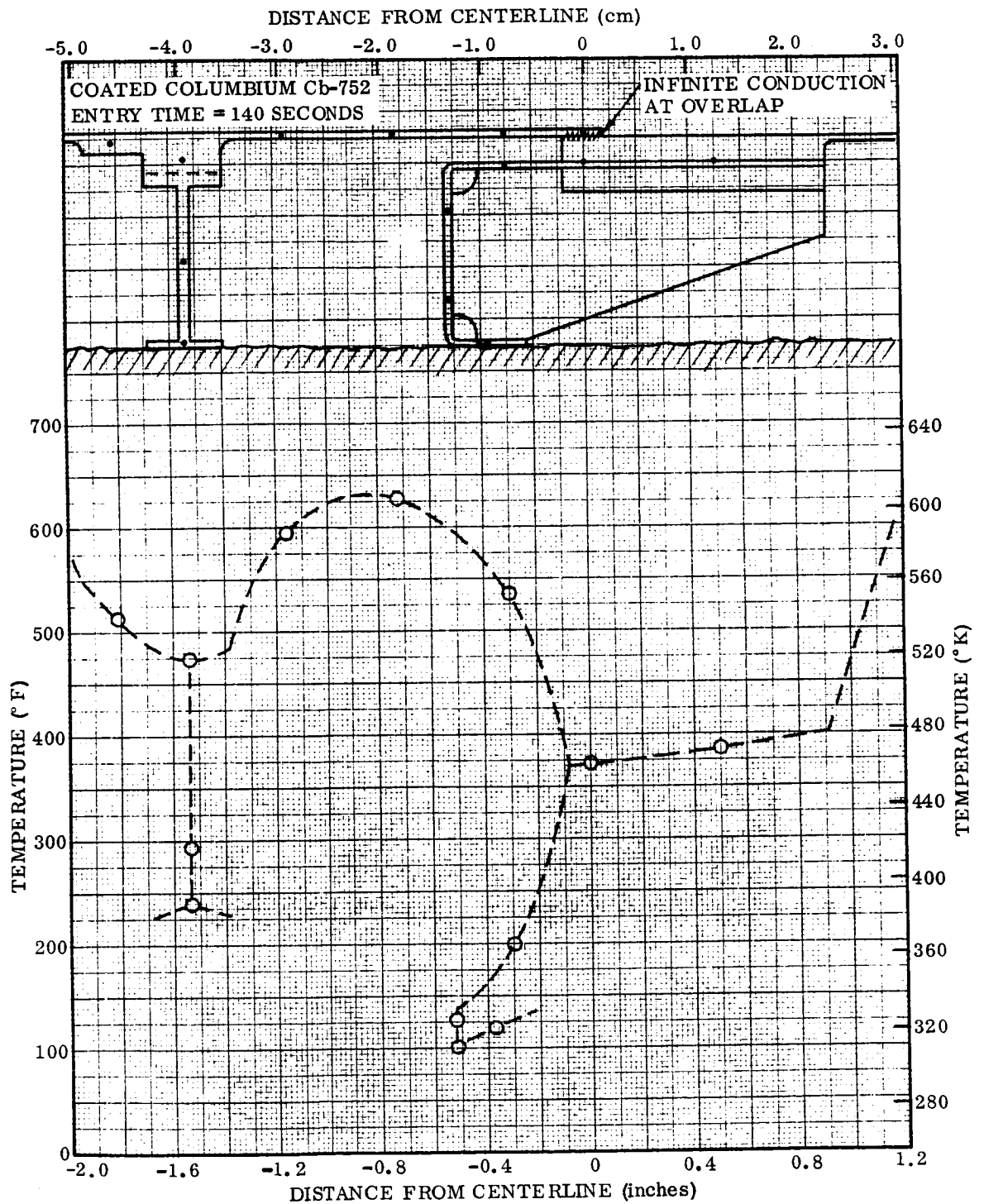


Figure 6-56. Predicted Corrugated Panel Overlapped Edge Structure Temperature Distribution Assuming Infinite Contact Conductance at Interface

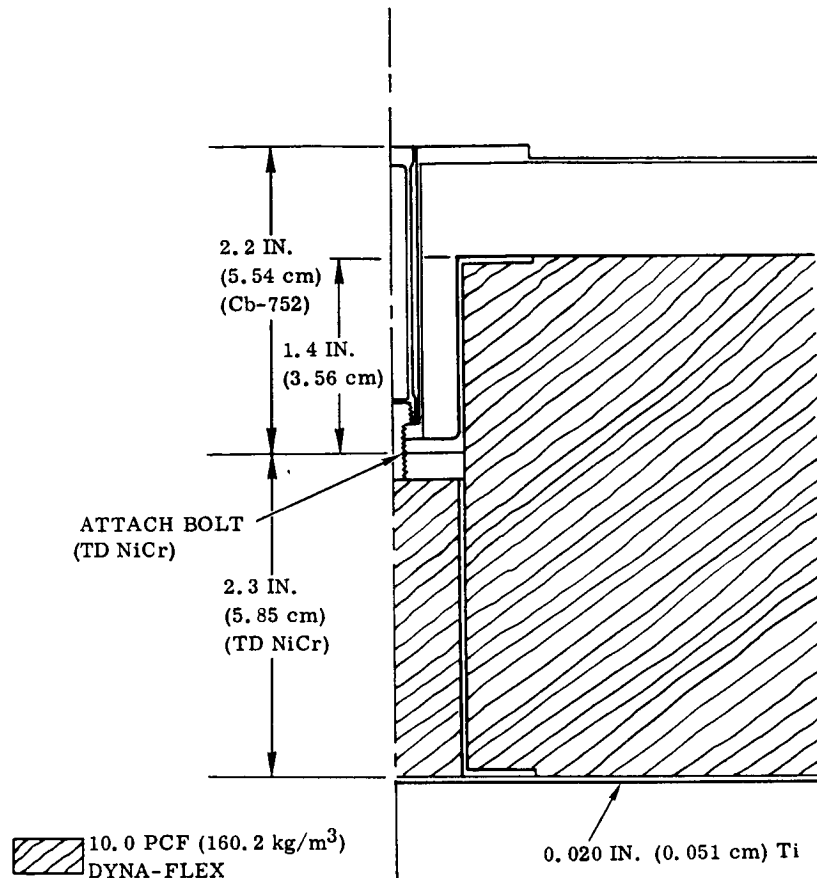


Figure 6-57. Panel Support-Post Schematic

in the insulation. Although primary structure temperatures shown in the vicinity of the base of the post are greater than the nominal titanium structural limit of 650° F (616° K), it is believed that local structure temperatures as high as 850° F (727° K) are acceptable for this application. The data presented in Figure 6-58 indicates that at distances greater than about 2.0 inches (5.1 cm) from the post, the structure will be below the 650° F (616° K) design limit until after orbiter landing.

The predicted temperature gradient along the length of the post at 950 seconds after entry is presented in Figure 6-59. Relatively low thermal gradients exist in the upper coated columbium alloy section of the post due to the relatively high thermal conductivity and the radiant heat transfer between post interior surfaces.

The analysis presented here assumes heat transfer to a 0.020-inch (0.051 cm) titanium primary structural plate, but no heat-sink effects of supporting I-beams or stiffeners were included. These effects will tend to lower temperatures of the primary structure.

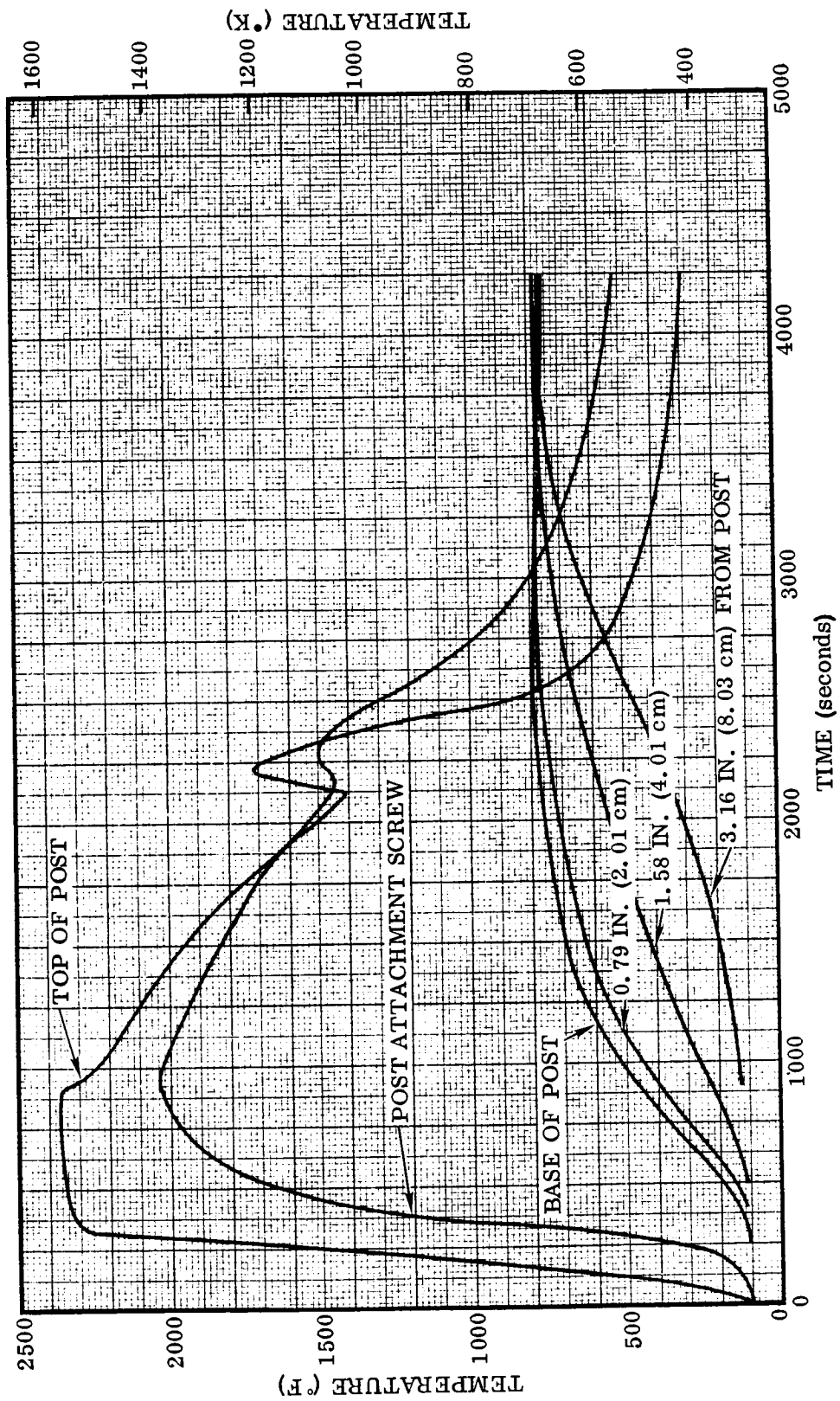


Figure 6-58. Predicted Panel Support-Post and Primary Structure Temperature Histories

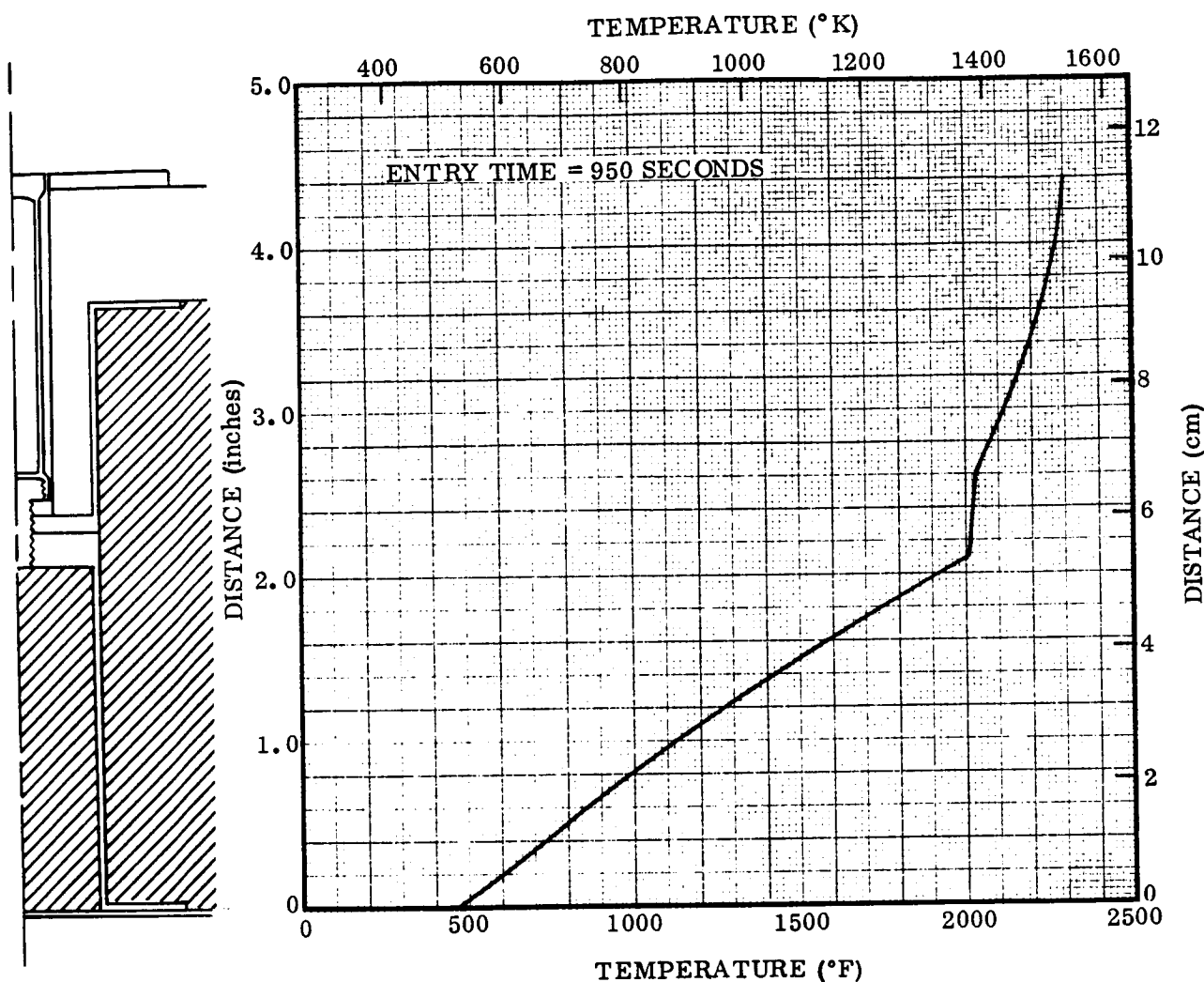


Figure 6-59. Predicted Support-Post Temperature Distribution

6.4 Small-Size TPS Structural Analysis

6.4.1 Summary. — The structural analysis is presented for two small-sized coated columbium alloy TPS. The panel configurations are (1) a tee-stiffened design with smooth outer skin, and (2) a corrugated skin design. The overall size of both panels is 12 by 16 inches (30.48 by 40.64 cm). Each panel is supported by six tubular posts, one of which serves to locate the panel and react inertia loads; the remaining posts support normal aerodynamic loads only via slip joints that permit free thermal expansion. Panel analyses are given for the predicted peak aerodynamic and thermal loads occurring during boost and reentry as given in the test loads profile (Figure 5-1). The support posts are analyzed for the boost engine vibration spectrum (Section 6.1.2).

The analysis is based on the preliminary material properties presented in Section 6.1.3. Since this data does not include stress-strain curves, all buckling analyses are based on the initial elastic modulus values at the appropriate temperature. Hence, in cases where the computed elastic buckling stress is a large percentage of the 0.2% offset yield strength, the required plasticity reduction factors (E_T/E or E_C/E) are not available. Therefore, true buckling stress cannot be determined. However, since the applied stress levels are low it is obvious that adequate margins of safety exist for these cases.

6.4.2 Method of analysis. — In both TPS panel designs the transverse stiffening elements, i. e. , ribs or corrugations, are assumed to behave essentially as simply supported beams when subjected to normal pressure loading. In addition to bending stresses due to the pressure loading, the panel section experiences thermal stresses due to nonuniform heating. The thermal stress analysis used is based on the finite sum solution given in Reference 28. In this procedure the cross section is broken down into a finite number of elemental areas so that the variation αT and E within each element is small. The solution is based on the assumption that plane cross sections remain plane. In the analysis the estimated effective material thickness after 100 flights is used. The effective thickness does not include the coating or diffusion zone.

The effective thickness of the coated columbium (Cb-752) sheet material after 100 flights is derived as follows.

Nominal coating thickness $t_c = 0.003$ in. (0.076 mm)

Initial diffusion on application $= \frac{t_c}{3} = 0.001$ inch/side (0.025 mm/side)

Assuming a linear rate of diffusion of the coating into the substrate of 0.00001 inch/side/flight (0.00025 mm/side/flight), the final effective thickness (t_e) after 100 flights is given by

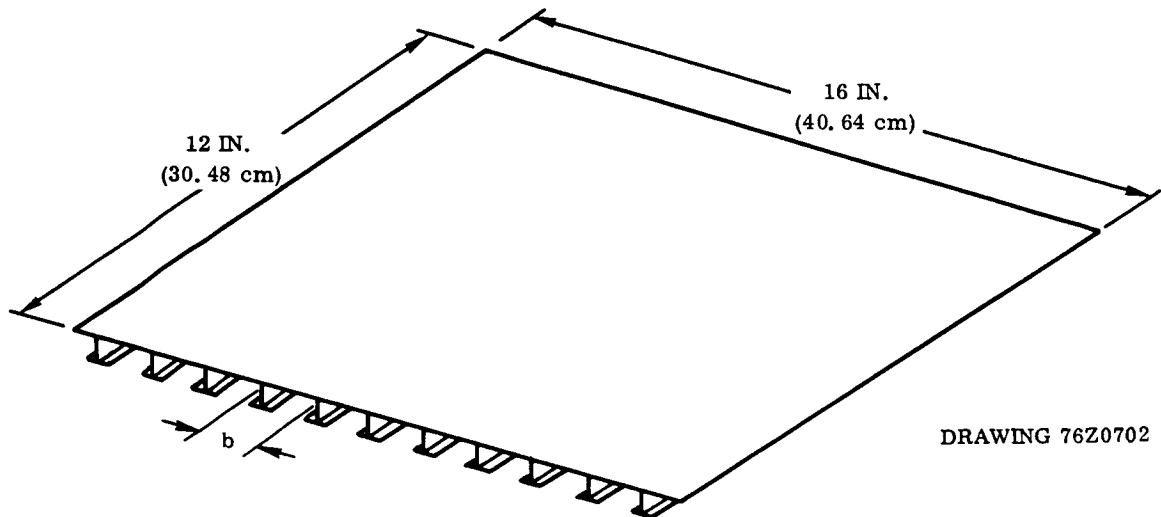
$$\begin{aligned} t_e &= t_s - 2 [0.001 + 100 (0.00001)] \\ &= t_s - 0.004 \end{aligned}$$

where

t_s = initial sheet thickness before coating

6.4.3 Tee-stiffened panel assembly. -

6.4.3.1 Bending analysis of tee stiffeners:



Design Condition

Boost Phase: Maximum pressure
(crushing)

Normal Pressure (p) = 3.0 psi
(20.7 kN/m²) (limit)

Temperature = 340° F (444° K)

Running Load/Stiffener (w) = (p) (b)
= (3.0) (1.4)
= 4.2 lb/in (7.35 N/cm)

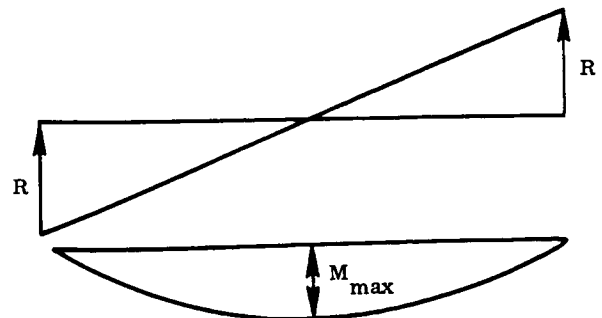
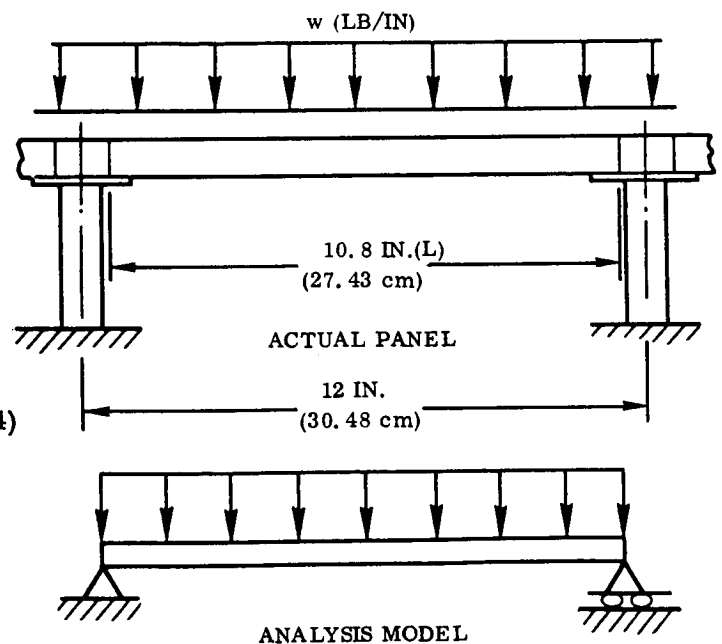
Reactions (R) = $\frac{wL}{2} = \frac{(4.2)(10.8)}{2}$

= 22.68 lb (100.9 N)

Maximum Bending Moment at Midspan

$= \frac{wL^2}{8} = \frac{(4.2)(10.8^2)}{8}$

= 61.24 in-lb (691.8 cm-N)



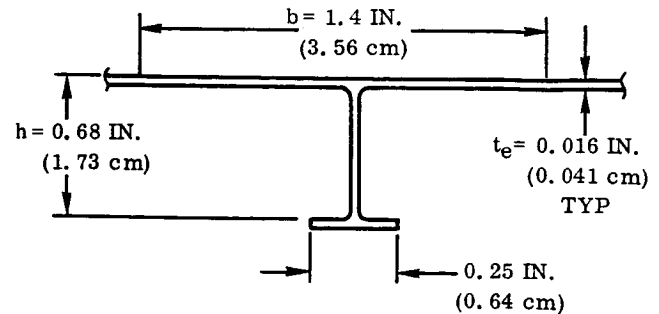
Bending Analysis

Condition: 3.0 psi (20.7 kN/m²) crushing

Maximum Bending Moment = 61.24 in-lb
(691.8 cm-N) (limit)

Section Properties

Item	b	h	\bar{y}
1	1.4	0.016	0.008
2	0.016	0.664	0.340
3	0.25	0.016	0.680



(Effective section 100th flight)

Note initial overall height with

$t_{stock} = 0.02$ in. (0.05 cm) is
0.70 in. (1.78 cm)

Material is coated Cb-752.

$$A = 0.037 \text{ in}^2 (0.239 \text{ cm}^2), \bar{y} = 0.176 \text{ inch} (0.447 \text{ cm}), I = 0.002323 \text{ in}^4 (0.0966 \text{ cm}^4)$$

Stress in Skin

$$f = \frac{M\bar{y}}{I} = \frac{(61.24)(0.176)}{0.002323} = -4640 \text{ psi } (-31.99 \text{ MN/m}^2)$$

$$F_{cr} = KE \frac{t^2}{b} \text{ [for simply supported edges, } K = 3.62; E \text{ Cb-752 at } 340^\circ \text{ F } (444^\circ \text{ K}) = 15.14 \times 10^6 \text{ (Figure 6-8)}]$$

$$= (3.62) (15.14 \times 10^6) \frac{0.016^2}{1.4} = 7158 \text{ psi } (49.4 \text{ MN/m}^2)$$

$$\therefore \text{ M. S. (skin buckling)} = \frac{7158}{(4640)(1.5)} - 1 = +0.028 \text{ (ULT)}$$

Stress in Flange

$$f = \frac{M(h-\bar{y})}{I} = \frac{61.24(0.68 - 0.176)}{0.002323} = 13,287 \text{ psi } (91.6 \text{ MN/m}^2)$$

For Cb-752 at 340° F (444° K)

$$F_{tu} = 54,860 \text{ psi } (378.3 \text{ MN/m}^2)$$

$$\therefore \text{ M. S. } = \frac{54,860}{(13,287)(1.5)} - 1 = +1.75 \text{ (ULT)}$$

Web Shear Analysis

Maximum Shear (S) = R = 22.68 lb (100.9 N)

$$f_s = \frac{S}{ht} = \frac{22.68}{(0.66)(0.016)} = 2147 \text{ psi (14.8 MN/m}^2\text{) (limit)}$$

Critical Buckling Stress ($F_{s_{cr}}$)

$$\begin{aligned} F_{s_{cr}} &= KE \left(\frac{t}{b} \right)^2 \text{ (for simply supported edges, } K = 4.84) \\ &= (4.84)(15.14 \times 10^6) \left(\frac{0.016}{0.66} \right)^2 = 43,064 \text{ psi (296.5 MN/m}^2\text{)} \end{aligned}$$

$$\therefore \text{M. S. (web buckling)} = \frac{43,064}{(2147)(1.5)} - 1 = + \text{ LARGE (ULT)}$$

Panel Deflection

Condition: $p = 3.0 \text{ psi (20.7 kN/m}^2\text{) crushing; Temperature} = 340^\circ \text{ F}$

Maximum bending deflection at midspan

$$\begin{aligned} \delta &= \frac{5}{384} \frac{wL^4}{EI} = \frac{5(4.2)(10.8^4)}{(384)(15.14 \times 10^6)(0.002323)} ; E \text{ (Cb-752 at } 340^\circ \text{ F)} \\ &= 15.14 \times 10^6 \text{ psi (Figure 6-8)} \\ &= 0.021 \text{ inch (0.053 cm)} \end{aligned}$$

where

$$w = 4.2 \text{ lb/in (7.35 N/cm)}$$

$$I = 0.002323 \text{ in}^4 (0.0966 \text{ cm}^4)$$

$$\text{Allowable deflection} = 0.10 + 0.04 L \left(\frac{BS - 12}{110} \right); \text{ mean body station BS} = 79.5 \text{ inches (201.9 cm)}$$

$$= 0.10 + 0.04 (12) \left(\frac{79.5 - 12}{110} \right)$$

$$= 0.395 \text{ inch (1.003 cm)}$$

$$\therefore \text{M. S. (deflection)} = + \text{ LARGE}$$

Bending Analysis

Condition

Boost Phase: 2.0 psi (13.8 kN/m²) (burst)

This gives compression in outstanding flange.

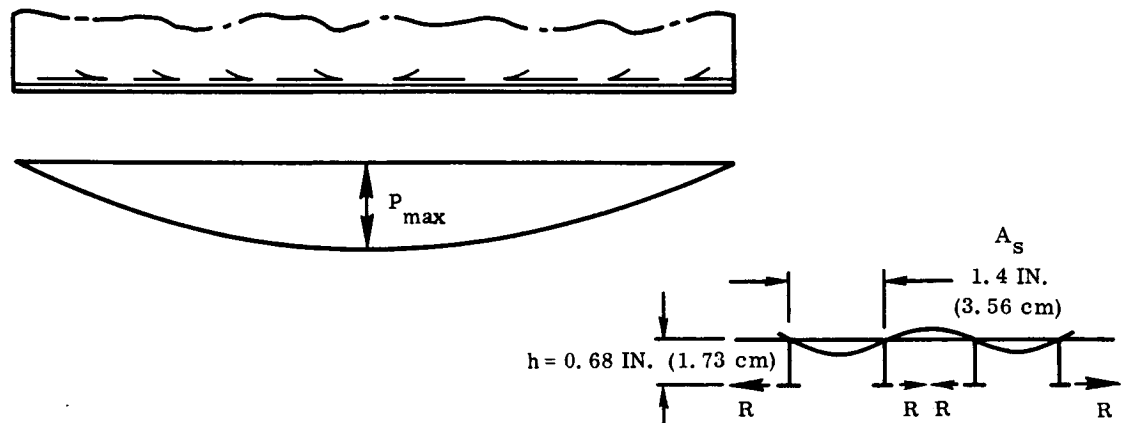
Stress in Flange

The flange stress is obtained by ratioing the stress for the 3.0 psi (20.7 kN/m²) crushing condition.

$$f = 13,287 \left(\frac{-2}{3} \right) = -8858 \text{ psi (61.1 MN/m}^2\text{)}$$

Flange Critical Buckling Stress

The flange is subjected to a distributed axial load, due to bending, as shown; the effective pin ended length is determined considering the lateral support provided by bending of the web and skin as an elastic support (Reference 29).



Lateral deflection of flange due to side load, R , lb/in

$$\delta = \frac{Rh^3}{3D_w} + \frac{Rh^2 A_s}{4D_s} = \frac{0.68^3}{(3)(5.68)} + \frac{(0.68^2)(1.4)}{(4)(5.68)} = 0.0469 \text{ in/lb (0.027 cm/N)}$$

for a unit length

where

$$D_w = D_s = \frac{Et^3}{12(1-\nu^2)} = \frac{(15.14 \times 10^6)(0.016^3)}{(12)(0.91)} = 5.68 \text{ in-lb (64.2 cm-N)}$$

(D_w and D_s = bending rigidities of web and skin)

The modulus of the equivalent elastic foundation

$$B = \frac{1}{\delta} = \frac{1}{0.0469} = 21.3 \text{ lb/in (37.3 N/cm)}$$

$$I_{zz} = [(0.016)(0.25^3)] / 12$$

$$= 2.083 \times 10^{-5} \text{ in}^4 (86.65 \times 10^{-5} \text{ cm}^4)$$

$$\frac{BI^4}{16 EI} = \frac{(21.3)(11^4)}{16(15.14 \times 10^6)(2.083 \times 10^{-5})} = 61.8$$

$$\therefore L = 0.317(l) = 3.49 \text{ inches (8.86 cm)}$$

$$A_2 = 0.005867 \text{ in}^2 (0.038 \text{ cm}^2) \text{ (Portion of web = } h/6 \text{ is included in area)}$$

$$\text{Radius of gyration} = \sqrt{I/A} = 0.0596 \text{ inch (0.151 cm)}$$

$$\therefore F_{cr} = \pi^2 \eta E \left(\frac{k}{L} \right)^2$$

$$= \pi^2 \eta (15.14 \times 10^6) \left(\frac{0.0596}{3.49} \right)^2 = 43,580 \eta \text{ psi (300.5 MN/m}^2\text{)}$$

$$\text{M. S. (lateral buckling)} = \frac{43,580}{(8858)(1.5)} - 1 = \text{LARGE}$$

Flange Crippling (Reference 30)

$$\sqrt{\frac{F_{cy}}{E}} \frac{b}{t} = \sqrt{\frac{43,050}{15.14 \times 10^6}} \left(\frac{0.125}{0.016} \right) = 0.417$$

$$\therefore \text{Use cutoff} = 1.1 F_{cy} = (1.1)(43,050) = 47,400 \text{ psi (326.8 MN/m}^2\text{)}$$

$$\therefore \text{Stress in flange} = -8858 \text{ psi (-61.1 MN/m}^2\text{) (limit)}$$

$$\therefore \text{M. S. (crippling)} = \frac{47,400}{(8858)(1.5)} - 1 = +2.57 \text{ (ULT)}$$

Thermal Stress Analysis - Boost Phase

Maximum temperature gradient during boost occurs at time = 440 seconds. (See Figure 6-37.)

Maximum Temperature = 760° F (677° K)

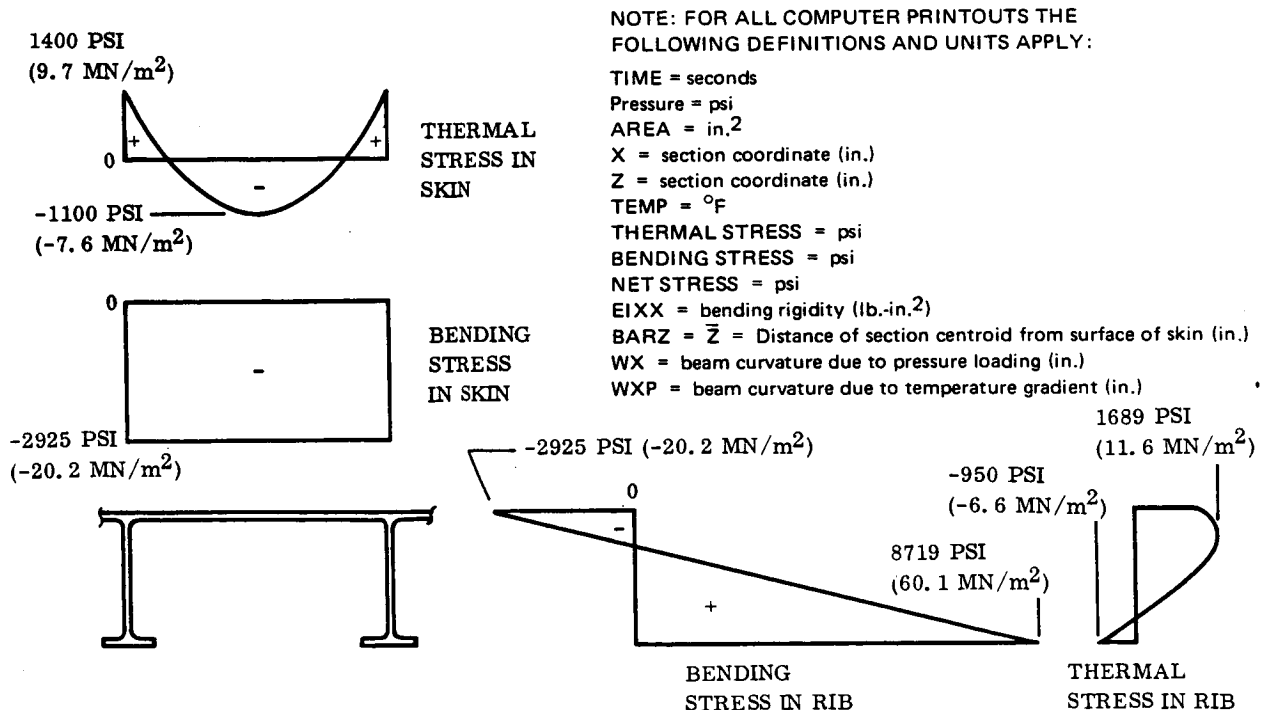
$\Delta T = 159^\circ \text{ F } (88^\circ \text{ K})$

Normal Pressure = 2.0 psi (13.8 kN/m²) crushing (see Figure 5-1.)

TEE-STIFFENED PANEL MATERIAL CR-752

	AREA	X	Z	TEMP	THERMAL STRESS	BENDING STRESS	NET STRESS
1	2.214E-03	6.308E-01	8.000E-03	7.600E+02	-1.133E+03	-2.925E+03	-4.013E+03
2	2.214E-03	4.924E-01	8.000E-03	7.575E+02	-9.394E+02	-2.926E+03	-3.865E+03
3	2.214E-03	3.540E-01	8.000E-03	7.515E+02	-5.701E+02	-2.927E+03	-3.497E+03
4	2.214E-03	2.156E-01	8.000E-03	7.420E+02	1.451E+01	-2.930E+03	-2.915E+03
5	2.214E-03	7.720E-02	8.000E-03	7.290E+02	8.148E+02	-2.933E+03	-2.118E+03
6	1.120E-03	4.000E-03	7.000E-02	7.013E+02	1.566E+03	-1.810E+03	-2.274E+02
7	1.120E-03	4.000E-03	2.100E-01	6.695E+02	1.699E+03	4.829E+02	2.172E+03
8	1.120E-03	4.000E-03	3.500E-01	6.440E+02	1.315E+03	2.857E+03	4.182E+03
9	1.120E-03	4.000E-03	4.900E-01	6.240E+02	5.384E+02	5.258E+03	5.857E+03
10	1.120E-03	4.000E-03	6.300E-01	6.080E+02	-3.585E+02	7.656E+03	7.287E+03
11	9.360E-04	3.725E-02	6.920E-01	6.020E+02	-8.644E+02	8.718E+03	7.854E+03
12	9.360E-04	9.575E-02	6.920E-01	6.010E+02	-8.037E+02	8.719E+03	7.916E+03
EIXX = 3.5487E+04 BARZ = 1.8157E-01							
WX = 1.1504E-03					WXP = -9.3515E-04		

The beam model and section geometry are as shown on Pages 204 and 205.



Maximum Compression Stress in Skin

$$= f_t + f_M = -1100 - 2925 = -4025 \text{ psi (27.8 MN/m}^2\text{) (limit)}$$

Skin Critical Buckling Stress

$$\begin{aligned} F_{cr} &= K E \left(\frac{t}{b}\right)^2 \\ &= 3.62 (14.65 \times 10^6) \left(\frac{0.016}{1.4}\right)^2 = 6927 \text{ psi (47.8 MN/m}^2\text{)} \end{aligned}$$

where

$$E = 14.65 \times 10^6 \text{ psi (101.0 GN/m}^2\text{) for Cb-752 at 760° F (677° K)}$$

$$M. S. = \frac{F_{cr}}{f_t + 1.5 f_M} - 1 = \frac{6927}{(1.0) 1100 + 1.5 (2925)} - 1 = +0.26 \text{ (ULT)}$$

Maximum Tension Stress in Flange

$$= 8719 - 950 = 7769 \text{ psi (53.6 MN/m}^2\text{)}$$

$$F_{tu} \text{ Cb-752 at 602° F (588° K) = 48,200 psi (332.3 MN/m}^2\text{)}$$

$$M. S. = + \text{LARGE}$$

Deflection Analysis — Boost Phase

Outward deflection due to temperature gradient.

$$\text{Curvature } \frac{1}{R} = WXP = -9.3513 \times 10^{-4} \text{ (Page 209)}$$

$$\therefore \delta_{\max} = \frac{L^2}{8R} = \frac{10.8^2}{8} (-9.3513 \times 10^{-4})$$

$$= -0.0136 \text{ inch (-0.0345 cm) (outward)}$$

Inward deflection due to normal press (2.0 psi) (13.8 kN/m²)

$$\delta_{\max} = \frac{5 W L^3}{384 EI} = \frac{5 (2.0) (1.4) (10.8) (10.8^3)}{384 (3.5487 \times 10^4)}$$

$$= 0.014 \text{ inch (0.0355 cm) (inboard)}$$

where

$$EI = 3.5487 \times 10^{-4} \text{ (Page 209)}$$

$$\therefore \text{Net deflection} = 0.014 - 0.0136 = 0.0004 \text{ inch (0.001 cm)}$$

$$\text{Allowable deflection} = 0.10 + 0.04 L \left(\frac{BS - 12}{110} \right) = 0.395 \text{ inch (1.003 cm)}$$

$$\therefore \text{M.S. (deflection)} = + \text{LARGE}$$

Thermal Stress Analysis: Reentry

Condition: Maximum temperature gradient

Reentry time = 140 seconds (see Figure 6-39)

Maximum temperature = 785° F (691° K)

$\Delta T = 252^\circ \text{ F (140° K)}$

Normal pressure = 0.15 psi (1.03 kN/m²)

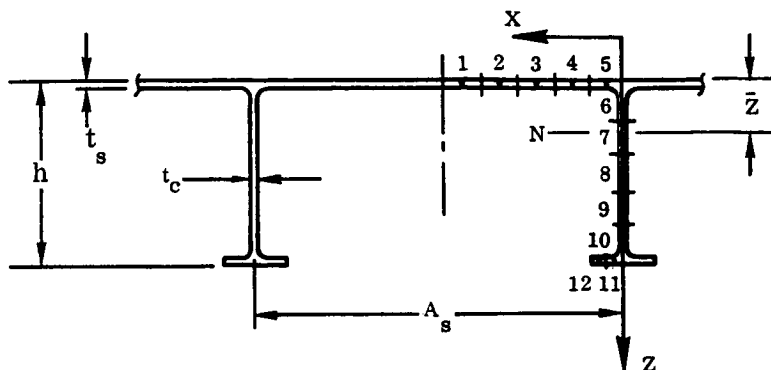
TEE-STIFFENED PANEL MATERIAL CB-752

TIME = 1.4000E+02 PFESSURE = 1.5000E-01

	AREA	X	Z	TEMP	THERMAL STRESS	BENDING STRESS	NET STRESS
1	2.214E-03	6.308E-01	8.000E-03	7.850E+02	-1.709E+03	-2.191E+02	-1.928E+03
2	2.214E-03	4.924E-01	8.000E-03	7.800E+02	-1.401E+03	-2.192E+02	-1.620E+03
3	2.214E-03	3.540E-01	8.000E-03	7.720E+02	-9.077E+02	-2.194E+02	-1.127E+03
4	2.214E-03	2.156E-01	8.000E-03	7.580E+02	-4.499E+01	-2.196E+02	-2.646E+02
5	2.214E-03	7.720E-02	8.000E-03	7.370E+02	1.249E+03	-2.200E+02	1.029E+03
6	1.120E-03	4.080E-03	7.000E-02	6.930E+02	2.624E+03	-1.422E+02	2.482E+03
7	1.120E-03	4.000E-03	2.100E-01	6.440E+02	2.607E+03	3.541E+01	2.642E+03
8	1.120E-03	4.000E-03	3.500E-01	6.020E+02	2.137E+03	2.144E+02	2.351E+03
9	1.120E-03	4.000E-03	4.900E-01	5.680E+02	1.123E+03	3.942E+02	1.518E+03
10	1.120E-03	4.000E-03	6.300E-01	5.470E+02	-6.777E+02	5.743E+02	-1.034E+02
11	9.360E-04	3.725E-02	6.920E-01	5.380E+02	-1.496E+03	6.542E+02	-8.414E+02
12	9.360E-04	9.575E-02	6.920E-01	5.330E+02	-1.193E+03	6.544E+02	-5.441E+02

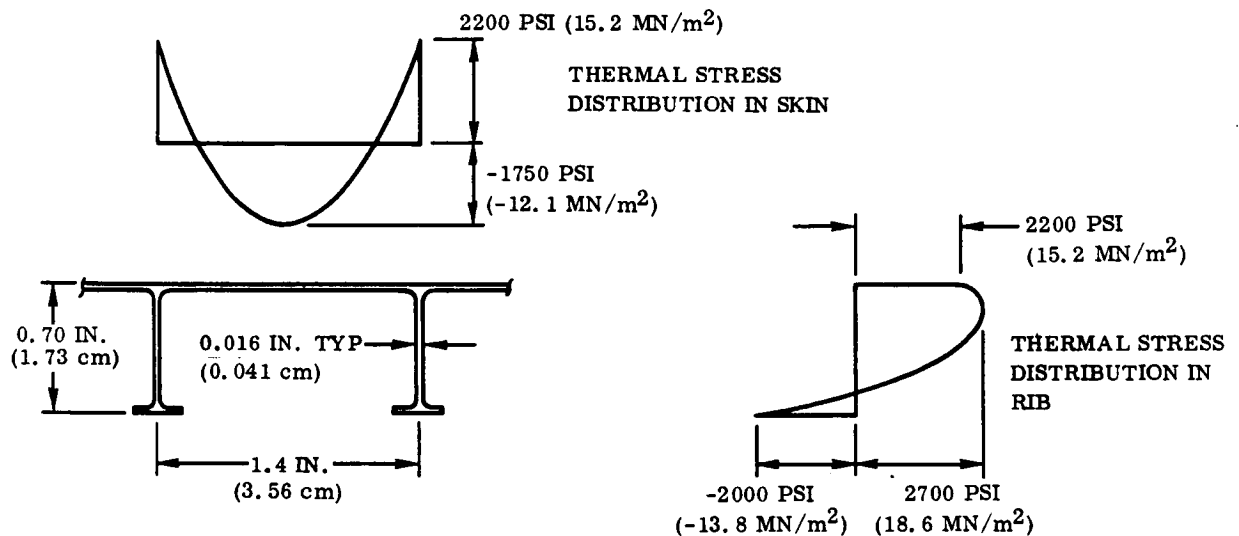
FIXY = 3.5581E+04 BARZ = 1.8219E-01
WXP = -1.4639E-03 WX = 8.6050E-05

Section Geometry



Note:

The analysis is made for half of the symmetrical section.



Total Stress in Skin

$$f_{\max} = f_{\text{thermal}} + f_{\text{pressure}}$$

$$= -1750 - 219 = -1969.0 \text{ psi } (-36.6 \text{ MN/m}^2)$$

Critical Buckling Stress

$$F_{\text{cr}} = KE \left(\frac{t}{b} \right)^2 = (3.62) (14.62 \times 10^6) \left(\frac{0.016}{1.4} \right)^2$$

$$= 6912 \text{ psi } (47.7 \text{ MN/m}^2)$$

where

$$E (\text{Cb-752}) = 14.26 \times 10^6 \text{ psi } (98.3 \text{ GN/m}^2), \text{ temperature} = 785^\circ \text{F } (691^\circ \text{K})$$

$$M. S. \text{ (skin buckling)} = \frac{6912}{1750 + 1.5 (219)} - 1 = +2.3 \text{ (ULT)}$$

Maximum tension stress occurs in tee web.

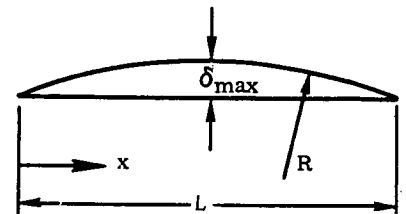
$$f_{\max} = 2700 \text{ psi (18.6 MN/m}^2\text{)}$$

$$F_{tu} \text{ Cb-752 at } 693^\circ \text{ F (540}^\circ \text{ K)} = 45,210 \text{ psi (311.7 MN/m}^2\text{)}$$

$$\therefore M. S. \text{ (tension)} = \frac{45,210}{(2700)(1.5)} - 1 = +10.2 \text{ (ULT)}$$

Panel Deflection

Assuming the temperature distribution is uniform along the length of the panel, then the panel deflects outward with a constant curvature $= 1/R$.



Hence from $d^2y/dx^2 = -1/R$, the maximum deflection at $x = L/2$ is given by:

$$\delta_{\max} = \frac{L^2}{8R} = \frac{10.8^2}{8} (1.464 \times 10^{-3}) = 0.021 \text{ inch (0.0533 cm)}$$

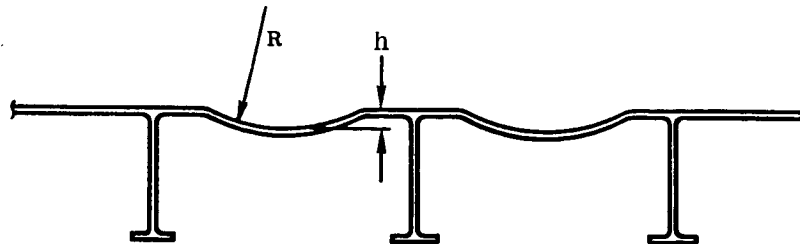
Note $1/R = WXP = 1.464 \times 10^{-3}$ (see Page 211).

$$\begin{aligned} \text{Allowable deflection} &= 0.1 + 0.04 L \left(\frac{BS - 12}{110} \right) \\ &= 0.1 + (0.04)(12) \left(\frac{79.5 - 12}{110} \right) = 0.395 \text{ inch (1.003 cm)} \end{aligned}$$

$$\therefore M. S. \text{ (deflection)} = + \text{ LARGE}$$

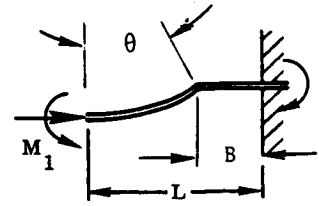
Note: The inward deflection due to the pressure loading [$p = 0.02 \text{ psi (137.9 N/m}^2\text{)}$] is conservatively neglected.

Transverse Thermal Stresses in Panel Skin



The differential thermal expansion between the skin and the relatively cool support beams gives rise to transverse axial and bending loads in the beaded skin.

The maximum temperature gradient during reentry at time = 140 seconds is given in Figure 6-43.



Maximum skin temperature = 783° F (690° K)

Average temperature in support beams = 450° F (505° K)

$$\therefore \Delta T = 783 - 450 = 333^\circ \text{ F } (185^\circ \text{ K})$$

The axial load (P) and bending moment (M) are derived using the method given in pages 228 through 230.

$$\theta = A \cos \left(\frac{R-h}{R} \right)$$

$$= 0.224 \text{ radians}$$

$$B = L - R \sin (\theta)$$

$$= 0.255 \text{ inch } (0.648 \text{ cm})$$

$$EI = \frac{(14.7 \times 10^6)(0.018^3)}{12.0} = 7.144 \text{ lb-in}^2 \text{ (205.01 N-cm}^2\text{)}$$

where 0.018 inch = initial thickness after coating, zero cycles.

$$\alpha_{11} = \frac{R^3}{EI} \left(\frac{3\theta}{2} - 2 \sin \theta + \frac{\sin \theta + \sin \theta \cos \theta}{2} \right) + \frac{h^2 B}{EI} = 1.2067 \times 10^{-4}$$

$$\alpha_{12} = \frac{R^2}{EI} (\theta - \sin \theta) + \frac{hB}{EI} = 2.832 \times 10^{-3}$$

$$\alpha_{22} = \frac{R\theta}{EI} + \frac{B}{EI} = 9.842 \times 10^{-2}$$

$$M = - \frac{P \alpha_{12}}{\alpha_{22}} = - 2.8774 \times 10^{-2} (P)$$

$$P \alpha_{11} + M \alpha_{12} = L \alpha \Delta T$$

$$P = \frac{L \alpha \Delta T}{(\alpha_{11} - 0.028774 \alpha_{12})} = 2.552 \times 10^4 (L \alpha \Delta T)$$

$$= 2.552 \times 10^4 (0.7) (4.0 \times 10^{-6}) (333) = 23.8 \text{ lb/in (41.67 N/cm)}$$

$$M = -2.8774 \times 10^{-12} (P) = -0.685 \text{ in-lb (-7.74 cm-N)}$$

$$\text{Stress in skin} = -\frac{P}{A} \pm \frac{Mc}{I} = -\frac{23.8}{0.018} \pm \frac{(6)(0.685)}{0.018^2} = 14,000 \text{ psi (96.5 MN/m}^2\text{)}$$

$$F_{tu} \text{ Cb-752 at } 780^\circ \text{ F (689}^\circ \text{ K)} = 44,500 \text{ psi (306.8 MN/m}^2\text{)}$$

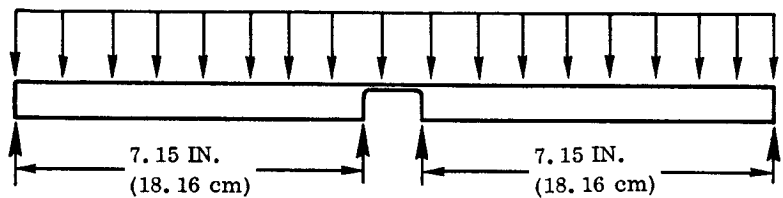
\therefore M. S. = + LARGE

6.4.3.2 Integral support beams

Condition: Boost Phase

Crushing Pressure =

$$3.0 \text{ psi (20.7 kN/m}^2\text{)}$$

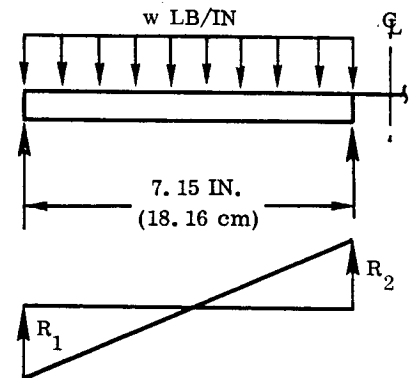


Beam is notched as shown at center support and hence is treated as two simply supported spans.

$$\text{Running load (w)} = p \frac{b}{2} = (3.0) \left(\frac{12}{2} \right) = 18 \text{ lb/in (31.5 N/cm)}$$

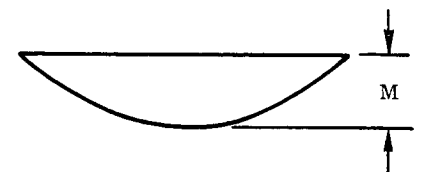
Reactions

$$R_1 = R_2 = \frac{w L}{2} = \frac{(18)(7.15)}{2} = 64.35 \text{ lb (286.23 N)}$$



Bending Moment

$$M = \frac{w L^2}{8} = \frac{(18)(7.15^2)}{8} = 115.0 \text{ in-lb (1299.3 cm-N)}$$



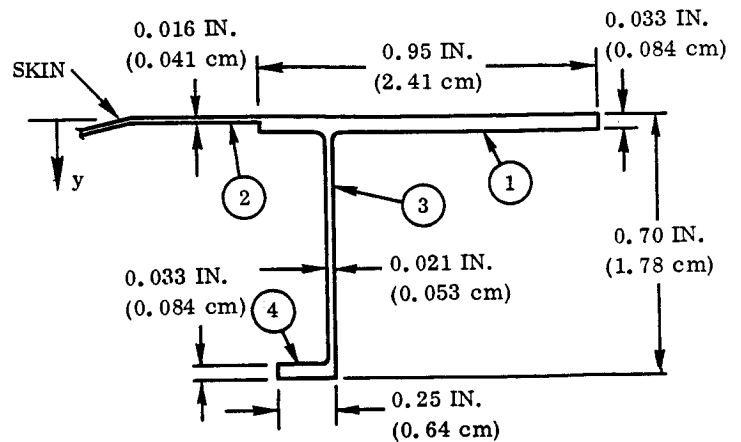
Section Properties

Item	b	h	y
1	0.95	0.033	0.0165
2	0.25	0.016	0.008
3	0.021	0.634	0.35
4	0.250	0.033	0.6835

$$\Sigma A = 0.057 \text{ in}^2 (0.368 \text{ cm}^2)$$

$$\bar{y} = 0.1898 \text{ in. } (0.482 \text{ cm})$$

$$I = 0.0039 \text{ in}^4 (0.162 \text{ cm}^4)$$



ASSUMED EFFECTIVE SECTION AFTER
100 FLIGHTS FOR -3 AND -5 BEAMS

Upper Flange

$$f_c = \frac{M\bar{y}}{I} = \frac{(115)(0.1898)}{0.0039} = 5597 \text{ psi } (38.6 \text{ MN/m}^2)$$

Critical Buckling Stress

$$F_{cr} = KE \left(\frac{t}{b} \right)^2$$

$$= (0.385)(15.14 \times 10^6) \left(\frac{0.033}{0.7} \right)^2 = 12,954 \text{ psi } (89.3 \text{ MN/m}^2)$$

where

$$K = 0.385 \text{ (One edge free, one edge and ends simply supported)}$$

$$E = 15.14 \times 10^6 \text{ psi } (104.4 \text{ GN/m}^2)$$

$$\text{M. S.} = \frac{12,954}{(5597)(1.5)} - 1 = +0.54 \text{ (ULT)}$$

Lower Flange

$$f_t = \frac{M(h - \bar{y})}{I} = \frac{(115)(0.7 - 0.1898)}{0.0039} = 15,044 \text{ psi } (103.7 \text{ MN/m}^2)$$

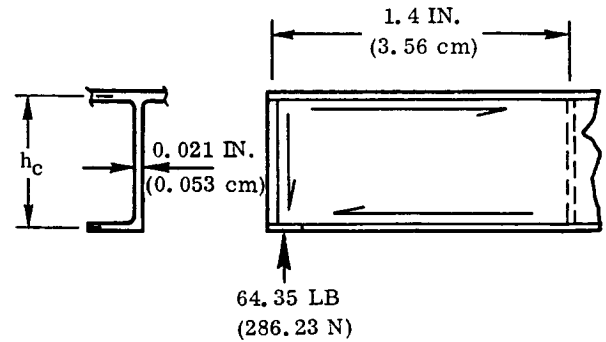
$$F_{tu} [\text{Cb-752 at } 340^\circ \text{ F } (444^\circ \text{ K})] = 54,860 \text{ psi } (378.3 \text{ MN/m}^2)$$

$$\text{M. S.} = \frac{54,860}{(15,044)(1.5)} - 1 = +1.43 \text{ (ULT)}$$

Web Shear Analysis

$$f_s = \frac{R_1}{h_c t} = \frac{64.35}{(0.70 - 0.033)(0.021)}$$

$$= 4594 \text{ psi (31.7 MN/m}^2\text{)}$$



Critical Buckling Stress

$$F_{scr} = K \eta E \left(\frac{t}{h} \right)^2$$

$$= 5.8 \eta 15.14 \times 10^6 \left(\frac{0.021}{0.667} \right)^2$$

$$= 87,044 \eta \text{ psi (600.2 } \eta \text{ MN/m}^2\text{)}$$

For simply supported edges

$$b/a = \frac{0.667}{1.4} = 4.77$$

$$K = 5.8$$

∴ M.S. = + LARGE

Thermal Stress Analysis: Reentry

EDGE MEMBER -TEE- STIFFENED PANEL CB-752

TIME = 1.4000E+02

PRESSURE = 0.

	AREA	X	Z	TEMP	THERMAL STRESS	BENDING STRESS	NET STRESS
1	3.850E-03	-6.522E-01	1.650E-02	5.980E+02	-1.206E+03	0.	-1.206E+03
2	3.850E-03	-5.355E-01	1.650E-02	5.950E+02	-1.027E+03	0.	-1.027E+03
3	3.850E-03	-4.188E-01	1.650E-02	5.890E+02	-6.696E+02	0.	-6.696E+02
4	3.850E-03	-3.022E-01	1.650E-02	5.820E+02	-2.525E+02	0.	-2.525E+02
5	3.850E-03	-1.855E-01	1.650E-02	5.770E+02	4.545E+01	0.	4.545E+01
6	3.850E-03	-6.883E-02	1.650E-02	5.670E+02	6.415E+02	0.	6.415E+02
7	3.778E-03	6.775E-02	1.650E-02	5.680E+02	5.819E+02	0.	5.819E+02
8	3.778E-03	1.822E-01	1.650E-02	5.770E+02	4.545E+01	0.	4.545E+01
9	5.000E-04	3.020E-01	8.000E-03	6.000E+02	-1.154E+03	0.	-1.154E+03
10	5.000E-04	4.270E-01	8.000E-03	6.320E+02	-3.097E+03	0.	-3.097E+03
11	5.000E-04	5.520E-01	8.000E-03	6.550E+02	-4.493E+03	0.	-4.493E+03
12	5.000E-04	6.770E-01	8.000E-03	6.710E+02	-5.465E+03	0.	-5.465E+03
13	2.450E-03	0.	5.833E-02	5.300E+02	2.003E+03	0.	2.003E+03
14	2.450E-03	0.	1.750E-01	4.820E+02	2.501E+03	0.	2.501E+03
15	2.450E-03	0.	2.917E-01	4.460E+02	2.274E+03	0.	2.274E+03
16	2.450E-03	0.	4.083E-01	4.180E+02	1.563E+03	0.	1.563E+03
17	2.450E-03	0.	5.250E-01	3.950E+02	5.527E+02	0.	5.527E+02
18	2.450E-03	0.	6.417E-01	3.760E+02	-6.923E+02	0.	-6.923E+02
19	4.122E-03	6.775E-02	6.820E-01	3.650E+02	-8.600E+02	0.	-8.600E+02
20	4.122E-03	1.822E-01	6.820E-01	3.600E+02	-5.613E+02	0.	-5.613E+02

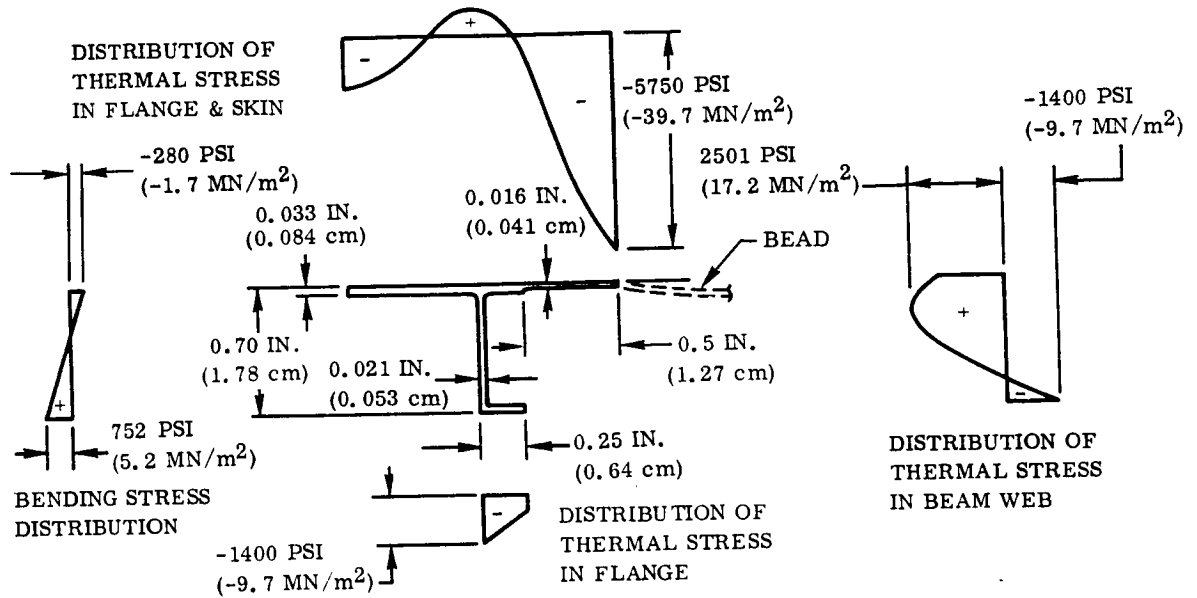
EIXX = 5.9124E+04 BARZ = 2.0477E-01
WXP = -1.3554E-03 WX = 0.

Maximum temperature gradient occurs at time = 140 seconds. (See Figure 6-42.)

Maximum temperature = 671° F (628° K)

$\Delta T = 311^\circ \text{F}$ (428° K)

Normal pressure = 0.15 psi (1.03 kN/m²)



Bending stresses due to pressure loading [$\Delta P = 0.15$ psi (1.03 kN/m²)] are obtained by factoring values for $\Delta P = 3.0$ psi (20.7 kN/m²) (Page 216).

Maximum stress in skin = $-5750 - 280 = -6030$ psi (-41.6 MN/m²)

Skin Critical Buckling Stress

$$F_{cr} = K \eta E \left(\frac{t}{b} \right)^2$$

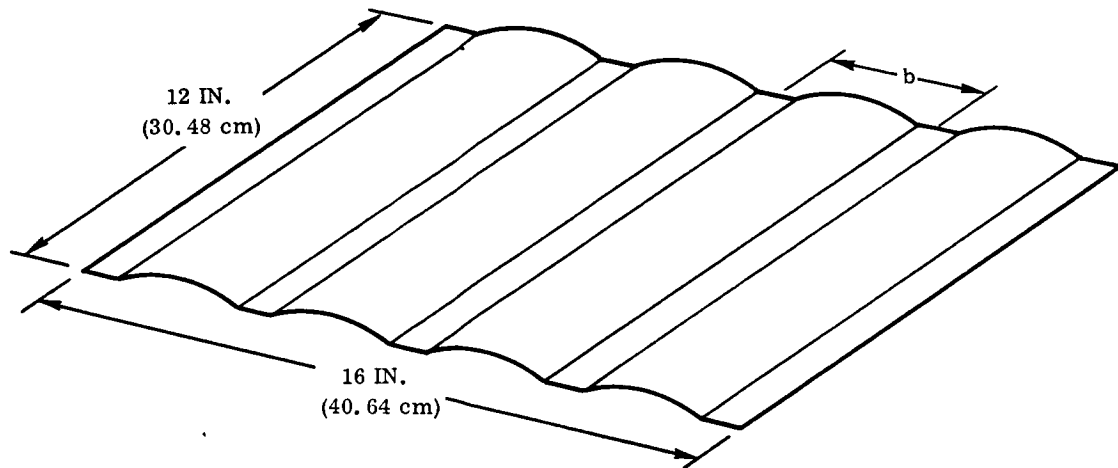
$$= (3.62) \eta (14.76 \times 10^6) \left(\frac{0.016}{0.5} \right)^2$$

$$= 54,713 \eta \text{ psi } (377.2 \eta \text{ MN/m}^2)$$

\therefore M.S. = + LARGE

Assuming skin is simply supported at junction of bead runout; i. e., $K = 3.62$, and E (Cb-752) at 670° F (627° K) = 14.76×10^6 psi (101.77 GN/m²).

6.4.4 Corrugated panel assembly. -



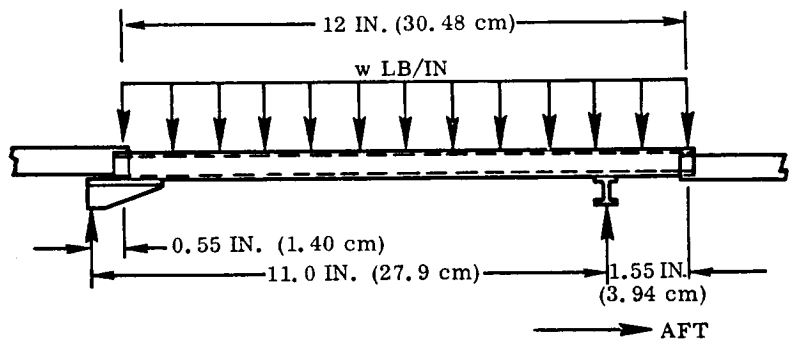
6.4.4.1 Corrugated panel - drawing 76Z0768:

Overall Bending Analysis

Condition: Boost Phase, $p = 3.0$ psi (20.7 kN/m²) crushing

Running Load Per Corrugation

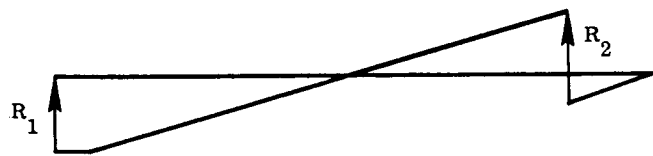
$$\begin{aligned} w &= pb = (3.0)(3.8) \\ &= 11.4 \text{ lb/in} \\ &\quad (19.96 \text{ N/cm}) \end{aligned}$$



Reactions

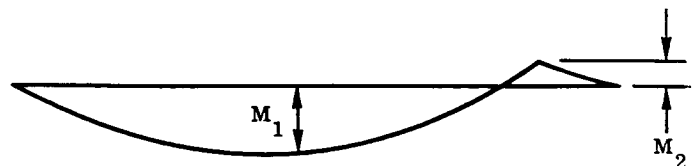
$$\begin{aligned} R_2 &= \frac{w L (L/2 + 0.55)}{11.0} \\ &= \frac{(11.4)(12)(6.55)}{11} = 81.46 \text{ pounds (362.33 N) (Limit)} \end{aligned}$$

$$R_1 = w L - R_2 = (11.4)(12) - 81.46 = 55.34 \text{ pounds (246.15 N) (Limit)}$$



Bending Moments

Maximum negative bending moment (M_1) occurs at $x = R_1/w + 0.55 = 5.40$ inches (13.72 cm)



Overall Section

Item	A	y	Ay	Ay ²	I _O
1	0.0562	0.3311	0.01861	0.00616	0.00126
2	0.0119	0.0	0.0	—	—
Total	0.0681		0.01861	0.00616	0.00126

$$\bar{y} = \frac{0.01861}{0.0681} = 0.2733 \text{ inch (0.694 cm)}$$

$$I_{N-N} = 0.00616 + 0.00126 - [(0.01861)(0.2733)] = 0.002326 \text{ in}^4 (0.0967 \text{ cm}^4)$$

Maximum Compression Stress in Circular Arc

$$f_c = \frac{M(h - \bar{y})}{I} = \frac{164.76(0.5 - 0.273)}{0.002326} = 16,058 \text{ psi (101.7 MN/m}^2\text{)}$$

Critical Buckling Stress

$$F_{cr} = KE \frac{t}{R} = 0.3 (15.14 \times 10^6) \frac{0.017}{2.6495} = 29,143 \text{ psi (200.9 MN/m}^2\text{)}$$

$$\therefore \text{M.S.} = \frac{29,143}{(16,058) 1.5} - 1 = +0.210 \text{ (ULT)}$$

Maximum Tension Stress in Flange

$$f_t = \frac{M\bar{y}}{I} = \frac{(164.76)(0.273)}{0.002326} = 19,359 \text{ psi (133.5 MN/m}^2\text{)}$$

$$F_{tu} = [\text{Cb-752 at } 340^\circ \text{ F (444}^\circ \text{ K)}] = 54,860 \text{ psi (378.3 MN/m}^2\text{)}$$

$$\therefore \text{M.S.} = \frac{54,860}{(19,359)(1.5)} - 1 = +0.89 \text{ (ULT)}$$

Condition: 2.0 psi (13.8 kN/m²) burst

The ultimate loads for this condition are equal to the limit loads for the 3.0 psi (20.7 kN/m²) crushing condition with signs reversed.

$$M_1 = R_1 x - \frac{w(x - 0.55)^2}{2}$$

$$= (55.34)(5.4) - \frac{11.4(5.4 - 0.55)^2}{2} = 164.76 \text{ in-lb (1861.5 cm-N) (Limit)}$$

$$M_2 = \frac{w \times 1.55^2}{2} = 13.70 \text{ in-lb (154.78 cm-N) (Limit)}$$

Maximum bending moment = -164.76 in-lb (-1861.5 cm-N) (Limit)

Section Properties

Circular Arc Segment

$$\alpha = 35.778^\circ = 0.6244 \text{ radians}$$

$$R_M = 2.66 - \frac{0.021}{2}$$

$$= 2.6495 \text{ inch (6.7297 cm)}$$

$$\text{Area} = 2\alpha R_M t_e$$

$$= 2(0.6244)(2.6495)(0.017)$$

$$= 0.05625 \text{ in}^2 (0.363 \text{ cm}^2)$$

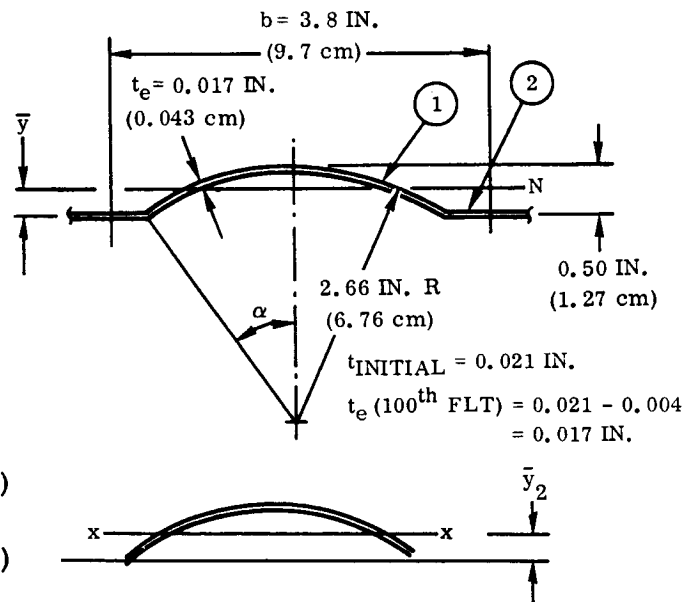
$$I_{x-x} = R_M^3 t_e \left(\alpha + \sin \alpha \cos \alpha - \frac{2 \sin^2 \alpha}{\alpha} \right)$$

$$= (2.6496^3)(0.017) \left(0.623 + \sin(0.624) \cos(0.624) - \frac{2 \sin^2(0.624)}{0.624} \right)$$

$$= 0.0012618 \text{ in}^4 (0.053 \text{ cm}^4)$$

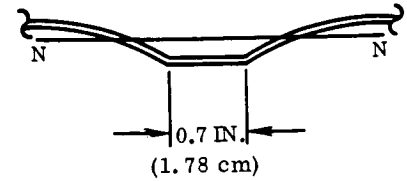
$$\bar{y}_2 = R_M \left(\frac{\sin \alpha}{\alpha} - \cos \alpha \right) = 2.6495 \left(\frac{\sin(0.624)}{0.624} - \cos(0.624) \right)$$

$$= 0.331 \text{ in. (0.841 cm)}$$



Maximum Compression Stress in Flange

$$f_{c(ult)} = 19,359 \text{ psi } (133.5 \text{ MN/m}^2)$$



Flange Critical Buckling Stress

$$F_{cr} = K E \left(\frac{t}{b} \right)^2 = (3.62) (15.14 \times 10^6) \left(\frac{0.017}{0.7} \right)^2 = 32,325 \text{ psi } (222.9 \text{ MN/m}^2)$$

$$\therefore \text{M.S.} = \frac{32,325}{19,359} - 1 = +0.67 \text{ (ULT)}$$

Panel Deflection Analysis

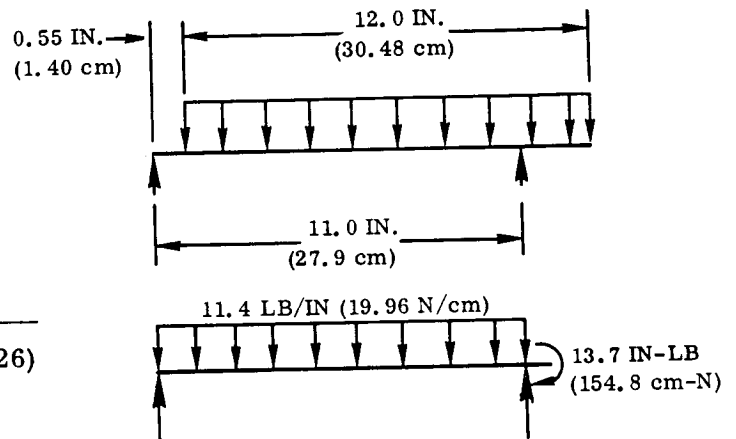
Deflection at Midspan

$$y = \frac{5 w l^4}{384 EI} - \frac{0.375 M_o l^2}{EI}$$

$$= \frac{(5) (11.4) (11^4)}{(384) (15.14 \times 10^6) (0.002326)}$$

$$- \frac{(0.375) (13.7) (11^2)}{(15.14 \times 10^6) (0.002326)}$$

$$= 0.0617 - 0.0177 = 0.044 \text{ inch } (0.112 \text{ cm})$$



$$\text{Allowable Deflection} = 0.10 + 0.04 L \left(\frac{BS - 12.0}{110} \right) = 0.395 \text{ inch } (1.003 \text{ cm})$$

$$\therefore \text{M.S.} = +(\text{LARGE})$$

Thermal Stress Analysis: Boost Phase

Maximum temperature gradient during boost occurs at time = 570 seconds

$$\text{Maximum temperature} = 1000^\circ \text{ F } (811^\circ \text{ K})$$

$$\Delta T = 12^\circ \text{ F } (262^\circ \text{ K})$$

$$\text{Normal pressure} = 2.0 \text{ psi } (13.8 \text{ kN/m}^2)$$

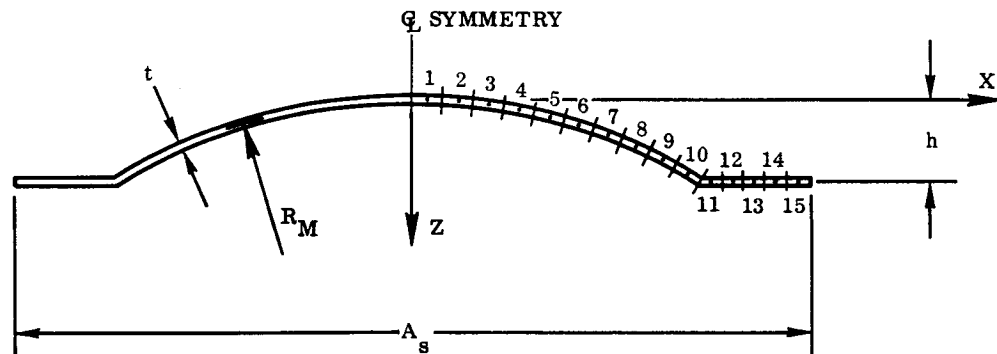
The beam model and section geometry are as shown in Figure 6-60.

CORRUGATED PANEL MATERIAL CR-752

TIME = 5.7000E+02 PRESSURE = 2.0000E+00

	AREA	X	Z	TEMP	THERMAL STRESS	BENDING STRESS	NET STRESS
1	2.813E-03	2.271E-02	1.291E-03	9.884E+02	6.118E+01	-1.062E+04	-1.056E+04
2	2.813E-03	2.478E-01	1.161E-02	9.888E+02	5.118E+01	-1.014E+04	-1.018E+04
3	2.813E-03	4.119E-01	3.222E-02	9.895E+02	3.718E+01	-9.163E+03	-9.126E+03
4	2.813E-03	5.745E-01	6.303E-02	9.905E+02	1.907E+01	-7.709E+03	-7.690E+03
5	2.813E-03	7.343E-01	1.139E-01	9.917E+02	2.726E+00	-5.779E+03	-5.776E+03
6	2.813E-03	8.922E-01	1.547E-01	9.934E+02	-3.023E+01	-3.392E+03	-3.412E+03
7	2.813E-03	1.046E+00	2.153E-01	9.955E+02	-7.403E+01	-5.262E+02	-6.012E+02
8	2.813E-03	1.196E+00	2.953E-01	9.980E+02	-1.290E+02	3.776E+03	2.647E+03
9	2.813E-03	1.341E+00	3.645E-01	1.000E+03	-1.594E+02	6.511E+03	6.352E+03
10	2.813E-03	1.481E+00	4.527E-01	1.000E+03	-3.191E+01	1.067E+04	1.064E+04
11	1.193E-03	1.584E+00	5.000E-01	9.995E+02	7.575E+01	1.290E+04	1.297E+04
12	1.193E-03	1.654E+00	5.000E-01	9.990E+02	1.060E+02	1.290E+04	1.300E+04
13	1.193E-03	1.725E+00	5.000E-01	9.987E+02	1.242E+02	1.290E+04	1.302E+04
14	1.193E-03	1.795E+00	5.000E-01	9.984E+02	1.424E+02	1.290E+04	1.304E+04
15	1.193E-03	1.865E+00	5.000E-01	9.983E+02	1.484E+02	1.290E+04	1.305E+04

FIXX = 3.3549E+04 DART = 2.2643E-01
WXP = 9.5597E-05 WX = 3.2740E-03



$$R_M = 2.6495 \text{ INCH (6.7297 cm)}$$

$$A_s = 3.80 \text{ INCH (9.65 cm)}$$

$$t = 0.017 \text{ INCH (0.043 cm)}$$

$$h = 0.50 \text{ INCH (1.27 cm)}$$

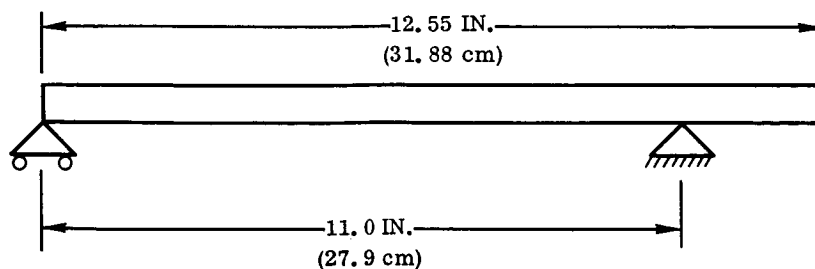


Figure 6-60. Beam Model and Typical Cross Section

The distributions of thermal and net stresses over the section are as shown.

Maximum compression stress in corrugation = -10,560 psi (-72.8 MN/m²) (Limit)

Critical buckling stress for circular arc segment.

[Cb-752 at 990° F (805° K), E = 14.41 × 10⁶ psi (99.4 GN/m²)]

$$F_{cr} = KE \frac{t}{R}$$

$$= (0.3) (14.41 \times 10^6) \left(\frac{0.017}{2.66} \right)$$

$$= 27,628 \text{ psi (190.5 MN/m}^2\text{)}$$

$$M.S. = \frac{27,628}{(10,560)(1.5)} - 1 = +0.74$$

Maximum tension stress

$$= 13,050 \text{ psi (89.9 MN/m}^2\text{)}$$

F_{tu} [Cb-752 at 1000° F (811° K)]

$$= 40,830 \text{ psi (281.5 MN/m}^2\text{)}$$

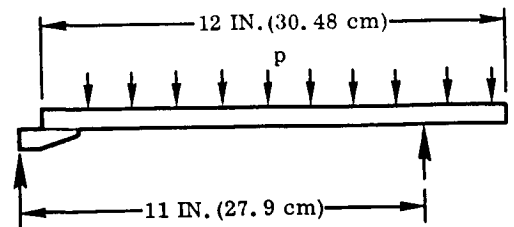
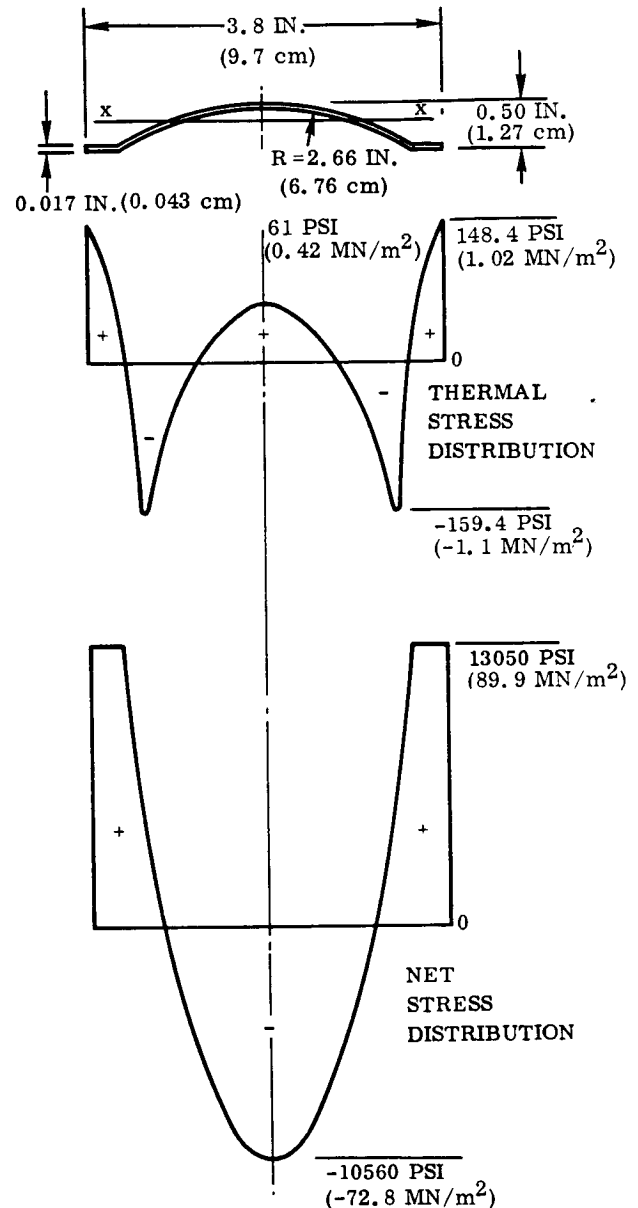
$$M.S. = \frac{40,830}{(13,050)(1.5)} - 1 = +1.08$$

Deflection Analysis

At time of maximum temperature gradient during boost (t = 570 seconds).

Outward deflection at midspan due to temperature gradient.

$$\text{Curvature} = 1/R = WXP = 9.5597 \times 10^{-5}$$



$$\delta_{\max} = \frac{L^2}{8R} = \frac{11.0^2}{8.0} (9.5597 \times 10^{-5}) = 0.00144 \text{ inch (0.00366 cm)}$$

Inward deflection due to normal pressure [2 psi (13.8 kN/m²)](neglecting relief from overhang)

$$\delta_{\max} = \frac{5wL^3}{384EI} = \frac{(5)(7.6)(11^3)}{(384)(3.3549 \times 10^4)} = 0.0039 \text{ inch (w=3.8 (p) = 7.6 lb/in) (13.3 N/cm)}$$

Net deflection = 0.0039 - 0.00144 = 0.00246 inch (0.00625 cm) (inward)

Allowable deflection = 0.395 inch (1.003 cm) (see Page 222)

Thermal Stress Analysis: Reentry

Maximum temperature gradient during reentry occurs at time = 450 seconds. (See Figure 6-50.)

Maximum temperature = 2438° F (1609° K)

$\Delta T = 40^\circ \text{ F (278}^\circ \text{ K)}$

Normal pressure = 0.15 psi (1.03 kN/m²)

CORRUGATED PANEL MATERIAL CB-752 AS=3.8, H=0.5, R=2.6495, TC=0.017

TIME = 4.5000E+02 PRESSURE = 1.5000E-01

	AREA	X	Y	TEMP	THERMAL STRESS	BENDING STRESS	NET STRESS
1	2.813E-03	8.271E-02	1.291E-03	2.398E+03	1.569E+02	-8.110E+02	-6.542E+02
2	2.813E-03	2.478E-01	1.161E-02	2.399E+03	1.377E+02	-7.720E+02	-6.344E+02
3	2.813E-03	4.119E-01	3.222E-02	2.401E+03	1.250E+02	-6.941E+02	-5.691E+02
4	2.813E-03	5.745E-01	6.333E-02	2.403E+03	1.001E+02	-5.775E+02	-4.774E+02
5	2.813E-03	7.348E-01	1.039E-01	2.407E+03	4.308E+01	-4.243E+02	-3.813E+02
6	2.813E-03	8.922E-01	1.547E-01	2.413E+03	-5.161E+01	-2.374E+02	-2.890E+02
7	2.813E-03	1.046E+00	2.153E-01	2.420E+03	-1.910E+02	-2.037E+01	-2.104E+02
8	2.813E-03	1.196E+00	2.953E-01	2.430E+03	-4.679E+02	2.208E+02	-2.471E+02
9	2.813E-03	1.341E+00	3.645E-01	2.438E+03	-5.943E+02	4.836E+02	-1.107E+02
10	2.813E-03	1.481E+00	4.527E-01	2.438E+03	-2.579E+02	7.819E+02	5.240E+02
11	1.193E-03	1.584E+00	5.000E-01	2.432E+03	1.908E+02	9.543E+02	1.145E+03
12	1.193E-03	1.654E+00	5.000E-01	2.420E+03	3.980E+02	9.635E+02	1.362E+03
13	1.193E-03	1.725E+00	5.000E-01	2.425E+03	5.294E+02	9.692E+02	1.439E+03
14	1.193E-03	1.795E+00	5.000E-01	2.424E+03	6.137E+02	9.724E+02	1.576E+03
15	1.193E-03	1.865E+00	5.000E-01	2.424E+03	6.303E+02	9.735E+02	1.604E+03

EJXX = 2.0130E+04 IAR7 = 2.2105E-01
WXP = 4.2244E-04 WY = 4.0924E-04

The beam model and section geometry are as shown in Figure 6-60.

The thermal and net stress distributions are as shown.

Maximum compression stress in corrugation = -654 psi (-4.5 MN/m²)

Critical buckling stress for circular arc segment.

[Cb-752 at 2400° F (1589° K), $E = 8.98 \times 10^6$ psi (61.9 GN/m²)]

$$\begin{aligned} F_{cr} &= K\eta E \left(\frac{t}{R} \right) \\ &= (0.3)\eta(8.98 \times 10^6) \left(\frac{0.017}{2.6495} \right) \\ &= 17,286 \eta \text{ psi } (119.2 \eta \text{ MN/m}^2) \\ \therefore \text{M.S.} &= \frac{17,286 \eta}{(654)(1.5)} - 1 = + \text{LARGE} \end{aligned}$$

Maximum tension stress = 1604 psi (11.1 MN/m²)

F_{tu} [Cb-752 at 2485° F (1636° K)] = 14,650 psi (101.0 MN/m²)

$$\therefore \text{M.S.} = \frac{14,650}{(1604)(1.5)} - 1 = +5.1$$

Outward deflection at midspan due to temperature gradient.

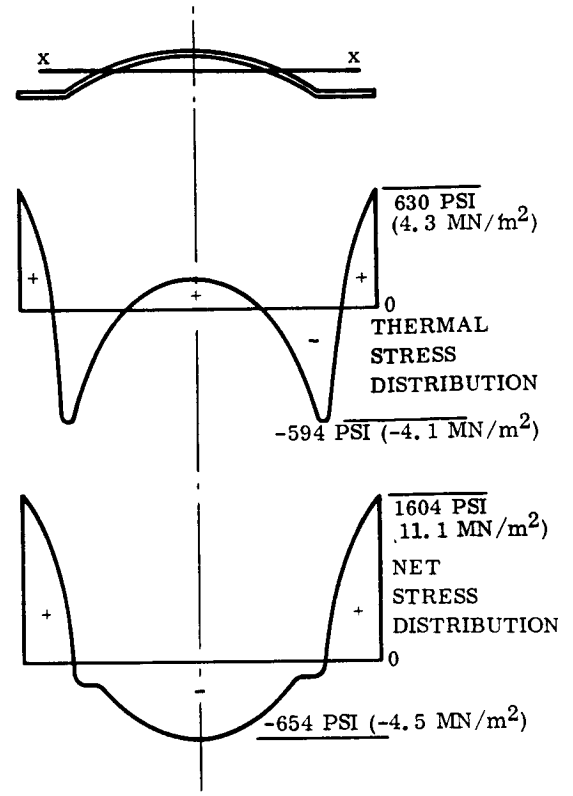
Beam curvature = $1/R = WXP = 4.22 \times 10^{-4}$ (see Page 225)

$$\therefore \delta_{\max} = \frac{L^2}{8R} = \frac{11.0^2}{8} (4.22 \times 10^{-4}) = 0.0064 \text{ inch } (0.163 \text{ cm})$$

Inward deflection due to normal pressure:

$$\delta_{\max} = \frac{5wL^3}{384EI} = \frac{(5)(3.8)(0.15)(11^3)}{(384)(2.013 \times 10^4)} = 0.00049 \text{ inch } (0.00125 \text{ cm}); (w = 3.8 \text{ p})$$

Net deflection = 0.0064 - 0.00049 = 0.0059 inch (0.0151 cm) (outward)



Allowable deflection = 0.395 inch (1.003 cm) (see Page 222).

Maximum temperature gradient in corrugation next to joint occurs at time = 140 seconds.
(See Figures 6-54 and 6-55.)

Maximum temperature = 879° F (744° K)

$\Delta T = 119^\circ \text{ F } (321^\circ \text{ K})$

Normal pressure = 0.15 psi (1.03 kN/m²)

CORRUGATED PANEL MATERIAL CB-752 AS=3.8, M=0.5, R=2.6495, TC=0.017

TIME = 1.4000E+02 PRESSURE = 3.0000E-01

	AREA	X	7	TEMP	THERMAL STRESS	BENDING STRESS	NET STRESS
1	2.839E-03	2.505E-01	5.000E-01	8.000E+02	3.292E+03	4.859E+02	3.777E+03
2	2.939E-03	4.175E-01	5.000E-01	8.190E+02	2.143E+03	4.852E+02	2.628E+03
3	6.250E-03	6.537E-01	3.979E-01	8.385E+02	1.225E+03	3.021E+02	1.527E+03
4	6.250E-03	9.786E-01	2.263E-01	8.535E+02	7.553E+02	-3.951E+00	7.514E+02
5	6.250E-03	1.324E+00	1.014E-01	8.600E+02	6.799E+02	-2.266E+02	4.534E+02
6	6.250E-03	1.684E+00	2.547E-02	8.623E+02	7.337E+02	-3.618E+02	3.719E+02
7	6.250E-03	2.050E+00	J.	8.650E+02	6.353E+02	-4.071E+02	2.282E+02
8	6.250E-03	2.416E+00	2.547E-02	8.676E+02	4.137E+02	-3.617E+02	5.210E+01
9	6.250E-03	2.776E+00	1.014E-01	8.702E+02	6.412E+01	-2.264E+02	-1.623E+02
10	6.250E-03	3.121E+00	2.263E-01	8.727E+02	-4.036E+02	-3.946E+00	-4.075E+02
11	6.250E-03	3.446E+00	3.978E-01	8.750E+02	-9.772E+02	3.014E+02	-6.758E+02
12	5.966E-03	3.775E+00	5.000E-01	8.690E+02	-8.747E+02	4.835E+02	-3.911E+02
13	5.966E-03	4.125E+00	5.000E-01	8.690E+02	-8.747E+02	4.835E+02	-3.911E+02
14	1.125E-02	4.581E+00	3.239E-01	8.700E+02	-1.031E+03	1.635E+02	-8.612E+02
15	1.125E-02	5.195E+00	8.222E-02	8.780E+02	-3.591E+02	-2.614E+02	-6.184E+02
16	1.125E-02	5.850E+00	J.	8.770E+02	-8.923E+01	-4.958E+02	-4.959E+02
17	1.125E-02	6.505E+00	3.222E-02	8.780E+02	-3.581E+02	-2.614E+02	-6.184E+02
18	1.125E-02	7.119E+00	3.239E-01	8.794E+02	-1.155E+03	1.635E+02	-8.853E+02
19	5.966E-03	7.575E+00	5.000E-01	8.710E+02	-9.953E+02	4.835E+02	-5.118E+02
20	2.839E-03	8.349E+02	5.100E-01	7.740E+02	4.907E+03	4.859E+02	5.394E+03

EIXX = 1.3442E+05 BARZ = 2.2851E-01
WXP = -1.7453E-04 WX = 1.2257E-04

The beam model is shown in Figure 6-60.

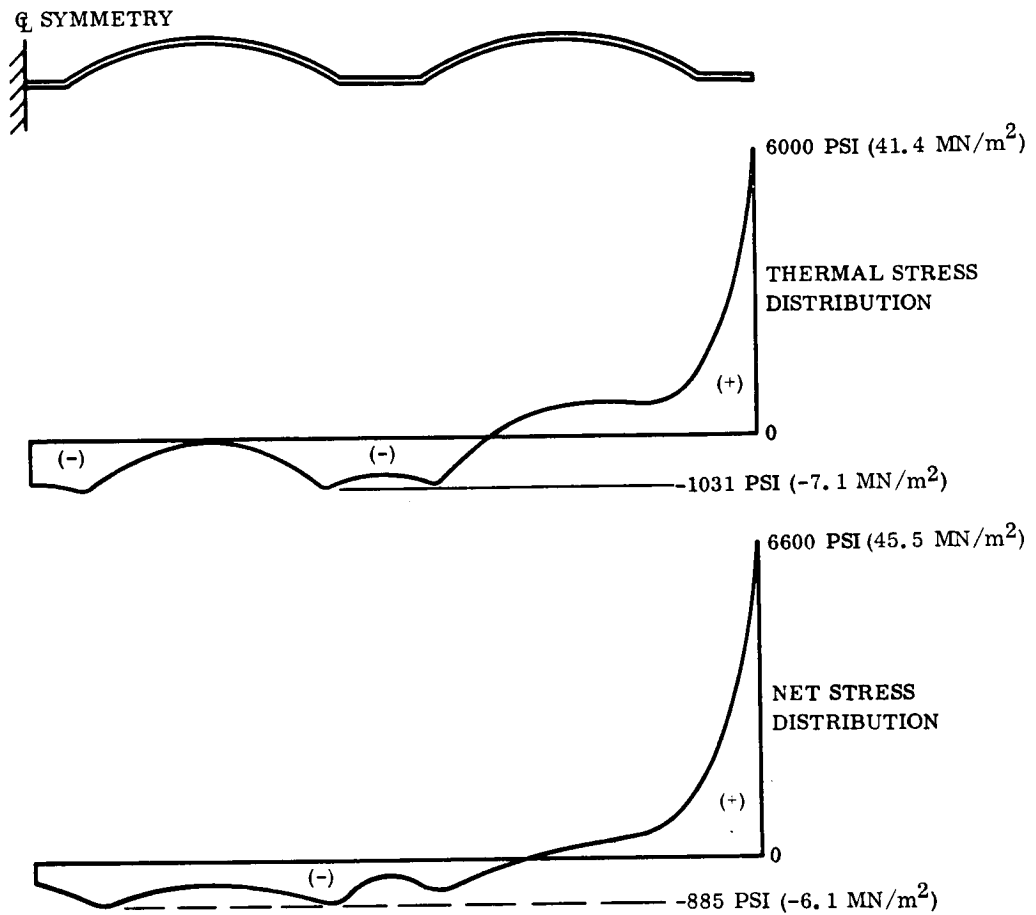
The distribution of thermal and net stresses over the panel are shown on Page 228.

At limit load the maximum tension stress at panel edge = 6600 psi (45.5 MN/m²)

Ultimate stress = $1.25(f_t) + 1.5(f_b) = 1.25(6000) + 1.5(600) = 8400 \text{ psi } (57.9 \text{ MN/m}^2)$
(see Page 228)

$F_{tu} [\text{Cb-752 at } 760^\circ \text{ F } (677^\circ \text{ K})] = 45,000 \text{ psi } (310.3 \text{ MN/m}^2)$

$$\therefore \text{ M. S. } = \frac{45,000}{8,400} - 1 = + \text{ LARGE}$$



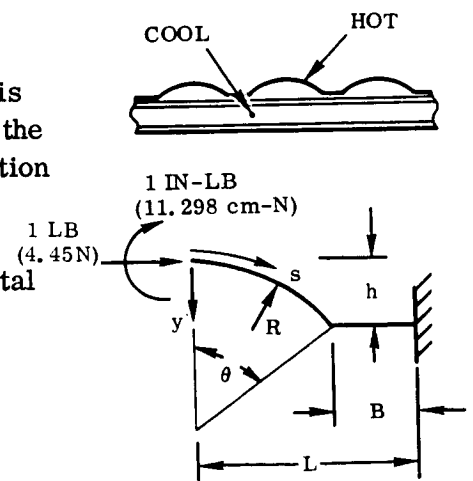
Transverse Thermal Stresses in the Corrugated Skin

Transverse thermal expansion of the corrugated skin is restrained by the relatively cool transverse beams at the panel ends. The thermal loads induced in the corrugation are derived by the method of virtual work as follows.

Consider the half-corrugation as shown. The horizontal deflection due to a unit horizontal load is given by

$$\alpha_{11} = \frac{1}{EI} \int_0^L m_1^2 ds$$

$$= \frac{R^3}{EI} \left(\frac{3\theta}{2} - 2 \sin \theta + \frac{\sin \theta \cos \theta}{2} \right) + \frac{h^2 B}{EI}$$



$$\theta = 0.62445 \text{ Radian}$$

$$R = 2.6495 \text{ INCH (6.73 cm)}$$

$$h = 0.50 \text{ INCH (1.27 cm)}$$

$$B = 0.351 \text{ INCH (0.891 cm)}$$

$$= \frac{0.08429}{EI} + \frac{0.08775}{EI} = \frac{0.12704}{EI}$$

where

$$m_1 = 1.0 \text{ y}$$

The rotation at the centerline is given by

$$\begin{aligned} \alpha_{12} &= \frac{1}{EI} \int_0^L m_1 m_2 ds \\ &= \frac{R^2}{EI} [\theta - \sin(\theta)] + \frac{hB}{EI} = \frac{0.279381}{EI} + \frac{0.1755}{EI} = \frac{0.45488}{EI} \end{aligned}$$

where

$$m_2 = 1.0 \text{ in-lb (11.289 cm-N)}$$

This rotation at the centerline due to a unit bending moment is given by

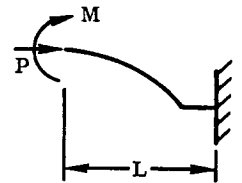
$$\alpha_{22} = \frac{1}{EI} \int_0^L m_2^2 ds = \frac{1}{EI} (R\theta) + \frac{B}{EI} = \frac{1.6544787}{EI} + \frac{0.351}{EI} = \frac{2.0055}{EI}$$

The net slope at the centerline is equal to zero from symmetry.
Hence,

$$P \alpha_{12} + M \alpha_{22} = 0$$

$$\therefore \text{bending moment at centerline} = M = -\frac{P \alpha_{12}}{\alpha_{22}}$$

$$= -\frac{0.454488P}{2.0055} = -0.226819P$$



Therefore, the net transverse deflection due to an axial load P is given by

$$\delta_x = P \alpha_{11} + M \alpha_{12} = P \left(\frac{0.12704}{EI} \right) - 0.226819P \left(\frac{0.45488}{EI} \right) = \frac{0.068865}{EI}$$

Hence the thermal loads induced in the corrugation by a differential thermal expansion ($L\alpha T$) are given by

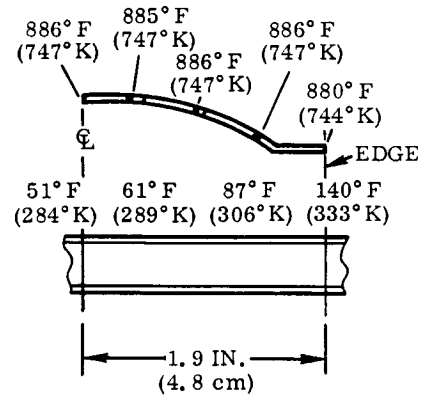
$$P = \frac{EI(L\alpha T)}{0.068865} = 14.5212 EI (L\alpha T)$$

$$M = -0.2268 P$$

The maximum temperature gradient between the skin and edge beams occurs at reentry time = 140 seconds.

The temperature distributions in the skin and forward edge beam flange are as shown. Assuming a uniform skin temperature = 886° F (747° K) and an average flange temperature

$$T = \frac{51 + 61 + 87 + 140}{4} = 85^\circ \text{ F } (302^\circ \text{ K})$$



$$\text{Differential expansion} = L (\alpha_1 \Delta T_1 - \alpha_2 \Delta T_2)$$

$$= 1.9 [(4 \times 10^{-6}) (886 - 70) - (3.75 \times 10^{-6}) (85 - 70)]$$

$$= 0.0061 \text{ inch } (0.0155 \text{ cm})$$

$$\therefore \text{ Axial load at centerline} = (14.5212) (EI) (0.0061)$$

Considering a 1.0 in. (2.54 cm) width of skin

$$I = \frac{1.0 \times 0.021^3}{12} = 0.77 \times 10^{-6} \text{ in}^4 (32.03 \times 10^{-6} \text{ cm}^4)$$

Note: the sheet thickness after coating of 0.021 in. (0.053 cm) is used since the induced loads are proportional to $(t)^3$.

$$\therefore P = (14.5212) (14.5 \times 10^6) (0.77 \times 10^{-6}) (0.0061)$$

$$= 0.989 \text{ lb } (4.399 \text{ N})$$

$$\text{Bending moment (M) at centerline} = (-0.2268) (0.989)$$

$$= -0.2243 \text{ in-lb } (-2.534 \text{ cm-N})$$

$$\text{Bending moment at edge} = P(h) + M_{\text{CL}} = (0.989) (0.50) - 0.2243$$

$$= 0.2702 \text{ in-lb } (3.053 \text{ cm-N})$$

Stress in skin at edge

$$f = -\frac{P}{A} \pm \frac{M\bar{y}}{I} = -\frac{0.989}{0.021} \pm \frac{(6)(0.2702)}{0.021^2} = -47.1 \pm 3676.0$$

$$= -3723.1 \text{ psi } (-25.7 \text{ MN/m}^2) \text{ or } +3628.9 \text{ psi } (25.02 \text{ MN/m}^2)$$

$$\text{Allowable } F_{\text{beam}} [\text{Cb-752 at } 880^\circ \text{ F } (744^\circ \text{ K})] = F_{\text{tu}} = 34,000 \text{ psi } (234.4 \text{ MN/m}^2)$$

$$\therefore \text{M.S. (bending)} = \frac{34,000}{3723.1 (1.25)} - 1 = + \text{LARGE}$$

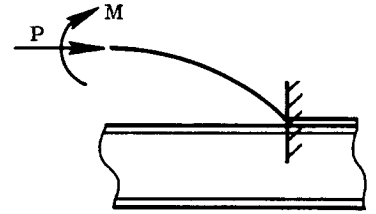
Local Stresses in Corrugation at Transverse Beams

Locally at the support beams, the flat portion of the corrugation is diffusion bonded to the beam flanges and hence bending deformation is prevented by the relatively stiff beams. Therefore, thermal loads are computed assuming corrugation is fixed at edge of flat.

The deflection coefficients are as before with the second terms representing the flat portion deleted.

Hence for zero slope at centerline,

$$M = -\frac{P \alpha_{12}}{\alpha_{22}} = -\frac{P(0.279381)}{1.6544787} = -0.16886P$$



\therefore net transverse deflection due to axial load P is given by

$$\begin{aligned} \delta_x &= P \alpha_{11} + M \alpha_{12} = P \left(\frac{0.08429}{EI} \right) - 0.16886 \left(\frac{0.279381}{EI} \right) \\ &= \frac{0.037113P}{EI} = L \alpha \Delta T \end{aligned}$$

Hence the thermal loads induced in the corrugation are given by

$$P = \frac{EI (L \alpha T)}{0.037113} = 26.945 EI (L \alpha T)$$

$$M = -0.16886P$$

Local Thermal Stresses in Corrugated Skin at Aft Support Beam

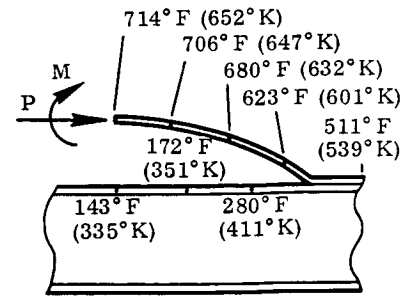
Differential expansion is based on average temperatures.

$$t_{\text{skin}} = \frac{(714 + 706 + 680 + 623 + 511)}{5} = 647^\circ \text{F} (615^\circ \text{K})$$

$$t_{\text{beam}} = \frac{(143 + 172 + 280 + 511)}{5} = 221^\circ \text{F} (378^\circ \text{K})$$

$$L\alpha\Delta T = L(\alpha_S \Delta T_S - \alpha_B \Delta T_B)$$

$$= 1.9 \times 10^{-6} [3.95(647 - 70) - 3.8(221 - 70)] = 0.00324 \text{ inch} (0.00823 \text{ cm})$$



Therefore the thermal loads per unit width of corrugation are

$$P = 26.945 EI (0.00324) = (26.945)(14.8 \times 10^{-6})(20.83 \times 10^{-6})(0.00324)$$

$$= 26.914 \text{ pounds} (119.713 \text{ N})$$

$$\text{Bending moment (BM) at centerline} = (-0.16886)(26.914) = -4.5446 \text{ in-lb} (-51.345 \text{ cm-N})$$

$$\text{BM at edge} = P(h) + M_{\bar{C}_L} = (26.914)(0.50) - 4.5446 = 8.912 \text{ in-lb} (100.638 \text{ cm-N})$$

$$I = \frac{(0.063)^3}{12} = 20.83 \times 10^{-6} \text{ in}^4 (866.53 \times 10^{-6} \text{ cm}^4)$$

where

$$0.063 \text{ inch} (0.160 \text{ cm}) = \text{effective thickness after coating}$$

The maximum stresses at the junction of corrugation and flat are:

$$f = -\frac{P}{A} \pm \frac{M\bar{y}}{I} = -\frac{26.914}{0.063} \pm \frac{(6)(8.912)}{(0.063)^2} = -427 \pm 13,472$$

$$= -13,900 \text{ psi} (-95.8 \text{ MN/m}^2) \text{ or } +13,045 \text{ psi} (89.9 \text{ MN/m}^2)$$

$$\text{Allowable } F_{\text{beam}} [\text{Cb-752 at } 623^\circ \text{F} (601^\circ \text{K})] = F_{tu} = 48,000 \text{ psi} (331 \text{ MN/m}^2)$$

$$\therefore \text{M.S. (bending)} = \frac{48,000}{13,900 (1.25)} - 1 = 1.76$$

6.4.4.2 Corrugation test panel

Support Beam - Aft

Pressure loading on panel is applied to beam as concentrated forces at flats on corrugations.

Condition: Boost phase 3.0 psi (20.7 kN/m²) crushing

Load/Corrugation = P = 81.46 lb (362.33 N)
(Limit) (see Page 219).

Reactions:

$$R_1 = \frac{P}{2} \left(\frac{3a^2L - a^3}{L^3} \right) + \frac{P}{2}$$

$$= \frac{81.46}{2} \left[\frac{(3)(3.8^2)(7.3) - 3.8^3}{7.3^3} \right]$$

$$+ \frac{81.46}{2} = 27.36 + 40.73$$

$$= 68.09 \text{ lb (302.86 N) (Limit)}$$

$$R_2 = 4P - 2R_1 = (4)(81.46) - (2)(68.09)$$

$$= 189.66 \text{ lb (843.61 N) (Limit)}$$

Bending Moments

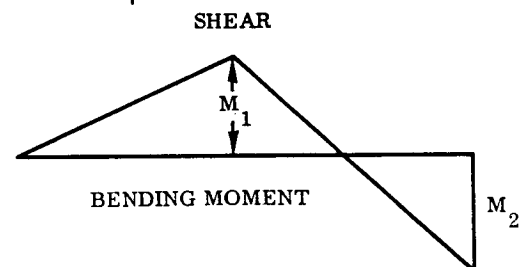
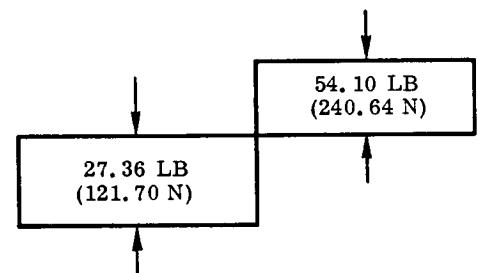
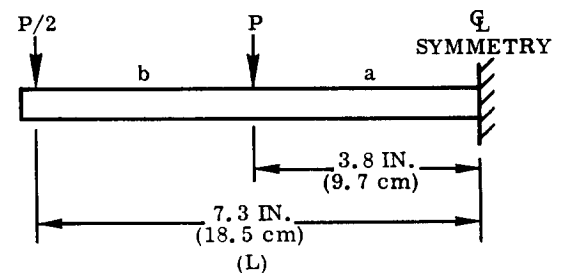
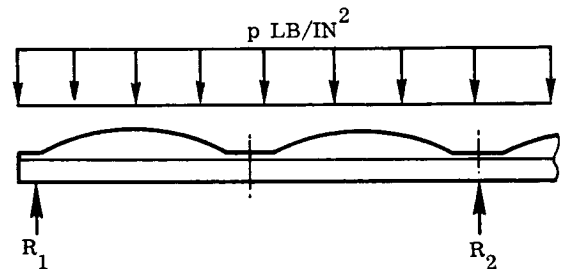
$$M_1 = \left(R_1 - \frac{P}{2} \right) (7.3 - 3.8)$$

$$= \left(68.09 - \frac{81.46}{2} \right) 3.5$$

$$= 95.76 \text{ in-lb (1081.90 cm-N) (Limit)}$$

$$M_2 = \left(R_1 - \frac{P}{2} \right) 7.3 - 3.8P$$

$$= -109.82 \text{ in-lb (-1240.75 cm-N) (Limit)}$$



Bending Section at Centerline

Material Cb-752, Temperature = 340° F (444° K)

$$I = \frac{(0.02)(0.7^3)}{12} + \frac{(0.30)(0.02)(0.68^2)}{2}$$

$$= 0.00196 \text{ in}^4 \text{ (0.0815 cm}^4\text{)}$$

$$f_b = \pm \frac{M\bar{y}}{I} = \pm \frac{(109.82)(0.35)}{0.00196}$$

$$= 19,610 \text{ psi (135.2 MN/m}^2\text{)}$$

Flange Critical Buckling Stress

$$F_{cr} = K \eta E \left(\frac{t}{b}\right)^2$$

$$= \eta (0.385)(15.14 \times 10^6) \left(\frac{0.02}{0.16}\right)^2$$

$$= 103,625 \eta \text{ psi (714.5 } \eta \text{ MN/m}^2\text{)}$$

(For ends and one side simply supported, one side free, $K = 0.385$)

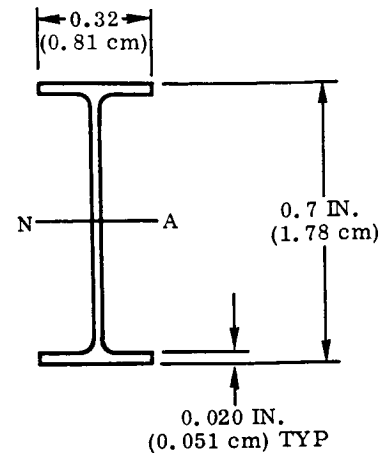
$$\therefore \text{ Use cutoff} = 1.1 F_{cy}$$

$$= (1.1)(43,050)$$

$$= 47,355 \text{ psi (326.5 MN/m}^2\text{)}$$

$$\therefore \text{ M. S.} = \frac{47,355}{(19,610)(1.5)} - 1$$

$$= + 0.61 \text{ (ULT)}$$



6.4.4.3 Corrugation test panel

Support Beam - Forward

Pressure loading on panel is applied to beam as concentrated forces at flats on corrugations.

Conditions: 3.0 psi (20.7 kN/m²) crushing

Load/Corrugation = $P = 55.34$ lb (Limit)
(246.15 N) (see Page 219)

Reactions

$$R_1 = \frac{P}{2} \left(\frac{3a^2 - a^3}{L^3} \right) + \frac{P}{2}$$

$$= \frac{55.34}{2} \left[\frac{(3)(3.8^2)(7.3) - 3.8^3}{7.3^3} \right] + \frac{55.34}{2}$$

$$= 18.59 + 27.67 = 46.26$$

$$R_2 = 4P - 2R_1$$

$$= (4)(55.34) - (2)(46.26)$$

$$= 128.84 \text{ pounds (573.1 N)}$$

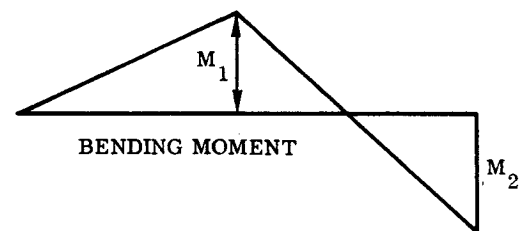
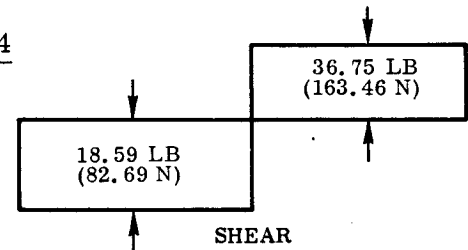
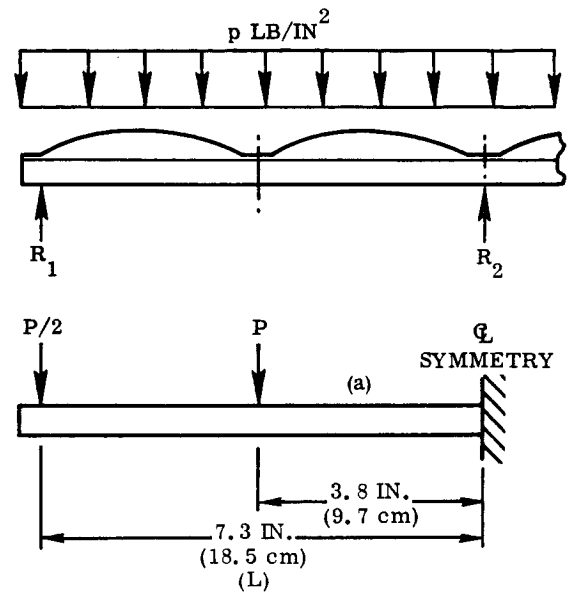
Bending Moments

$$M_1 = \left(R_1 - \frac{P}{2} \right) (7.3 - 3.8) = \left(46.26 - \frac{55.34}{2} \right) (3.5)$$

$$= 65.07 \text{ in-lb (735.16 cm/N) (Limit)}$$

$$M_2 = \left(R_1 - \frac{P}{2} \right) 7.3 - P(3.8)$$

$$= \left(46.26 - \frac{55.34}{2} \right) 7.3 - 55.34(3.8) = -74.59 \text{ in-lb (-842.72 cm-N) (Limit)}$$



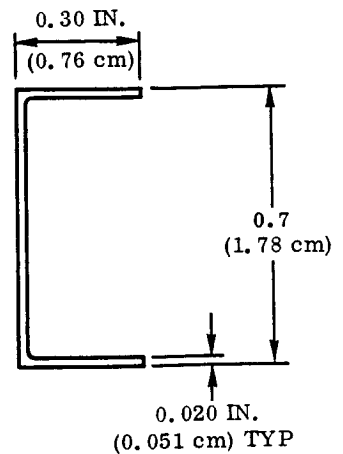
Bending Section at Centerline

Material, Cb-752; Temperature = 340° F (444° K)

$$I = \frac{(0.020)(0.7^3)}{12} + \frac{(0.28)(0.020)(0.680^2)}{2}$$

$$= 0.001866 \text{ in}^4 \text{ (0.0776 cm}^4\text{)}$$

$$f_b = \pm \frac{M\bar{y}}{I} = \frac{(74.59)(0.35)}{0.001866} = 13,990 \text{ psi (96.5 MN/m}^2\text{)}$$



Flange Critical Buckling Stress

$$F_{cr} = KE \left(\frac{t}{b} \right)^2$$

$$= (0.385)(15.14 \times 10^6) \left(\frac{0.020}{0.28} \right)^2 = 29,739 \text{ psi (205.1 MN/m}^2\text{)}$$

(For ends and one edge simply supported, one edge free, $K = 0.385$)

$$\therefore \text{M.S.} = \frac{29,739}{(13,990)(1.5)} - 1 = +0.417 \text{ (ULT)}$$

Support Beams: Thermal Stress Analysis

The support beams are continuous over three supports (page 237) and hence the curvature induced by a temperature gradient is restrained. Therefore, thermal stresses arise from the temperature gradient across the section and from the overall bending due to the restraint of free curvature. The net thermal stresses are computed by superimposing the local and overall stress systems.

Overall Bending Due to Restraint of Free Curvature

The temperature varies along the span. Hence the overall bending loads are computed for average flange temperatures.

Consider beam with center support released and free curvature due to temperature gradient permitted.

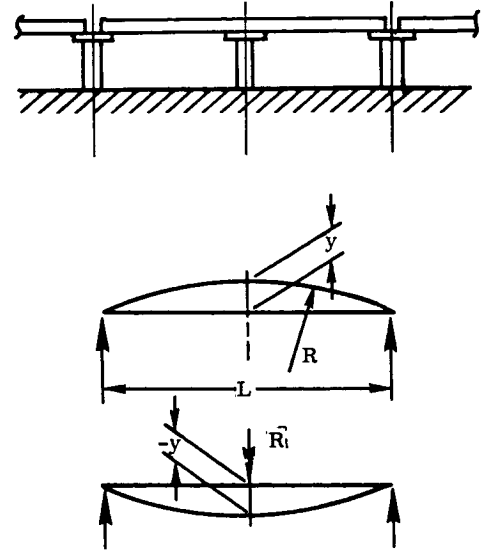
$$\text{Curvature} = \frac{1}{R} = \frac{\alpha \Delta T}{h}$$

$$\text{Maximum deflection} = y_{\max} = \frac{L^2}{8R} = \left(\frac{L^2}{8}\right) \left(\frac{\alpha \Delta T}{h}\right)$$

Deflection of simply supported beam due to unit load at midspan = $-L^3/192 EI$. Hence, for zero deflection at center post:

$$\left(\frac{L^2}{8}\right) \left(\frac{\alpha \Delta T}{h}\right) - R \left(\frac{L^3}{192 EI}\right) = 0$$

$$\therefore R = \left(\frac{L^2 \alpha \Delta T}{8h}\right) \left(\frac{192 EI}{L^3}\right) = \frac{24 EI \alpha \Delta T}{Lh}$$



Aft Support Beam: Thermal Stress Analysis Overall Bending Due to Restraint at Center Post

Condition: Reentry time = 140 seconds

Outer flange average temperature = 277° F (409° K)

Inner flange average temperature = 189° F (360° K)

$$\Delta T = 277 - 189 = 87^\circ \text{ F } (321^\circ \text{ K})$$

For Cb-752 at 230° F (383° K)

$$E = 15.3 \times 10^6 \text{ psi } (105.5 \text{ GN/m}^2)$$

$$\alpha = 3.85 \times 10^{-6} \text{ in/in/}^\circ \text{ F } (6.93 \times 10^{-6} \text{ cm/cm/}^\circ \text{ C})$$

$$I = 0.00196 \text{ in}^4 (0.0815 \text{ cm}^4) \text{ (see Page 234)}$$

\therefore Reaction at center post

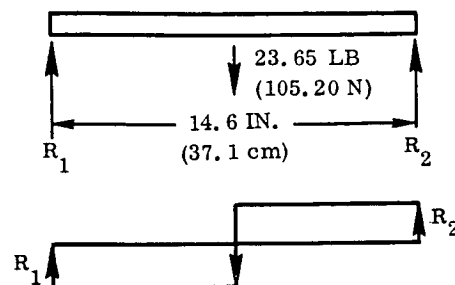
$$R = \frac{24 EI \alpha \Delta T}{Lh} = \frac{(24) (15.3 \times 10^6) (0.00196) (3.85 \times 10^{-6}) (87.25)}{(14.6)(0.7)}$$

$$= 23.65 \text{ pounds } (105.20 \text{ N})$$

Reactions

$$R_1 = R_2 = \frac{23.65}{2}$$

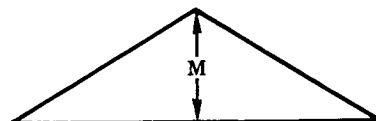
$$= 11.82 \text{ pounds (52.58 N)}$$



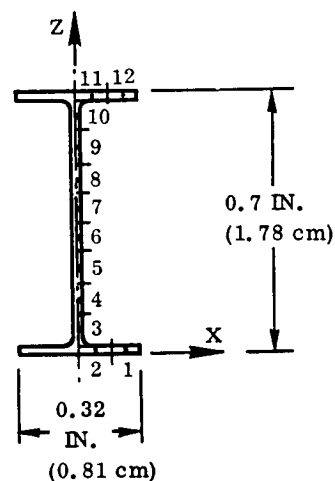
Bending Moment

$$M = \frac{R_1 L}{2} = \frac{(11.82)(14.6)}{2}$$

$$= 86.32 \text{ in-lb (975.24 cm-N)}$$



Thermal stresses due to local temperature gradient over section at midspan (unrestrained beam), entry time = 140 seconds.



CORRUGATED PANEL AFT SUPPORT BEAM MATERIAL CU-752

TIME = 1.4040E+02 PRESSURE = -0.

	AREA	X	Y	TEMP	THERMAL STRESS	BENDING STRESS	NET STRESS
1	1.600E-03	1.200E-01	1.000E-02	2.730E+02	-1.096E+03	0.	-1.096E+03
2	1.600E-03	4.000E-02	1.000E-02	2.730E+02	-1.096E+03	0.	-1.096E+03
3	8.250E-04	5.000E-03	6.125E-02	2.810E+02	-5.945E+02	0.	-5.945E+02
4	8.250E-04	5.000E-03	1.437E-01	2.925E+02	3.175E+02	0.	3.175E+02
5	8.250E-04	5.000E-03	2.262E-01	3.050E+02	1.157E+03	0.	1.157E+03
6	8.250E-04	5.000E-03	3.087E-01	3.200E+02	1.942E+03	0.	1.942E+03
7	8.250E-04	5.000E-03	3.912E-01	3.350E+02	2.464E+03	0.	2.464E+03
8	8.250E-04	5.000E-03	4.737E-01	3.565E+02	2.810E+03	0.	2.810E+03
9	8.250E-04	5.000E-03	5.562E-01	3.810E+02	2.910E+03	0.	2.910E+03
10	8.250E-04	5.000E-03	6.387E-01	4.190E+02	2.205E+03	0.	2.205E+03
11	1.600E-03	4.000E-02	6.900E-01	5.110E+02	-2.287E+03	0.	-2.287E+03
12	1.600E-03	1.200E-01	6.900E-01	5.110E+02	-2.287E+03	0.	-2.287E+03

IXX = 2.9466E+04 PARZ = 3.4793E-01
 IXP = 1.2628E-03 MY = 0.

Section at Center Post

The distribution of thermal stresses over the section is as shown.

Overall Bending

Bending moment = 86.32 in-lb
(975.24 cm-N)

$$f_b = \pm \frac{(86.32)(0.35)}{0.00196}$$

$$= \pm 15,400 \text{ psi}$$

$$(\pm 106.2 \text{ MN/m}^2)$$

Combined stresses due to overall bending and local temperature gradient.

Upper flange is critical.

$$f_{\text{net}} = -15,400 - 2287 = -17,687 \text{ psi } (-122 \text{ MN/m}^2)$$

Critical Buckling Stress

$$F_{\text{cr}} = KE \left(\frac{t}{b} \right)^2 = (0.385)(15.24 \times 10^6) \left(\frac{0.02}{0.16} \right)^2 = 91,678 \text{ psi } (632.1 \text{ MN/m}^2)$$

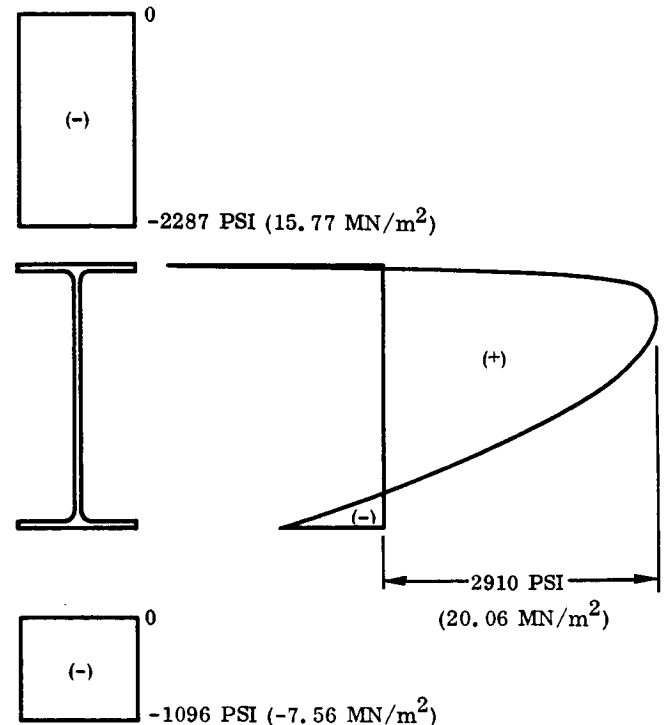
where

$$K = 0.385$$

$$E = 15.24 \times 10^6 \text{ psi } (105.1 \text{ GN/m}^2)$$

$$\therefore \text{Use cutoff} = 1.1 F_{\text{cy}} = (1.1)(39,650) = 43,615 \text{ psi } (300.7 \text{ MN/m}^2)$$

$$\therefore \text{M.S.} = \frac{43,615}{(-17,687)(1.25)} - 1 = 0.97$$



Overall Bending Due to Restraint at Center Post

Condition: Reentry time = 200 seconds

Outer flange average temperature = 981° F (800° K)

Inner flange average temperature = 906° F (759° K)

$$\Delta T = 981 - 906 = 75^\circ \text{ F } (315^\circ \text{ K})$$

For Cb-752 at 950° F (783° K)

$$E = 14.4 \times 10^6 \text{ psi } (99.3 \text{ GN/m}^2)$$

$$\alpha = 4.0 \times 10^{-6} \text{ in/in/}^\circ \text{ F } (7.2 \times 10^{-6} \text{ cm/cm/}^\circ \text{ C})$$

$$I = 0.00196 \text{ in}^4 (0.0815 \text{ cm}^4) \text{ (see Page 234)}$$

∴ Reaction at center post

$$\begin{aligned} R &= \frac{24 E \alpha \Delta T}{L h} \\ &= \frac{(24)(14.4 \times 10^6)(0.00196)(4.0 \times 10^{-6})(75)}{(14.6)(0.7)} \\ &= 19.9 \text{ pounds } (88.5 \text{ N}) \end{aligned}$$

Reactions

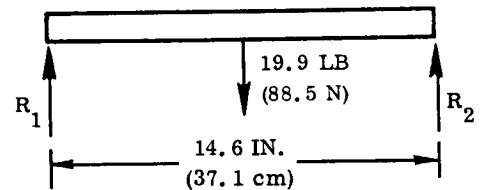
$$R_1 = R_2 = \frac{19.9}{2} = 9.95 \text{ pounds } (44.26 \text{ N})$$

Bending Moment

$$M = \frac{R_1 L}{2} = \frac{(9.95)(14.6)}{2} = 72.64 \text{ in-lb } (820.69 \text{ cm-N})$$

Thermal stresses due to local temperature gradient over section at midspan (unrestrained beam) at entry time = 200 seconds.

Section is as shown on Page 238.



CORRUGATED PANEL AFT SUPPORT BEAM MATERIAL C8-752

TIME = 2.0040E+02 PRESSURE = -0.

	AREA	X	Z	TEMP	THERMAL STRESS	BENDING STRESS	NET STRESS
1	1.600E-03	1.200E-01	1.000E-02	9.460E+02	-6.563E+02	0.	-6.563E+02
2	1.600E-03	4.000E-02	1.000E-02	9.460E+02	-6.563E+02	0.	-6.563E+02
3	8.250E-04	5.000E-03	6.125E-02	9.520E+02	-3.331E+02	0.	-3.331E+02
4	8.250E-04	5.000E-03	1.437E-01	9.610E+02	2.250E+02	0.	2.250E+02
5	8.250E-04	5.000E-03	2.262E-01	9.710E+02	7.234E+02	0.	7.234E+02
6	8.250E-04	5.000E-03	3.087E-01	9.820E+02	1.159E+03	0.	1.159E+03
7	8.250E-04	5.000E-03	3.912E-01	9.952E+02	1.460E+03	0.	1.460E+03
8	8.250E-04	5.000E-03	4.737E-01	1.010E+03	1.655E+03	0.	1.655E+03
9	8.250E-04	5.000E-03	5.562E-01	1.029E+03	1.586E+03	0.	1.586E+03
10	8.250E-04	5.000E-03	6.387E-01	1.062E+03	6.552E+02	0.	6.552E+02
11	1.600E-03	4.000E-02	6.900E-01	1.103E+03	-1.182E+03	0.	-1.182E+03
12	1.600E-03	1.200E-01	6.900E-01	1.103E+03	-1.182E+03	0.	-1.182E+03

FIXX = 2.8040E+04 HAZZ = 3.4868E-01
WXP = 9.2613E-04 WY = 0.

Section at Center Post

The distribution of thermal stresses over the section is as shown.

Overall Bending

Bending moment = 72.64 in-lb (820.69 cm-N)

$$f_b = \pm \frac{(72.64)(0.35)}{0.00196}$$

$$= \pm 12,950 \text{ psi } (\pm 89.3 \text{ MN/m}^2)$$

Combined Stresses Due to Overall Bending and Local Temperature Gradient

Outer flange is critical.

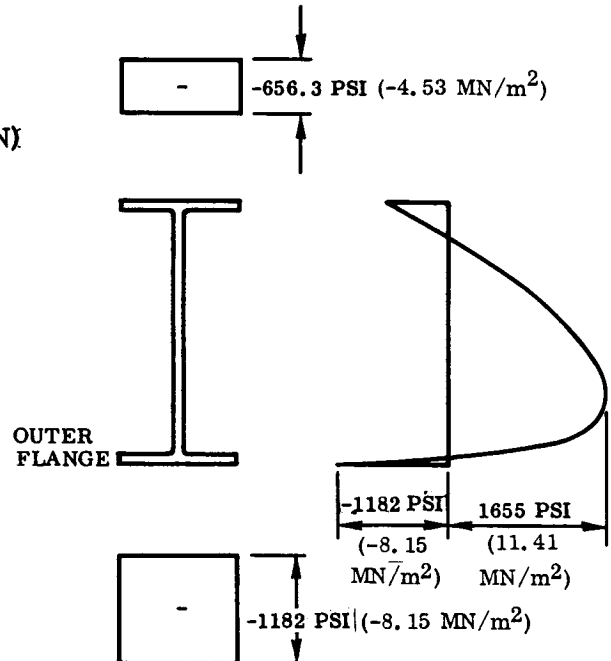
$$f = -12,950 - 1182$$

$$= -14,132 \text{ psi } (-97.4 \text{ MN/m}^2)$$

$$F_{cr} = KE \left(\frac{t}{b} \right)^2 = (0.385)(14.45 \times 10^6) \left(\frac{0.02}{0.16} \right)^2 = 86,925 \text{ psi } (599.3 \text{ MN/m}^2)$$

where

$$K = 0.385, E = 14.45 \times 10^6 \text{ psi } (99.6 \text{ GN/m}^2)$$



$$\therefore \text{Use cutoff} = 1.1 F_{cy} = (1.1)(31,570) = 34,720 \text{ psi } (239.4 \text{ MN/m}^2)$$

$$\therefore \text{M.S.} = \frac{34,720}{(14,132)(1.25)} - 1 = +0.96$$

Forward Support Beam: Thermal Stress Analysis

Overall Bending Due to Constraint at Center Post

Condition: Reentry time = 140 seconds

Outer flange average temperature = 85° F (302° K)

Inner flange average temperature = 21° F (267° K)

$$\therefore \Delta T = 85 - 21 = 64^\circ \text{ F } (309^\circ \text{ K})$$

Cb-752 at 50° F (283° K)

$$E = 15.5 \times 10^6 \text{ psi } (106.96 \text{ N/m}^2)$$

$$\alpha = 3.8 \times 10^{-6} \text{ in/in/}^\circ \text{ F } (6.8 \times 10^{-6} \text{ cm/cm/}^\circ \text{ C})$$

$$I = 0.001866 \text{ in}^4 (0.0776 \text{ cm}^4) \text{ (see Page 234)}$$

\therefore Reaction at center post

$$R = \frac{24 EI \alpha \Delta T}{Lh} = \frac{(24)(15.5 \times 10^6)(0.001866)(3.8 \times 10^{-6})(64.25)}{(14.6)(0.7)}$$

$$= 16.6 \text{ pounds } (73.8 \text{ N})$$

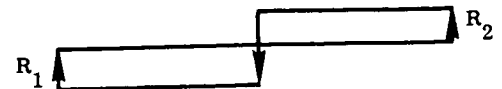
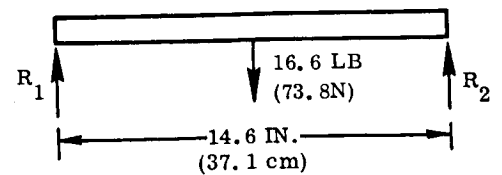
Reactions

$$R_1 = R_2 = \frac{16.6}{2} = 8.3 \text{ pounds } (36.9 \text{ N})$$

Bending Moment

$$M = \frac{R_1 L}{2} = \frac{(8.3)(14.6)}{2}$$

$$= 60.59 \text{ in-lb } (684.55 \text{ cm-N})$$



Section at Center Post

The distribution of thermal stresses over the section is shown in the sketch.

Overall Bending

Bending Moment = 60.59 in-lb (684.55 cm-N)

$$f_b = \pm \frac{Mc}{I} = \frac{(60.59)(0.35)}{0.001866}$$

$$= \pm 11,365 \text{ psi } (\pm 78.4 \text{ MN/m}^2)$$

Combining overall bending and temperature gradient stresses:

Total stress in upper flange

$$= -2850 - 11,365 = -14,215 \text{ psi } (-98.0 \text{ MN/m}^2)$$

Critical Buckling Stress

$$F_{cr} = KE \left(\frac{t}{b} \right)^2$$

$$= (0.385)(15.3 \times 10^6) \left(\frac{0.02}{0.28} \right)^2 = 30,053 \text{ psi } (207.2 \text{ MN/m}^2)$$

(For ends and one side simply supported, one side free, $K = 0.385$)

$$\therefore \text{M.S.} = \frac{30,053}{(14,215)(1.25)} - 1 = +0.69 \text{ (ULT)}$$

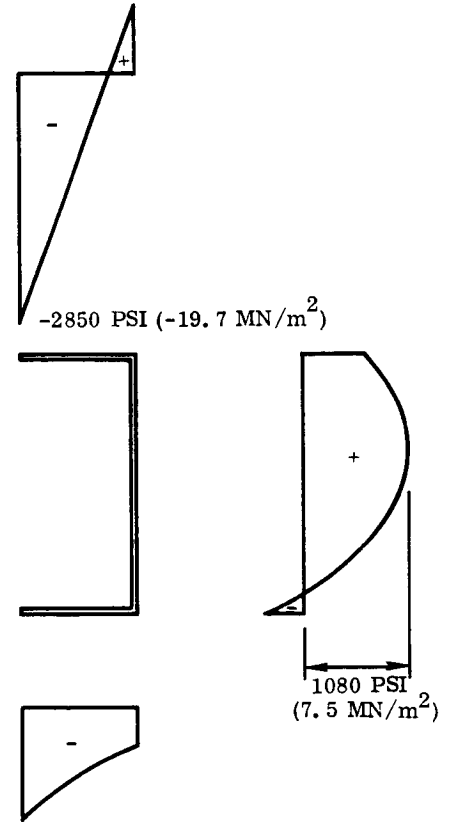
Overall Bending Due to Constraint at Center Post

Condition: Reentry time = 200 seconds

Outer flange average temperature = 815° F (708° K)

Inner flange average temperature = 684° F (635° K)

$$\therefore \Delta T = 814.5 - 683.5 = 131.0^\circ \text{ F } (346^\circ \text{ K}) \text{ (maximum temperature gradient)}$$



Cb-752 at 750° F (672° K)

$$E = 14.66 \times 10^6 \text{ psi (101.1 GN/m}^2\text{)}$$

$$\alpha = 3.96 \times 10^{-6} \text{ in/in/}^\circ\text{F (7.12} \times 10^{-6} \text{ cm/cm/}^\circ\text{C)}$$

$$I = 0.00186 \text{ in}^4 \text{ (0.0776 cm}^4\text{) (see Page 236)}$$

∴ Reaction at Center Post

$$R = \frac{24 EI \alpha \Delta T}{Lh} = \frac{(24)(14.66 \times 10^6)(0.00186)(3.96 \times 10^{-6})(131)}{(14.6)(0.7)}$$

$$= 33.22 \text{ pounds (147.76 N)}$$

Reactions

$$R_1 = R_2 = \frac{33.22}{2}$$

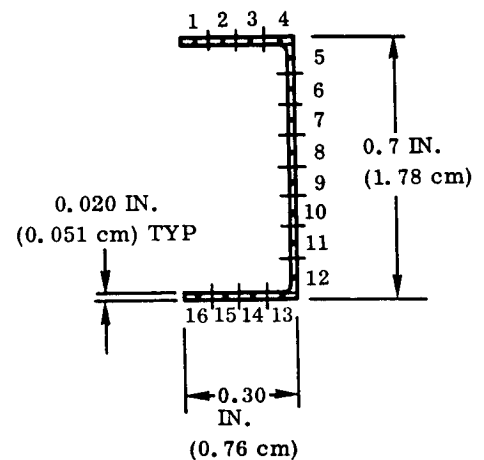
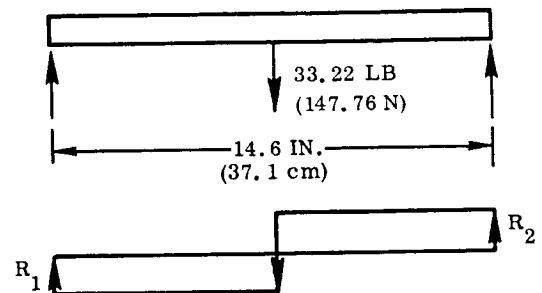
$$= 16.61 \text{ pounds (73.88 N)}$$

Bending moment

$$M = \frac{R_1 L}{2} = \frac{(16.61)(14.6)}{2}$$

$$= 121.25 \text{ in-lb (1369.88 cm-N)}$$

Thermal stresses due to local temperature gradient over section at midspan (unrestrained beam):



CORRUGATED PANEL FORWARD SUPPORT BEAM MATERIAL CB-752

TIME = 2.0040E+02 PRESSURE = -0.

	AREA	X	Z	TEMP	THERMAL STRESS	BENDING STRESS	NET STRESS
1	1.500E-03	2.625E-01	1.000E-02	7.540E+02	2.194E+02	0.	2.194E+02
2	1.500E-03	1.875E-01	1.000E-02	7.533E+02	2.625E+02	0.	2.625E+02
3	1.500E-03	1.125E-01	1.000E-02	7.520E+02	3.427E+02	0.	3.427E+02
4	1.500E-03	3.750E-02	1.000E-02	7.500E+02	4.653E+02	0.	4.653E+02
5	1.650E-03	1.000E-02	6.125E-02	7.480E+02	2.393E+02	0.	2.393E+02
6	1.650E-03	1.000E-02	1.437E-01	7.445E+02	-1.086E+02	0.	-1.086E+02
7	1.650E-03	1.000E-02	2.262E-01	7.400E+02	-3.953E+02	0.	-3.953E+02
8	1.650E-03	1.000E-02	3.087E-01	7.340E+02	-5.912E+02	0.	-5.912E+02
9	1.650E-03	1.000E-02	3.912E-01	7.260E+02	-6.629E+02	0.	-6.629E+02
10	1.650E-03	1.000E-02	4.737E-01	7.180E+02	-7.363E+02	0.	-7.363E+02
11	1.650E-03	1.000E-02	5.562E-01	7.080E+02	-6.879E+02	0.	-6.879E+02
12	1.650E-03	1.000E-02	6.387E-01	6.975E+02	-6.098E+02	0.	-6.098E+02
13	1.500E-03	3.750E-02	6.900E-01	6.875E+02	-3.488E+02	0.	-3.488E+02
14	1.500E-03	1.125E-01	6.900E-01	6.770E+02	2.943E+02	0.	2.943E+02
15	1.500E-03	1.875E-01	6.900E-01	6.660E+02	9.680E+02	0.	9.680E+02
16	1.500E-03	2.625E-01	6.900E-01	6.540E+02	1.703E+03	0.	1.703E+03

EIXX = 2.7337E+04 BARZ = 3.5070E-01
WXP = -4.6559E-04 WX = 0.

Reentry time = 200 seconds

Section at Center Post

The distribution of thermal stresses over the section is as shown.

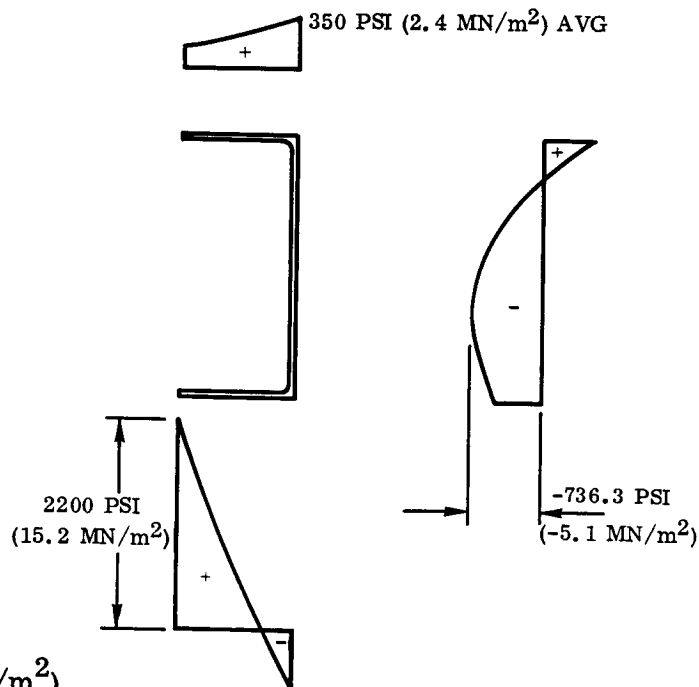
Overall Bending

Bending moment = 121.25 in-lb
(1369.88 cm-N)

(See Page 244.)

$$f_b = \pm \frac{M\bar{y}}{I} = \frac{(121.25)(0.35)}{0.00186}$$

$$= \pm 22,816 \text{ psi } (\pm 157.3 \text{ MN/m}^2)$$



Combining overall bending and temperature gradient stresses

Maximum stress in lower flange = $2200 + 22,816 = -25,016$ psi (-172.5 MN/m²)

$$F_{tu} [\text{Cb-752 at } 654^\circ \text{ F (619}^\circ \text{ K)}] = 47,150 \text{ psi (325.1 MN/m}^2\text{)}$$

$$\therefore \text{M.S.} = \frac{47,150}{(25,016)(1.25)} - 1 = +0.51$$

Upper Flange Stress

$$f_c = -22,816 + 350 = -22,466 \text{ psi (-154.9 MN/m}^2\text{)}$$

Flange Critical Buckling Stress

$$F_{cr} = K E \left(\frac{t}{b} \right)^2 = (0.385) (14.61 \times 10^6) \left(\frac{0.02}{0.28} \right)^2 = 28,698 \text{ psi (197.9 MN/m}^2\text{)}$$

(For ends and one side simply supported, one side free, $K = 0.385$)

$$\therefore \text{M.S.} = \frac{28,698}{(22,466)(1.25)} - 1 = +0.022$$

Overall Bending Due to Restraint at Center Post

Condition: Reentry time = 210 seconds.

Outer flange average temperature = $967^\circ \text{ F (792}^\circ \text{ K)}$

Inner flange average temperature = $844^\circ \text{ F (724}^\circ \text{ K)}$

\therefore Average $\Delta T = 967 - 841 = 126^\circ \text{ F (342}^\circ \text{ K)}$

Cb-752 at $900^\circ \text{ F (755}^\circ \text{ K)}$

$$E = 14.5 \times 10^6 \text{ psi (99.9 GN/m}^2\text{)}$$

$$\alpha = 4.0 \times 10^{-6} \text{ in/in/}^\circ \text{ F (7.2 cm/cm/}^\circ \text{ C)}$$

$$I = 0.00186 \text{ in}^4 (0.0774 \text{ cm}^4)$$

\therefore Reaction at center post

$$R = \frac{24 EI \alpha \Delta T}{Lh} = \frac{(24)(14.5 \times 10^6)(0.00186)(4 \times 10^{-6})(126)}{(14.6)(0.7)}$$

$$= 31.92 \text{ pounds (141.98 N)}$$

Reactions

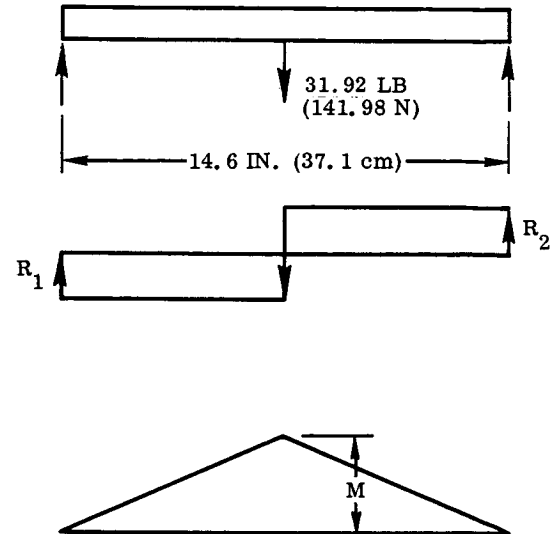
$$R_1 = R_2 = \frac{33.19}{2}$$

$$= 15.96 \text{ pounds (70.99 N)}$$

Bending Moment

$$M = \frac{R_1 L}{2} = \frac{(15.96)(14.6)}{2}$$

$$= 116.51 \text{ in-lb (1316.33 cm-N)}$$



Thermal stresses due to local temperature gradient over section at midspan (unrestrained beam).

Section is as shown on page 244.

CORRUGATED PANEL FORWARD SUPPORT BEAM MATERIAL CR-752

TIME = 2.1040E+02 PRESSURE = -0.

	AREA	X	Z	TEMP	THERMAL STRESS	BENDING STRESS	NET STRESS
1	1.500E-03	2.625E-01	1.000E-02	8.800E+02	7.069E+02	0.	7.069E+02
2	1.500E-03	1.875E-01	1.000E-02	8.885E+02	6.767E+02	0.	6.767E+02
3	1.500E-03	1.125E-01	1.000E-02	8.890E+02	6.465E+02	0.	6.465E+02
4	1.500E-03	3.750E-02	1.000E-02	8.893E+02	6.284E+02	0.	6.284E+02
5	1.650E-03	1.000E-02	6.125E-02	8.897E+02	2.701E+02	0.	2.701E+02
6	1.650E-03	1.000E-02	1.437E-01	8.900E+02	-2.858E+02	0.	-2.858E+02
7	1.650E-03	1.000E-02	2.262E-01	8.897E+02	-8.055E+02	0.	-8.055E+02
8	1.650E-03	1.000E-02	3.087E-01	8.865E+02	-1.155E+03	0.	-1.150E+03
9	1.650E-03	1.000E-02	3.912E-01	8.800E+02	-1.297E+03	0.	-1.297E+03
10	1.650E-03	1.000E-02	4.737E-01	8.710E+02	-1.292E+03	0.	-1.292E+03
11	1.650E-03	1.000E-02	5.562E-01	8.580E+02	-1.048E+03	0.	-1.048E+03
12	1.650E-03	1.000E-02	6.387E-01	8.440E+02	-7.432E+02	0.	-7.432E+02
13	1.500E-03	3.750E-02	6.900E-01	8.290E+02	-1.744E+02	0.	-1.744E+02
14	1.500E-03	1.125E-01	6.900E-01	8.150E+02	6.697E+02	0.	6.697E+02
15	1.500E-03	1.875E-01	6.900E-01	8.010E+02	1.514E+03	0.	1.514E+03
16	1.500E-03	2.625E-01	6.900E-01	7.800E+02	2.318E+03	0.	2.318E+03

FIXX = 2.7039E+04 HAFX = 3.5055E-01
WXP = -4.4926E-04 WYX = 0.

Beam Section at Center Post

The distribution of thermal stresses over the section is as shown.

Overall Bending

$$M = 116.51 \text{ in-lb (1316.33 cm-N)}$$

$$f_b = \pm \frac{Mc}{I} = \frac{(116.51)(0.35)}{0.00186}$$

$$= \pm 21,924 \text{ psi } (\pm 151.2 \text{ MN/m}^2)$$

Combined Stresses Lower Flange

$$f_t = 2830 + 21,924$$

$$= 24,754 \text{ psi (170.1 MN/m}^2)$$

$$F_{tu} [\text{Cb-752 at } 788^\circ \text{ F (693}^\circ \text{ K)}]$$

$$= 44,530 \text{ psi (307.0 MN/m}^2)$$

$$\therefore \text{ M. S. } = \frac{44,530}{(24,754)(1.25)} - 1 = +0.44$$

Upper Flange

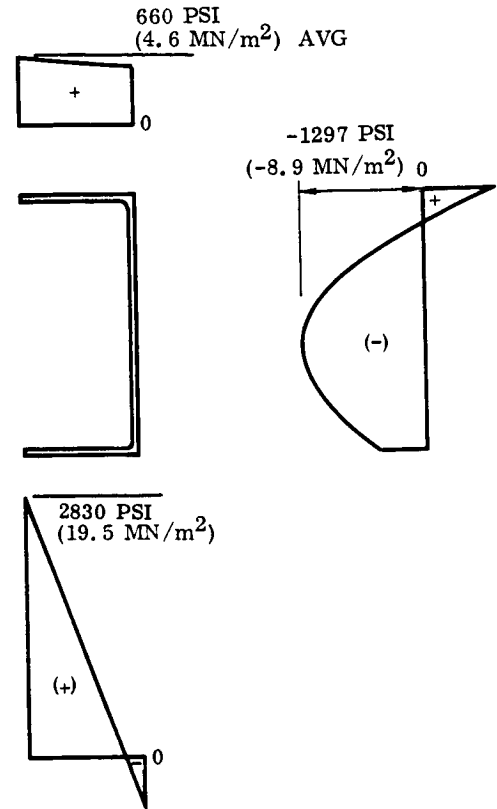
$$f_c = -21,924 + 660 = -21,264 \text{ psi } (-146.6 \text{ MN/m}^2)$$

Flange Critical Buckling Stress

$$F_{cr} = KE \left(\frac{t}{b} \right)^2 = (0.385)(14.51 \times 10^6) \left(\frac{0.02}{0.28} \right)^2 = 28,500 \text{ psi (196.5 MN/m}^2)$$

[For ends and one side simply supported, one side free, $K = 0.385$. $E = 14.51 \times 10^6 \text{ psi}$ (100.0 GN/m^2) at $888^\circ \text{ F (749}^\circ \text{ K)}$]

$$\therefore \text{ M. S. } = \frac{28,500}{(21,264)(1.25)} - 1 = +0.072$$



6.4.5 Panel flutter. — The design criteria for panel flutter are given in Section 2.2.2. Panel flutter analyses are presented for both the tee-stiffened and the corrugated skin panel designs.

The analysis is based on the procedure of Reference 31, for an orthotropic panel with flexible edge supports. The required factor of 1.5 on dynamic pressure is included by incrementing the equivalent airspeed (V_E) by $0.225 V_E$ at constant Mach number and constant altitude as shown in Figure 6-61, and, hence, computing the dynamic pressure using incremented values of V_E . In the region $M = 1$ to $M = 2$ the flutter parameter is computed using $f(M)$ in place of $B = \sqrt{M^2 - 1}$ (Reference 32, Figure 1).

6.4.5.1 Tee-stiffened panel: The material is Cb-752. The maximum value of $q/\sqrt{M^2 - 1}$ occurs during boost at time = 62.5 seconds.

Conditions:

Altitude = 29,000 feet (8839 m)

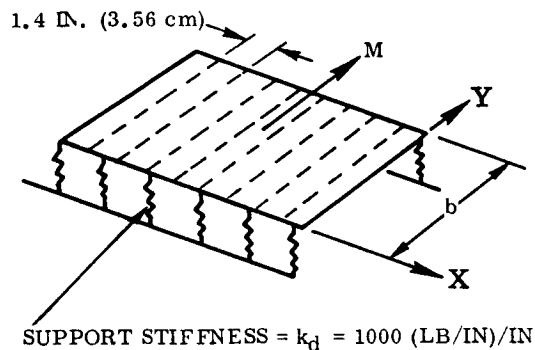
$V = 1150$ ft/sec (350.5 m/sec)

$M = 1.15$

$q = 935$ psf (44.8 kN/m²)

$f(M)^\dagger = 0.482$

$$\lambda = \frac{2qb^3}{D_2 f(M)^{1/2}} = \frac{(2)(935)(12^3)}{(24,900)[(144)(0.482)]^{1/2}} = 1.294$$



where

$$D_2 = \frac{EI}{1.4} = \frac{(15.5 \times 10^6)(0.002323)}{1.4} = 25,719 \text{ in-lb (2906 m-N)}$$

$$K_D = \frac{k_d b^3}{\pi^3 D_2} = \frac{(1000)(12^3)}{\pi^3 (25,719)} = 2.167$$

$$\frac{1}{K_D} = \frac{1}{2.167} = 0.4615$$

[†] Note: $B = \sqrt{M^2 - 1}$ is replaced by $f(M)$ (Reference 32).

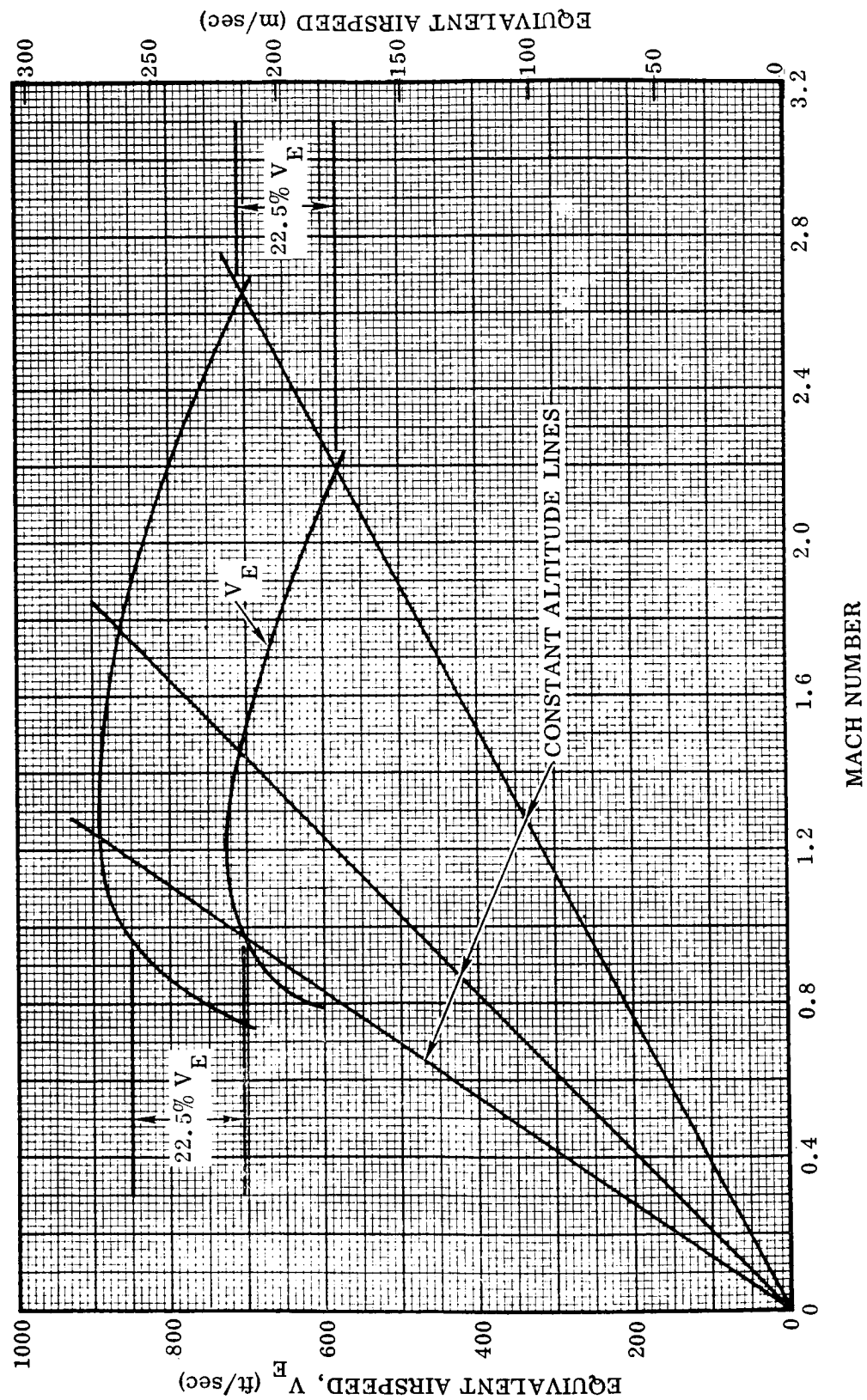


Figure 6-61. Equivalent Airspeed Versus Mach Number During Boost Phase

From Reference 31, Figure 8

$$\lambda_{cr} \sim 60$$

$$\therefore \text{M.S. (panel flutter)} = \frac{\lambda_{cr}}{\lambda} - 1 = \frac{60}{1.294} - 1 = + \text{LARGE}$$

Corrugated Panel: The material is Cb-752. The maximum value of $q \sqrt{M^2 - 1}$ occurs during boost at time = 62.5 seconds.

Conditions:

Altitude = 29,000 feet (8839 m)

V = 1150 ft/sec (350.5 m/sec)

M = 1.15

q = 935 psf (44.8 kN/m²)

f(M)[†] = 0.482

$$\lambda = \frac{2 q b^3}{D_2 [f(M)]^{1/2}}$$

$$= \frac{(2)(935)(12^3)}{(8984.2)[(144)(0.482)]^{1/2}} = 3.6$$

where

$$D_2 = \frac{EI}{3.8} = \frac{(15.5 \times 10^6)(0.00227)}{3.8} = 9259.2 \text{ in-lb (1046 m-N)}$$

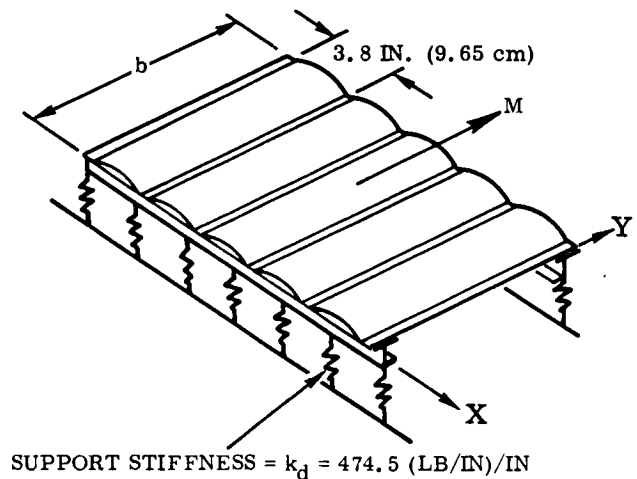
$$K_D = \frac{k_d b^3}{\pi^3 D_2} = \frac{(474.5)(12^3)}{\pi^3 (9259.2)} = 2.856 ; \quad \frac{1}{K_D} = \frac{1}{2.856} = 0.35$$

From Reference 31, Figure 8

$$\lambda_{cr} \sim 80$$

$$\therefore \text{M.S. Panel Flutter} = \frac{\lambda_{cr}}{\lambda} - 1 = \frac{80}{3.6} - 1 = + \text{LARGE}$$

[†] Note: $B = \sqrt{M^2 - 1}$ is replaced by f(M) (Reference 32)



Conclusion. The flutter analysis for both the tee-stiffened and corrugated panels indicates that the panels have large margins of safety for the axial flow condition considered (i. e. , with the panel stiffeners aligned with the flow direction). However, for a cross flow condition these margins could be substantially reduced or eliminated as indicated in Reference 33.

6.4.5.2 Support posts: Each TPS panel is supported by posts at six locations, i. e. , at each corner and at the center of each long side. The four corner posts and the center post at the forward edge react normal pressure loads only; slip joints permit the panel to expand freely. The aft center post serves to locate the panel and hence reacts in-plane inertia as well as normal pressure loads. In addition to supporting the heat shield, it is required that the post provide a minimum heat leakage path to the vehicle structure and permit the installation and removal of a single panel. This latter requirement dictated the minimum post diameters, and hence the minimum wall thicknesses of the tubular posts were established based on manufacturing considerations of structural requirements. The critical design loads are derived from the boost engine vibration spectrum for the heat shield attachment points (Figure 6-5).

Post model and system response: The heat-shield panel and the cantilever support posts are represented as a single-degree-of-freedom system with a frequency determined by idealizing the post as a massless cantilever beam with a concentrated mass at the free end (Figure 6-62). The response of a single-degree-of-freedom system in G_{rms} to an input described by a power spectral density curve is given by

$$G_{rms} = \sqrt{\frac{\pi}{4} f_n \frac{S_N}{\zeta}}$$

where

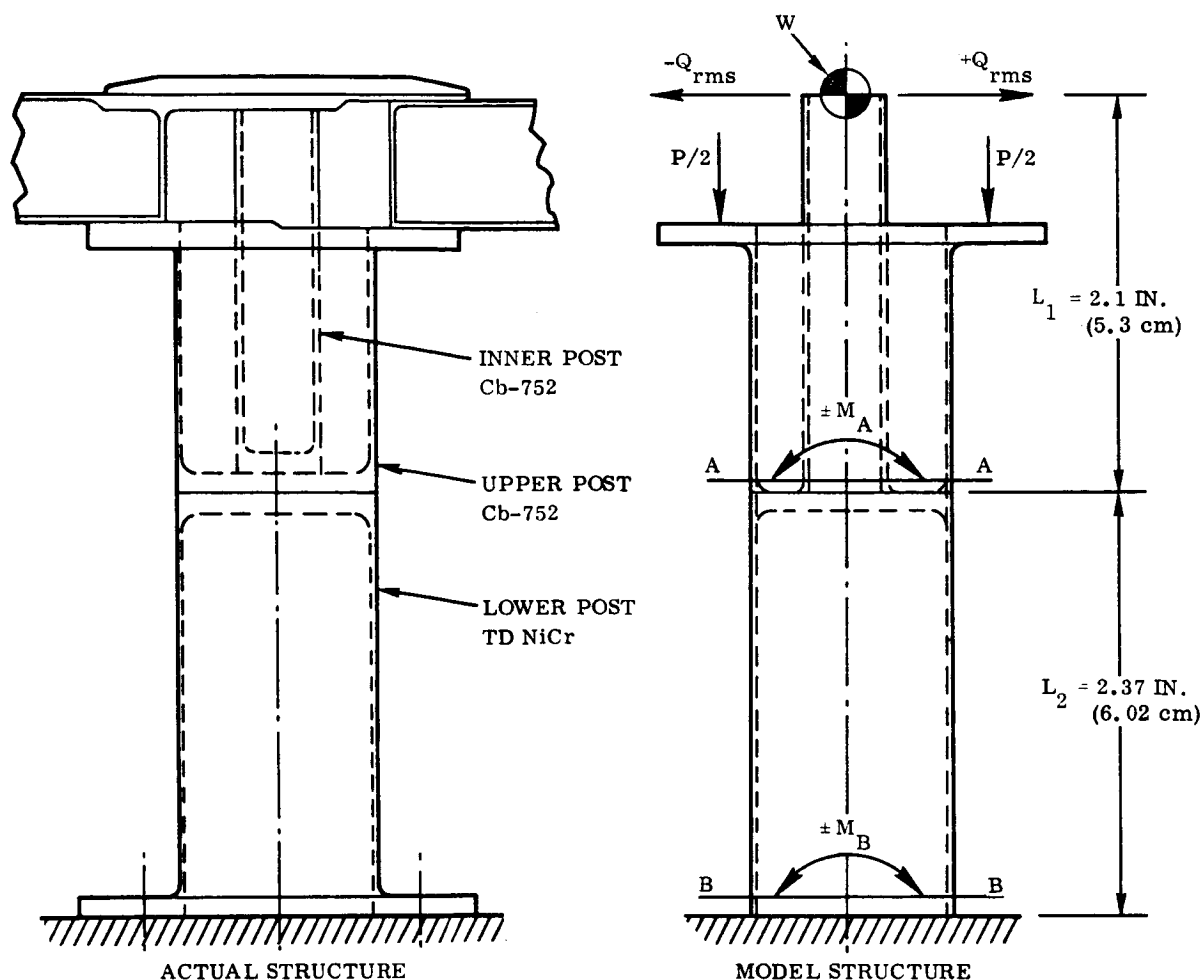
f_n is the system frequency

ζ is the damping ratio

S_N is the amplitude of the power spectral density function in G^2/cps at f_n

Vibration environment: The boost engine vibration environment specified for the heat shield attachment design is shown in Figure 6-5. An exposure of four seconds per flight is assumed.

Design requirements: The support post is designed to satisfy the following requirements.



E = MODULUS OF ELASTICITY

I = MOMENT OF INERTIA

P = AXIAL LOAD

W = WEIGHT OF VIBRATING MASS = PANEL WEIGHT

G_{rms} = rms ACCELERATION

$Q_{rms} = \pm G_{rms} \times W =$ LATERAL LOAD (rms)

$$f_n = \frac{1}{2\pi} \sqrt{\frac{386.4}{\delta_{STATIC}}}$$

$$\delta_{STATIC} = \frac{W L_2}{E_2 I_2} \left(\frac{L_2^2}{3} + L_1^2 + L_1 L_2 \right) + \frac{W L_1^3}{3 E_1 I_1}$$

= LATERAL DEFLECTION UNDER STATIC LOAD W

Figure 6-62. Post Model

- (1) The applied ultimate 3σ -stress in the tube walls must not exceed cutoff values equal to $1.1 F_{cy}$.
- (2) The applied ultimate 3σ -stress must not exceed the load buckling stress of the tube walls.
- (3) The applied limit 1σ -stress must not exceed the allowable fatigue stress determined from random S-N curves for a life equal to four times the required life.
- (4) The tube wall thicknesses must be equal to or greater than specified minimum values [0.012 in. (0.031 cm) for Cb-752 tubes and 0.015 in. (0.038 cm) for TD NiCr tube].

Applied stress levels: The stress levels at sections A-A and B-B (Figure 6-62) are determined for the lateral inertia loads resulting from the acceleration of the concentrated mass. Axial compressive stresses due to the maximum normal pressure loading of 3.0 psi (20.7 kN/m²) on the panel also act at section B-B.

Ultimate 3σ -load condition: The maximum ultimate bending moments M_A and M_B were computed using 3σ values of the lateral load and an ultimate factor of safety of 1.5. A beam column analysis was used. The bending moments are given by

$$M_B = 1.5 (Q L + P y_2)$$

$$M_A = 1.5 (Q L_1 + P y_1)$$

where

$$Q = 3Q_{rms} = \text{lateral load}$$

$$y_i = \text{relative lateral displacement of point of application of axial load and section considered}$$

Limit 1σ -load condition: The alternating bending moments at sections A-A and B-B due to the rms acceleration acting on the weight W are:

$$M_A = Q_{rms} L_1 + P y_1$$

$$M_B = Q_{rms} L + P y_2$$

S-N Data: Random S-N data is used in the post fatigue analysis. The Cb-752 random S-N curve (Figure 6-63) is derived from the alternating stress fatigue data discussed in Section 6.4.6, using the method given in Reference 34. The TD NiCr

data (Figure 6-64) is derived similarly from an S-N curve given in Reference 35. The fatigue allowable stresses were obtained from these curves for the number of applied cycles given by

$$N = 4 (N_F) (T) (f_n)$$

where

N_F = number of flights (= 100).

T = duration of vibration environment per flight (=4 seconds).

f_n = natural frequency of vibrating system.

The factor four is a fatigue life scatter factor.

Post sizing procedure: Minimum post diameters were established by installation requirements. The sizing of the tube wall thickness was accomplished by an iterative procedure as follows:

- (1) Select initial tube wall thicknesses t_A and t_B (minimum gauges).
- (2) Compute tube section properties.
- (3) Compute model structure response.
- (4) Compute bending moments and stresses.
- (5) Check compliance with design requirements.
- (6) Modify t_A and t_B as a function of the most critical applied allowable stress ratio.
- (7) Repeat Steps 2 through 6 until convergency tolerance is met.

Results: The analysis was performed using a computer program based on the previously given procedure. Required tube wall thickness were established for a range of panel weights combined with maximum axial loads of 308.5 and 318.5 pounds (1372.2 and 1416.7 N) corresponding to the maximum design values for the tee-stiffeners and corrugated panels respectively. A damping ratio (ζ) equal to 0.05 was used. Based on prior vibration tests of similar post supported panels in which a damping ratio of 0.1 was obtained, this is considered to be a conservative value (Reference 36). The system response G_{rms} versus panel weight is shown in Figure 6-65. The required thickness t_A of the upper post versus panel weight is shown in Figure 6-66. The minimum gauge of 0.015 inch (0.038 cm) specified for the lower post (t_B) satisfied the structural requirements for all conditions. The ultimate and limit design bending moment distributions for an estimated panel weight of 2.75 pounds (12.49 kg) are given in Figure 6-67.

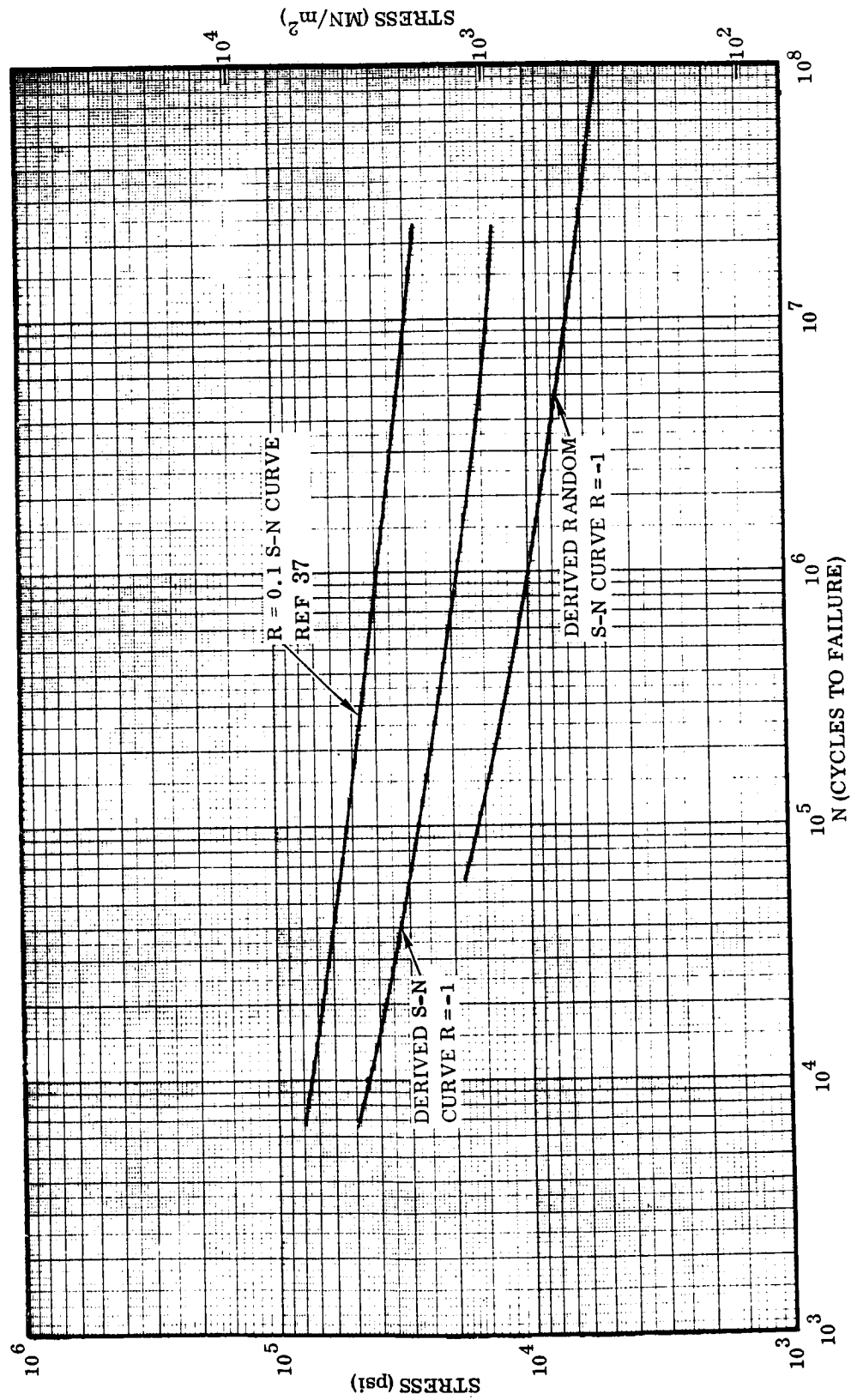


Figure 6-63. $R = 0.1$ and Random S-N Curves for Coated Cb-752

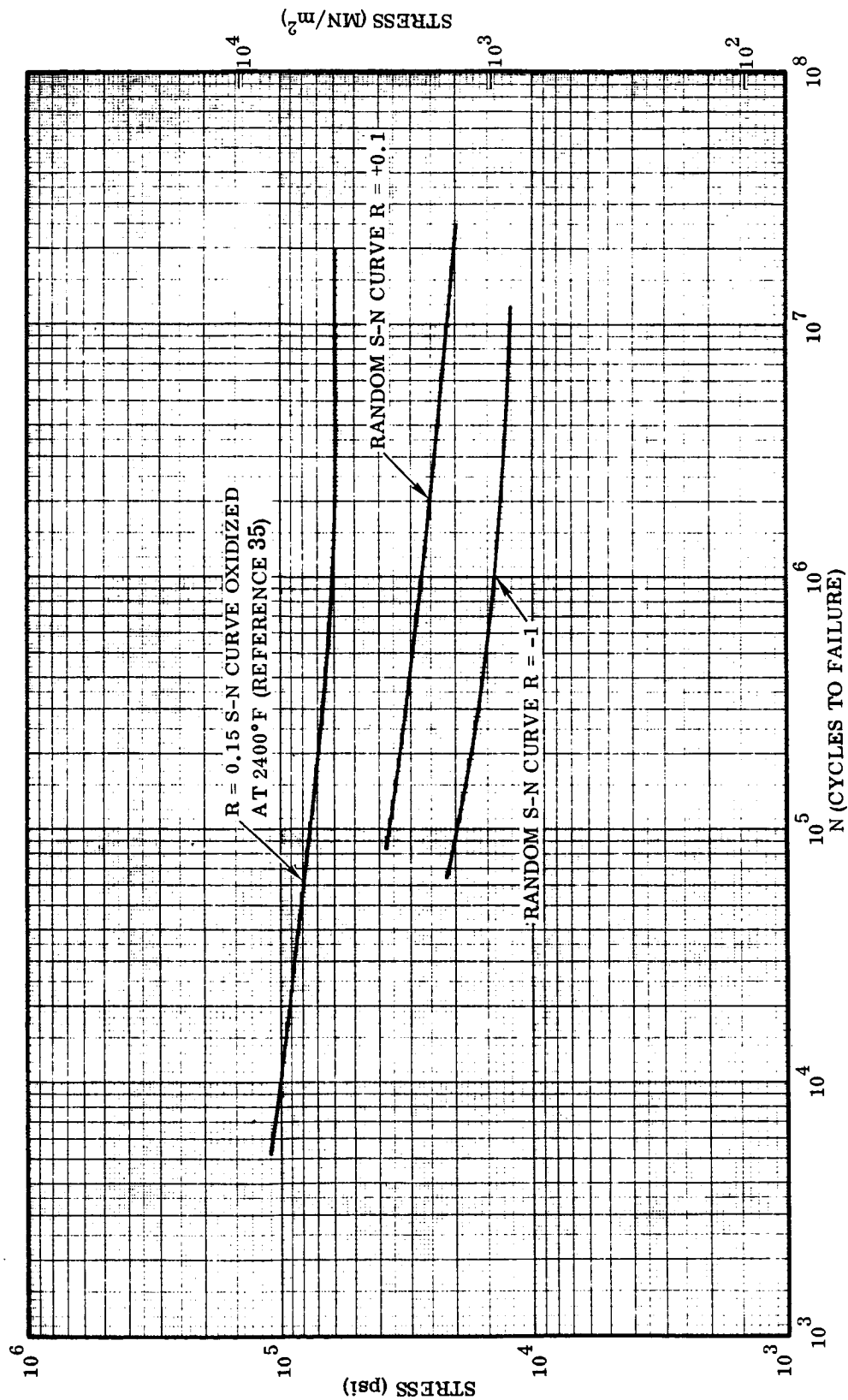


Figure 6-64. R = 0.15 and Random S-N Curves for TD NiCr

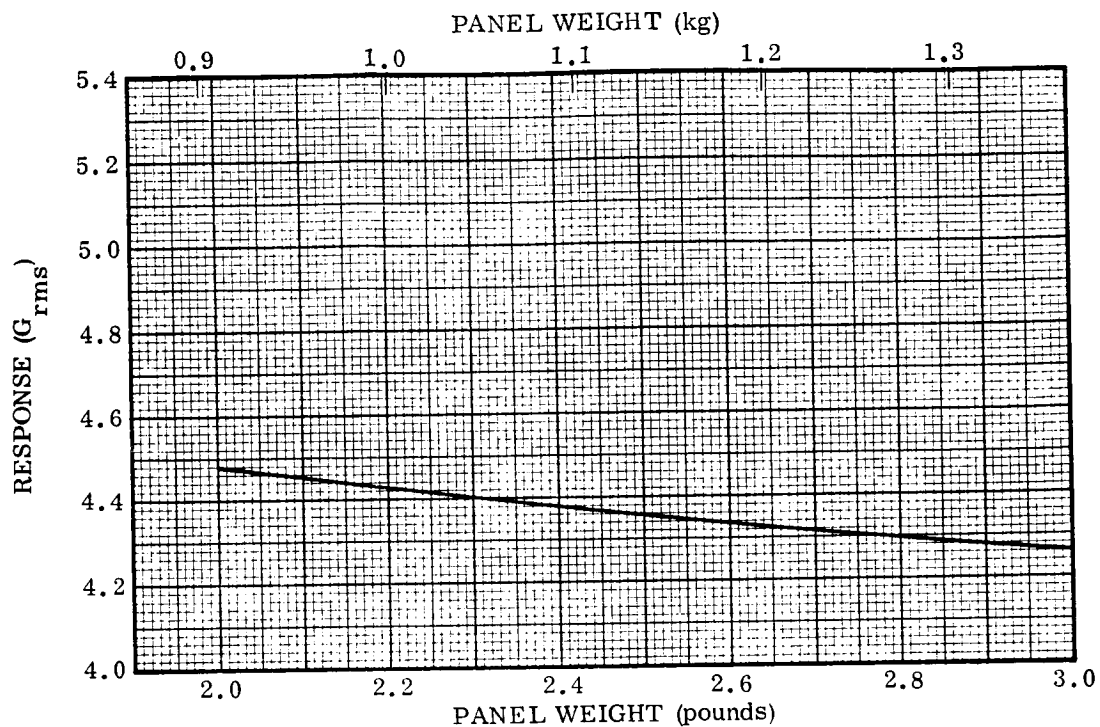


Figure 6-65. Response Acceleration (G_{rms}) Versus Panel Weight

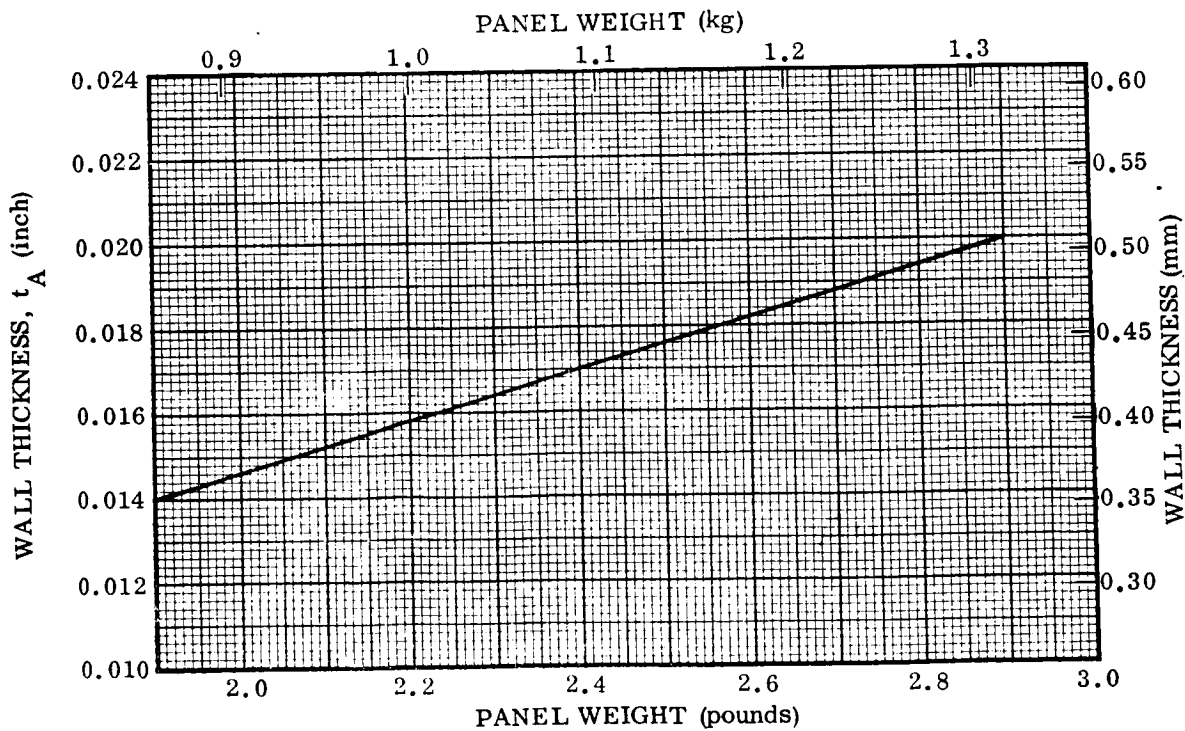


Figure 6-66. Inner Post Wall Thickness Versus Panel Weight

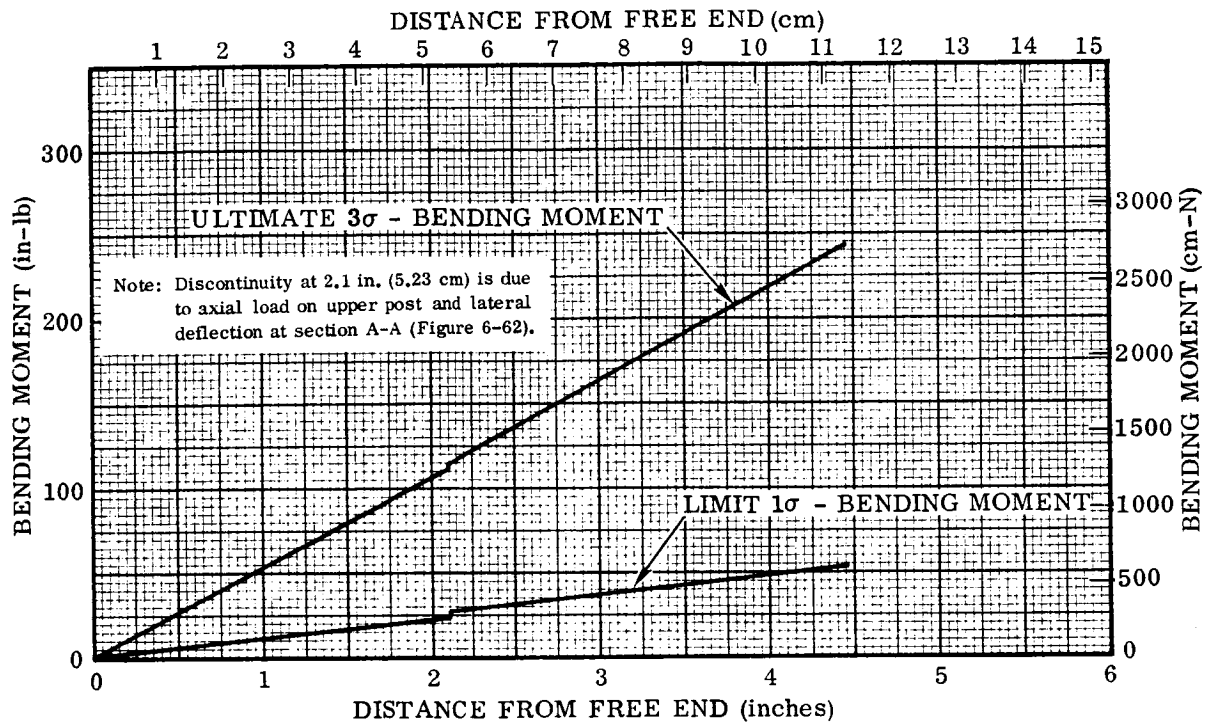


Figure 6-67. Ultimate and Limit Bending Moment Distributions for a 2.75-Pound (12.49 kg) Panel

6.4.5.3 Inner post: - The material is Cb-752.

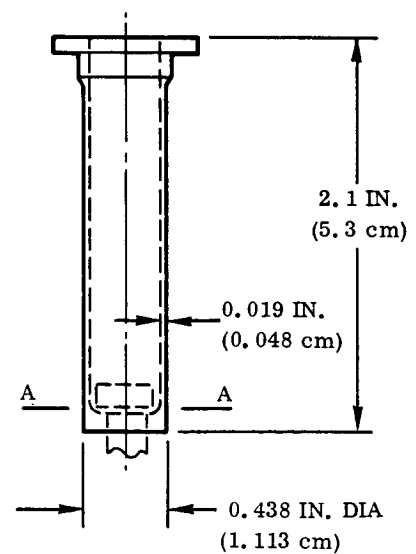
Bending at Section A-A

Ultimate (3σ) Loads

Bending Moment = 112 in-lb (1265 cm-N)

Section Properties

$$\begin{aligned}
 I &= \pi R_M^3 t = \pi (0.2095^3) (0.019) \\
 &= 0.000549 \text{ in}^4 (0.0228 \text{ cm}^4) \\
 f_b &= \frac{M\bar{y}}{I} = \frac{(112)(0.219)}{0.000549} \\
 &= \pm 44,700 \text{ psi } (\pm 308.2 \text{ MN/m}^2)
 \end{aligned}$$



Tube Critical Buckling Stress

$$F_{cr} = K \eta E \frac{t}{b} = 0.3 \eta (15.7 \times 10^6) \left(\frac{0.019}{0.2095} \right) = 427,159 \eta$$

$$\therefore \text{Use cutoff} = 1.1 (F_{cy}) = (1.1)(49,300) = 54,250 \text{ psi } (374.1 \text{ MN/m}^2)$$

$$\therefore \text{M. S.} = \frac{54,250}{44,700} - 1 = +0.215 \text{ (ULT)}$$

Fatigue Analysis (1 σ loads)

Bending moment = ± 25.0 in-lb (± 282.5 cm-N)

$$f_b = \frac{M \bar{y}}{I} = \frac{(25.0)(0.219)}{0.000549} = \pm 9980 \text{ psi } (\pm 68.8 \text{ MN/m}^2)$$

$$f_{\text{fatigue}} = (\pm f_b)(K_T) = (\pm 9980)(1.5) = \pm 14,950 \text{ psi } (\pm 103.1 \text{ MN/m}^2)$$

$$\text{Number of cycles} = 4 (N_F)(t)(f_n) = (4)(100)(4)(78.64) = 1.26 \times 10^5$$

$$\therefore \text{Allowable stress} = \pm 15,350 \text{ psi } (\pm 105.8 \text{ MN/m}^2) \text{ (Figure 6-63)}$$

$$\therefore \text{M. S.} = \frac{15,350}{14,950} - 1 = +0.027 \text{ (FATIGUE)}$$

6.4.5.4 Upper post attachment bolt:
The material is TD NiCr.

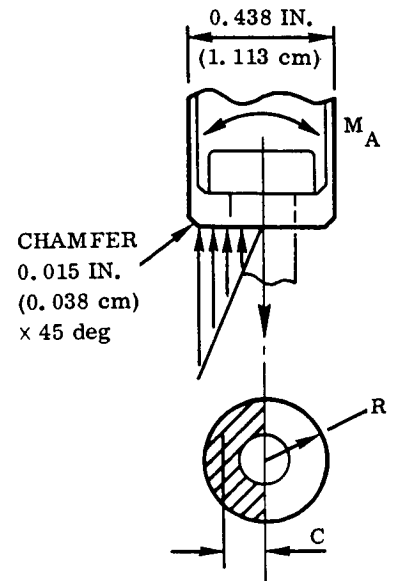
Diameter at base of post

$$= 0.438 - 2(0.015) = 0.408 \text{ inch } (1.036 \text{ cm})$$

\therefore Couple arm = C

$$= \frac{3\pi R}{16} = \frac{3\pi (0.408)}{32}$$

$$= 0.12 \text{ inch } (0.31 \text{ cm})$$



Ultimate Strength Analysis (Upper Attachment Bolt)

Bending moment = 112 in-lb (1265 cm-N)

$$\therefore \text{Bolt load} = \frac{112}{0.12} = 933 \text{ pounds (4150 N)}$$

Root area (10-32 bolt) = 0.018074 in² (0.117 cm²)

$$f_t = \frac{P}{A} = \frac{933}{0.018074} = 51,700 \text{ psi (356.5 MN/m}^2\text{)}$$

$$F_{tu} = 110,000 \text{ psi (758.5 MN/m}^2\text{) (Reference 38)}$$

$$\therefore \text{M. S.} = \frac{110}{(51,700)(1.2^*)} - 1 = +0.77 \text{ (ULT)}$$

Fatigue Analysis (Upper Attachment Bolt)

Bending moment = ± 25.0 in-lb (± 282.5 cm-N)

$$\text{Bolt load} = \frac{M}{C} = \frac{25.0}{0.12} = 208 \text{ pounds (925 N)}$$

$$\text{Fatigue stress} = \frac{P}{A_{\text{net}}} K_T = \left(\frac{208}{0.018074} \right) (2.2) = 25,300 \text{ psi (174.4 MN/m}^2\text{)}$$

where

$$K_T = 2.2 \quad (\text{Reference 39})$$

Number of cycles

Bolt experiences two cycles of axial load for each bending cycle.

$$\therefore N = 2 (1.258 \times 10^5) = 2.516 \times 10^5$$

\therefore Allowable stress = 31,000 psi (213.7 MN/m²) (see Figure 6-64).

$$\text{M. S.} = \frac{31,000}{25,300} - 1 = +0.22 \text{ (FATIGUE)}$$

*Fitting factor.

6.4.5.5 Lower post: The material is TD NiCr.

Bending at Section C-C

Ultimate (3σ) Loads

Bending moment = 243 in-lb (2745 cm-N) (Figure 6-67)

Axial load = 462.7 pounds (2058.1 N)

$$I = \pi R^3 t = \pi (0.5075^3) (0.015) = 0.00616 \text{ in}^4 (0.256 \text{ cm}^4)$$

$$A = \pi D t = \pi (1.015) (0.015) = 0.0478 \text{ in}^2 (0.308 \text{ cm}^2)$$

$$f_c = \frac{P}{A} + \frac{M\bar{y}}{I} = \frac{462.7}{0.0478} + \frac{(243)(0.5075)}{0.00616} = 9680 + 20,020 = 29,700 \text{ psi } (204.8 \text{ MN/m}^2)$$

Tube Critical Buckling Stress

$$F_{cr} = K \eta E \frac{t}{R} = 0.3 \eta (21.0 \times 10^6) \left(\frac{0.015}{0.5075} \right) = 186,206 \eta$$

$$\therefore \text{Use cutoff} = 1.1 (F_{cy}) = 91,570 \text{ ksi } (631.4 \text{ MN/m}^2) \text{ (Reference 35)}$$

$$\therefore \text{M.S.} = \frac{91,570}{29,700} - 1 = +2.08$$

Fatigue Analysis (1σ) Loads

Bending moment = 53 in-lb (598.8 cm-N)

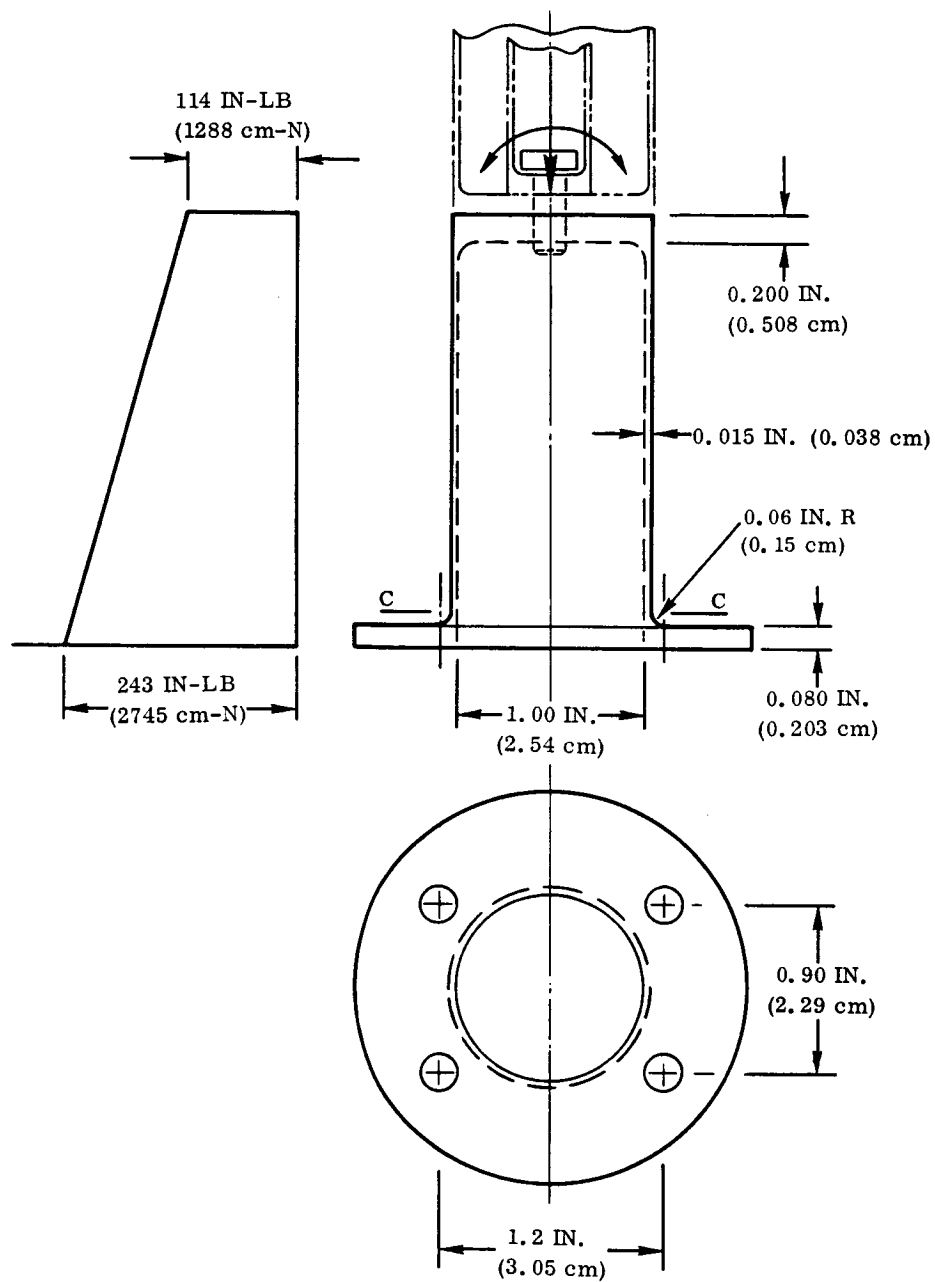
Axial load 308 pounds (1370 N)

Fatigue Stresses

$$\text{Axial compression } f_c = \frac{P}{A} = \frac{308}{0.0478} = 6440 \text{ psi } (44.4 \text{ MN/m}^2)$$

$$\text{Bending } f_b = \pm \frac{M\bar{y}}{I} = \frac{(53)(0.5075)}{0.00616} = \pm 4360 \text{ psi } (\pm 30.1 \text{ MN/m}^2)$$

The axial compression stress is greater than the bending stress; hence, the net stress is always compressive. Since cycling in compression gives negligible damage, the axial load is taken as zero in the fatigue analysis.



Stress Concentration Factor (see Reference 35).

$$\frac{R}{t} = \frac{0.06}{0.015} = 4, \quad \frac{h}{R} = \text{LARGE}$$

$$\therefore K_T \approx 1.5$$

$$\text{Number of cycles} = f_n t N_F S_F = (78.7)(4.0)(100)(4) = 1.26 \times 10^5$$

where

f_n = Natural frequency, Hertz

t = Exposure time per flight

N_F = Number of flights

S_F = Scatter factor

$$\text{Fatigue stress} = (f_b)(K_T) = (\pm 4360)(1.5) = \pm 6540 \text{ psi } (\pm 45.1 \text{ MN/m}^2)$$

$$\text{Allowable stress} = 29,000 \text{ psi } (199.9 \text{ MN/m}^2) \quad (\text{see Figure 6-64}).$$

\therefore M.S. (fatigue) = + LARGE

Stresses in Brazed Joint at Flange

Condition: ultimate (3σ) loads

Applied Loads

$$P = 318.5 \text{ pounds } (1416.7 \text{ N})$$

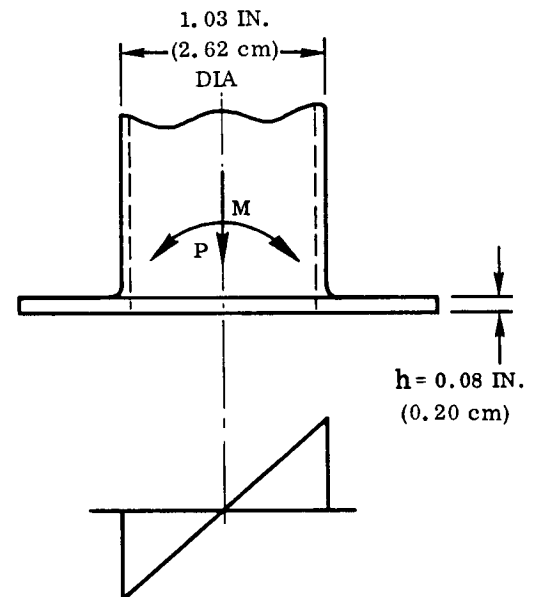
$$M = 243.0 \text{ in-lb } (2745 \text{ cm-N})$$

The shear stresses on the annular joint area are assumed distributed in the same manner as the bending and axial stress in the tube.

$$\begin{aligned} f_{s_{\max}} &= \frac{P}{\pi D_h} + \frac{MR}{\pi R^3 h} \\ &= \frac{318.5}{\pi (1.03)(0.08)} + \frac{243}{\pi (0.515^3)(0.08)} \\ &= 1230 + 3645 = 4875 \text{ psi } (33.6 \text{ MN/m}^2) \end{aligned}$$

$$\text{Allowable stress} = 20,000 \text{ psi } (138 \text{ MN/m}^2)$$

\therefore M.S. = + LARGE



$$R_B = (0.6^2 + 0.45^2)^{1/2} = 0.75 \text{ inch (1.91 cm)}$$

$$\theta = \tan^{-1} \left(\frac{0.45}{0.60} \right) = 36.87^\circ$$

$$A = 0.50 + 0.50 \cos \theta$$
$$= 0.9 \text{ in. (2.29 cm)}$$

Bending moment = 243 in-lb (2745 cm-N)
ultimate (Figure 6-67)

$$\text{Couple loads} = \frac{243}{A} = 270 \text{ pounds (1201 N)}$$

$$\text{Load/bolt} = \frac{270}{2} = 135 \text{ pounds (601 N)}$$

$$\begin{aligned}\text{Bolt reaction (R}_B\text{)} &= \frac{135 (0.243 + 0.207)}{0.207} \\ &= 294 \text{ pounds (1308 N)}\end{aligned}$$

Allowable load NAS 1003 bolt
= 2530 pounds (11.3 kN)

$$\therefore \text{M.S. (bolt tension)} = + \text{LARGE}$$

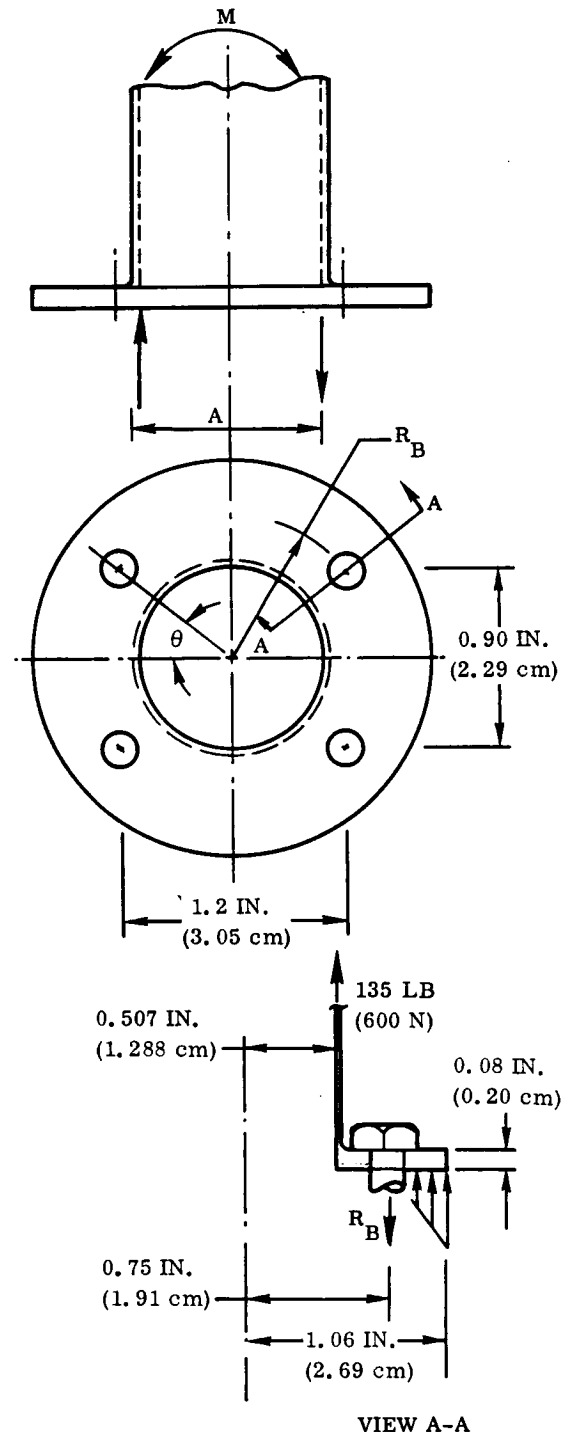
Flange Bending

Bending moment at bolt centerline

$$= 32.8 \text{ in-lb (371 cm-N)}$$

Assuming 0.75-inch (1.91 cm) width of flange is effective,

$$f_b = \frac{6M}{bt^2} = \frac{(6)(32.8)}{(0.75)(0.08^2)} = 41,000 \text{ psi } (282.7 \text{ MN/m}^2)$$



$$\text{Allowable } F_B = F_{tu} = 125,000 \text{ psi } (861.9 \text{ MN/m}^2) \quad (\text{Reference 35})$$

$$\therefore \text{M. S.} = + \text{LARGE}$$

Fatigue Analysis

$$\text{Bending moment } (1\sigma) = 53.0 \text{ in-lb } (599 \text{ cm-N})$$

$$\therefore \text{Flange bending stress} = f_{ult} \left(\frac{M_{fatigue}}{M_{ult}} \right) = 41,000 \left(\frac{53}{243} \right) = 8930 \text{ psi } (61.57 \text{ MN/m}^2)$$

$$\text{Fatigue stress} = f_b K_T = (8930)(3) = 26,790 \text{ psi } (184.7 \text{ MN/m}^2)$$

$$\text{Number of cycles} = 1.26 \times 10^5$$

$$\therefore \text{Allowable stress} = 35,500 \text{ psi } (244.8 \text{ MN/m}^2) \quad (\text{Figure 6-64}).$$

$$\therefore \text{M. S.} = \frac{35,500}{26,790} - 1 = +0.32$$

6.4.5.6 Inner post retainer: The material is Cb-752.

Design Condition: 2.0 psi (13.8 kN/m²) burst

Post reaction = 308.5 pounds (1372 N) ultimate

Loads on retainer are assumed to act at points of intersection of panel ribs and edge members.

Section A-A

$$\text{Bending moment} = \frac{308.5}{2} (0.70 - 0.125) = 88.69 \text{ in-lb } (1002 \text{ cm-N})$$

Section Properties

$$A = 0.1(1.70 - 0.39) - \frac{(0.064)(0.5)}{2} = 0.131 - 0.016 = 0.115 \text{ in}^2 \quad (0.74 \text{ cm}^2)$$

$$\bar{y} = \frac{(0.131)(0.05) - (0.016)(0.0787)}{0.115} = 0.046 \text{ inch } (0.117 \text{ cm})$$

$$I = \frac{(1.31)(0.1^3)}{12} + 0.115(0.05 - 0.046)^2$$

$$- \left[\frac{(0.064^3)(0.5)}{36} + 0.016(0.0786 - 0.046)^2 \right]$$

$$= 0.00009 \text{ in}^4 (0.00374 \text{ cm}^4)$$

$$f_b = \frac{M(h-y)}{I}$$

$$= \frac{88.69(0.1 - 0.046)}{0.00009}$$

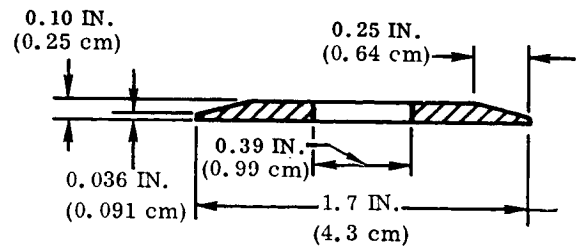
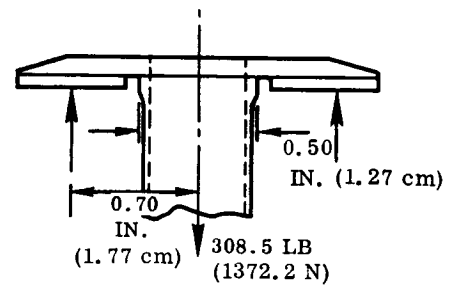
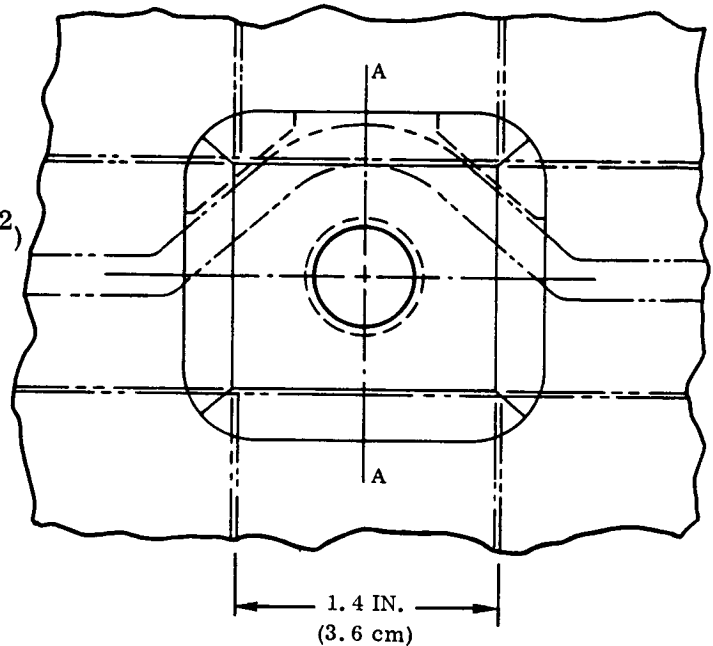
$$= 52,700 \text{ psi } (363.4 \text{ MN/m}^2)$$

$$\text{Allowable } F_B = F_{tu}$$

$$= 54,860 \text{ psi } (378.3 \text{ MN/m}^2)$$

[Cb-752 at 340° F (444° K)]

$$\therefore \text{M. S.} = \frac{54,860}{52,700} - 1 = +0.04$$



SECTION A-A

6.4.5.7 Tee-stiffened panel retainer assembly: The material is Cb-752.

Condition: 2.0 psi (13.8 kN/m²) (burst)

Reaction at corner post = 267.5 pounds (1189.8 N) ultimate

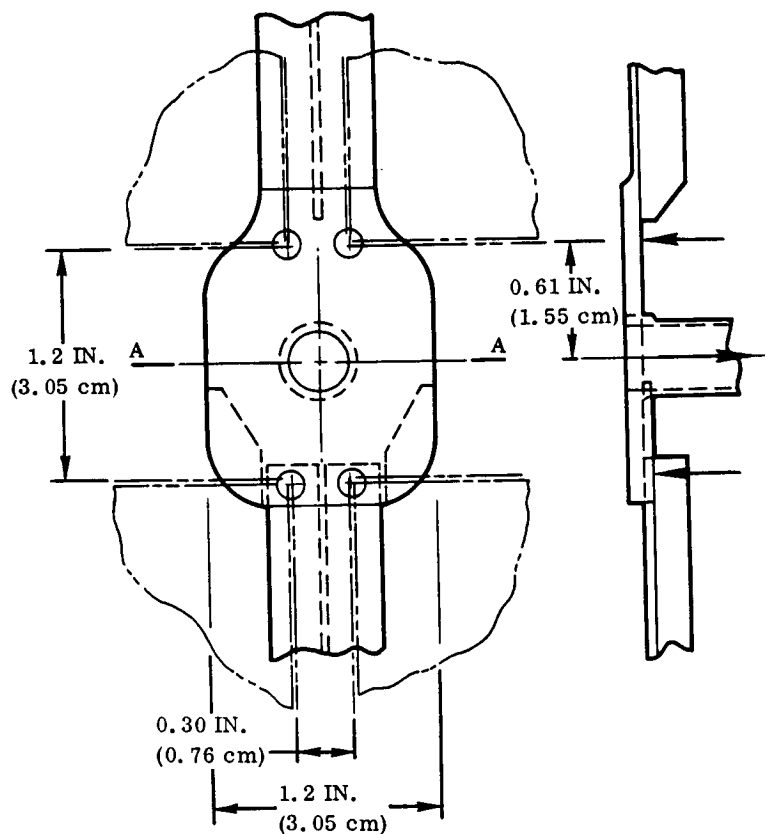
Bending at Section A-A

$$\text{Bending moment} = \frac{267.5}{2} (0.61 - 0.125) = 65.0 \text{ in-lb (734 cm-N)}$$

$$f_b = \frac{6M}{Bt^2} = \frac{(6)(65)}{(1.2 - 0.4)(0.096)} = 52,900 \text{ psi (374.7 MN/m}^2\text{)}$$

$$\text{Allowable } F_B = F_{tu} = 54,860 \text{ psi (378.3 MN/m}^2\text{) [Cb-752 at 340}^\circ\text{F (444}^\circ\text{K)]}$$

$$\therefore \text{M.S.} = \frac{54,860}{52,900} - 1 = +0.035 \text{ (ULT)}$$



6.4.6 Acoustic fatigue analysis. - The acoustic fatigue analyses of the tee-stiffener and the corrugated columbium heat shields were made using Convair Aerospace computer program P5454. This program computes sound pressure levels from basic engine and aerodynamic data, computes the dynamic response characteristics of the TPS panels as a function of the material properties, geometry, damping and restraint, computes equivalent static and dynamic stresses, and computes fatigue life. A description of the program is given in Appendix C.

The analysis is made for the acoustic excitation derived from the booster engines during liftoff and ascent. The total exposure times for 100 flights are:

Liftoff - 1000 seconds

Ascent - 4000 seconds

The acoustic input from other sources (e.g., turbulent boundary layer noise, jet flyback noise) is considered to be negligible (Reference 40). The analysis was conservatively made for a total exposure of 5000 seconds under the conditions at liftoff.

The input parameters used to compute the sound pressure levels due to rocket engine noise based on the Convair B9U booster (Reference 41) are:

Rocket engine thrust = $(12)(550,000) = 6,600,000$ lb (29.4 MN)

Weight flow = $(12)(1372) = 16,464$ lb/sec (7475 kg/sec)

Equivalent nozzle exit diameter = 20 ft (6.1m)

Local speed of sound = 1116 ft/sec (340 m/sec)

Distance to nozzle exit (X_i) = 287 ft (87.5m)

Distance from exit to reflecting surface (D_{ref}) = 60 ft (18.3m)

Local vehicle diameter (D_{veh}) = 5.3 ft (1.6m)

The vehicle configuration is shown in Figure 6-68. The fatigue data used in the analysis is presented in Section 6.4.5.

6.4.6.1 Results: The tee-stiffened and corrugated panel installations considered are as shown in Figures 6-27 and 6-28 respectively. In both panels the transverse reinforcing ribs or corrugations are supported by integral beams and posts at the long sides. The short sides of the panels are unsupported. In the acoustic fatigue analysis the panel stiffnesses and stresses are based on the estimated effective material thickness after 100 exposure cycles. The mass distribution is based on the initial stock thickness plus the coating mass.

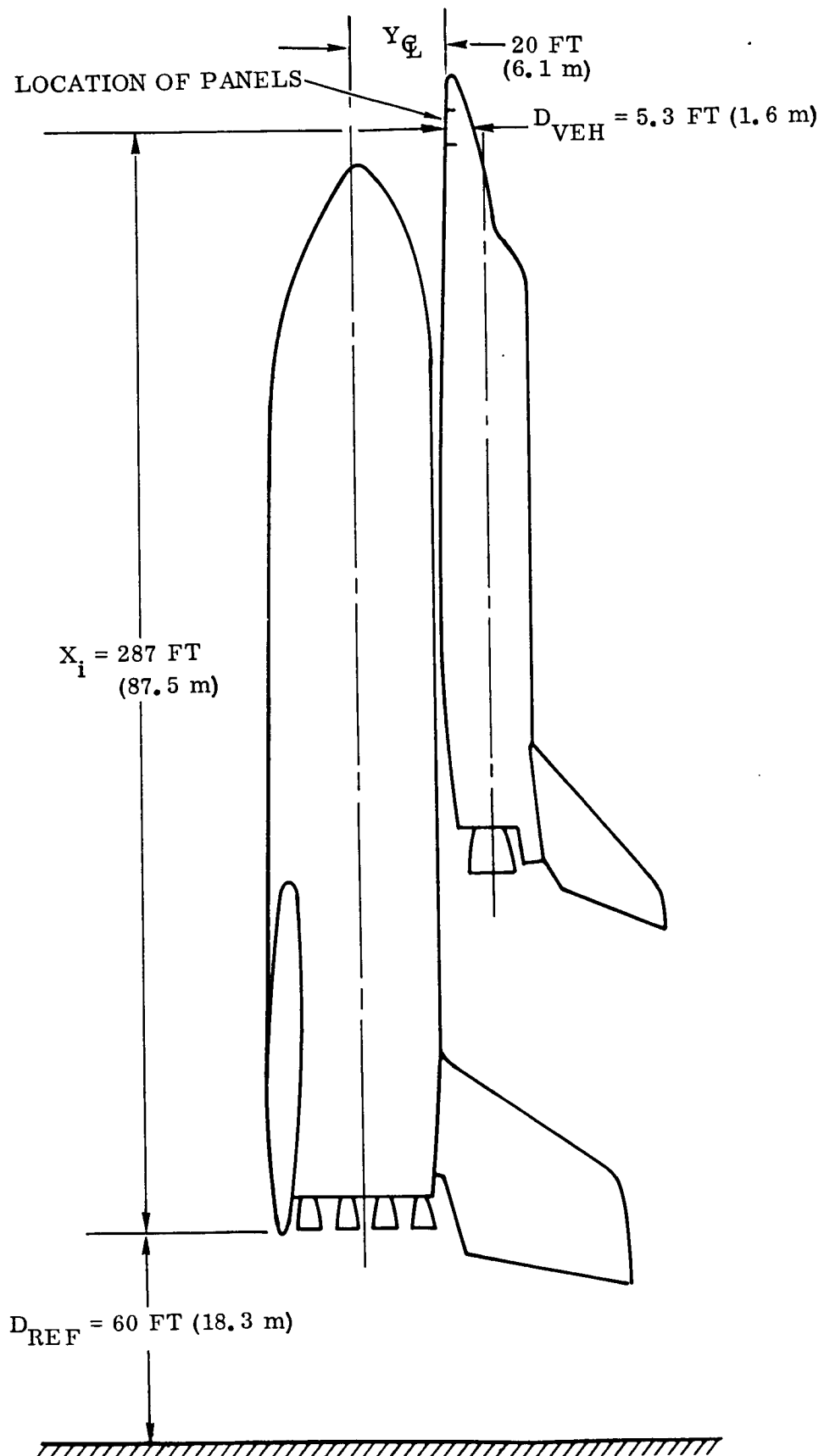
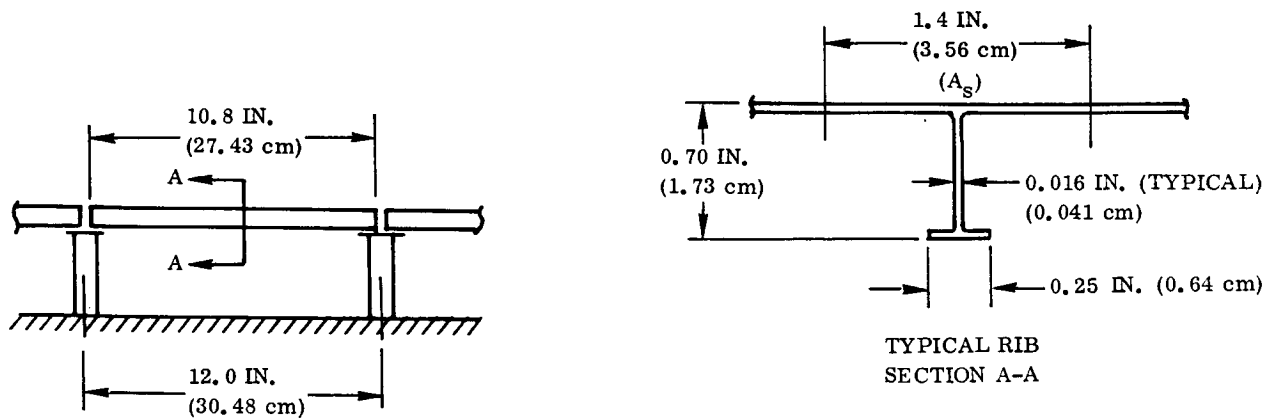


Figure 6-68. Mated Vehicle Configuration (on Pad)

Tee-Stiffened Panel

The panel support configuration and typical rib cross section are as shown.



Two independent analyses were made for this panel:

- (1) An overall analysis of the integrally stiffened 12 by 16 in. (30.48 by 40.64 cm) panel with simple supports at the long sides.
- (2) A local analysis of the rectangular isotropic skin panels 1.4 by 10.8 in. (3.56 by 27.43 cm) between stiffeners assuming all sides are simply supported.

Overall Analysis

Panel bending stiffness per inch width

$$= \frac{EI}{A_s} = \frac{(15.5 \times 10^6) (0.002323)}{1.4} = 25,719 \text{ in-lb (29,052 cm-N)}$$

Panel mass (m) per square inch

$$= \frac{1}{A_G} \{A_i \rho + A_c w_c\}$$

where

A_i = Area of rib cross section based on initial sheet thickness of 0.020 in² (0.051 cm²)

A_c = Surface area of rib and skin per inch run

ρ = Density of Cb-752 = 0.326 lb/in³ (9.02 g/cm³)

$$w_c = \text{Coating weight} = 0.00284 \text{ lb/in}^2 (19.6 \text{ N/m}^2)$$

$$G = 386.4 \text{ in/sec}^2 (981.5 \text{ cm/sec}^2)$$

$$A_s = \text{Rib spacing}$$

$$\therefore m = \frac{1}{(1.4)(386.4)} \left\{ \frac{(0.037)(0.02)}{(0.016)} [0.326] + 2(1.4 + 0.66 + 0.25)(0.000284) \right\}$$

$$= 0.0000303 \text{ in-lb sec}^2/\text{in}^2 (0.0000530 \text{ cm-N sec}^2/\text{cm}^2)$$

Computer program P5454 yields:

Panel fundamental frequency (f) = 388.0 Hz

Sound pressure level at panel frequency (SPL_f) = 110.8 dB

Critical stress (F_{cr}) = 170.9 psi (1178 kN/m²)

Number of stress reversals (N_{cr}) = 4.91 × 10⁶

Allowable stress (F_{all}) = 15,570 psi (107.4 MN/m²)

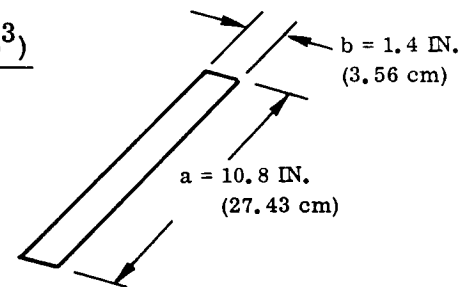
∴ M.S. = + LARGE

Local analysis of skin panels between ribs.

Panel bending rigidity

$$D_X = D_Y = D = \frac{E t^3}{12(1-h^2)} = \frac{(15.5 \times 10^6)(0.016^3)}{12(1-0.3^2)}$$

$$= 5.8 \text{ in-lb} (6.6 \text{ cm-N})$$



Panel mass (m) per square inch

$$= \frac{1}{G} (t_i \rho + 2 w_c)$$

$$= \frac{1}{386.4} [(0.02)(0.326) + (2)(0.00284)] = 3.157 \times 10^{-5} \text{ in-lb sec}^2/\text{in}^2$$

$$(0.0000553 \text{ cm-N sec}^2/\text{cm}^2)$$

Computer program P5454 yields:

Panel fundamental frequency (f) = 872 Hz

Sound pressure level at panel frequency (SPL_f) = 102.5 dB

Critical stress (F_{cr}) = 262.5 psi (1810 kN/m²)

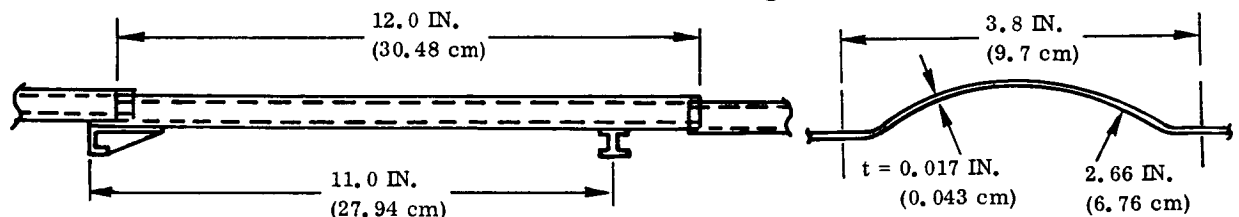
Number of stress reversals (N_{cr}) = 8.875×10^6

Allowable stress (F_{all}) = 14,083 psi (97,102 kN/m²)

\therefore M.S. = + LARGE

Corrugated Panel

The panel support configuration and typical corrugation cross section are as shown.



Panel bending stiffness per inch width

$$= \frac{EI}{A_c} = \frac{(15.5 \times 10^6)(0.002326)}{3.8} = 9.488 \times 10^4 \text{ in-lb (107.2 m-N)}$$

Panel mass (m) per square inch

$$= \frac{1}{A_s G} (A_i \rho + A_c w_c)$$

where

A_i = Area of corrugation cross section, based on initial sheet thickness of 0.021 in. (0.053 cm)

A_c = Surface area of corrugation per inch run

ρ = Density of Cb-752 = 0.326 lb/in³ (9.02 g/cm³)

w_c = Coating weight = 0.000284 lb/in² (1.96 N/m²)

G = 386.4 in/sec² (981.5 cm/sec²)

$$\therefore m = \frac{1}{3.8 \times 386.4} \left(\frac{(0.0681)(0.021)}{0.017} + \frac{(0.0681)(2)}{0.017} (0.000284) \right)$$

$$= 2.023 \times 10^{-5} \text{ in-lb sec}^2/\text{in}^2 (0.354 \mu\text{m-Nsec}^2/\text{cm}^2)$$

Computer program P5454 yields:

Panel fundamental frequency (f) = 281.6 Hz

Sound pressure level at panel frequency (SPL_f) = 115.0 dB

Critical stress (F_{cr}) = 1274.5 psi (8788 kN/m²)

Number of stress reversals (N_{cr}) = 1.561 × 10⁶

Allowable stress (F_{all}) = 17,859 psi (123 MN/m²)

∴ M.S. = + LARGE

6.4.6.2 Conclusions: Based on the preceding analysis both the tee stiffened and corrugated panel designs are shown to have large margins of safety for acoustic fatigue arising from excitation due to booster engine noise. However, the analysis considers only the effect of concurrent thermal and mechanical load cycles in that the estimated thickness of the Cb-752 substrate on the one-hundredth flight is used. Insufficient data on the degradation of fatigue properties due to thermal cycling and the resulting coating diffusion, creep strain, and oxidation are available to permit an evaluation of these effects.

6.4.6.3 S-N data: The acoustic fatigue analysis procedure requires conventional S-N data for reversed loading ($R = F_{\min}/F_{\max} = -1$). Since all published data for coated Cb-752 material is for tension-tension loading ($R = 0$) it is necessary to extrapolate to obtain the required values. The basic S-N data used in this analysis is for a stress ratio $R = +0.1$ taken from Figure 101 of Reference 37. The extrapolated values for $R = -1$ are derived using Gerber's parabolic equation:

$$\sigma_a = \alpha \left[1 - \left(\frac{\sigma_m}{F_{tu}} \right)^2 \right]$$

where

α = value of σ_a when $\sigma_m = 0$ ($R = -1$)

σ_a = alternating stress amplitude

σ_m = mean stress

Hence the allowable alternating stress for a selected fatigue life is given by:

$$\alpha = \frac{\sigma_a}{1 - \left(\frac{\sigma_m}{F_{tu}} \right)^2}$$

The basic data and the derivation of α for a range of cyclic lives (N) are:

1	2	3	4	5	6
N (cycles)	σ_{\max} R = +0.1 Ref 37 (psi)	σ_{\min} $0.1 \times \textcircled{2}$ (psi)	σ_m $(\textcircled{2} + \textcircled{3})/2$ (psi)	σ_a $(\textcircled{2} - \textcircled{3})/2$ (psi)	α R = -1 (psi)
10^4	74,000	7400	40,700	33,300	44,930
10^5	53,000	5300	29,150	23,850	27,500
10^6	39,500	3950	21,725	17,775	19,190
10^7	30,000	3000	16,500	13,500	14,100

The extrapolation is shown graphically on a constant life fatigue diagram (Figure 6-69). The derived S-N curve is given in Figure 6-63.

6.4.7 Creep. - Preliminary flight simulation creep test results (Ref. 3) which became available during the design of small-size TPS panels, yielded creep strains much larger than values predicted using preliminary creep data. Based on these results it was considered that no reliable creep analysis could be made until completion of the creep tests and analysis of the data. Hence a maximum limit stress of 20,000 psi (138 MN/m²) was used for panel design in lieu of a creep analysis. This stress corresponds to the maximum pressure [3.0 psi (20.7 kN/m²)] in the flight simulation test profile, Figure 6-8, and is based on the effective section in the one-hundredth flight. The corresponding stress at time of maximum temperature [2400° F at 0.15 psi (1589° K at 1.03 kN/m²)] based on the estimated effective section after coating is 846 psi (5.8 MN/m²). (The nominal stress level in the simulation tests at this time was 1075 psi (7.4 MN/m²)).

The design stress is based on the assumption that the relationship $\dot{\epsilon} \sim \sigma^n$ is applicable and hence a small reduction in stress would yield a relatively large reduction in creep strain. Final test results indicate the relationship $\dot{\epsilon} \sim \sigma$ rather than σ^n ; hence, permissible values of creep strain and deflection may be exceeded for the corrugated panel design. The estimated maximum creep strain for a stress of 20,000 psi (138 MN/m²) is derived below from the preliminary simulation test results for Cb-752/R-512E. Using the relationship previously stated, an approximate creep deflection analysis for the corrugated panel is also given.

Maximum test load = 140 pounds (623 N)

Estimated effective area of nominal [0.015 in. by 0.5 in. (0.038 cm by 1.27 cm)] specimen after 100 flights = 0.5 (0.015 - 0.004) = 0.0055 in² (0.0355 cm²).

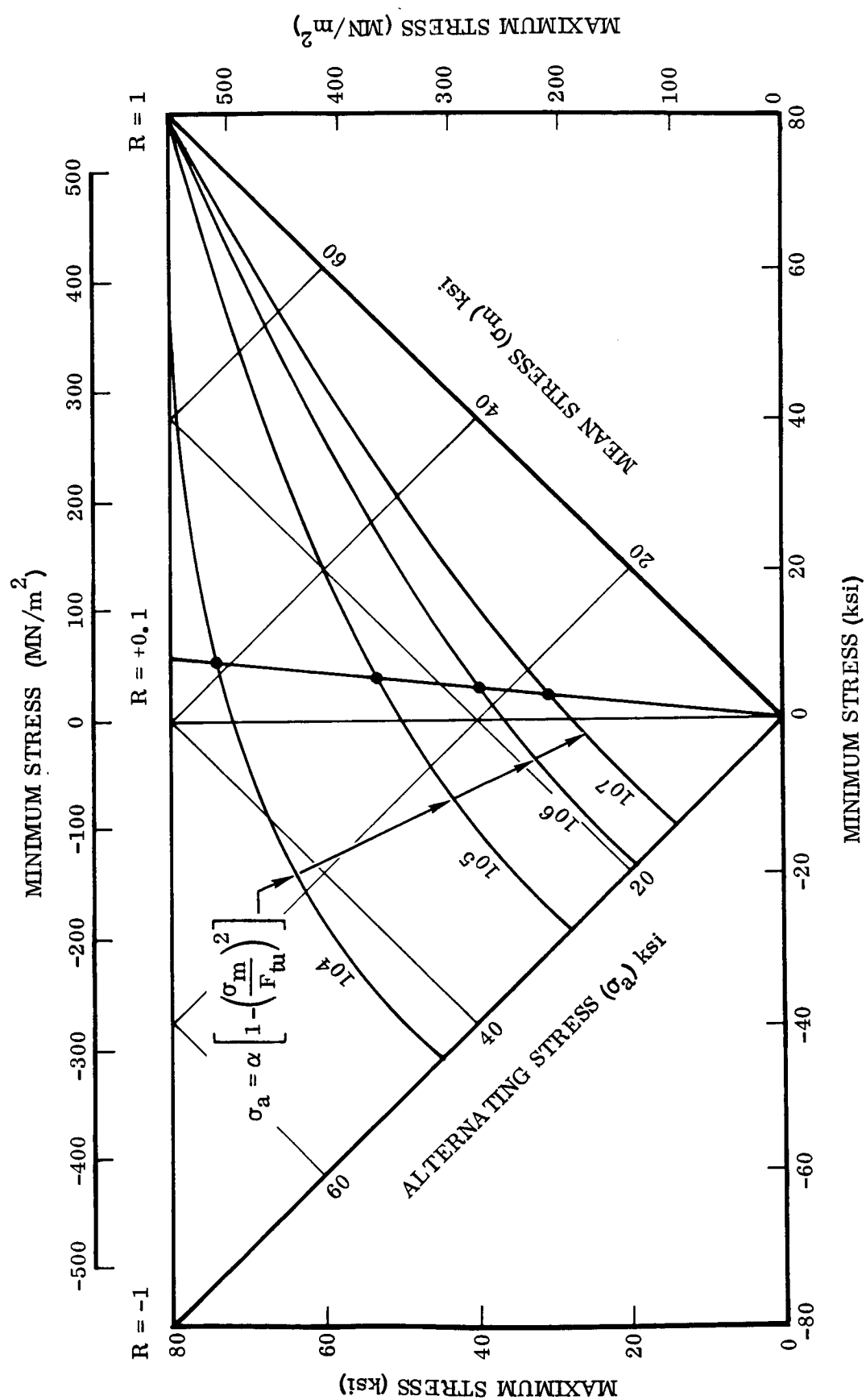


Figure 6-69. Constant Life Fatigue Diagram for Coated Cb-752

$$\therefore \text{Maximum test stress} = \frac{140}{0.0055} = 25,455 \text{ psi (175.5 MN/m}^2\text{)}$$

$$\text{Creep strain (100 flights)} = 2.2\%$$

The majority of the creep in the test cycle occurs in the time interval at maximum temperature and minimum stress; hence, the relationship $\dot{\epsilon} \sim \sigma^n$ was assumed. Hence total creep strain $\epsilon \sim \sigma^n$.

Taking $n = 4.5$

$$\epsilon = K \sigma^{4.5} = 0.022$$

$$\therefore K = \frac{\epsilon}{\sigma^{4.5}} = \frac{0.022}{25,455^{4.5}} = 3.258 \times 10^{-22}$$

Hence for $\sigma = 20,000 \text{ psi (138 MN/m}^2\text{)}$

$$\begin{aligned} \epsilon_{\max} &= (3.25 \times 10^{-22}) (20,000^{4.5}) \\ &= 0.0074 \text{ in/in (0.0074 cm/cm)} \end{aligned}$$

This estimate is applicable to an axially loaded member in which no stress redistribution occurs. In a beam member, stress redistribution would reduce the extreme fiber stresses and hence the maximum creep strain.

Creep Deflection

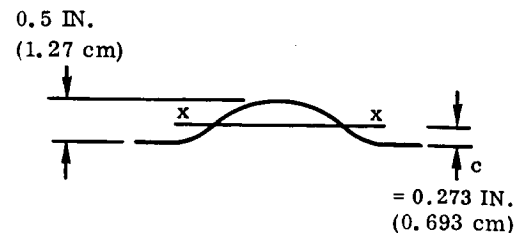
The maximum limit stress in the tee-stiffened panel is 13,287 psi (91.6 MN/m²) (see Page 205) and hence is not considered critical for creep deflection.

Corrugated Panel

$$f_{\max} = 19,359 \text{ psi (133.5 MN/m}^2\text{)}$$

Neglecting the effect of stress redistribution and assuming ϵ_{\max} as computed above for $\sigma = 20,000 \text{ psi (138 MN/m}^2\text{)}$ beam curvature at midspan

$$= \frac{1}{R} = \frac{\epsilon_{\max}}{c} = \frac{0.0074}{0.273}$$



Assuming average curvature $\approx \frac{2}{3} \left(\frac{\epsilon_{\max}}{c} \right)$

then

$$\delta_{\max} = \frac{2}{3} \frac{\epsilon_{\max}}{c} \frac{L^2}{8} = \frac{(2)(0.0074)(11.0^2)}{(3)(0.273)(8)} = 0.273 \text{ inch (0.693 cm)}$$

Elastic deflection = 0.044 in (0.112 cm) (see Page 222)

\therefore Total deflection = 0.273 + 0.044 = 0.317 inch (0.805 cm)

$$\begin{aligned} \text{Allowable deflection} &= 0.10 + 0.04L \left(\frac{\text{BS}-12}{110} \right) = 0.10 + 0.04L \left(\frac{79.5 - 12}{110} \right) \\ &= 0.395 \text{ inch (1.003 cm)} \end{aligned}$$

\therefore Deflection is satisfactory.

7 FABRICATION OF TPS HARDWARE

The fabrication of test hardware for the metallic thermal protection system involved the use of a variety of conventional processes familiar to the aerospace industry. These included standard machining, electrical discharge machining, chemical milling, electron beam and resistance spot welding, vacuum brazing, heat treating and creep flattening, and standard sheet metal processing. Only the materials used and the application of oxidation resistant coatings could be considered as unconventional.

7.1 Configurations

The TPS hardware involved fabrication of two configurations for test - open corrugation and tee-stiffened heat shields. In each case, the panels were approximately 12 inches (30.5 cm) wide by 16 inches (40.6 cm) long. The complete TPS for test, including the high temperature fibrous insulation and panel support posts was 4.2 inches (10.7 cm) thick.

Figure 7-1 is an exploded illustration of the open corrugation and support structure. The illustration shows the TPS panel with retainer straps and posts atop the blanket of high temperature insulation and the support posts. All the surface hardware and the upper half of the support posts are columbium alloy Cb-752, coated with R-512E. The lower half of each support post is a dispersion strengthened nickel alloy, TD NiCr. All fasteners are TD NiCr, except the two horizontal bolts and nuts and the filler plugs in each post which are Cb-752.

Figures 7-2 and 7-3 show a completely assembled and brazed open corrugation panel. The view in Figure 7-2 is of the exterior or skin side of the panel. Figure 7-3 shows the interior side of the panel on which may be seen the built-up brazed forward beam and the machined aft beam. Also visible are the two panel stiffeners (produced by chemical milling of the panel skin) running transverse to the corrugations and located beneath each beam.

Figure 7-4 is an exploded illustration of a tee-stiffened heat shield and support structure showing the tee-stiffened panel, retainers, support posts, and the insulation. All the surface hardware, the top half of the support posts, and the filler plugs are coated columbium alloy Cb-752. The lower halves of the support posts and all fasteners are made of TD NiCr.

Figures 7-5 and 7-6 show one of the completed tee-stiffened heat shields ready for test. These panels are completely assembled by electron beam welding, each panel containing over 30 feet (9.2 m) of weld applied without straightening or intermediate heat treating of the parts.

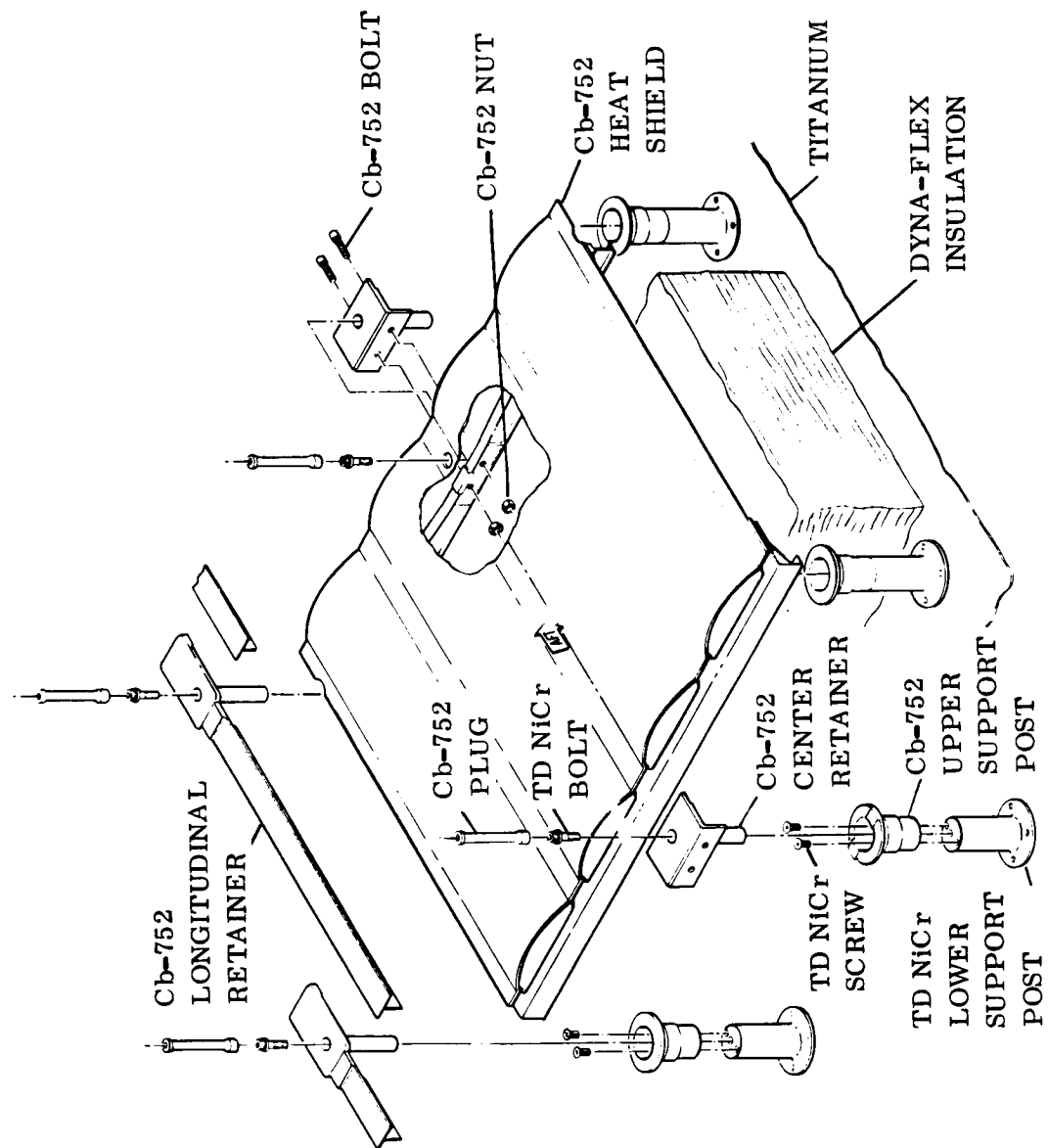


Figure 7-1. Open-Corrugated TPS Exploded Assembly

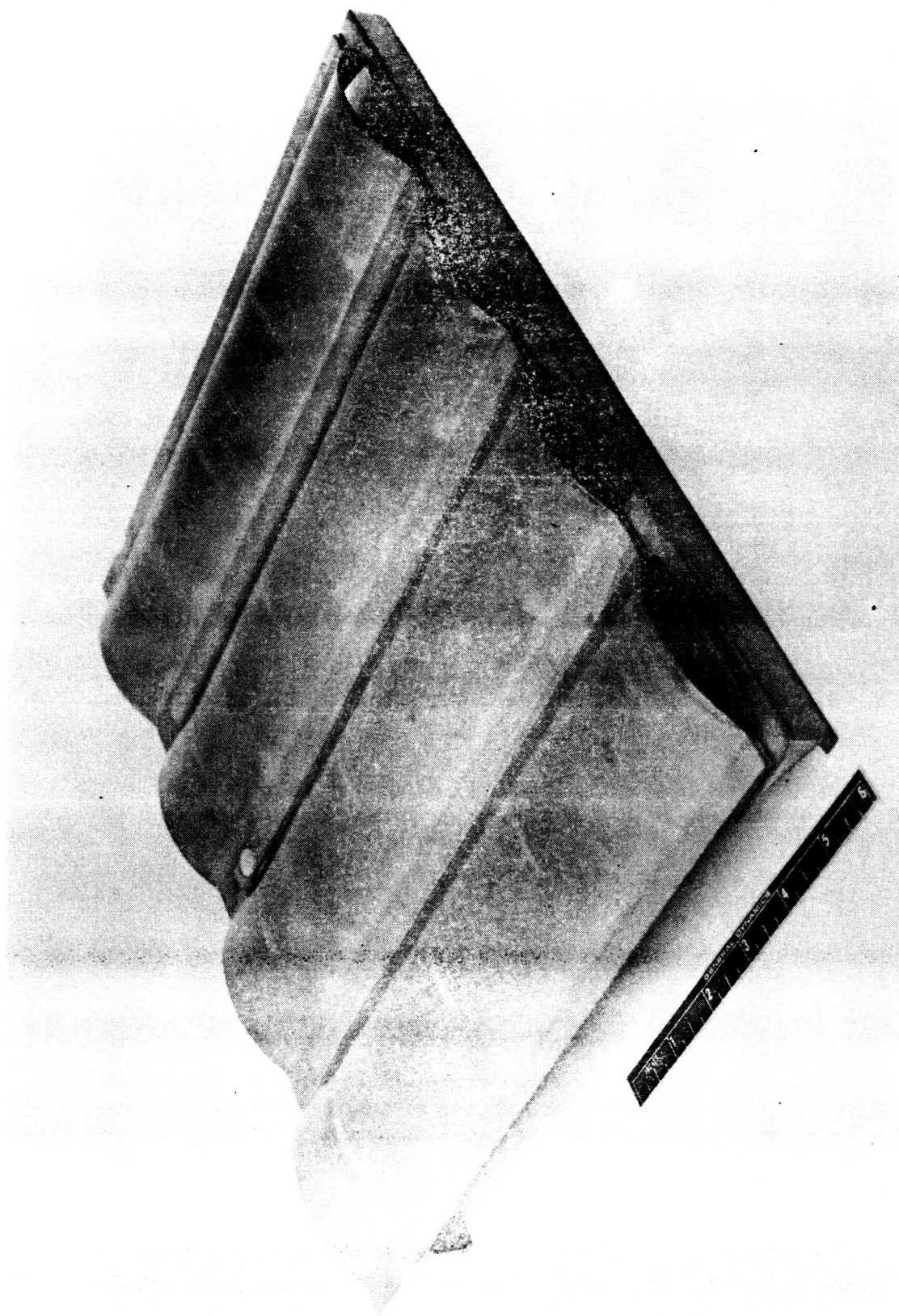


Figure 7-2. Exterior View of Brazed Cb-752 Open Corrugation Heat Shield (Photo No. 126974B)

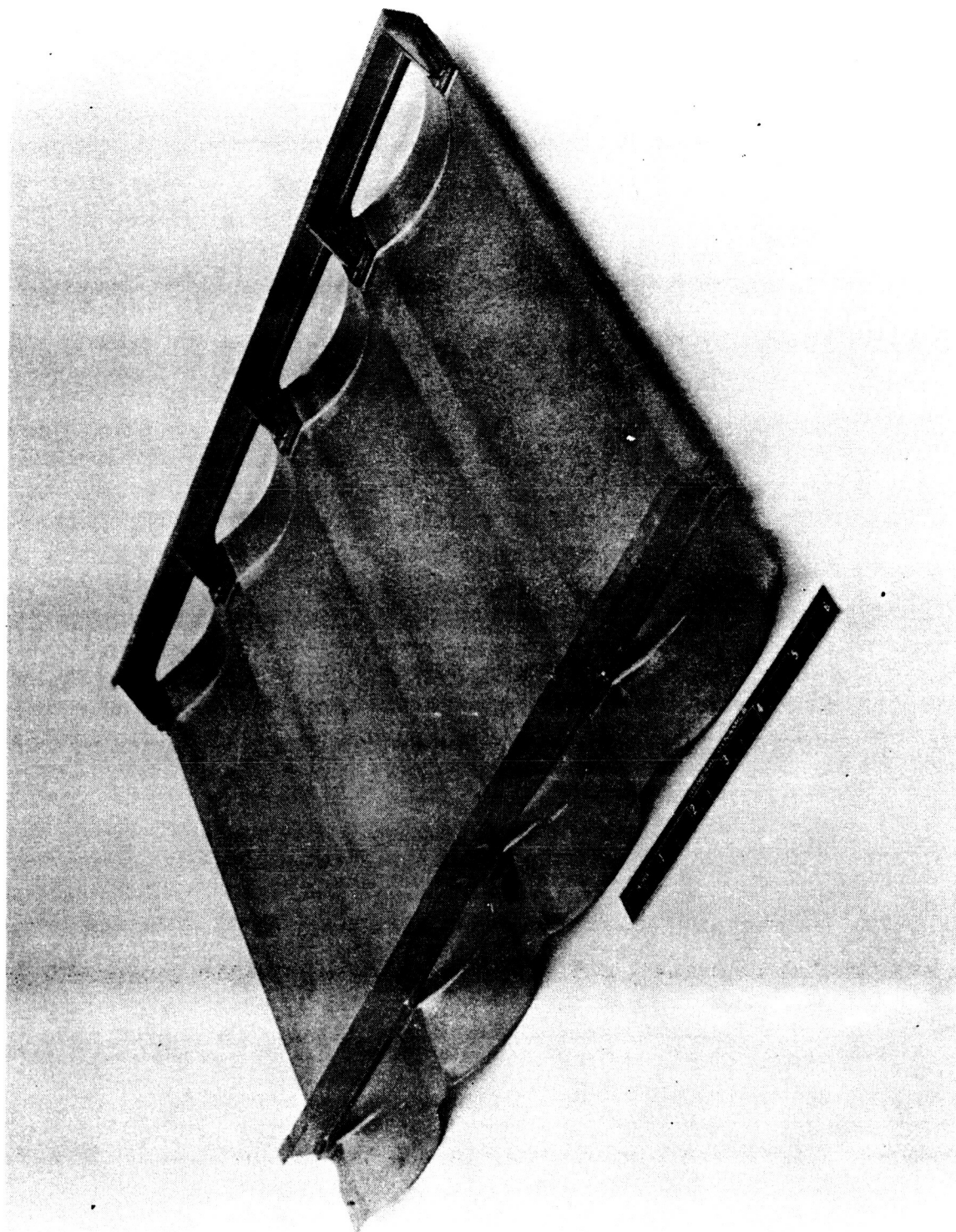


Figure 7-3. Interior View of Brazed Cb-752 Open Corrugation Heat Shield (Photo No. 126980B)

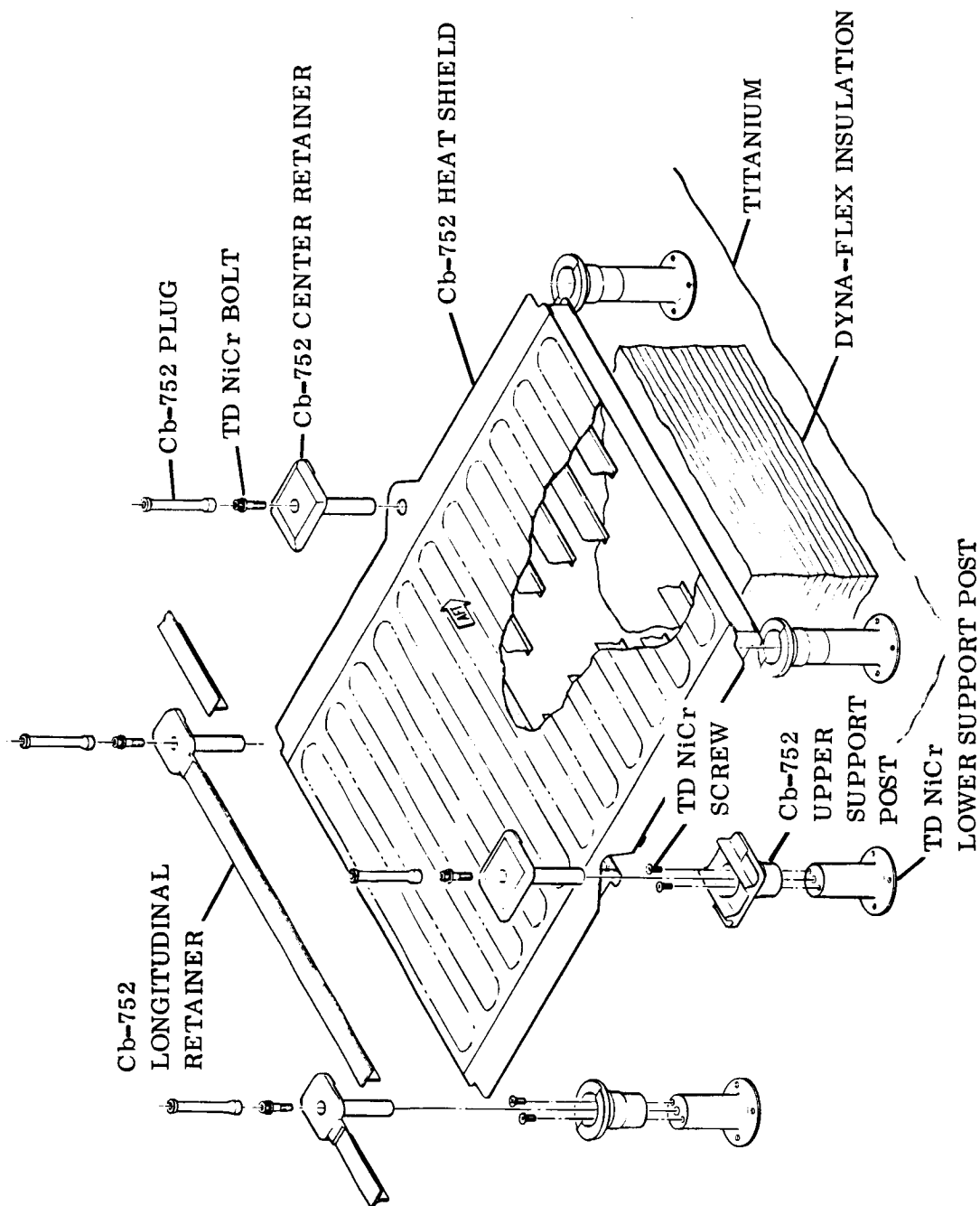


Figure 7-4. Tee-Stiffened TPS Exploded Assembly

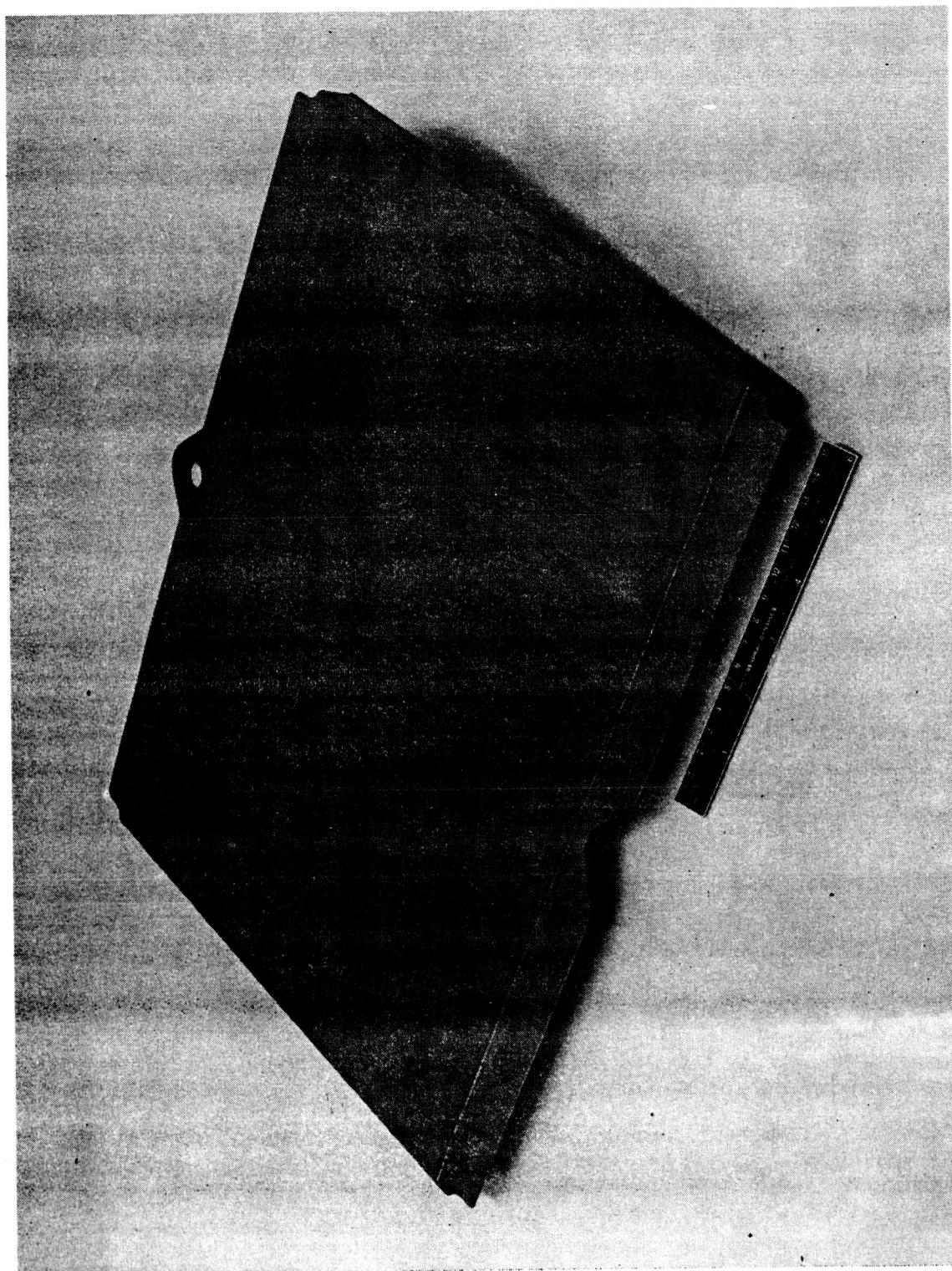


Figure 7-5. Tee-Stiffened Cb-752 Heat Shield Panel — Skin Side Ready for Coating (Photo No. 128327B)

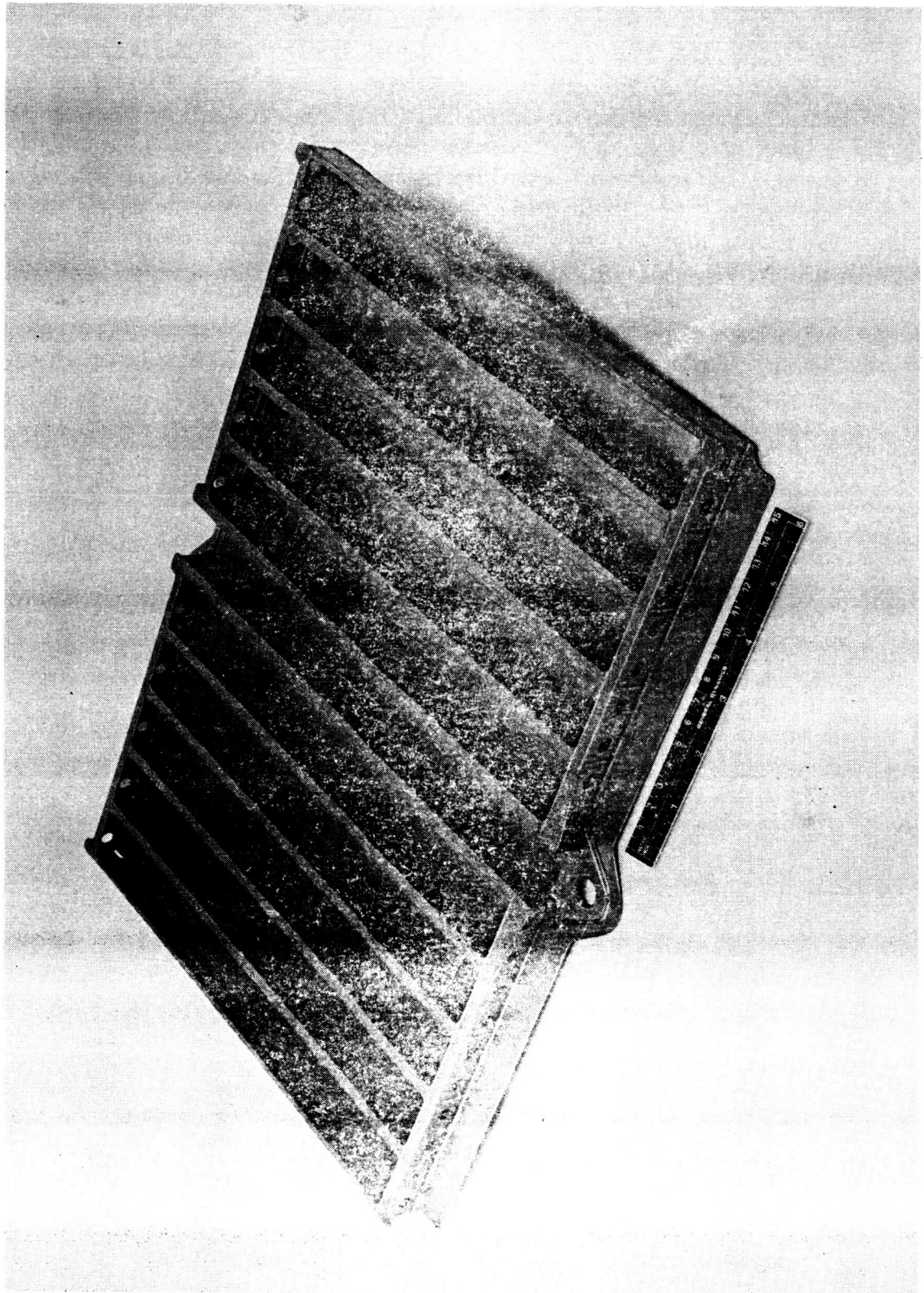


Figure 7-6. Tee-Stiffened Cb-752 Heat Shield Panel -- Interior Side Ready for Coating (Photo No. 128326B)

The panel skin, ribs, and flange or cap skin were first cleaned and then assembled into the weld tooling for electron beam welding. The tooling was designed to permit the completion of all the burn-through longitudinal tee welds on both panel faces - approximately 12 feet (3.7 m) of welding in each side - without removing the assembly from the tooling. The maximum distortion resulting from this welding was 0.050 inch (0.127 cm) in the panel long dimension. Transverse distortion was negligible. Skin distortion resulting from welding was also negligible. The panel subassemblies composed of the skin, cap skin, and ribs were subsequently machined to receive the end closure beams for welding.

Closeout electron beam welding joined the panel subassembly to the end closure beams. This consisted of an additional 5 feet (1.5 m) of step-butt weld and 24 burn-down tee slot welds interconnecting the ribs and the beam webs. For the panel skin to beam welds, the parts were placed in weld tooling which held the skin in contact with the machined step of the beam flange during welding on both sides of the panel. No interior tooling was necessary. No weld tooling was needed for the tee slot welds.

Figure 7-7 shows the welded panel subassembly and the closure beams prior to closure welding. Details of the top and bottom transverse step-butt welds and the tee slot welds for attaching the panel to a closure beam, can be seen in Figure 7-8. The same joint, closed for welding is seen in Figure 7-9.

This welding approach was possible since: (1) the parts and subassemblies were designed to be self-locating, (2) the welding equipment could be precisely regulated, (3) the operator was able to observe, manipulate, and control the welding beam during all welding.

7.2 Materials

The materials used in the fabrication of the TPS test hardware were: (1) columbium alloy Cb-752 for the heat shield and guard panels, panel retainers, the upper support posts, plugs and some fasteners; (2) the dispersion strengthened nickel alloy, TD NiCr, for the threaded fasteners, and the lower half of the support posts; (3) oxidation resistant coatings for columbium and for TD NiCr, (4) high temperature fibrous insulation blankets.

7.2.1 Metals. — The columbium alloy used was Cb-752 (Cb-10W-2.5 Zr) produced by Wah Chang Albany Corporation, Albany, Oregon and furnished in the fully recrystallized condition. Typical chemical compositions taken from supplier certifications are presented in Table 7-1.

TD NiCr was supplied by NASA-Lewis Research Center from material produced by Fansteel under NASA Contract NAS3-13490. A typical chemical analysis for TD NiCr is given in Table 7-2.

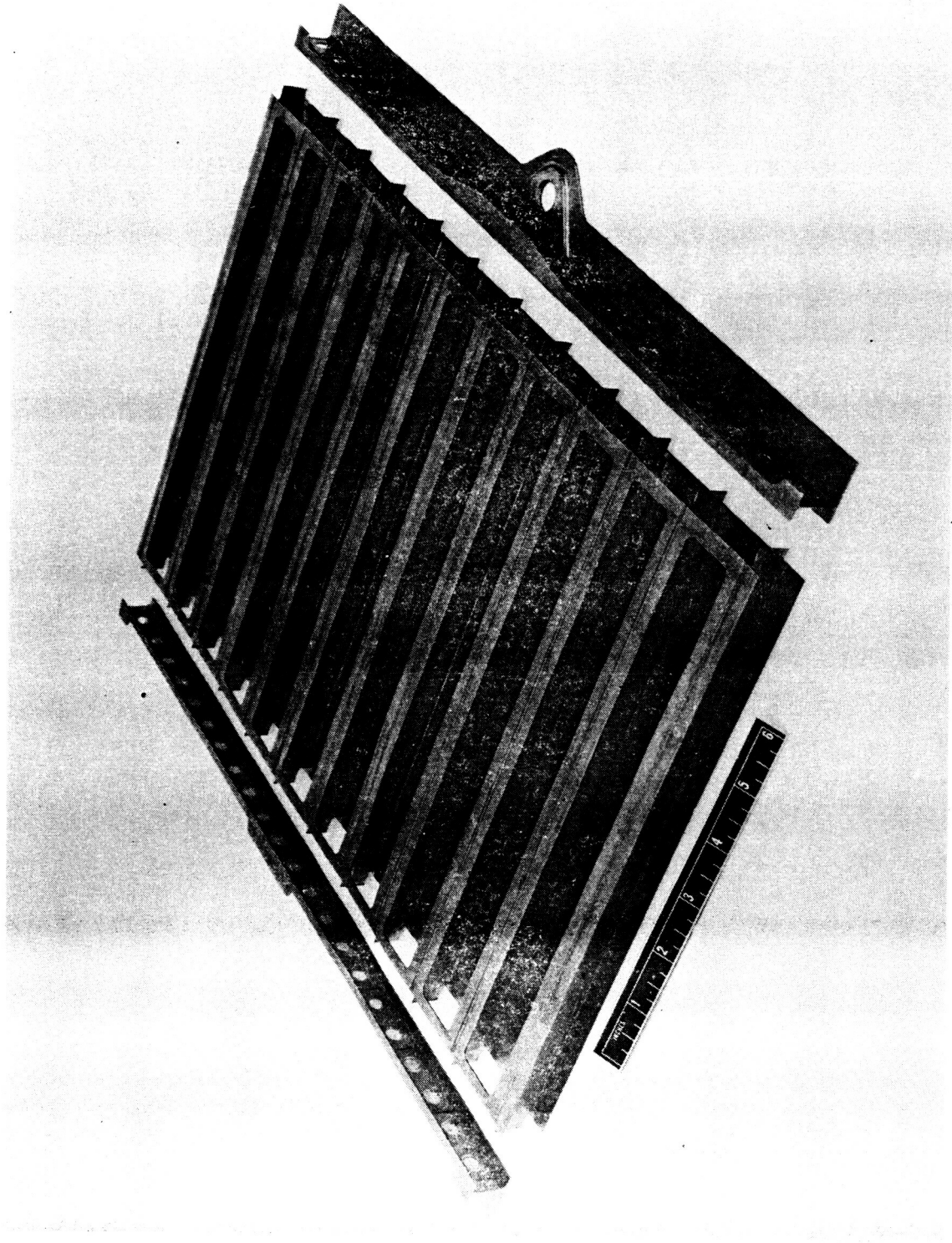


Figure 7-7. Tee-Stiffened Cb-752 Heat Shield Panel — Interior Side Prior to Final Weld (Photo No. 128070B)

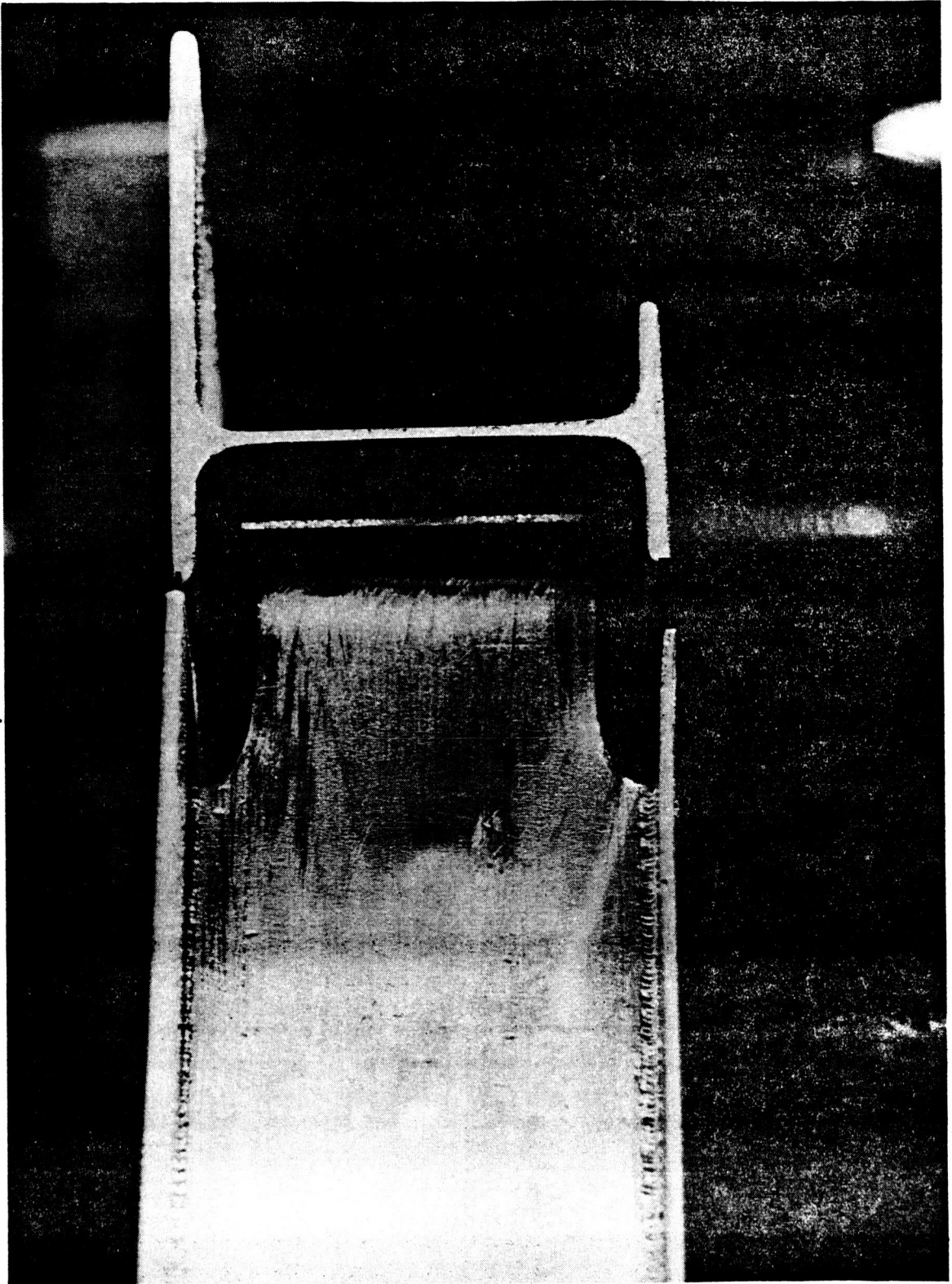


Figure 7-8. Details of Closure Welds — Welded Panel to Beam — Tee-Stiffened Cb-752 Heat Shield Panel (Photo No. 128069B)

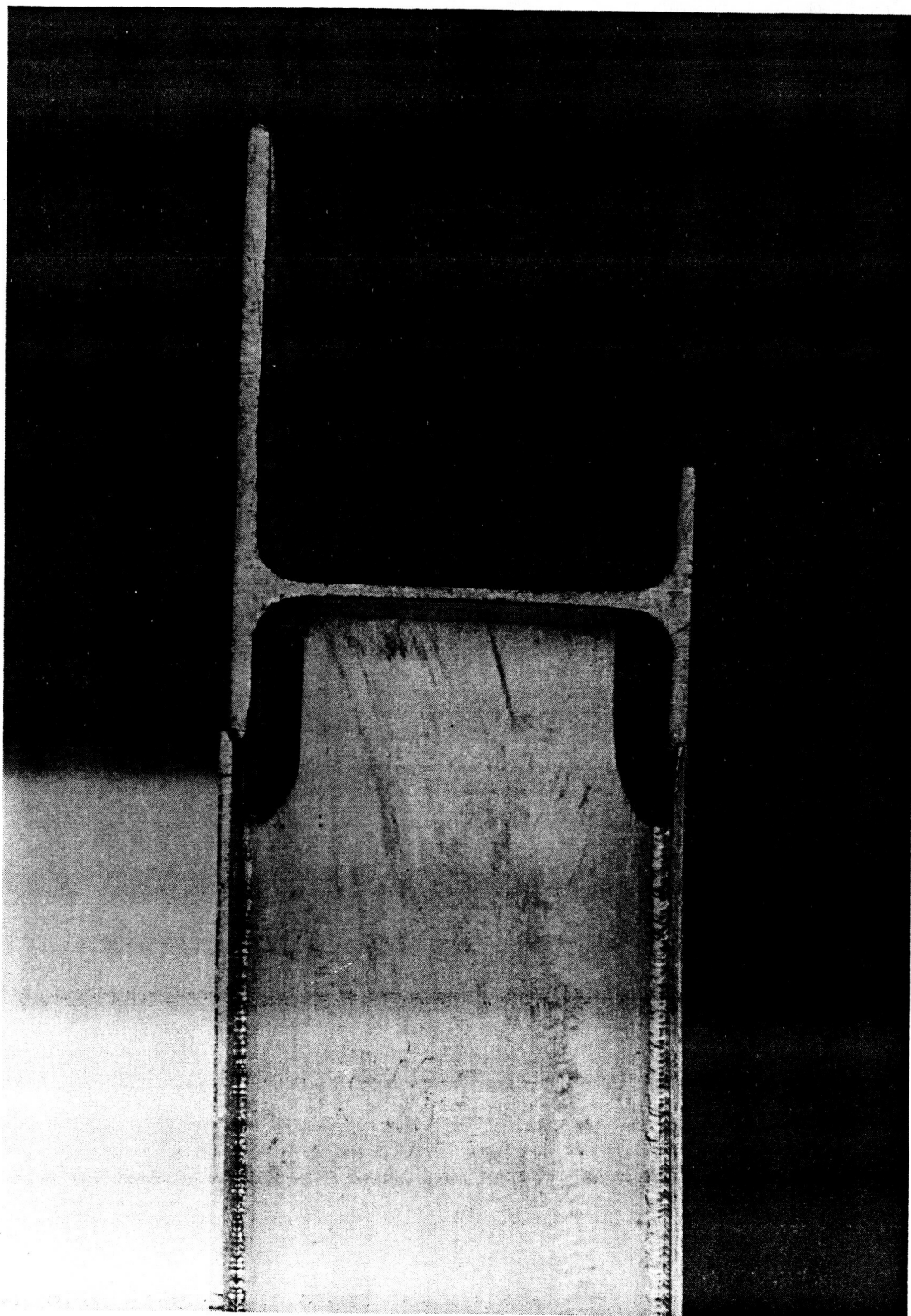


Figure 7-9. Detail of Closure Welds — Welded Panel to Beam — Ready for Welding.
Tee-Stiffened Cb-752 Heat Shield Panel (Photo No. 128068B)

Table 7-1. Chemical Analysis of Small Size TPS Columbian Alloy Cb-752
Heat Treat Condition: Fully recrystallized
Form: Sheet, Bar and Rod

Ingot Analysis - In Percent

<u>Element</u>	<u>Heat 70035</u>	<u>Heat 70036</u>	<u>Heat 70043</u>
W	9.7/9.8	9.1/9.6	10.2/10.2
Zr	2.8/2.4	2.6/2.6	2.5/2.6
Cb	Balance	Balance	Balance
C	70/80 ppm	30/30 ppm	60/<30 ppm
O	<50/90 ppm	90/140 ppm	70/<50 ppm
N	63/15 ppm	64/47 ppm	45/27 ppm
H	2.5/2.8 ppm	1.3/1.8 ppm	<5/5 ppm
Ta	2700/3000 ppm	2950/2750 ppm	4000/3800 ppm
All others	<3000 ppm	<3000 ppm	<3000 ppm

Product Chemistry - in PPM

C	30	<30	<30
O	80	<50	<50
N	47	50	40
H	<5	<5	<5

Table 7-2. Typical Chemical Analysis of
Small Size TPS TD NiCr

Heat Treat Condition: Stress relieved

Form: Rod

Heat Number: 3817

Source: Fansteel Inc., Metals Division

Chemical Analysis in % —

Carbon	-	0.0152
Sulphur	-	0.0025
Chromium	-	19.73
Thoria (ThO ₂)	-	1.65
Nickel	-	Balance

7.2.2 Coatings. — Coatings used were a silicide coating for Cb-752 and an aluminide coating for the TD NiCr. The columbium coating was R-512E, a Si-20% Cr-20% Fe fused silicide coating applied by HiTemCo. This coating was applied to columbium hardware following chemical or mechanical cleaning. Chemical cleaning was accomplished in a HNO₃-HF acid solution, and mechanical cleaning was by grit blasting with iron particles. The coating slurry was applied by dipping and spraying with all edges overcoated or beaded using a miniature stripping roller. Spray overcoating was employed on edges when the geometry of a part prevented using the stripping roller. After coating application, the parts were air dried at room temperature, followed by insertion into a high temperature vacuum furnace where they were baked at a low temperature, 400 to 600° F (478 to 589° K) to remove the coating binder and other volatiles. The furnace temperature was then increased to 2600° F (1700° K) where the coating fuses and flows evenly over all surfaces of the parts. This temperature was held for 60 minutes under a vacuum of less than one micron (133 mN/m²) and the parts were then furnace cooled to room temperature. The thickness of the unfired or "green" coating was specified to be 20 to 25 mg/cm², which resulted in a fused coating thickness of 0.003 (0.076 mm) to 0.004 inch (0.102 mm).

All TD NiCr parts were coated with an aluminide to increase oxidation resistance and as a protective measure to avoid any incompatibility between the TD NiCr and the silicide coatings on the columbium. This coating is a Vac Hyd proprietary aluminide coating, VH-28 (Cr-Co-Al-Y). In tests, columbium coupons coated with R-512E were placed in

contact with TD NiCr coupons coated with VH-28 and heated in an air furnace. There was no evidence of incompatibility of the two coatings after cyclic testing to 2200°F (1478°K) in air for 72 hours.

In order to complete the design of the tee-stiffened panels, it was necessary to perform limited tests to establish panel design features which would facilitate coating application and would assure an even distribution of coating to the beam ends of the panels. Also the best dipping position for a panel was needed. The design features under consideration were the size and location of the drain holes in the beam web, and the width of the cut-out slots at the ends of the ribs where they terminate with the beams. These had to be sized so that the coating would distribute evenly on the interior of the beam webs and flanges and so that the coating would properly cover the 0.020 inch (0.051 cm) wide edge of the rib in the cut-out slot area.

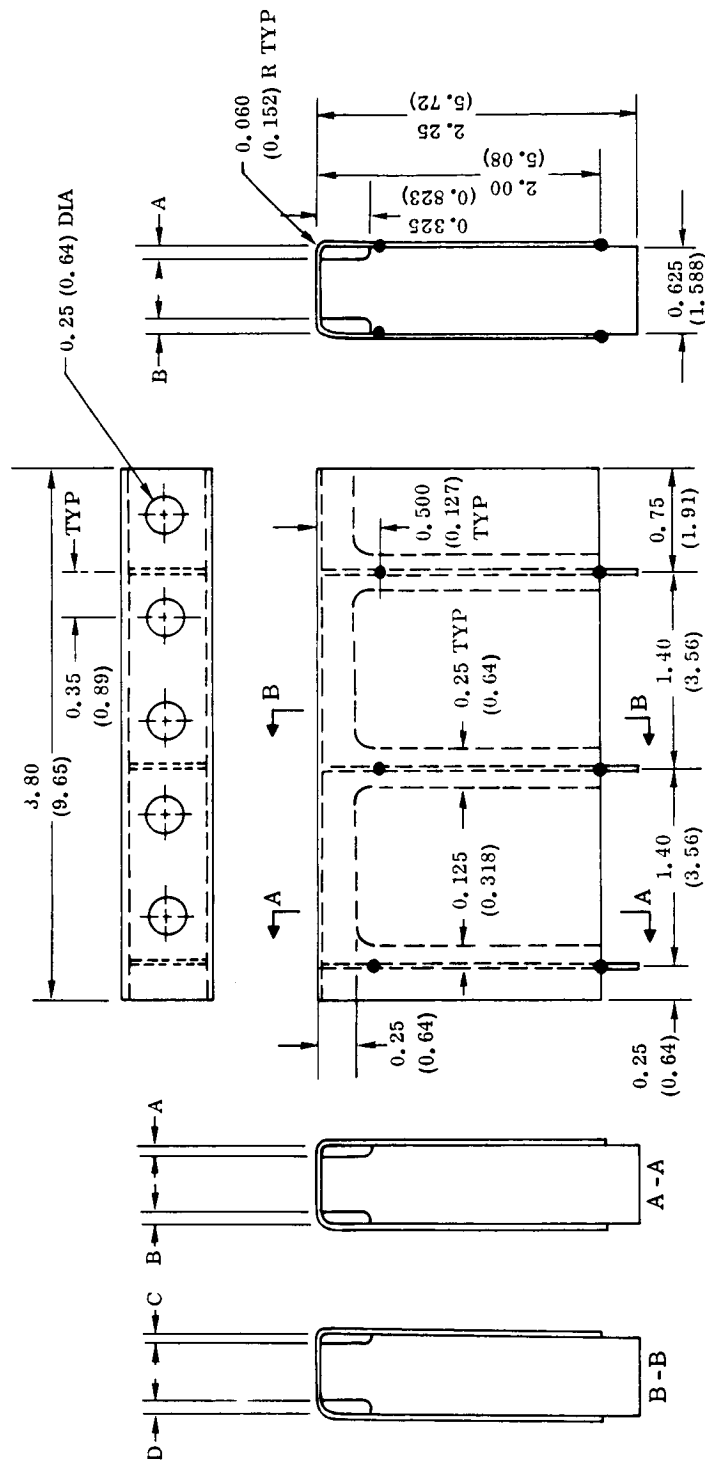
For these tests, specimens which simulated the corners and beam end conditions of the panels were prepared, (Figure 7-10). Drain holes and cut-out slots of various size combinations and locations were placed in the specimens. Specimens were immersed in the coating slurry with either the beam face up or face down to determine the effect of dipping position. The coating thickness was measured and visually examined before and after firing. Metallographic sectioning was used for final evaluation of coating thickness and distribution.

7.2.3 Insulation. — The high temperature insulating material selected for use between the metallic heat shield panels and the primary load structure was Dyna-Flex having a density of 10 pcf (160.2 kg/m³). This material is a product of Johns-Manville of Manville, New Jersey, and is composed of aluminum silicate fibers coated with chromia. It was supplied in nominal 1/4-inch (0.64 cm) thick blankets. After specimen buildup and prior to testing the insulation was baked at 800°F (700°K) for 4 hours to drive out the acrylic resin binder.

7.3 Fabrication Sequence

Typical fabrication sequences for each panel configuration are shown in Figures 7-11 and 7-12. Both the corrugation stiffened and the tee-stiffened panels employ familiar aircraft fabrication processes. The preparation for coating is perhaps unique to coated refractory metals and consists of rounding or radiusing edges and corners either manually or by vibratory finishing. This prepares the edges and corners with the best condition for the application of the silicide coating. In general a radius of 0.015 inch (0.038 cm) was specified for all Cb-752 components.

7.3.1 Welding. — The manufacture of the subsize tee-stiffened heat shield panels for Part 1 of Phase II (Section 4) clearly demonstrated the practicality of fabricating columbium TPS hardware with electron beam welding.



- NOTES
1. All material Cb-752 - 0.020 in. (0.051 cm) thick.
 2. Electron beam spotweld 5 places each rib.
 3. No. 69 [0.029 (0.074)] drill - 9 holes for rib locators.
 4. All slots and drain holes to be radiused for coating.
 5. Coat with silicide R-512E - 0.003 to 0.004 in. (0.008 to 0.010 cm) thick.
 6. Parenthesized dimensions in cm; all others in in.

	SLOT WIDTH			
	END RIBS		CTR RIBS	
	A	B	C	D
SPECIMEN 1	0.04 (0.10)	0.06 (0.15)	0.04 (0.10)	0.08 (0.20)
SPECIMEN 2	0.08 (0.20)	0.10 (0.25)	0.08 (0.20)	0.06 (0.15)

Figure 7-10. Coating Application Test Specimen

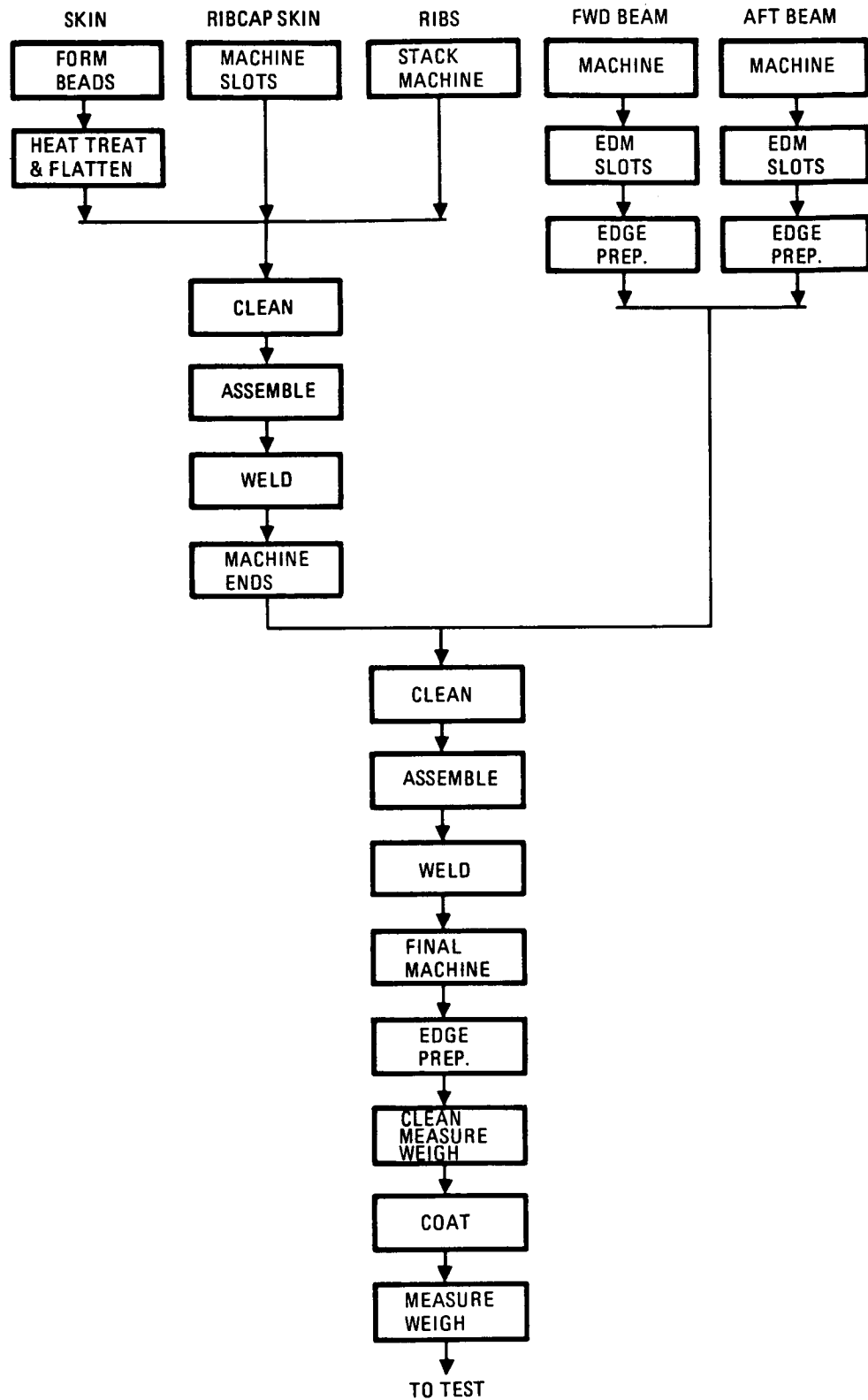


Figure 7-11. Tee-Stiffened Heat Shield Panel Fabrication Sequence

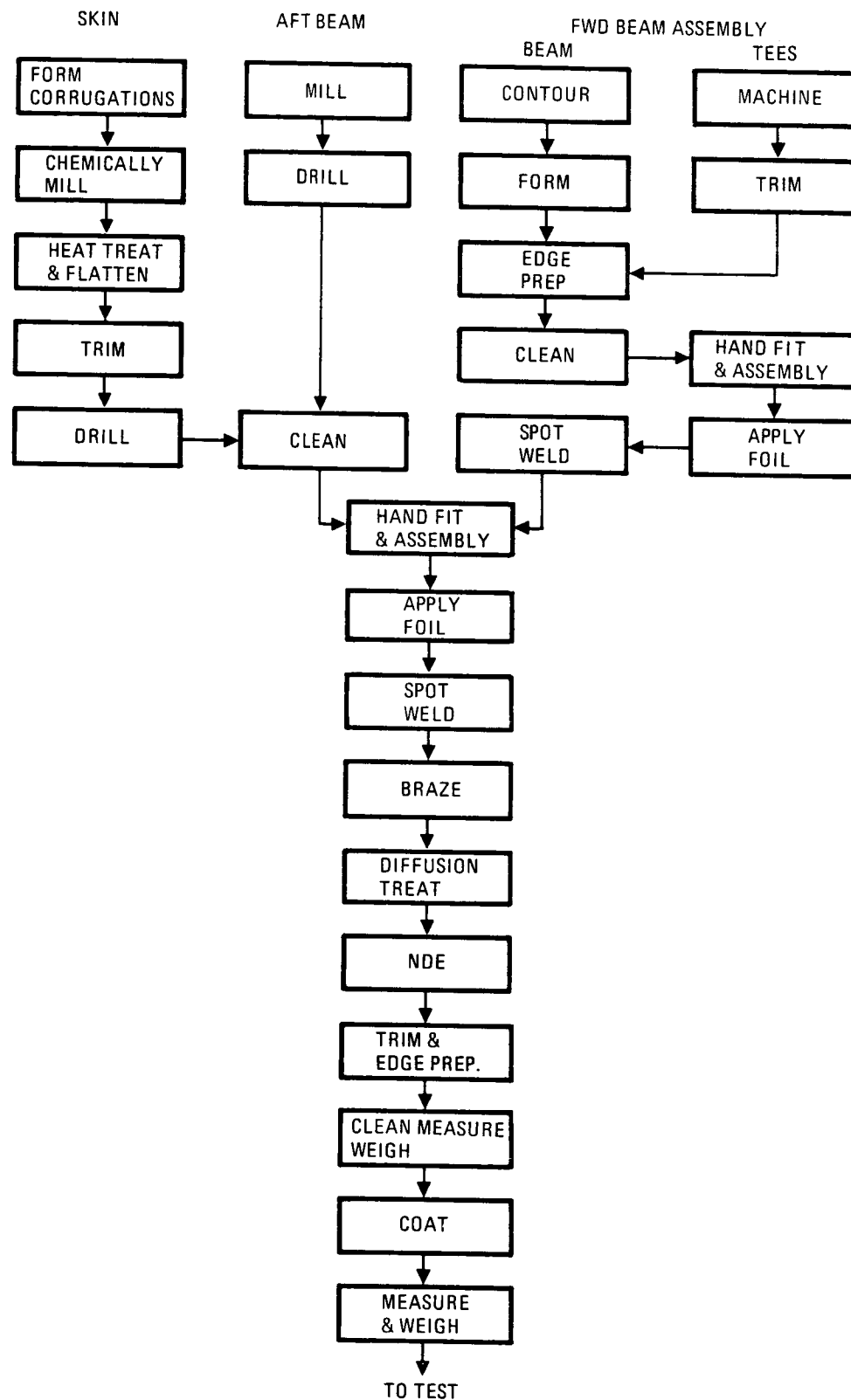


Figure 7-12. Open Corrugation Heat Shield Panel Fabrication Sequence

The electron beam welding used on the tee-stiffened panels involved three types of weld joints: (1) burn-through tee welds between ribs and skins and rib caps, (2) step-butt welds between skins and rib cap skins, and closure beams, (3) burn-down tee slot welds between rib end tangs and beam webs. All welds required 100% joint fusion with full penetration and fillet formation and conformance with specification MIL-W-46132. Welds were made using chrome-plated copper and aluminum hard tooling. Hard chromium was applied to copper tooling to prevent contamination of the columbium during welding and assembly operations. As further insurance, all welded parts were bathed in nitric acid to remove residual copper prior to each heating or welding operation.

Before fabrication of the electron beam welded heat shields, a program was initiated for weld qualification and tool development to assure quality and repeatable production welds. The program shown in Figure 7-13 involved a step-by-step, parallel development of weld qualifications and weld tooling for each of the three major weld joint types required. Materials used and sample joint preparation were identical to those planned for production.

The initial tooling requirements were selected to be appropriate for production panels. Using sample tooling, weld specimens were prepared for each joint type and evaluated for weld quality, part distortion, and tooling adequacy. Figure 7-14 illustrates joint specimen designs, except for the burn-down tee slot joint for which sample specimens were not required. From this step, final weld certifications and tooling concepts were developed and were used to check prototype tooling and to prepare prototype weld specimens for evaluation. Production weld tooling was then manufactured and one or more final weld qualification panels were welded and evaluated. These panels were a three or four rib, tee-stiffened configuration shown in Figure 7-15. All parts used were of the same alloy, material gage, and joint preparation as planned for production panels. The burn-through tee welds were the identical length planned for production. Only this type weld was made in the final qualification panels since these welds represent the greatest potential source of problems with panel distortion, tooling, and weld quality.

It was determined from the simulated test joints that there would be no need for mold tooling for the step-butt and the tee slot joints since satisfactory welds could be made with proper control of the electron beam process and equipment.

7.3.2 Heat treatment. — Formed and welded parts were simultaneously annealed and creep flattened to assure stress free and properly fitting parts. This operation was performed at 2400° F (1589° K) for one hour in a vacuum of at least 5×10^{-5} torr (6.67 mN/m²). Parts were loaded with refractory metal weights to effect creep flattening during annealing. Prior to final machining, all test panels were also vacuum annealed.

7.3.3 Brazing. — It became known prior to the start of fabrication of the small size TPS specimens that the planned press diffusion bonding would have to be abandoned due to

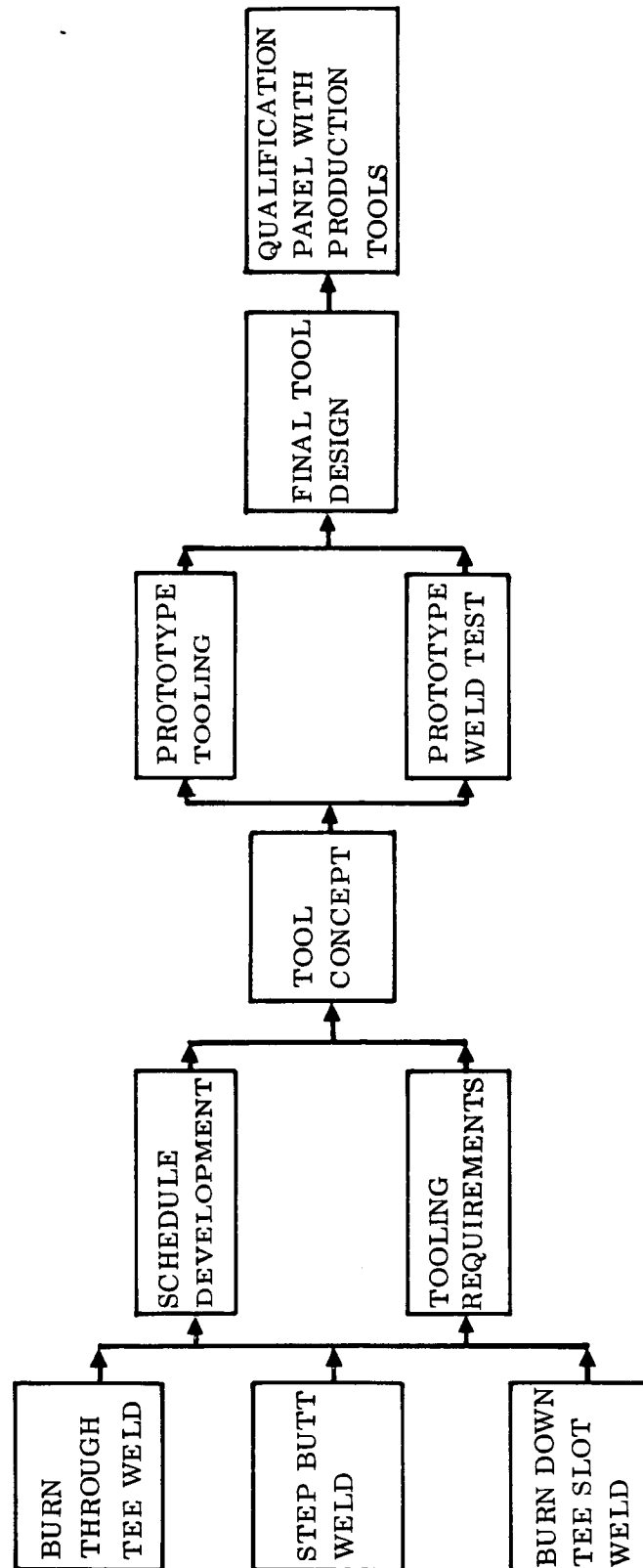
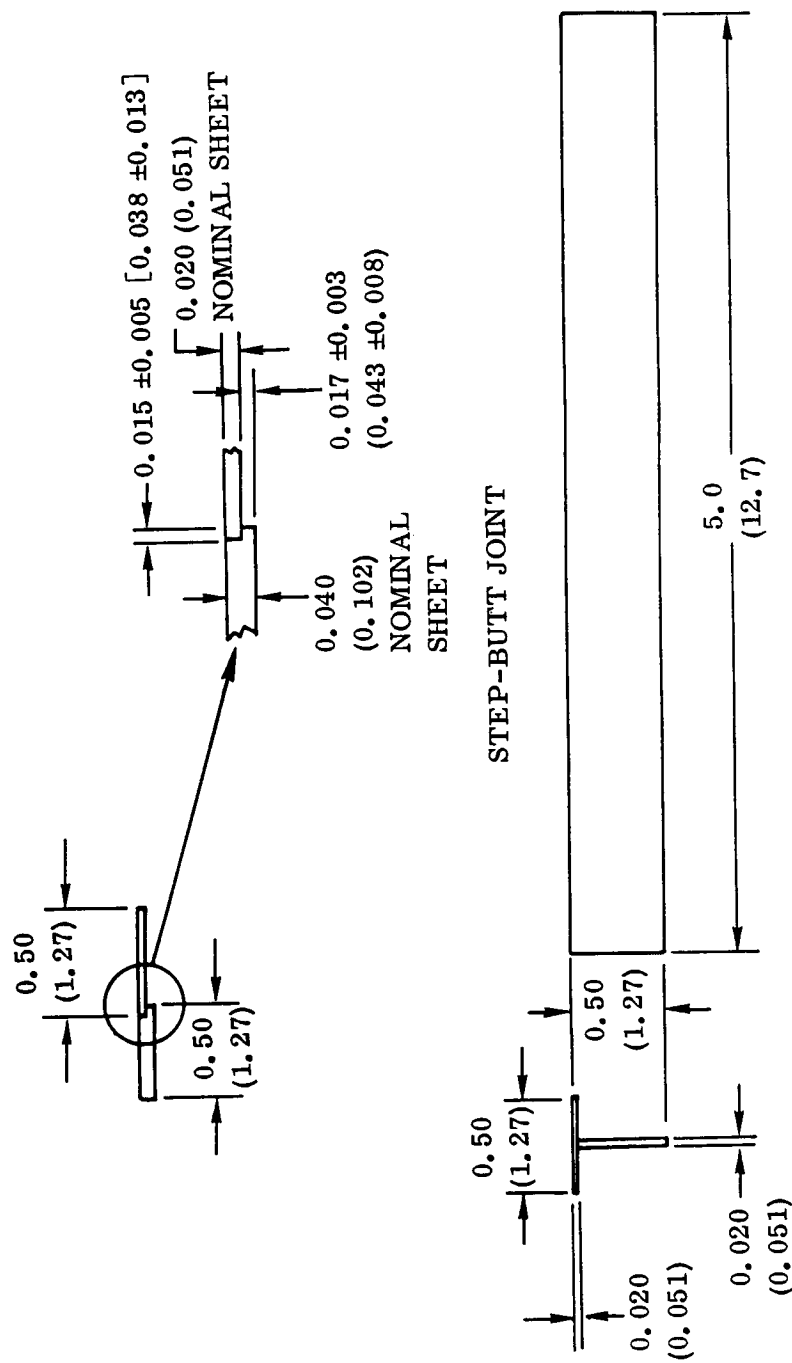


Figure 7-13. Electron Beam Weld Qualification and Tool Development

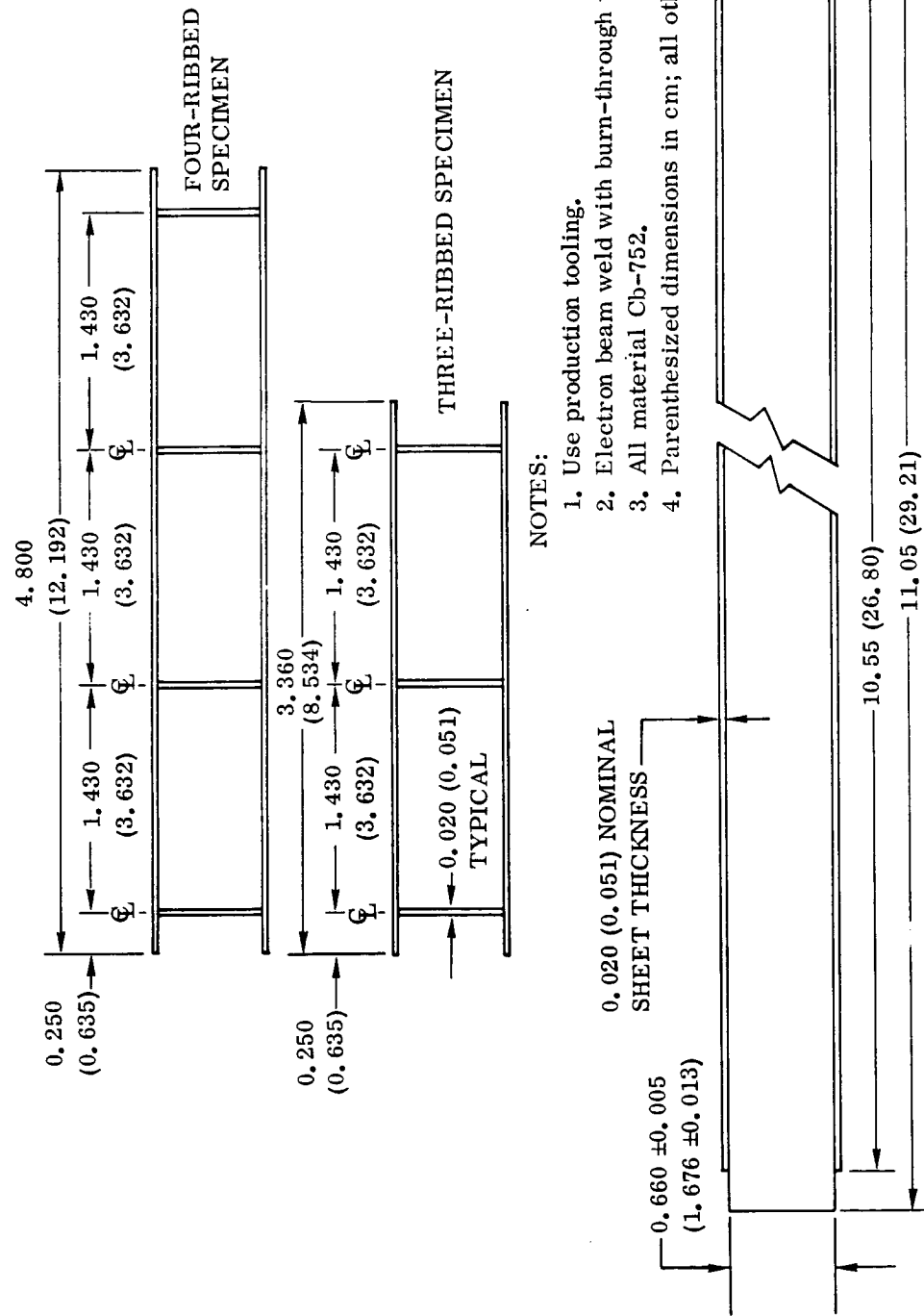


NOTES:

1. All material Cb-752.
2. Parenthesized dimensions in cm; all others in in.

BURN-THROUGH TEE JOINT

Figure 7-14. Sample Weld Joint Configurations



NOTES:

1. Use production tooling.
2. Electron beam weld with burn-through tee welds.
3. All material Cb-752.
4. Parenthesized dimensions in cm; all others in in.

Figure 7-15. Final Weld Qualification Panel

the subcontractor's projected excessive costs and schedule delays. Thus, it was necessary to select an alternate bonding source or method or to re-design for welding. Since no source for a state-of-the-art diffusion bonding process was available and time considerations eliminated a redesign, high temperature brazing was chosen to replace diffusion bonding. Both processes involve lap joints of reasonable area enabling the retention of the basic original hardware designs. Of significant concern was the potential reaction between heavily titanium alloyed braze materials and the silicide coating. However, Northrop Corporation-Aircraft Division had successfully brazed columbium alloy honeycomb heat shields between 1962 and 1966 (References 42, 43, 44). More recently Northrop brazed TPS hardware of C-129Y and Cb-752 for NASA-MSFC.

To qualify brazing for this program, it was decided that two mutually supporting development and test programs were essential. One to qualify a brazing system for Cb-752 TPS hardware and the other to develop adequate procedures for the preparation, assembly, and brazing of production heat shields. Both programs ran concurrently in order to minimize delays created by the change from diffusion bonding to brazing.

The principal development program shown in Figure 7-16 was for the selection of a brazing system and procedures adequate for production brazing. The second program shown in Figure 7-17 was to qualify typical braze joints, following essentially the same plan used in Phase I on elemental specimens for welding and diffusion bonding. Details of the supplemental braze qualification program are given in Appendix D.

The process development program shown in Figure 7-16 was carried out by Northrop and Convair Aerospace. Initially, previous works involving columbium brazing and coating were reviewed and a braze alloy and processing parameters best suited to this program were selected. Using this braze alloy and Cb-752 sheet, sample joints were prepared, brazed, and evaluated for flow and filleting using visual, penetrant and ultrasonic methods. Sample joints of actual hardware were then brazed utilizing the planned processing and part positioning and holding methods. After evaluation of these samples, the initial production corrugated panel was alloyed, assembled and brazed. Post braze analysis of this panel indicated deficiencies in the flow and filleting characteristics of the braze alloy under production conditions. Since efforts to improve these characteristics were not successful, action was taken to circumvent the problems: (1) by hand fitting all braze joints to improve fit-up, (2) by providing additional locator spot welds, (3) by adding braze alloy external to the joints in the fillet regions.

As a result of these corrections, satisfactory brazing was accomplished on all the corrugated panels. Final acceptance was by visual inspection of all joints to MIL-B-7883, Grade A except for the use of X-ray and internal defect limits. C-scan ultrasonics was utilized on joints where feasible to verify the internal quality of the braze bonds.

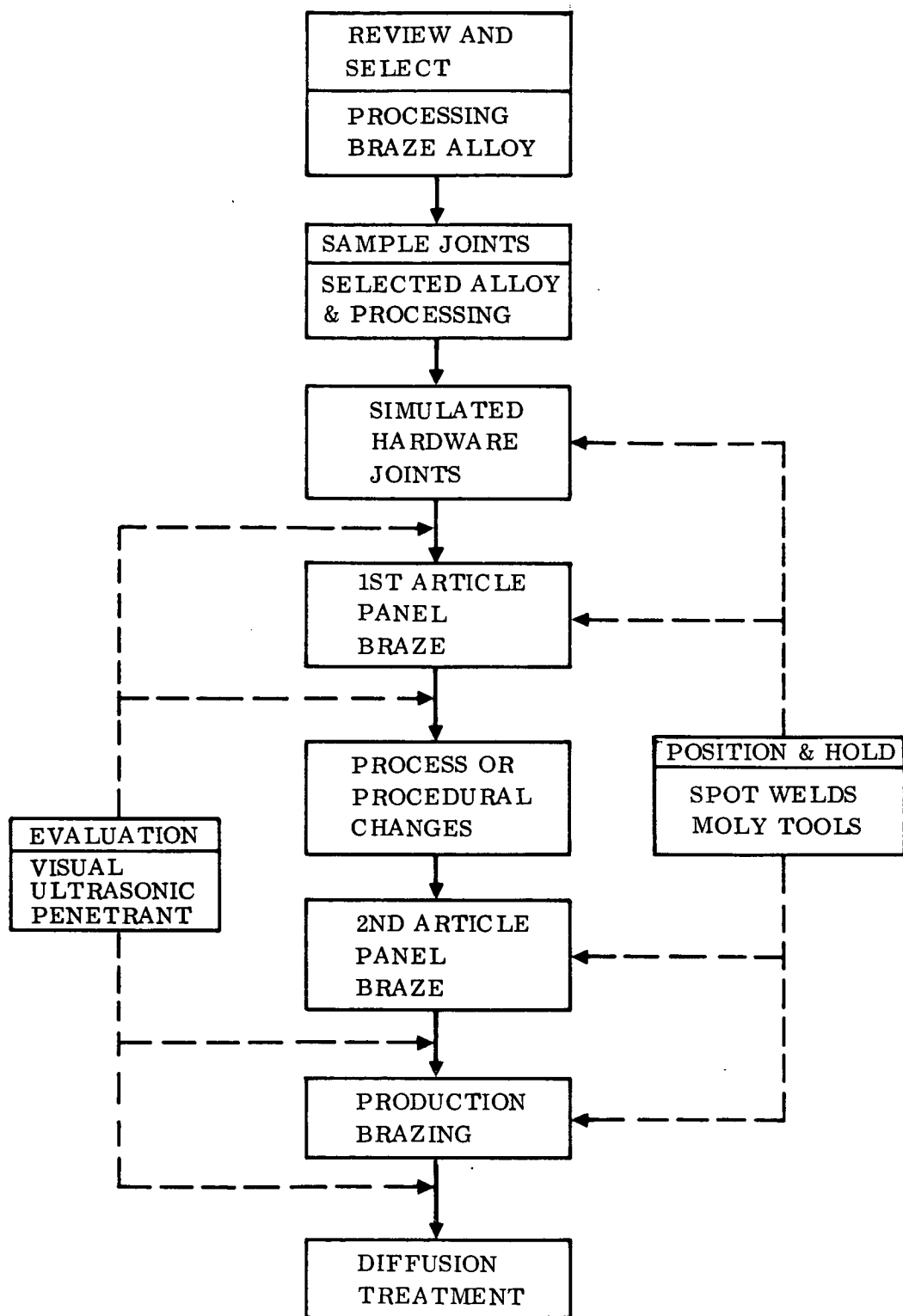


Figure 7-16. Braze Process Development Program

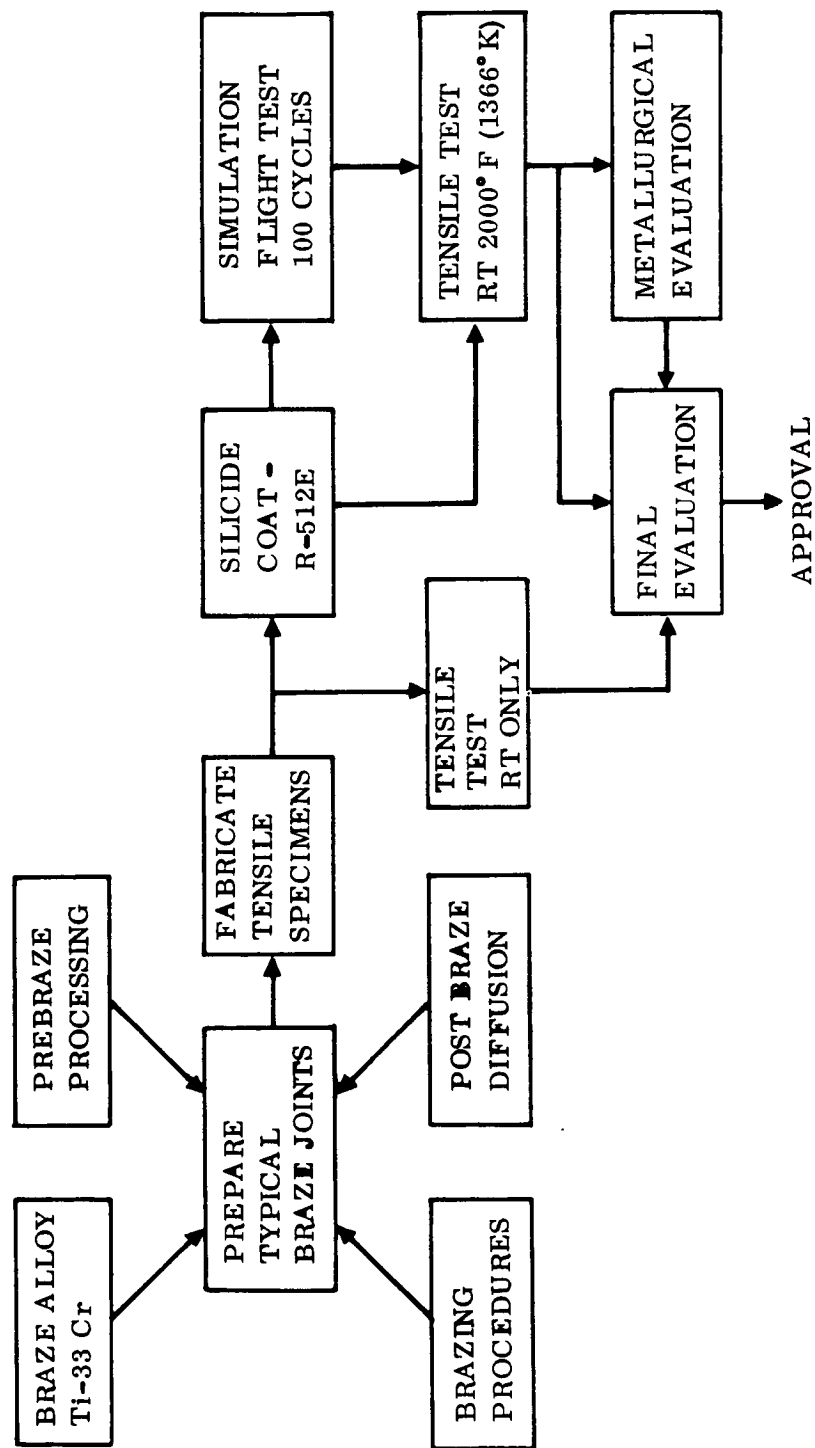


Figure -17. Brace Qualification Program for Columbian Alloy Cb-752

Brazing of the open corrugation panels employed the use of Ti-33Cr titanium-chromium braze alloy foil, 0.002 inch (0.051 mm) thick. This braze alloy was available only as foil. Brazing was followed by a high temperature diffusion treatment. Due to the characteristics of the Ti-33Cr alloy, it was necessary to make metal-to-metal fits in all joints to assure satisfactory flow and filleting of the braze alloy. The joint fit-up and the braze alloy were held in position by resistance spot welding.

Columbium brazing was accomplished in a vacuum furnace under a half atmosphere of high purity argon (<2 ppm O_2), by heating to $2400^\circ F$ ($1589^\circ K$) and stabilizing for 5 minutes followed by a temperature increase to $2700^\circ F$ ($1756^\circ K$) and an 8 minute hold at temperature. After brazing, the parts were either furnace cooled to room temperature, or cooled with high purity argon or helium at temperatures below $500^\circ F$ ($533^\circ K$). Simple, lightweight molybdenum tooling was used to hold and support parts during brazing.

After brazing, the columbium parts were diffusion treated by heating at $2400^\circ F$ ($1589^\circ K$) in a vacuum for a period of 16 hours. During the diffusion treatment, the parts were protected from possible contamination from the furnace atmosphere during the long time at temperature, by wrapping with tantalum foil. Cooling methods were similar to those used for brazing.

The brazing of TD NiCr permitted the joining of the flange to the main body of the lower support posts. This involved conventional vacuum brazing at $2350^\circ F$ ($1561^\circ K$) and holding for 4 minutes before cooling. TD-6 (Ni-16Cr-4Si-5W-17Mo) was used as the braze alloy.

The completed components are shown in layout positions after coating in Figures 7-18 through 7-21.

7.4 System Weights

A breakdown of the TPS component weights, both before and after coating, is presented in Table 7-3. For the tee-stiffened configuration the resulting unit weight of the metallic (Cb-752 and TD NiCr) components before coating was 2.44 lb/ft^2 (0.103 kg/m^2). After coating the weight increased to 2.67 lb/ft^2 (0.113 kg/m^2). Using 10 pcf (160.2 kg/m^3) density Dyna-Flex, the insulation unit weight was 3.08 lb/ft^2 (0.130 kg/m^2). This resulted in a total system unit weight for the tee-stiffened TPS of 5.75 lb/ft^2 (0.243 kg/m^2) in the as-coated condition.

The unit weight of the open corrugation TPS metallic components before coating was 2.60 lb/ft^2 (0.110 kg/m^2) and 2.75 lb/ft^2 (0.116 kg/m^2) after coating. With the 3.7-inch (9.4 cm) thick Dyna-Flex the total system unit weight was 5.83 lb/ft^2 (0.246 kg/m^2). These resulting system unit weights for both configurations were in agreement with the general target weight of 6.0 lb/ft^2 (0.253 kg/m^2) that was considered acceptable at the

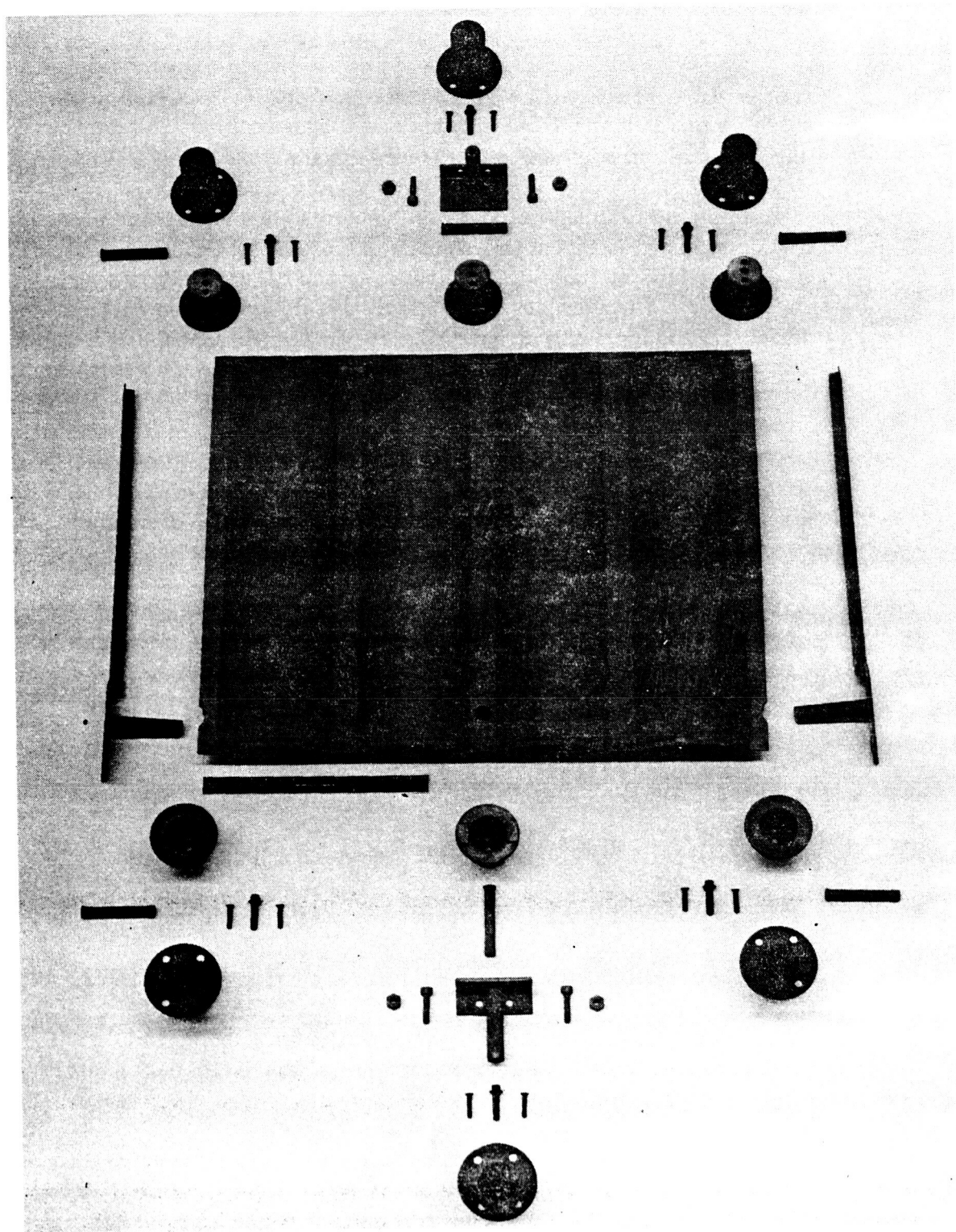


Figure 7-18. Open Corrugation TPS Components Prior to Testing (Photo No. 130748B)

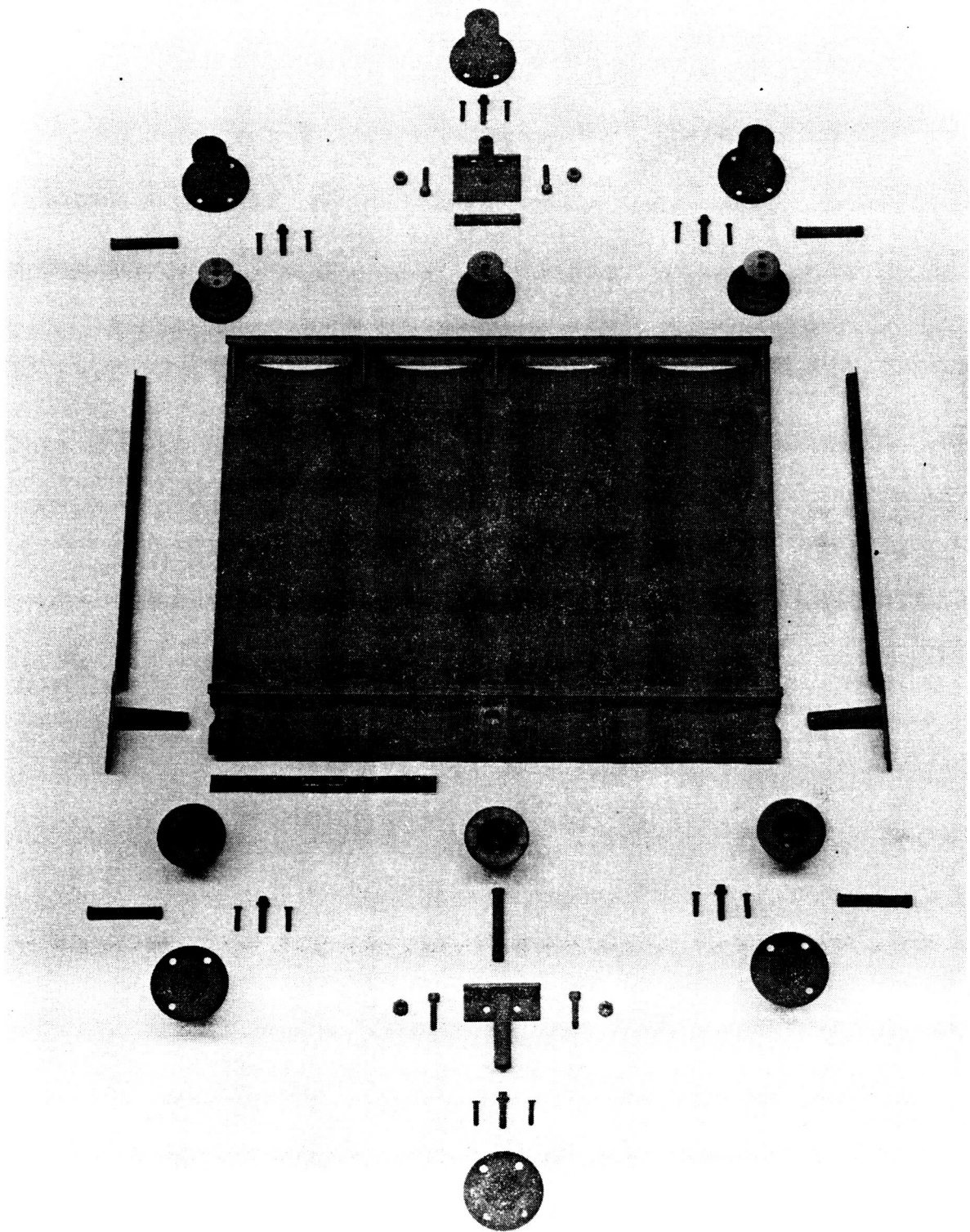


Figure 7-19. Open Corrugation TPS Component Prior to Testing (Photo No. 130749B)

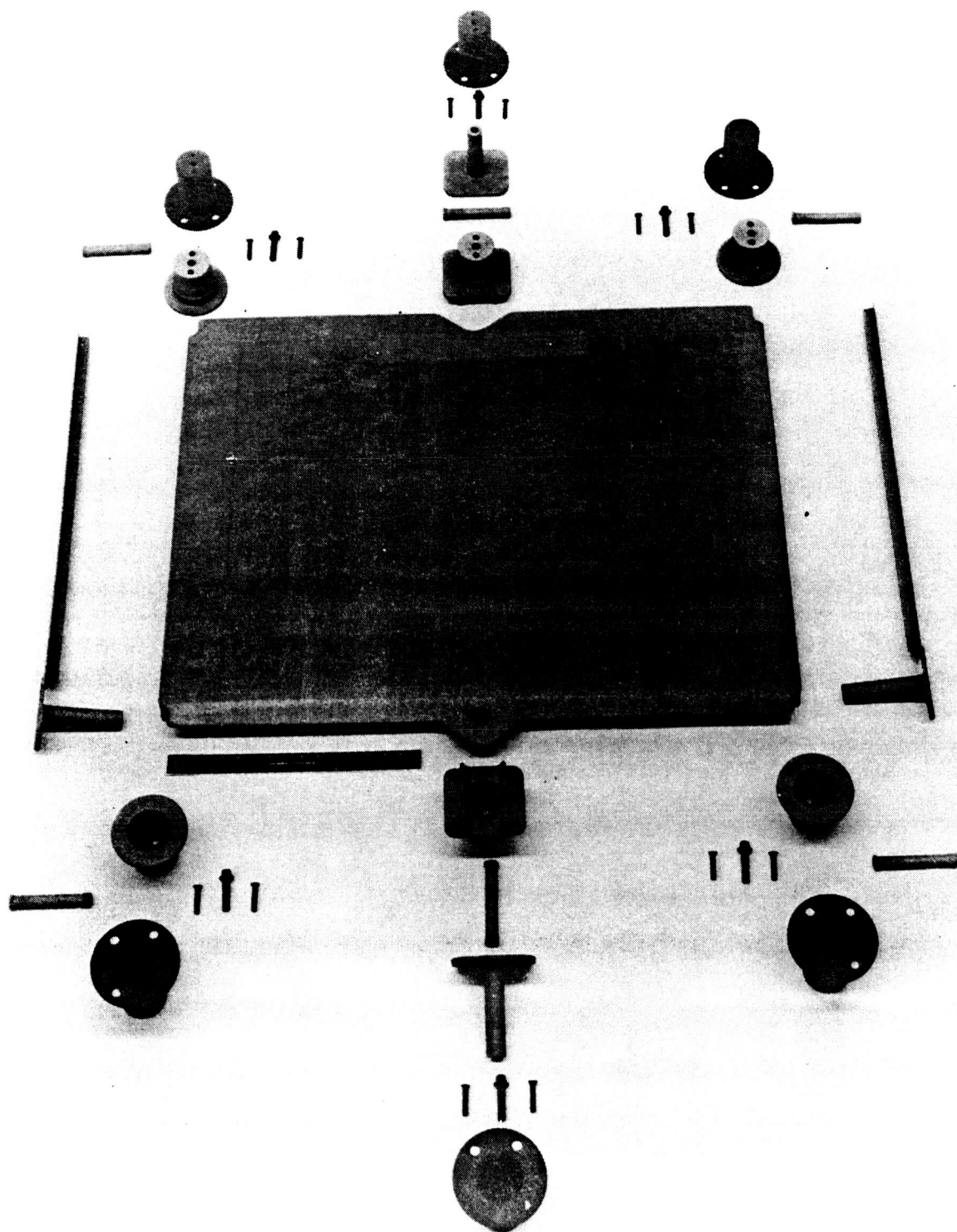


Figure 7-20. Tee-Stiffened TPS Component Prior to Testing (Photo No. 129895B)

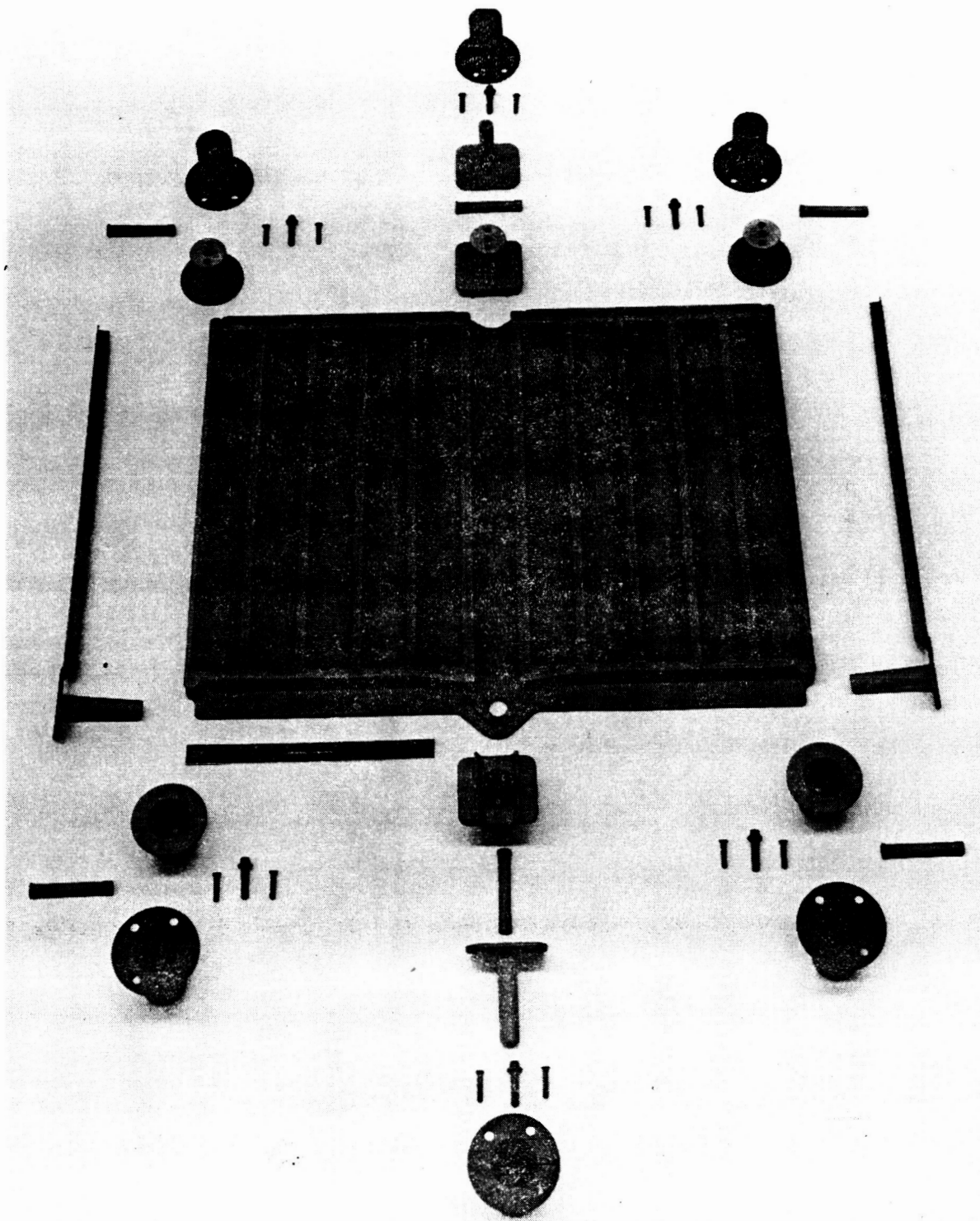


Figure 7-21. Tee-Stiffened TPS Components Prior to Testing (Photo No. 129894B)

Table 7-3. TPS Components Weight Breakdown

Component	Alloy	Tee-Stiffened		Open Corrugation	
		Wt. before coating, grams	Wt. after coating, grams	Wt. before coating, grams	Wt. after coating, grams
Heat Shield	Cb-752	1091.5	1208.3	1153.2	1233.2
Retainer, side	Cb-752	95.2	100.2	120.7	125.4
Post, center, upper	Cb-752	101.9	105.0	71.1	73.9
Post, corner, upper	Cb-752	70.1	72.3	71.4	73.3
Retainer, center	Cb-752	52.9	55.3	68.4	70.4
Plug	Cb-752	9.6	9.7	9.6	9.7
Post, Lower	TD NiCr	58.2	58.9	57.7	58.4
Bolt	TD NiCr	3.4	3.5	3.4	3.5
Screw	TD NiCr	0.9	1.0	0.9	1.0
Bolt	Cb-752	—	—	4.0	4.1
Nut	Cb-752	—	—	3.5	3.6

initiation of the parametric trade study. However, the detail design phase and subsequent fabrication resulted in the tee-stiffened TPS having a lower weight than the open corrugation TPS. This was not anticipated as a result of the parametric study (Table 3-4). It is, therefore, obvious that the trade study was deficient for not examining in more detail the heat shield attachments, closeouts, support structure, and insulation.

The actual weight of the as-coated tee-stiffened heat shield was 2.66 lb (1208.3 g) and its associated support structure was 0.90 lb (406.9 g). The as-coated open corrugation heat shield weighed 2.71 lb (1233.2 g) and its support structure was 0.95 lb (432.0 g). For both systems the insulation weighed 4.10 lb (1864.0 g).

7.5 System Costs

The cost data presented herein is based on the actual fabricating costs for constructing seven panels of each configuration. This represents an area of less than 10 ft² (1 m²) for each concept. The costs include raw material, machining, forming, joining (welding and/or brazing), chemical milling, and coating. For the tee-stiffened concept (including heat shield, support system, and insulation) the cost was \$518.21/lb (\$1141.43/kg). For the open corrugation concept the cost was \$557.80/lb (\$1228.64/kg). The percentage breakdown for the various fabrication processes is shown in Table 7-4.

The individual components cost data has been combined into an nth unit cost format and the costs projected for 5 orbiter vehicles plus spares. This information is shown in Table 7-5.

The assumptions were that 24 heat shields would be required per vehicle; the current actual costs were baseline; there would be no reduction in per pound material cost; and there would be approximately a 85% learning factor applied to all other fabrication parameters (machining, joining, coating, etc.). The cumulative average cost for n units is shown in Figure 7-22 for both corrugated and tee-stiffened configurations.

When studying the fabrication processes of Table 7-4 it can be seen that with a significant amount of machining done on bar stock there was a large amount of waste material that accompanied the machining costs. With the excellent joint efficiencies attained with welding, diffusion bonding, and brazing during the elemental and subsize evaluations (and subsequently the small size TPS specimens reported in Chapter 8), fabrication costs can be significantly reduced by employing these joining methods. For the Phase III evaluations different fabrication methods will be used to take advantage of welding thereby adding supplemental data to the cost projection curve.

Table 7-4. TPS Fabrication Cost Breakdown*

Process	Percent of Total Cost	
	Tee-Stiffened	Open Corrugation
Material	34.2	30.8
Machining	31.1	25.4
Forming/Finishing	5.8	6.8
Welding	11.3	0.3
Brazing	0.2	17.3
Chemical Milling	—	3.3
Coating	17.4	16.1

*Based on approximately 10 ft² (1 m²) of fabricated hardware per configuration

Table 7-5. Columbia Alloy TPS Cost Projection¹

<u>Type Panel</u>	Quantity Produced ²							
	<u>1</u>	<u>10</u>	<u>24</u>	<u>50</u>	<u>100</u>	<u>120</u>	<u>150</u>	<u>200</u>
Open Corrugation (composite rate = 87%)								
nth unit cost	0.419	0.264	0.221	0.191	0.166	0.160	0.153	0.145
cumulative cost (n units)	0.419	3.126	6.446	11.732	20.573	23.833	28.534	35.950
cumulative average cost (n units)	0.419	0.313	0.269	0.235	0.206	0.199	0.190	0.180
Tee-Stiffened (composite rate = 89%)								
nth unit cost	0.381	0.259	0.223	0.197	0.176	0.170	0.164	0.156
cumulative cost (n units)	0.381	2.976	6.291	11.697	20.955	24.414	29.432	37.414
cumulative average cost (n units)	0.381	0.298	0.262	0.234	0.210	0.203	0.196	0.187

1 Costs in thousands of 1972 dollars exclusive of TPS assembly effort

2 Estimated 24 heat shield sets per orbiter vehicle [$32 \text{ ft}^2 (3\text{m}^2)$]; 5 production orbiter vehicles

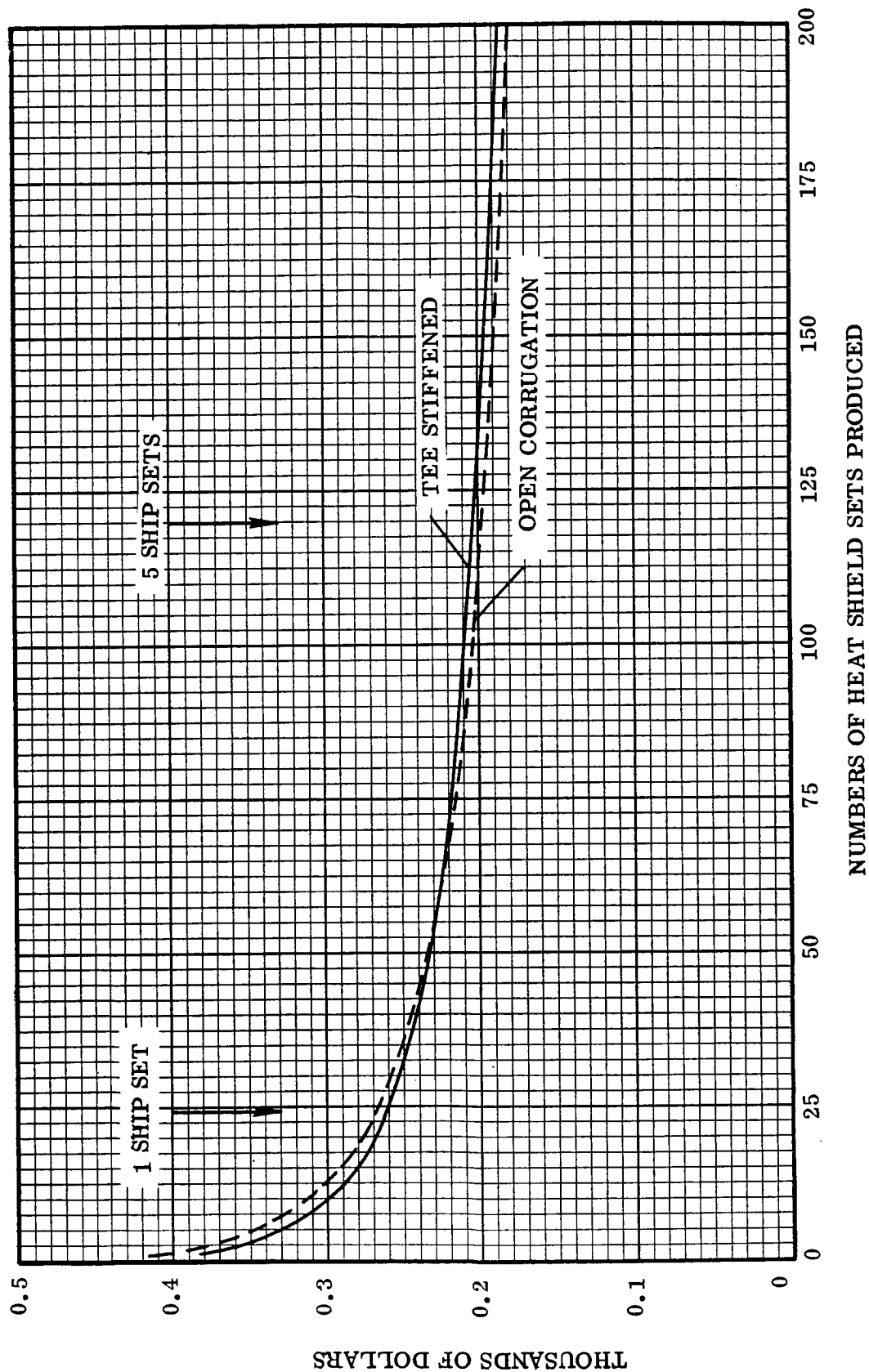


Figure 7-22. Columbia Alloy TPS Cumulative Average Cost

8 SMALL SIZE FULL SCALE ENVIRONMENTAL TESTING

The two heat shield concepts had been evaluated by test in subsize configurations (Chapter 5). Both the tee-stiffened and open corrugation models were found to be viable candidates for TPS application. Since the Cb-752/R-512E system was found to be a better performer than C-129Y/R-512E, the major remaining task was to environmentally test an entire TPS to assess the interrelated effects of temperature, pressure, load, and acoustic fatigue on the system.

Two types of thermal testing were undertaken. The first was conducted in a hot gas flow facility to investigate the system structural integrity and leakage effects. The second was conducted in a radiant heat chamber to investigate the system response while undergoing temperature, pressure differential loading and local surface pressure conditions. All specimens also were exposed to representative acoustic excitation before and after thermal testing.

8.1 Hot Gas Flow Tests

8.1.1 Test equipment and procedure. — The specimen assembly was installed in a holding frame enclosing the specimen on all four sides with the upper and lower surfaces exposed. The holding frame was constructed from copper plate and incorporated water cooling coils on the exterior surfaces. This assembly was installed in the shroud test section of the Simulated Entry and Aerothermodynamic Research (SEAR) facility (Figure 8-1) at the Harbor Drive Test Facility.

The SEAR facility incorporates a shroud test section which, when the specimen is installed, provides a flat flow channel across the exposed heat shield surface. The panel surface is exposed to a hot gas flow in one direction over the surface, thus allowing system thermal response evaluation in an environment similar to the boundary layer flow field existing on the TPS surfaces during reentry. A hydrogen/oxygen combustor is attached to the shroud section and generates the hot gas flow environment through the flow channel 22 inches (55.9 cm) wide by approximately 1.75 inches (4.45 cm) in height. The combustor design incorporates fixed throttling fuel injector nozzles arrayed span wise across the width of the combustor for lateral combustion uniformity.

For reentry test specimen temperature profiles, the combustion is controlled with a near stoichiometric mixture ratio (O_2 to H_2 by weight of 8/1 to 8.3/1) for varying total flow rates. Thus, the total flow rate determines the flow channel wall convective heating rate. The temperature response of a heat shield surface, relative to the convective heating, determines the surface equilibrium temperature. The primary test parameter is a specimen surface temperature profile (Figure 8-2) starting at ambient. The

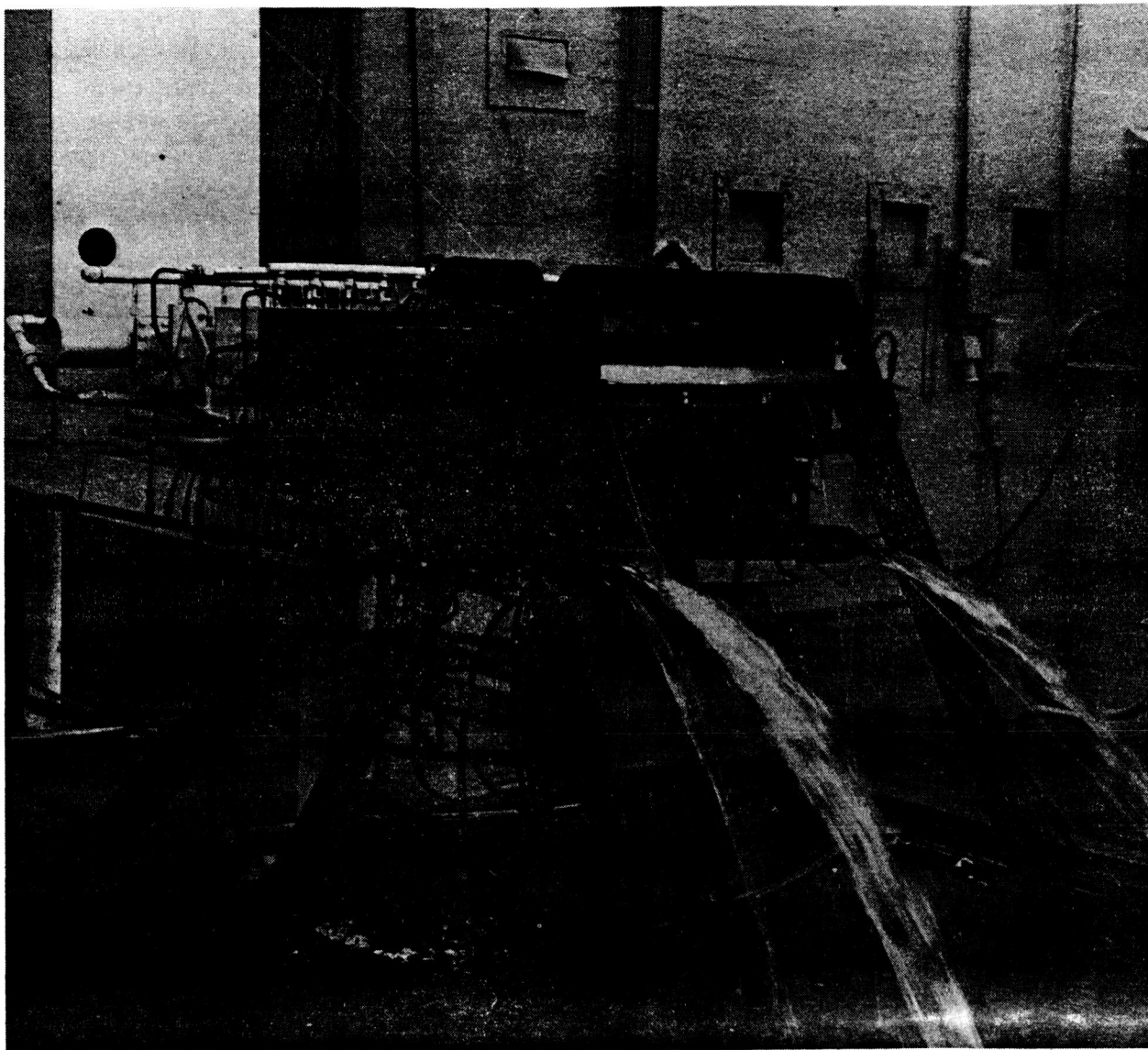


Figure 8-1. SEAR Test Facility (Photo No. 01129M)

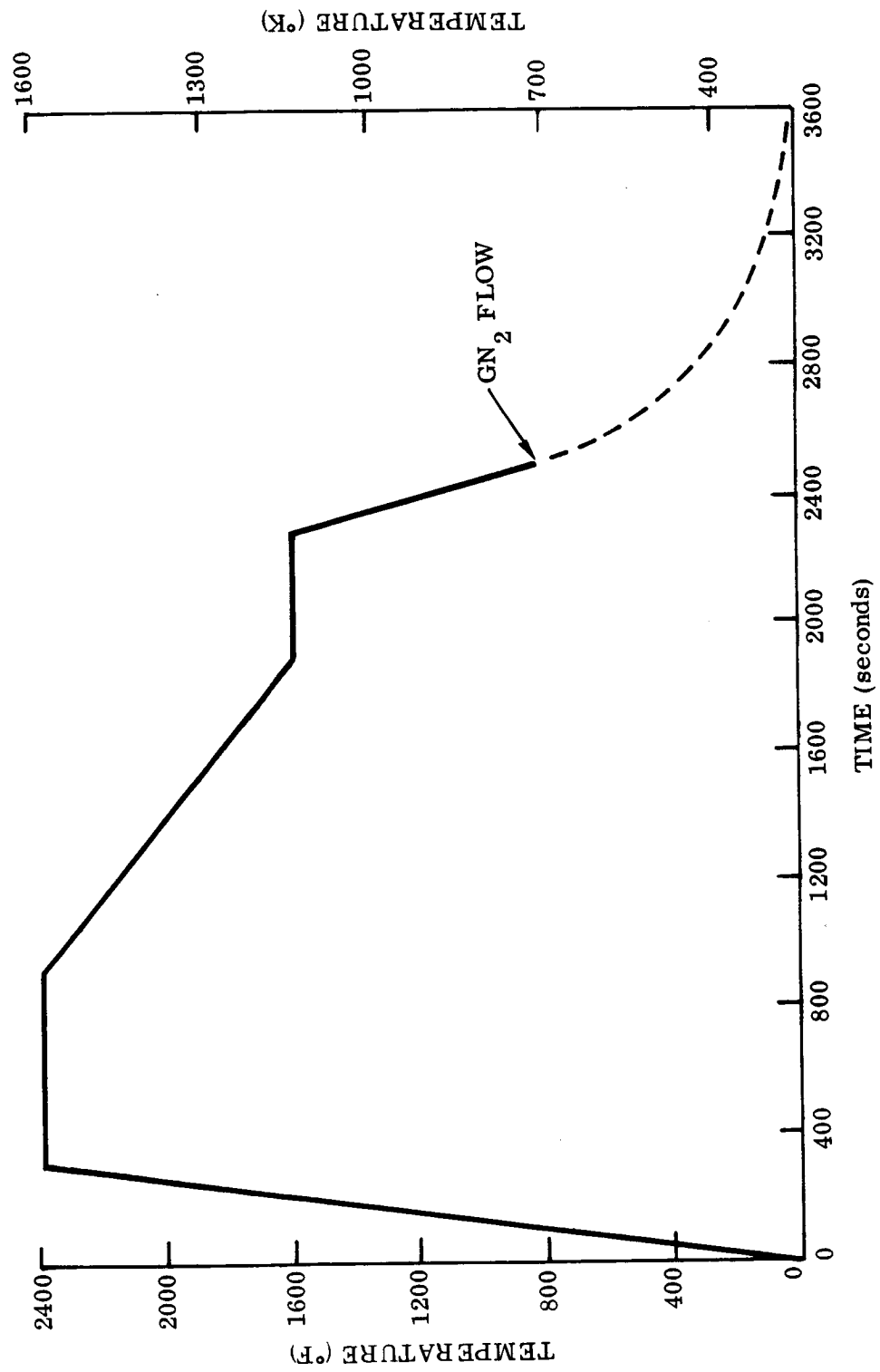


Figure 8-2. Hot Gas Flow Test Profile

surface temperature was increased linearly to 2400°F (1589°K) in 300 seconds. This temperature was maintained for 600 seconds then decreased linearly to 1600°F (1144°K) during the next 1000 seconds. The temperature was maintained at 1600°F (1144°K) for the next 400 seconds then decreased linearly to approximately 400°F (478°K) during the next 300 seconds. The next thermal cycle is begun when the highest specimen temperature is near ambient. It is hypothesized that one cycle conducted at one atmosphere in an oxidizing environment is the equivalent of four to five reduced pressure cycles. The combustor flow rates are controlled by the SEAR programmer/control console (Figure 8-3), incorporating combustion safety interlock devices, automatic sequencing ignition and shut down controls, and a closed-loop mass flow control system.

The specimens were instrumented with Tungsten-5% Rhenium/Tungsten-26% Rhenium thermocouple probes installed against the back surface of the heat shield panel and chromel/alumel thermocouples installed at discrete locations within the assembly and on the titanium primary structure sheet (Figures 8-4 and 8-5). All thermocouple leads were attached to terminals of a 150° F (339°K) reference junction. The facility instrumentation lines were routed from the reference junction, at the test specimen, to a Dymec digital data acquisition system. Test section heat flux calorimeter signals and hydrogen and oxygen mass flow rate sensor output signals were also input to the Dymec system. Data was recorded for each channel at 10 second intervals during the first 1300 seconds of each thermal cycle. The recording interval was increased to one minute from 1300 seconds to 3600 seconds and to 10 minutes from 3600 seconds to 5400 seconds elapsed time.

The same operational sequence was used for each test run and is described below:

Instrumentation and control circuits were calibrated.

The test site was secured for hazardous testing and all primary gas supply systems were pressurized.

Test shroud and combustor cooling water flow was started.

A countdown was initiated and the test run conducted as follows:

T minus 60 seconds - Preignition nitrogen purge was started through the combustor with O₂ flow at the initial heat level flow rate.

T minus 35 seconds - The hydrogen pilot was ignited.

T minus 30 seconds - The main flame combustion was started at the minimum heating conditions.

T minus 25 seconds - Hydrogen pilot automatically extinguished and operational characteristics were monitored for stability.

T Zero - The program function generator chart drive was started; recorders were started.

T Zero to T plus 2460 seconds - Specimen temperatures were monitored on recorder and specimen surface was visually monitored with TV and by direct observation.

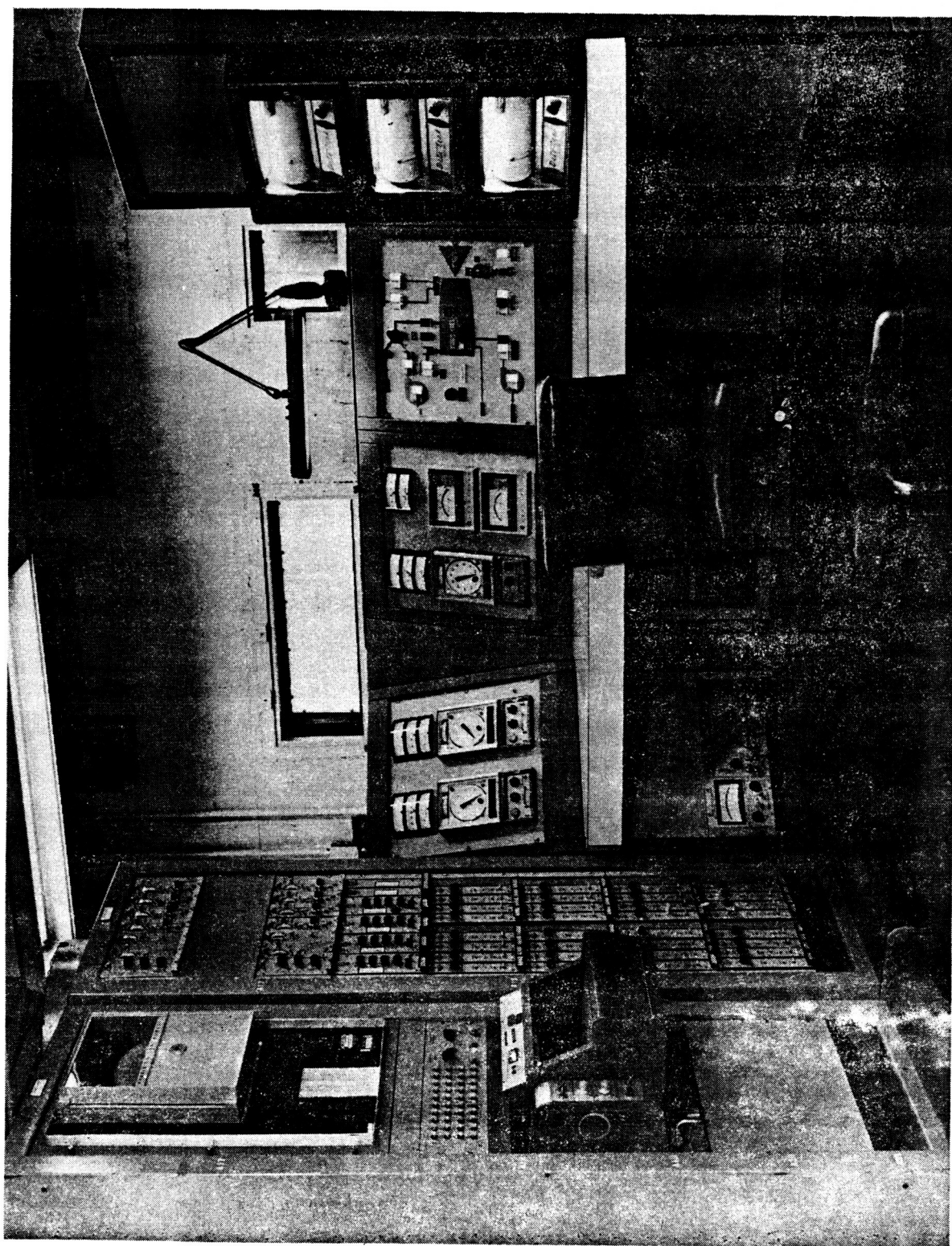
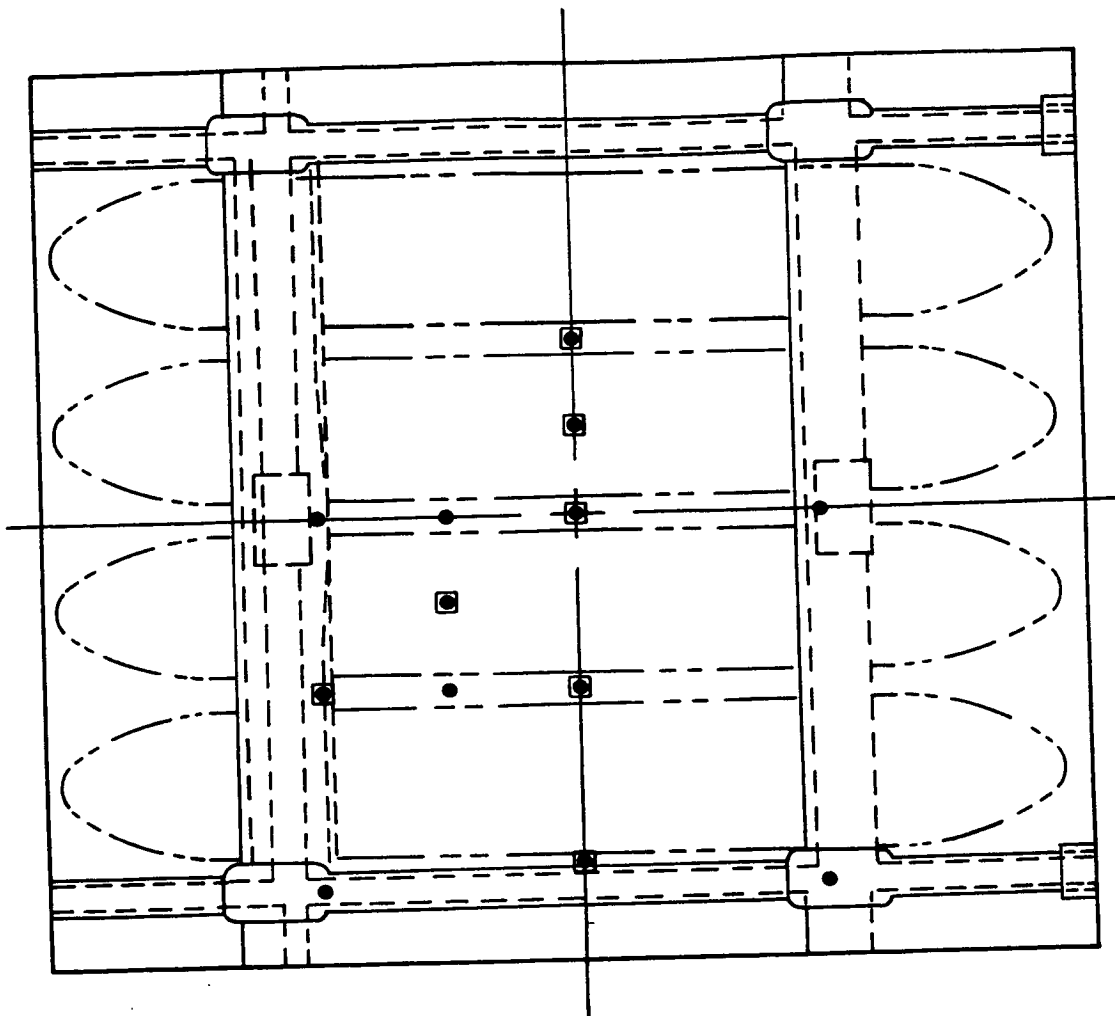


Figure 8-3. SEAR Facility Control, Programming, and Data Acquisition Center (Photo 97110)



□ W-5 Re/W-26 Re

● Cr/Al

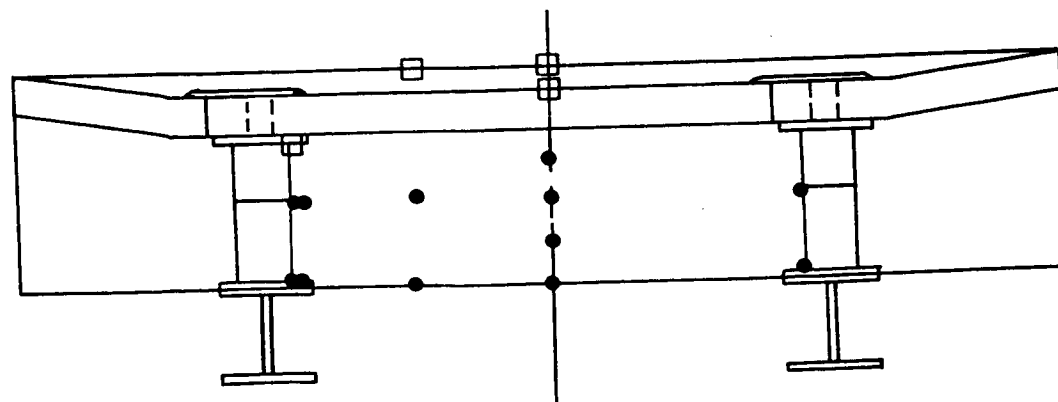


Figure 8-4. Thermocouple Locations for Open Corrugation TPS

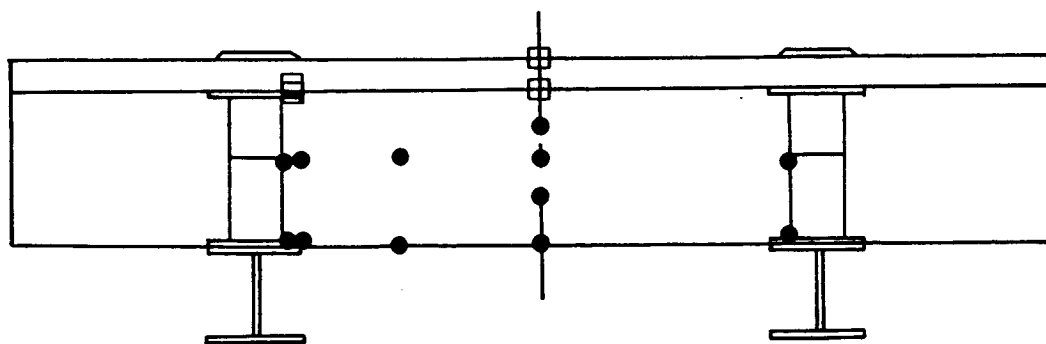
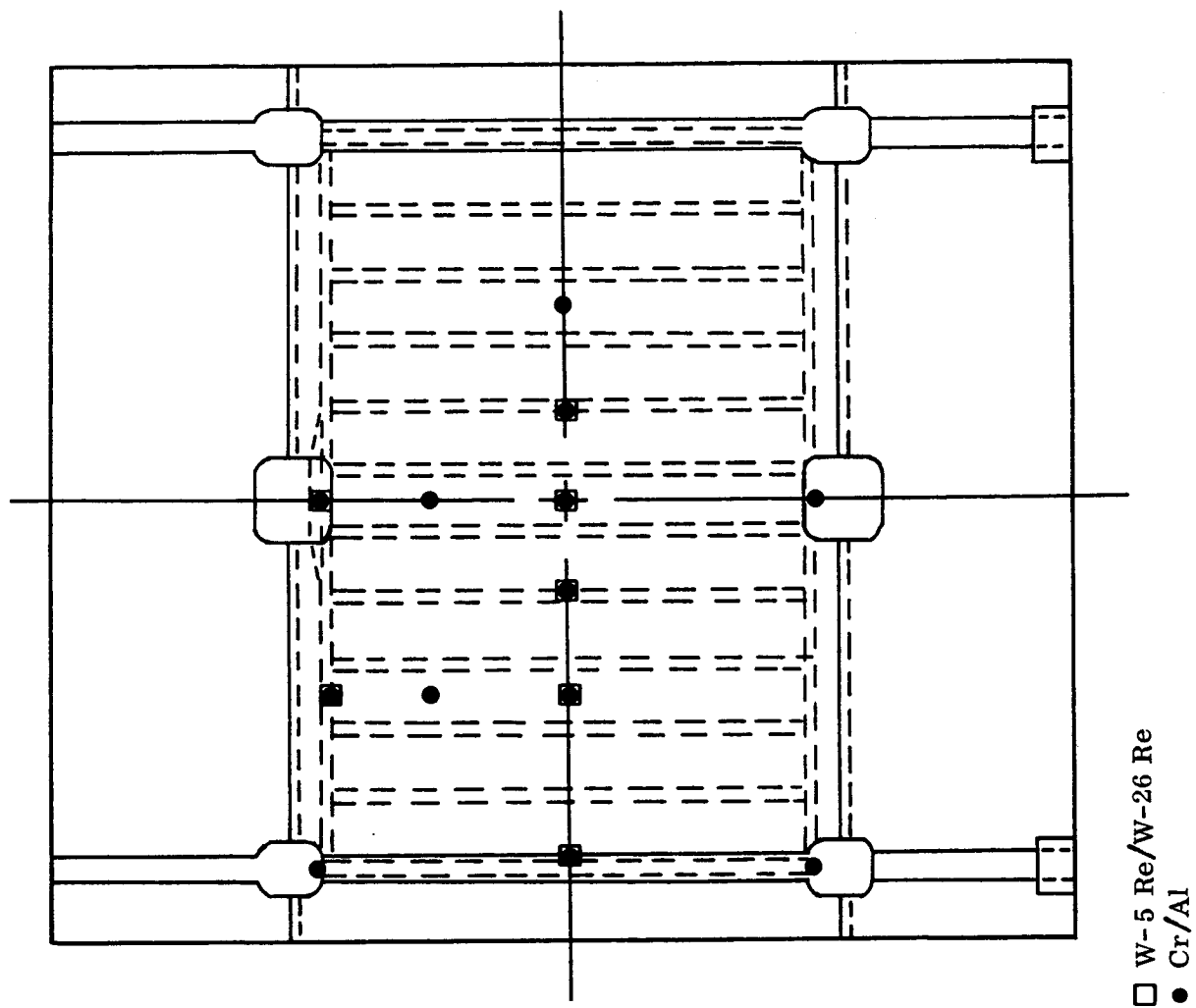


Figure 8-5. Thermocouple Locations for Tee-Stiffened TPS

- T plus 2460 seconds - Combustion terminated and post test nitrogen purge initiated.
Function generators "OFF".
- T plus 2580 seconds - Purge terminated. Primary gas supply systems depressured,
cooling water flow stopped, flow control circuits on "Standby."
- T plus 5400 seconds - Recorders OFF, post-test calibrations.

The test specimen surface was examined visually and the specimen was cooled down to ambient temperatures prior to conducting the next thermal cycle.

8.1.2 Test observations and results. -

8.1.2.1 Open corrugation TPS: The specimen is shown in Figure 8-6 installed in the SEAR facility prior to test initiation. The specimen was subjected to three calibration heating cycles prior to the first full heating cycle. Each cycle was approximately 600 seconds duration with peak temperatures of 1900, 2000, and 2300° F (1311, 1366, and 1533° K) respectively. Full thermal flow cycles 1 through 10 were conducted with cold wall heating rates up to 69 Btu/ft²-sec (783 kW/m²) measured to produce nominal peak heating surface temperatures of 2400° F (1589° K). The temperature corrected maximum nominal velocity₂ was M = 0.8. The flat plate static pressure at peak temperature was 0.025 psig (172N/m²).

Although not specifically recorded, it was observed that wind gusts at the test site, in the direction counterflow to the SEAR hot gas exhaust flow, caused hot gas to recirculate beneath the specimen assembly in the vicinity of the titanium primary structure. The wind gusts were sporadic and infrequent; consequently, no specific correlation is available with respect to specimen cold face temperature response and no attempt was made to provide additional shielding of the specimen cold face.

The specimen assembly was removed from the shroud for inspection after Run No. 10 following a cooling system failure. Evaluation after the test run revealed that water ingestion had occurred in the flow channel with residual deposits evidenced on the specimen surface. The shroud was repaired by local rewelding. Also included at this time was the brushing (polishing) of the interior wall surfaces. This operation had not been performed prior to this time during the test program. A perceptible improvement in surface reflectivity was observed. Subsequent examinations and cleaning operations were able to maintain this surface condition during the remainder of the test operations.

During this specimen inspection period it was found that the leading edge of the main heat shield had separated from the forward auxiliary panel (Figure 8-7). In the normal installed position the closeout panel overlaps the heat shield by 0.20 inch (0.51 cm). As noted in Figure 8-8 the panel sustained some local damage that required removal of the contaminated region and repair by the glass frit method discussed in Section 10.3.3. The partially disassembled specimen is shown in Figure 8-9.

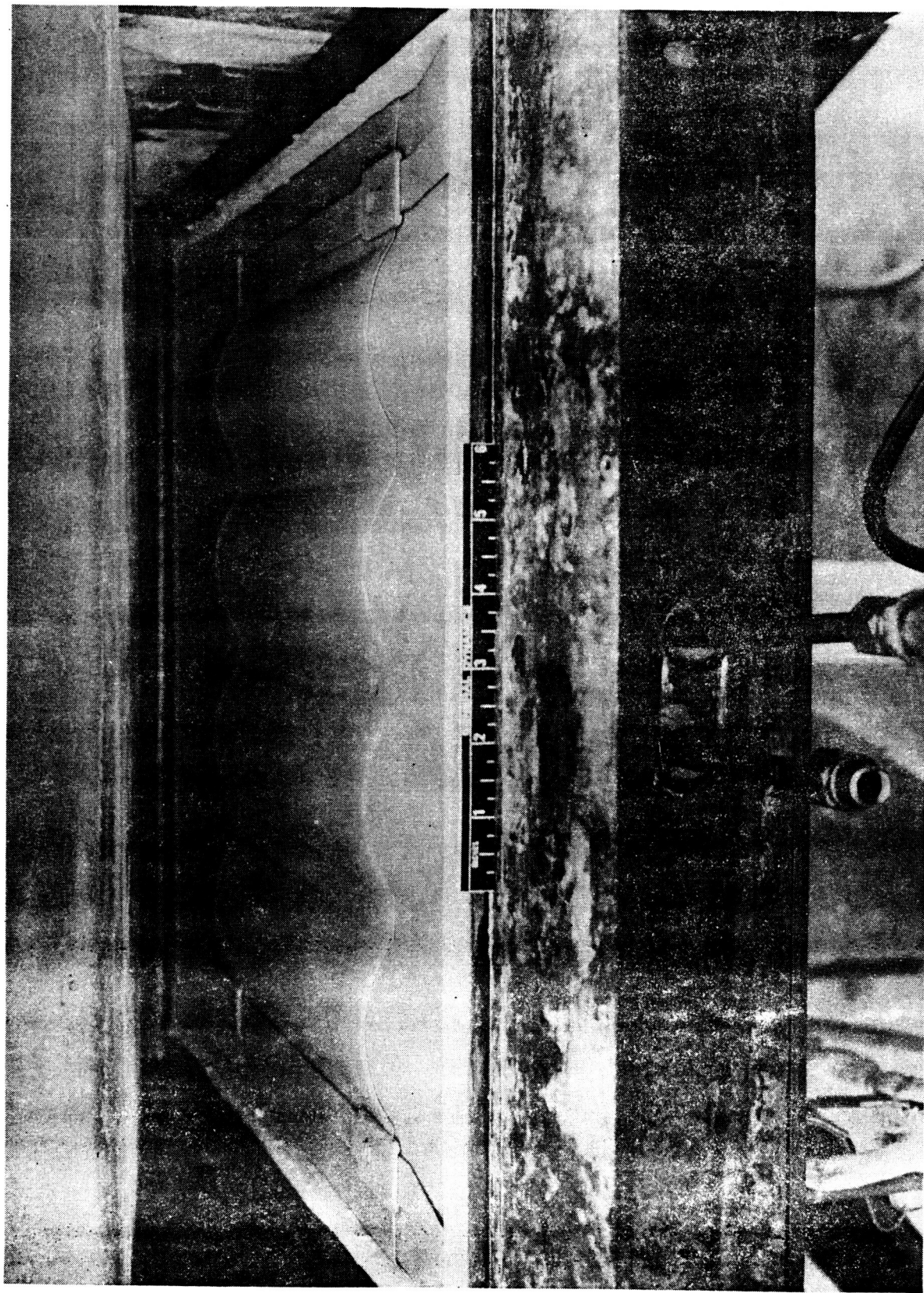


Figure 8-6. Open Corrugation TPS Specimen Installed in SEAR Facility Prior to Testing (Photo 132620B)

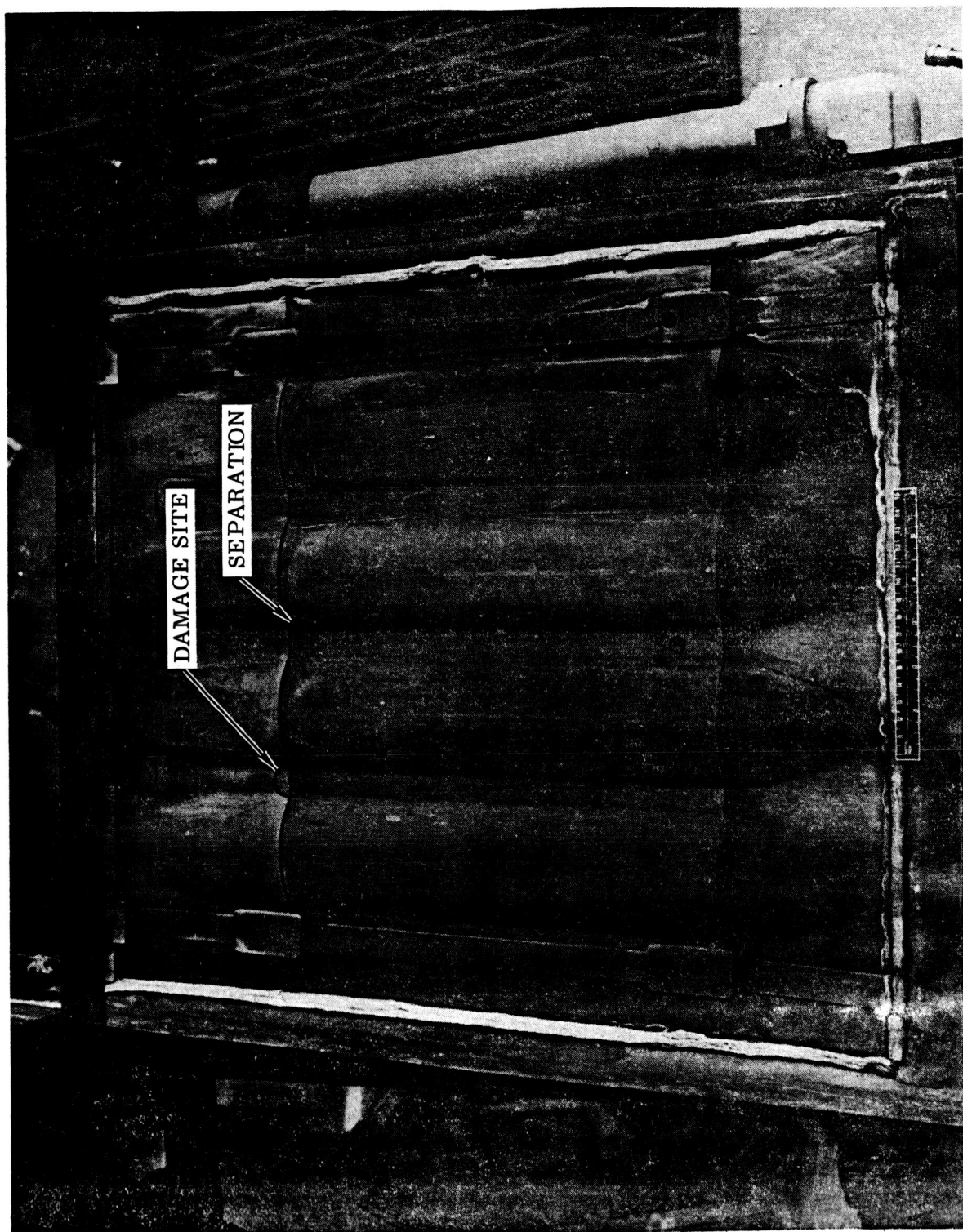


Figure 8-7. Open Corrugation TPS Specimen After 10 Hot Gas Flow Cycles (Photo 132917B)



Figure 8-8. Panel Separation and Edge Damage of Open Corrugation TPS Specimen After 10 Hot Gas Flow Cycles (Photo 132919B)

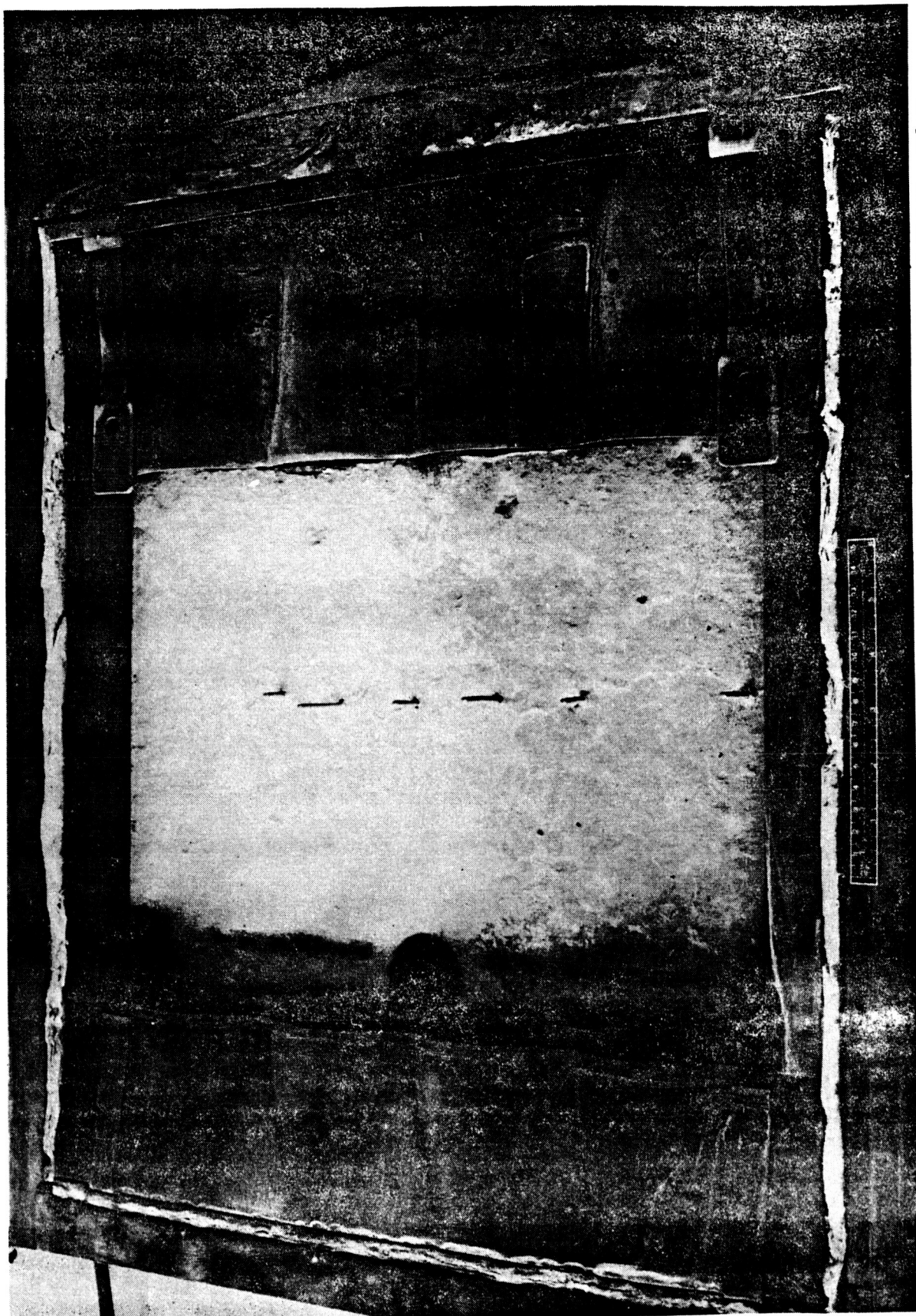


Figure 8-9. Open Corrugation TPS Specimen with Main Heat Shield Removed After 10 Hot Gas Flow Cycles (Photo 132916B)

The in-plane displacement of the panels that permitted the overlapping edges to butt is attributed to excessive clamp-up and/or interference which prevented free thermal expansion [approximately 0.12 inch (0.30 cm) at 2400°F (1589°K)]. It can also be attributed to the flexibility of the support beams in the test fixture which react the panel support post bending loads in torsion. It is considered that the thermal expansion of the heat shield was accommodated by forcing the support posts apart rather than by sliding. The resulting misalignment of the heat shield and post flanges prevented the posts from returning to their initial position on cool-down. Hence, under repeated thermal cycles the panel edge was progressively withdrawn from underneath the overlapped edge of the closeout panel.

Thermal testing was reinitiated following repair of the shroud and specimen. With all combustor operating parameters indicating stable conditions at levels used during the previous runs, the specimen surface temperature data indicated a peak of 2707°F (1759°K) at 300 seconds elapsed time. After approximately four minutes of stabilized operation, manual control was exercised to reduce the surface temperature to 2400°F (1589°K) in approximately one minute. A normal control profile was maintained for the remainder of the cycle.

A similar excursion was experienced during Cycle 12 when the peak surface temperature reached 2653°F (1729°K) for three minutes. These excursions were attributed to the change of shroud interior reflectance. The operating conditions of the combustor were altered to resume the normal profile. Structurally, no detrimental effects were noted due to these temperature excursions indicating a comfortable overshoot capability for the columbium alloy system. As a result of the maximum excursion the titanium substructure reached a maximum temperature of approximately 900°F (755°K). The predicted normal temperature was 750°F (673°K).

Testing was continued for the remaining eight cycles for a total of twenty. No further anomalies were observed. The specimen is shown after 20 cycles in Figure 8-10. As was the case after 10 cycles, no difficulties were encountered during disassembly examination following the twentieth thermal cycle and 100 acoustic cycles. No additional repairs were made to the specimen. The five repair sites exhibited no further oxidation or crack propagations.

Since the repair was accomplished by removing the heat shield from the test setup and firing the glass frit mixture in a furnace, the practicality of field repair was demonstrated. It is believed that an in-place repair also could have been made using either the glassy matrix composition technique or the R-512E preform fired by a high intensity heat lamp (Reference 45) except for the desire to remove the potentially contaminated region by grinding. It is, therefore, believed that the repair techniques developed under contract NAS8-26121 and employed herein are viable and should be considered state-of-the-art for coated columbium alloys.

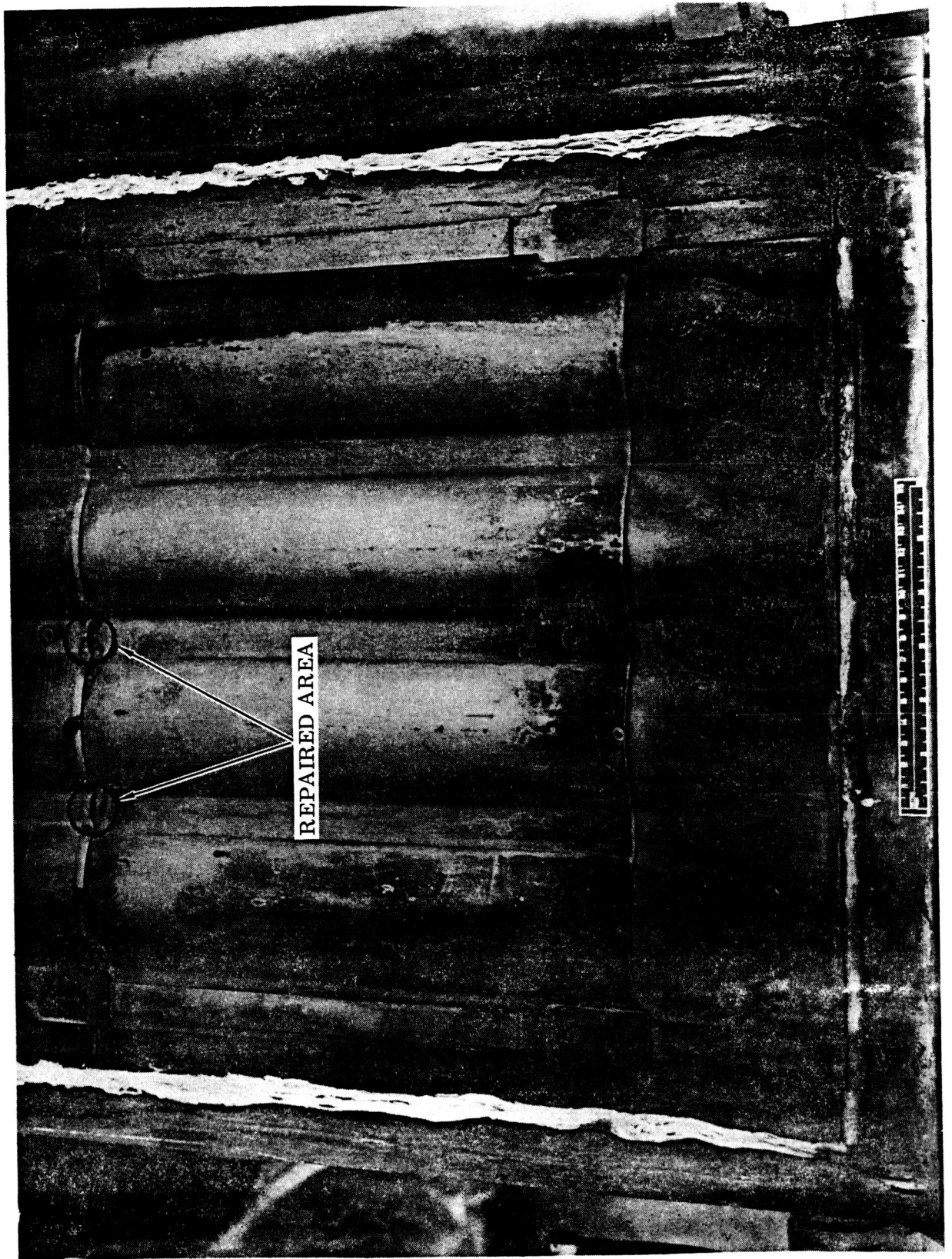


Figure 8-10. Open Corrugation TPS Specimen After 20 Hot Gas Flow Cycles (Photo 133245B)

Due to an error made during the design stage the TD NiCr lower support posts were machined to a height of 1.90 inches (4.83 cm) instead of 2.30 inches (5.84 cm). Since it was not practical to refabricate the posts, new thermal predictions were made for the overall and support post temperature distributions. These predictions are presented in Figures 8-11, 8-12, and 8-13. They replace Figures 6-34, 6-58, and 6-59 respectively. It is shown that the titanium structure at the center of the specimen was predicted to reach a maximum temperature of 750° F (673° K). The base of the TD NiCr post was predicted to reach 915° F (764° K).

In reviewing the data from the 18 runs (excluding the two runs with excessive heating rates) it was found that the actual temperatures were within an acceptable tolerance of those predicted. A summary of the data for four critical locations of the open corrugation specimen is presented in Table 8-1. The data average shows that the peak heat shield temperature at the center of the specimen was 2401° F (1590° K) versus a nominal temperature of 2400° F (1589° K). For thermocouples located near the support post interface between the upper Cb-752 post and the lower TD NiCr post the average peak temperature was 2136° F (1442° K) versus a predicted 2150° F (1450° K). At the base of the TD NiCr posts the average recorded temperature was 910° F (761° K) compared to a predicted 915° F (764° K). The thermocouple located at the center of the specimen on the titanium skin recorded an average temperature of 759° F (677° K). The predicted temperature for this region was 750° F (672° K). Data plots of the average temperature history for these four locations are shown in Figure 8-14.

After completion of the 20 thermal cycles the specimen was subjected to 99 simulated boost acoustic cycles (Section 8.3).

8.1.2.2 Tee-stiffened TPS: The specimen was subjected to 20 complete thermal flow heating cycles with no calibration cycles prior to start of tests. Surface temperatures monitored during each cycle indicated temperatures of 2400° F (1589° K) during the peak heating of approximately 60 Btu/ft²-sec (681 kW/m²). A corresponding total mass flow rate, through the 1.75 inch (4.45 cm) by 22 inch (55.9 cm) rectangular cross section gas flow channel, was 0.259 pounds (0.118 kg) per second. Static wall pressures at peak heating were measured spanwise across the flow channel during calibration runs. The measured static pressure was 0.025 psig (172 N/m²). The temperature corrected Mach number was 0.8.

No anomalies were encountered during this test series. The specimen surface was visually inspected after each thermal cycle during the cool down period. The specimen was physically removed from the shroud after cycle 10 and inspected by removing the longitudinal retainers and main heat shield. No unusual surface changes or structural changes were observed. Following inspection the specimen was reassembled and subjected to an additional 10 thermal cycles. For comparison, two views of the tee-stiffened TPS specimen are shown before exposure and after 20 thermal cycles in Figures 8-15 through 8-18.

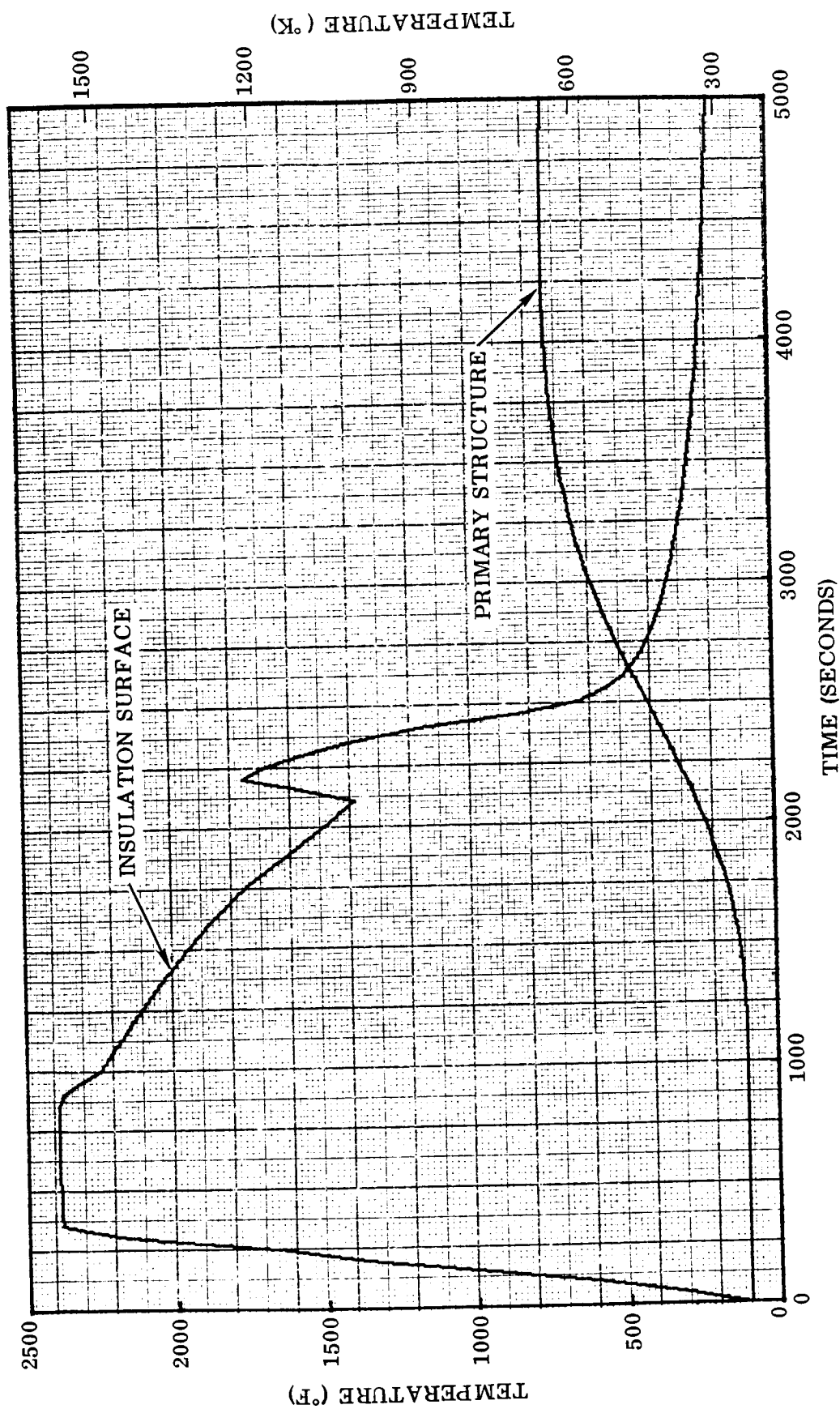


Figure 8-11. Predicted Structure and Insulation Surface Temperature History (Revised)

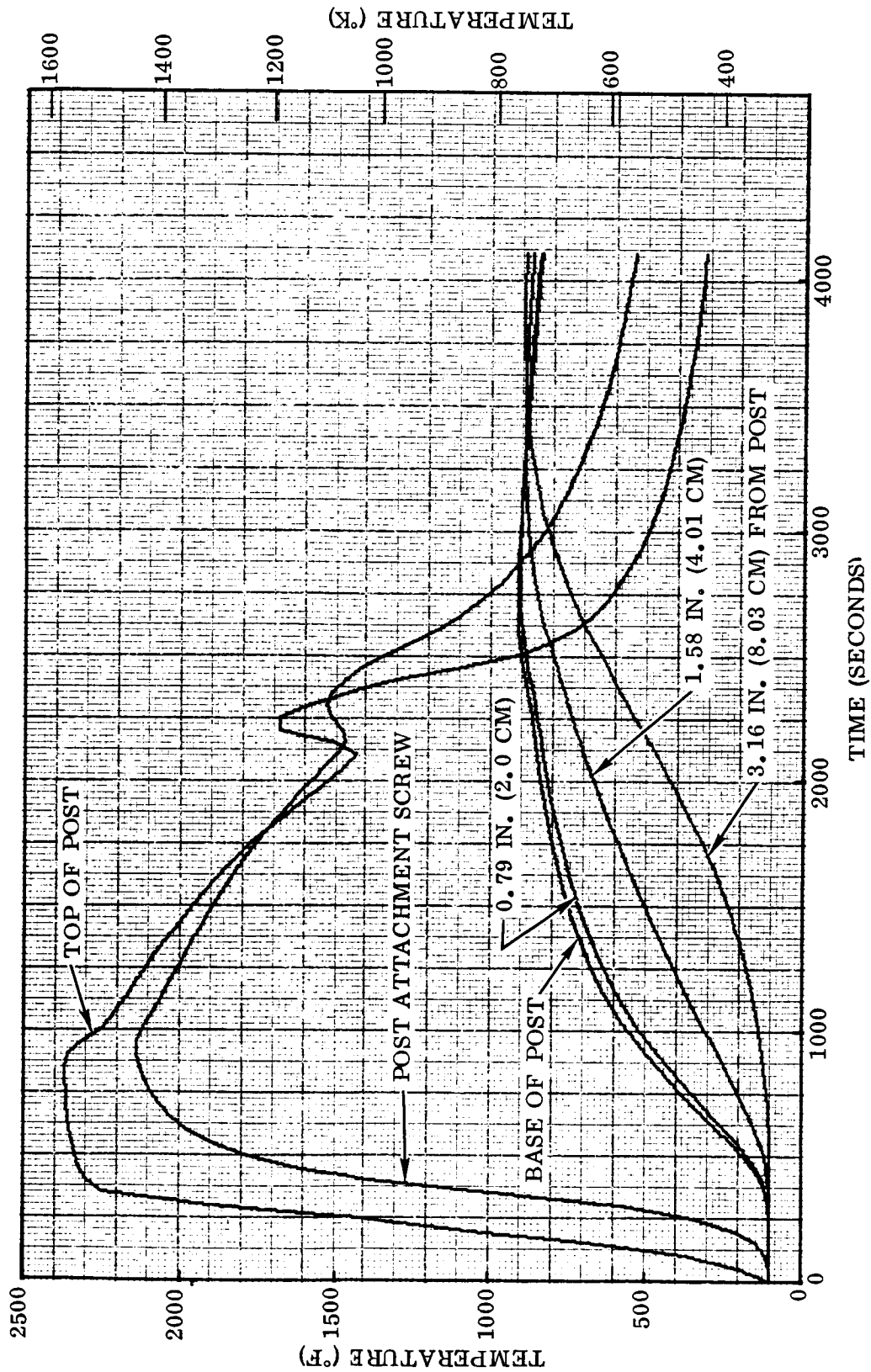


Figure 8-12. Predicted Panel Support Post and Primary Structure Temperature Histories (Revised)

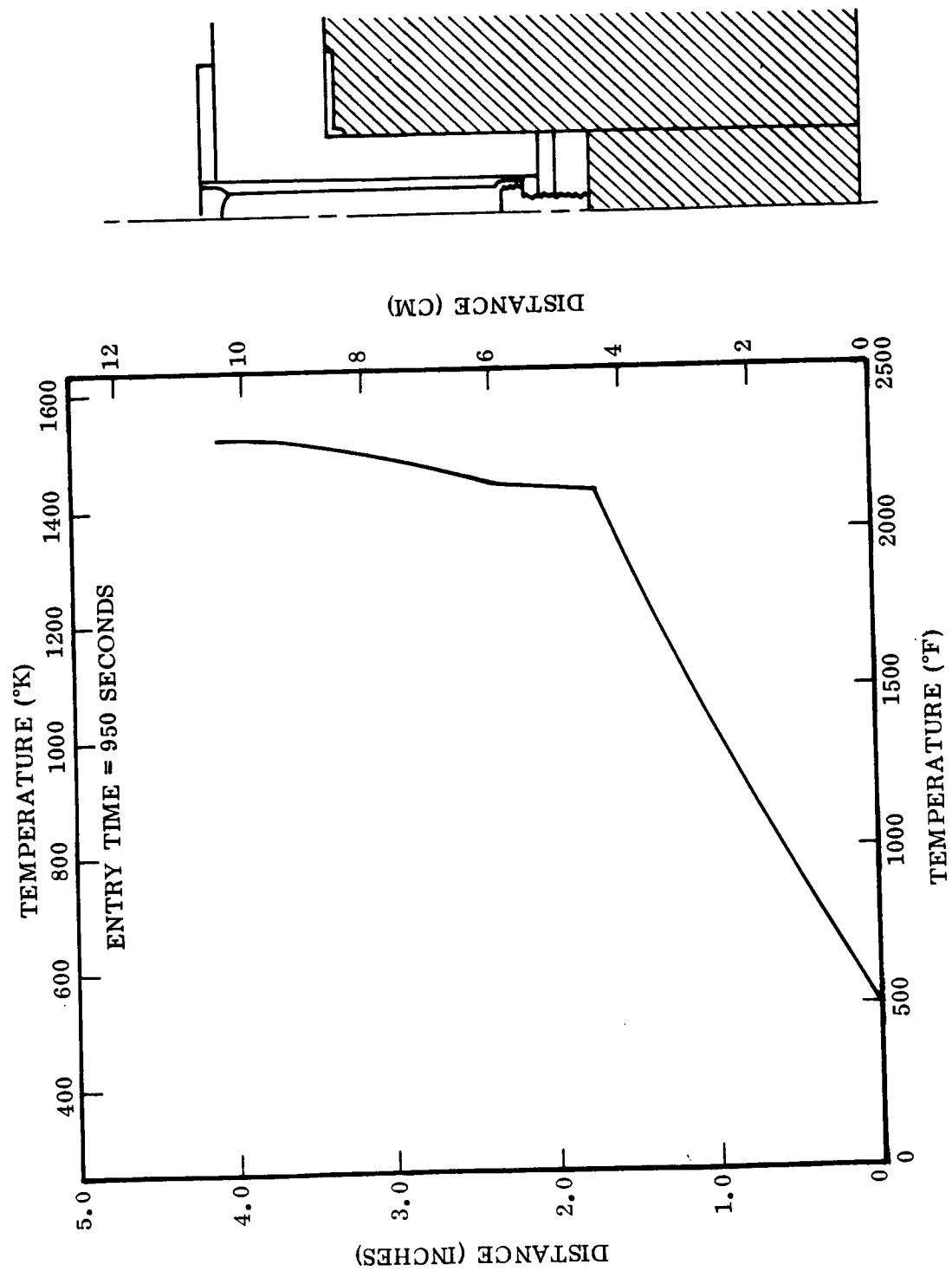


Figure 8-13. Predicted Support Post Temperature Distribution (Revised)

Table 8-1. Open Corrugation TPS Hot Gas Flow Test Thermal Summary

Run Number	Max. Heat Shield Temp. at Specimen Center		Cb-752/TD NiCr Support Post Interface		TD NiCr Support Post Base		Titanium Structure at Specimen Center	
	°F	°K	°F	°K	°F	°K	°F	°K
1	2397	1587	2130	1439	905	758	755	675
2	2402	1590	2132	1440	910	761	760	678
3	2400	1589	2137	1443	914	763	760	678
4	2405	1592	2140	1444	917	765	763	679
5	2401	1589	2133	1441	906	759	762	679
6	2398	1588	2133	1441	900	756	759	677
7	2399	1588	2132	1440	898	754	761	678
8	2402	1590	2137	1443	908	760	765	691
9	2400	1589	2139	1444	906	754	760	678
10	2405	1592	2141	1445	915	764	771	684
11	2707	1759	2363	1568	1116	876	905	758
12	2653	1729	2302	1534	1076	853	892	751
13	2410	1594	2148	1449	922	768	773	685
14	2401	1589	2135	1442	915	764	761	678
15	2401	1589	2136	1442	915	764	757	676
16	2397	1587	2130	1439	904	758	750	672
17	2395	1586	2130	1439	896	753	750	672
18	2402	1590	2135	1442	913	763	752	673
19	2404	1591	2136	1442	917	765	752	673
20	2406	1592	2140	1444	919	766	753	674
Average*	2401	1590	2136	1442	910	761	759	677
Tolerance	{ ⁺⁹ -6}	{ ⁺⁴ -4}	{ ⁺¹² -6}	{ ⁺⁷ -3}	{ ⁺⁹ -14}	{ ⁺⁷ -8}	{ ⁺¹⁴ -9}	{ ⁺⁸ -5}

*Runs 11 and 12 not included.

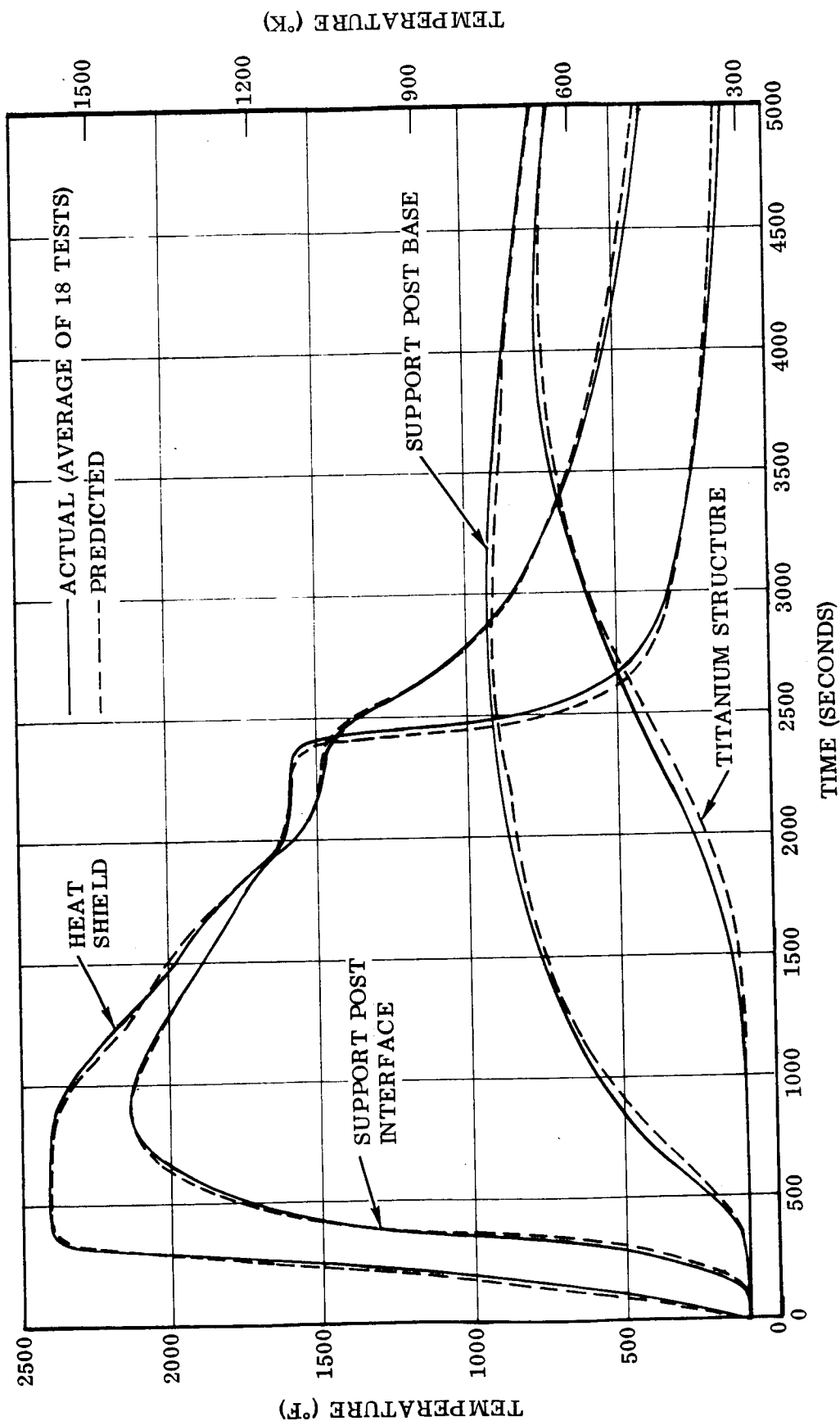


Figure 8-14. Hot Gas Flow Test Composite Temperature Distribution — Open Corrugation TPS

A summary of the thermocouple readings for four critical locations are presented in Table 8-2. The peak heat shield temperature during this test series was 2425° F (1603° K). The average maximum temperature of the heat shield for the 20 cycles was 2404° F (1591° K) compared to a nominal 2400° F (1589° K). The average maximum temperature near the bi-metal post interface was 2162° F (1456° K) versus a predicted value of 2150° F (1450° K). The thermocouples located at the base of the TD NiCr posts indicated a maximum temperature of 920° F (767° K) versus a predicted level of 915° F (764° K). The average maximum temperature experienced by the titanium skin at the center of the specimen was 766° F (681° K) compared to a prediction of 750° F (672° K). Data plots of the average temperature history for these four locations are shown in Figure 8-19.

Following the examination of the tee-stiffened TPS specimen after 20 hot gas flow simulated reentry cycles, the specimen was returned to the acoustic chamber for 99 additional simulated boost mission cycles (Section 8.3).

8.1.3 Test summary. — In comparing the hot gas flow test performance of the open corrugation and tee-stiffened TPS specimens, little differentiation could be found. The material systems performed well with no coating failures on either specimen (with the exception of the mechanically induced edge defect on the corrugation specimen). No post-test structural defects were found in the tee-stiffened specimen. The structural difficulty encountered with the corrugation specimen was believed to have been induced by an improperly assembled specimen. In addition there is some reason to suspect the quality of the forward beam brazement. The insulation performed well and appeared to be unaffected by hot gas leakage into the system or by moisture due to humidity. (The average relative humidity during the 21 days of elapsed time for the open corrugation TPS series was 70%; the average relative humidity during the 16 days of elapsed time for the tee-stiffened TPS series was 71%.)

8.2 Radiant Heat Tests

8.2.1 Test equipment and procedure. — This test series was conducted in the Convair Cryotherm/Radiant Heat Lamp facility (Figure 8-20). The heat chamber, which is 32 inches (81.4 cm) square and 13 inches (33 cm) deep (Figure 8-21), is water cooled on the sides and bottom at a flow rate of 1.5 gallons per minute ($94.8 \mu\text{m}^3/\text{sec}$). Inside the heat chamber is a perforated stainless steel basket supporting 2 inch (5.1 cm) thick insulation and providing an open path to the sides of the test specimen from the pump opening in the bottom of the chamber.

Heating is provided by 28 heat lamps, General Electric 5M/T3/ICL/HT-(575-625V), mounted in quartz-tube cooling jackets. The lamps are arranged to provide additional heating at the edge of the specimen when necessary for uniform hot-face temperatures.

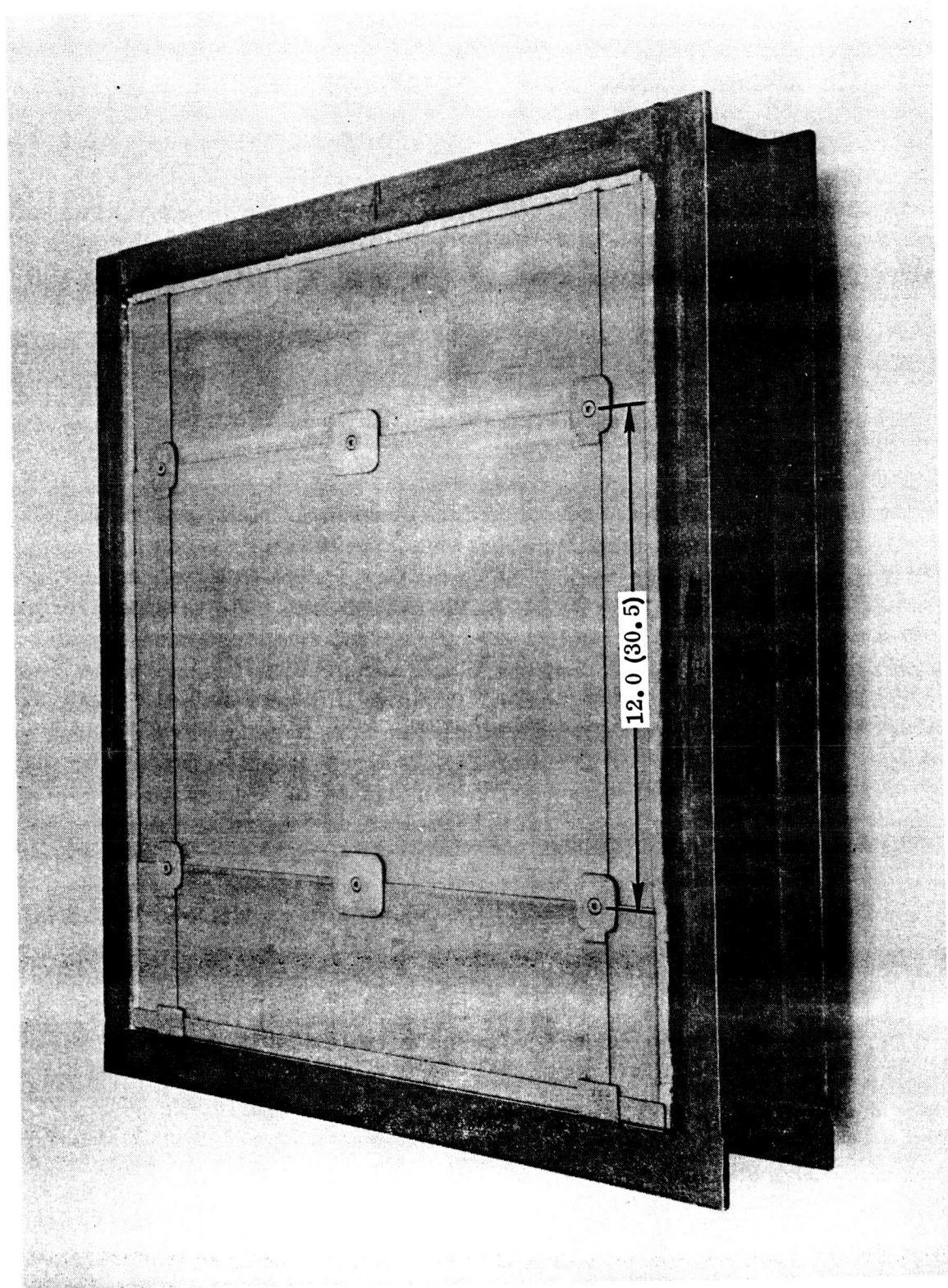


Figure 8-15. Unexposed Tee-Stiffened TPS Specimen -- Side View (Photo 120327B)

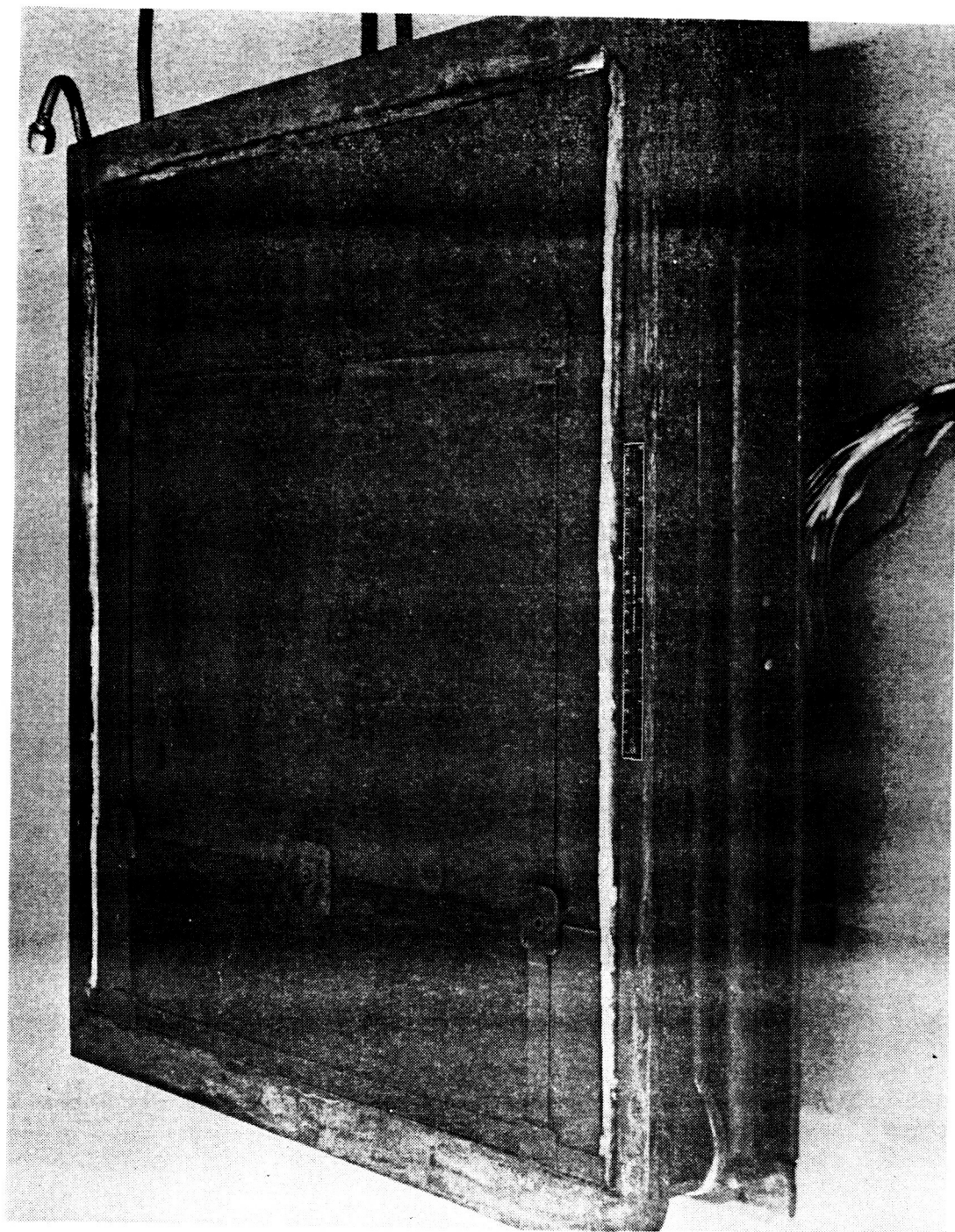


Figure 8-16. Tee-Stiffened TPS Specimen After 20 Hot Gas Flow Cycles — Side View (Photo 133659B)

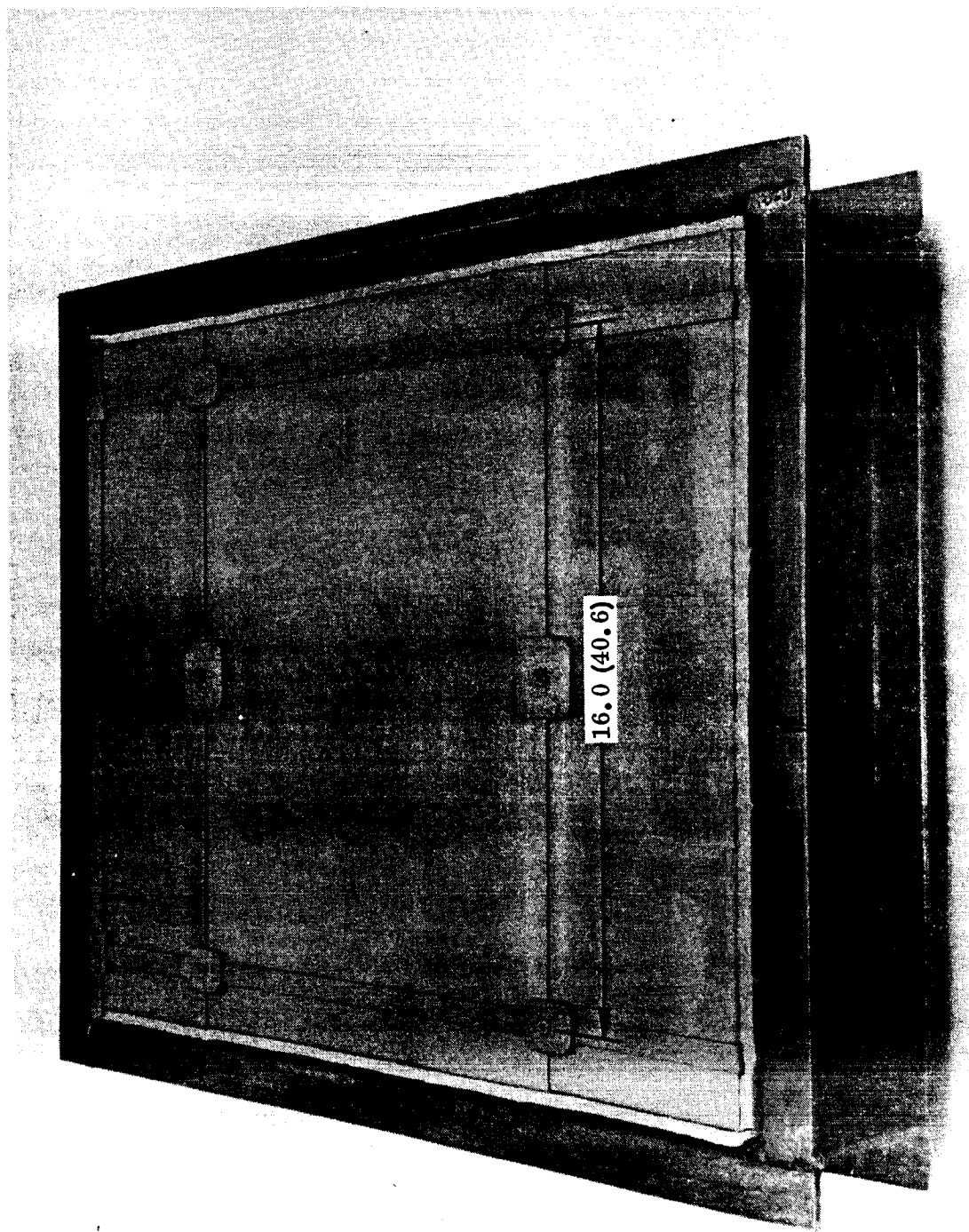


Figure 8-17. Unexposed Tee-Stiffened TPS Specimen -- End View (Photo 130328B)

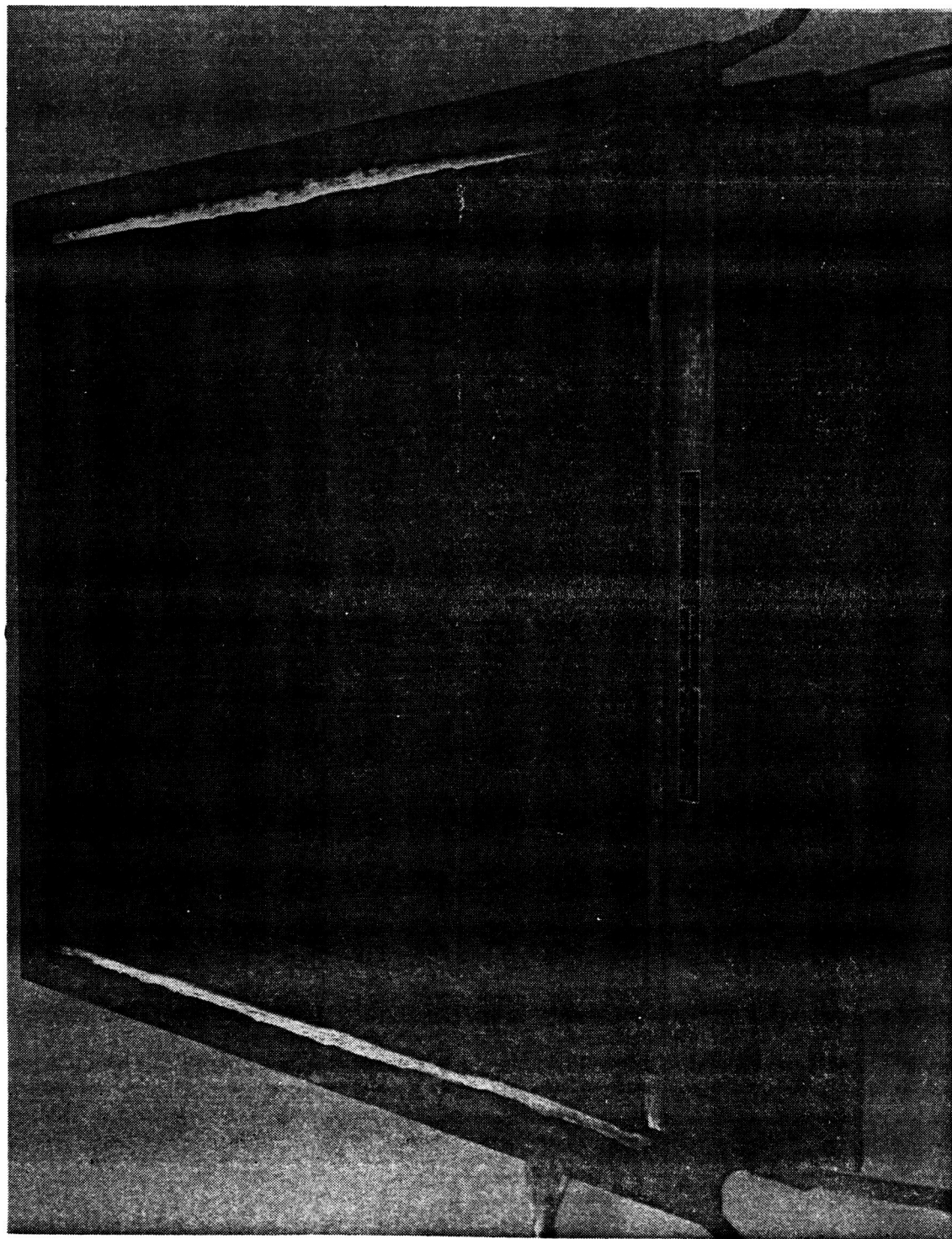


Figure 8-18. Tee-Stiffened TPS Specimen After 20 Hot Gas Flow Cycles — End View (Photo 133658B)

Table 8-2. Tee-Stiffened TPS Hot Gas Flow Test Thermal Summary

Run Number	Max. Heat Shield Temp. at Specimen Center		Cb-752/TD NiCr Support Post Interface		TD NiCr Support Post Base		Titanium Structure at Specimen Center	
	°F	°K	°F	°K	°F	°K	°F	°K
1	2406	1592	2167	1459	922	768	770	683
2	2404	1591	2162	1457	922	768	769	683
3	2400	1589	2161	1456	920	767	768	682
4	2402	1590	2160	1456	921	767	768	682
5	2410	1594	2170	1461	927	771	775	686
6	2415	1597	2172	1462	930	772	776	687
7	2408	1593	2167	1459	923	768	768	682
8	2400	1589	2158	1454	919	766	765	681
9	2395	1586	2152	1451	913	763	760	678
10	2398	1588	2160	1456	915	764	762	679
11	2393	1585	2149	1449	912	762	760	678
12	2409	1594	2167	1459	925	769	770	683
13	2418	1599	2173	1463	931	773	778	688
14	2425	1603	2176	1464	935	775	780	689
15	2402	1590	2159	1455	915	764	760	678
16	2400	1589	2156	1453	916	764	761	678
17	2397	1587	2152	1451	913	763	758	677
18	2397	1587	2153	1452	912	762	755	675
19	2402	1590	2158	1454	915	764	759	677
20	2405	1592	2159	1455	916	764	758	677
Average	2404	1591	2162	1456	920	767	766	681
Tolerance	{ $\begin{pmatrix} +21 \\ -7 \end{pmatrix}$ }		{ $\begin{pmatrix} +14 \\ -13 \end{pmatrix}$ }		{ $\begin{pmatrix} +15 \\ -8 \end{pmatrix}$ }		{ $\begin{pmatrix} +12 \\ -11 \end{pmatrix}$ }	
	{ $\begin{pmatrix} +12 \\ -6 \end{pmatrix}$ }		{ $\begin{pmatrix} +8 \\ -7 \end{pmatrix}$ }		{ $\begin{pmatrix} +8 \\ -5 \end{pmatrix}$ }		{ $\begin{pmatrix} +8 \\ -6 \end{pmatrix}$ }	

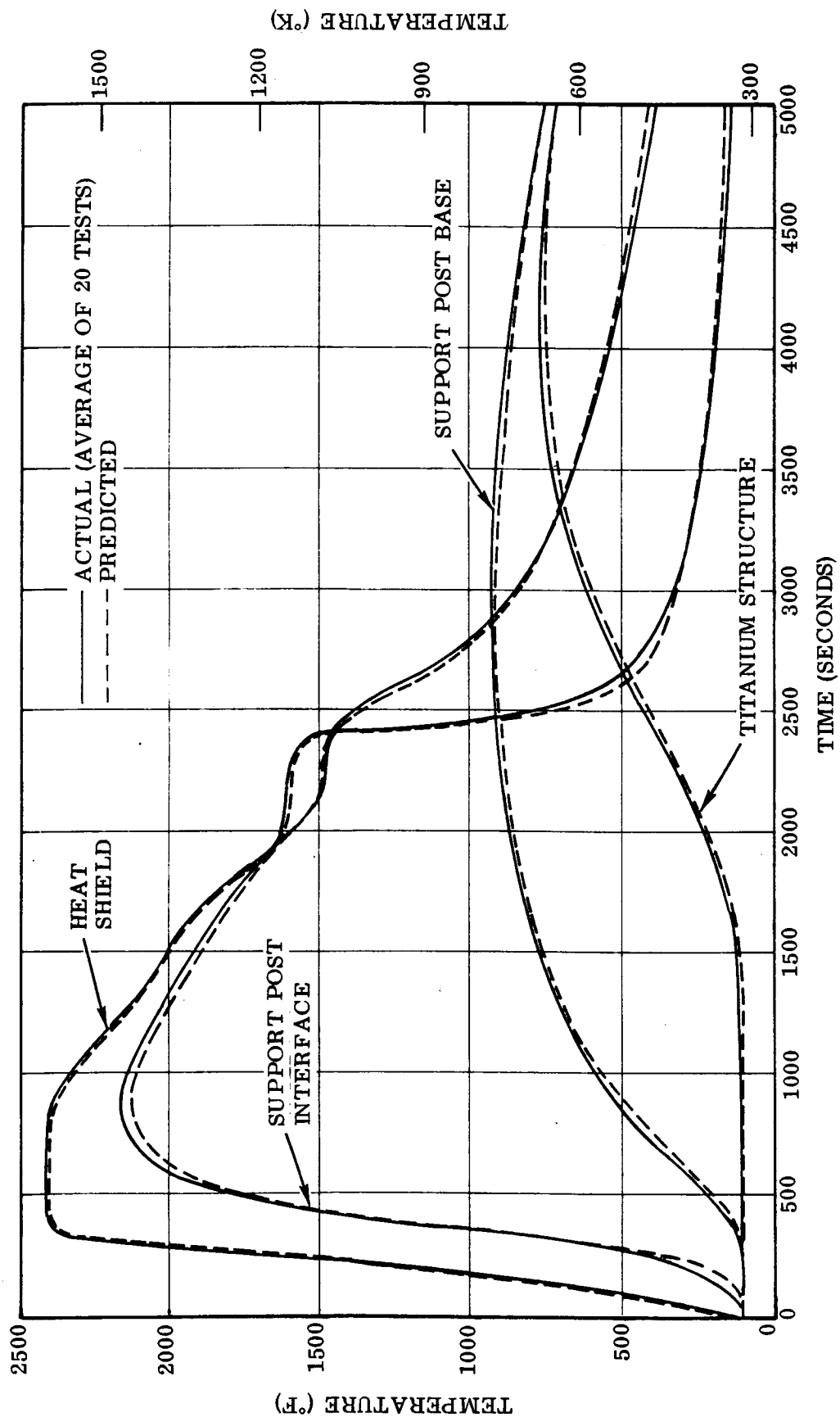


Figure 8-19. Hot Gas Flow Test Composite Temperature Distribution -- Tee-Stiffened TPS

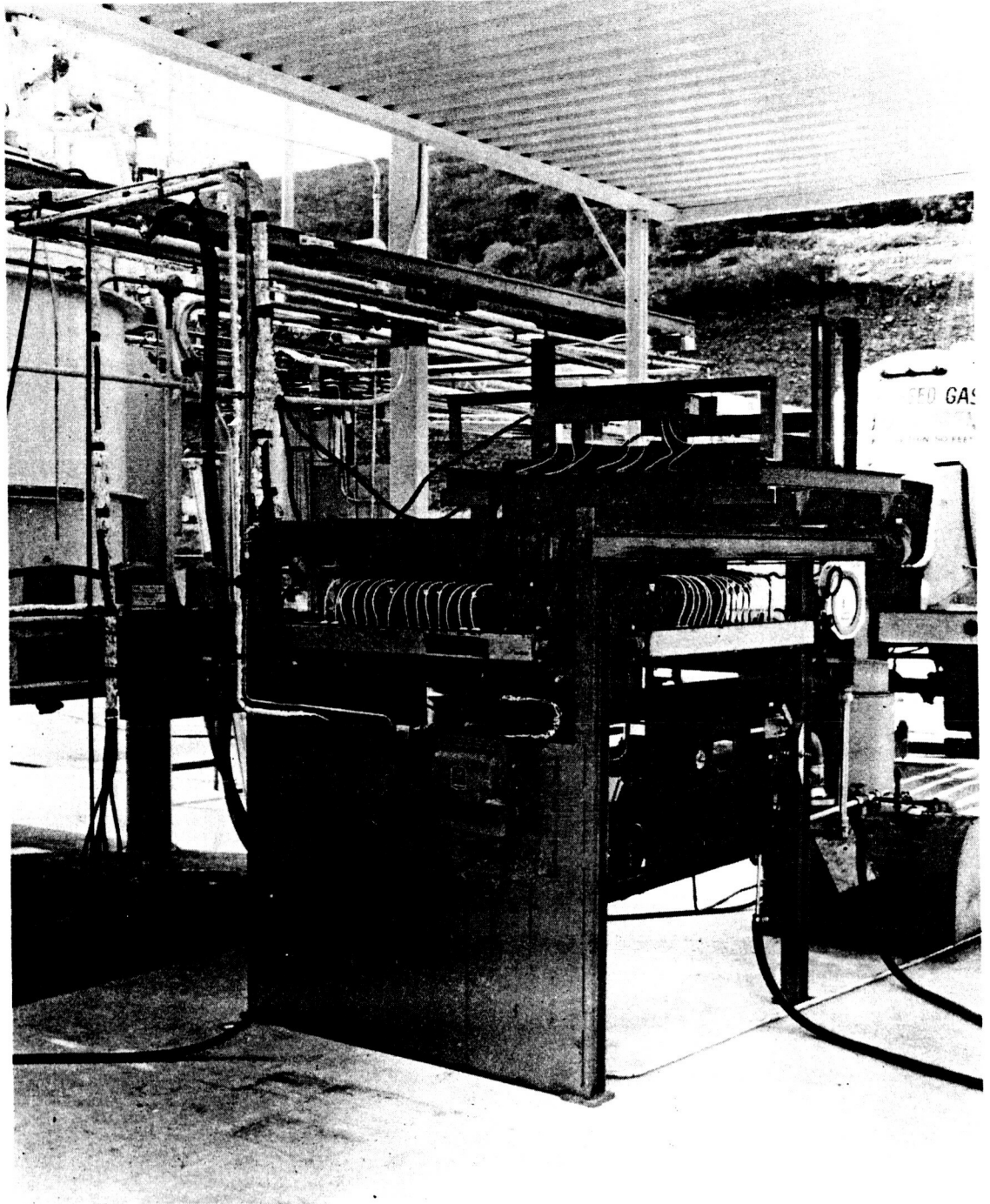


Figure 8-20. Cryotherm/Radiant Heat Lamp Facility
(Photo No. 99084B)

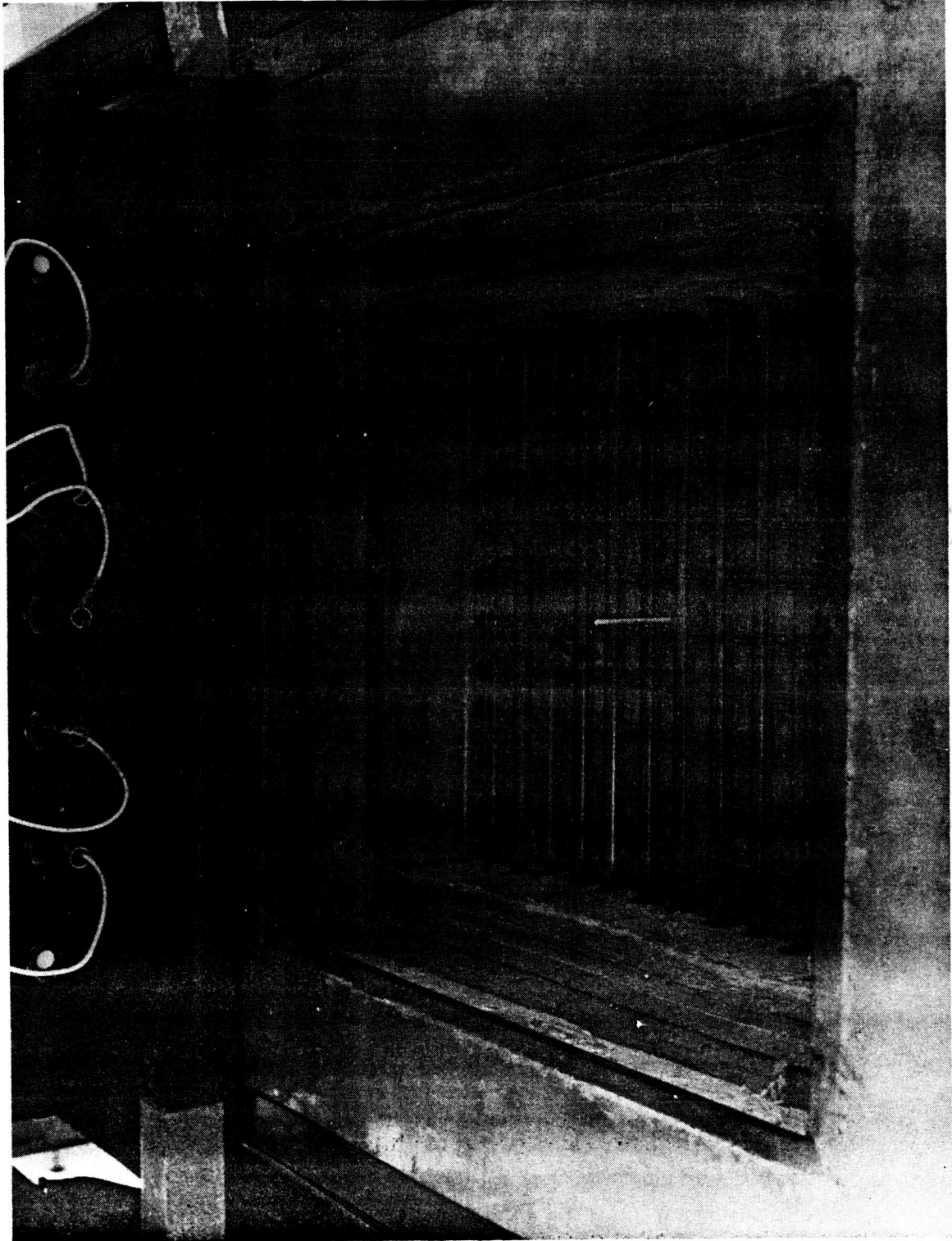


Figure 8-21. Cryotherm Heat Chamber (Photo 132764B)

O-ring fittings provide a vacuum-tight seal where the quartz tubes pass through the sides of the heat chamber. The O-rings at the nitrogen outlet end of the quartz tubes are water cooled to prevent deterioration of the O-ring materials. Up to 200 thermocouples from the test specimen can be fed out of the heat chamber through O-ring-sealed fittings.

The specimen cold face is backed by seven 5000-watt lamps controlled by a separate set of ignitrons. These guard lamps are driven to balance any heat loss from the specimen cold face by maintaining a zero output from a differential thermocouple installed on two thin stainless steel sheets, one inch (2.54 cm) apart and located between the specimen cold face and the guard lamps.

Temperatures are recorded from thermocouples carefully installed to prevent emf junction errors. Liquid nitrogen is used as a reference junction for thermocouples, and the installation permits automatic scanning of up to 80 thermocouples. The test chamber pressure can be varied from atmospheric pressure to 1×10^{-4} mm Hg (13.3 mN/m²) with a vacuum pumping system consisting of a CVC PMC-4100 [10 inch (25.4 cm)] diffusion pump, a Kinney KDH 130 mechanical pump, and a Beach-Russ Model 250 mechanical pump. Valves and controls are provided to vary the gas composition and pressure during test runs. A system schematic is shown in Figure 8-22.

The specimens were instrumented as shown in Figures 8-4 and 8-5. The temperature-pressure profile is shown in Figure 5-1.

Each test began with the maximum evacuation of the chamber to maintain the required chamber pressure and pressure differential across the face of the heat shield. Following the boost phase of the profile the specimen required approximately one hour to return to a maximum internal temperature of less than 100°F (311°K). The entry phase of the profile began with the chamber fully evacuated and the pressure increased by bleeding in air/nitrogen at a controlled rate and mixture to maintain the required surface pressure. At the conclusion of each cycle, the chamber was backfilled to ambient pressure with GN₂. Cycling was resumed when the maximum recorded internal temperature at the center of the insulation was less than 100°F (311°K). The chamber was opened approximately every ten cycles for specimen inspection until the completion of 50 cycles.

8.2.2 Test observation and results. —

8.2.2.1 Open corrugation TPS: Following specimen assembly and prior to the initiation of acoustic and thermal testing the heat shield surface contour was measured at 15 sites. These measurements were made in an effort to determine the amount of permanent deflections sustained by the thermal/load cycling.

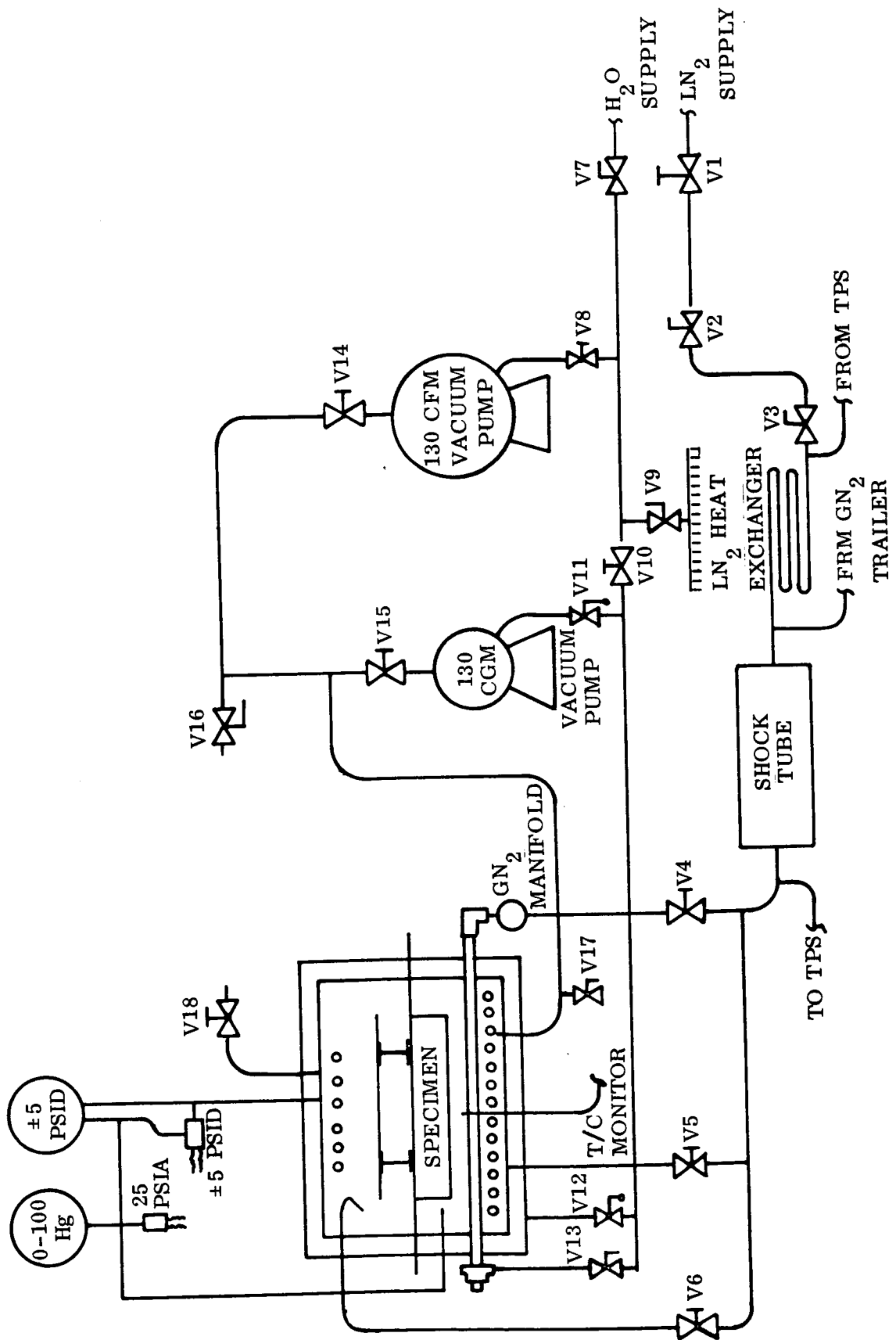


Figure 8-22. Cryotherm/Radiant Heat Chamber System Schematic

Three 0.19 inch (0.48 cm) diameter balls were attached to the primary structure of the specimen to serve as a locating plane. All measurements were made with a dial indicator located above the specimen; both rested on a surface table.

The post test measurements indicated an outward deflection. This was a result of excessive force exerted outward by the vertically positioned temperature probes. This condition also existed on the tee-stiffened heat shield, thereby negating the deflection measurement data.

No unusual conditions were observed as a result of the radiant heat tests. The specimen evidenced no sign of coating failure, substrate erosion, or structural degradation. Two views of the specimen after 50 thermal cycles are shown in Figures 8-23 and 8-24. As can be seen, the specimen exhibited a non-uniform pattern of coloration. As with all previous specimens (elemental and subsize panels) the random coloration was not deleterious to the system performance.

The temperature measurements for the entire test series showed good temperature uniformity [$\pm 21^{\circ}\text{F}$ ($\pm 12^{\circ}\text{K}$) at peak temperature] over the surface of the specimen. A summary of the data for four critical locations is presented in Table 8-3. The data was reduced for cycles 1 through 5 and every five cycles thereafter. The average maximum temperature at the center of the heat shield surface was 2400°F (1589°K) which was the programmed temperature. The bi-metallic post interface temperature maximum was 2149°F (1450°K) versus a predicted peak of 2150°F (1450°K). The maximum average temperature at the base of the TD NiCr post was 921°F (767°K) compared to a predicted value of 915°F (764°K). The average temperature maximum at the center of the titanium skin was 747°F (671°K) compared to a predicted level of 750°F (672°K). Data plots of the average temperature history for these four locations are shown in Figure 8-25. After completion of the 50 thermal cycles the specimen was subjected to 75 simulated boost acoustic cycles (Section 8.3).

8.2.2.2 Tee-stiffened TPS: Similar to the open corrugation TPS test series the specimen experienced a uniform temperature distribution with the peak heat shield temperatures ranging from a minimum of 2395°F (1586°K) to a maximum of 2410°F (1594°K). A thermal data summary is shown in Table 8-4. The maximum average temperature at the Cb-752/TD NiCr support post interface was 2153°F (1452°K) compared to a prediction of 2150°F (1450°K). The support post base experienced an average peak temperature of 927°F (771°K) compared to a predicted level of 915°F (764°K). The actual support structure skin temperature exceeded the prediction by 7°F (5°K) attaining an average of 757°F (767°K). The average temperature data history for the four locations on the tee-stiffened TPS specimen is shown in Figure 8-26.

For comparison the specimen is shown in Figures 8-27 through 8-30 before exposure and after 50 thermal cycles. Again, the varied surface patterns can be seen in the post test photographs. No sites of substrate oxidation, impending coating failure, or structural

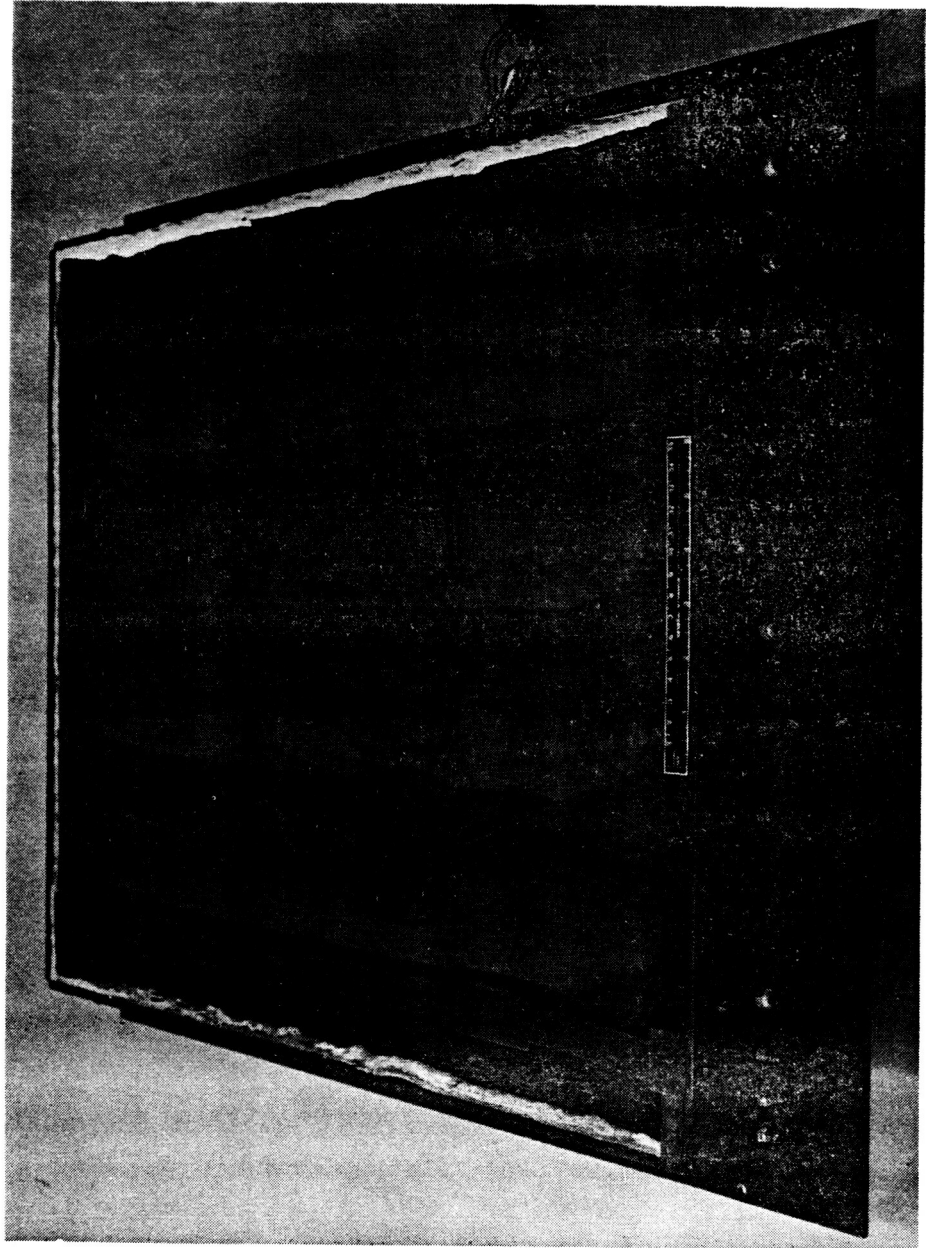


Figure 8-23. Open Corrugation TPS Specimen After 50 Radiant Heat/Pressure/Load Cycles — View Looking Downstream (Photo 133517B)

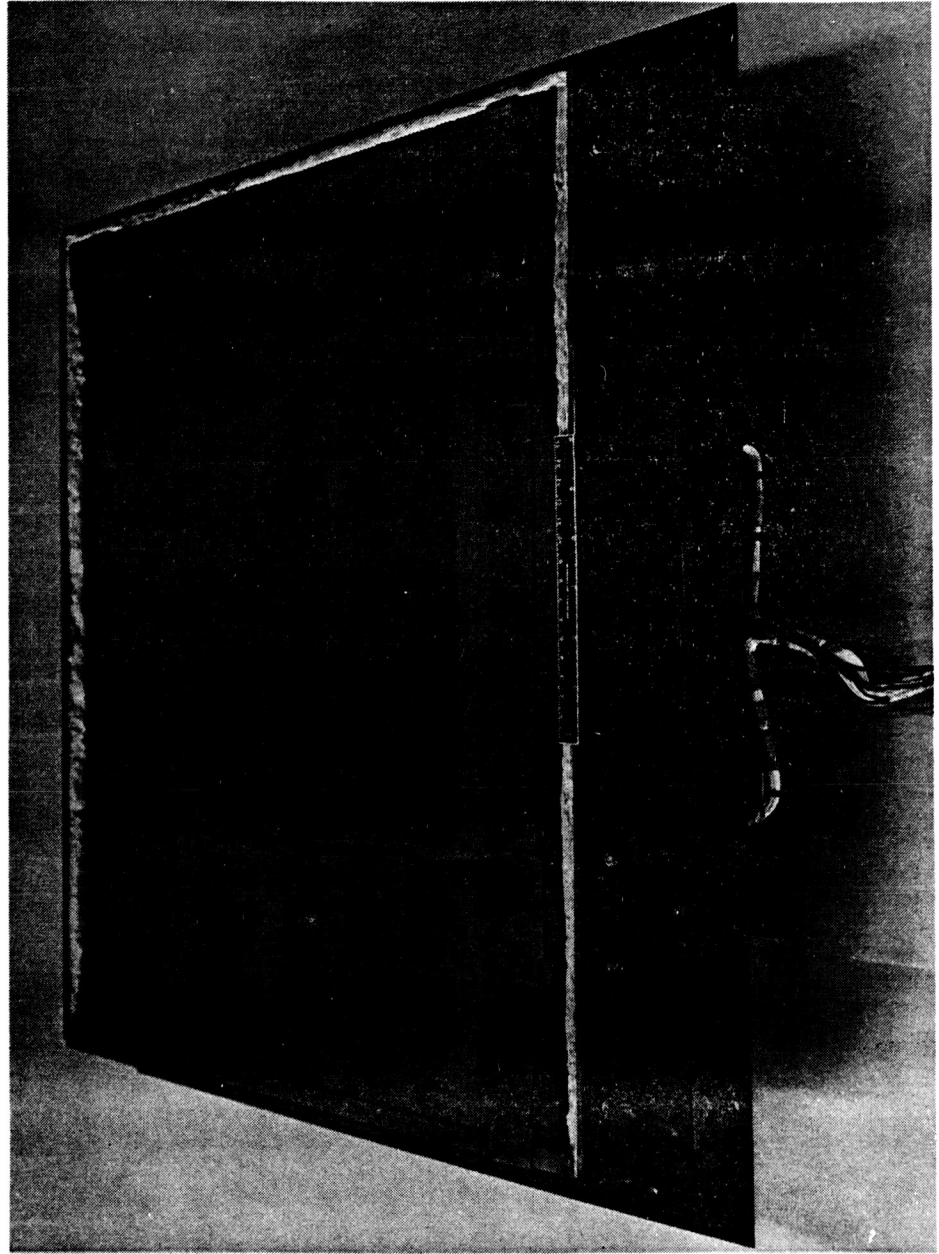


Figure 8-24. Open Corrugation TPS Specimen After 50 Radiant Heat/Pressure/Load Cycles — Side View (Photo 133518B)

Table 8-3. Open Corrugation TPS Radiant Heat Test Thermal Summary

Run Number	Max. Heat Shield Temp. at Specimen Center		Cb-752/TD NiCr Support Post Interface		TD NiCr Support Post Base		Titanium Structure at Specimen Center	
	°F	°K	°F	°K	°F	°K	°F	°K
1	2392	1584	2146	1448	920	767	746	670
2	2398	1588	2150	1450	922	768	751	672
3	2401	1589	2151	1451	922	768	752	673
4	2403	1591	2151	1451	923	768	755	675
5	2400	1589	2149	1449	920	767	748	671
10	2400	1589	2150	1450	923	768	751	672
15	2400	1589	2148	1449	922	768	753	674
20	2396	1587	2146	1448	918	766	745	669
25	2399	1588	2150	1450	919	766	745	669
30	2403	1591	2151	1451	920	767	745	669
35	2400	1589	2149	1449	920	767	743	668
40	2405	1592	2153	1452	925	769	746	670
45	2401	1589	2150	1450	920	767	742	668
50	2398	1588	2147	1448	918	766	740	667
Average	2400	1589	2149	1450	921	767	747	671
Tolerance	{ (+5) (-8)	{ (+3) (-5)	{ (+4) (-3)	{ (+2) (-2)	{ (+4) (-3)	{ (+2) (-1)	{ (+8) (-5)	{ (+4) (-3)

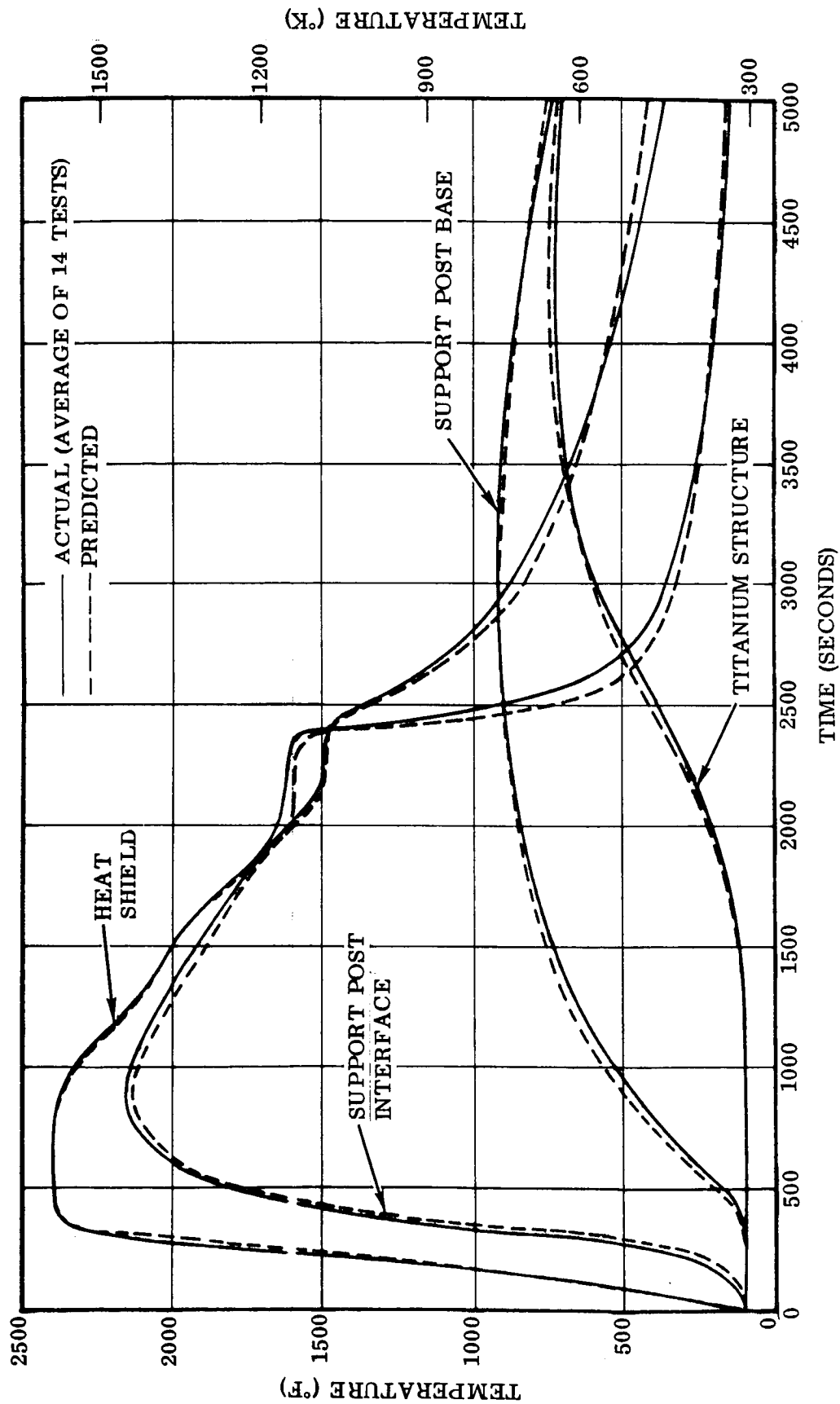


Figure 8-25. Radiant Heat Test Composite Temperature Distribution — Open Corrugation TPS

Table 8-4. Tee-Stiffened TPS Radiant Heat Test Thermal Summary

Run Number	Max. Heat Shield Temp. at Specimen Center		Cb-752/TD NiCr Support Post Interface		TD NiCr Support Post Base		Titanium Structure at Specimen Center	
	°F	°K	°F	°K	°F	°K	°F	°K
1	2410	1594	2162	1457	931	773	761	678
2	2403	1591	2156	1453	929	772	760	678
3	2396	1587	2152	1451	927	771	758	677
4	2398	1588	2153	1453	927	771	756	676
5	2401	1589	2154	1452	928	771	757	676
10	2402	1590	2153	1453	926	770	756	676
15	2405	1592	2158	1454	930	772	758	677
20	2400	1589	2154	1452	928	771	757	676
25	2401	1589	2153	1452	928	771	756	676
30	2397	1587	2149	1449	926	770	755	675
35	2403	1591	2152	1451	927	771	757	676
40	2395	1586	2148	1449	925	769	753	674
45	2399	1588	2151	1451	926	770	757	676
50	2402	1590	2150	1450	925	769	756	676
Average	2401	1589	2153	1452	927	771	757	676
Tolerance	+9	+5	+9	+5	+4	+2	+4	+2
	-6	-3	-5	-3	-2	-2	-4	-2

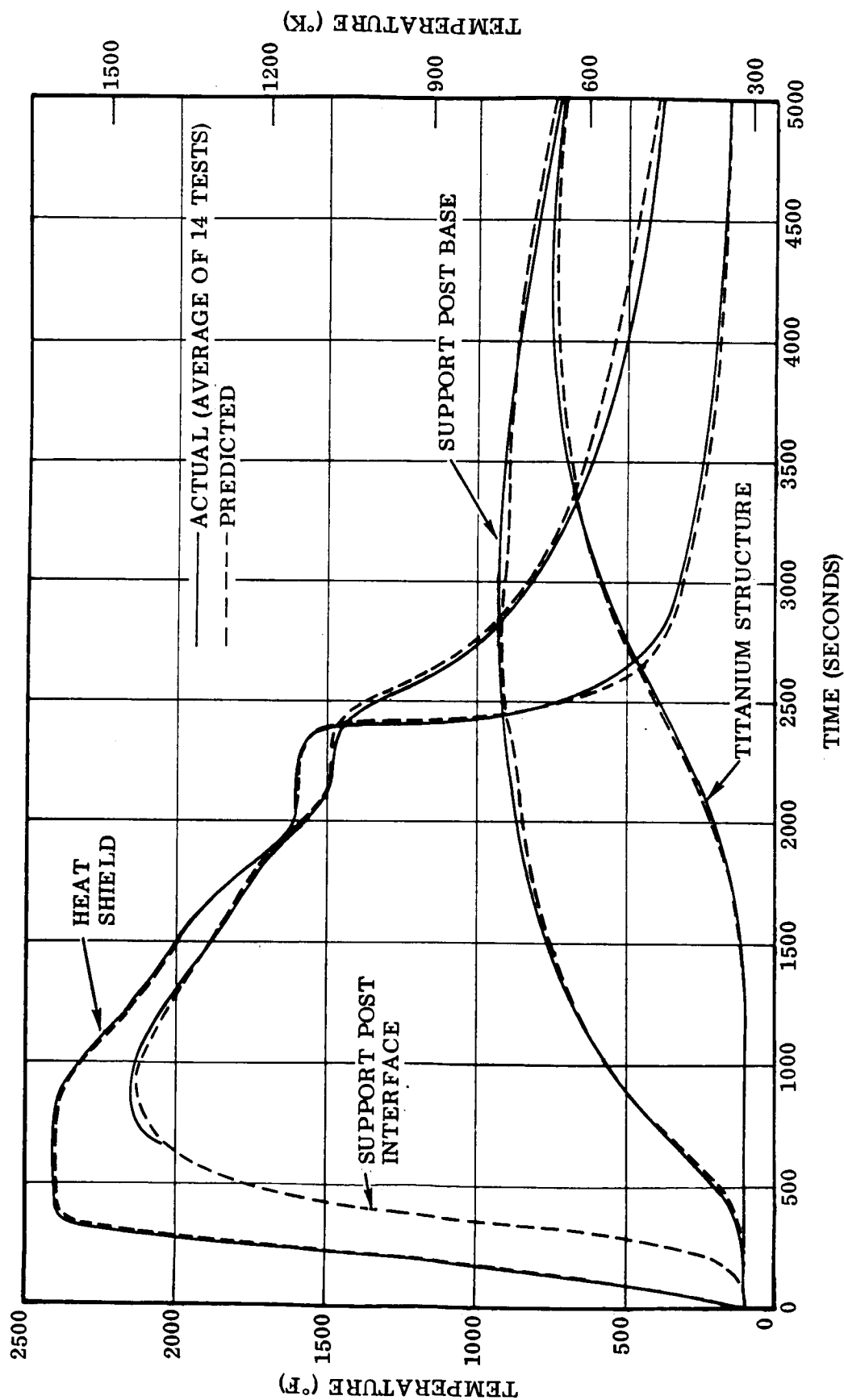


Figure 8-26. Radiant Heat Test Composite Temperature Distribution — Tee-Stiffened TPS

deterioration were found. Following the 50 thermal cycle exposure the specimen was exposed to acoustic excitation as described in Section 8.3.

8.2.3 Test summary. — Both types of specimens performed well during the radiant heat test series. The temperature distributions through the depth of the specimens were near the predicted levels. No structural failures were found on either specimen. The concept of sliding, coated surfaces did not cause any difficulties; that is, no excessive wear appeared in those regions of overlap. In addition, the concept of buried fasteners provided for relatively easy panel and insulation inspection. No incompatibility between the silicide coated columbium alloy and the aluminide coated TD NiCr was found.

Based on this test series no clear preference could be made between the two configurations. Therefore, the selection of the tee-stiffened TPS as the system for Phase III evaluation was based on its slightly lower unit weight and cost.

8.3 Acoustic Tests

The objective of the acoustic test series was to determine the structural response of each of the two TPS configurations to acoustic excitation. The acoustic energy levels were to be representative of those predicted during orbiter boost for the region of investigation (see Figure 6-1) and according to the parameters discussed in Section 6.4.6.

8.3.1 Test equipment and procedure. — All specimens were mounted vertically (as positioned during boost) through the side wall of the Convair Aerospace 1000 ft³ (28.3 m³) reverberation chamber as shown in Figures 8-31 and 8-32. The Endevco Model 2222B miniturized accelerometers were bonded to Mylar tape with Eastman 910 adhesive. The Mylar tape adhered well to the coated heat shield during the test duration.

Each of the four specimens was subjected to an acoustic cycle consisting of an overall sound pressure level (OASPL) of 155 dB for 10 seconds followed by an OASPL of 152 dB for 40 seconds. The spectrum of each level is shown in Figures 8-33 through 8-36. The acoustic levels were measured 18 inches (45.7 cm) from the test specimen face and were recorded on magnetic tape for later reduction to octave band sound pressure level (OBSPL) spectrum plots.

The test sequence for the specimens was:

For Radiant Heat Test Specimens —

- Acoustic test (25 cycles)
- Disassemble and inspect
- Thermal test (50 cycles)
- Acoustic test (75 cycles)
- Disassemble and inspect

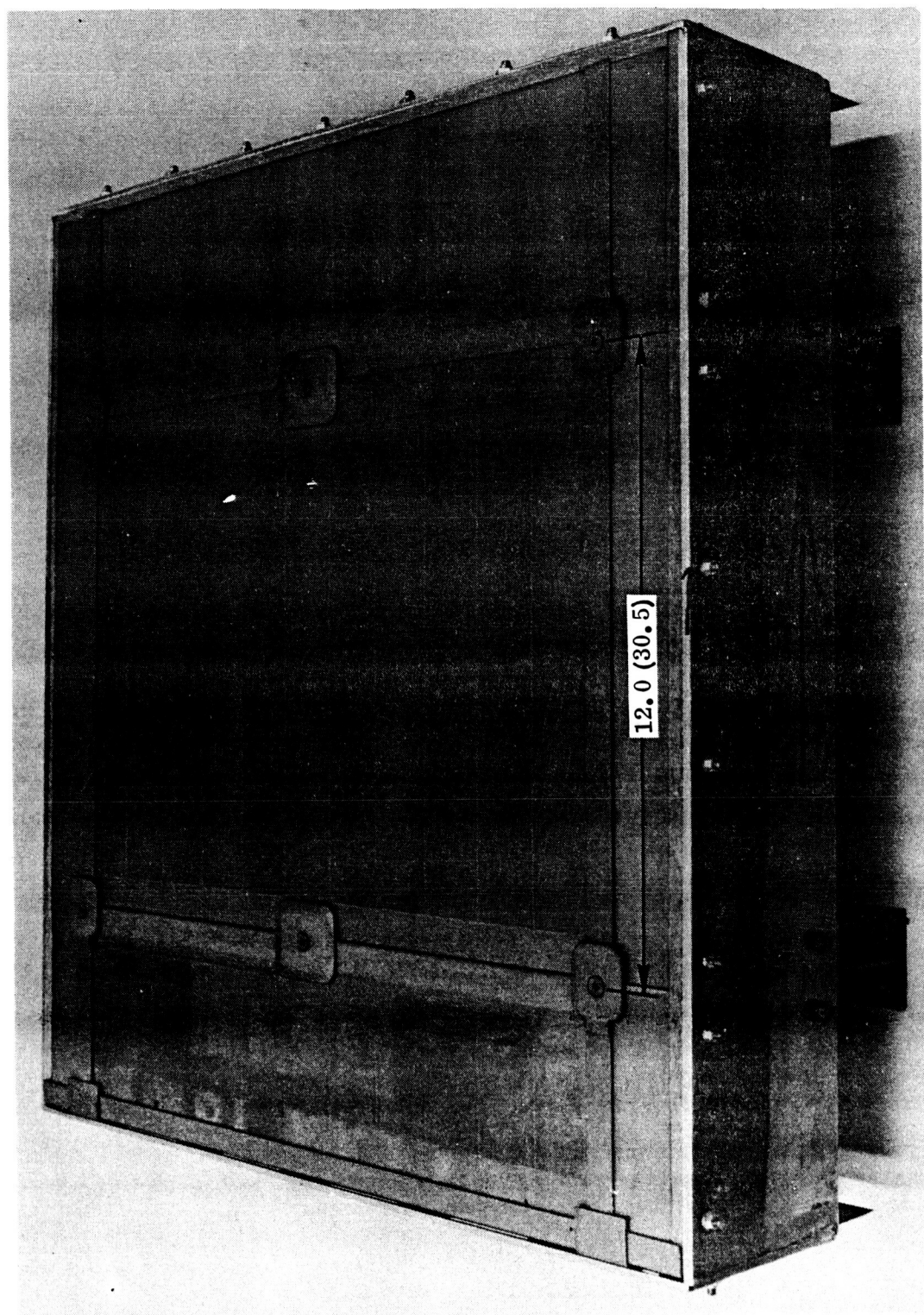


Figure 8-27. Tee-Stiffened TPS Specimen Before Thermal Cycling — Side View (Photo 130836B)

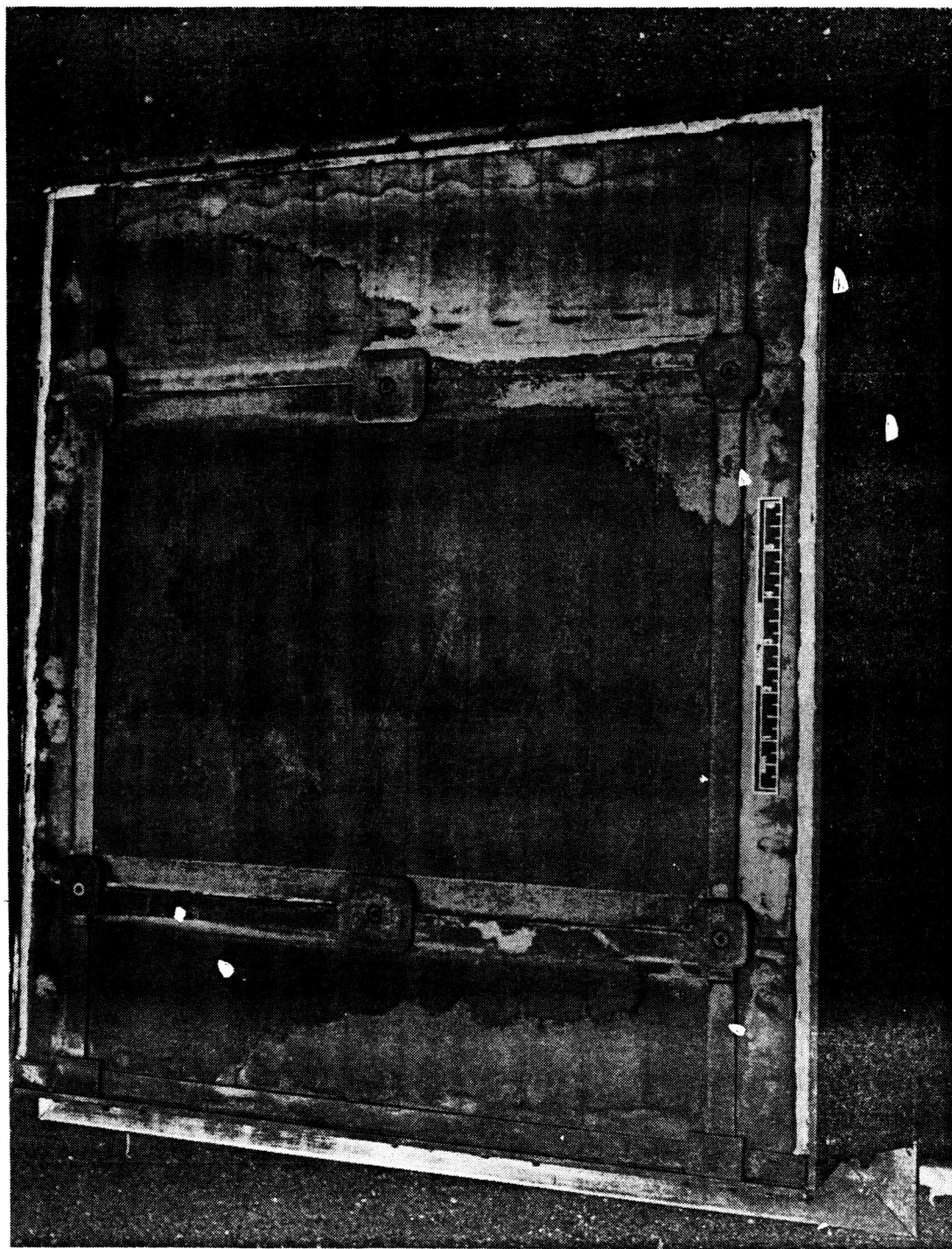


Figure 8-28. Tee-Stiffened TPS Specimen After 50 Radiant Heat/Pressure/Load Cycles — Side View (Photo 132766B)

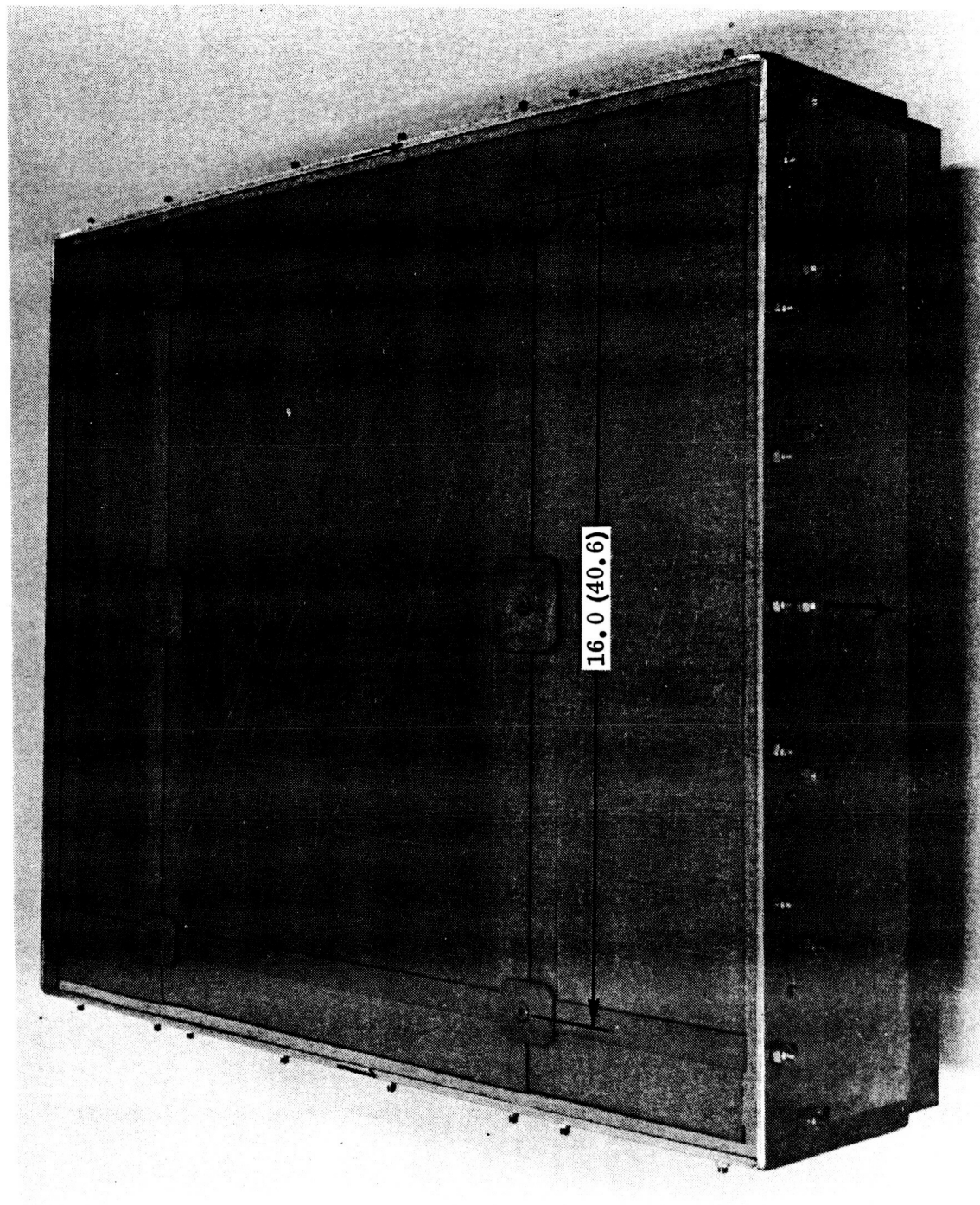


Figure 8-29. Tee-Stiffened TPS Specimen Before Thermal Cycling — View Looking Upstream (Photo 130838B)

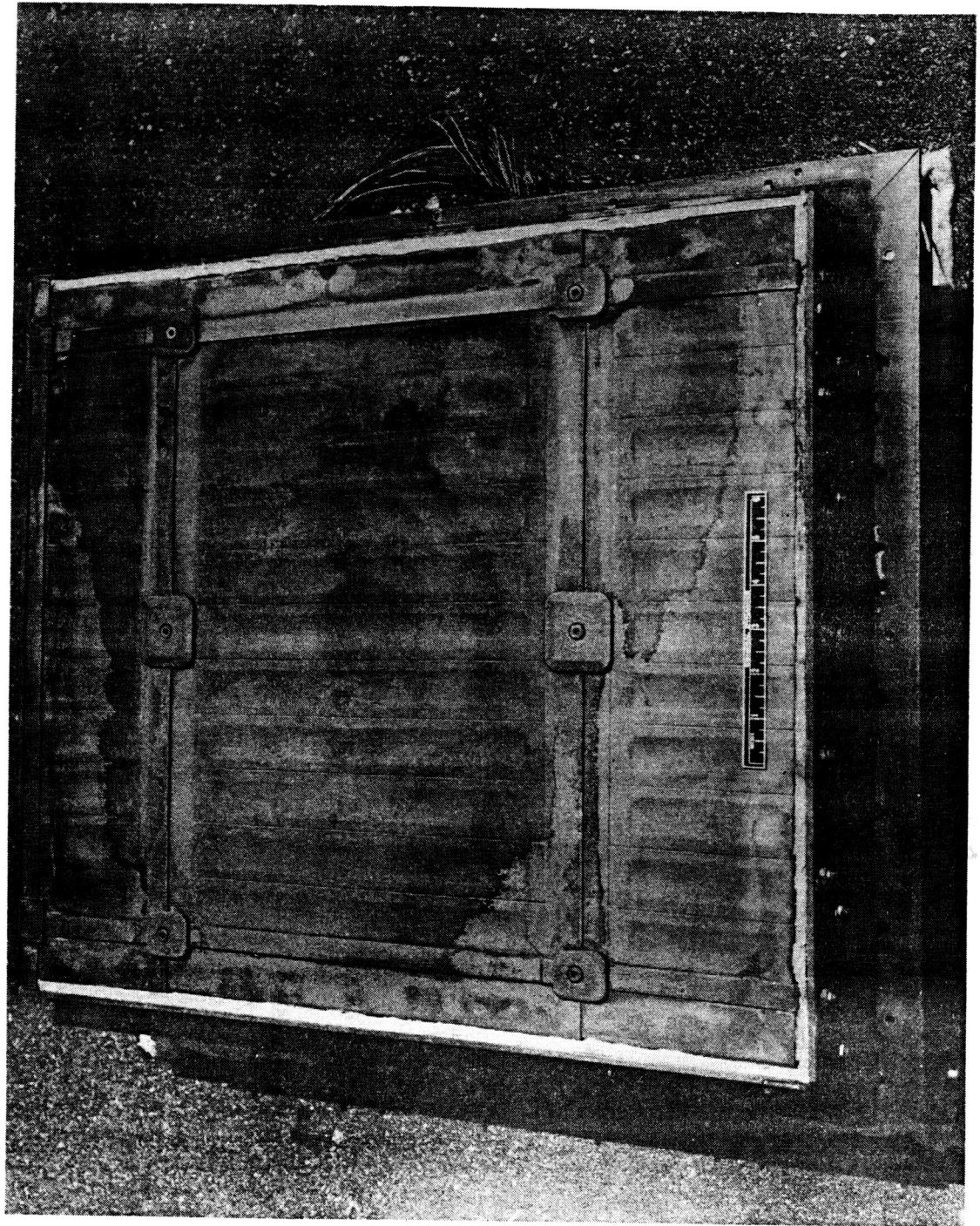


Figure 8-30. Tee-Stiffened TPS Specimen After 50 Radiant Heat/Pressure/Load Cycles — View Looking Upstream (Photo 132767B)

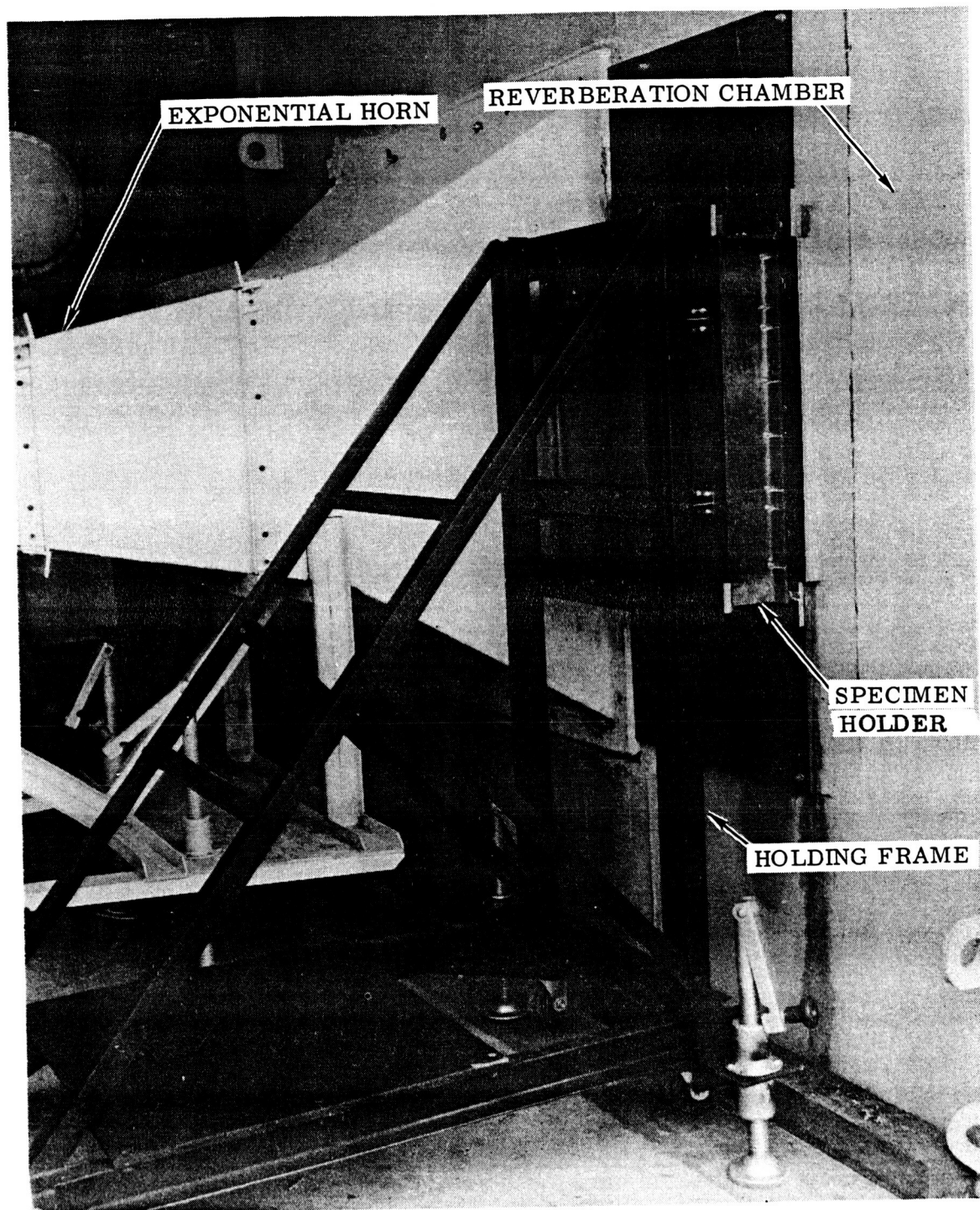


Figure 8-31. TPS Specimen Mounting Technique for Acoustic Testing

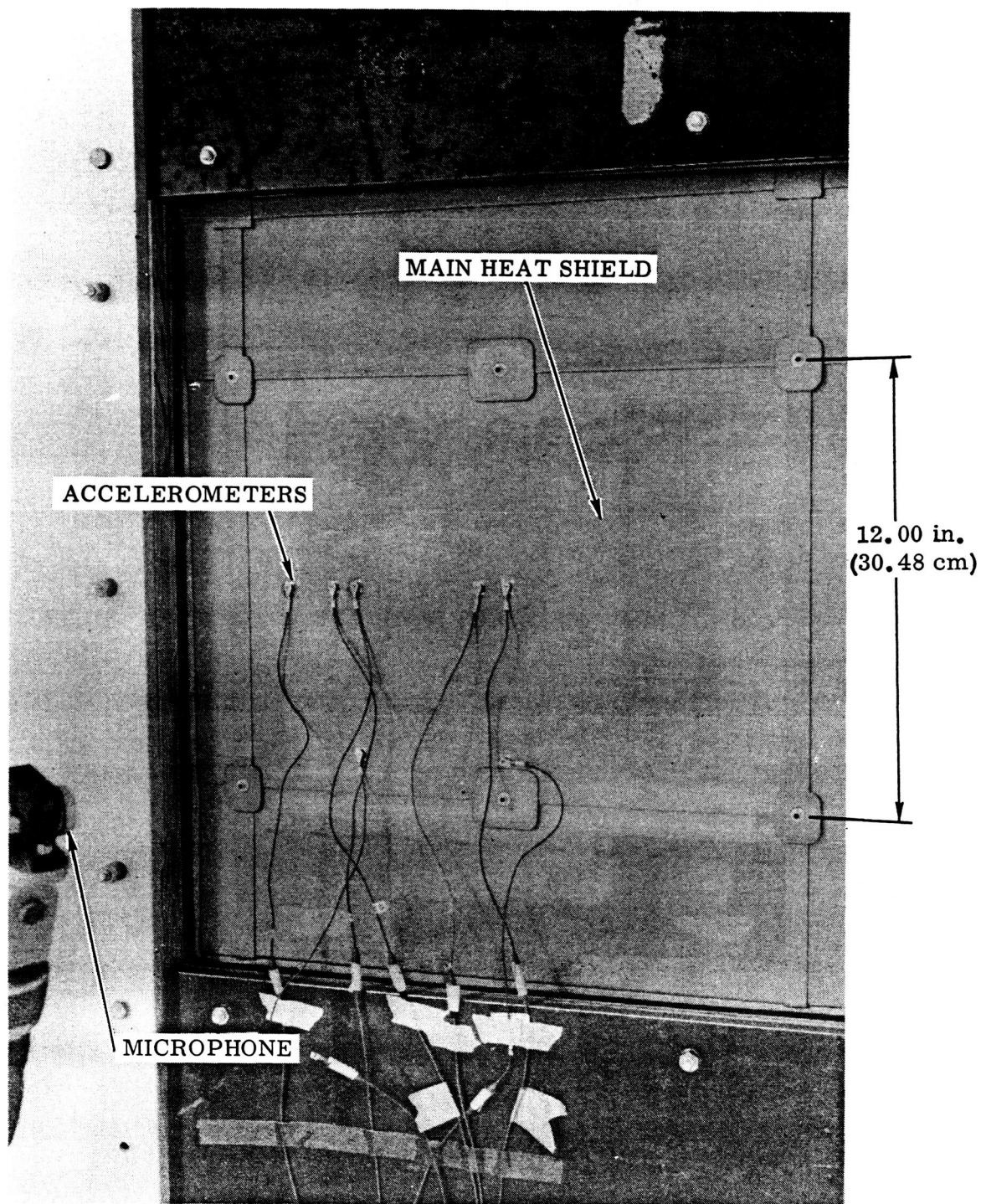


Figure 8-32. Tee-Stiffened TPS Specimen Mounted in Reverberation Chamber Wall

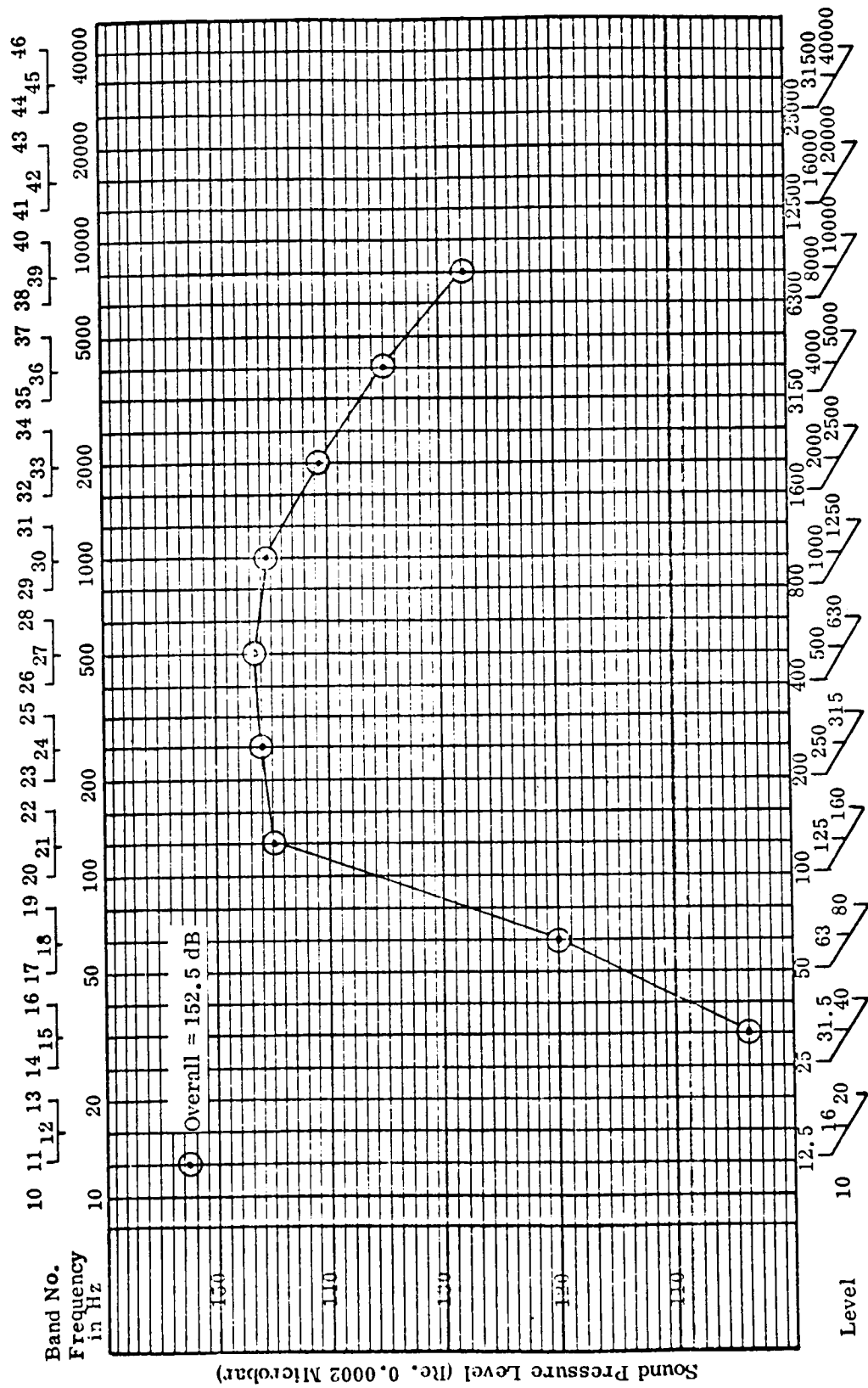


Figure 8-33. 1/3 Octave and Octave Band Center Frequencies - 152 dB OASPL (Pre-thermal Tests)

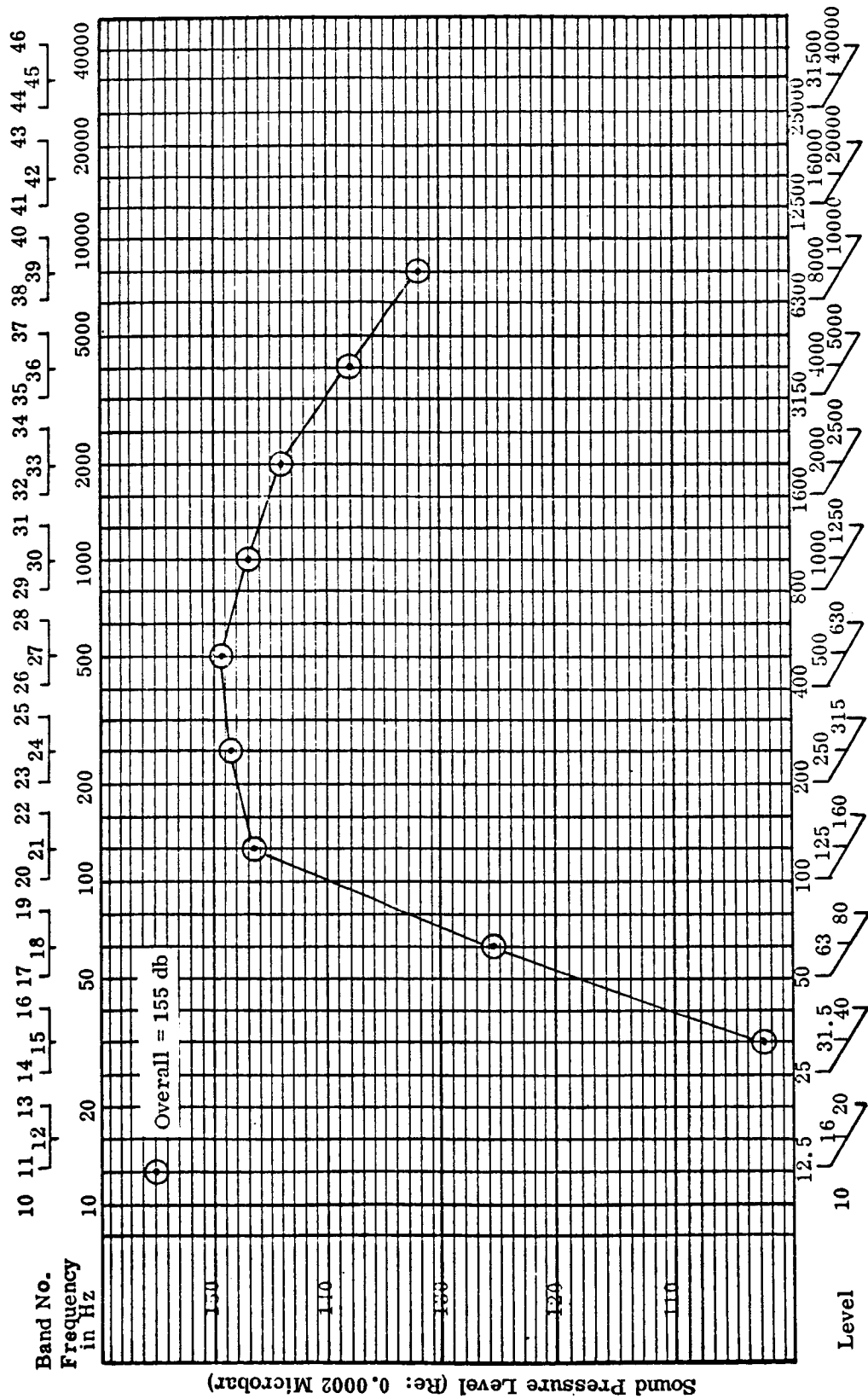


Figure 8-34. 1/3 Octave and Octave Band Center Frequencies - 155 dB OASPL (Pre-thermal Tests)

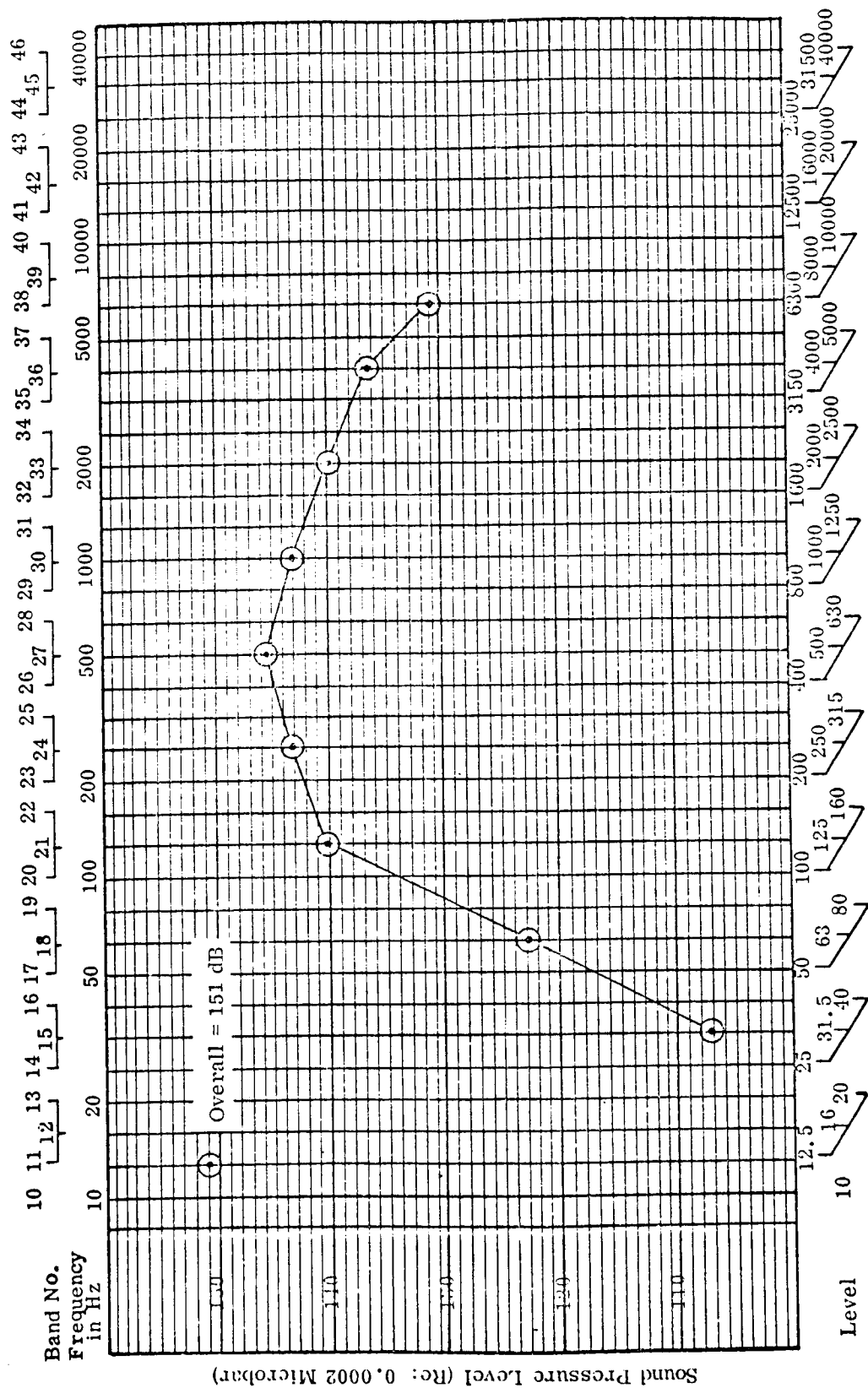


Figure 8-35. 1/3 Octave and Octave Band Center Frequencies - 152 dB OASPL (Post-thermal Tests)

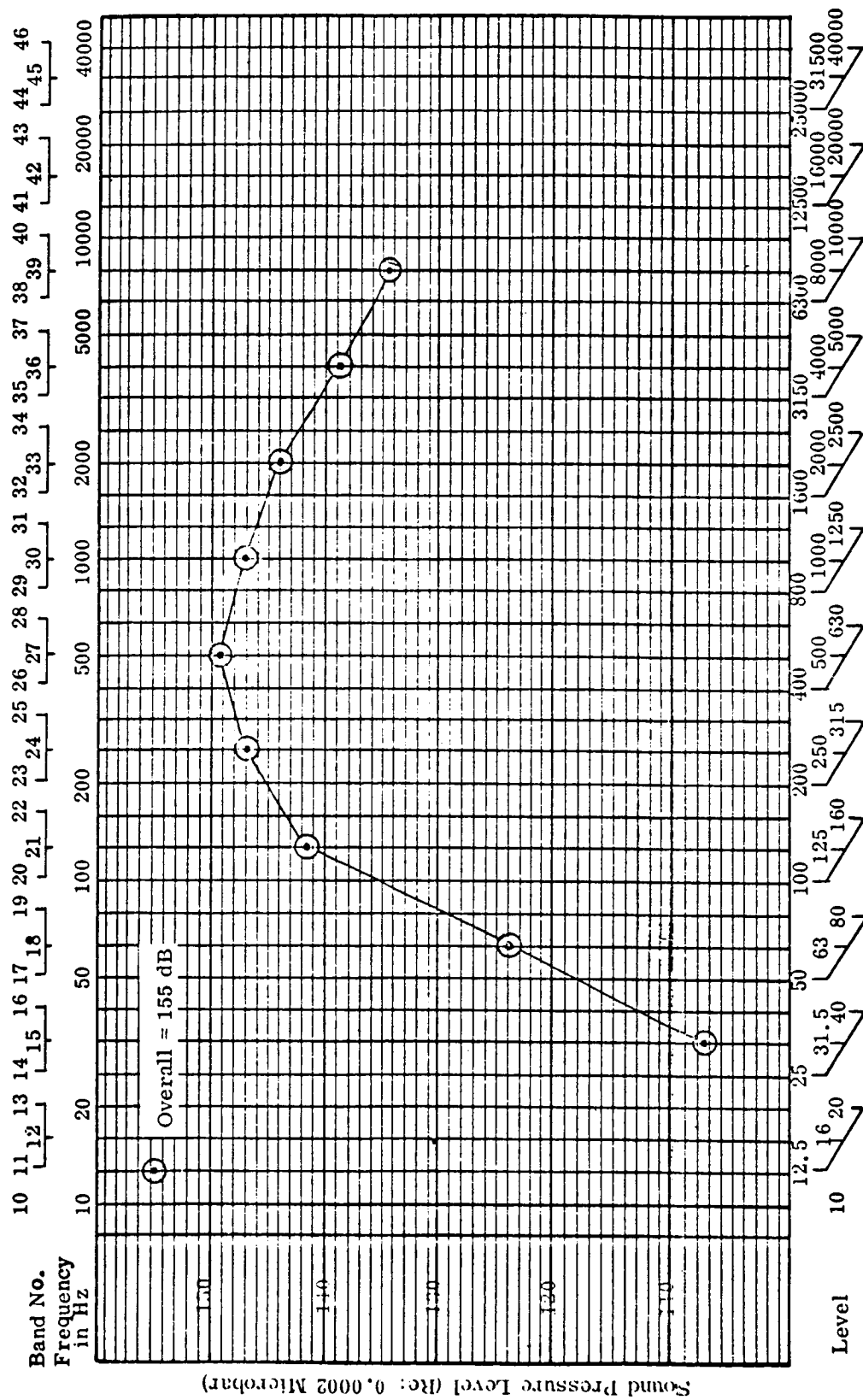


Figure 8-36. 1/3 Octave and Octave Band Center Frequencies - 155 dB OASPL (Post-thermal Tests)

For Hot Gas Flow Test Specimens —

- Acoustic test (1 cycle)
- Disassemble and inspect
- Thermal tests (20 cycles)
- Acoustic test (99 cycles)
- Disassemble and inspect

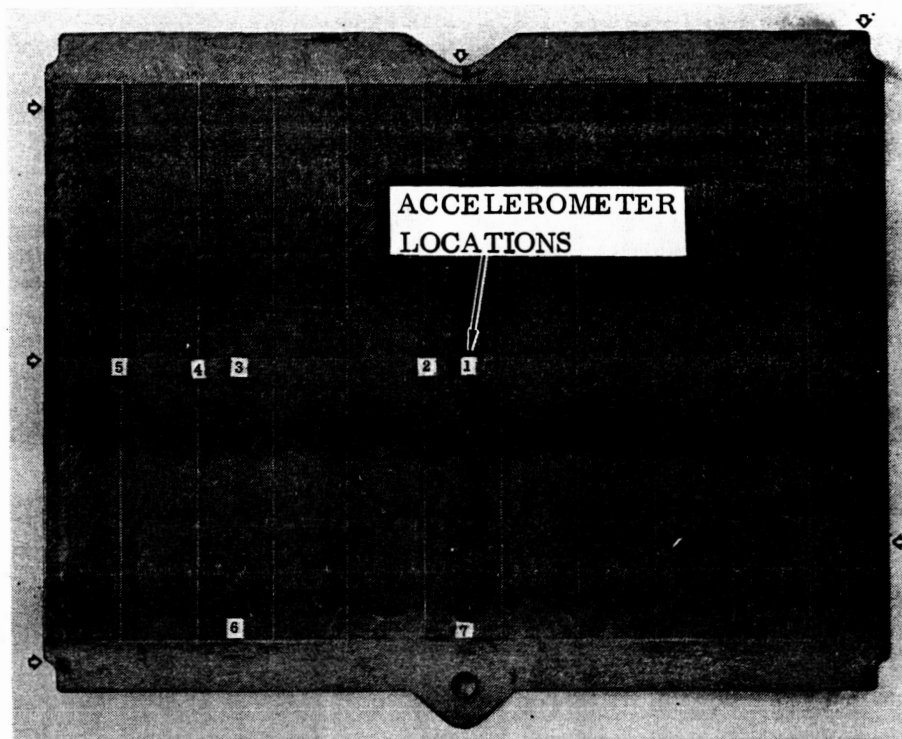
8.3.2 Test observations and results. — For the tee-stiffened and open corrugation TPS specimens that were to subsequently be tested thermally in the radiant heat chamber no damage or degradation was observed at the end of the first 25 acoustic cycles. Visual checks of the specimens were made at five cycle intervals.

8.3.2.1 Tee-stiffened TPS: The tee-stiffened heat shield is shown in Figure 8-37. Several areas of rubbing can be seen around the periphery of the panel at locations where adjacent panels and retainers were in contact. The rubbing action resulted in a blackened powder that generally was removed by brushing. The powder was created by a wearing down of the unsmooth surface of the coating.

Comparable areas of rubbing were found on the upper bearing surfaces of the Cb-752 support post and can be seen circled in Figure 8-38. Most of the abrasions were caused by the fore and aft support beam pads of the heat shield. Additional abrasions were caused by the bearing leg of the longitudinal side closeout panels. These abrasions were deeper than those caused by the beam pads. It would have been preferable to have designed the auxiliary panels with a return flange for a better distribution of the bearing load. All of these regions received special attention during the thermal test interim inspection periods. No substrate oxidation was noted at any time.

Test data are presented in Appendix E for three accelerometer locations, at both OASPL for four test periods. These data are typical of that recorded for all accelerometers.

The specimens were disassembled twice; after 25 and 100 cycles for the radiant heat tested specimen and after 1 and 20 cycles for the hot gas flow exposed specimen. An example of a disassembled specimen is shown in Figures 8-39 and 8-40. No difficulty was encountered during the disassemblies. The breakaway torque to remove the Cb-752/R-512E plug from the coated TD NiCr bolt ranged from 17 to 23 in-lb (191 to 259 cm-N) compared to the applied setting torque of 15 in-lb (169 cm-N). The TD NiCr bolts were removed from the Cb-752/R-512E support post by applying between 17 and 24 in-lb (191-270 cm/N). No significant differences were noted in the removal qualities with regard to type of thermal test or exposure duration.



Arrows indicate regions of rubbing

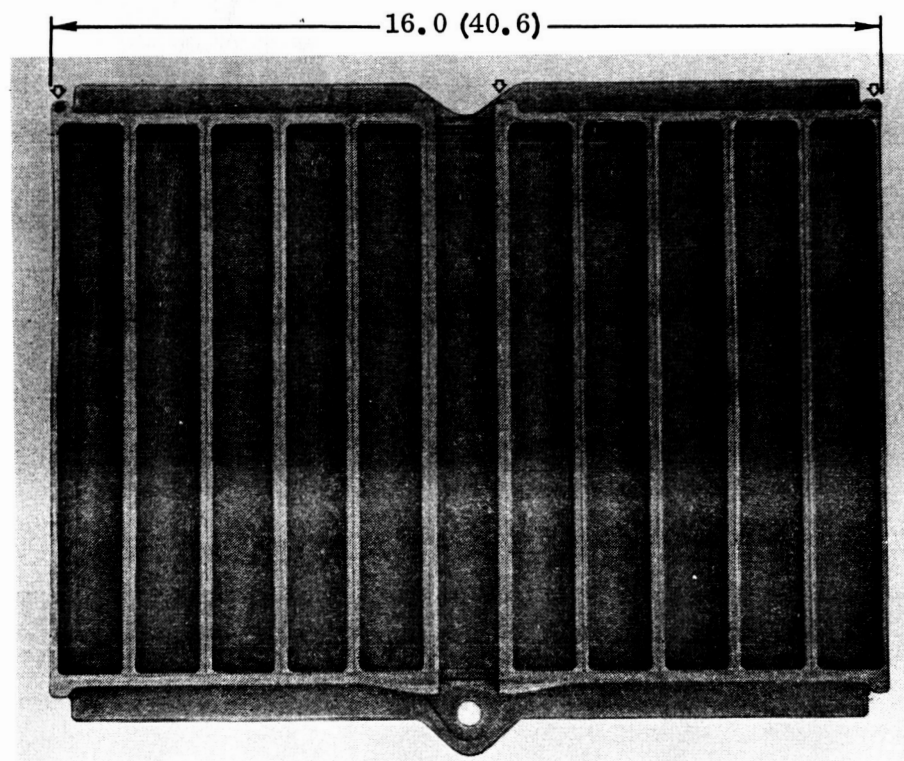


Figure 8-37. Tee-Stiffened Heat Shield after 25 Acoustic Cycles
[Photo No. 130962B (upper) and 130961B (lower)]

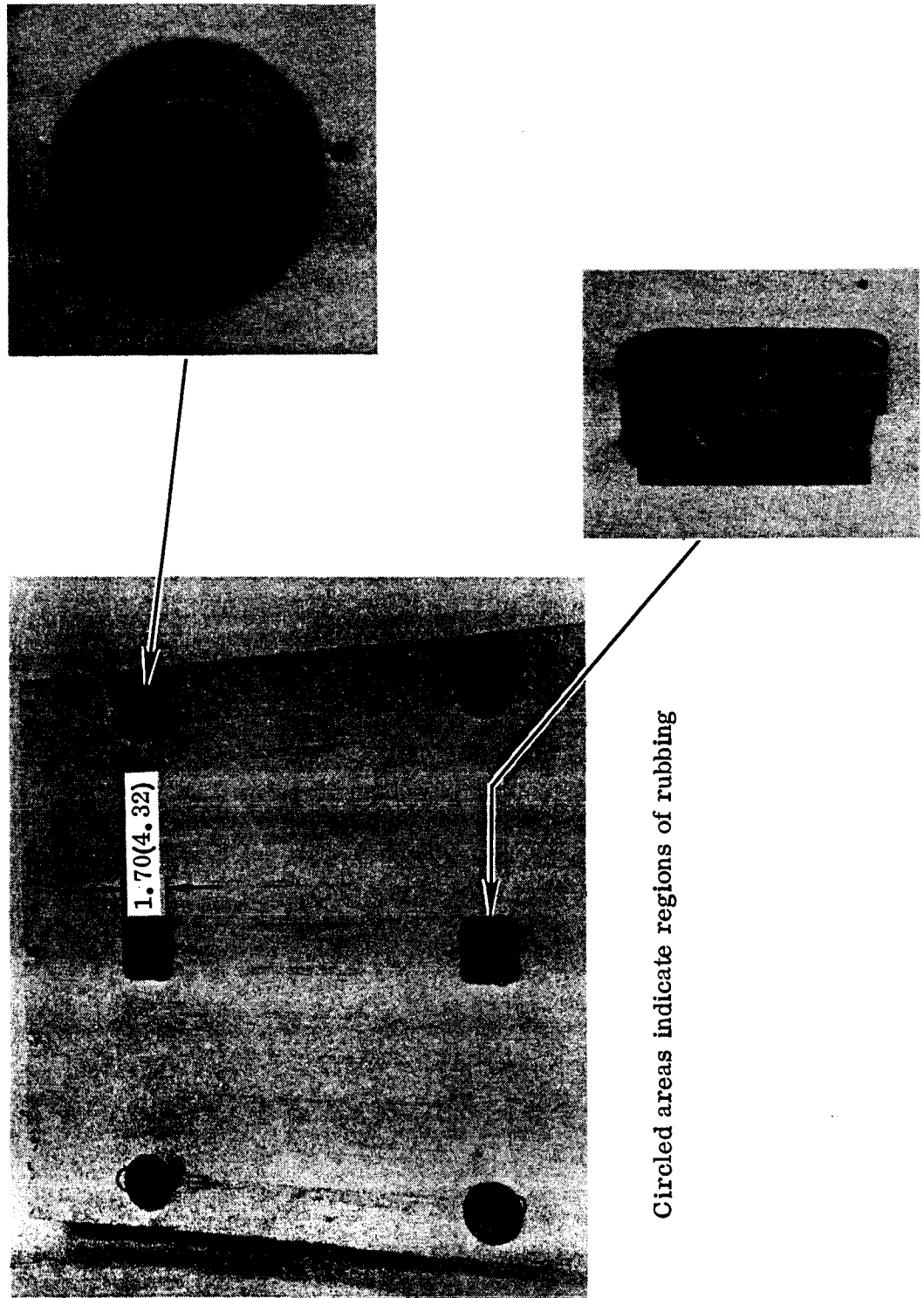


Figure 8-38. Tee-Stiffened TPS Support Posts and Insulation after 25 Acoustic Cycles (Photo No. 130963B)

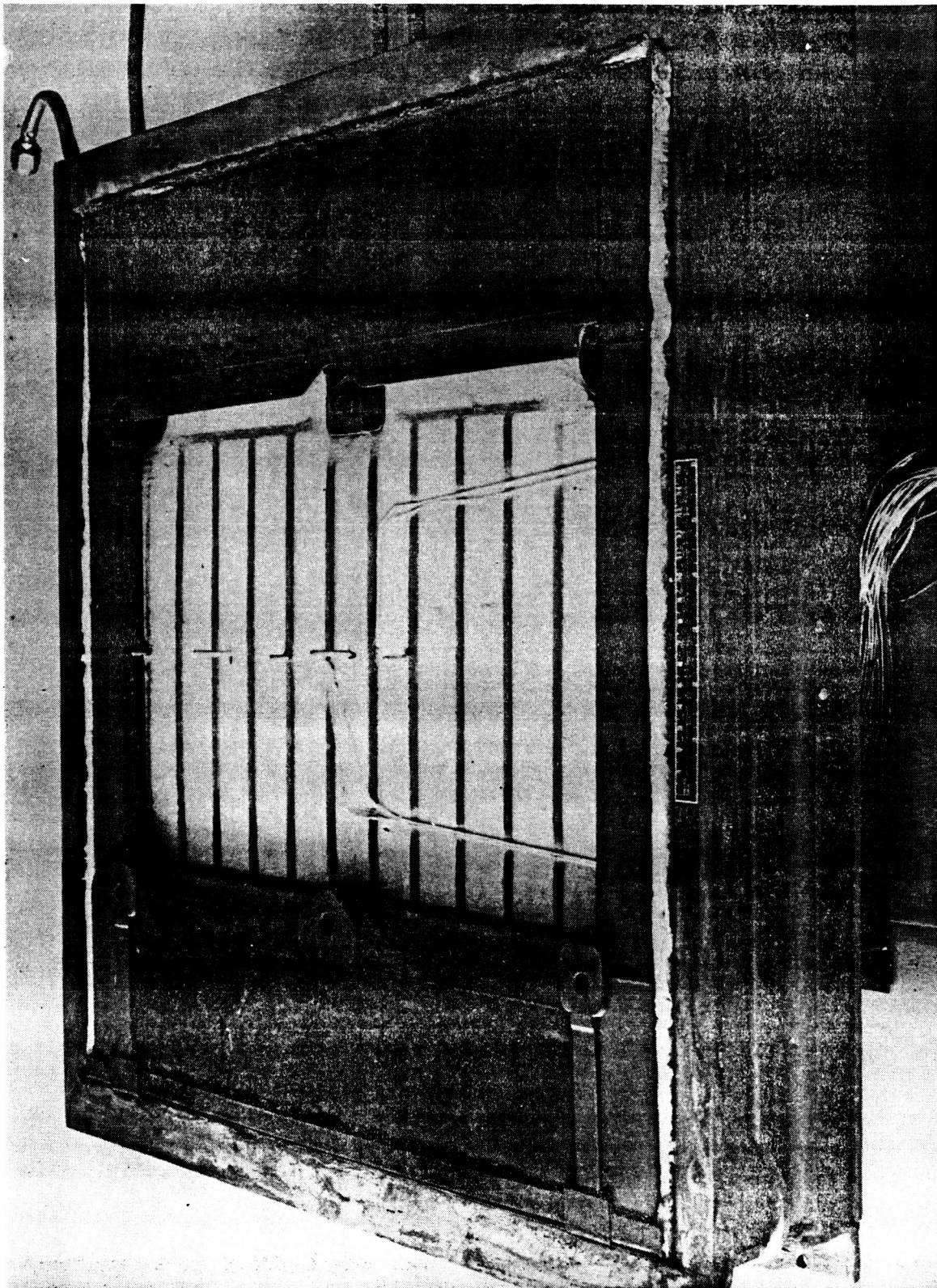


Figure 8-39. Partially Disassembled Tee-Stiffened TPS After 20 Hot Gas Flow Thermal Cycles and 100 Acoustic Cycles (Photo 133769B)

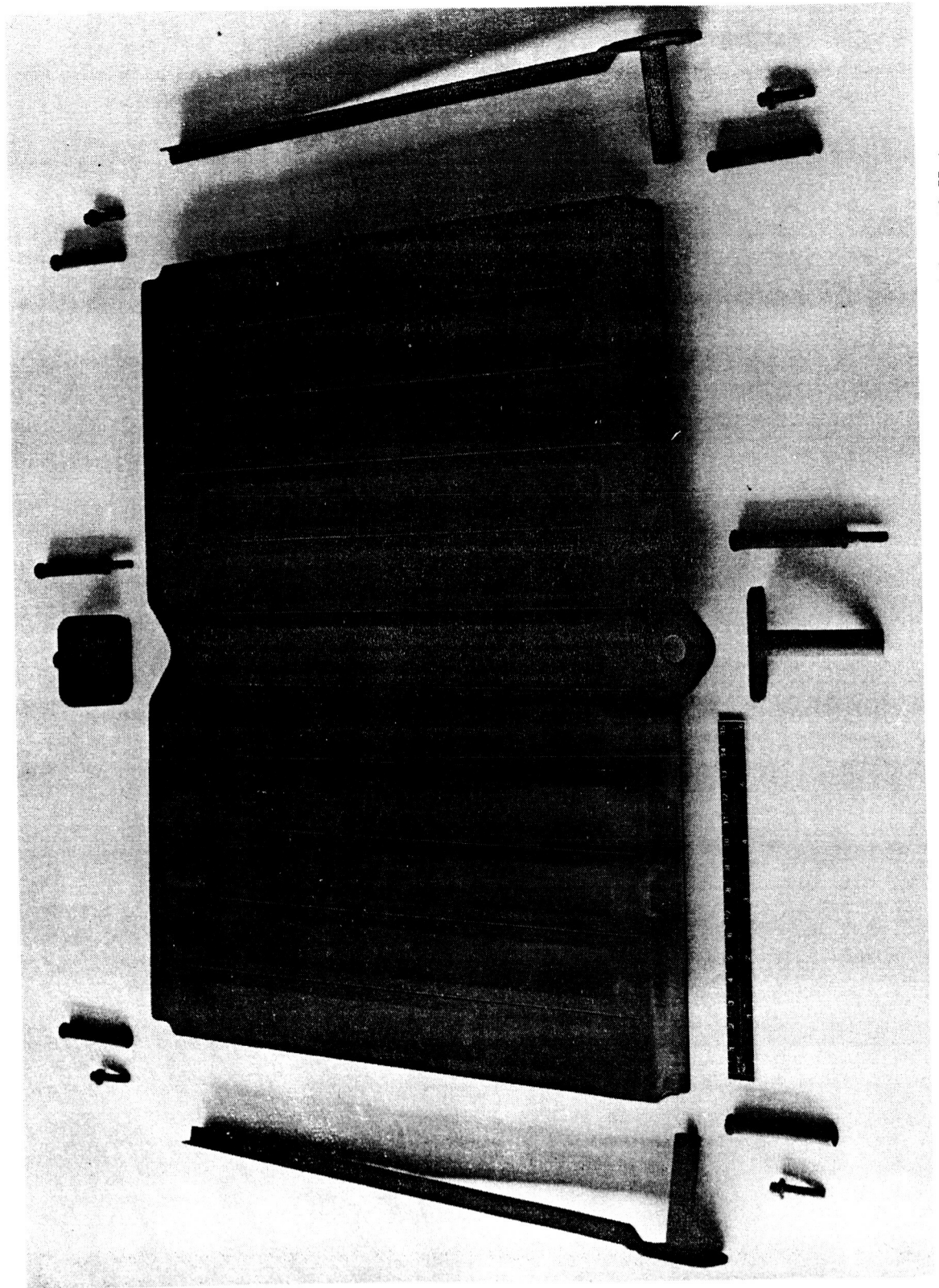


Figure 8-40. Tee-Stiffened Heat Shield (Exterior Side) and Attachments After 20 Hot Gas Flow Thermal Cycles and 100 Acoustic Cycles (Photo 133768B)

8.3.2.2 Open corrugation TPS: The heat shield of the open corrugation TPS scheduled for the radiant heat test series is shown in Figure 8-41 after 25 acoustic cycles. Regions of rubbing similar to those on the comparable tee-stiffened heat shield can be seen. Again, these areas of abraded coating were not sites of premature oxidation during the thermal tests.

The insulation and heat shield bearing surfaces of the Cb-752 support posts are shown in Figure 8-42. The abrasions were again caused by the fore and aft beams of the heat shield and the legs of the auxiliary closeout panels. No accelerated oxidation was noted at any of these locations following thermal cycling.

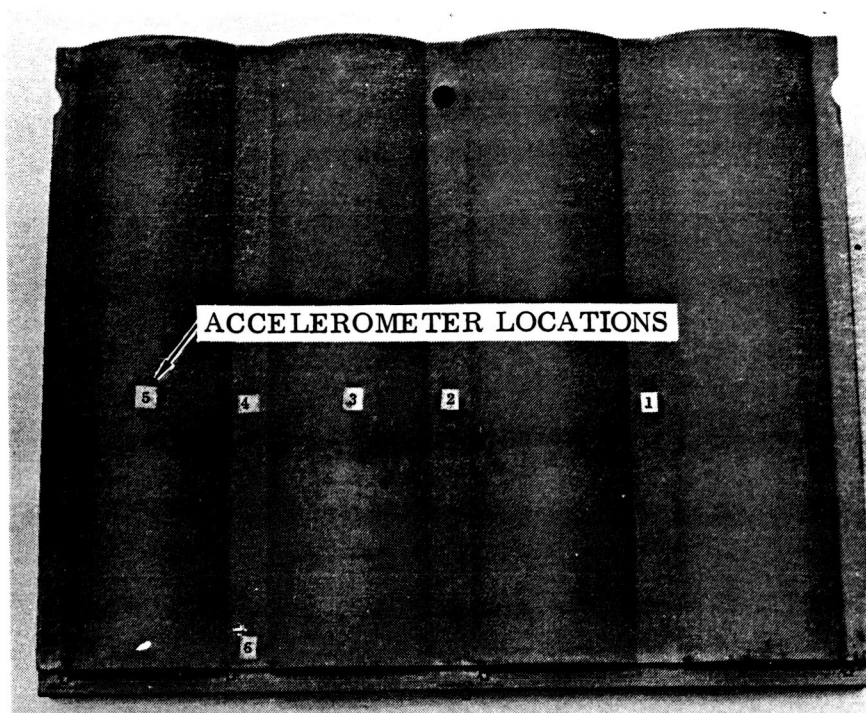
Typical accelerometer response data for three locations for cycles 1, 25, 26, and 100 are presented in Appendix E.

The degree to which the specimen was disassembled is shown in Figures 8-43 through 8-47. These display the main heat shield, side retainers and plugs, all of Cb-752/R-512E, and the TD NiCr bolts. All Cb-752/R-512E plugs were easily removed from the aluminide coated TD NiCr bolts. The breakaway torque required to remove the plugs ranged from 15 to 19 in-lb (169 to 215 cm-N). The initial setting torque was 13 in-lb (147 cm-N). The breakaway torque required to remove the same TD NiCr bolts from the Cb-752/TD NiCr support post ranged from 18 to 21 in-lb (203 to 237 cm-N). The initial setting torque was 15 in-lb (169 cm-N). No chipping of the coating or thread damage was noted during the disassembly.

No coating damage was found on the heat shield or any other Cb-752 components. Evidence of rubbing of the lapped surfaces was noted but this appeared to be related to the outer oxide layer. After a total of 100 acoustic cycles no evidence of fatigue was found. However, the forward transverse beam of the hot gas flow specimen separated from the skin at the braze locations. Four of the five joints were disbonded; the remaining joint was pried apart using little force (Figure 8-48). The disbonded condition of the heat shield was noted after thermal cycle 19 when apparent separation occurred. It is probable that the braze joint failure was initiated by the simultaneous occurrence of high restraint loads due to panel separation as previously discussed and the maximum temperature. It is also probable that inferior braze existed since examination revealed a lack of complete diffusion of the braze foil.

8.3.3 Test summary. — Both heat shield configurations survived the acoustic test program without any damage attributable to sonic fatigue. Therefore, an evaluation was made to compare analytical and test results in order to validate sonic fatigue prediction procedures used herein.

Test panel responses to acoustic excitation were measured by accelerometers located as shown in Figures 8-32 and 8-41. Response data are presented as plots of acceleration spectral density in G^2/Hz versus frequency in Hz. However, acoustic fatigue analysis of



Arrows indicate regions of rubbing

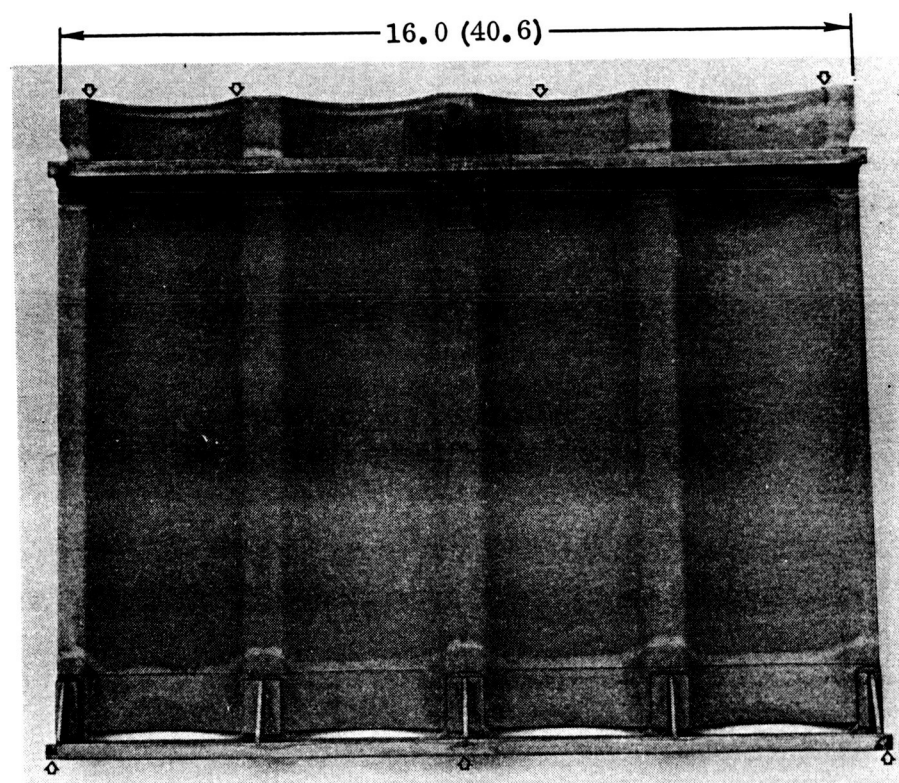


Figure 8-41. Open Corrugation Heat Shield after 25 Acoustic Cycles
 [Photo No. 131395B (upper) and 131396B (lower)]

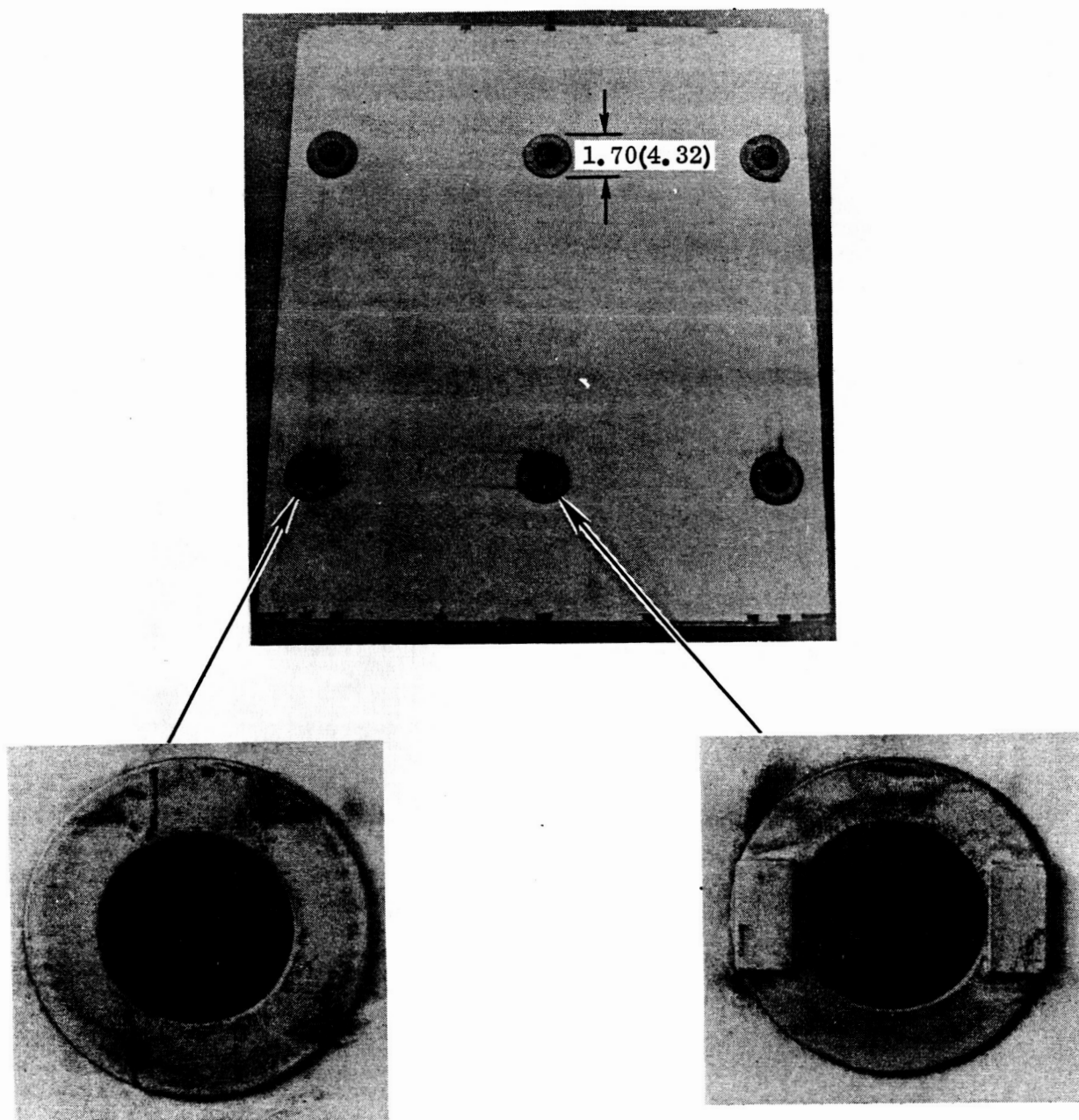


Figure 8-42. Open Corrugation TPS Support Posts and Insulation after 25 Acoustic Cycles
(Photo No. 131397B)

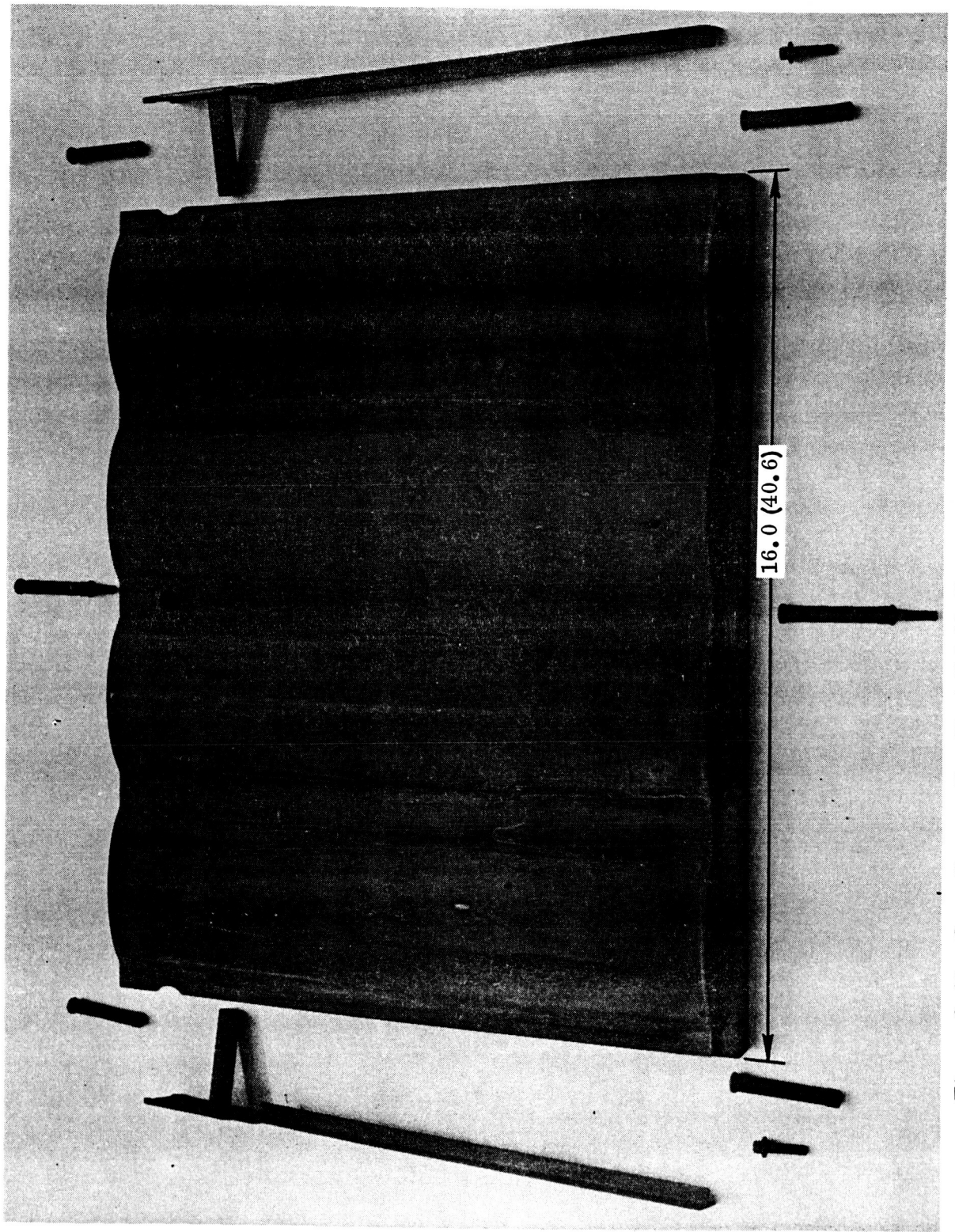


Figure 8-43. Open Corrugation Heat Shield (Exterior Side) and Attachments After 20 Hot Gas Flow Cycles and 100 Acoustic Cycles (Photo 132914B)

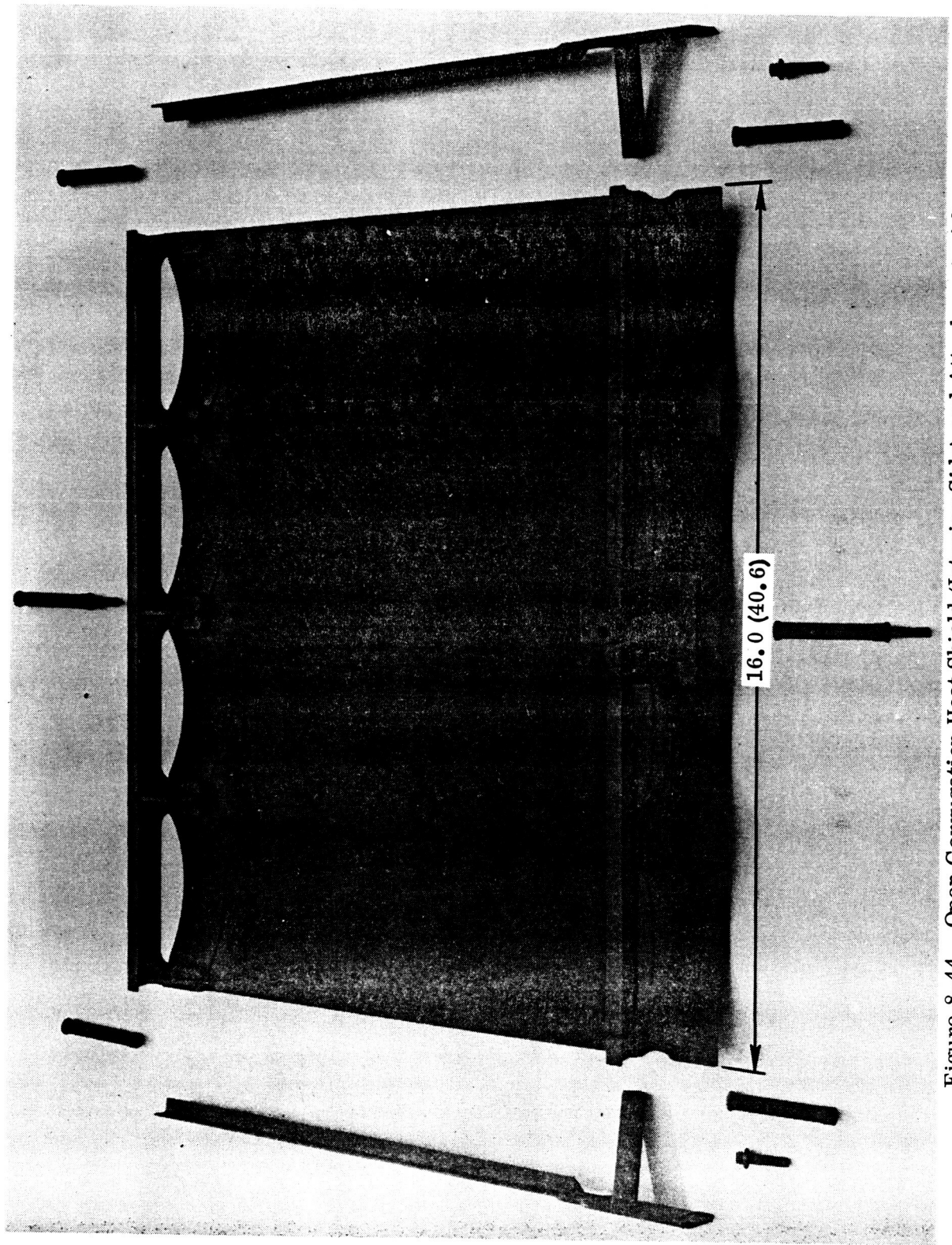


Figure 8-44. Open Corrugation Heat Shield (Interior Side) and Attachments After
20 Hot Gas Flow Cycles and 100 Acoustic Cycles (Photo 132915B)

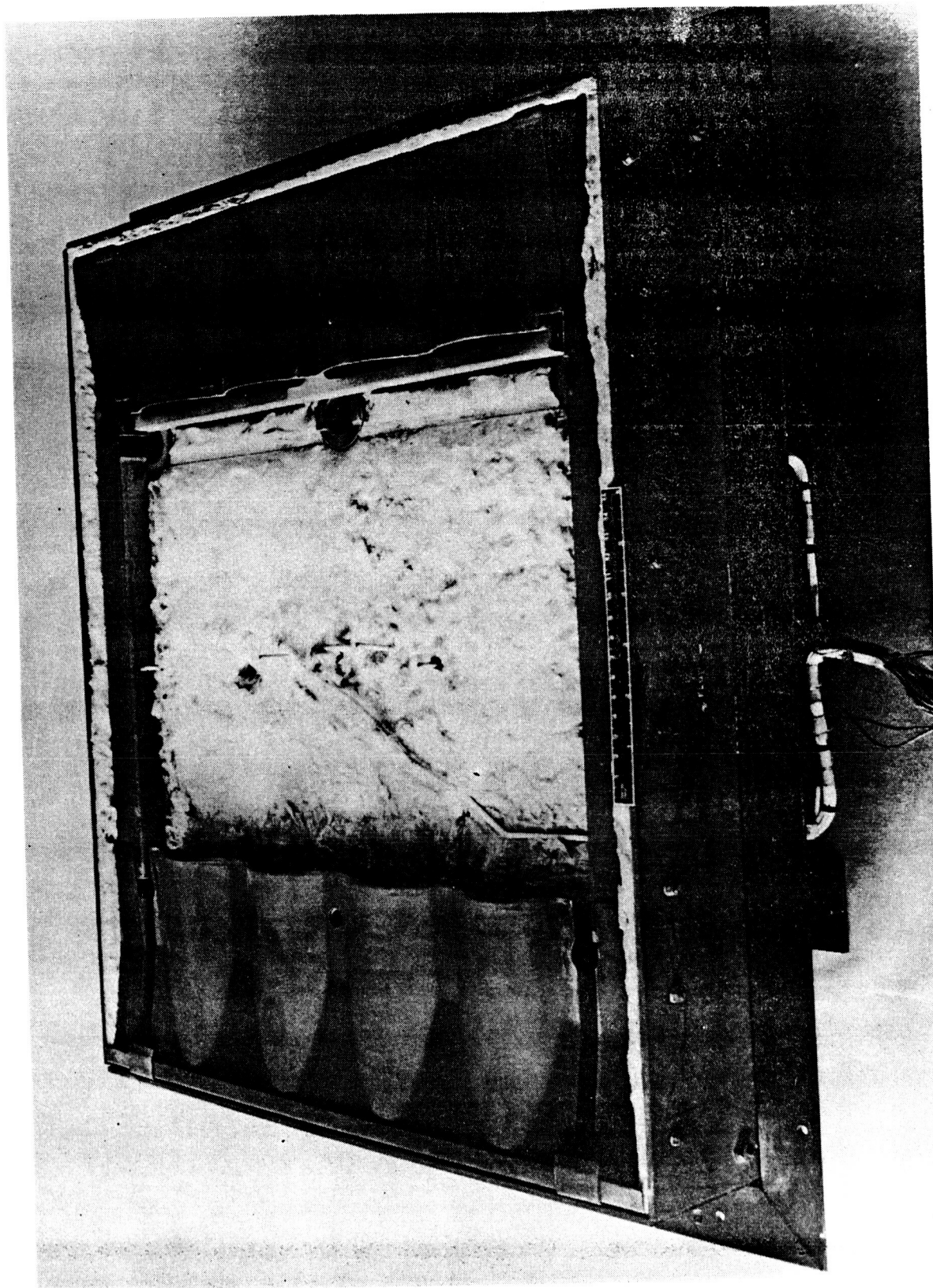


Figure 8-45. Partially Disassembled Open Corrugation TPS After 50 Radiant Heat Thermal Cycles and 100 Acoustic Cycles (Photo 133772B)

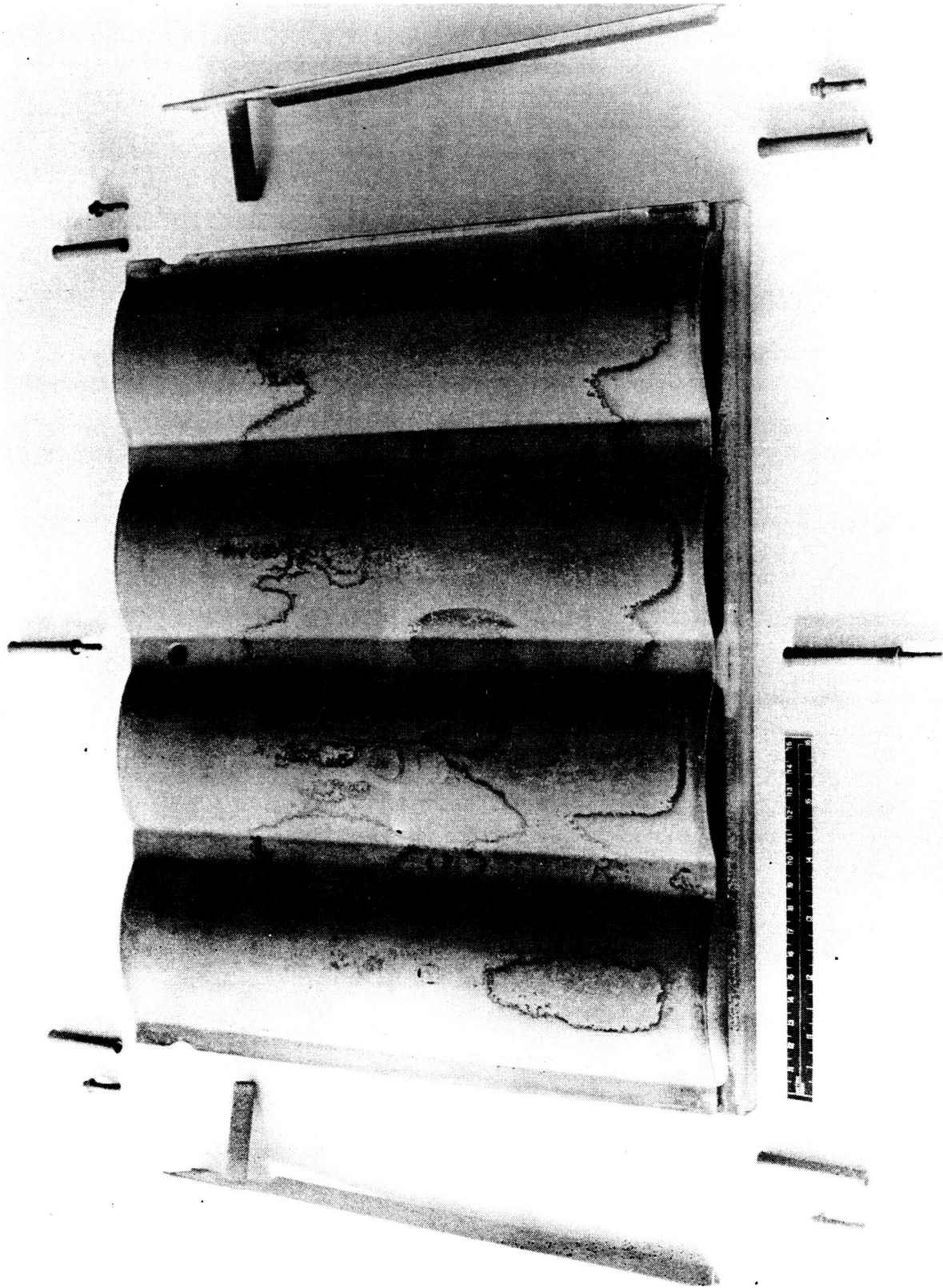


Figure 8-46. Open Corrugation Heat Shield (Exterior Side) and Attachments After 50 Radiant Heat Thermal Cycles and 100 Acoustic Cycles (Photo 133771B)

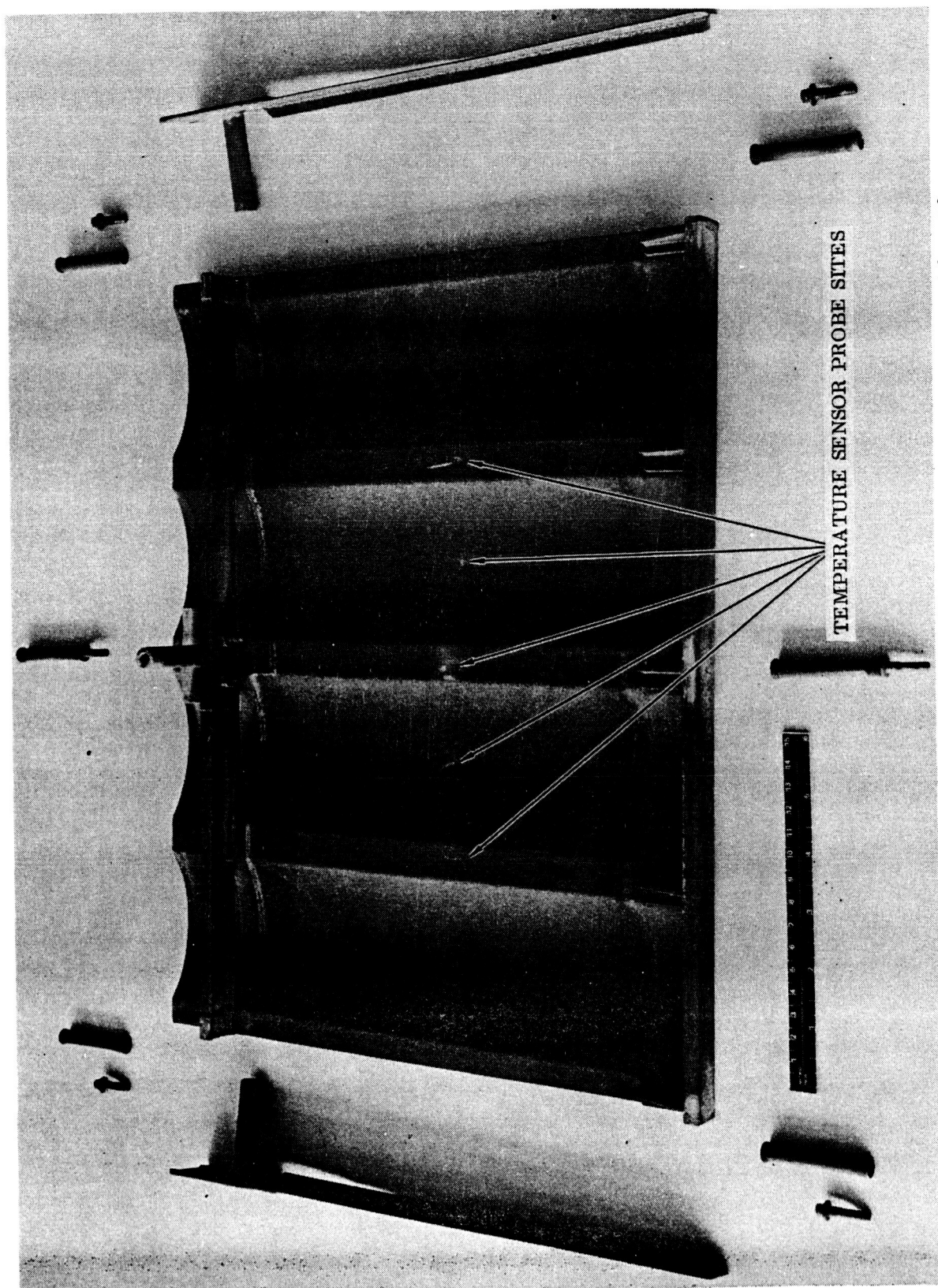


Figure 8-47. Open Corrugation Heat Shield (Interior Side) and Attachments After 50 Radiant Heat Thermal Cycles and 100 Acoustic Cycles (Photo 133770B)

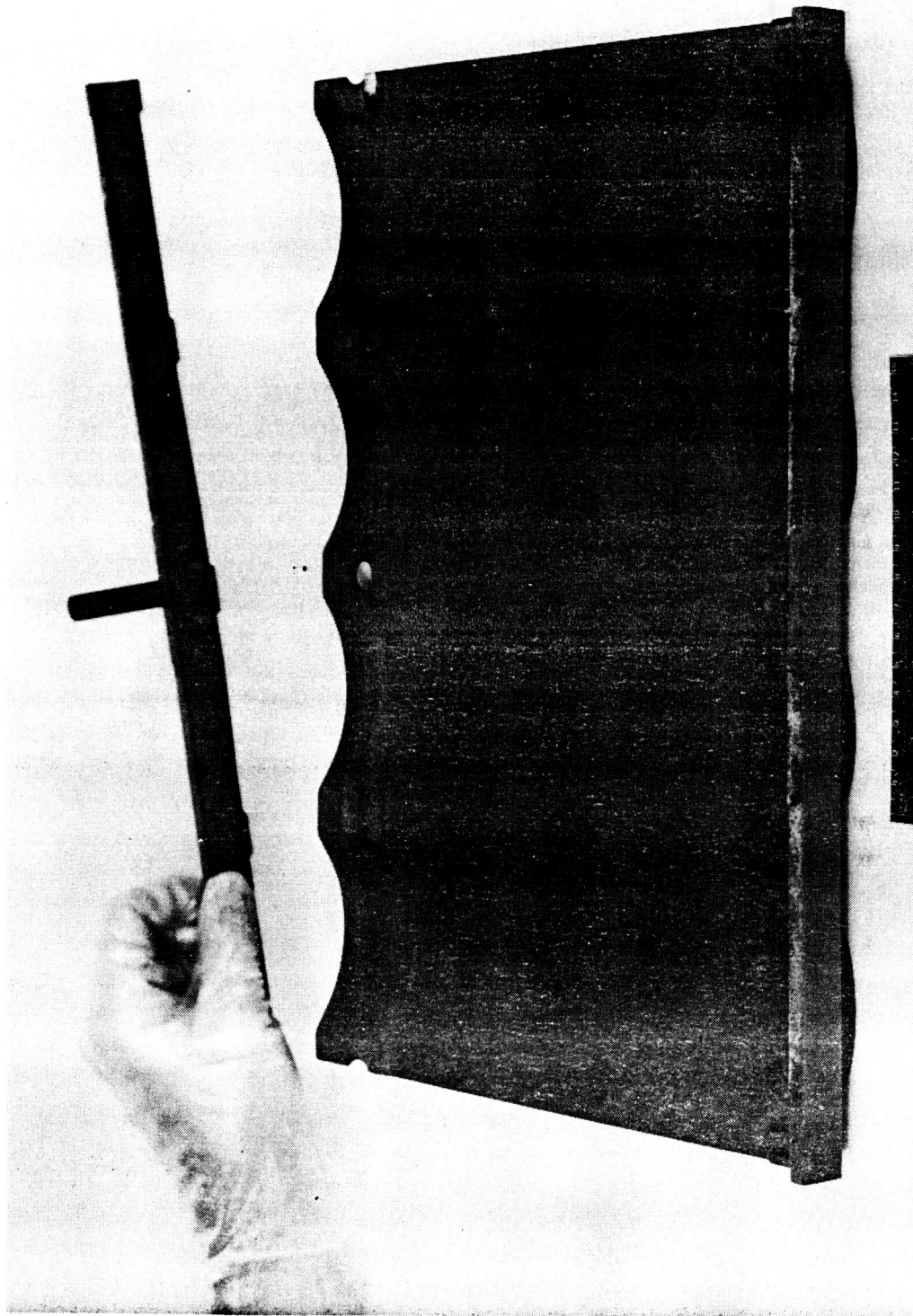


Figure 8-48. Open Corrugation Heat Shield Showing Forward Beam Disbond After 20 Thermal Cycles and 100 Acoustic Cycles (Photo 133249B)

the panels was made using Convair Aerospace computer program P5454, which computes panel responses in terms of dynamic stresses. It was necessary, therefore, to estimate the dynamic stresses corresponding to the measured accelerations in order to establish a compatible basis for comparing analytical and test results.

The panels, being effectively supported only at two ends, were considered as simply supported beams. A simply supported beam under a uniformly distributed load has its maximum bending deflection and stress at mid-span,

$$y_{\max} = \left(\frac{5}{384} \right) \left(\frac{W \ell^3}{EI} \right), \text{ and } f_{\max} = \frac{Mc}{I} = \left(\frac{1}{8} \right) \left(\frac{W \ell c}{I} \right)$$

For essentially the same size panels exposed to the same acoustic pressure, the acoustic pressure applied statically can be substituted for W . By ratioing the normalized stress to the normalized deflection, i.e., $(f_{\max}/W)/(y_{\max}/W)$, the following expression is obtained,

$$f = \frac{48Ec y}{5 \ell^2}$$

where c is the distance from the neutral axis of the beam to the extreme fiber.

For the test panels, it was assumed that under acoustic excitation all points vibrated in phase at their fundamental resonant frequencies. Thus, the rms vibratory acceleration of the center of the panel relative to the ends is obtained by subtracting, for example, the output of accelerometer 6 from that of accelerometer 3 (Figure 8-41). Dividing the rms acceleration in in/sec^2 by the square of the resonant frequency in radians per second yields the rms displacement in inches. Substituting this displacement in the equation yields the dynamic rms stress in psi.

The responses of the test panels include the effects of their inherent damping (dynamic magnification) but do not include the effects of local stress raisers. Analytically computed responses include both an arbitrarily selected damping coefficient, $c/c_c = 0.02$, and the stress raiser, $K_T = 4.0$. Analytical results can be adjusted for the stress raiser. However, no adjustment can be made for the actual damping of the test panels compared to 2%, because the structural bandwidth is less than that of the 20 Hz bandwidth of the analyzer used in reducing the test data. The half-power points on the acceleration spectral density plots then merely reflect the analyzer bandwidth.

With all the assumptions involved in converting panel responses in terms of acceleration spectral density into dynamic stresses, agreement between test and analytically derived normalized stresses, i.e., stress divided by applied acoustic pressure, was good. For the tee-stiffened heat shield, agreement was within 15%; for the open corrugated panel, agreement was within 30%. In both cases, analytically derived stresses were higher.

9 LIGHTNING STRIKE TESTS

The effect of lightning strikes on coated columbium alloy heat shields had not been defined prior to the initiation of this program. However, it was anticipated that problems with electrical bonding and intrastructural arcing could be aggravated by the presence of the non-conductive silicide coating. Also, it was theorized that charges induced by climatic electrical fields could build to a large potential at the coating surface and eventually break down the dielectric protection at attachments and edges of the heat shields. The resulting arcing could interfere with the operation of electrical systems or cause damage to the coating and expose the substrate to oxidation. Hence, two simulated heat shields were fabricated and tests established to investigate the phenomena of lightning discharge. All discharge tests were made at the Lightning and Transients Research Institute (LTRI) of St. Paul, Minnesota.

9.1 Mechanism of Lightning Discharge

The basic mechanism of lightning stroke approach to an aerospace vehicle of any type is as follows. The lightning discharge step leader advances in discrete steps of approximately 50 meters in length from a cloud charge region and induces streamering off the vehicle extremities as it approaches. The streamers may be induced off any extremity including metallic components under non-conducting plastic sections. As the stroke comes near the vehicle it finally contacts one of the streamers to follow it into the vehicle and then exits through streamers from the opposite extremity to another cloud charge region or to the earth. The sequence is illustrated in Figure 9-1. An example of the streamering from a laboratory model is shown in Figure 9-2.

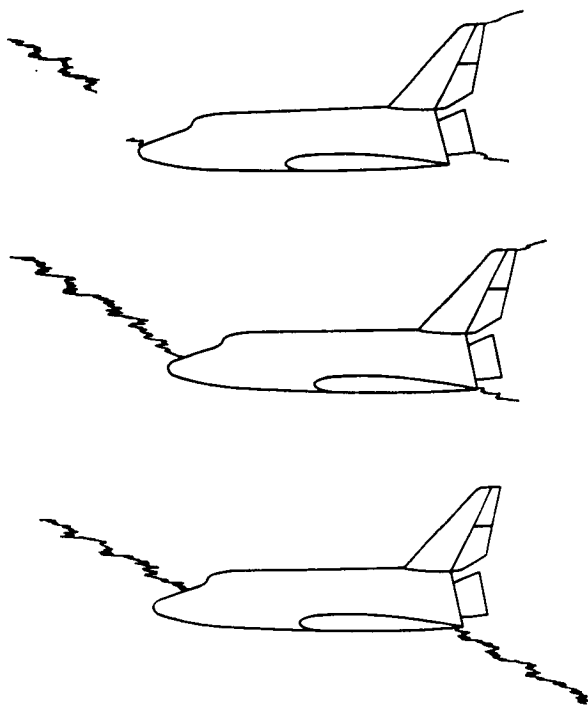


Figure 9-1. Mechanism of Lightning Step Leader Approach and Passage Through an Aerospace Vehicle

The discharge will normally strike some extremity and if the extremity is on the leading edge of the vehicle, the contact point of the discharge channel will be swept to the rear over the surface producing a series of pit marks as it moves, finally hanging on to the trailing edge, as illustrated in Figure 9-3, for an extensive

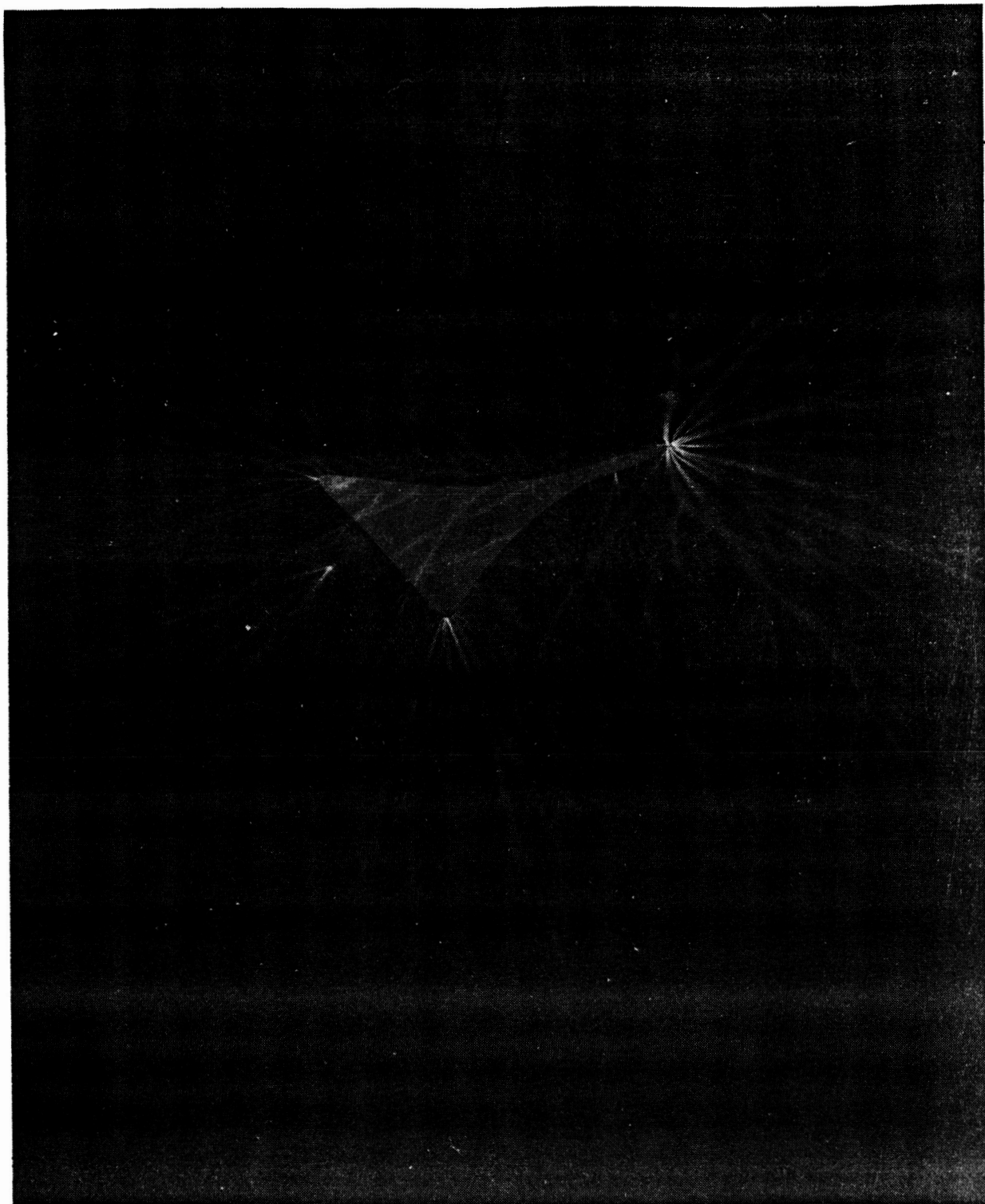


Figure 9-2. Streamering from Model in Laboratory Illustrates Induced Streamering from Approaching Natural Lightning Discharge That Guides Stroke into Vehicle

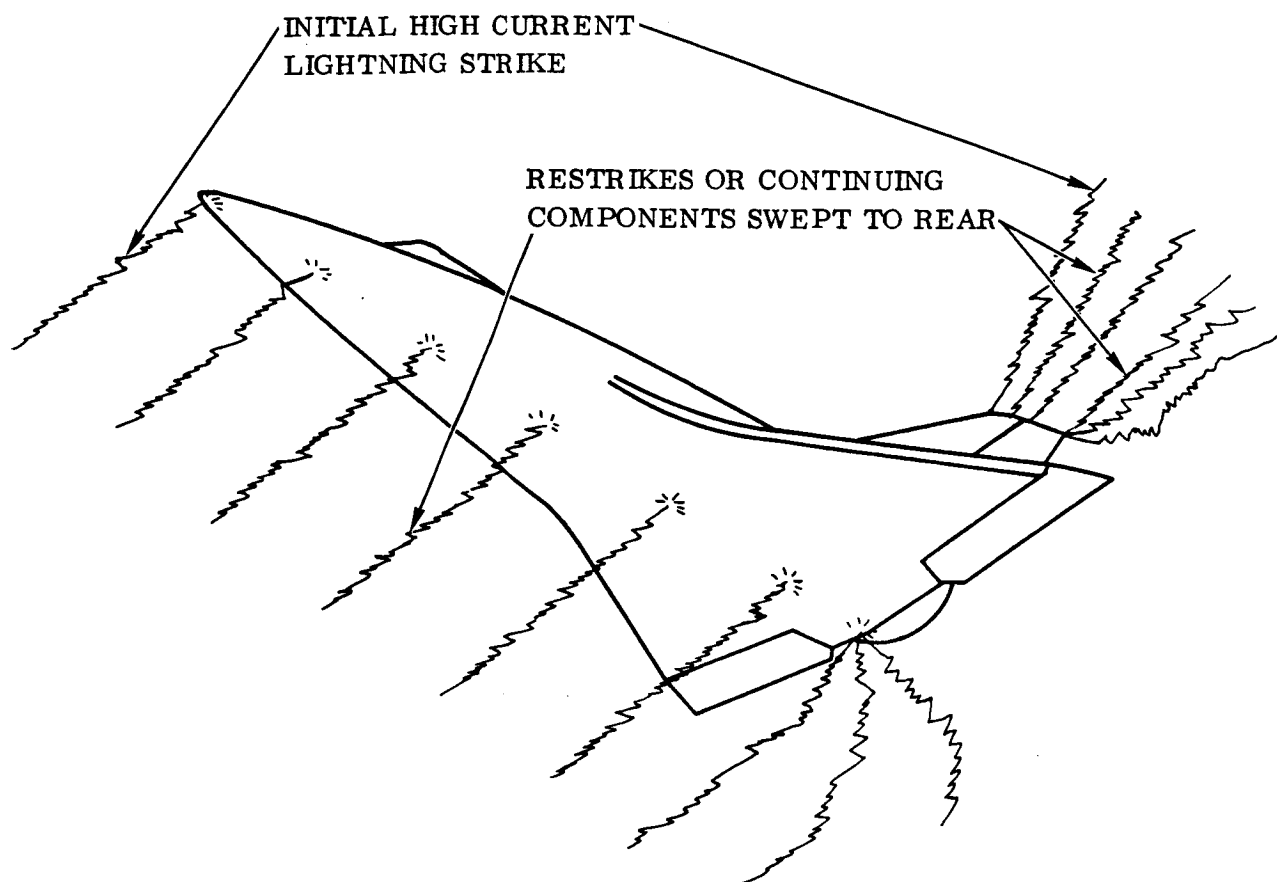


Figure 9-3. Stroke Off Nose is Swept Back Over Undersurface of Vehicle to Produce Pit Marks and a Few Holes in Undersurface

period. A simplified waveform of the lightning discharge currents is presented in Figure 9-4. The initial step leader has very low currents insufficient to produce more than a very slight marking of the vehicle.

As the step leader contacts the earth for a cloud-to-ground discharge, a high current return stroke in the form of an ionization wave follows back up the channel to the vehicle and produces the initial high current pitting during which time the vehicle has moved a slight distance in the few milliseconds required for the step leader to travel to the opposite charge region (or earth) and return. Thus, the initial pitting may be expected to strike a few feet behind the leading edge of the wing or nose, whichever may be the strike point. The high current return stroke exhibits a pseudo skin effect in which only a few thousandths thickness of the skin surface is melted. This initial high current return stroke is followed by an intermediate current component consisting of a slower waveform with maximum currents of 1000 to 10,000 amperes and time durations of milliseconds. This discharge, because of its relatively long time duration shows no pseudo skin effects such as are seen in the high current discharges and is

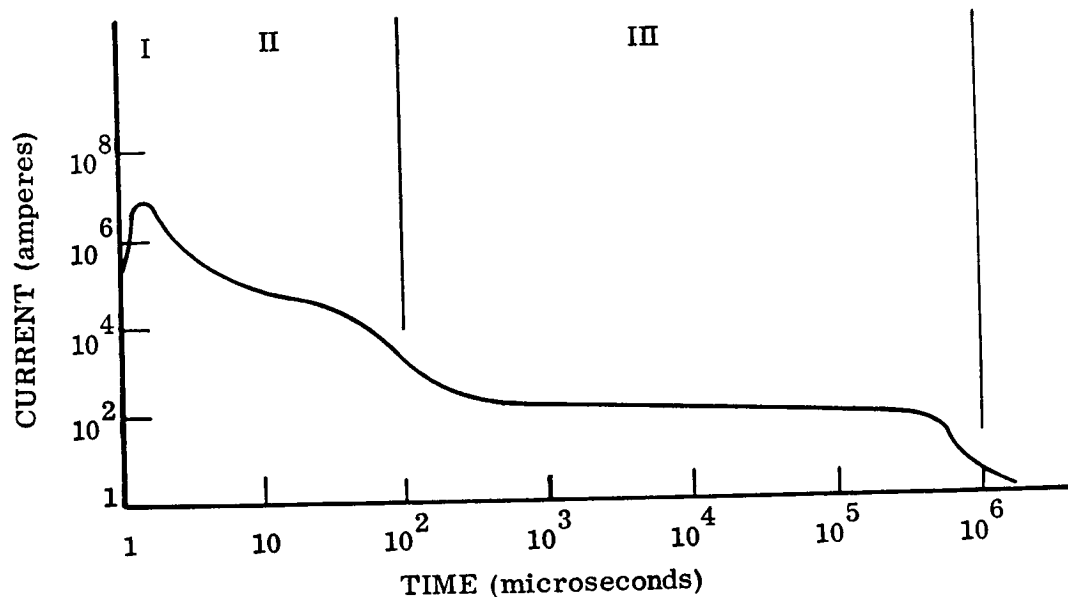


Figure 9-4. Composite Current Waveform of Natural Lightning Discharge Showing Three Main Phases: High Current, Intermediate Current, and Low Current Long Duration

therefore capable of producing the maximum skin penetration effects from a moving discharge.

The final phase of the discharge, a continuing current of a few hundred amperes lasting for periods up to one second, is swept across the full length of the vehicle up to the trailing edge where it may hang on producing fairly large holes up to several inches in diameter.

These three major high current components, the initial high current return stroke of several hundred thousand amperes, the intermediate current component of a few thousand amperes lasting for a few milliseconds, and the continuing current of a few hundred amperes lasting for seconds, represent fairly well the major components of a natural lightning discharge. These components may be followed by restrikes, which differ principally in having a continuous dart leader. The major phases are illustrated in Figure 9-5.

The damage produced by the three major high current components includes: (1) high current sparking of metallic joints, slight melting of the external skin surface, and induced voltages in the vehicle wiring, (2) intermediate currents produce skin puncture effects even when the discharge is moving and maximum internal pressure effects by vaporization of metallic or insulating materials to produce extensive internal blast damage, and (3) continuing currents which produce minor pitting of the skin while moving across the surface but fairly large holes several inches in diameter at trailing edge surfaces as the discharge hangs on.

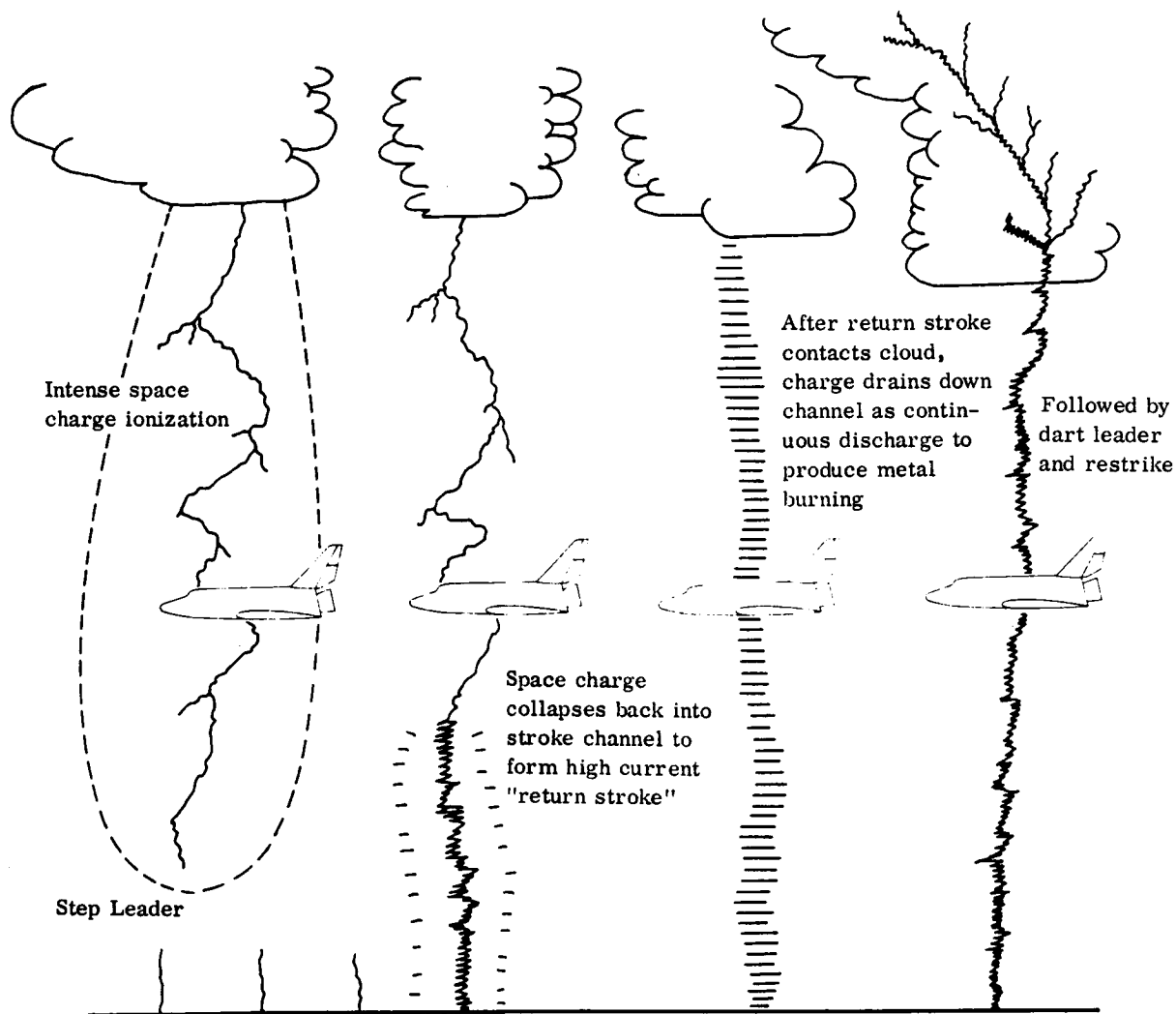


Figure 9-5. Illustration of Spacecraft Contact Mechanism and Movement Through Lightning Channel

The mechanism of stroke hang-on to the trailing edge surfaces is illustrated in Figure 9-6. The initial wing-to-wing strike is stretched out by motion of the vehicle for nearly a full second as the vehicle moves forward to produce fairly large pitting in the trailing edge corresponding quite closely to the effect of an arc welding torch held at the trailing edge for a full second.

9.2 Test Specimen Fabrication

Two sets of specimens were fabricated from Cb-752 and coated with R-512E. The components of one specimen are shown prior to assembly in Figure 9-7. The heat

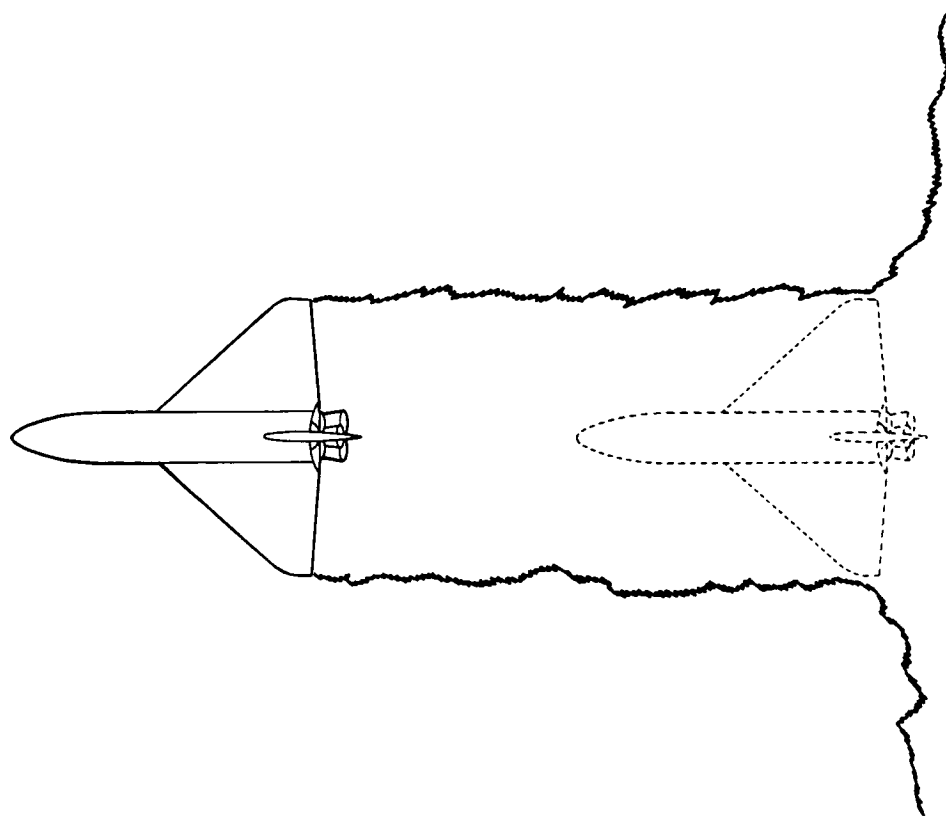


Figure 9-6. Mechanism of Stroke Hang-on

shield was unstiffened and of the dimensions 10.5 by 10.5 by 0.015 inches (26.7 by 26.7 by 0.038 cm). The overall specimen size was 15 by 15 by 2 inches (38.1 by 38.1 by 5.08 cm). All components were coated with 0.003 inch (0.076 mm) R-512E. The heat shields were examined by electron emission radiography and thermoelectric probe and found to have a uniform coating.

Prior to performing electrical resistance mapping measurements, one specimen was oxidized at 2400° F (1589° K) at one atmosphere for one hour in air. The second specimen was mapped in the unexposed condition thereby giving a relative comparison of electrical resistance between a first flight panel and one that had been thermally exposed. Before measuring for resistance, a six foot (1.83 m) number 4 gage cable was attached to each panel for grounding. The electrical resistance measurements for each panel are shown in Figure 9-8. For the oxidized panel the resistance measurements were taken with a General Radio Megohmmeter Type 1862-C with a 0.25 in² (1.61 cm²) wiper at two inch (5.08 cm) intervals. For the unoxidized panel all measurements were taken with a wheatstone bridge. As noted, the resistance of the oxidized panel was found to be significantly greater than that of the unexposed panel.

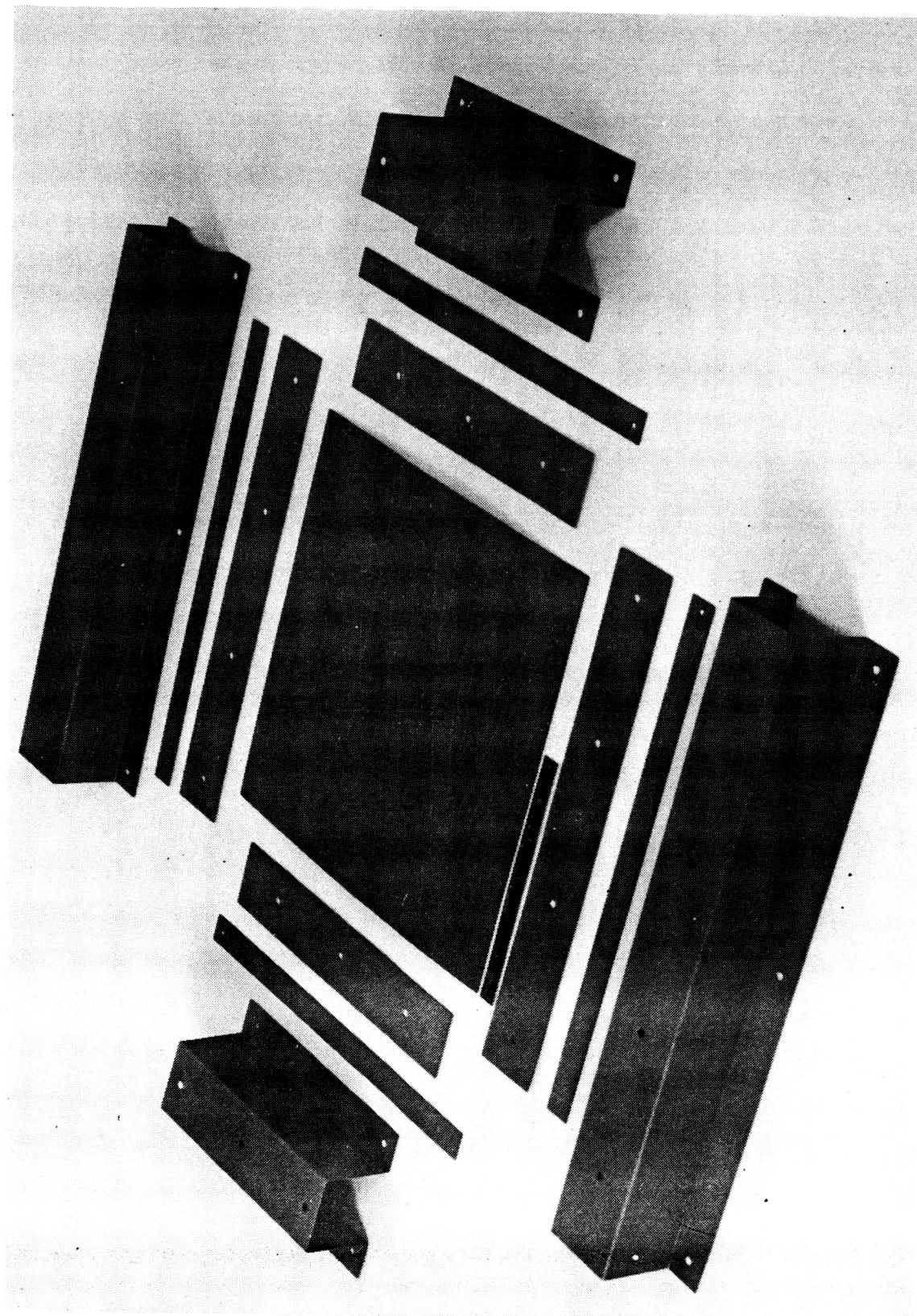


Figure 9-7. Cb-752/R-512E Lightning Strike Specimen Components
Prior to Assembly (Photo 117844B)

Figure 9-8. Electrical Resistance Measurements of Lightning Strike Specimens

9.3 Lightning Strike Testing

To reproduce the various lightning strike effects on a columbium alloy heat shield three types of tests were conducted. The first was a high current rise discharge (maximum dI/dt) of 100,000 amperes per microsecond fired into the specimen as specified in MIL-B-5087B. The high rate of rise is intended to produce induced surges in wiring, but also is an assessment of the ability of a material to dissipate (conduct) a charge away from a localized area without burning or damage. The results of this test on each skin was very slight pitting but no visible perforation to the substrate. The test arrangement is shown in Figure 9-9.

The second test was a maximum energy (maximum Q) test that is typical of a cloud-to-cloud, cloud-to-vehicle, or the second component of a cloud-to-ground discharge during which relatively low currents (less than 10,000 amperes) and long dwells (milliseconds rather than microseconds) occur. Typically, this results in burned holes 0.25 to 0.75 inch (0.64 to 1.91 cm) diameter at wing trailing edges of an aircraft as charges accumulate and try to leave the wing. When brass electrodes were used, the results were slight pitting of the surface of each skin. However, during the arcing, the brass electrode was bombarded by columbium ions. Thus, brass sputtered from the electrode and onto the strike area of the panels. Since the presence of brass could cause premature coating failure or eutectic alloying with the columbium during subsequent thermal exposure, it was decided to use a tungsten electrode in the remaining test.

Thus, the test was repeated with a tungsten electrode and in the initial test the electrode apparently produced puncture of the skin through mechanical force. To produce a more realistic test in view of these two non-inflight effects, an intermediate discharge was triggered to the panels using a high voltage, low current trigger generator to establish an arc of three inches (7.62 cm) in length down to the test panel. The test arrangement is shown in Figure 9-10.

The results of the test showed very minor pitting on both samples and rather extensive spreading of the discharge contact points over an area of several square inches. Thus both panels passed the intermediate current, intermediate duration discharge tests with only minor pitting but some damage to the coating on the skin. Oscillograms of the test current waveforms are shown in Figure 9-11.

The third type of test was a high current discharge of 200,000 amperes. This would be typical of a major cloud-to-ground lightning strike and would normally puncture the aluminum skin of an aircraft. The hole would largely be the result of a mechanical shock wave.

For both specimens, the discharges tore the skin resulting in a fairly large hole in the columbium. It should be noted however that a 200,000 ampere return stroke would

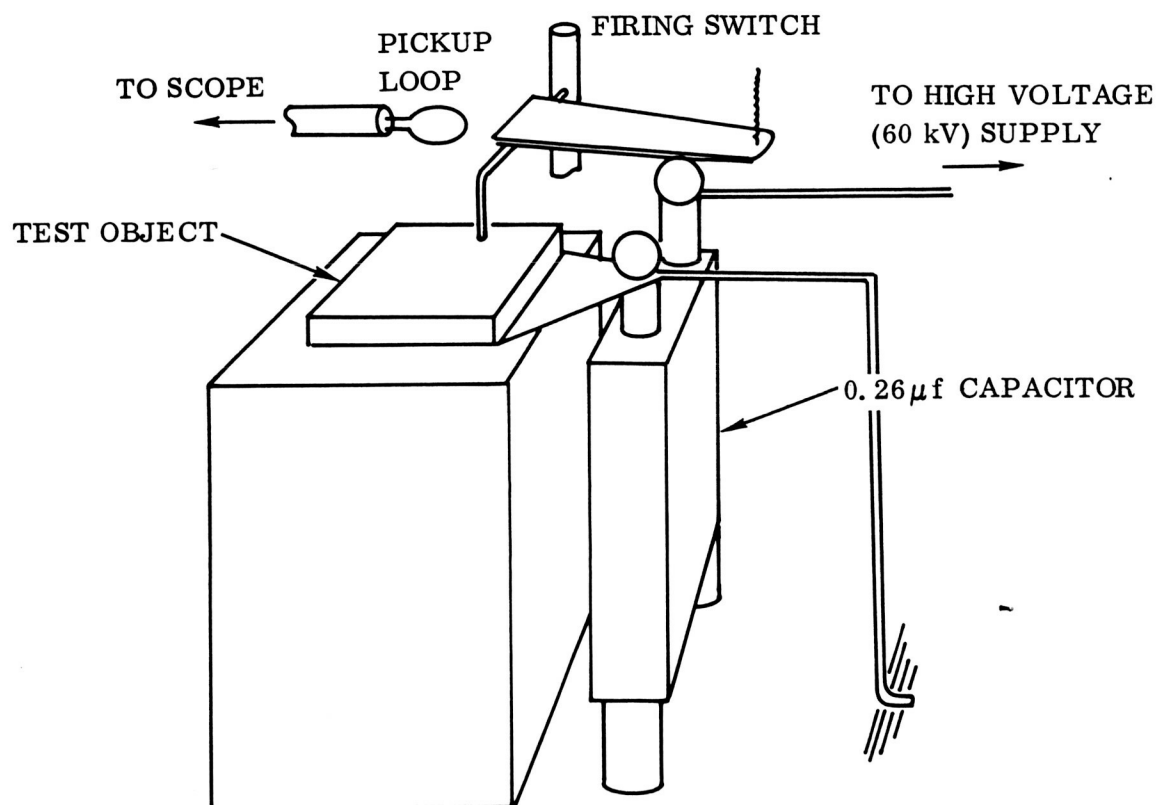
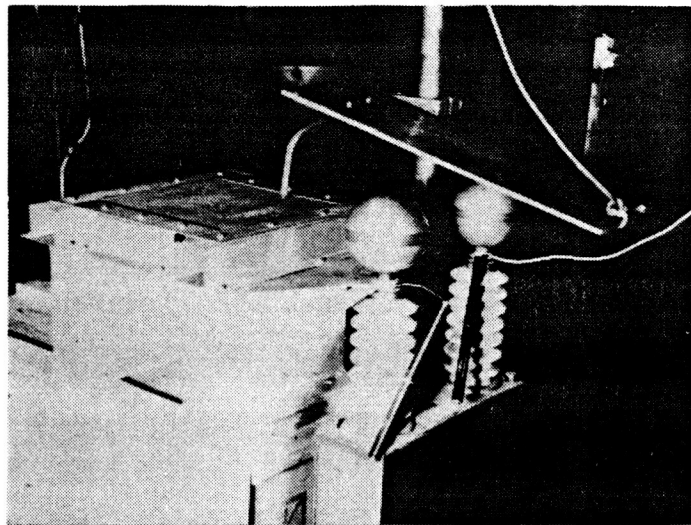


Figure 9-9. Test Arrangement for High Rate of Rise Test

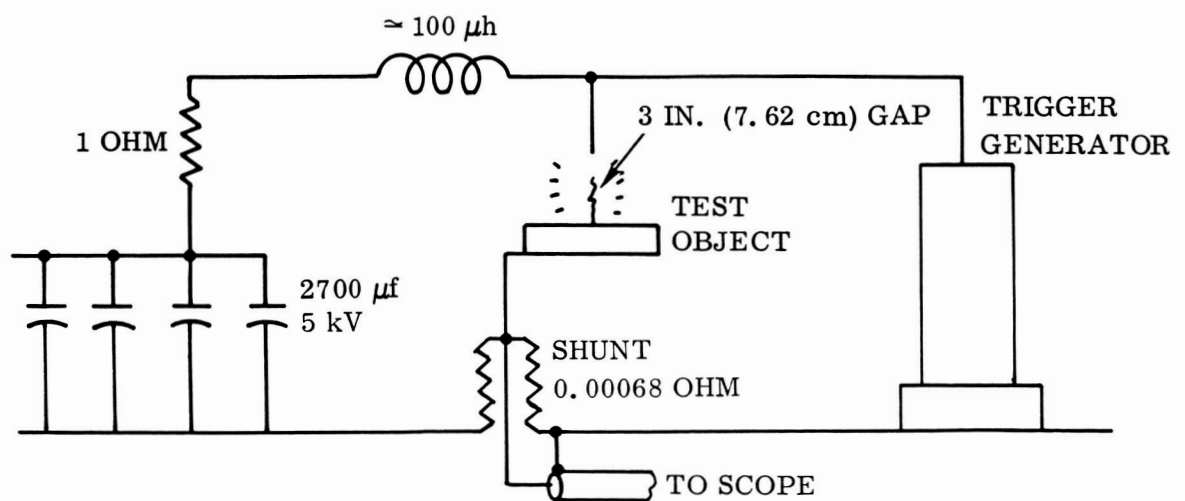
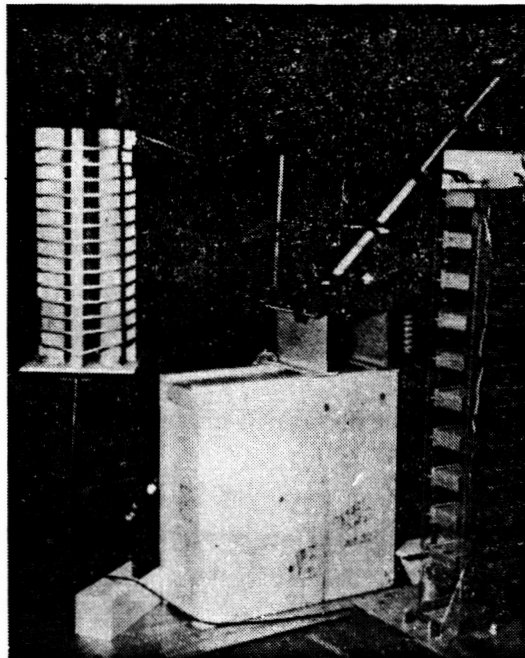


Figure 9-10. Test Arrangement for the Intermediate Current Test

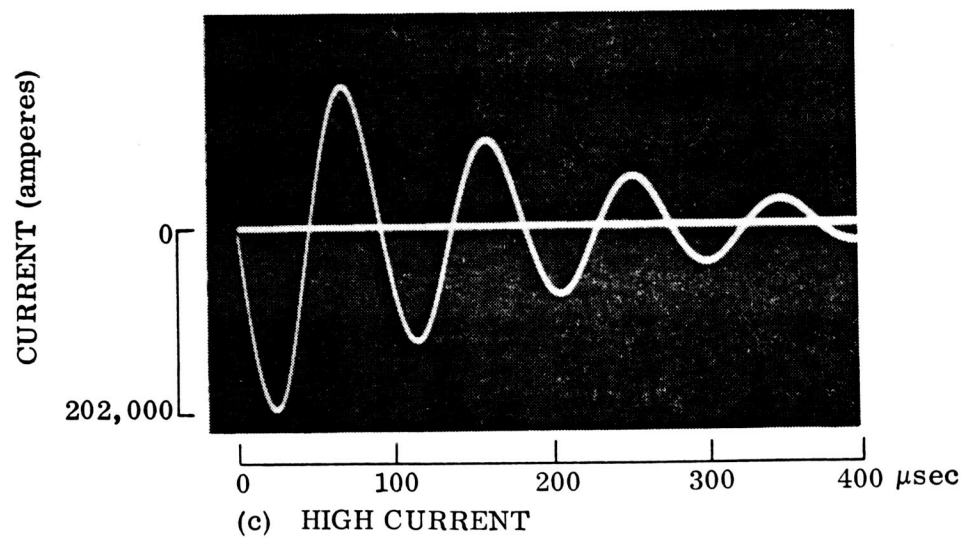
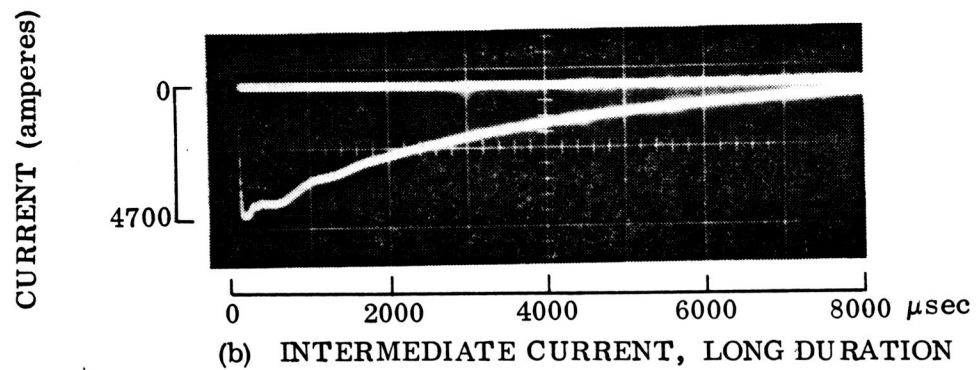
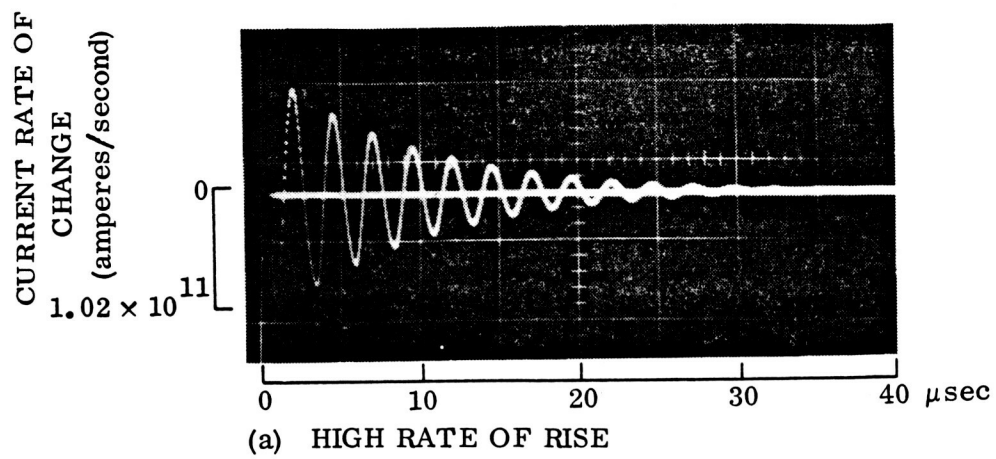


Figure 9-11. Oscillograms of Lightning Waveforms Used in Test of Columium Heat Shield Panels

be expected to strike an extremity and not a mid-chord area, which is generally contacted by restrikes or continuing components. This current with a 20,000 ampere crest and a time duration of nearly 40 microseconds represented the initial high current component of a natural lightning discharge.

The test specimen without prior thermal exposure and the pre-oxidized specimen are shown in Figures 9-12 and 9-13 respectively. Upon return of the specimens from LTRI each specimen was exposed to two 1/2-hour cycles to 2400° F (1589° K) in air to determine the oxidation resistance of the struck areas. As expected, the ruptured areas

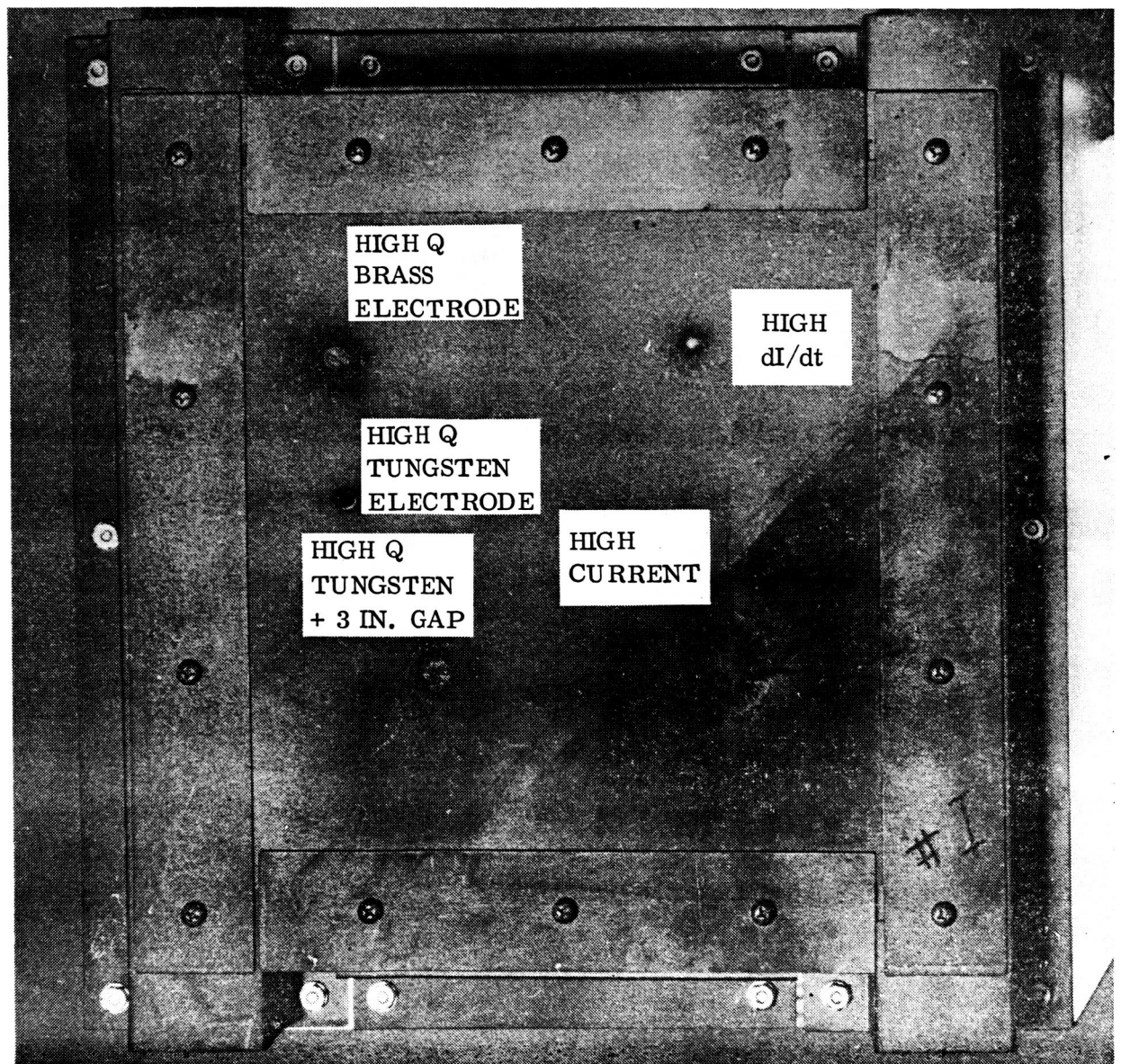


Figure 9-12. As-Coated Cb-752 Test Specimen After Lightning Strike Test Sequence

developed a heavy columbium oxide and the arc burns developed a light oxide. The arc burns could easily have been repaired but the test results indicate that, had a strike of this nature occurred during flight, the mission and recovery would not have been jeopardized.

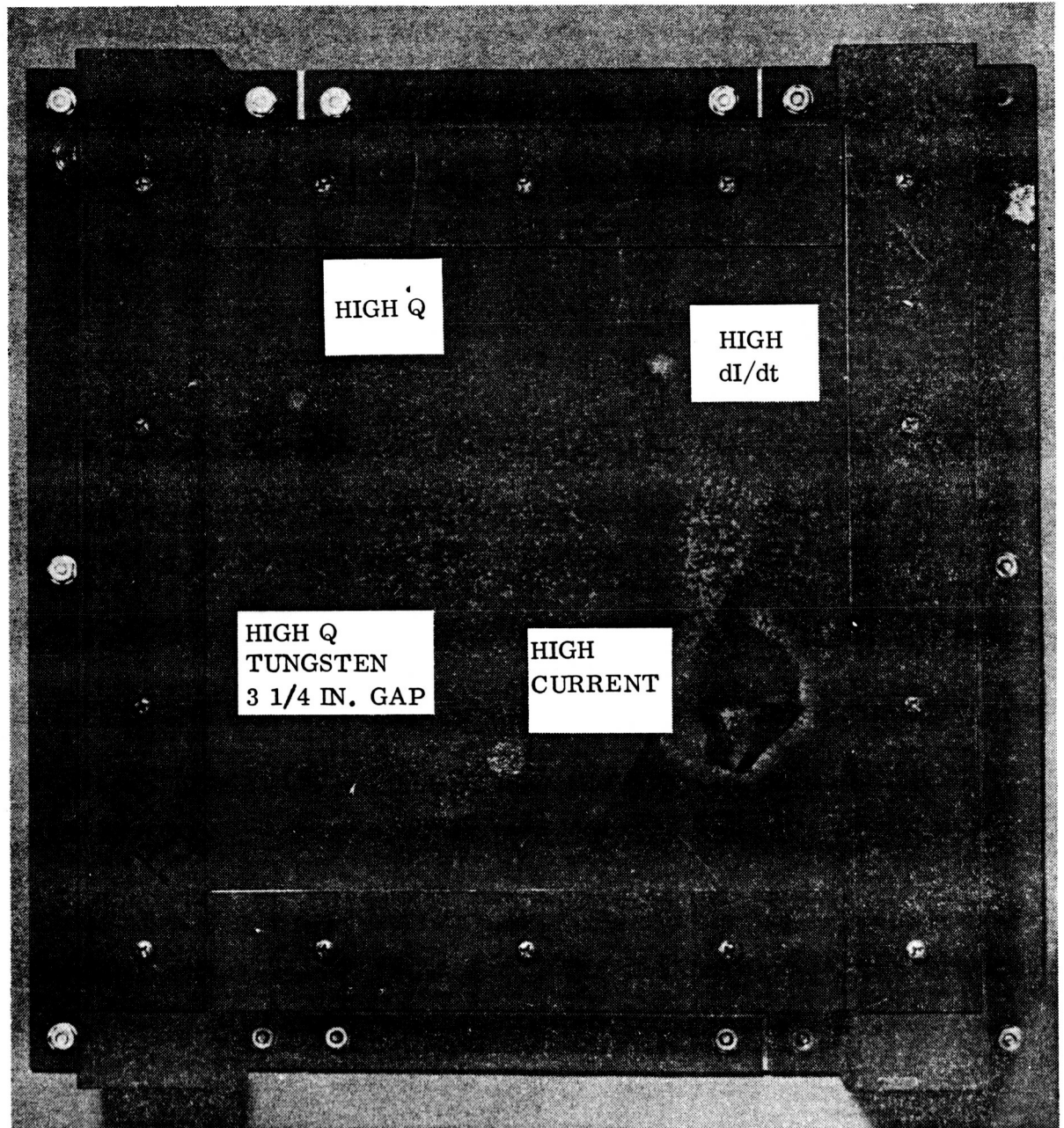


Figure 9-13. Pre-Oxidized Cb-752 Test Specimen After Lightning Strike Test Sequence

The heat shield that had not been preoxidized prior to lightning strike testing is shown after thermal exposure in Figure 9-14. The preoxidized heat shield exhibited similar substrate oxidized regions. Both panels were measured for electrical resistance as previously described following testing. The resistance of both panels was similar to that recorded for the oxidized panel prior to the lightning strikes.

In summary, the following observations were made:

(1) The panels could withstand the maximum current use rate (dI/dt) and a typical cloud-to-cloud discharge (high Q) without perforation. Some coating damage is possible within approximately a 1/2-inch (1.27 cm) radius. However, it is expected that at least one successful reentry could be made.

(2) The maximum current strike, typical of a cloud-to-ground bolt, ruptured the panels causing the material to rip. Rips of approximately 2.50 to 5.25 inches (6.35 to 13.34 cm) along with inward bending of the ripped areas occurred. A panel damaged in such a manner would be unsatisfactory for reentry due to ingestion of the air stream. It would, therefore, require repair or replacement prior to atmospheric entry. However, since the strike condition was an example of an on-the-pad mode, it is unlikely that the vehicle would be launched with a noticeably damaged heat shield.

Finally, the strike probabilities will be affected by the following factors:

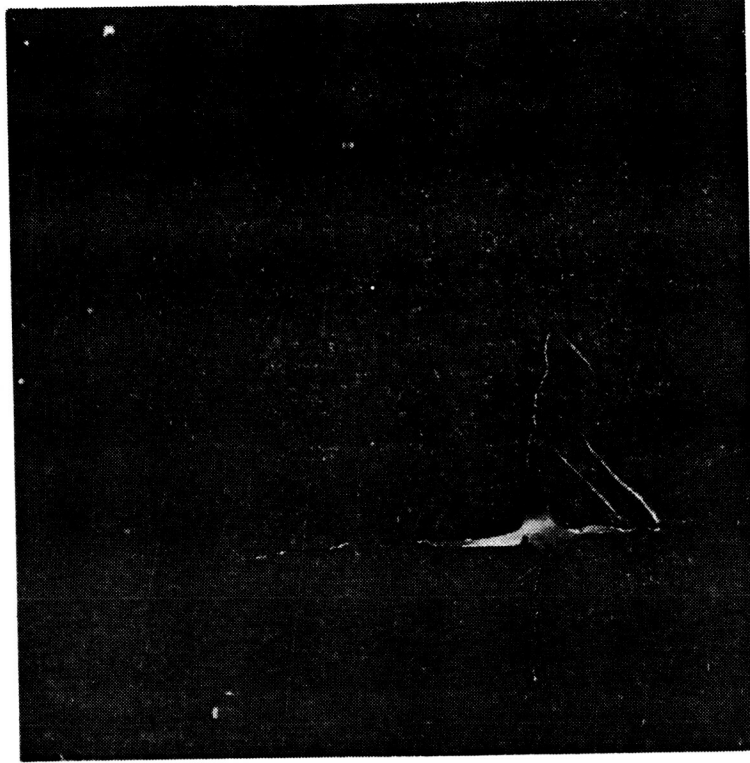
(1) The shuttle will avoid weather on reentry to a much greater extent than is possible with commercial airliners.

(2) The probability of a 200,000 ampere stroke is low as it is estimated that only one such stroke occurs every year for all U. S. commercial aircraft.

(3) The coincidence of a 200,000 ampere stroke occurring as a restrike during the time a stroke is sweeping over the columbium panels is extremely remote.

(4) A typical strike to the heat shield would be one swept from the nose to the tail producing pit marks and occasional small holes.

In summary, the shuttle will have a reduced probability of being struck, most strikes that do occur will occur to the extremities, but the few strokes that do occur will be swept over the columbium panel to produce pit marks and probably some small holes with the remote possibility of a larger hole of about one to two inches (2.54 to 5.08 cm) in diameter. The major saving factor is thus movement of the swept stroke almost continuously by the air stream over the surface of the heat shield.



INTERNAL SURFACE
(Photo 121491B)



EXTERNAL SURFACE
(Photo 121490B)

Figure 9-14. Cb-752/R-512E Heat Shield Following Lightning Strike Tests and Thermal Exposure

10 MICROMETEOROID IMPACT TESTS

10.1 Introduction

It is required that the Space Shuttle orbiter be designed to tolerate prolonged exposure to the micrometeoroid environment without undue hazard to the crew and without excessive maintenance of the exposed surfaces. Preliminary meteoroid hazard analysis (Reference 46) has indicated that thermal protection systems based on the use of thin heat-resistant materials will sustain erosion, cratering, and a few punctures of the outer surface, which could be incompatible with this requirement. The testing of coated columbium alloy specimens under this program was intended to provide data for representative heat shield gages. The tests and data would then be related to post-impact thermal exposure, repair techniques, and verification of penetration mechanics.

The three types of damage of interest required the use of different test facilities and the cooperation of four companies (GDCA, NRSD, MDAC-E, and HiTemCo) plus two NASA centers (LaRC and MSC).

10.2 Test Specimens

Two types of specimens were provided for testing: 1) 2 by 2 by 0.020 inch (5.08 by 5.08 by 0.051 cm) coupons, and 2) standard 0.015 inch (0.038 cm) thick tensile specimens from Phase I of the program (see Figure 4-1, Reference 3). All specimens were coated with a 0.003 inch (0.008 cm) nominal thickness of R-512E. Two types of the square coupons were impacted - eight as-coated/unexposed and eight that were subjected to 50 simulated flight cycles to 2400°F (1589°K). Of the six tensile specimens two had sustained 50 Phase I flight simulation cycles and four were as-coated. These four specimens were exposed to 50 flight simulation cycles after bombardment. Properties of the materials used for theoretical damage correlation are presented in Table 10-1.

10.3 Impact Testing

10.3.1 Erosion tests. - Erosion testing was performed in a Vandergraph facility at LaRC. Six tensile specimens were supplied as part of the Phase I flight simulation test program. To conduct this test series it was necessary to establish the total number of microparticle impacts the vehicle would receive during the design life. The region of the orbiter considered was the lower surface with an area of 4607 in² (29,724 cm²). Using a design life of 700 days, the meteoroid environment of Reference 47, and a test particle mass of 2.62×10^{-10} grams, it was computed that the vehicle would

Table 10-1. Columbium Alloy Room Temperature Properties

	C-129Y/R-512E(a)		Cb-752/R-512E(a)	
	Unexposed	Exposed	Unexposed	Exposed
e, %	15.2	4.8	13.0	2.5
F _{tu} , psi (MN/m ²)	90.5 (624)	86.6 (597)	89.7 (618)	80.3 (554)
F _{ty} , psi (MN/m ²)	71.0 (489)	76.6 (528)	67.4 (465)	62.8 (433)
E, psi × 10 ⁶ (GN/m ²)	16.0 (110)	18.4 (127)	16.3 (112)	20.0 (138)
Hardness, Base Metal KHN (BHN)	—	200 (157) ^(b)	—	176 (139) ^(b)
Hardness, Coating KHN (BHN)	(c)	1128 (824) ^(b)	(c)	1088 (798) ^(b)
ρ, lb/in ³ (g/cm ³)	0.343 (9.49)	0.343 (9.49)	0.326 (9.02)	0.326 (9.02)

(a) Nominal coating thickness was 0.003 in. (0.008 cm) applied to 0.020 in. (0.051 cm) base metal.

(b) Hardness values are averages of 6 points each on subsize panel Specimens YSC-3 and BSC-5 after 100 cycles.

(c) Material too hard for effective reading.

receive 0.14 impacts per square centimeter by micrometeoroids with a mass equal to or larger than the largest test particle. To account for the upward range from the test particle mass, the number of test impacts was increased to 700 per square centimeter to account for 1) the very reduced material removal by the smaller test particles in each cloud and 2) the increased material removal by micrometeoroids larger than the largest test particle.

Of the six specimens subjected to hypervelocity impact, four had been previously exposed to 50 flight simulation cycles and two had no previous exposure. After bombardment all specimens were visually examined. Using magnifications up to 250X no difference could be detected between the material surface in the impact zone and that of the surrounding region. This indicated that the microparticles had caused negligible damage to the material system. Two of the specimens were metallographically examined but no effect of the bombardment was revealed.

The remaining four specimens were subjected to 50 flight simulation cycles. No unusual surface conditions were observed following this exposure. These specimens were subsequently tensile tested, and the results are shown in Table 10-2.

Table 10-3 shows a comparison of the average room temperature tensile properties for bombarded/thermally cycled specimens, 100 cycled flight simulation specimens, and unexposed specimens.

Table 10-2. Tensile Test Results for Bombarded Specimens After 50 Thermal Cycles

Material System	Specimen No.	F_{tu} , * ksi (MN/m ²)	F_{ty} , * ksi (MN/m ²)	e, % in 2 in.	E, * psi $\times 10^6$ (GN/m ²)
C-129Y/VH-109	YVD-19	81.9 (564.7)	67.6 (466.1)	8.5	16.9 (116.5)
C-129Y/VH-109	YVD-13	77.2 (532.3)	64.4 (444.0)	-	14.6 (100.7)
Cb-752/R-512E	BSD-11	67.8 (467.5)	52.9 (364.7)	12.0	14.1 (97.2)
Cb-752/VH-109	BVD-20	76.8 (529.5)	62.4 (430.2)	9.0	16.0 (110.3)

* Values based on original uncoated cross sections.

Table 10-3. Average Tensile Properties for Diffusion Bonded Specimens

Condition	Material System	F_{tu} † ksi (MN/m ²)	F_{ty} † ksi (MN/m ²)	E† psi $\times 10^6$ (GN/m ²)
As-coated/unexposed	C-129Y/VH-109	83.4 (575.0)	67.0 (462.0)	15.6 (107.6)
Bombarded/50 F.S.C. *		79.6 (548.8)	66.0 (455.1)	15.7 (108.3)
100 F.S.C.		69.2 (477.1)	58.8 (405.4)	14.7 (101.4)
As-coated/unexposed	Cb-752/VH-109	77.0 (530.9)	60.4 (416.5)	15.4 (106.2)
Bombarded/50 F.S.C.		76.8 (529.5)	62.4 (430.2)	16.0 (110.3)
100 F.S.C.		**	—	—
As-coated/unexposed	C-129Y/R-512E	73.4 (506.1)	56.9 (392.3)	14.4 (99.3)
Bombarded/50 F.S.C.		67.8 (467.5)	52.9 (364.7)	14.1 (97.2)
100 F.S.C.		61.6 (424.7)	56.9 (392.3)	15.8 (108.9)

* F.S.C. — Flight Simulation Cycles

** No Cb-752/VH-109 specimens sustained 100 cycles.

† Values based on uncoated cross sections.

10.3.2 Cratering test. — Eight specimens were provided for the cratering tests — six C-129Y/R-512E and two Cb-752/R-512E. Prior to bombardment, four of these specimens were subjected to 50 slow reduced pressure cycles to 2400° F (1589° K) at Sylvania. These specimens were examined before and after thermal exposure and mapped by electron emission radiography. The specimens appeared to be in generally good condition after the initial 50 thermal cycles and exhibited no visible base metal oxidation. These specimens together with the thermally exposed specimens used in the perforation tests are shown in Figure 10-1.

The cratering tests were conducted in the electrostatic launching facility at North American Rockwell Space Division. The test projectiles were 0.002 inch (0.005 cm) diameter glass spheres having a density of 2.3g/cm³ and a mass of 1.57 × 10⁻⁷ gram. The particle velocities ranged from 5 to 15 km/sec. The particles were energetic enough to cause visible craters in the surface of the specimens but not powerful enough to cause perforation. Each crater was inspected with an optical microscope and measurements of the diameter and depth were recorded. These data are presented in Tables 10-4 through 10-6. The specimens as shown in Figure 10-2 after bombardment.

The cratering data of tables 10-4 through 10-6 were correlated with the following equation from Reference 48:

$$P_{\infty} = \frac{8.15 \times 10^{-4} m_p^{0.367} \rho_p^{0.133} V_p^{2/3}}{H_t^{1/4} \rho_t^{1/6}}, \text{ cm} \quad (1)$$

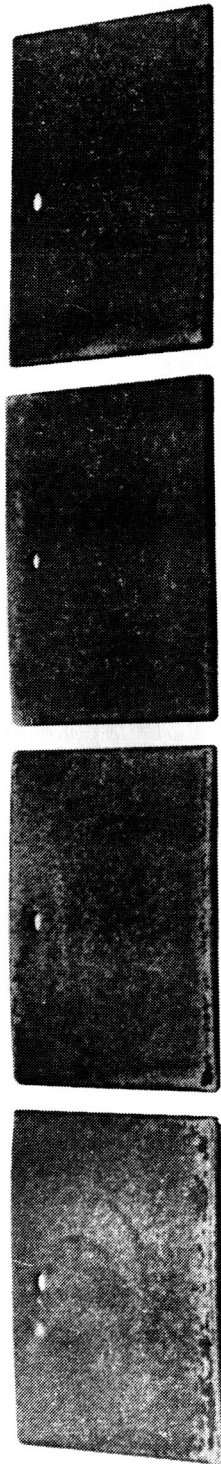
where

ρ = density, grams/cm ³	H = Brinell hardness, kg/mm ²
m = mass, grams	p = particle
V = velocity, cm/sec	t = target

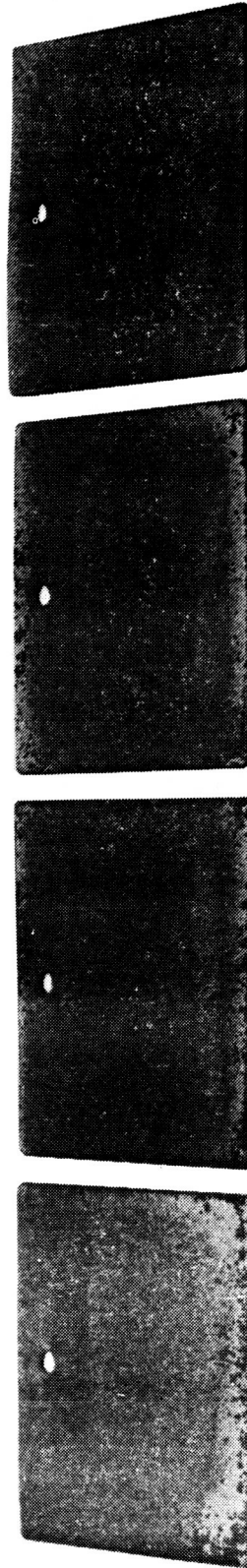
For this correlation, the hardness and density of the base metal were used, and predicted crater depths ranged from correct to 13% low, relative to the nominal test values. To obtain better accuracy it is recommended that penetrations up to the thickness of the coating be determined by Equation 2 using the tabulated K_1 values. Penetrations through the coating and into the base metal should be computed using Equation 1 and base metal properties.

$$P_{\infty} = K_1 m_p^{0.367} \rho_p^{0.133} V_p, \text{ cm} \quad (2)$$

Material	Condition	K_1	Material	Condition	K_1
Cb-752	Unexposed	1.44×10^{-6}	C-129Y	Unexposed	1.44×10^{-6}
	Exposed	1.61×10^{-6}		Exposed	1.61×10^{-6}



C-129-Y/R-512E



Cb-752/R-512E



Figure 10-1. Columbium Alloy Coupons After 50 Thermal Cycles Prior to Bombardment

Table 10-4. Cratering Data for Unexposed C-129Y/R-512E

Firing	Target No.	Target Location	Velocity		Crater Depth		Crater Diameter	
			ft/sec	km/sec	in.	cm	in.	cm
1	1	1	38,000	11.5	0.0024	0.0061	0.0139	0.0353
			33,400	10.1	0.0014	0.0036	0.0066	0.0168
2	1	2	46,200	14.0	0.0025	0.0065	0.0093	0.0236
			31,300	9.5	0.0023	0.0058	0.0093	0.0236
			30,800	9.4	0.0022	0.0056	0.0100	0.0254
			30,400	9.2	0.0013	0.0033	0.0068	0.0173
			43,500	13.7	0.0025	0.0064	0.0093	0.0236
3	1	3	35,400	10.7	0.0023	0.0058	0.0122	0.0310
4	1	4	34,400	10.4	0.0021	0.0053	0.0104	0.0264
1	2	1	35,400	10.7	0.0024	0.0061	0.0116	0.0295
			34,800	10.5	0.0023	0.0058	0.0104	0.0264
			33,700	10.2	0.0020	0.0051	0.0106	0.0269
2	2	2	33,000	10.0	0.0021	0.0053	0.0083	0.0211
3	2	3	49,800	15.1	0.0030	0.0076	0.0126	0.0320
			49,500	15.0	0.0031	0.0079	0.0121	0.0307
			45,300	13.7	0.0025	0.0064	0.0098	0.0249
			43,000	13.0	0.0024	0.0061	0.0092	0.0234
			36,300	11.0	0.0021	0.0053	0.0094	0.0239
4	2	4	35,000	10.6	0.0022	0.0056	0.0116	0.0295
			32,400	9.8	0.0021	0.0053	0.0098	0.0249
1	3	1	33,000	10.0	0.0020	0.0051	0.0077	0.0196
2	3	2	44,300	13.4	0.0023	0.0058	0.0111	0.0282
			34,300	10.4	0.0020	0.0051	0.0100	0.0254
			33,000	10.0	0.0019	0.0048	0.0096	0.0244
			32,200	9.75	0.0018	0.0046	0.0094	0.0239
			31,200	9.5	0.0017	0.0043	0.0088	0.0224
3	3	3	38,000	11.5	0.0023	0.0058	0.0100	0.0254
			36,300	11.0	0.0022	0.0056	0.0111	0.0282
			35,000	10.6	0.0021	0.0053	0.0092	0.0234
4	3	4	39,400	11.9	0.0022	0.0056	0.0121	0.0307
			31,400	9.5	0.0020	0.0051	0.0089	0.0226
			28,000	8.5	0.0017	0.0043	0.0086	0.0218
			25,900	7.75	0.0014	0.0036	0.0057	0.0145
1	4	1	35,500	10.7	0.0022	0.0056	0.0116	0.0295
			27,200	8.25	0.0015	0.0038	0.0085	0.0216
2	4	2	49,300	15.0	0.0033	0.0084	0.0172	0.0437
			48,300	14.6	0.0025	0.0064	0.0144	0.0366
			48,300	14.6	0.0025	0.0064	0.0141	0.0358
			48,300	14.6	0.0026	0.0066	0.0126	0.0320
			39,600	12.0	0.0024	0.0061	0.0113	0.0287
3	4	3	33,000	10.0	0.0019	0.0048	0.0083	0.0211
			25,900	7.85	0.0017	0.0043	0.0085	0.0216
			25,000	7.6	0.0016	0.0041	0.0086	0.0218
			21,400	6.5	0.0013	0.0033	0.0076	0.0193
4	4	4	33,200	10.1	0.0022	0.0056	0.0105	0.0267
			33,000	10.0	0.0019	0.0048	0.0094	0.0239
			28,700	8.7	0.0017	0.0043	0.0098	0.0249
			26,400	8.0	0.0015	0.0038	0.0086	0.0218
			20,400	6.2	0.0013	0.0033	0.0086	0.0218
			18,600	5.65	0.0012	0.0030	0.0095	0.0241

Note: Projectile — 0.0020 in. (0.0051 cm) diameter glass sphere; density = 2.3 g/cm³; mass = 1.57 × 10⁻⁷ g

Table 10-5. Cratering Data for Exposed C-129Y/R-512E

Firing	Target No.	Target Location	Velocity		Crater Depth		Crater Diameter	
			ft/sec	km/sec	in.	cm	in.	cm
1	7	1	36,000	11.5	0.0028	0.0071	0.0123	0.0312
2	7	2	43,000	13.0	0.0030	0.0076	0.0131	0.0333
			42,300	12.8	0.0029	0.0074	0.0137	0.0348
			35,600	10.8	0.0024	0.0061	0.0120	0.0305
3	7	3	43,300	13.1	0.0031	0.0079	0.0150	0.0381
			38,300	11.6	0.0028	0.0071	0.0131	0.0333
			33,400	10.1	0.0020	0.0051	0.0100	0.0254
4	7	4	37,400	11.3	0.0026	0.0066	0.0134	0.0340
			35,300	10.7	0.0025	0.0064	0.0125	0.0318
1	8	1	44,300	13.4	0.0030	0.0076	0.0135	0.0343
			41,500	12.6	0.0028	0.0071	0.0102	0.0259
			29,700	9.0	0.0019	0.0048	0.0093	0.0236
2	8	2	36,300	11.0	0.0025	0.0064	0.0127	0.0322
			33,400	10.1	0.0022	0.0056	0.0100	0.0254
			28,700	8.7	0.0019	0.0048	0.0094	0.0239
3	8	3	38,600	11.7	0.0027	0.0069	0.0116	0.0295
			28,400	8.6	0.0018	0.0046	0.0087	0.0221
4	8	4	34,700	10.5	0.0024	0.0061	0.0102	0.0259
			31,000	9.4	0.0022	0.0056	0.0100	0.0254

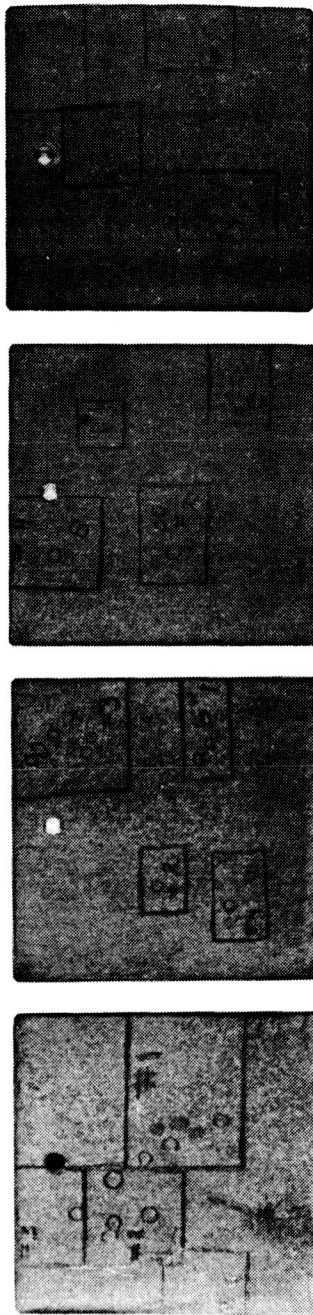
Note: Projectile — 0.0020 in. (0.0051 cm) diameter glass sphere; density = 2.3 g/cm³; mass = 1.57×10^{-7} g

Table 10-6. Cratering Data for Exposed Cb-752/R-512E

Firing	Target No.	Target Location	Velocity		Crater Depth		Crater Diameter	
			ft/sec	km/sec	in.	cm	in.	cm
1	7	1	43,000	13.0	0.0030	0.0076	0.0157	0.0399
			33,000	10.0	0.0022	0.0056	0.0115	0.0292
2	7	2	42,300	12.8	0.0029	0.0074	0.0145	0.0368
			41,500	12.6	0.0028	0.0071	0.0119	0.0302
			36,000	10.9	0.0023	0.0058	0.0155	0.0394
			35,400	10.7	0.0023	0.0058	0.0122	0.0310
			31,700	9.6	0.0020	0.0051	0.0097	0.0246
3	7	3	38,000	11.5	0.0024	0.0061	0.0115	0.0292
4	7	4	33,000	10.0	0.0022	0.0056	0.0125	0.0318
			30,000	9.1	0.0020	0.0051	0.0126	0.0320
			28,400	8.6	0.0018	0.0046	0.0100	0.0254
			27,800	8.4	0.0018	0.0046	0.0099	0.0251
1	8	1	39,000	11.8	0.0027	0.0069	0.0080	0.0203
			35,400	10.7	0.0024	0.0061	0.0101	0.0257
			33,700	10.2	0.0021	0.0053	0.0100	0.0254
			32,400	9.8	0.0020	0.0051	0.0137	0.0348
			25,100	7.6	0.0015	0.0038	0.0104	0.0264
2	8	2	33,000	10.0	0.0020	0.0051	0.0128	0.0325
3	8	3	33,400	10.1	0.0020	0.0051	0.0107	0.0272
4	8	4	33,000	10.0	0.0020	0.0051	0.0094	0.0239

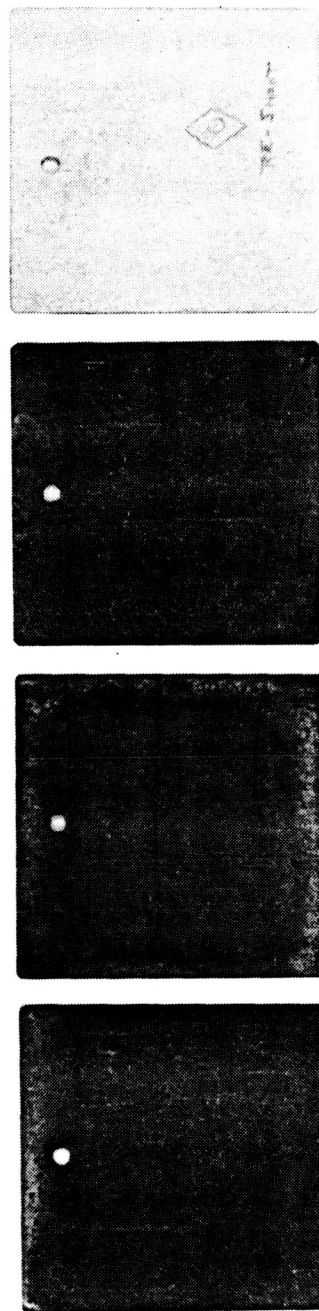
Note: Projectile — 0.0020 in. (0.0051 cm) diameter glass sphere; density = 2.3 g/cm³; mass = 1.57×10^{-7} g

NO THERMAL EXPOSURE/BOMBARDED



C-129Y/R-512E

THERMAL EXPOSURE/BOMBARDED



C-129Y/R-512E

Cb-752/R-512E



Figure 10-2. Columbium Alloy Coupons After Bombardment

Correlations of the penetration data with the penetration equation for the various material systems and conditions are shown in Figures 10-3 through 10-5.

Following bombardment and electron emission radiographic mapping all specimens were subjected to 50 slow reduced pressure cycles to 2400° F (1589° K). These specimens are shown in Figure 10-6. The top row of specimens have been exposed to 50 thermal cycles while those in the bottom row have been exposed to 100 thermal cycles. These specimens exhibited no unusual surface oxidation or erosion.

10.3.3 Perforation tests. — Eight specimens were also provided for the perforation tests — six Cb-752/R-512E and two C-129Y/R-512E. Two Cb-752/R-512E and two C-129Y/R-512E were thermally exposed (Figure 10-1) while four Cb-752/R-512E were unexposed.

The perforation tests were performed in the light gas gun facility at NASA/MSC. The test projectiles were 0.032 inch (0.081 cm) aluminum spheres having a density of 2.78 g/cm³ and a mass of 7.74×10^{-4} gram. The particle velocities ranged from approximately 3 to 7 km/sec. A 2024-T3 aluminum plate was located 1 inch (2.54 cm) behind the coupon to obtain data on the debris cloud particles. The perforation test data is presented in Table 10-7. A group of the specimens following bombardment and prior to subsequent thermal exposure is shown in Figure 10-7.

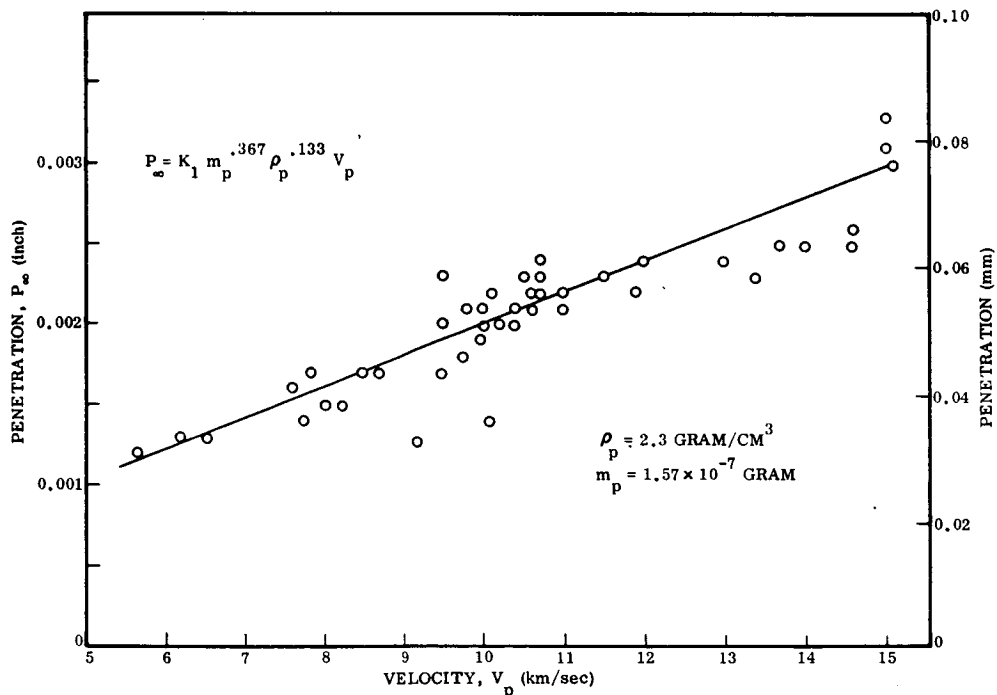


Figure 10-3. Hypervelocity Particle Penetration Into Unexposed C-129Y/R-512E Coupons

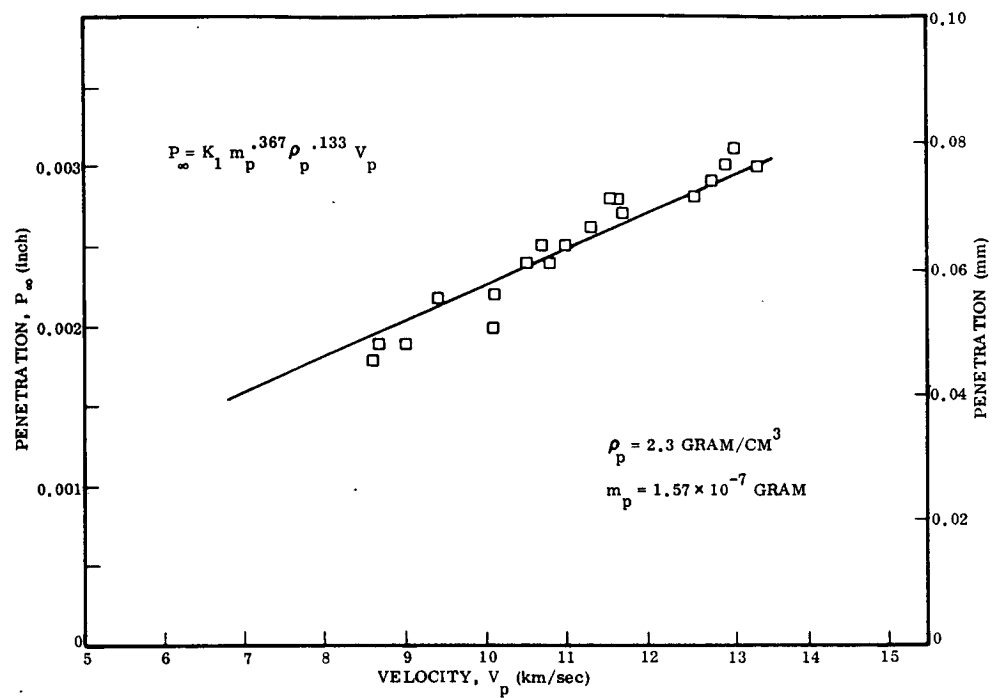


Figure 10-4. Hypervelocity Particle Penetration Into C-129Y/R-512E Coupons After Exposure to 50 Cycles to 2400° F (1589° K)

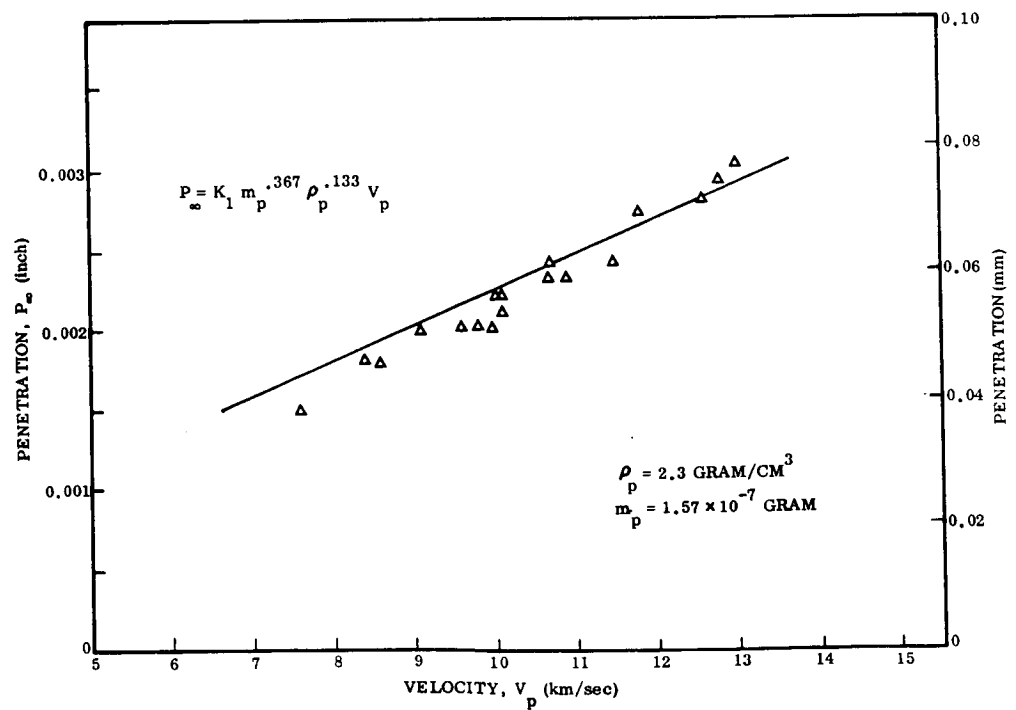


Figure 10-5. Hypervelocity Particle Penetration Into Cb-752/R-512E Coupons After Exposure to 50 Cycles to 2400° F (1589° K)

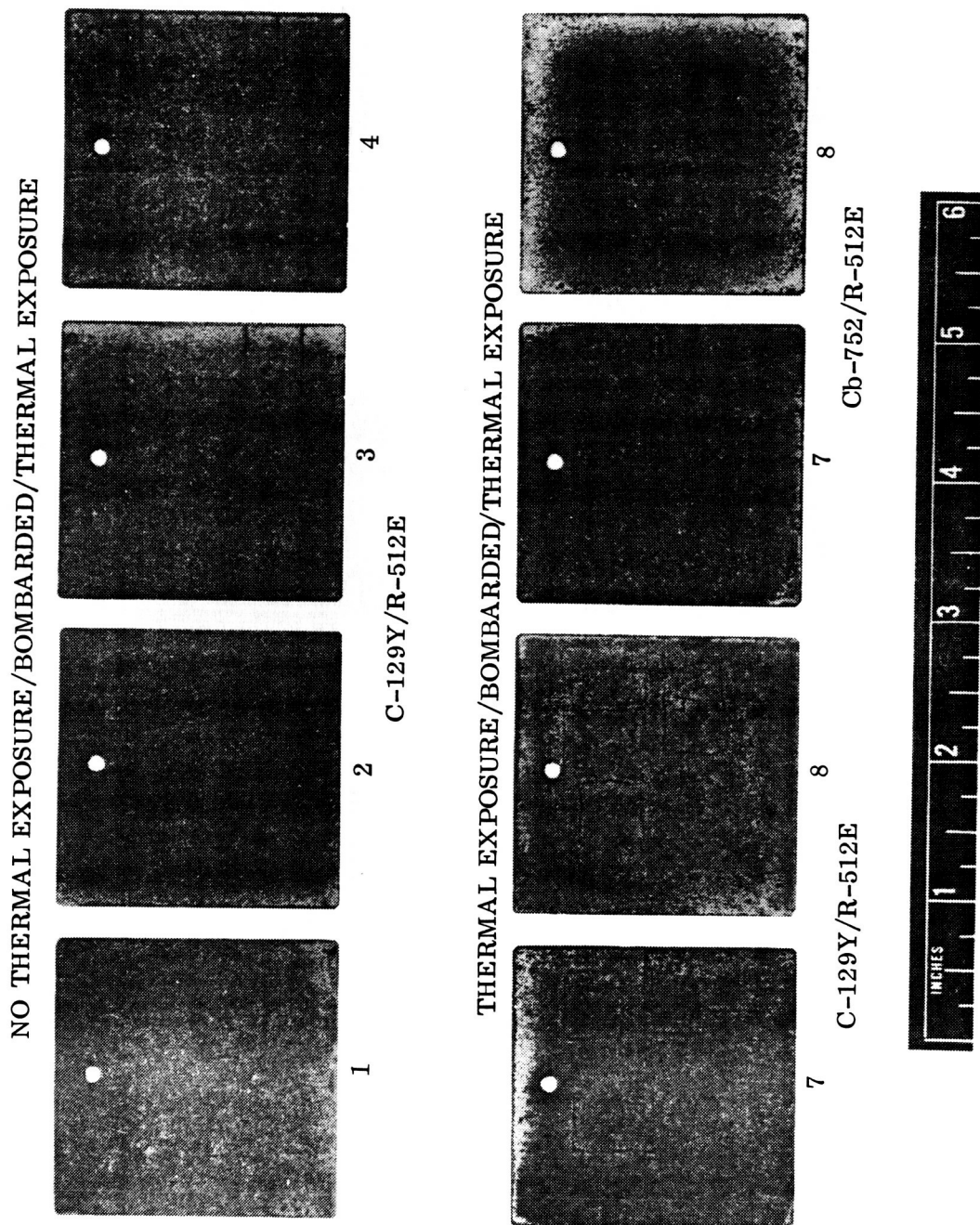
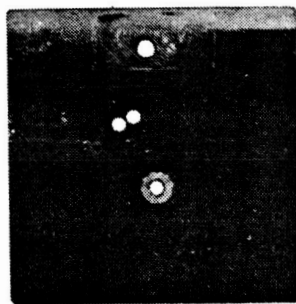


Figure 10-6. Columbium Alloy Coupons After Bombardment and Thermal Exposure

Table 10-7. Perforation Test Results

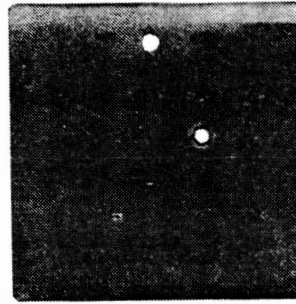
Material System	Specimen No.	Condition	Projectile Velocity		Hole Size				Maximum Rear Sheet Penetration			
					Actual		Predicted		Actual		Predicted	
			ft/sec	km/sec	in.	cm	in.	cm	in.	cm	in.	cm
Cb-752/R-512E	1	Unexposed	17,926	5.425	0.085	0.217	0.087	0.220	-	-	-	-
	2		19,529	5.910	0.093	0.235	0.091	0.230	-	-	-	-
	3		17,503	5.297	0.079	0.201	0.085	0.217	0.0121	0.0308	0.0118	0.0300
	4		22,007	6.660	0.085	0.216	0.097	0.246	0.0154	0.0390	0.0134	0.0340
	5	Exposed	21,214	6.420	0.079	0.201	0.079	0.200	0.0144	0.0365	0.0130	0.0330
	6		10,115	3.061	0.053	0.134	0.053	0.134	-	-	-	-
C-129Y/R-512E	5	Exposed	15,494	4.689	0.067	0.171	0.067	0.171	0.0094	0.0240	0.0106	0.0270
	6		9,791	2.963	0.053	0.134	0.052	0.133	-	-	-	-

NO THERMAL EXPOSURE/BOMBARDED



1

Cb-752/R-512E



2

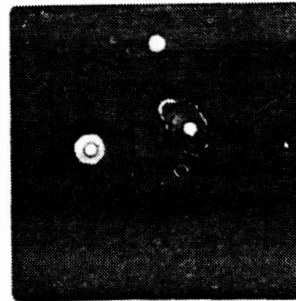
Cb-752/R-512E



3

Cb-752/R-512E

THERMAL EXPOSURE/BOMBARDED



5

Cb-752/R-512E



Figure 10-7. Columbium Alloy Coupons After Bombardment and Thermal Exposure

Hole sizes obtained in the specimens were correlated with the following equation from Reference 49:

$$D_h = K d \left(\frac{t}{d} \right)^{0.14} (e)^{0.22} \left(\frac{V}{10^5} \right) \exp \left[0.63 \left(\frac{t}{d} \right)^{0.43} \right], \text{ cm } (d \leq 2t) \quad (3)$$

where

$K = 0.658$

$d =$ projectile diameter, cm

$e =$ elongation, %

$V =$ velocity, cm/sec

$t =$ sheet thickness, cm

$h =$ hole

It was found that the predicted values obtained were within +12 to -20% of the actual values. To obtain better accuracy the following coefficient values are recommended, and the correlation of Table 10-7 is based on these values.

<u>Material</u>	<u>Condition</u>	<u>K</u>	<u>Material</u>	<u>Condition</u>	<u>K</u>
Cb-752/R-512E	Unexposed	0.658	C-129Y/R-512E	Unexposed	0.658
	Exposed	0.790		Exposed	0.586

The 2024-T3 aluminum rear sheets located behind the columbium alloy specimens were pitted over a 1.5 inch (3.81 cm) diameter area by impact of projectile and target fragments. Using an optical microscope the deepest pits were found to be located near the center of the damage circle and measured penetration values are presented in Table 10-7. Theoretical penetrations, as determined by the computer program of Reference 49, were correlated with these values, and it was found that predicted penetrations were low by an average of 4%. As this is probably less than the experimental scatter, it was concluded that these test results support the usage of the subject program for damage predictions on the two types of coupons tested.

Following bombardment at NASA/MSFC the four specimens shown in Figure 10-7 were forwarded to MDAC-E for examination and repair recommendations as delineated in Reference 45. Subsequently these specimens were forwarded to HiTemCo (Sylvania High Temperatures Composites Laboratory) for repair and thermal cycling. In Figure 10-7 it can be noted that in addition to the through-penetrations, the specimens also exhibit secondary damage sites. Specimens 1, 2, and 3 are shown in the as-bombarded condition with no thermal exposure. Specimen 5 sustained 50 thermal cycles prior to being bombarded.

If a vehicle was bombarded by micrometeoroids and sustained detectable damage while on station, the options are: 1) to replace the damaged heat shield (by ferrying a replacement part to the vehicle or by an on-board store), 2) repair the damaged areas

(this is feasible, especially by using the HiTemCo method), or 3) reenter the atmosphere without repair. The first two options present little or no problems for reentry. However, the question is posed whether or not a vehicle could safely reenter with damaged columbium alloy heat shields. (The problem of subsequent insulation damage or the thermal effects of hot air ingestion will not be broached at this time.)

Using the penetration test data presented in Table 10-7, where the projectile velocities ranged from approximately 3 to 7 km/sec, the resulting through-holes varied from 0.053 inch (0.135 cm) to 0.079 inch (0.201 cm) diameter for the specimens previously exposed to 50 thermal cycles. For the unexposed specimens, the hole size ranged from 0.079 inch (0.201 cm) to 0.093 inch (0.236 cm) diameter, with the hole size being velocity dependent in all cases. Referring to the recent defect tolerance work at Battelle Columbus Laboratories (Reference 50), it was shown that under dynamic flow conditions an initial through-defect in Cb-752/R-512E and C-129Y/R-512E could increase in diameter from 0.040 inch (0.102 cm) to 0.100-0.140 inch (0.254-0.356 cm) after one cycle. [This increase of 2.5 to 3.5 times is related to temperatures ranging from 2470 to 2510° F (1629 to 1650° K).] Using this relationship the size of the aforementioned holes could increase as shown below.

Specimen Condition	Original Hole Diameter*		Projected Hole Diameter After 1 Reentry Cycle	
	in.	(cm)	in.	(cm)
50 thermal cycles	0.053	(0.135)	0.133-0.186	(0.338-0.472)
	0.079	(0.201)	0.198-0.277	(0.503-0.704)
No thermal cycles	0.079	(0.201)	0.198-0.277	(0.503-0.704)
	0.093	(0.236)	0.233-0.326	(0.592-0.828)

* Hole sizes were velocity dependent - see Table 10-7.

Since field repairs of columbium alloys have been made on defects up to 0.50 inch (1.27 cm) diameter (Reference 45), it is not unreasonable to assume that holes of the projected size could be repaired successfully and the heat shield reused.

Three of the four coupons shown in Figure 10-7 were repaired. Specimen 3 (the unrepaired specimen) was subsequently exposed to slow cyclic temperature to 2400° F (1589° K) at reduced pressures in the as-defected condition. The base metal oxide was visible at the first inspection after six cycles. Testing was continued to 13 cycles, after which time the 0.079 inch (0.201 cm) diameter holes had grown to 0.26 inch (0.66 cm) diameter. No evidence of base metal oxidation was noted at secondary damage sites.

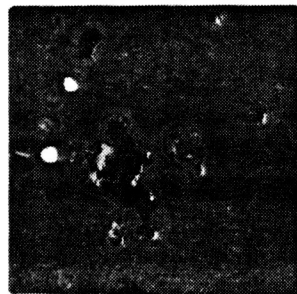
Specimen 2 was repaired at HiTemCo using the high intensity spot heater. The 0.093 inch (0.235 cm) diameter hole was drilled out to 0.17 inch (0.43 cm) and a pure columbium plug was inserted. The specimen was repaired in five places on one side and four places on the other side to cover primary and secondary damage sites. After 20 cycles, base metal oxide was observed at an edge at the location of an accidental chip. Testing was continued to 50 cycles with no evidence of base metal oxide at any of the repair sites.

Specimens 1 and 5 were repaired at MDAC-E using the glass repair method designated MRC-3. The repair mixture was composed of the following: 60 w/o -325 mesh Pyrex frit, 30 w/o -270 mesh aluminum oxide (flame spray powder grade), 10 w/o -325 boron (amorphous). The composition is mixed in a Nichrobrazor or lacquer vehicle and fired in a vacuum at 2100° F (1422° K) for approximately five minutes or until the composition flows.

Since Specimens 1 and 5 exhibited the most primary and secondary damage, it was thought that the glass repair would give the best coverage and protection. Most of the sites were well covered. After 20 cycles a hole developed through the specimen at one of the repair sites. No evidence of base metal oxide was observed at 50 cycles nor did the hole enlarge significantly. Specimen 5 developed base metal oxide and a through hole after 20 cycles. This appeared to be at the site of an improperly repaired defect. Two additional sites of base metal oxide were observed after 38 cycles in unrepaired areas. All specimens are shown in Figure 10-8 following thermal exposure.

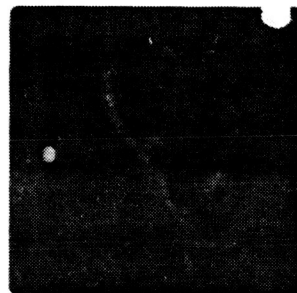
With the specimens employed it is apparent that good field repairs can be made and that heat shield sustaining severe damage (such as through-penetrations) can be made serviceable for many additional cycles. In observing the effects of the two repair processes there was no preference of one over the other. It appears that for relatively large holes the heat lamp and plug method offers the surest repair. However, the process does concentrate heat over a rather small area and could cause localized panel distortion. The amount of distortion probably would be aerodynamically acceptable. The glass repair method appears to be simpler and affords excellent coverage and protection for a wide variety of damage sites.

NO THERMAL EXPOSURE/BOMBARDED/
REPAIRED/THERMAL EXPOSURE



1

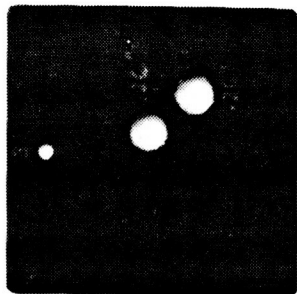
Cb-752/R-512E



2

Cb-752/R-512E

NO THERMAL EXPOSURE/BOMBARDED/
THERMAL EXPOSURE



3

Cb-752/R-512E

THERMAL EXPOSURE/BOMBARDED/
REPAIRED/THERMAL EXPOSURE



5

Cb-752/R-512E



Figure 10-8. Columbium Alloy Coupons After Bombardment, Repair, and Thermal Cycling

11 CONCLUDING REMARKS

The studies presented in this report were directed toward the selection of one columbium alloy substrate and coating system and one thermal protection system configuration after exposure to a typical simulated mission environment. The results of these evaluations would then be employed in the fabrication and testing of a full-scale multi-heat shield array in the third and final phase of the program.

As a result of the Phase I study two material systems were selected: Cb-752/R-512E and C-129Y/R-512E. Each alloy was used to fabricate tee-stiffened and open corrugation subsize heat shields for simulated thermal and applied load missions testing. Conventional aerospace forming and joining practices were used during the fabrication phase. The primary method of joining was electron beam fusion welding. Excellent joint efficiencies and panel flatness were produced. Subsequently, brazing with Ti-33 Cr foil was evaluated as an alternate joining method to diffusion bonding (Phase I). Compared with welding and diffusion bonding similar efficiencies were achieved with the braze and no adverse reaction was observed between the braze and the silicide coated columbium alloy.

Environmental testing of the subsize heat shields confirmed the structural adequacy through 100 cycles of the two configurations. Of the two material systems evaluated Cb-752/R-512E performed better than C-129Y/R-512E. No structural failures of either systems resulted from the testing although severe substrate erosion occurred on the C-129Y/R-512E tee-stiffened panels. Field repair techniques were also evaluated during the subsize heat shield testing. Areas of coating degradation and/or substrate oxidation were clearly identifiable thereby enabling a component to be removed and repaired. Repaired areas that were properly prepared by removing the contaminated region were proven completely successful after continued cycling.

Several conventional NDE methods were used throughout the program to determine the quality of the applied coating. In addition, a new technique of radioactive labeling was used to analyze the coating process. It is believed that the radionuclide tag (^{147}Pm), for the first time, showed the wetability of edges and limitations of the coating that require special consideration. The degree of difficulty encountered when dipping as well as the sensitivity of the unfired (green state) coating to handling and abrasion was shown.

The effects of lightning strikes on coated columbium alloy heat shields had not been defined prior to the initiation of this program. It was anticipated that the non-conductive silicide coating could accentuate problems with electrical bonding and intrastructural arcing. From a series of tests employing simulated heat shields and supports it was concluded that (1) although some local damage was possible the TPS could withstand a typical cloud-to-cloud discharge without perforation, and (2) a maximum current strike, typical of a cloud-to-ground strike, would cause extensive damage. In the latter case, however, the damaged

area would be clearly identifiable before launch, thereby enabling component repair or replacement. Although a strike to the vehicle is considered a small probability, a typical strike would be one swept from the nose to the tail producing pit marks and occasional small holes but would not jeopardize the mission due to structural failure.

Impact tests simulating a micrometeoroid environment were also conducted. These tests consisted of microparticle erosion, small particle cratering, and penetration. Test velocities ranged up to 15 km/sec. The tests were conducted on coated specimens without thermal exposure and on those having 50 thermal cycles. No coating or substrate damage was observed as a result of either the erosion or cratering conditions. The perforated specimens were repaired by field repair techniques and subsequently successfully cycled 50 times through a simulated entry temperature profile.

The two heat shield configurations (tee-stiffened and open corrugation) evaluated as subsize panels were designed into small size, full scale TPS models that included split bi-metal (Cb-752 and TD NiCr) support posts, retainers, close-outs, and insulation. The fabrication processes used in fabricating four models (two of each configuration) included machining, sheet metal forming, electrical discharge machining, welding, brazing, heat treating, and creep flattening. All were employed without difficulty and resulted in high quality components. Electron beam welding was demonstrated to be highly flexible and versatile when it was possible to view and optically track a joint during welding. This permitted the economical weld fabrication of many articles of hardware heretofore considered impractical and too expensive. The extremely high and local input energy levels inherent to high voltage electron beam welding permitted the use of minimum tooling and resulted in few weld distortion problems.

Two types of thermal testing were conducted on each small size configuration. The first test was intended to investigate structural integrity and system leakage effects under convective hot gas flow. The second test involved the simultaneous exposure of temperature, local surface pressure, and pressure differential loading. In addition, all specimens were exposed to acoustic excitation at levels up to 155 dB simulating 100 missions.

Each specimen that was exposed to 20 hot gas flow cycles in a one atmosphere oxidizing environment experienced no substrate oxidation or structural degradation. The open corrugation TPS, however, did suffer a braze disbond between the skin and a transverse beam. This condition was attributed to a combination of substandard braze diffusion and an improperly assembled specimen.

Two specimens were also exposed to 50 cycle radiant heat profiles. These specimens exhibited no structural degradation or coating failure. All systems responded well to the thermal environments and the temperature distributions were within close tolerances of the predicted levels. No disruption or deterioration of the insulation was found after any of the

tests. All systems were able to be disassembled as required between cycles or at the conclusion of the test series. Although the TD NiCr fasteners and Cb-752 plugs were intended to be replaced after each disassembly, these could be and were reused without detrimental effects to the system performance.

In conclusion, both thermal protection systems evaluated performed well and are considered to be viable candidates for the space shuttle. The unit weight of both systems as presently designed is less than the target of 6 lb/ft² (0.253 kg/m²). Of this weight 54% is assigned to the fibrous insulation blankets. It is believed that the weight of the metallic components cannot be reduced by more than 10% with the present criteria. Hence, the major weight saving must be related to reducing the density of the insulation without degrading the thermal efficiency or the physical performance. (From cursory investigations at Convair Aerospace and by other investigators, it is believed that an insulation exists that will fulfill the thermal/mechanical requirements for TPS performance. Further evaluation will be undertaken during Phase III that could reduce the present insulation weight by up to 40%.)

As fabricated within this phase there was approximately a 6% difference in cost between the two systems with the tee-stiffened TPS being less expensive. A significant cost factor for the open corrugation was the development nature of the braze system. The cost of this operation can be reduced by 55 to 65% without difficulty.

The system selected for further application and study as applied to a multi-heat shield array was the tee-stiffened TPS. This selection was based on a slightly lower unit weight and cost and the relative performance during the thermal/acoustic tests.

San Diego operation of Convair Aerospace Division
General Dynamics Corporation
San Diego, California, August 31, 1973

PRECEDING PAGE BLANK NOT FILMED

APPENDIX A

CONVERSION OF U.S. CUSTOMARY UNITS TO SI UNITS

The International System of Units (designated SI) was adopted by the Eleventh General Conference on Weights and Measures in 1960. The units and conversion factors used in this report are taken from or based on NASA SP-7012, "The International System of Units, Physical Constants and Conversion Factors — Revised, 1969".

The following table expresses the definitions of miscellaneous units of measure as exact numerical multiples of coherent SI units, and provides multiplying factors for converting numbers and miscellaneous units to corresponding new numbers of SI units.

The first two digits of each numerical entry represent a power of 10. An asterisk follows each number that expresses an exact definition. For example, the entry "-02 2.54*" expresses the fact that 1 inch = 2.54×10^{-2} meter, exactly, by definition. Most of the definitions are extracted from National Bureau of Standards documents. Numbers not followed by an asterisk are only approximate representations of definitions, or are the results of physical measurements.

ALPHABETICAL LISTING

<u>To convert from</u>	<u>to</u>	<u>multiply by</u>	
atmosphere (atm)	newtons/meter ² (N/m ²)	+05	1.0133*
British thermal unit, mean (Btu)	joule (J)	+03	1.056
Fahrenheit (F)	kelvin (K)	$t_k = (5/9) (t_f + 459.67)$	
foot (ft)	meter (m)	-01	3.048*
inch (in.)	meter (m)	-02	2.54*
mil	meter (m)	-05	2.54*
millimeter of mercury (mm Hg)	newton/meter ² (N/m ²)	+02	1.333
nautical mile, U.S. (n.mi.)	meter (m)	+03	1.852*

APPENDIX A -- Continued

<u>To convert from</u>	<u>to</u>	<u>multiply by</u>	
pound force (lb _f)	newton (N)	+00	4.448*
pound mass (lb _m)	kilogram (kg)	-01	4.536*
torr	newton/meter ² (N/m ²)	+02	1.333

PHYSICAL QUANTITY LISTING

<u>Acceleration</u>			
foot/second ² (ft/sec ²)	meter/second ² (m/sec ²)	-01	3.048*

<u>Area</u>			
foot ² (ft ²)	meter ² (m ²)	-02	9.290*
inch ² (in ²)	meter ² (m ²)	-04	6.452*
inch ² (in ²)	centimeter ² (cm ²)	+00	6.452

<u>Density</u>			
pound mass/foot ³ (pcf, lb _m /ft ³)	kilogram/meter ³ (kg/m ³)	+01	1.602
pound mass/inch ³ (lb _m /in ³)	kilogram/meter ³ (kg/m ³)	+04	2.768
pound mass/inch ³ (lb _m /in ³)	gram/centimeter ³ (g/cm ³)	+01	2.768

<u>Energy</u>			
British thermal unit, mean (Btu)	joule (J)	+03	1.056

<u>Energy/Area Time</u>			
Btu/foot ² second (Btu/ft ² sec)	watt/meter ² (W/m ²)	+04	1.135

<u>Force</u>			
kilogram force (kg _f)	newton (N)	+00	9.807*
pound force (lb _f)	newton (N)	+00	4.448*

APPENDIX A — Continued

<u>To convert from</u>	<u>to</u>	<u>multiply by</u>	
<u>Length</u>			
foot (ft)	meter (m)	-01	3.048*
inch (in.)	meter (m)	-02	2.54*
micron	meter (m)	-06	1.00*
mil	meter (m)	-05	2.54*
mile, U.S. nautical (n.mi.)	meter (m)	+03	1.852*
<u>Mass</u>			
pound mass (lb _m)	kilogram (kg)	-01	4.536*
<u>Pressure</u>			
atmosphere (atm)	newton/meter ² (N/m ²)	+05	1.013*
millimeter of mercury (mm Hg)	newton/meter ² (N/m ²)	+02	1.333
pound/foot ² (psf, lb _f /ft ²)	newton/meter ² (N/m ²)	+01	4.788
pound/inch ² (psi, lb _f /in ²)	newton/meter ² (N/m ²)	+03	6.895
<u>Temperature</u>			
Fahrenheit (F)	Kelvin (K)	$t_K = (5/9) (t_F + 459.67)$	
<u>Volume</u>			
foot ³ (ft ³)	meter ³ (m ³)	-02	2.832*
inch ³ (in ³)	meter ³ (m ³)	-05	1.639*
inch ³ (in ³)	centimeter ³ (cm ³ , cc)	-01	1.639

APPENDIX A — Concluded

PREFIXES

The names of multiples and submultiples of SI units may be formed by application of the prefixes:

Multiple	Prefix
10^{-6}	micro (μ)
10^{-3}	milli (m)
10^{-2}	centi (c)
10^{-1}	deci (d)
10^3	kilo (k)
10^6	mega (M)
10^9	giga (G)

APPENDIX B
NONDESTRUCTIVE EVALUATION
THERMOELECTRIC TESTING

Thermoelectric testing utilizes a hot and cold junction between dissimilar elements (modifiers) in the coating to detect changes in coating composition and, within limits, coating thickness. A lead wire is affixed to the specimen and to one terminal of a micro-volt meter. A second lead wire connected to a heated probe and the other meter terminal completes the electrical circuit. When heat is applied, an electromotive force is developed across the heated junction; its magnitude depends upon the electrochemical potential difference between elements at each junction and upon temperature gradient.

The difference in electromotive force (emf) corresponding to a given temperature gradient is known as the Seebeck coefficient; it varies significantly between elements contained in most silicide coatings. Accordingly, thermoelectric devices have been used to detect changes in the Seebeck coefficient thereby detecting segregation of these elements, and to measure coating thickness.

It may be shown with thermoelectric testing that small temperature gradients and variations in coating chemistry between junctions complicate thermoelectric response. In the most typical case, thermoelectric readings are attributable to a multiplicity of effects, which may include local resistivity, Seebeck coefficient, variation in the diffusion layer, and time and temperature conditions. Also in thin coatings, the thermal conductivity of the coating may be short circuited by the substrate. While oversimplified in Figure B-1, a change in the heat flow rate by a highly conductive substrate reduces the temperature gradient between the junctions. In thick coatings, the relatively poor conductivity of the coating contains the heat within a short distance from the probe thus reducing this heat sinking effect. Accordingly, the thermoelectric response becomes asymptotic as the coating thickness exceeds a maximum limit. For the complex columbium silicide coatings, this limit is between 0.004 and 0.005 inch (0.101 and 0.127mm).

By substituting various materials for one side of the junction, a thermoelectric series may be developed in reference to the constant junction material. The resulting emfs display both amplitude and sign, which are compared to those for a known standard. For the R-512E coating, the voltage input to a high-impedance meter is set to read zero on a bare columbium alloy sample. A signal response ranging from 0 to 3 millivolts is displayed and recorded as a function of thickness and uniformity of the coating.

The average thermoelectric reading for the R-512E coating ranges between 1 and 1-1/2 millivolts for a temperature gradient of about 550° F (561° K). However, it

APPENDIX B — Continued

should be pointed out that this is relative and not an absolute value. For the normal application of thermoelectric testing, a reading of less than 0.5 millivolt would indicate thin coating. Also, since the resolution of the test is determined by the probe diameter, it is conceivable that a small defect, i.e., thinning or segregation, may be overlooked by the thermoelectric test or not detected because of an adjacent good area in contact with the probe (sensor) at the same time.

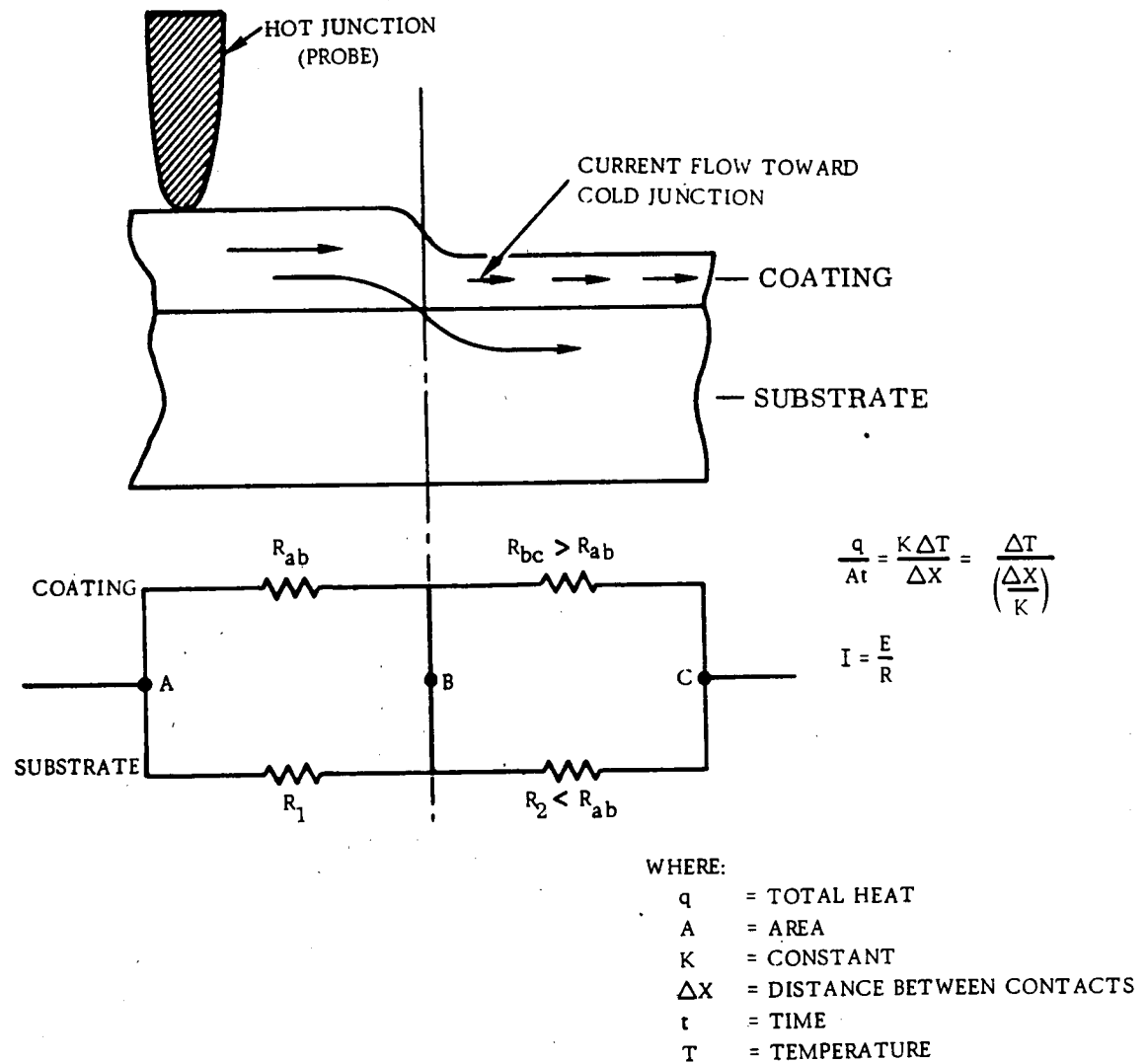


Figure B-1. Sketch Illustrating Heat Sinking Effect of Substrate and Equivalent Electrical Circuit During Thermoelectric Testing of Thin Coating

APPENDIX B — Continued

The sensitivity of the thermoelectric test is determined by the material selected for the common junction and by temperature gradient. It has been determined that stainless steel is an ideal junction material since it is less susceptible to oxidation and wear than most alternate conductors, e.g., copper. The temperature of the probe (hot junction) is generally maintained between 550 and 650°F (561 and 617°K).

For testing large structures, a perimeter or surface area contact, e.g., a flat plate, for the cold junction reduces many of the variables encountered with the thermoelectric test since the temperature gradient is maximum and relatively unaffected by location of the sensor (hot junction). Also, losses are minimal since there are more available paths for current flow between the junctions. Voltage rather than current is generally displayed with a high-impedance meter to minimize the effects of variations in local resistivity and probe contact.

Most silicide coatings are non-uniform. Temperature gradients and variation in coating constituents between junctions may result in a higher emf than would otherwise be generated. While incorporation of both contacts, i.e., hot and cold junction, into a single probe device (Figure B-2) can increase the resolution of the test (for the same scan area), it is difficult to separate effects such as opposing variance at both junctions. Also, if not properly insulated, the temperature gradient, and thus the sensitivity of the test, is reduced as the cold junction is heated either by radiation or conduction through the coating.

Limitations

Thermoelectric testing is not suitable for examining large surfaces. Considering the local manner in which coatings fail, more area is overlooked by this point-by-point method than can be practically inspected with any reasonable plan. Accordingly, thermoelectric testing is used by most coating manufactures to examine edges of specimens, corners, radii, etc., less suitable for alternate inspection. A meaningful examination of corners and edges can be accomplished using this method. A non-conductive oxide developed on the surface of the coating does not permit thermoelectric testing to be performed following thermal exposure of the shield.

Application to Program

Thermoelectric testing was used for the subsize and small size heat shield components to examine edges and assist the interpretation of alternate NDE data from selected regions on the panels. The test apparatus comprised a 40-watt heating element with a stainless steel tip to which a thermocouple and lead wire were attached by resistance welding. The heating element contained a thermostat with rapid feedback

APPENDIX B — Continued

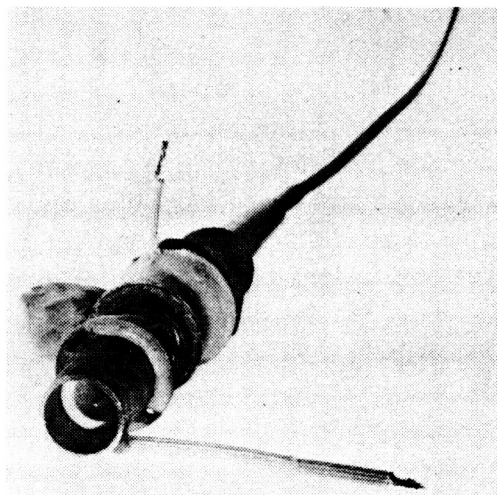


Figure B-2. Single-Probe Thermoelectric Device

control. Thermocouple wires, input to a potentiometer during operation of the device, showed the temperature at the stainless steel tip to be about 617°F (598°K) with regulation within ± 1 per cent. A wire coil served to radiate the heat from the hot junction to ambient temperature for lead input to a high-impedance microvolt meter. A second lead wire from the meter input (ground) was connected to a stainless steel plate (cold junction) on which the heat shields were placed. The thermoelectric response was displayed and simultaneously recorded to provide a permanent record; see Figure B-3.

STIMULATED ELECTRON-EMISSION RADIOGRAPHY

This technique employs the use of secondary radiation emission produced by bombarding the specimen with X- or gamma rays. The radiation is recorded by single-emulsion X-ray film placed in contact with the surface of the coating. The uniformity of the coating - relative thickness and distribution of major constituents - may be observed in the developed radiograph(s).

A method for distinguishing between electron and photon (X-ray) interaction is possible due to the difference in laws governing their absorption. All materials absorb about the same quantity of electrons for the same mass penetrated. X-ray absorption, however, is dependent on the atomic number of the absorber for the same mass penetrated. Accordingly, step tablets of thin aluminum and Mylar were placed in contact with an uncoated columbium alloy to determine the relative transmissibility of radiation emitted under X-ray stimulation (see Figure B-4).

Eastman Kodak single emulsion R X-ray film was placed in contact with the surface of the step tablets (emulsion side toward specimen). A nylon bag was placed around the experiment and evacuated. An exposure was made using a maximum X-ray energy of 0.3 MeV; the source to detector distance used was about 40 inches (100 cm).

APPENDIX B - Continued

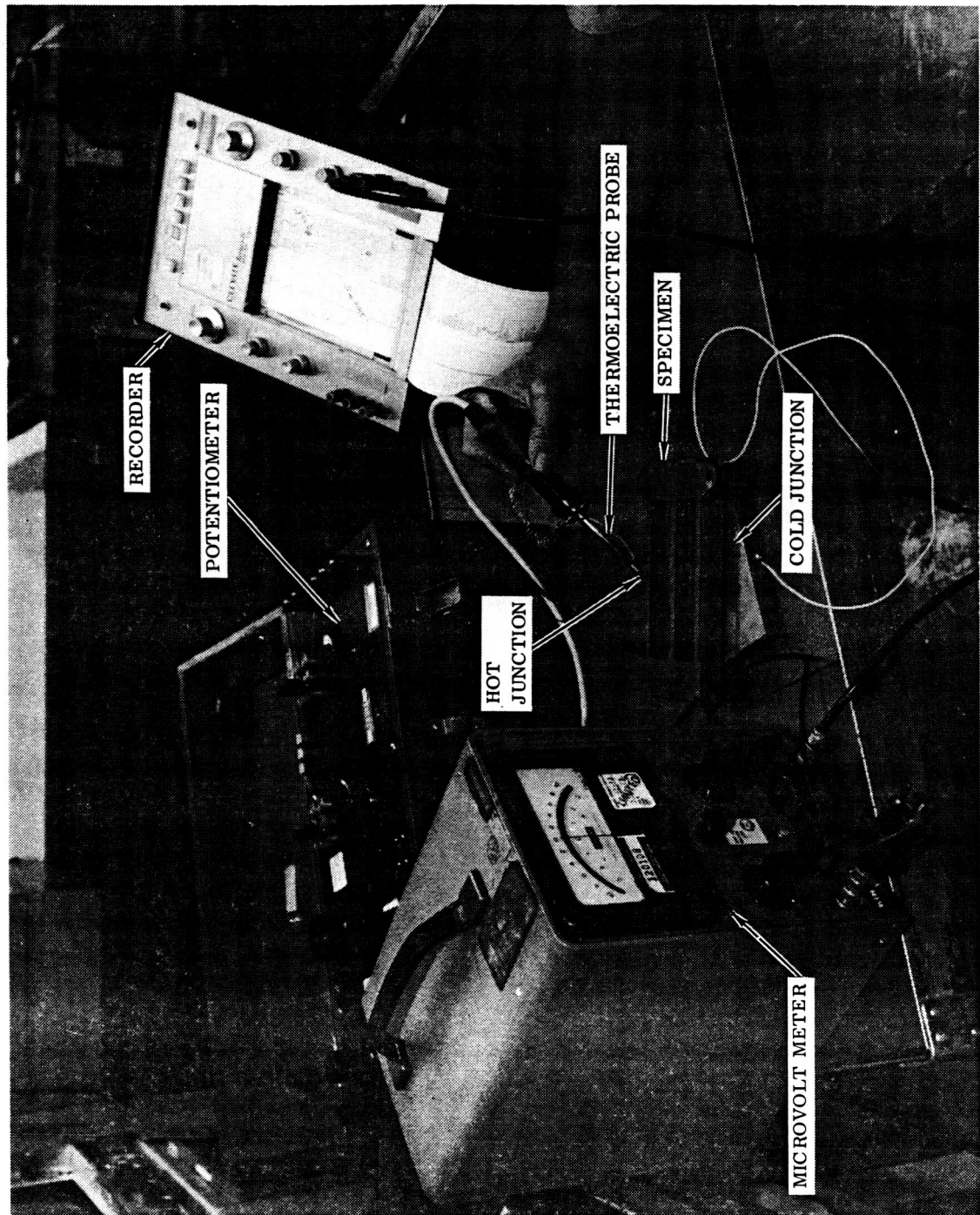


Figure B-3. Thermoelectric Testing Apparatus

APPENDIX B — Continued

During the exposure, a 0.020 inch (0.051 cm) lead filter was placed in the X-ray beam, between the X-ray tube and test specimen, to remove low energy photons (primary X-ray beam) to which the film is highly sensitive. The arrangement is shown in Figure B-5.

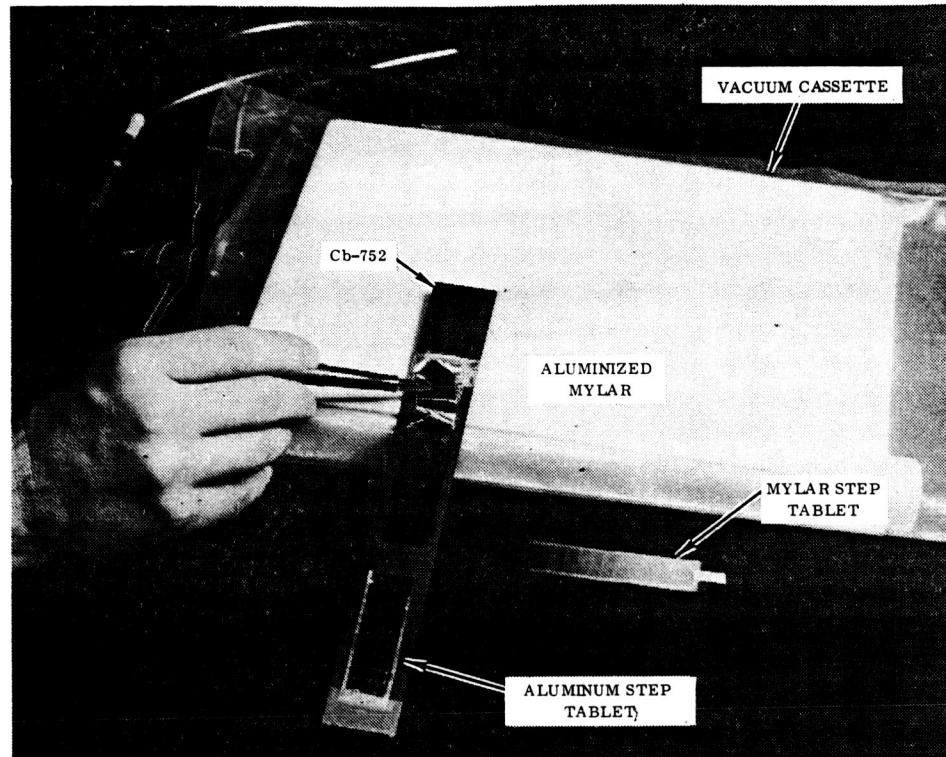


Figure B-4. Step Tablets Used to Determine Nature of Backscatter from Uncoated Cb-752

Following development of the radiographs, the image of the step tablets was traced using a scanning densitometer. Density values $\left(\log_{10} \frac{I_t}{I_0} \right)$, where I_0 = initial and I_t = transmitted light through the radiograph) obtained from parallel scans on opposite sides and equidistant from the center axis of the tables were averaged. Fog plus background readings were subtracted from each density; net density values were recorded for the various steps. Assuming linearity between density and exposure, the transmission of backscattered radiation was determined as a function of weight of the absorber. The relative intensity of secondary radiation (scatter) transmitted by the step tablets was plotted as a function of mass per square centimeter of absorber (range). The plot is shown in Figure B-6.

APPENDIX B — Continued

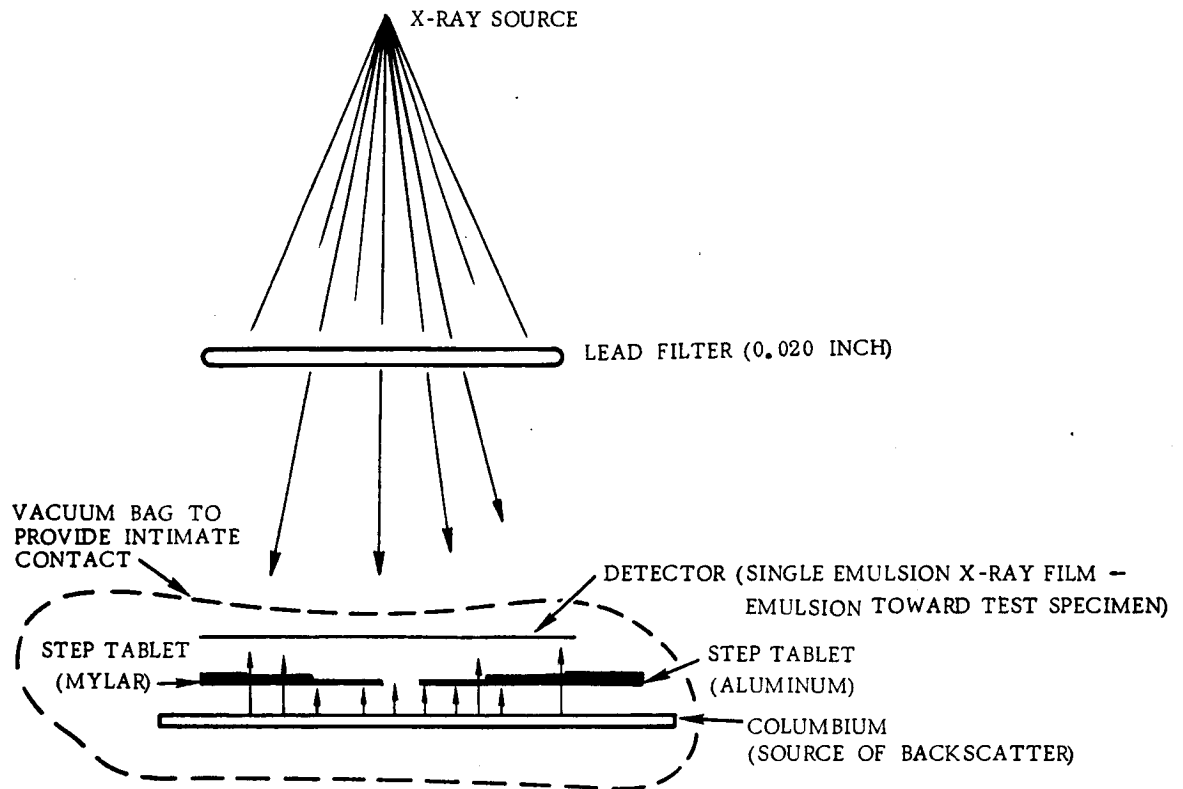


Figure B-5. Test Setup for Analysis of Backscatter

In Figure B-6, an intensity of 100 represents exposure due to both direct radiation (bombarding X-rays) and backscattered radiation with no absorbing material interposed. Within the limits of experimental error, the agreement between the transmission curves for both aluminum and Mylar is quite satisfactory; i.e., the curves have the same shape. It may be concluded, therefore, that the secondary radiation emission is primarily electrons. The horizontal portion of the curve is interpreted as indicating complete electron absorption, although a small amount of radiation is penetrating the thickest portions of the tablets. This radiation is attributed to characteristic K radiation from the columbium and to scattered X-rays, both of which are only slightly absorbed. The wavelength limits of the L series from columbium (4.6\AA to 5.2\AA) are mostly absorbed in aluminum of the thickness used for the experiment. The M series is for practical purposes completely absorbed by the first step in both the aluminum and Mylar.

APPENDIX B — Continued

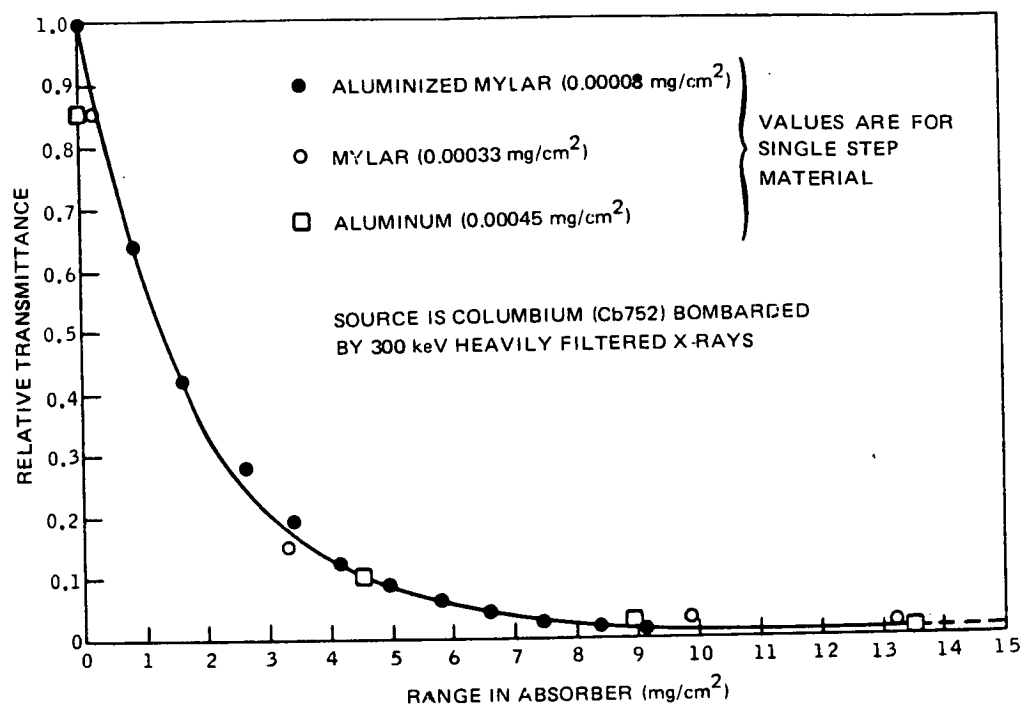


Figure B-6. Results Showing Nature of Back-Scattered Radiation from Surface of Columbium Test Specimen

The shape of the curve in Figure B-6 is not linear because the X-ray beam does not impart a uniform velocity to the electrons. Furthermore, even if the electrons were all from outer shells and due to 0.3 MeV X-rays, there would still be a wide range of velocities among those emitted because of partial absorption at various depths and angles in the columbium. This is why complete electron absorption occurs at about 10 milligrams per centimeter of absorber. While this corresponds to an energy of only about 0.085 MeV, few electrons approach the maximum bombarding X-ray energy. It is probable that the energy of electrons in sufficient abundance to be detected by the radiograph is less than 0.2 MeV. The emulsion used to trap these electrons accounts for about 0.02 MeV.

The electron image is qualitative. Since the range of electrons in the coating is controlled by the bombarding X-ray energy, it is possible to determine the nominal coating thickness from the resultant data. Accordingly, given a single energy-source, the time required to produce the latent image is an indirect measure of coating thickness.

It has been determined experimentally that the image produced by stimulated electron-emission radiography is attributable to photo-electrons ejected from the columbium

APPENDIX B - Continued

substrate as shown in Figure B-7 (Reference 51). However, for coating that contains high atomic number modifiers, such as VH-109, the coating itself may be the primary source of electrons. Also, depending on the thickness of the substrate, specifically the amount by which it absorbs the bombarding X-rays, either forward and/or back-emission techniques can be utilized as illustrated in Figure B-8.

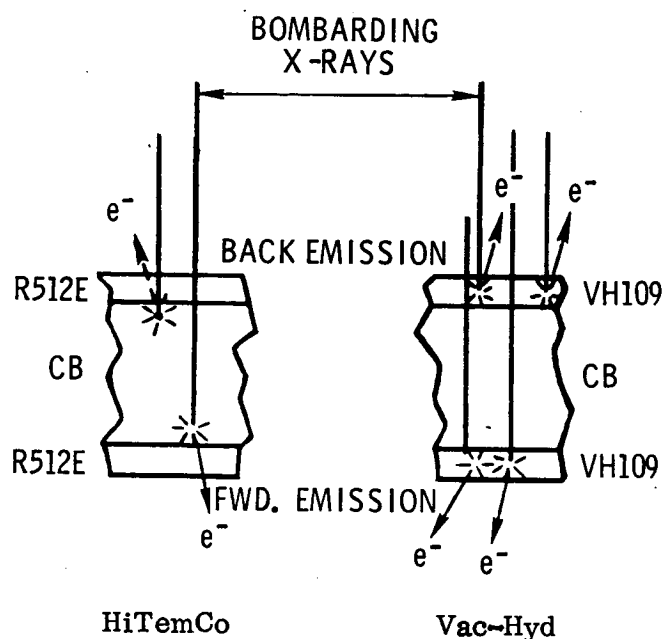


Figure B-7. Mechanics of Electron Emission

Of the various factors that must be considered in producing an optimum radiograph, film selection is perhaps most important. If the emulsion is not thick enough to remove sufficient energy from the electrons to prevent their penetration through the emulsion, the amount of energy transferred to the film grains will be about the same for both thick and thin regions of the coating. While extremely thin emulsions -e.g., less than 10 microns - may increase the ratio of electron signal to X-ray signal recorded by the radiograph, small changes in coating thickness will go undetected.

For inspecting complicated geometries where conformity to the surface is a problem, or where dark room handling is impractical, 1/4 mil aluminized Mylar has been used to protect the emulsion from light. Lead tape is used to complete the envelope thus providing shielding against scattered X-radiation on the back side of the film as seen in Figure B-9. Using this arrangement, film positioning may be accomplished in white light and film specimen contact observed. Various tools, e.g. vacuum bags, air bladders, and holding fixtures, have been developed to assist application of the test.

APPENDIX B - Continued

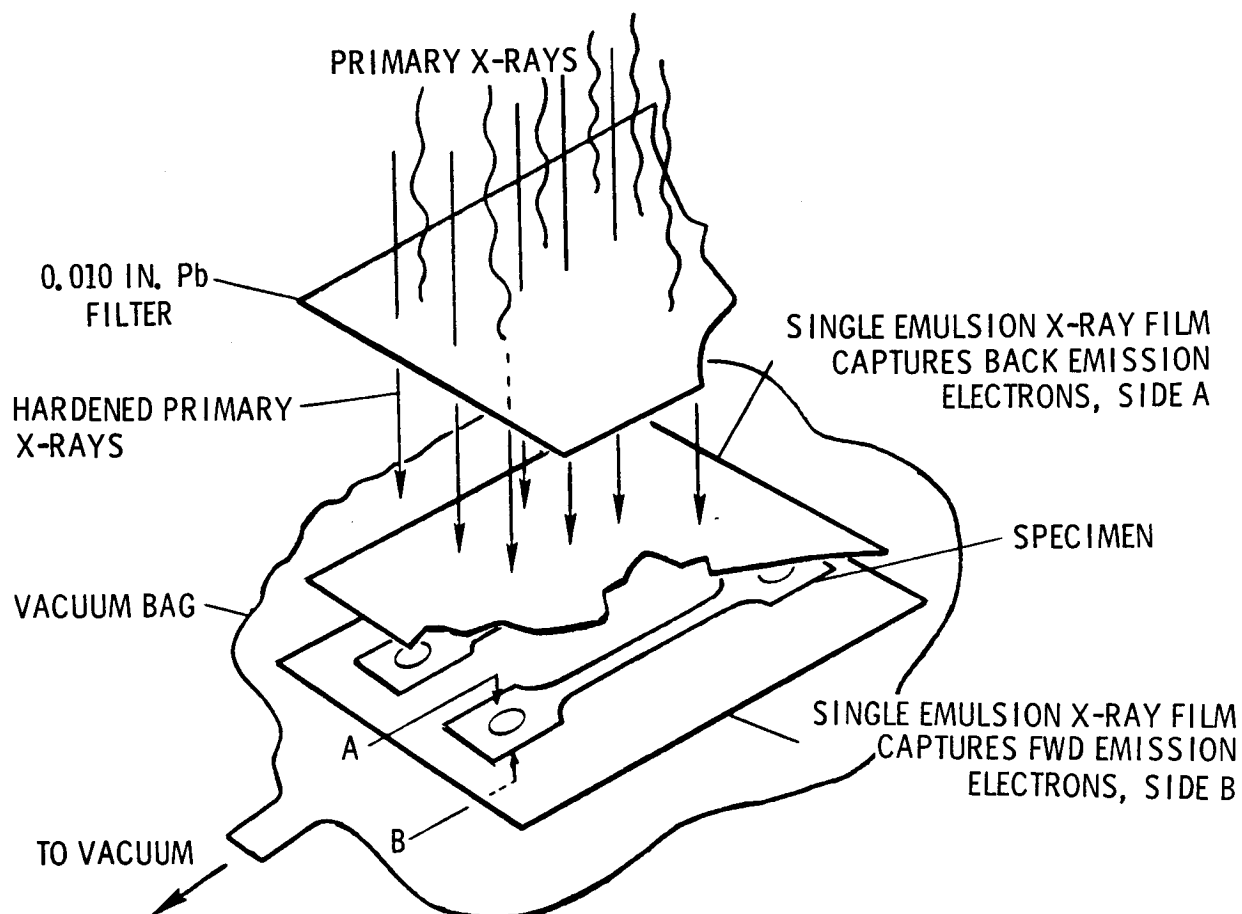


Figure B-8. Setup for Stimulated Electron-Emission Radiography

Figure B-10 shows improvement in the uniformity of early coatings resulting from the awareness provided by electron-emission radiography. Highly developed, the advantages of the method are wide coverage of the evaluated area, no required preparation such as gridding or extensive identification, and a permanent record.

Limitations

Stimulated-electron emission radiography has some limitations that must also be considered:

- (1) The relative uniformity of the X-ray bombardment and resulting distribution (emission) of electrons is dependent on shield geometry; it limits both inspection coverage and accessibility for exposure.

APPENDIX B — Continued

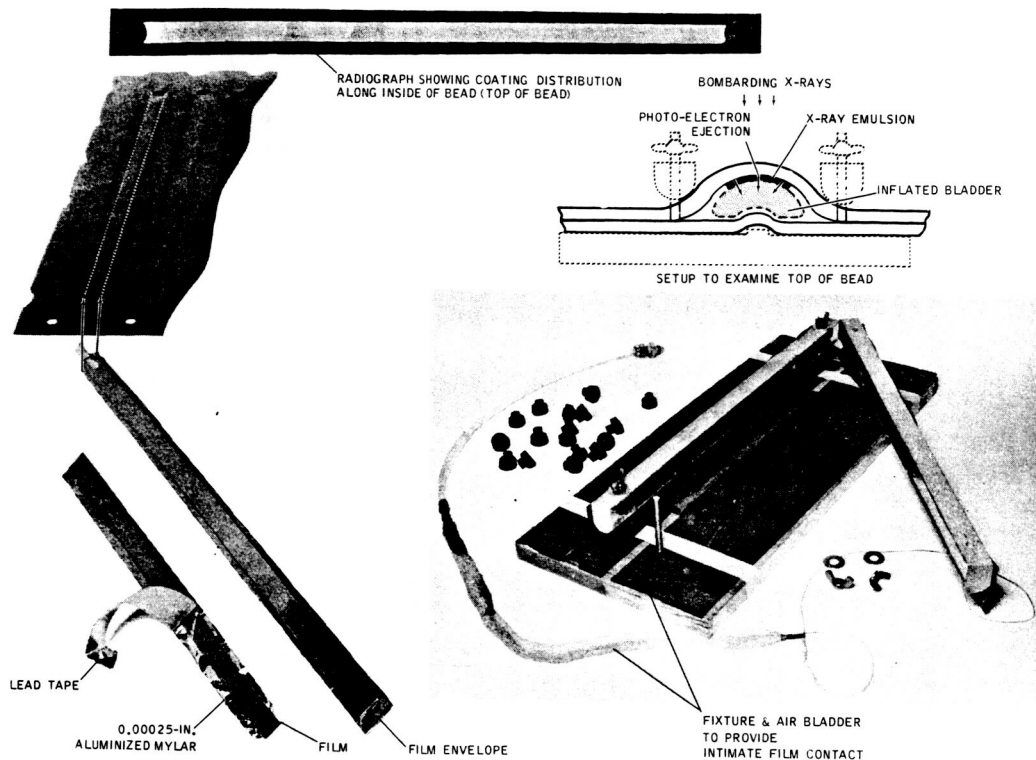
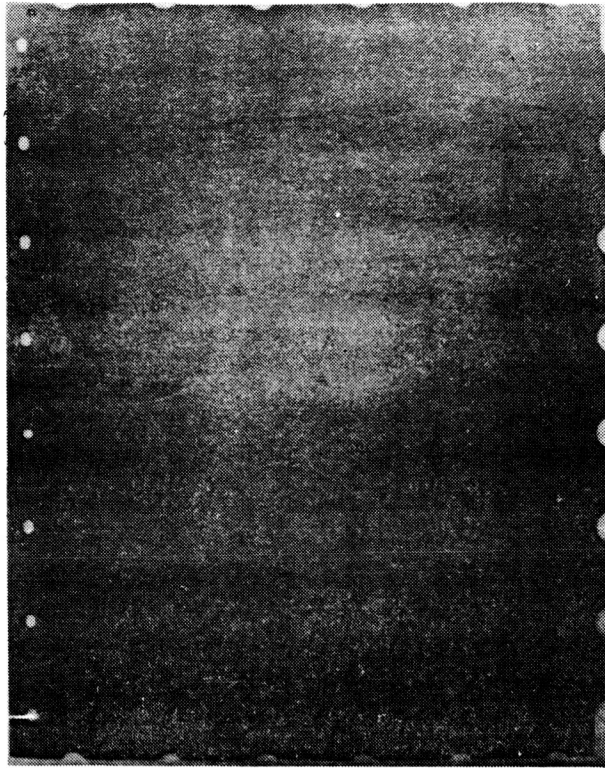


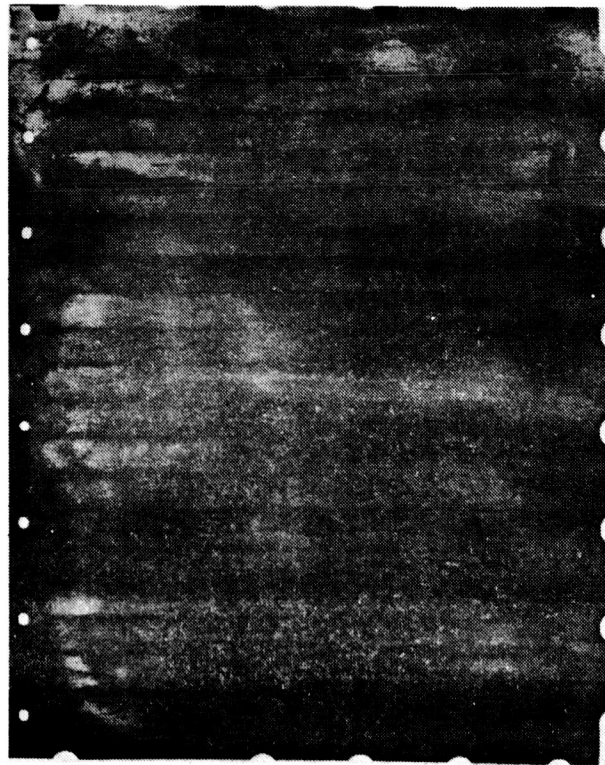
Figure B-9. Technique for Electron-Emission Radiography Inside Coating Surface

- (2) Safety restrictions to attendant personnel limit the amount and/or location of concurrent vehicle maintenance that may be performed during turnaround inspection.
- (3) A relatively large number of exposure setups are required.

APPENDIX B — Continued



RECENTLY COATED HEAT SHIELD



EARLY COATED HEAT SHIELD

Figure B-10. Stimulated Electron-Emission Radiography
Shows Improvement in Coating Uniformity

APPENDIX B — Continued

RADIOACTIVE LABELING

During 1970, the mechanics of coating behavior were studied through independent research and development (Reference 5) and techniques investigated to measure the service life of coated columbium. A major accomplishment of that program was the use of radioactive labeling (Reference 51) to provide inherent radiation emission properties to the coating to measure integrity and service remainder. The findings were used to design a coating system that, together with suitable apparatus, would provide means for inspecting the coating during shuttle turnaround in less time and at less cost than previously possible. The method is safe, requires minimum attendance, requires no down-time or restrictions to personnel affecting scheduled maintenance of the vehicle.

Isotope Selection

Consideration of the special service requirements for a reusable TPS, such as minimum cost, safety, and service life, indicated that ideally the radionuclide for incorporation into the coating should:

- (1) Have a half-life of several years — sufficient for longevity required for practical usage, yet short enough to provide a high specific activity and to minimize possible contamination concern.
- (2) Be a pure β -emitter, with emission of β -particles of medium energy.
- (3) Be a radionuclide of an element that is essentially nonvolatile at temperatures as high as 1500°C, whether in the form of the metal, the metal oxide, the metal nitride, or the metal silicide.
- (4) Be a radionuclide that is commercially available, at a suitable specific activity, in a suitable chemical form, at a reasonable price.
- (5) Be a radionuclide of an element that is chemically compatible with incorporation in the silicide layer during repeated reentry cyclings.

By reason of its refractory nature, favorable half-life (2.62 years), and favorable radiation (emits beta particles only and with ≤ 0.224 MeV), promethium-147 was chosen as the radioactive tag for the initial tests. The oxide properties were primarily of interest since they are stable and easy to prepare. While no data on the melting point or boiling point of Pm_2O_3 exists, all of the rare earths have remarkable similarity of chemical and physical properties. The melting point of lanthanum oxide, also a rare earth, is 2315°C; its boiling point is 4200°C.

APPENDIX B — Continued

Two columbium (Cb-752) coupons, 5 cm by 5 cm, were coated with a Vac-Hyd VH-101 coating containing ^{147}Pm . The carrier used was lanthanum oxide; it was selected because of its orbital structure (similar to promethium) and dispersion characteristics. Prior to coating, the tagged slurry was shaken in a paint mixer for about two hours. The samples were weighed in still air. The coating was then applied by spraying. Following spraying, the coatings were outgassed, then fired at approximately 1500°C in vacuum to form the silicide.

The total amount of carrier added to the slurry was 9.8 mg of lanthanum oxide, which contained 10 microcuries of ^{147}Pm . The spray was gaged at 20% utilization. Therefore, each side of each coupon contained 0.5 microcuries (1.1×10^6 disintegrations per minute) of radioactivity.

After coating, the specimens were reweighed, and, by difference, the weights of the coatings were calculated. The radioactivity of each surface, counted with a Geiger-Muller counter, was measured at 0.5-cm intervals along the surface of the coating using a collimated detector (3.2-mm aperture); the results were compared with a recount under exactly the same conditions following abrasion of the coating. For a decrease in coating thickness of 0.5 mil, the average counting rate at the surface of the coating was shown to decrease by 21%. The correspondence of relative levels of radioactivity was not changed by the abrasion process.

Each surface was autoradiographed by contact with Kodak Type-T film. The resulting pictures indicated some degree of segregation and unevenness of the tag. The radiographs were then compared with the results of electron-emission radiography of the same specimens. It was noted that indications apparent in the electron-emission radiographs were identically mirrored in the autoradiographs. The results of microprobe analysis to attribute these indications are shown in Figure B-11. As evidenced by both the X-ray scanning image and transverse scan through the defective area, the indications are attributable to segregations of a major coating element.

The results of autoradiography following induced compression spall (Figure B-12) showed the technique to indicate losses to the coating that are likely to occur in service. In related tests, with only a fraction of the initial radioactivity loading level remaining following removal of all visible evidence of the coating (by abrasion), the coating remainder was evident by autoradiography adjacent to induced spall.

Significant diffusion of the rare-earth oxides within the refractory coating at temperatures up to 2700°F (1755°K) was not expected. On theoretical grounds, the comparatively large atomic radii of the rare earths may be cited; e.g., the covalent

APPENDIX B - Continued

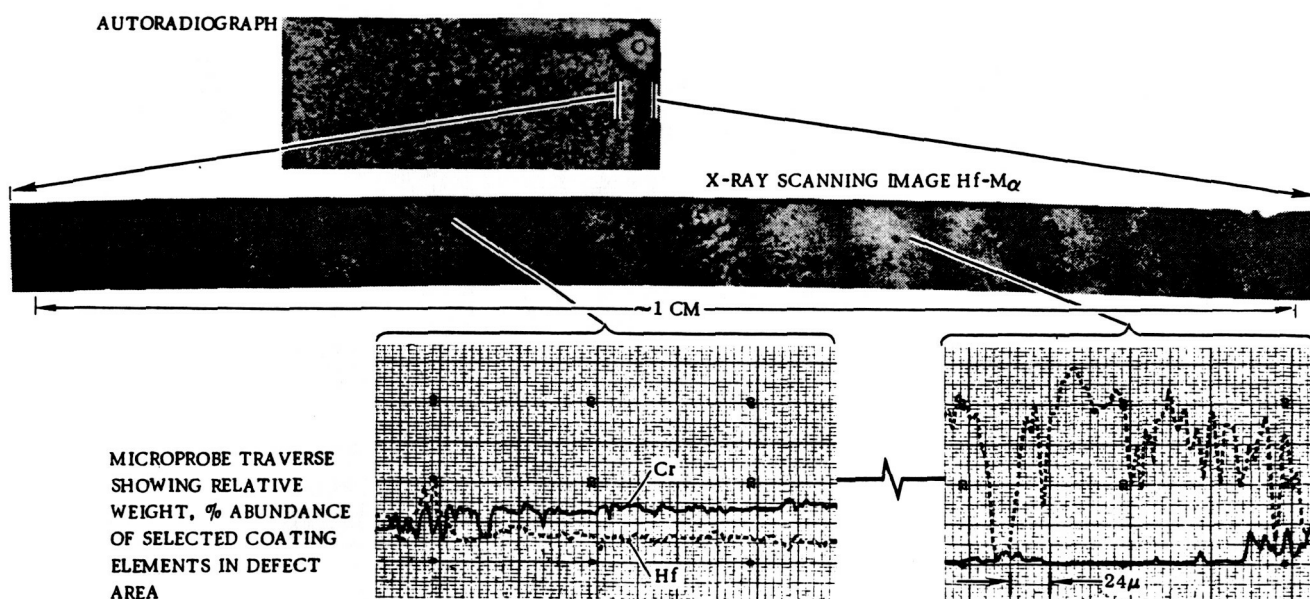


Figure B-11. Microprobe Analysis to Attribute Coating Variation
radii of the various coating elements expressed in angstrom units (10^{-8}cm) are oxygen 0.73, silicon 1.11, chromium 1.17, iron 1.165, hafnium 1.44, niobium 1.43, promethium 1.65 and lanthanum 1.69. Furthermore, the rare-earth oxides have 87.5% of their kinetic energy in rotational and vibrational modes while only 12.5% is in the translational mode at the same temperature. Consequently, for a given energy input, the rare-earth oxides experience relatively less displacement than silicon dioxide. Metal modifiers in the coating, having relatively high translational energy, are even more active.

The results of high-temperature exposure to verify this theory may be seen in Figure B-13. A comparison between autoradiographs before and after continuous exposure shows no evidence of redistribution of radioactivity.

Perhaps the most significant result of early experiments with the radioactive tag was the correlation between lack of coating protection shown by autoradiography and resulting oxidation attack during thermal test. It should be noted that the lack of protection was not attributable to the absence of coating, but to absence of constituents (modifiers) in the coating necessary for oxidation resistance. The condition was not visible on the surface of the coating even with knowledge of its location.

Figure B-14 identifies areas of the autoradiograph which indicate lack of coating at discrete locations along the edge of the test coupon. Corresponding oxidation attack during thermal exposure is evident in the bottom photograph.

APPENDIX B – Continued

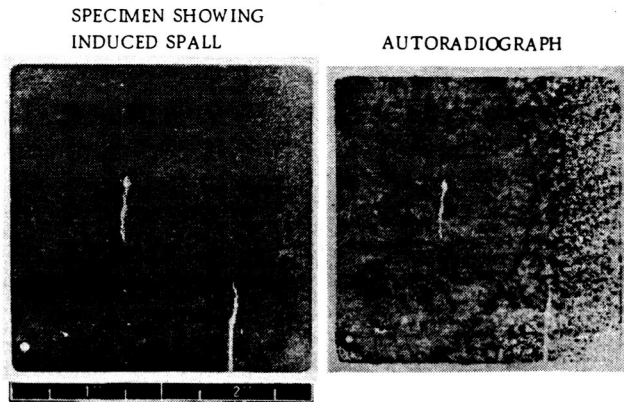


Figure B-12. Coating Spall and Resulting Indication in Autoradiograph

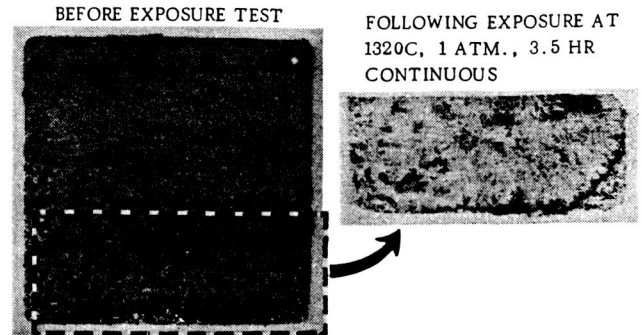


Figure B-13. Autoradiographs Before and After Exposure Showing No Redistribution of Radioactivity

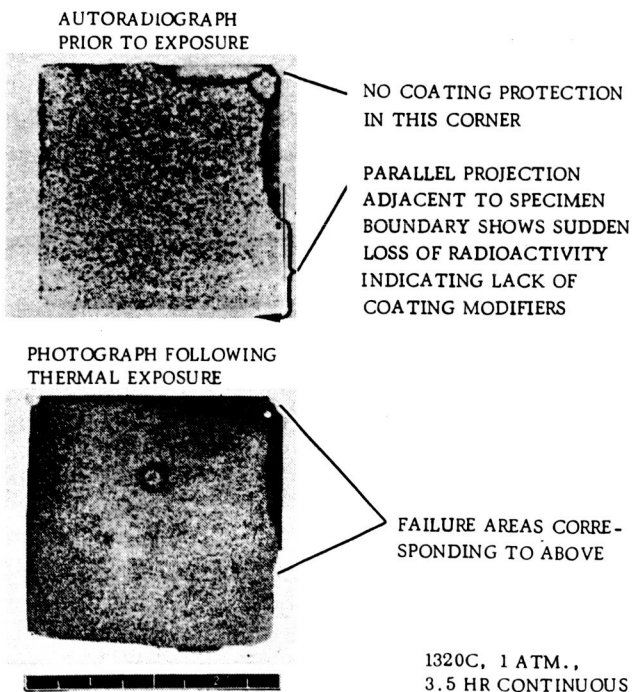


Figure B-14. Autoradiograph Showing Lack of Coating Versus Resulting Oxidation Attack During Thermal Test

Early experiments with the radioactive tag (^{147}Pm) demonstrated the feasibility of the technique to provide inherent radiation emission properties to the coating to detect variations in coating thickness and uniformity. Within the short inspection time requirements for the Space Shuttle, the technique was shown to provide two categories of nondestructive measurement: 1) autoradiography, which provides a very detailed and high resolution picture of the coating, and 2) direct counting, which before and after abrasion tests demonstrate to correlate with coating thickness, and which can provide a measure of coating uniformity. Since adjacent films can be exposed simultaneously, complete autoradiography interrogation of a large coated area, e. g., the leading edge of a wing, could be completed in a matter of hours without attendant personnel; scheduled maintenance of the vehicle could be conducted concurrently. An artist's concept of a counting device to measure the thickness of the coating is shown in Figure B-15.

APPENDIX B - Continued

Safety Aspects

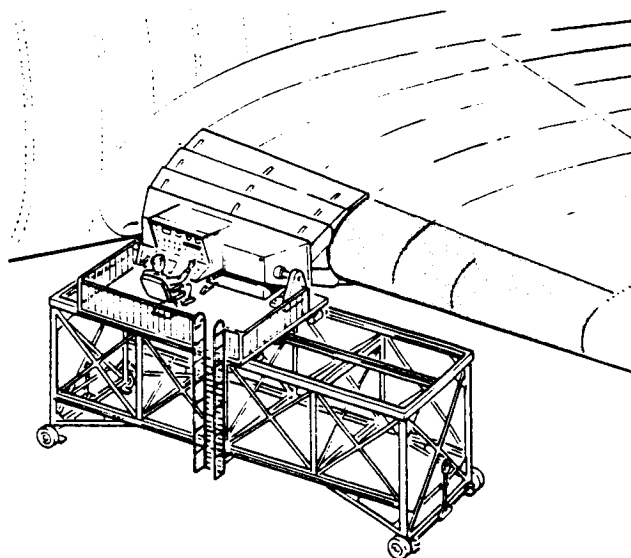


Figure 15. Inspection of Leading Edges

The health physics aspects of the radiation from ^{147}Pm locked in the refractory coating considered the radiation dose delivered by the beta particles to the skin. The maximum range of the beta particles is about 55 mg/cm^2 . Since the density of the air is 1.29 mg/cm^3 , no radiation exposure may be obtained beyond 42.7 cm (about 17 inches) from the coating. If desired, gloves having an area density of at least 55 mg/cm^2 may be worn to completely shield the radiation when contacting the surface of the coating.

The radioactivity loading level required for practical implementation of this method is 0.02 microcuries of ^{147}Pm per cm^2 of coating. The amount of radioactive material to be incorporated into the coating is less than 0.1 ppm based on a nominal coating thickness of 22.5 mg/cm^2 . A breakdown of the mr/hr calculated for a 22.5 mg/cm^2 coating containing $0.02 \mu\text{c } ^{147}\text{Pm/cm}^2$ and measured with an ion chamber (having a 7 mg/cm^2 window) at 1 cm from the surface of the coating is:

- Factors: (A). $(0.02 \mu\text{c}) (3.7 \times 10^4 \text{ dps}/\mu\text{c}) (7 \times 10^5 \text{ eV/d}) = 5.2 \times 10^7 \text{ eV/sec-cm}^2$ emitted.
- (B). 1:1 correspondence between coating and detector window areas.
- (C). Geometry = 50% (max); transmission from infinite thickness = 12%; transmission through 1.29 mg/cm^2 air plus 7 mg/cm^2 window = 30.6%.
- (D). Energy retention of β 's reaching sensitive volume of detector is 8% of original 70 keV .
- (E). Absorption in 1 cm air path (specified distance to surface of shield): $1 - e^{-0.144} = 0.13$.

Calculation: $(5.2 \times 10^7 \text{ eV/sec}) (0.5 \text{ geom}) (0.12 \text{ trans}_1) (0.306 \text{ trans}_2) (8 \times 10^{-2} \text{ energy remaining}) = 7.6 \times 10^4 \text{ eV/sec-cm}^2 = \text{energy reaching sensitive volume of ion chamber; thus}$

APPENDIX B - Continued

$$\left[\frac{(7.6 \times 10^4) (4.8 \times 10^{-10} \text{ esu/ion})}{32.5 \text{ eV/ion}} \right] (3.6 \times 10^3 \text{ sec/hr}) (0.13)$$

$$= 5.25 \times 10^{-4} \text{ r/hr} = 0.53 \text{ mr/hr.}$$

Given: $1 \text{ r} = 83 \text{ ergs}$; $(0.83) (0.53) = 0.44 \text{ mrads/hr.}$

Where: $c = \text{curies: Unit strength of radioactivity; } 1c = 3.7 \times 10^{10} \text{ atomic disintegrations per second}$

$\text{dps} = \text{disintegrations per second}$

$r = \text{roentgen: ionization potential for X and } \gamma \text{ rays equivalent to } 83 \text{ ergs per gram (dry air)}$

$\text{rad} = \text{radiation absorbed dose equivalent to } 100 \text{ ergs per gram (any medium)}$

The U. S. Atomic Energy Commission, Division of Materials Licensing, has developed "GUIDELINES FOR DECONTAMINATION OF FACILITIES AND EQUIPMENT PRIOR TO RELEASE FOR UNRESTRICTED USE OR TERMINATION OF LICENSES FOR BYPRODUCT, SOURCE, OR SPECIAL NUCLEAR MATERIAL (April 22, 1970)." The total radiation level, 0.44 mrad/hr beta radiation only, calculated for the surface of the shield is approximately equal to the 0.4 mrad/hr level established by these guidelines for unrestricted release of previously contaminated facilities for public use.

The high temperature stability of the rare-earth radioactive tag provides an important advantage to the safety of the technique. Nonvolatility and significant diffusion assure that the tag will not be removed any faster, proportionally, than the refractory coating. Thus, the chance of ingesting this material is no greater than the chance of ingesting the coating itself. Less stable tags could not meet this important safety criterion.

While the relatively low level of the beta radiation required for the method is approximately equal to that established by the U. S. Atomic Energy Commission for unrestricted release of previously contaminated facilities for public use, a heat shield incorporating this amount of radioactivity would, in addition, be an external component of an extraordinarily large vehicle, easily accounted for and easily controlled. However, should a component from such a vehicle be lost

APPENDIX B — Continued

in a populated area, the radioactivity level, already insignificant, would not persist. The 2.62-year half-life of the promethium would lower the radiation level making it virtually impossible for a significant exposure to be accumulated should an unprotected extremity, e.g., a bare hand or foot, be placed directly on the shield surface for an indefinite period.

Present Application

Although the potential of radioactive labeling as an important tool for the analysis of coated columbium was demonstrated prior to this study, use of the technique in conjunction with the program raised several problems: 1) the method while reduced to practice, was not state-of-the-art; preliminary experiments would be necessary to demonstrate compatibility between the radioactive tag and coating system selected for use during the program; 2) the cost of radioactive labeling was beyond the program budget; finally, 3) vendor facilities for application of the coating lacked the license necessary to handle promethium-147 in the quantities required.

While coatings known to be defective were purposely not selected for flight simulation during Phase I, it became clear that conventional NDE beyond initial inspection checkout was not meaningful for predicting coating life. Accordingly, radioactive labeling was proposed to better understand the mechanism of coating failure. Authorization was obtained from the state of New York to conduct studies with the tag using HiTemCo facilities under the direct supervision of licensed Convair Aerospace personnel.

Earlier experiments had shown the radioactive tag to report the wetting characteristics of the coating (green state) as well as the formation of ternary eutectics during siliciding. It was concluded that use of the tag on selected small size panels would assist the analysis of the coating process while providing invaluable information on the coatability of candidate shield configurations.

Use of radioactive labeling was approved for Phase II in order to better understand the mechanics of the coating process, particle size distribution and wetting characteristics fundamental to coatability and performance.

APPENDIX B - Concluded

On the basis of coupon tests showing compatibility between the radionuclide (^{147}Pm) and R-512E coating, five tee-stiffened panels (including one spare) were coated with a modified R-512E containing the dispersed radionuclide. Funded independently by Convair Aerospace, the information provided new insight as to possible drawbacks of selected coating systems. The effect of edges, small radii and general configuration of the shield on distribution and uniformity of the coating was observed, possibly for the first time. The results of these evaluations are reported in Section 5.8.

APPENDIX C

ACOUSTIC FATIGUE ANALYSIS PROGRAM (P5454)

Program P5454 uses panel structural parameters to compute the fundamental frequency of a rectangular isotropic plate, an integrally stiffened panel, or a corrugated panel. It computes the expected spectrum noise level at the panel fundamental frequency for boundary layer noise, rocket engine noise, flyback engine (jet) noise, and noise due to scrubbing of the jet engine exhaust. It computes the dynamic stress response of the structural panel to each noise excitation and/or an input spectral fluctuating pressure. It compares the Rayleigh probability distribution of stresses for the computed dynamic stress response and number of stress reversals in the expected life of the panel with an appropriate S-N curve, selects the critical stress, and computes the equivalent number of stress reversals for a sinusoidally applied effective stress for each noise. The program then computes a composite critical stress and an equivalent number of stress reversals for a sinusoidally applied effective stress for all noise sources. It compares each of the S-N points with an appropriate S-N curve for the material and indicates whether the panel has adequate fatigue life. It also computes the allowable stress for that number of cycles associated with each critical stress. The program prints out each of the preceding computed values.

Panel Fundamental Frequencies

The equations used in the program for the computation of the fundamental frequencies of the three panel types considered in the accompanying analysis are:

- (1) Rectangular isotropic plate

$$f = \frac{K_1}{2\pi a^2 \sqrt{M/D}} f^*$$

$$D = \frac{E h^3}{12 (1 - \nu^2)}$$

- (2) Integrally stiffened panel (see Figure C-1)

$$f = \frac{\sqrt{\frac{K_T}{M}}}{2\pi} f^*$$

APPENDIX C - Continued

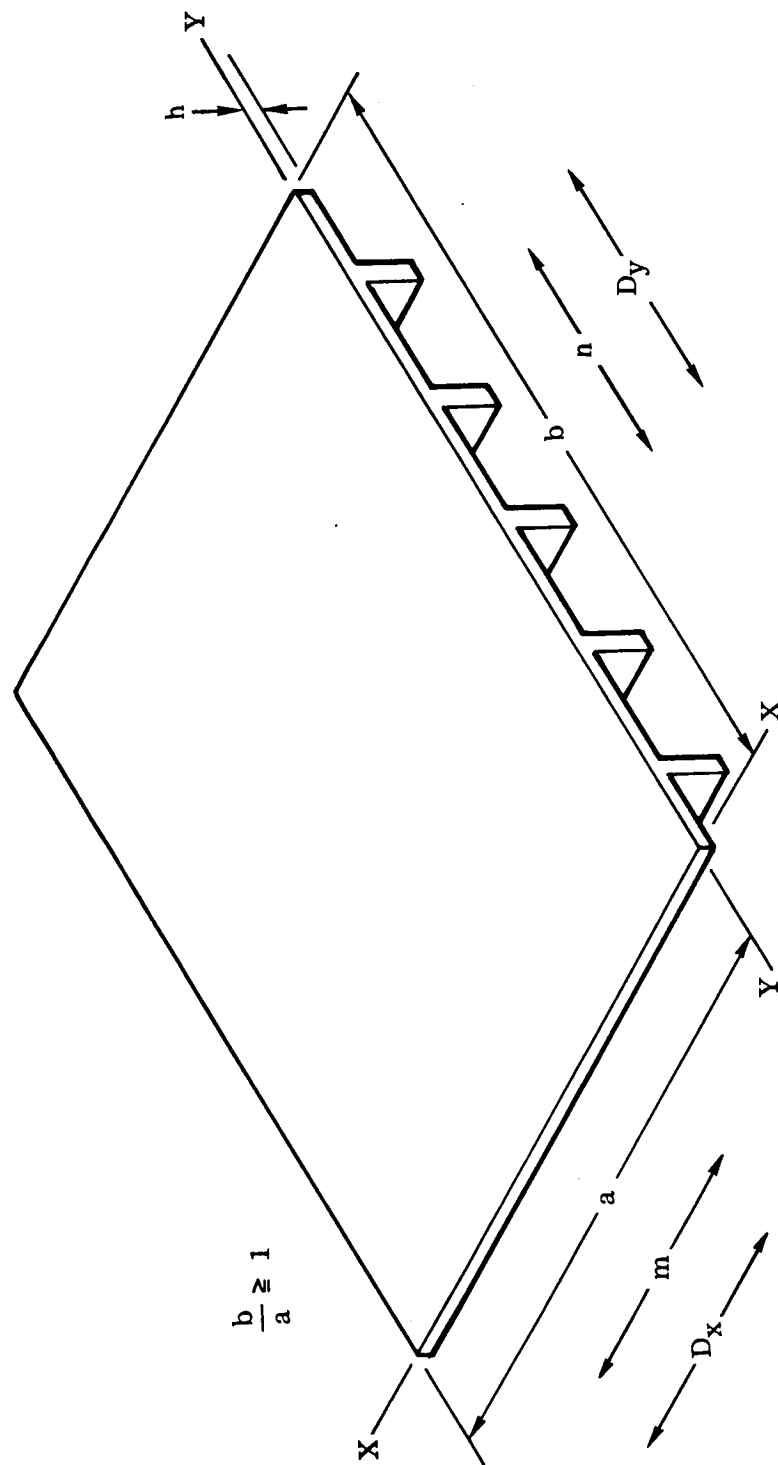


Figure C-1. Integrally Stiffened Panel.

APPENDIX C - Continued

$$K_T = \left[\left(\frac{D_x}{12} \right)^{\frac{1}{2}} K_m^2 + \left(\frac{D_y}{12} \right)^{\frac{1}{2}} K_n^2 \right]^2$$

$$D_y = D = \frac{E h^3}{12 (1 - \nu^2)}$$

$$D_x = D + \frac{EI}{12b}$$

$$K_m = \frac{m\pi}{a}$$

$$K_n = \frac{n\pi}{b}$$

(3) Corrugated panel

$$f = \sqrt{\frac{\frac{K_T}{M}}{12}} \frac{1}{2\pi} f^*$$

$$K_T = \left[\left(\frac{D_x}{12} \right)^{\frac{1}{2}} \left(\frac{\pi}{a} \right)^2 + \left(\frac{D_y}{12} \right)^{\frac{1}{2}} \left(\frac{\pi}{b} \right)^2 \right]^2$$

$$D_y = \frac{EI_x}{12a}$$

$$D_x = \frac{EI_y}{12b}$$

Acoustic Noise Prediction

The program computes the spectrum sound pressure level at the panel fundamental frequency for rocket engine noise as follows:

$$\bar{p}(f) = \text{antilog} (\text{SPL}_f \times 2.09 \times 10^{-8})$$

$$\text{SPL}_f = \text{OBSPL} - 10 \log BW$$

$$\text{OBSPL} = 10 \log (0.676 v) + \text{SPL}_0 - 20 \log R + \Delta B'$$

$$\text{SPL}_0 = 70 + 16.6 \log \left(\frac{S}{0.003} \right) \text{ for } S \leq 0.016$$

APPENDIX C - Continued

$$\text{SPL}_0 = 82 \quad \text{for } 0.016 \leq S < 0.152$$

$$\text{SPL}_0 = 70 - 16.6 \log \left(\frac{S}{0.8} \right) \quad \text{for } 0.152 \leq S$$

$$\text{In flight, } R = x_i + x_o$$

On Pad:

$$\text{when } x_o > (D_{\text{ref}} + y_{\text{cl}}), \quad R = \sqrt{(x_i + D_{\text{ref}})^2 + (x_o - D_{\text{ref}})^2}$$

$$\text{when } D_{\text{ref}} < x_o \leq (D_{\text{ref}} + y_{\text{cl}}),$$

$$R = \sqrt{(x_i + D_{\text{ref}})^2 + (y_{\text{cl}} - x_o + D_{\text{ref}})^2}$$

$$\text{when } x_o \leq D_{\text{ref}}, \quad R = \sqrt{(x_i + x_o)^2 + y_{\text{cl}}^2}$$

$$\text{for } S > 0.175, \quad x_o = D_e \times 10^{-0.222 - 1.315 \log S}$$

$$\text{for } S \leq 0.175, \quad x_o = D_e \times 10^{0.625 - 0.202 \log S}$$

The spatial parameters involved in the computation of rocket engine noise are illustrated in Figure C-2.

Dynamic Stress Computation

The program provides for computation of the panel maximum rms dynamic stress induced by the rms acoustic pressure acting on the panel at its fundamental frequency. For each panel type, the rms acoustic pressure is computed by

$$\bar{p} = p(f) \times (BW)^{\frac{1}{2}}$$

where BW is the effective bandwidth of the resonant peak.

$$BW = 2 \times \frac{c}{c_c} \times f$$

APPENDIX C - Continued

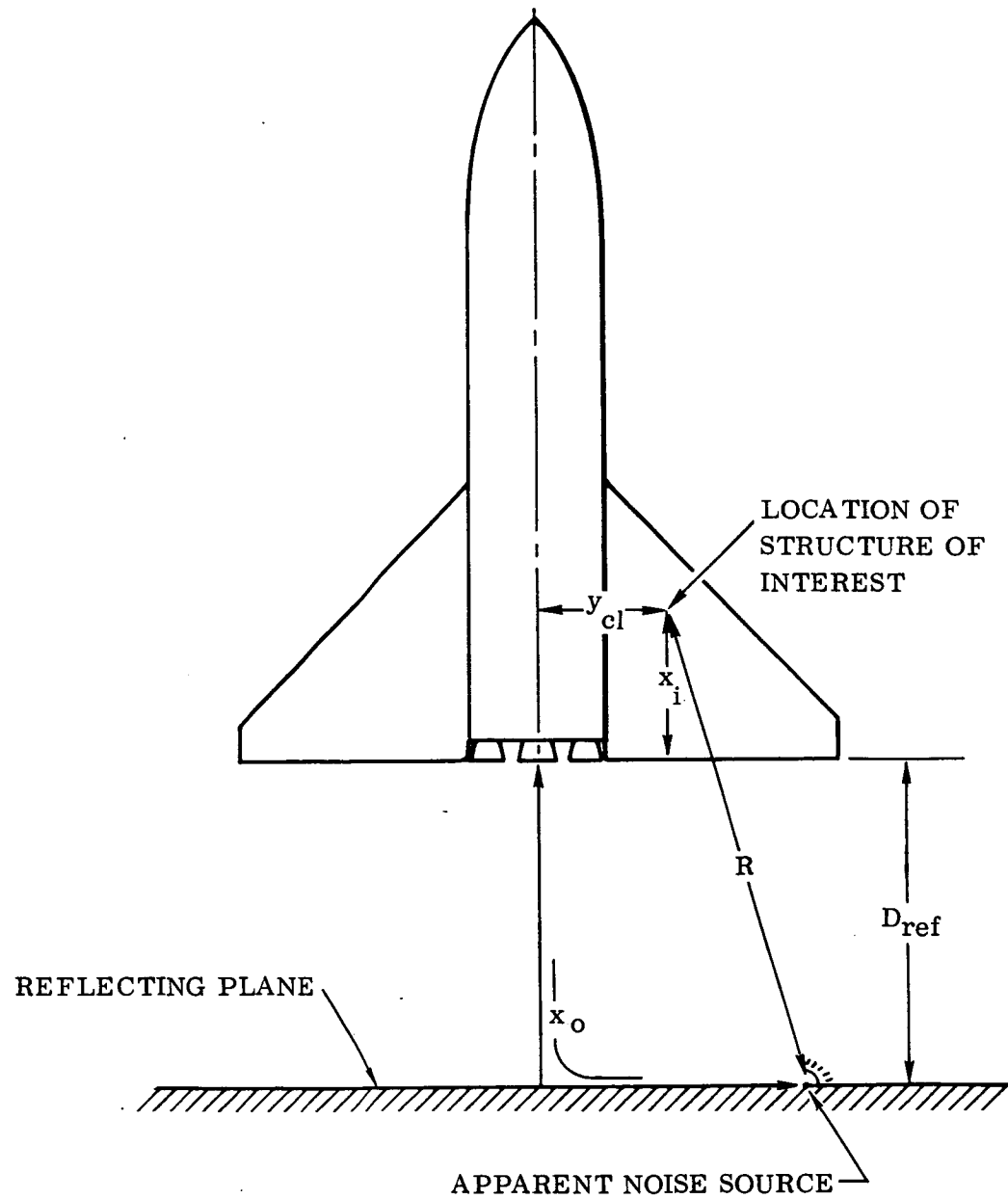


Figure C-2. Rocket Noise Spatial Parameters

APPENDIX C - Continued

(1) Rectangular isotropic plate

The maximum bending stress for rigid and symmetrical supporting structure is computed by:

$$S_{\max} = \frac{0.5 \bar{p} a^2}{h^2}$$

$$Y_{\max} = \frac{4.089 \bar{p} a^4}{E h^3}$$

For flexible and/or unsymmetrical structure:

$$S_{\max} = \frac{0.75 \bar{p} a^2}{h^2}$$

$$Y_{\max} = \frac{20.445 \bar{p} a^4}{E h^3}$$

Assuming a dynamic magnification factor

$$Q = \frac{1}{2(c/c_c)} = 25$$

and a local stress raiser due to edge conditions, $k_r = 4$, the local dynamic stress is

$$S_{1d} = Q k_r S_{\max} = 100 S_{\max}$$

(2) Integrally stiffened panel

$$\text{Substitute } h_{eq} = h (r_s)^{1/3}$$

(3) Corrugated panel

Substitute

$$h_{eff} = \left\{ \frac{10.9}{12} \left[\frac{\left(\frac{I_y}{b} \right)^{\frac{1}{2}} \left(\frac{1}{a^2} \right) + \left(\frac{I_x}{a} \right)^{\frac{1}{2}} \left(\frac{1}{b^2} \right)}{\left(\frac{1}{a^2} + \frac{1}{b^2} \right)} \right]^2 \right\}^{1/3}$$

APPENDIX C - Continued

Stress Reversals for Vehicle Lifetime

For each local dynamic rms stress of interest, the program computes the number of stress reversals at the fundamental frequency. It is assumed that stress levels equal to or greater than the rms stress occur only 61% of the time.

$$N_L = f \times \Delta t(0.61)$$

Critical Stress Levels and Number of Stress Reversals

The program computes a Rayleigh distribution envelope of the computed dynamic stress induced by the acoustic environment for the number of stress reversals the panel must withstand during its service life. This is accomplished by curve fit equations for the two parts of the integrated Rayleigh distribution:

$$\left(p > S_{app} \right) = e^{-\frac{1}{2} \left(\frac{S_{app}}{S_{ld}} \right)^2}$$

where $\left(p > S_{app} \right)$ is the probability of exceeding S_{app} in percent and $\frac{S_{app}}{S_{ld}}$ is the ratio of peak stress to rms stress. It is assumed that

$$S_{app_{max}} = 4 \times S_{ld}$$

The curve fit equations are:

$$S_{app} = \frac{2}{\pi} \cos \left[1 - \frac{\pi}{1.212} \left(1 - \frac{N}{N_L} \right) \right] S_{ld} \text{ for } 0.455 < \frac{N}{N_L} < 1.0$$

$$S_{app} = \left\{ \frac{-c_2 - \sqrt{c_2^2 - 4c_3 \left[c_1 - \log \left(\frac{N}{N_L} \right) \right]}}{2c_3} \right\} S_{ld} \text{ for } \frac{N}{N_L} < 0.455$$

where

$$c_1 = 2.631102 \times 10^{-2}$$

$$c_2 = -2.635 \times 10^{-2}$$

$$c_3 = -4.939331 \times 10^{-1}$$

APPENDIX C - Continued

An appropriate S-N curve for the panel material is also represented in the program by a third order polynomial

$$S_{all} = 1000 (c_1 + c_2x + c_3x^2 + c_4x^3)$$

The coefficients c_1 , c_2 , c_3 and c_4 are input into the program, having been determined by a least squares fit of the S-N curve where the stress is in ksi and x is the logarithm of N .

At this point in the analysis, a rationale is needed for relating the random environment (represented by the Rayleigh probability distribution envelope) to the material fatigue characteristics (represented by the sinusoidal S-N curve). It is assumed that some fixed amount of input energy is needed to fail a component in fatigue. It is further assumed that this energy is proportional to the area bounded by the number of cycles where failure occurs and the sinusoidal stress level from the S-N curve at that number of cycles. This may be said to represent the "allowable" energy. The "applied" energy due to the acoustic loading is assumed to be proportional to the area under the integrated Rayleigh distribution curve.

A comparison of the areas under the two curves indicates whether failure will or will not occur during the operating life of the component. This comparison is facilitated by selecting a critical stress level, S_{cr} , and a number of cycles, N_{cr} , such that the rectangular area for $S_{cr} \times N_{cr}$ is equal to the area under the applied stress curve. S_{cr} is selected as the stress on the applied curve where its slope is equal to the slope of the allowable curve. N_{cr} is determined numerically by the equation:

$$N_{cr} = \frac{1.261 N_L S_{ld}}{S_{cr}}$$

Now the work accomplished by N_{cr} reversals of stress, S_r , is theoretically equal to that accomplished by the required number of stress reversals of the randomly varying stresses.

The service life equivalent exposure, $S_{cr}N_{cr}$, is compared in the program to the S-N curve for the panel. It predicts failure of the panel if $S_{cr}N_{cr}$ is above the S-N curve and prints out the stress from the S-N curve at N_{cr} cycles to indicate the magnitude of improvement required to make the panel adequate for its noise environment.

If $S_{cr}N_{cr}$ is below the S-N curve, the program indicates the panel is good for its environment and also prints out the stress from the S-N curve at N_{cr} cycles to indicate the margin of safety.

APPENDIX C - Continued

NOMENCLATURE FOR SONIC FATIGUE ANALYSIS PROGRAM

a	panel short dimension, ft
A_e	area, jet exit nozzle, ft ²
b	panel long dimension, ft
BW	frequency bandwidth, Hz, selected by FUNCTION BANDW from standard octave bandwidths stored in the program
C_a	local speed of sound, ft/sec
c/c_c	critical damping coefficient - assumed to be 0.02
D	diameter or distance, ft

Subscripts:

e	effective diameter of rocket nozzles
J	jet exit diameter
ref	distance from reflecting surface to rocket exhaust plane
veh	vehicle diameter
x	jet diameter at x_j
E	Young's modulus of elasticity, psi
f	frequency, Hz
f_0	characteristic frequency, Hz
f^*	support structure stiffness multiplier = 1.0 for rigid and symmetrical supporting structure = 0.25 for flexible and/or unsymmetrical supporting structure
g_0	gravitational constant = 32.2 ft/sec ²
h	thickness, in.

Subscripts:

c	honeycomb sandwich core
eff	effective
eq	equivalent
f	honeycomb sandwich face

APPENDIX C - Continued

I moment of inertia, in ⁴

k_r local stress raiser due to edge conditions

K flexural stiffness

Subscripts:

1,2 coefficients interpolated by FUNCTION TABLE from
table stored in program

i isotropic panel

s,t stiffened panel

m mode number = 1 for simply supported beam

M mass term = $\frac{\rho h}{32.2}$, lb sec² in /ft⁴

Mach local mach number

n mode number = 1 for simply supported beam

N number of stress reversals

Subscripts:

cr associated with critical stress

L for vehicle lifetime

\bar{N}_{cr} number of stress reversals associated with composite critical stress

OASPL overall sound pressure level, db

Subscripts:

200 at 200 ft from jet exit nozzle

nf in near field at distance less than 200 ft

x from grazing jet at distance x

OBSPL octave band sound pressure level, db

\bar{P} root mean square acoustic pressure, psf

Subscripts:

x from grazing jet at distance x

APPENDIX C - Continued

$\bar{p}(f)$	spectrum sound pressure at panel fundamental frequency, psf
q	local dynamic pressure, psf
Q	dynamic modification factor = $\frac{1}{2(c/c_c)}$
r_s	stiffness ratio = $\frac{K_s}{K_i}$
R	radial distance between noise source location and panel, in.
Re_y	Reynold's number of the flow
S	Strouhal number = $\frac{f Pe}{v}$
S	stress, psi
Subscripts:	
	all allowable
	app applied
	cr critical
\bar{S}_{cr}	composite critical stress, psi
SPL	sound pressure level, db
Subscripts:	
	o reference octave level for $R = 1$ ft
	f spectrum level at panel frequency
t	rocket total thrust, lb
T_j	jet thrust, lb
u	local freestream velocity, fps
v	exhaust gas velocity, = $\frac{tg_o}{w}$, fps
Subscripts:	
	j jet
	R relative
w	engine total weight flow, lb /sec

APPENDIX C - Concluded

x	distance, ft
	Subscripts:
	o to noise source location along jet
	i from panel to rocket exhaust plane
	j from panel to jet exhaust plane
	l from vehicle leading edge to panel
y	distance, ft
	Subscripts:
	cl from vehicle centerline to panel
	p from jet engine centerline to panel
δ	local boundary layer thickness, ft
$\Delta B'$	correction for ambient conditions
	$= 0 \text{ for } f < \frac{C_a}{(\pi D_{veh})}$
	$= 6 \text{ db for } f \geq \frac{C_a}{(\pi D_{veh})}$
Δt	time duration of acoustic stress, sec
ν	Poisson's ratio $\cong 0.3$ for materials of interest
π	$= 3.14159$
ρ	density, lb /ft ³
	$= \frac{w}{a_e v_j}$ for flow
ω	circular frequency, rad/sec

APPENDIX D

BRAZE SYSTEM QUALIFICATION

The intent of this supplemental test series was to qualify brazing as an alternate joining method. The level of effort, however, was considerably less than that conducted for electron beam welding and diffusion bonding during Phase I. Since considerable work had been done since 1964 with the Ti-33 Cr foil system with columbium alloys by Freedman and Mikus of Northrop (References 43 and 44), was believed that the system qualification could be made with a minimal effort.

TEST PROGRAM

Braze joints were selected which were representative of those found on the open corrugation heat shields. Material thicknesses and joint overlaps were typical of those found in the production hardware. The brazing foil was Ti-33 Cr, 0.002 inch (0.005 cm) thick. Brazed specimens were coated with R-512E. All preparations for brazing and for coating, the brazing process and the post brazing diffusion treatment were the same as those planned for production hardware.

The braze system specimen panels using a combination of 0.023 and 0.040 inch (0.058 and 0.102 cm) thick material with an 0.080 inch (0.203 cm) overlap were prepared per Figure D-1. The size of the brazed portion was selected to accommodate laboratory brazing furnaces and extensions were added by electron beam welding. Two additional specimen panels with 0.065 to 0.065 inch (0.165 cm) thick overlap material with a 0.300 inch (0.762 cm) overlap were prepared with welded extensions (see Figure D-2). Following brazing, the specimen panels were diffusion treated for 16 hours at 2400° F (1589° K) in a vacuum.

Each of the brazed specimen panels were evaluated by NDT - visual and C-scan ultrasonics - and cut into 18 tensile specimens - 9 with an 0.080 inch (0.203 cm) overlap and 9 with a 0.300 inch (0.762 cm) overlap - as shown in Figure D-3. All 18 tensile specimens were identically prepared for coating, with 16 specimens coated with R-512E. The remaining two specimens were used for comparing room temperature properties of uncoated with coated specimens. Four coated specimens of each overlap were exposed to a simulated flight environment for 100 entry cycles (Ref. Phase I Report). All flight simulation tested specimens and eight unexposed as-coated specimens (4 of each overlap) were tensile tested, one half at room temperature and half at 2200° F (1478° K) in air.

Six specimens were selected at random for metallographic evaluation of the braze bond and the braze alloy/coating/base metal interactions. Particular attention was

APPENDIX D - Continued

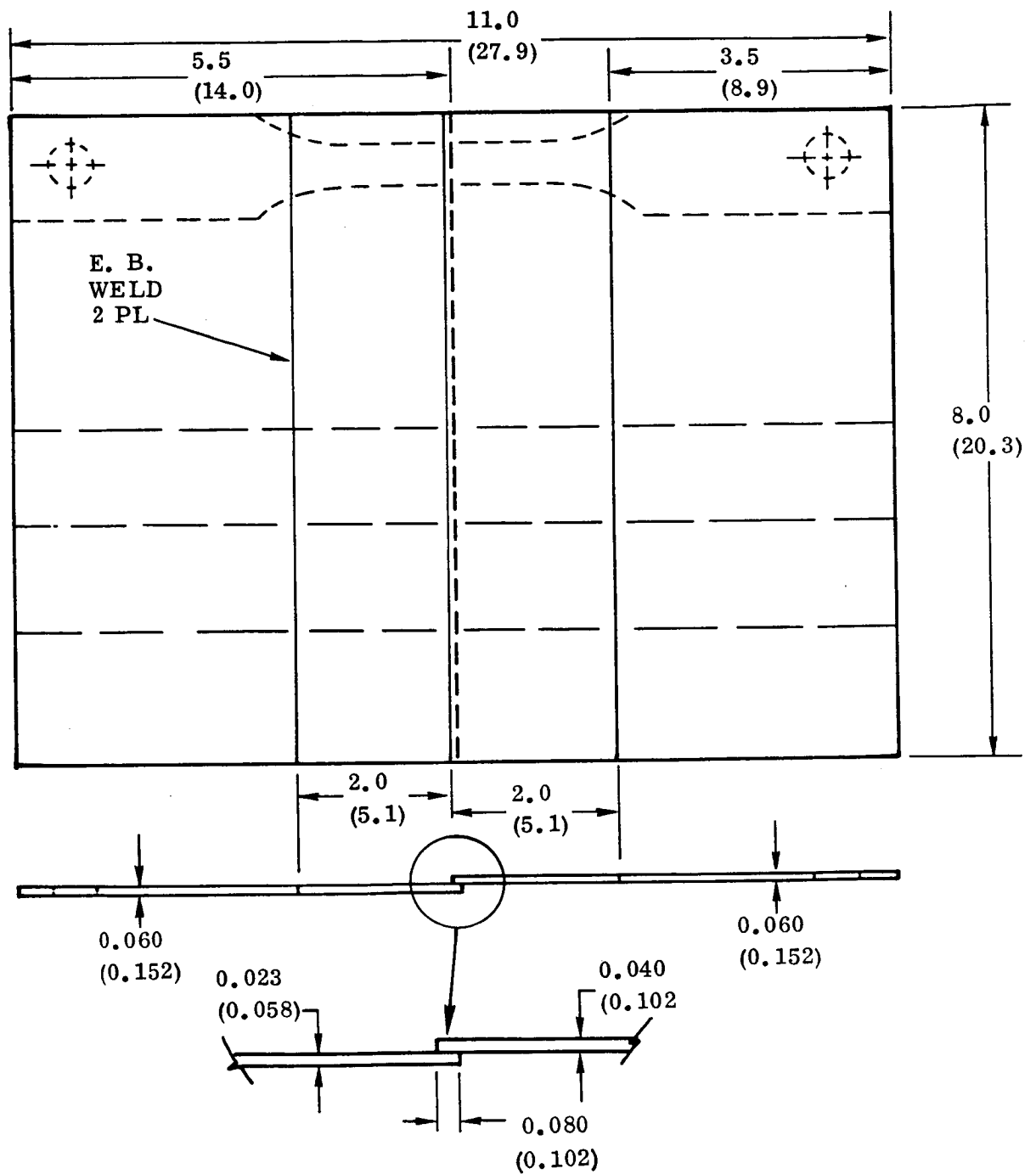


Figure D-1. Cb-752/Ti-33 Cr Braze System Test Specimen

APPENDIX D -- Continued

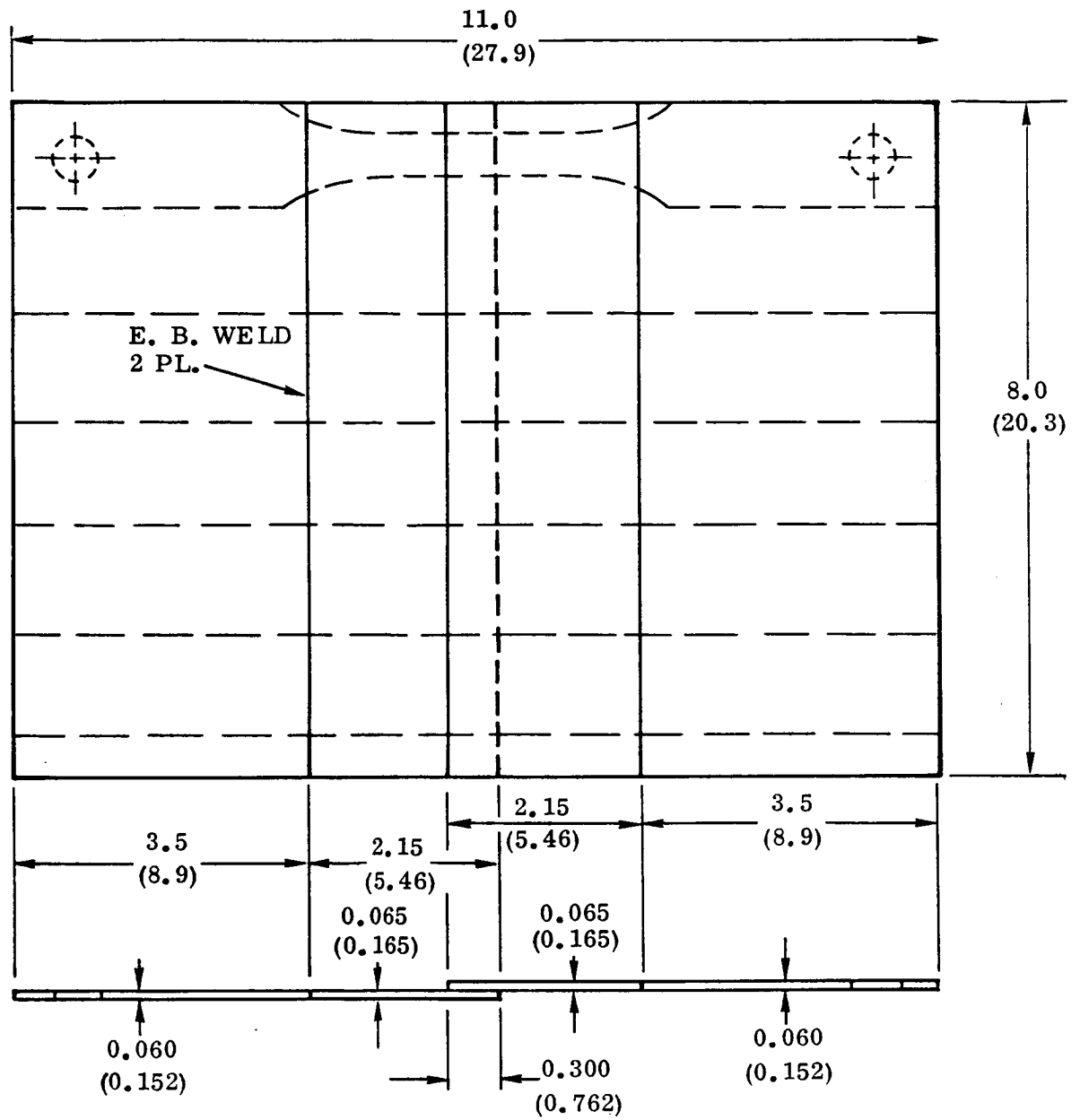


Figure D-2. Cb-752/Ti-33 Cr Braze System Test Specimen

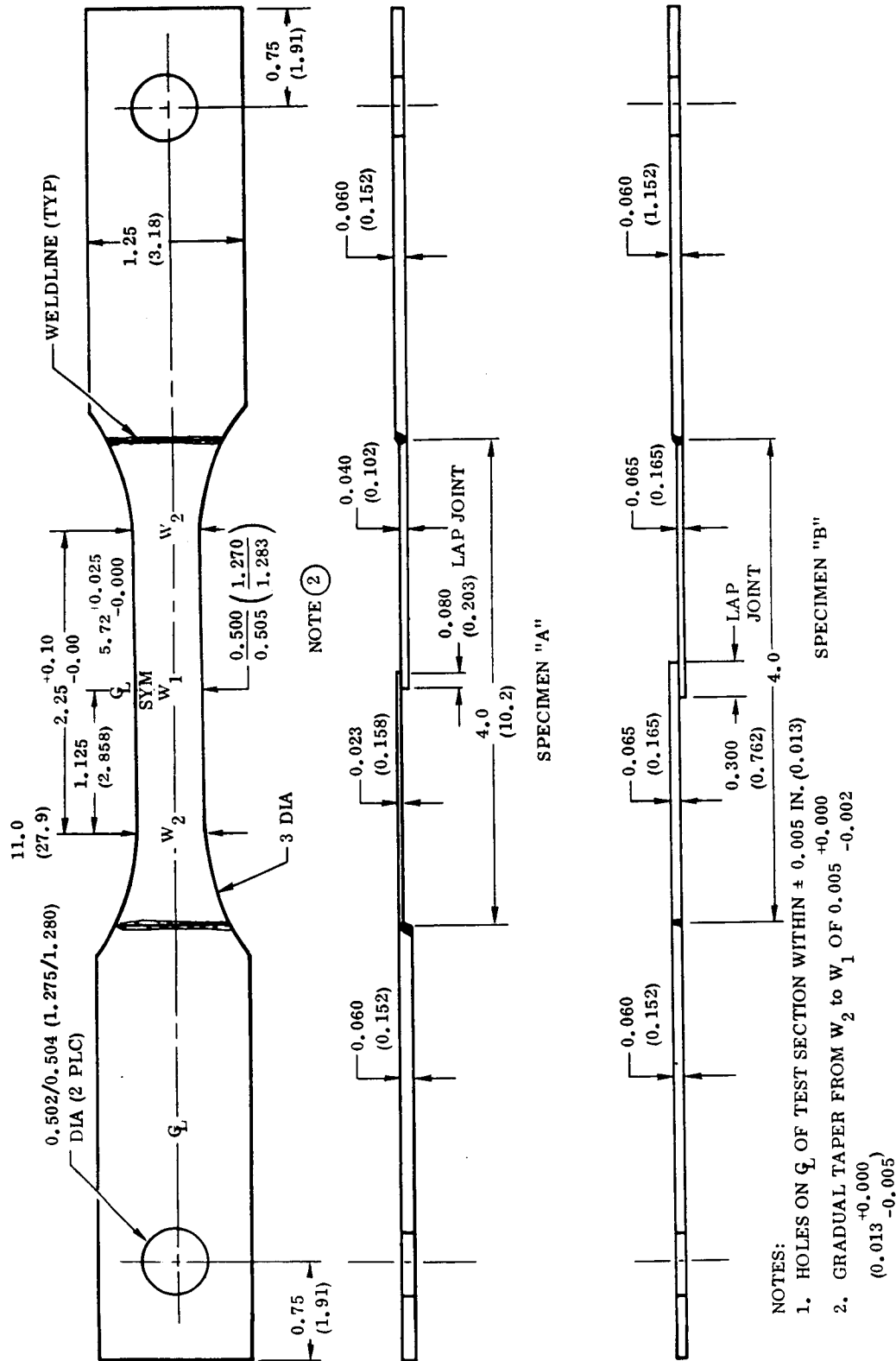


Figure D-3. Brazed Flight Simulation Tensile Specimen Details

APPENDIX D - Continued

given to conditions at the edges of coated braze joints for both entry exposed and unexposed specimens.

TEST RESULTS AND OBSERVATIONS

Test specimens were examined for coating uniformly, weight gain and thickness increase after coating, and inspected for any visible coating anomalies resulting from the presence of the braze alloy. None were found.

All eight specimens exposed to flight simulation completed the 100 cycle life test in excellent condition. No areas of localized coating failure or substrate erosion were observed on any of the samples. There were the normal color changes (to a grey brown, somewhat darker in the reduced section than at the ends) and a slight coating spall. No reactions were visible in or near the brazed overlap regions. There was some bending of the specimens on either side of the joint as a result of the geometry of an overlap braze which imparts a bending moment in this region. Eight specimens are shown in Figures D-4 and D-5.

The eight specimens which completed 100 cycle testing along with the eight coated but unexposed specimens and the two uncoated specimens were tensile tested with results shown in Table D-1. All tensile fractures occurred in the base metal with more than half the fractures located near the edge of the joint. This failure location can be attributed to a bending moment imparted to the specimen in the region of a stress discontinuity.

A comparison of the average ultimate tensile strengths for welded and diffusion bonded joints in Cb-752 performed in Phase I (Reference 3) with brazed joints is presented in Table D-2. It can be seen that the data compare quite favorably, particularly for joints tests after 100 simulated flight cycles.

METALLOGRAPHY

Figures D-6 and D-7 show microsections of the brazed region of two uncoated specimens. A good fillet and some substrate erosion can be seen in Figure D-6. Both sections show a braze zone thickness of approximately 0.006 inch (0.015 cm) which represents an increase of 0.004 inch (0.010 cm) from the 0.002 inch (0.005 cm) foil thickness after the diffusion cycle. Figure D-8 shows an example of the porosity found in two of the specimens. This porosity was apparently not detrimental since tensile fractures occurred away from the joint. Figure D-9 is a photomicrograph of a coated and unexposed specimen and illustrates the typical slight reaction between the R-512E coating and the braze foil. After cycling, no preferential oxidation or diffusion was found in the joint edge region. In fact, less of a reaction

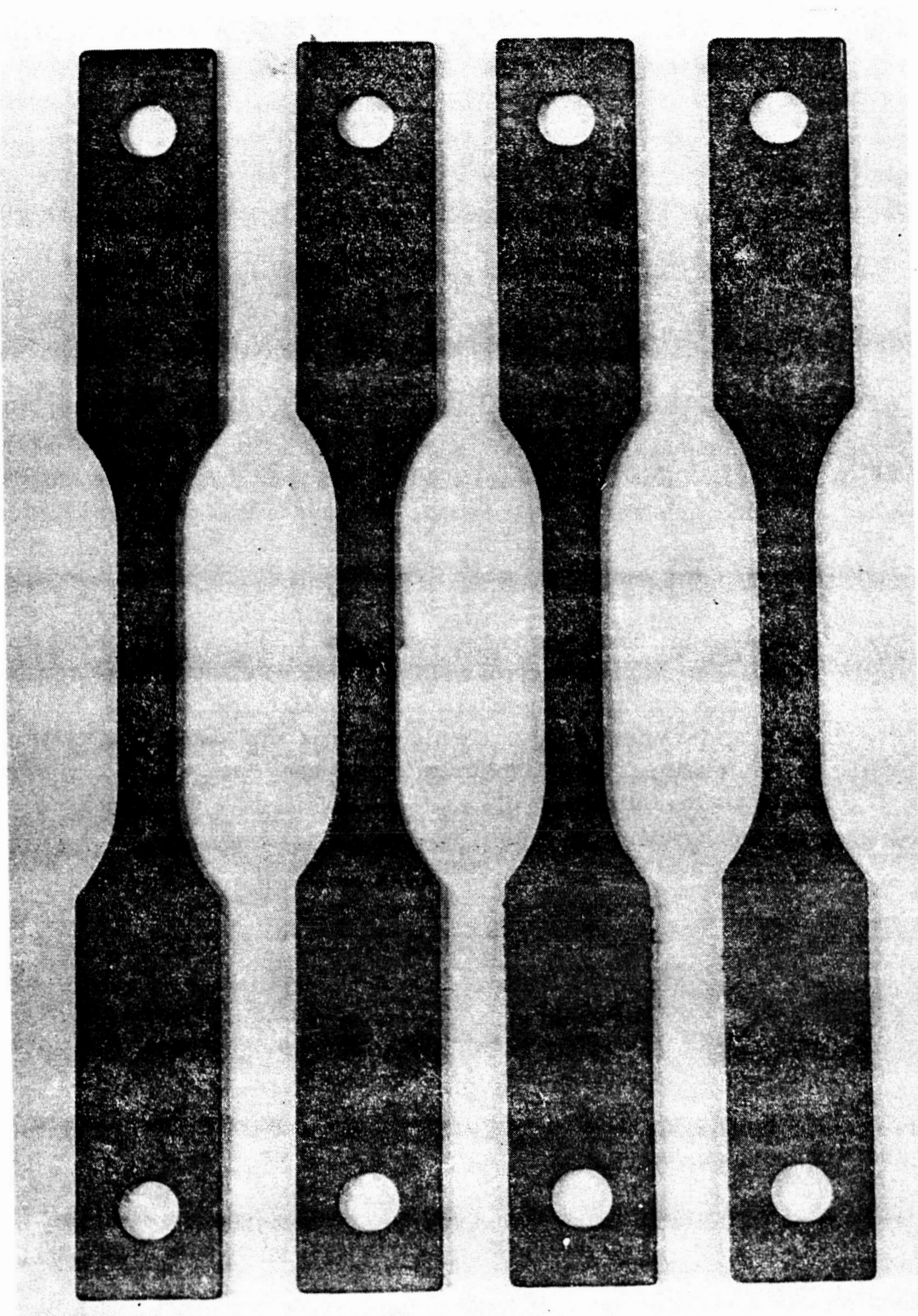


Figure D-4. Brazed Specimens [0.08 inch (0.203 cm) overlap] after 100 Flight Simulation Cycles (Photo No. 128381B)

APPENDIX D - Continued

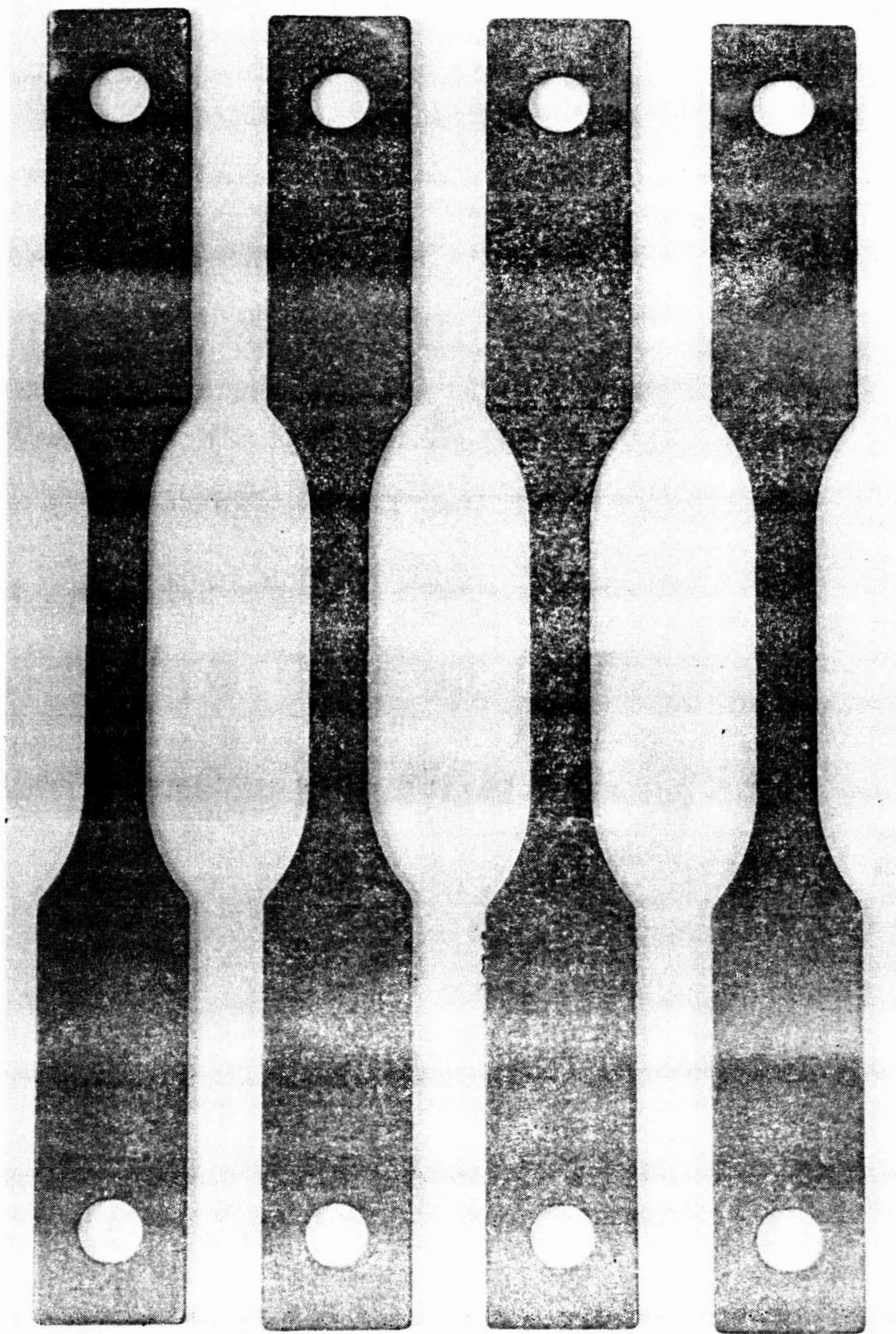


Figure D-5. Brazed Specimens [0.30-inch (0.76 cm)] Overlap After 100 Flight Simulation Cycles (Photo 128382B)

Table D-1. Brazed Cb-752/R-512E Specimens Tensile Test Results

Spec No.	Cycles	Temperature		F _{tu} [*]		F _{tu} ^{**}		% Elong.	Failure Location
		°F	°K	ksi	MN/m ²	ksi	MN/m ²		
BSB-08-9 0.08 in. (0.20cm) overlap	0 (Bare)	75	297	76.7	528.8	—	—	14.0	Base metal
	0	75	297	72.0	496.4	85.0	586.1	6.5	Base metal
	0	75	297	69.4	478.5	81.2	559.9	8.0	Base metal
	100	75	297	59.8	412.3	69.4	478.5	1.0	Edge of bond
	100	75	297	56.9	392.3	66.0	455.1	1.5	Edge of bond
	0	2000	1366	29.2	201.3	34.5	237.9	1.0	Edge of bond
	0	2000	1366	29.0	200.0	34.2	235.8	2.0	Edge of bond
	100	2000	1366	31.9	220.0	37.3	257.2	1.0	Edge of bond
	100	2000	1366	30.7	211.7	35.9	247.5	1.0	Edge of bond
BSB-30-9 0.30 in. (0.76cm) overlap	0 (Bare)	75	297	77.9	537.1	—	—	23.5	Base metal
	0	75	297	74.2	511.6	78.7	544.0	20.0	Base metal
	0	75	297	74.1	510.9	78.5	541.3	20.0	Base metal
	100	75	297	72.5	499.9	76.9	530.2	††	Base metal
	100	75	297	72.3	498.5	76.6	528.2	15.0	Base metal
	0	2000	1366	29.5	203.4	31.3	215.8	3.5	Edge of bond
	0	2000	1366	29.7	204.8	31.8	219.3	3.0	Edge of bond
	100	2000	1366	29.7	204.8	31.5	217.2	3.0	Edge of bond
	100	2000	1366	28.3	195.1	30.0	206.9	2.0	Edge of bond

* Values based on original uncoated cross-sections

** Values based on calculated remaining substrate according to the relationship $F_{tu}^{**} = CF_{tu}^{*} \left(3 - \frac{2}{t_{oc}/t_o} \right)$;

† C-scan indicated poor bond

 t_{oc} = Thickness after coating

†† Lost gage marks

 t_o = thickness bare

APPENDIX D - Continued

Table D-2. Ultimate Tensile Strength Comparison* for Cb-752/R-512E

Test Temp.		Conditions	Cycles	E.B. Weld ⁽¹⁾		Diff. Bond ⁽¹⁾		Braze**	
°F	°K			ksi	MN/m ²	ksi	MN/m ²	ksi	MN/m ²
75	297	Bare	0	80.8	557.3	83.2	573.9	76.7	532.7
75	297	Coated	0	68.2	470.3	69.7	480.8	70.7	491.0
75	297	Coated	100	58.4	402.9	59.9	413.0	58.4	405.6
2000	1366	Coated	0	31.9	219.7	32.4	222.7	29.1	202.1

* Values based on original uncoated cross-sections

**0.08-inch (0.20 cm) overlap

(1) Reference 3

APPENDIX D - Continued

Magnification: 100X
Etch: HF-HNO₃-H₂O
Specimen No.: BSB-08-9
Flight Cycles: 0
Negative No.: D3402
Mount No.: 804P

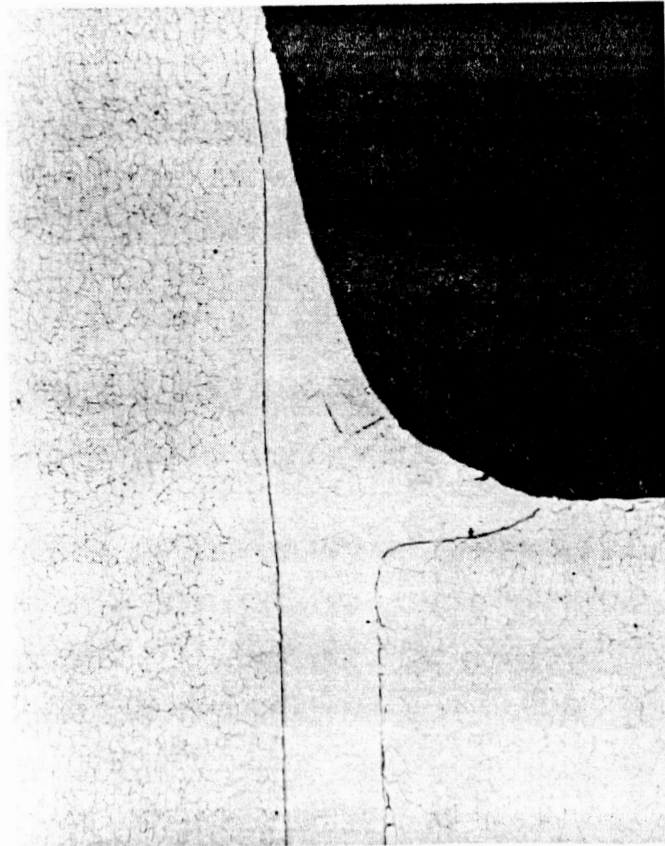
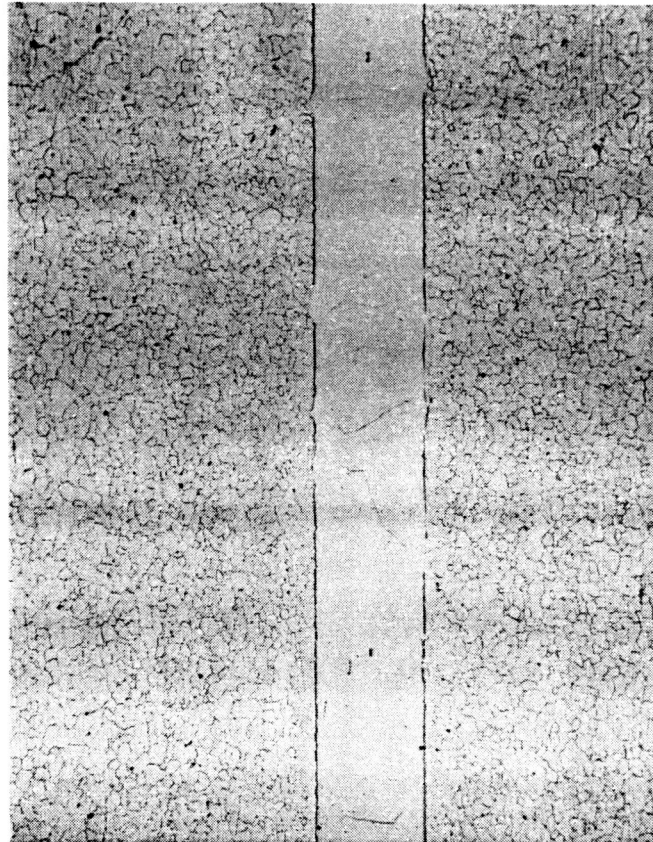


Figure D-6. Microstructure of Unexposed, Uncoated Cb-752 Brazed
Tensile Specimen Joint Edge

APPENDIX D - Continued



Magnification: 100X
Etch: HF-HNO₃-H₂O
Specimen No.: BSB-30-9
Flight Cycles: 0
Negative No.: D3408
Mount No.: 807P

Figure D-7. Microstructure of Unexposed, Uncoated Cb-752 Brazed
Tensile Specimen Joint

APPENDIX D - Continued

Magnification: 100X
Etch: HF-HNO₃-H₂O
Specimen No.: BSP-30-1
Flight Cycles: 0
Negative No.: D3404
Mount No.: 805P

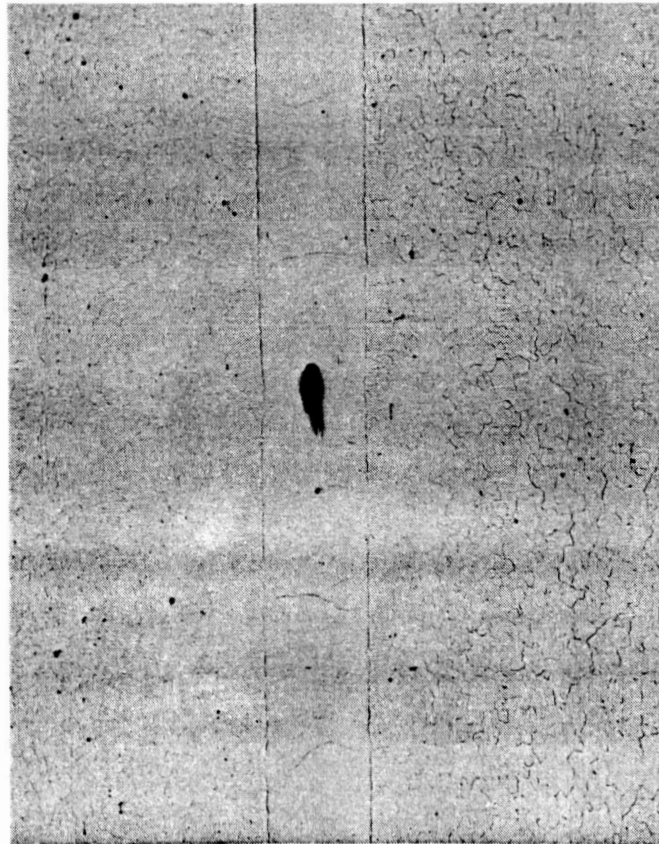
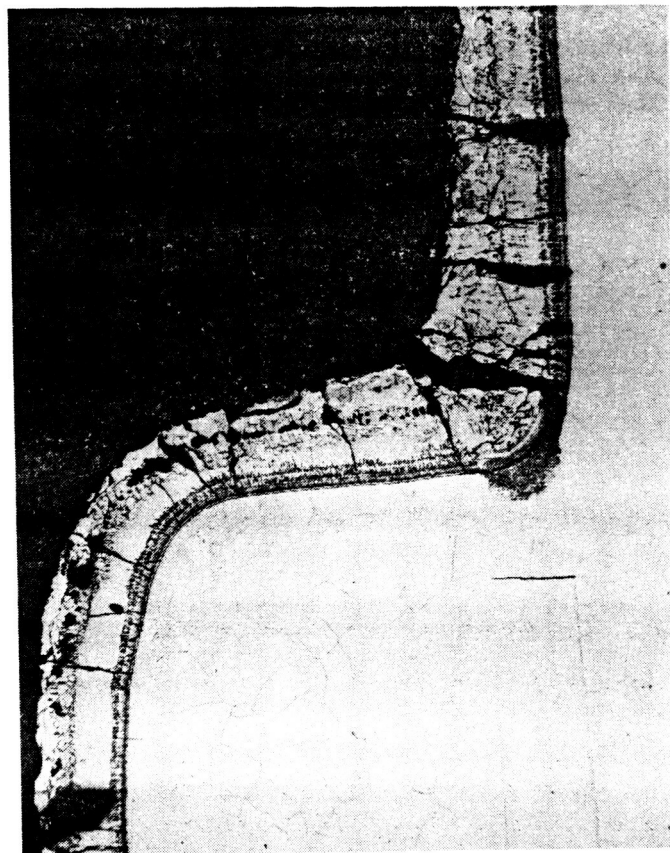


Figure D-8. Microstructure of Unexposed Cb-752/R-512E Brazed
Tensile Specimen Joint

APPENDIX D - Continued



Magnification:	100X
Etch:	HF-HNO ₃ -H ₂ O
Specimen No.:	BSB-08-1
Flight Cycles:	0
Negative No.:	D3398
Mount No.:	802P

Figure D-9. Microstructure of Unexposed Cb-752/R-512E Brazed
Tensile Specimen Joint Edge

APPENDIX D — Continued

occurred with the brazed specimens than with the diffusion bonded specimens (Reference 3) which employed a pure titanium foil interleaf.

Only one of the post-cycled specimens examined exhibited coating breakdown. This specimen is shown in Figure D-10. Failure nodes emanating from the oxide-filled cracks are clearly identifiable. About the nodes are hemispheres of oxygen-contaminated substrate. The darker areas along the perimeter of the hemispheres are extensions of contamination along these regions of high defect density.

Hardness readings were made using a 200 gram load on select locations on this specimen. The highest reading was 502 KHN for a location in the coating-effected braze joint area. The magnitude of this reading was predictable considering the high chromium content of the braze foil. The unaffected substrate was found to have a reading of 174 KHN; a reading of 204 KHN was recorded at the center of the large contaminated hemisphere; the inner contamination band was found to be less hard with a recording of 192 KHN.

CONCLUSIONS

As a result of this test series, it was concluded that the Ti-33 Cr braze system joints could be made and that these joints would have satisfactory structural properties for heat shield applications.

APPENDIX D — Concluded

Magnification: 100 X
 Etch: Anodized
 Specimen No.: BSB-08-6
 Flight Cycles: 100
 Mount No.: 803P

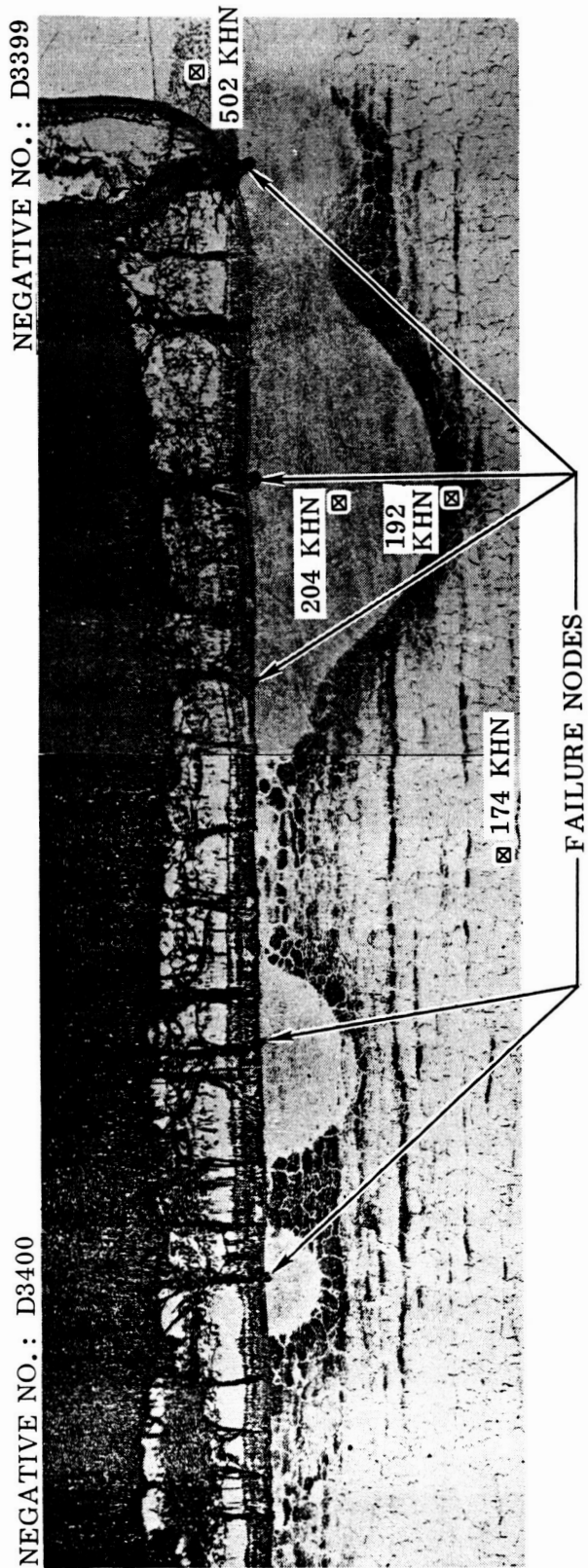


Figure D-10. Microstructure of Exposed Cb-752/R-512E Brazed Tensile Specimen

PRECEDING PAGE BLANK NOT FILMED

APPENDIX E

ACOUSTIC TEST DATA

The data presented herein are accelerometer power spectral density plots of three locations per specimen at two OASPL for cycles 1, 25, 26 and 100. The accelerometer outputs were recorded on magnetic tape and reduced to the form of power spectral density plots. Acoustic levels were measured 18 inches (45.7 cm) from the test specimen face. Acoustic levels were also recorded on magnetic tape and reduced to octave band sound pressure levels (Figures 8-33 through 8-36). Since the data shows no significant shift in the recorded fundamental frequency, it was assumed that no structural degradation of the system had occurred. Post test disassembly and examination confirmed this assumption.

APPENDIX E — Continued

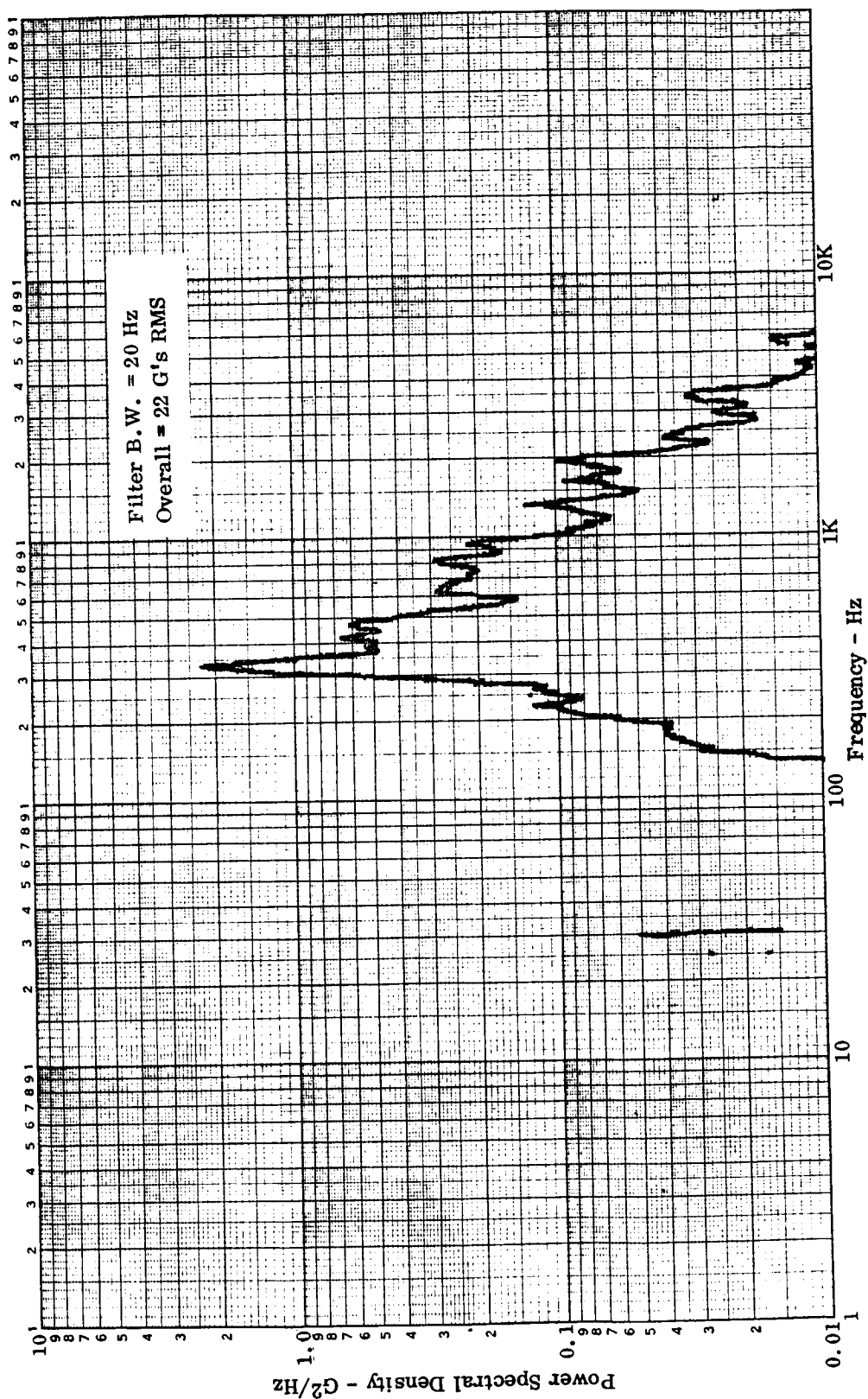


Figure E-1. Tee-Stiffened TPS, Accelerometer No. 2, 155 dB OASPL, Cycle No. 1

APPENDIX E — Continued

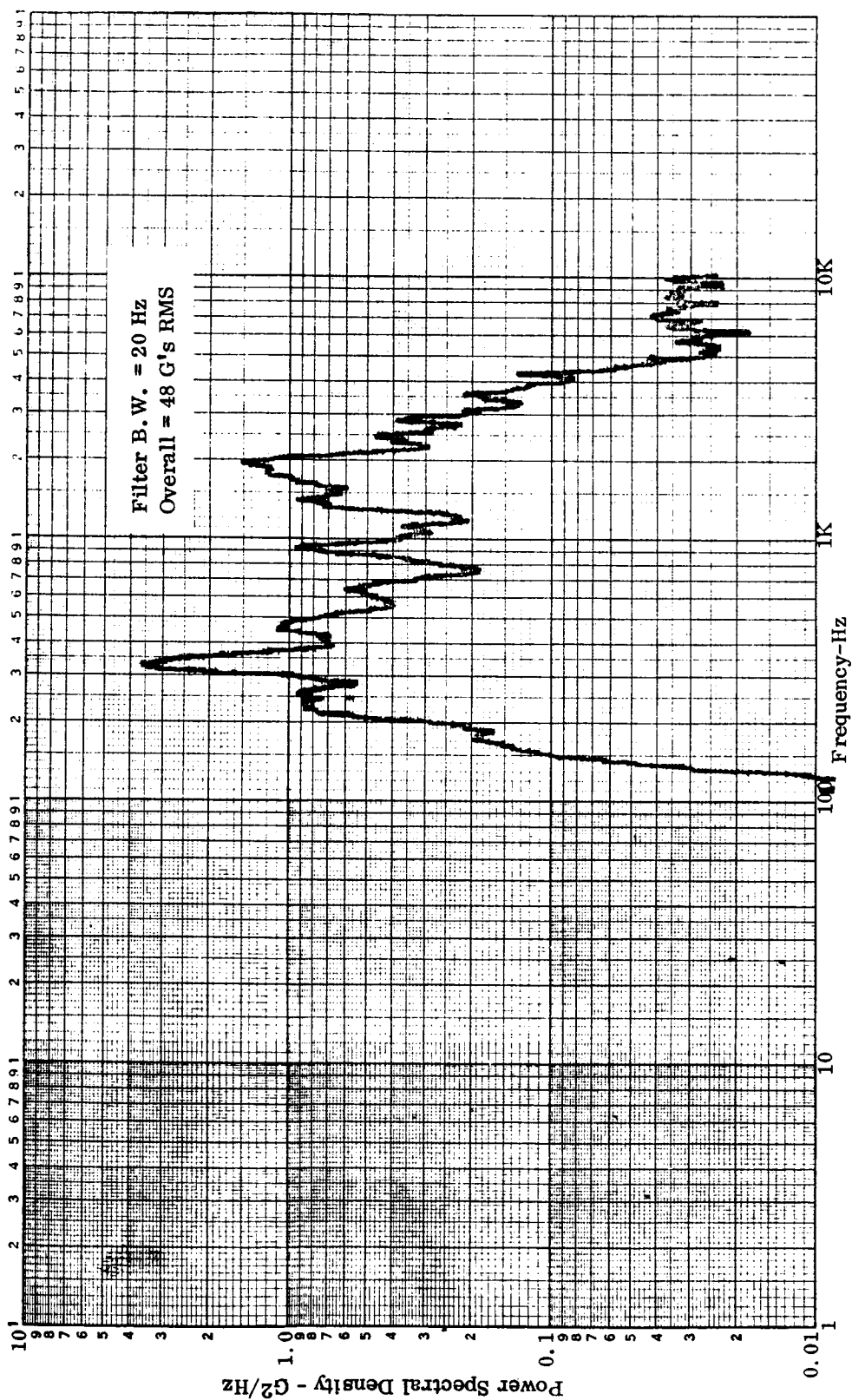


Figure E-2. Tee-Stiffened TPS, Accelerometer No. 3, 155 dB OASPL, Cycle No.1

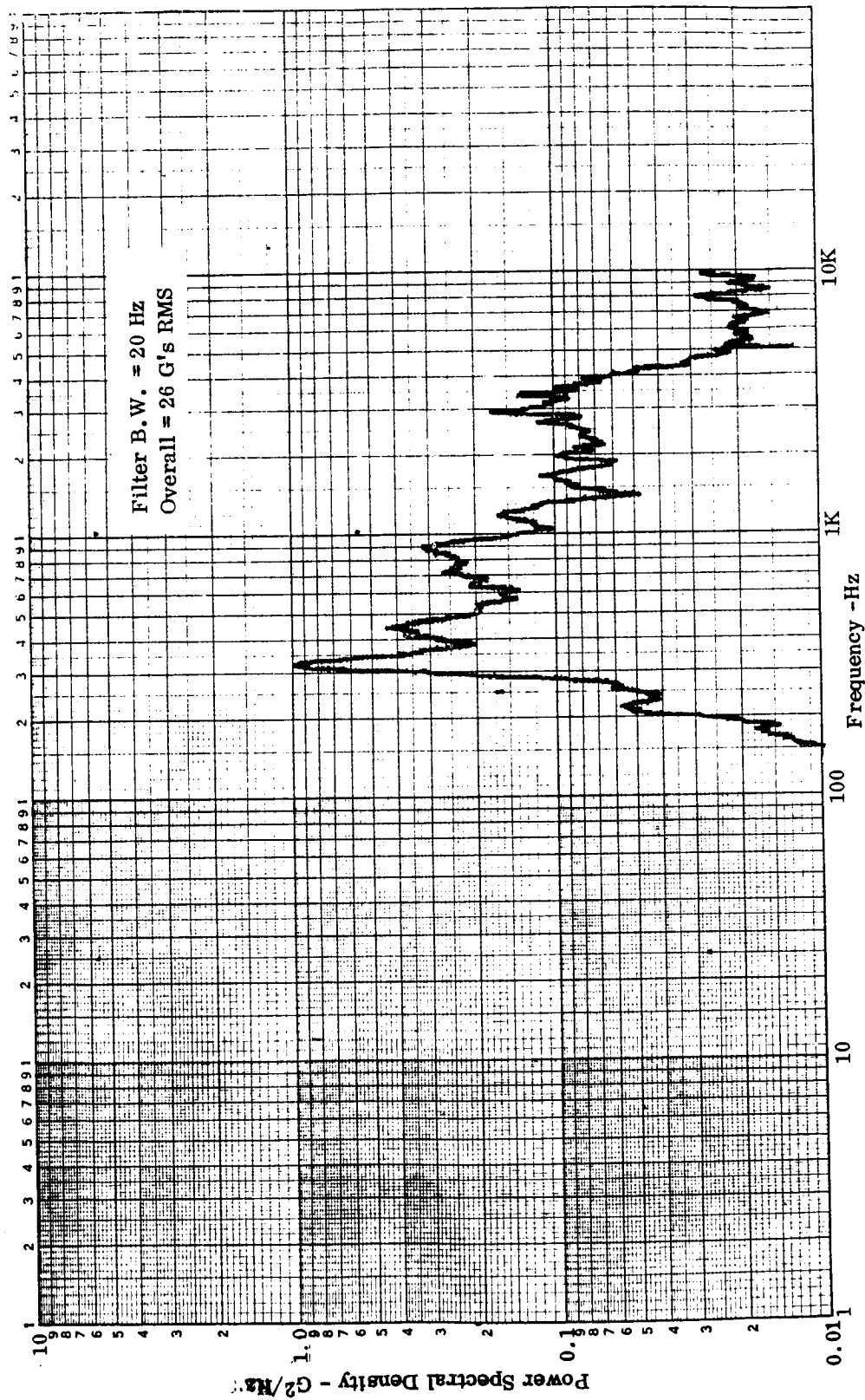


Figure E-3. Tee-Stiffened TPS, Accelerometer No. 6, 155 dB OASPL, Cycle No. 1

APPENDIX E — Continued

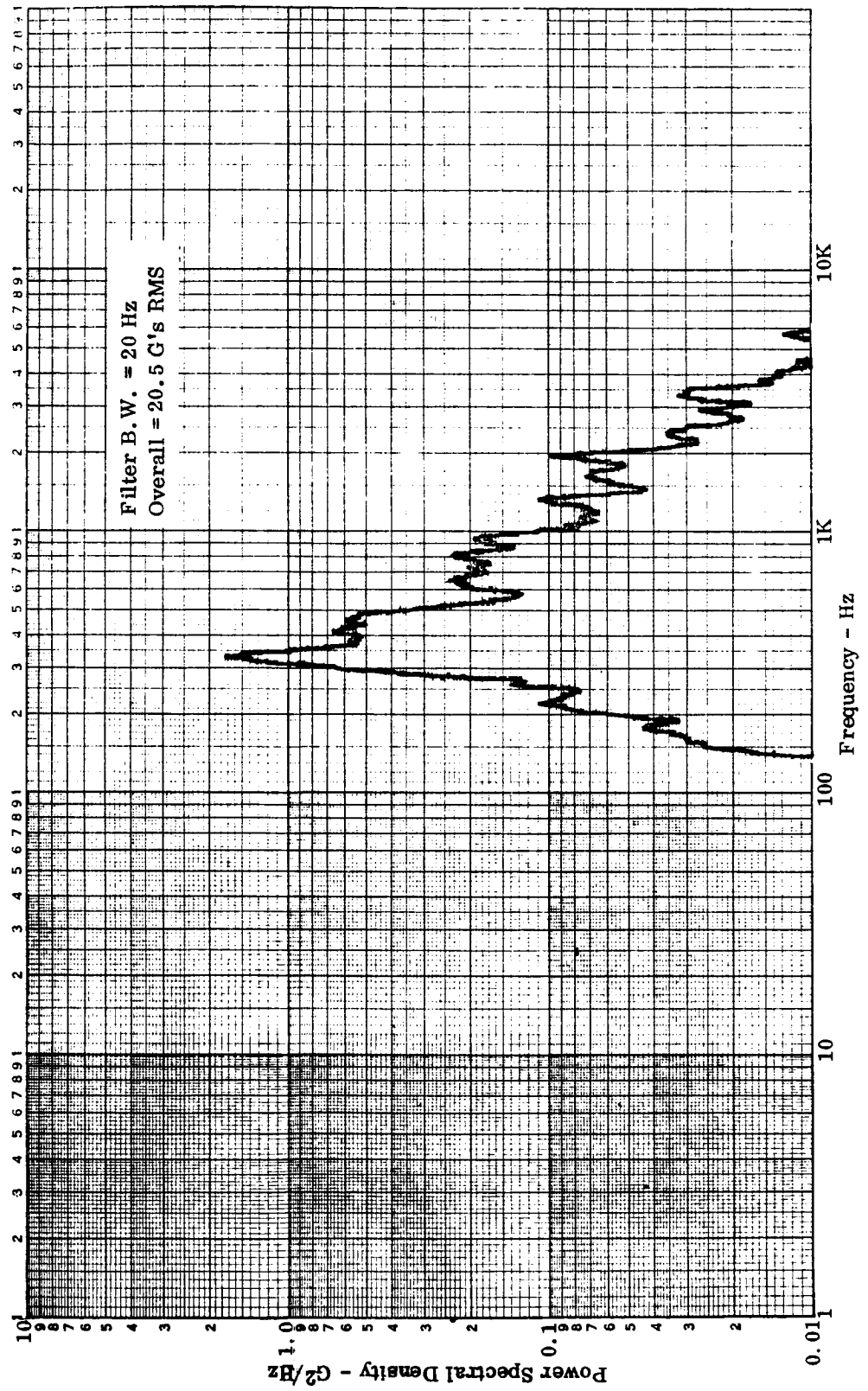


Figure E-4. Tee-Stiffened TPS, Accelerometer No. 2, 152 dB OASPL, Cycle No. 1

APPENDIX E — Continued

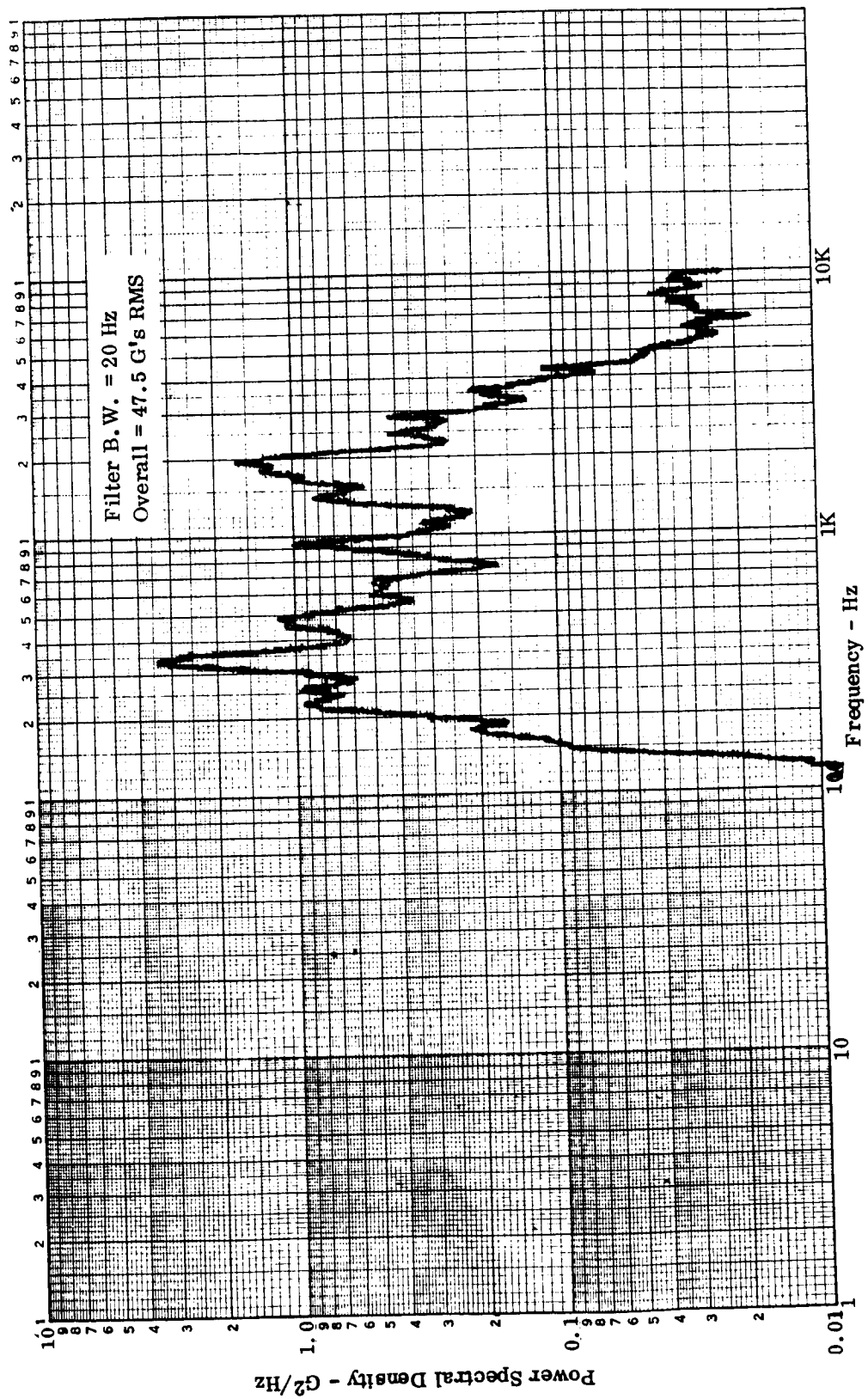


Figure E-5. Tee-Stiffened TPS, Accelerometer No. 3, 152 dB OASPL, Cycle No. 1

APPENDIX E — Continued

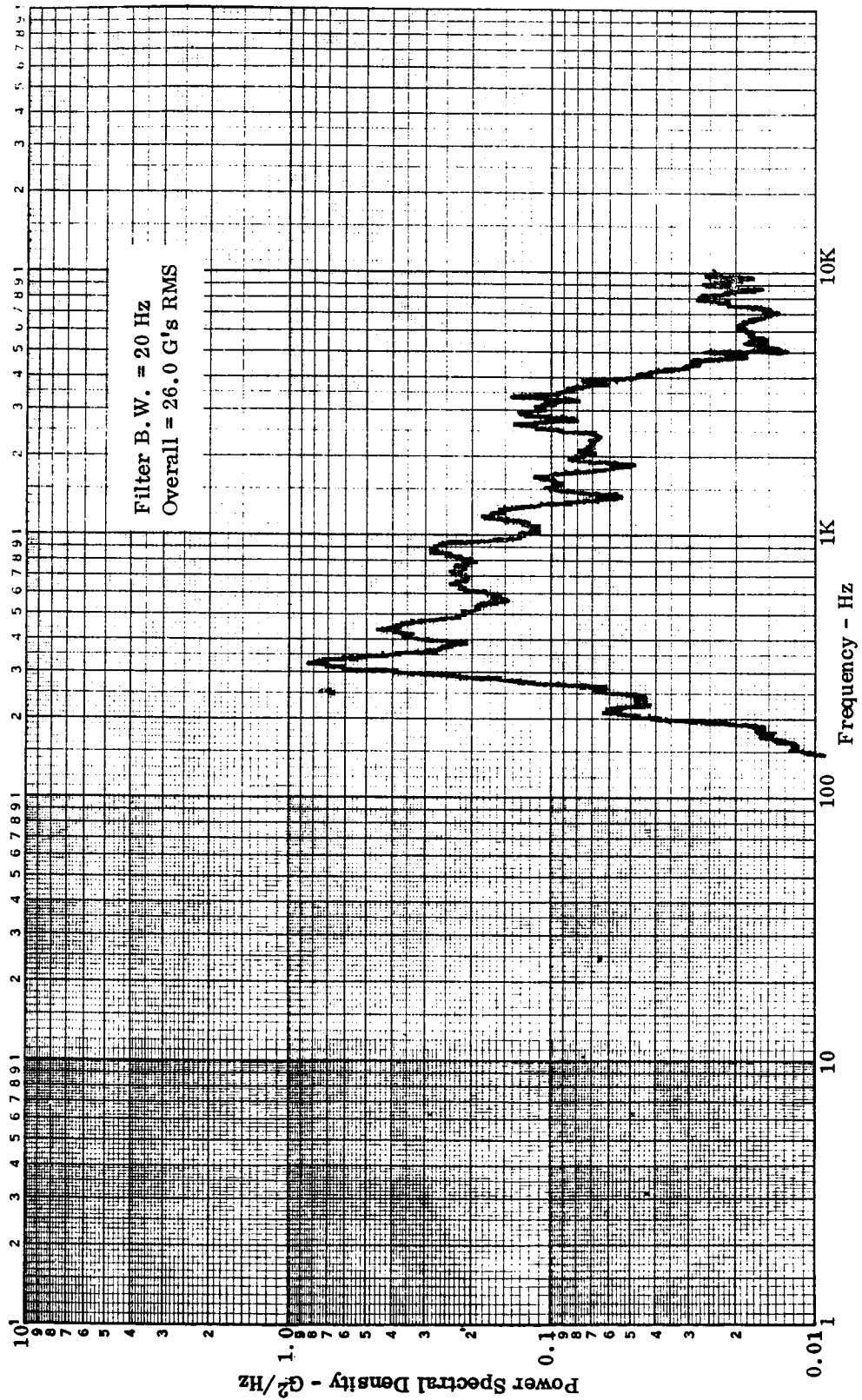


Figure E-6. Tee-Stiffened TPS, Accelerometer No. 6, 152 dB OASPL, Cycle No.1

APPENDIX E — Continued

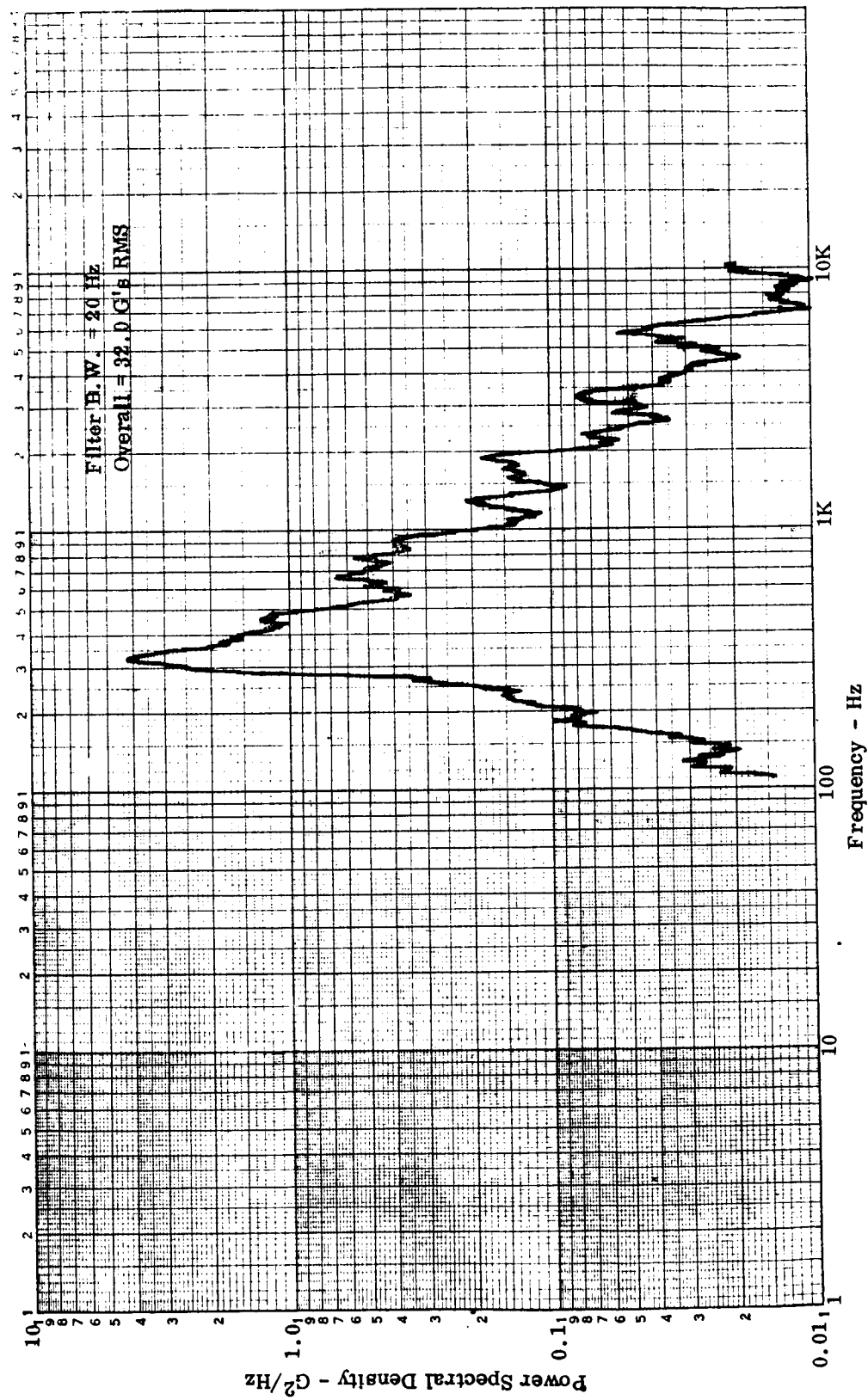


Figure E-7. Tee-Stiffened TPS, Accelerometer No. 2, 155 dB OASPL, Cycle No. 25

APPENDIX E — Continued

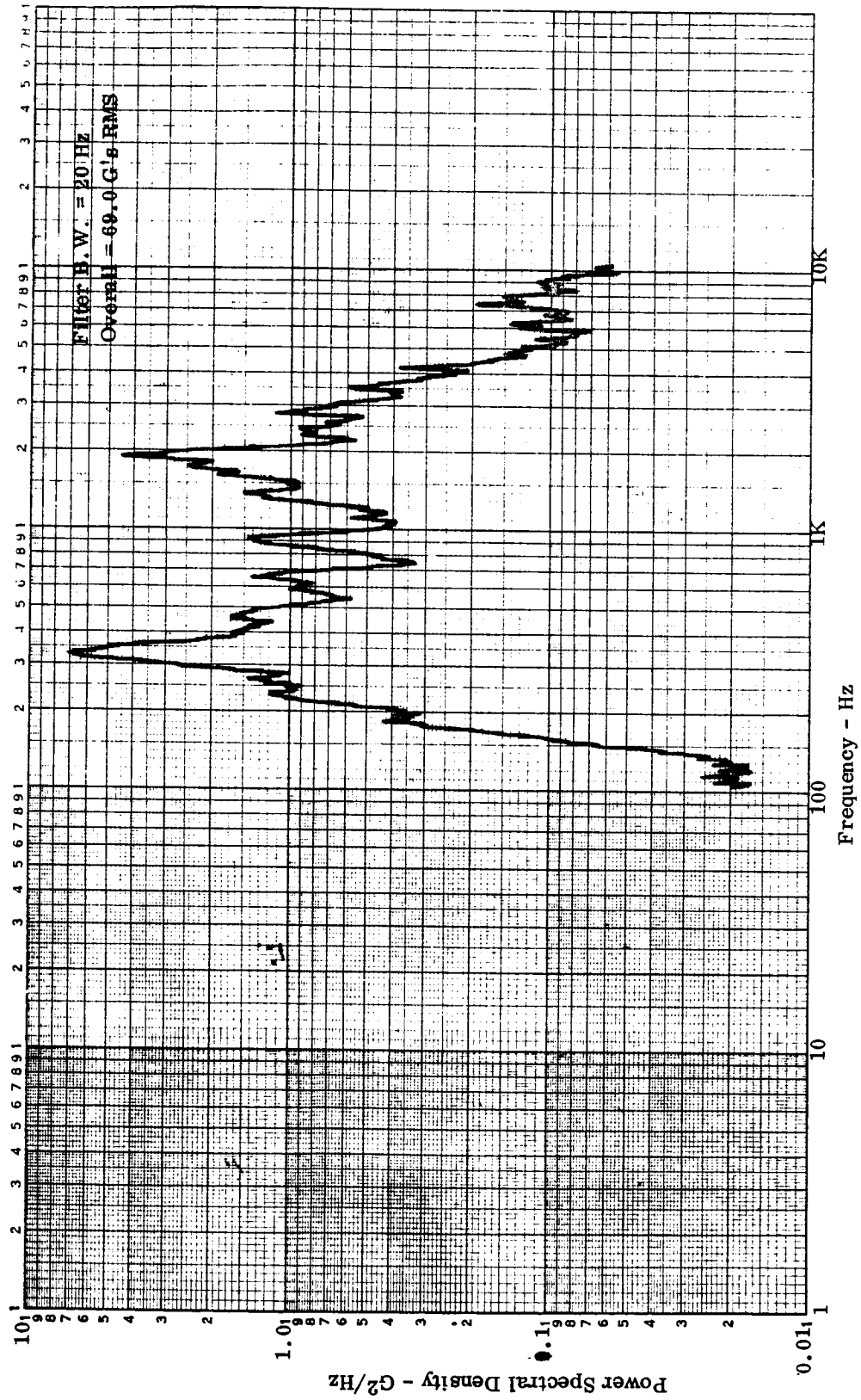


Figure E-8. Tee-Stiffened TPS, Accelerometer No. 3, 155 dB OASPL, Cycle No. 25

APPENDIX E — Continued

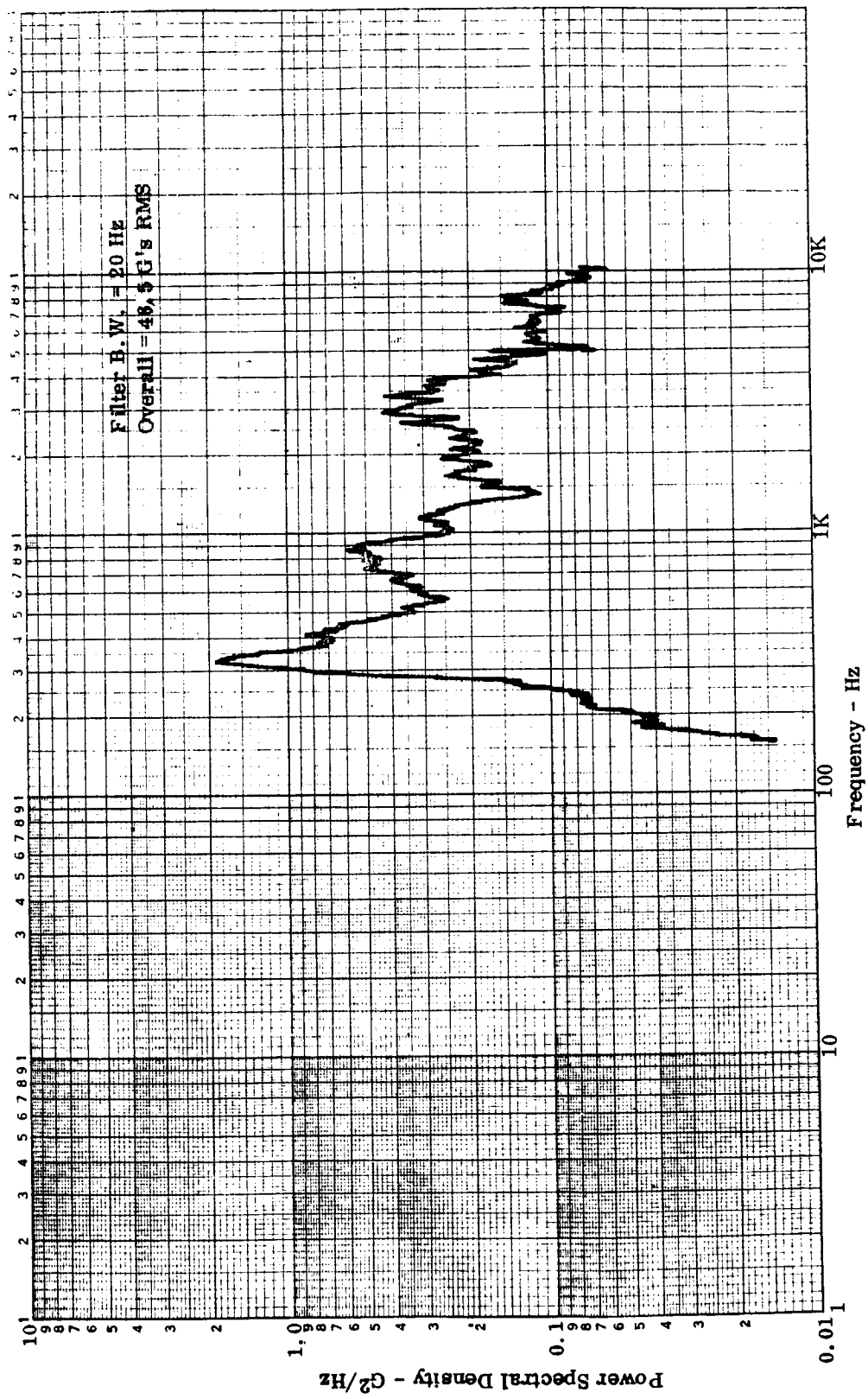


Figure E-9. Tee-Stiffened TPS, Accelerometer No. 6, 155 dB OASPL, Cycle No. 25

APPENDIX E — Continued

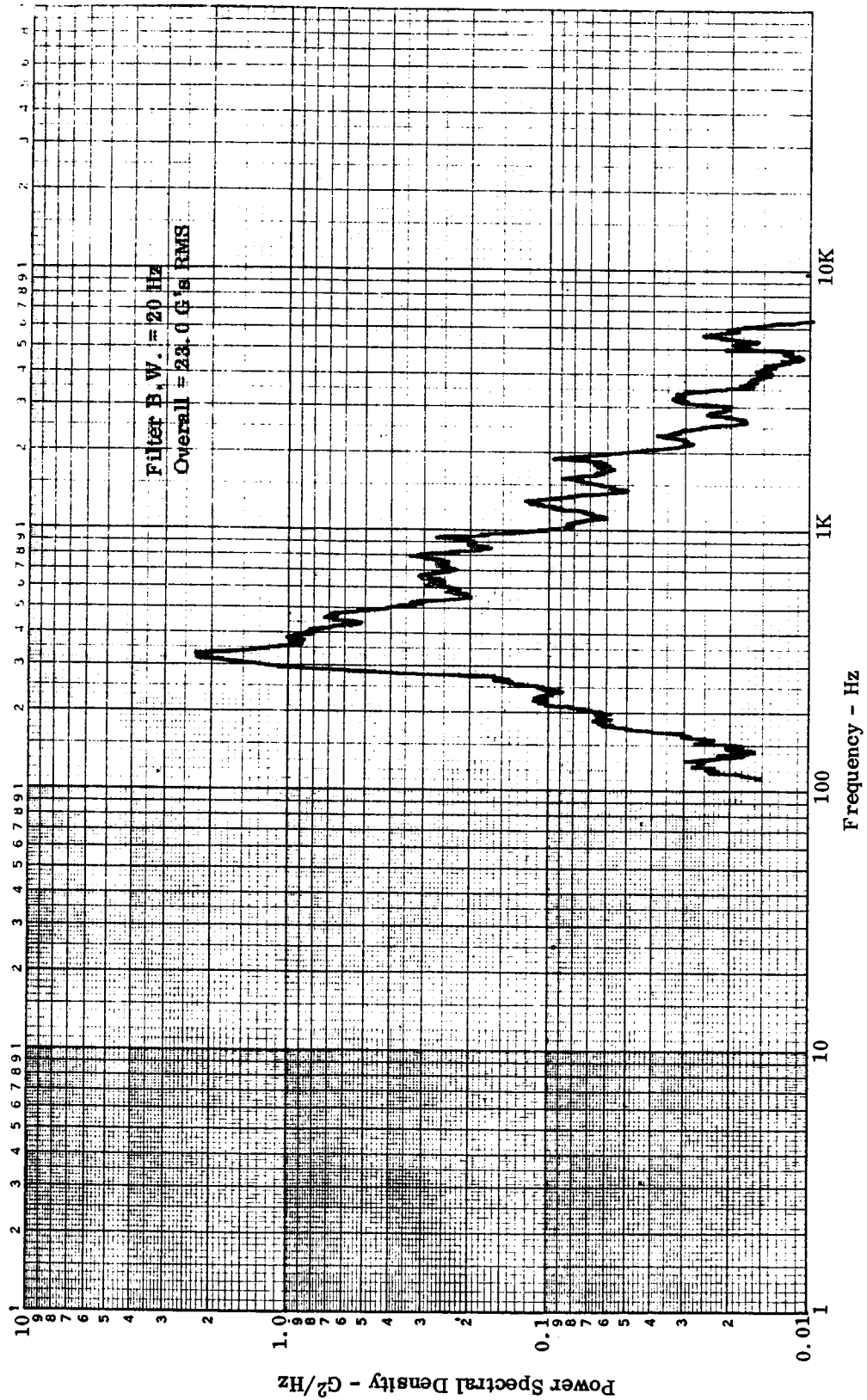


Figure E-10. Tee Stiffened TPS, Accelerometer No. 2, 152 dB OASPL, Cycle No. 25

APPENDIX E — Continued

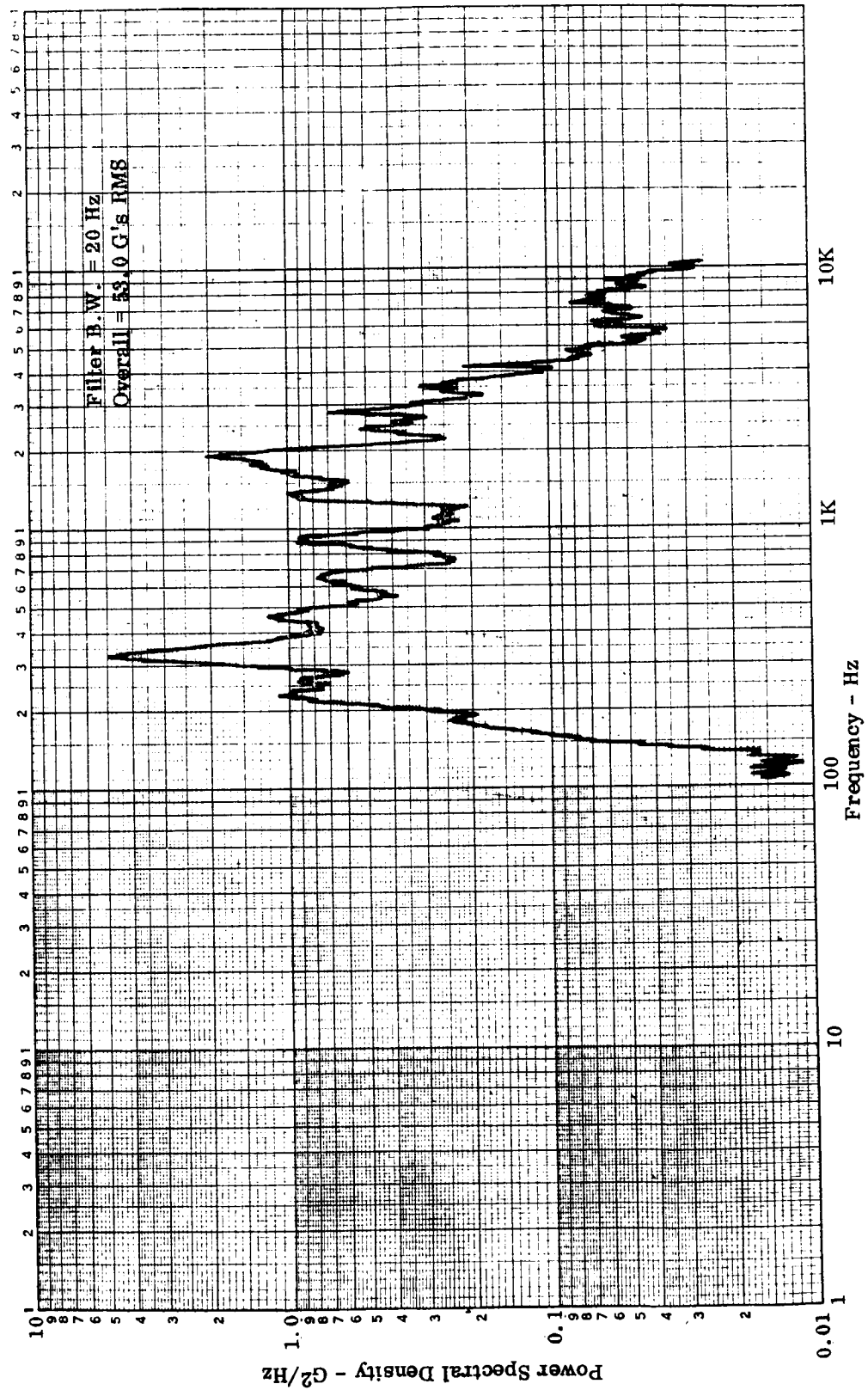


Figure E-11. Tee-Stiffened TPS, Accelerometer No. 3, 152 dB OASPL, Cycle No. 25

APPENDIX E — Continued

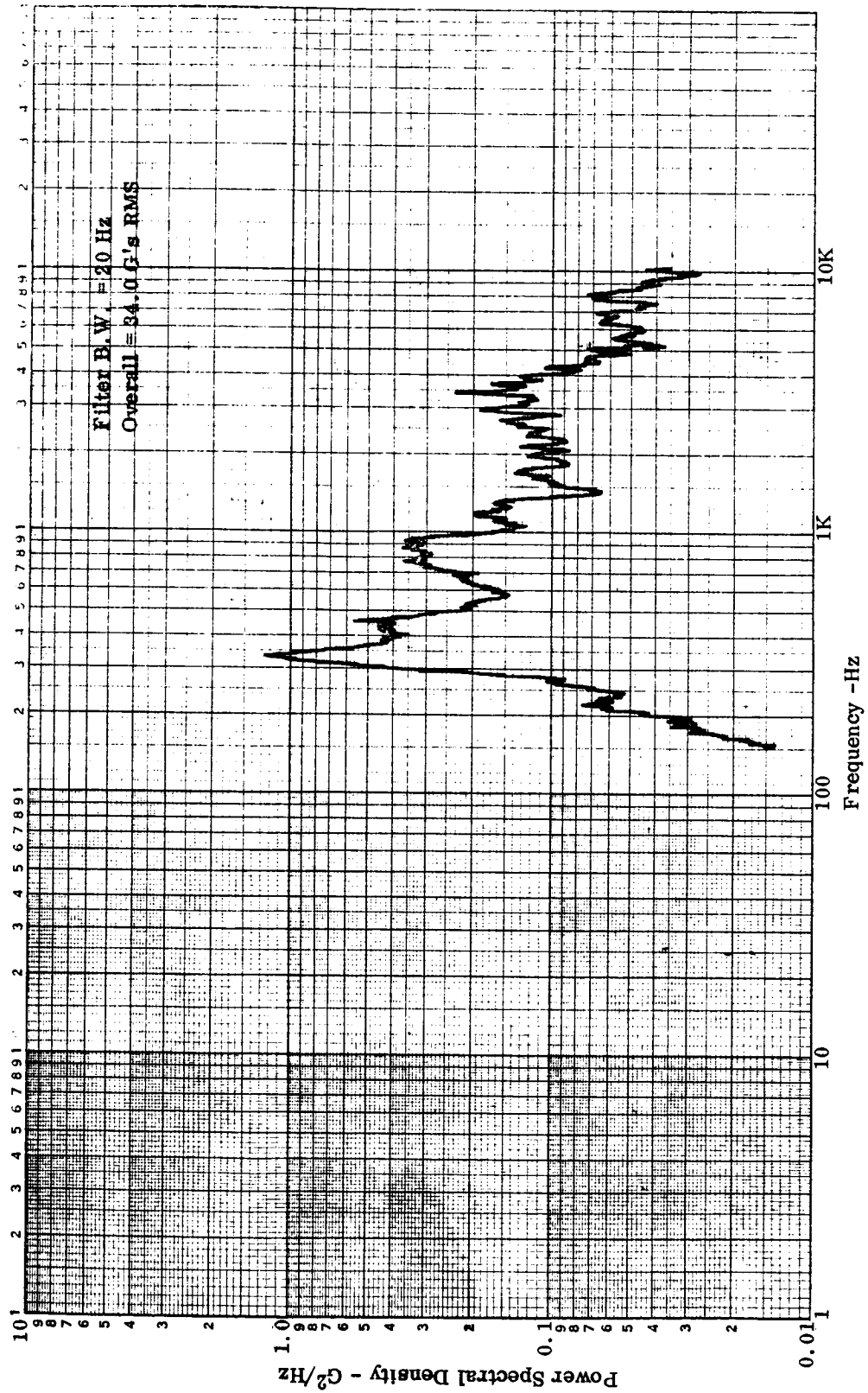


Figure E-12. Tee-Stiffened TPS, Accelerometer No. 6, 152 dB OASPL, Cycle No. 25

APPENDIX E — Continued

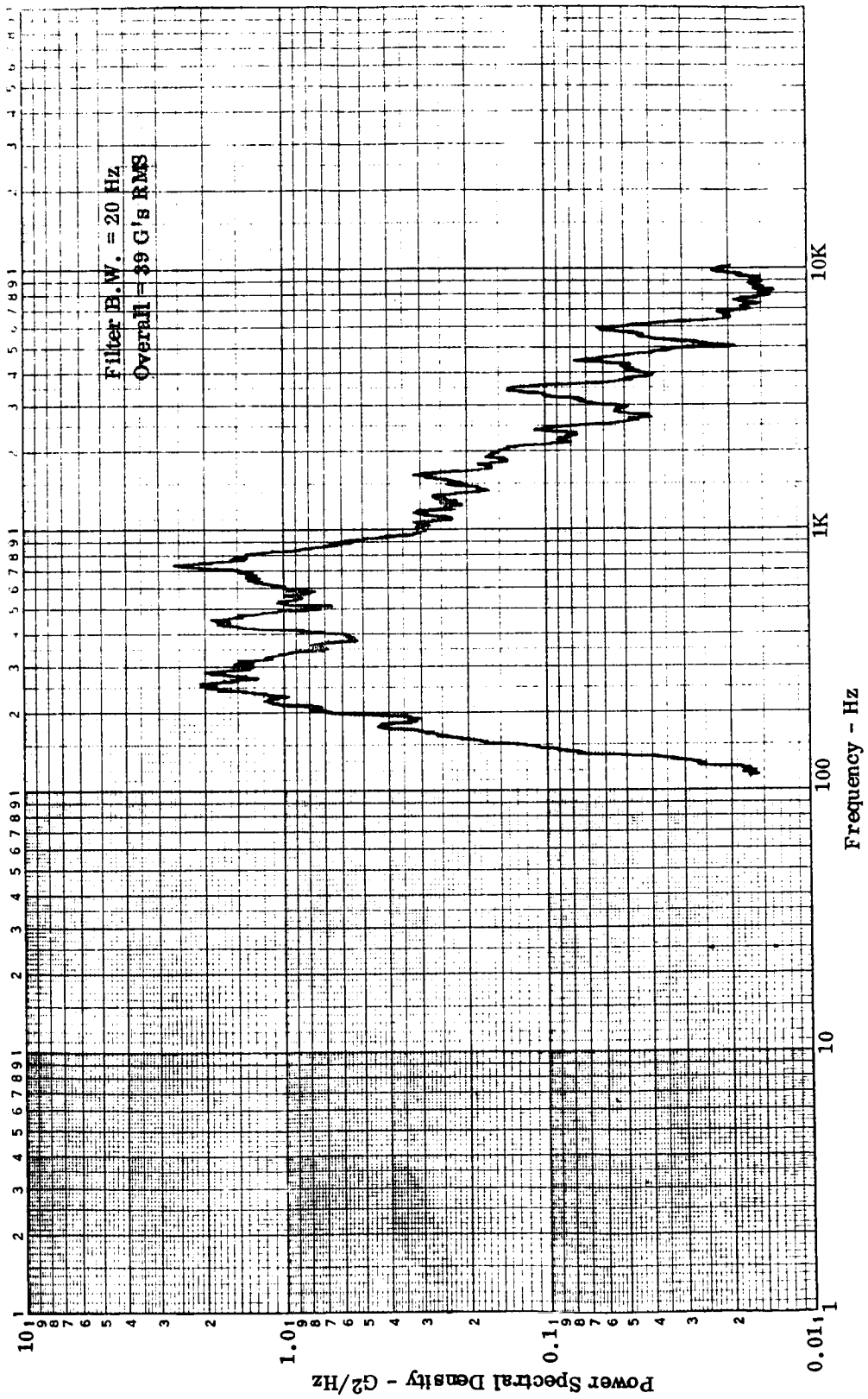


Figure E-13. Tee-Stiffened TPS, Accelerometer No. 2, 155 dB OASPL, Cycle No. 26

APPENDIX E — Continued

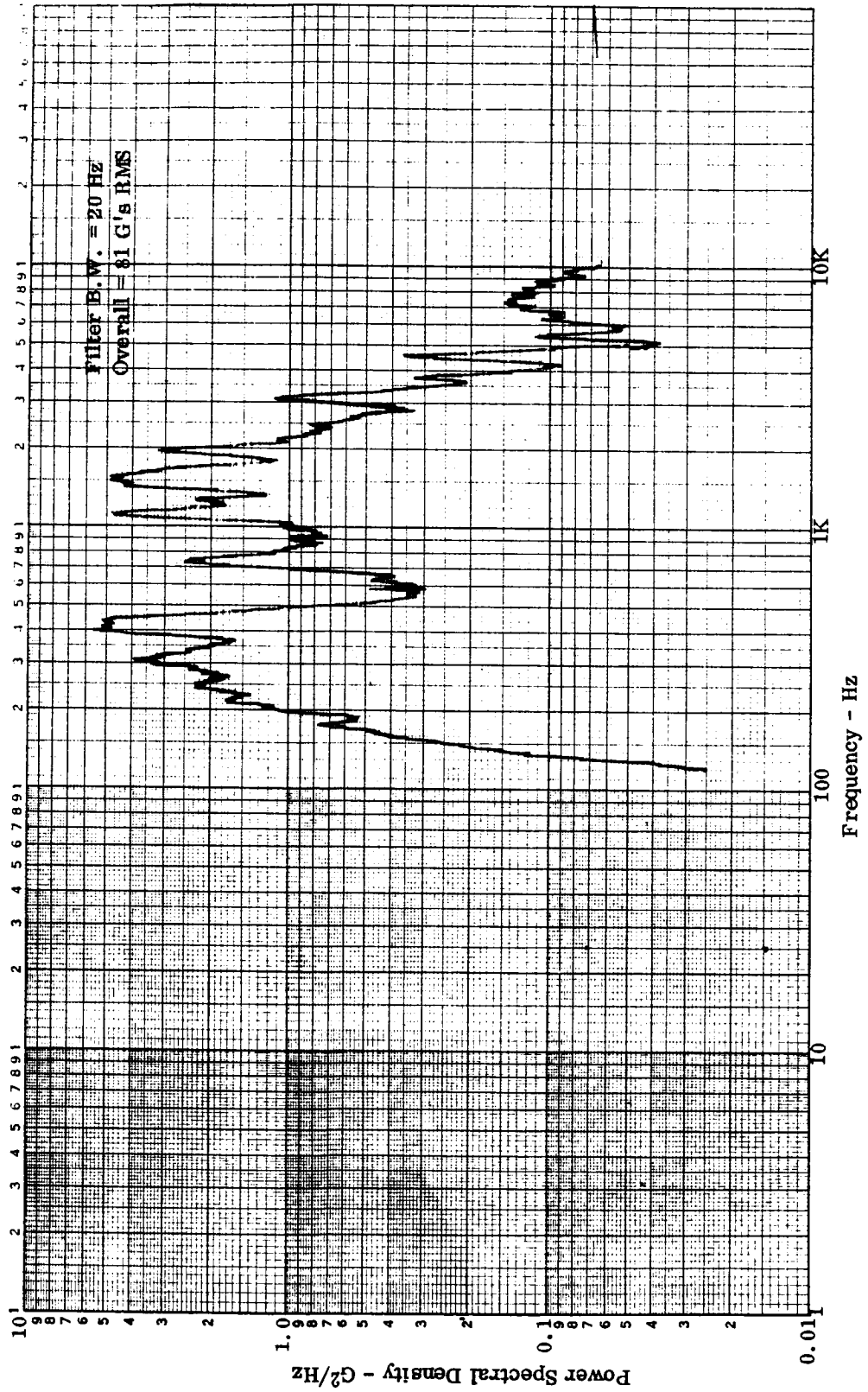


Figure E-14. Tee-Stiffened TPS, Accelerometer No. 3, 155 dB OASPL, Cycle No. 26

APPENDIX E — Continued

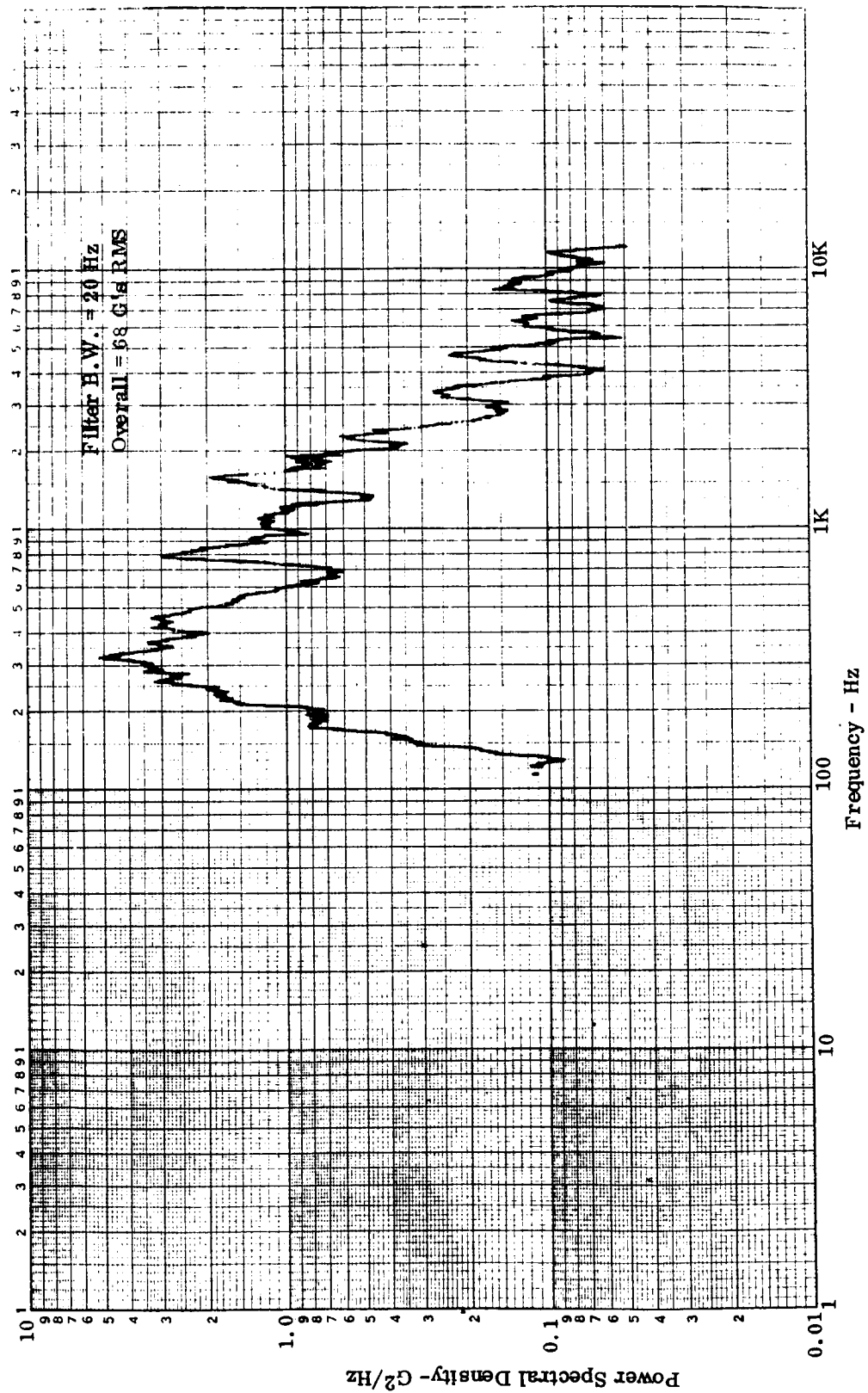


Figure E-15. Tee-Stiffened TPS, Accelerometer No. 6, 155 dB OASPL, Cycle No. 26

APPENDIX E — Continued

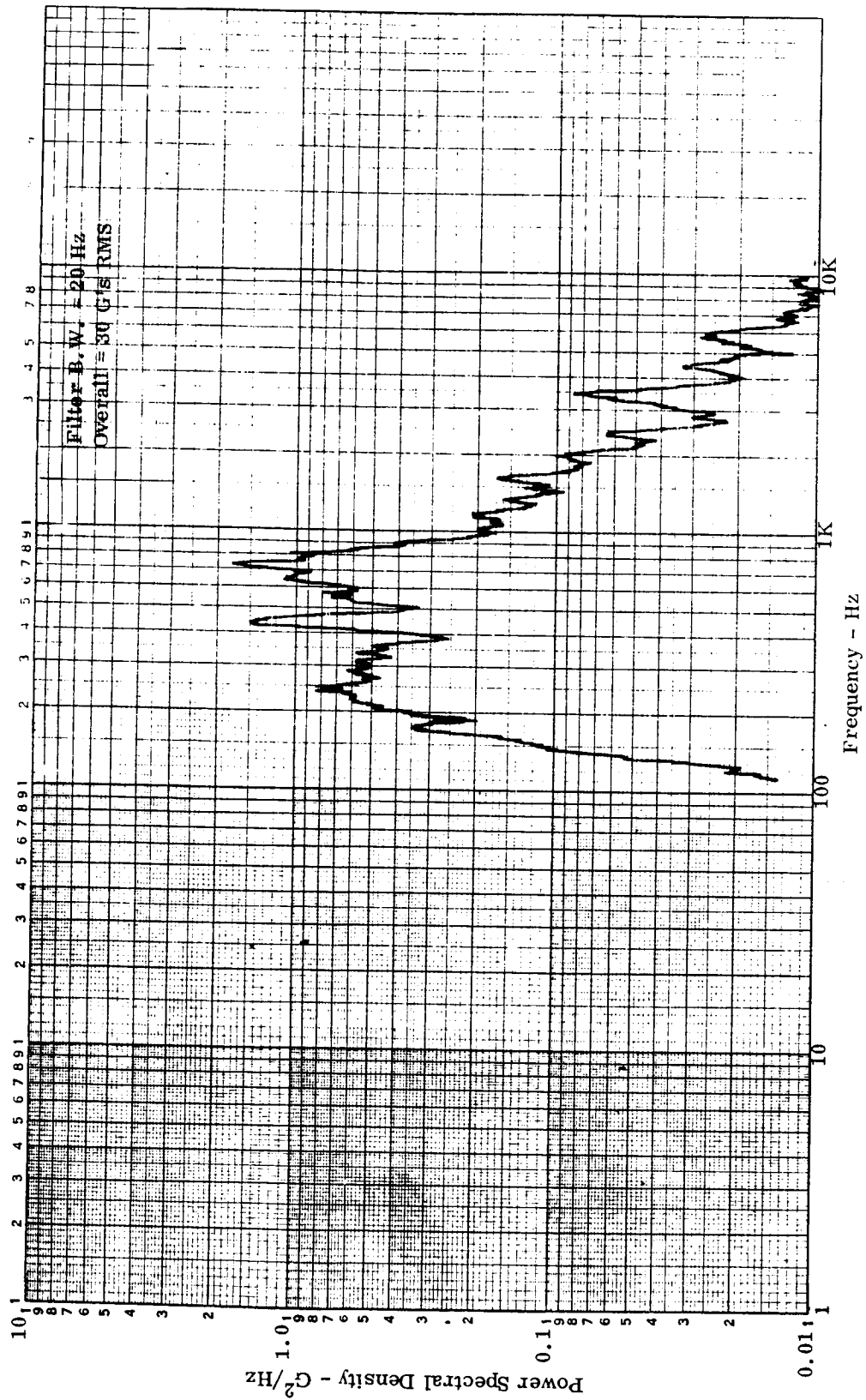


Figure E-16. Tee Stiffened TPS, Accelerometer No. 2, 152 dB OASPL, Cycle No. 26

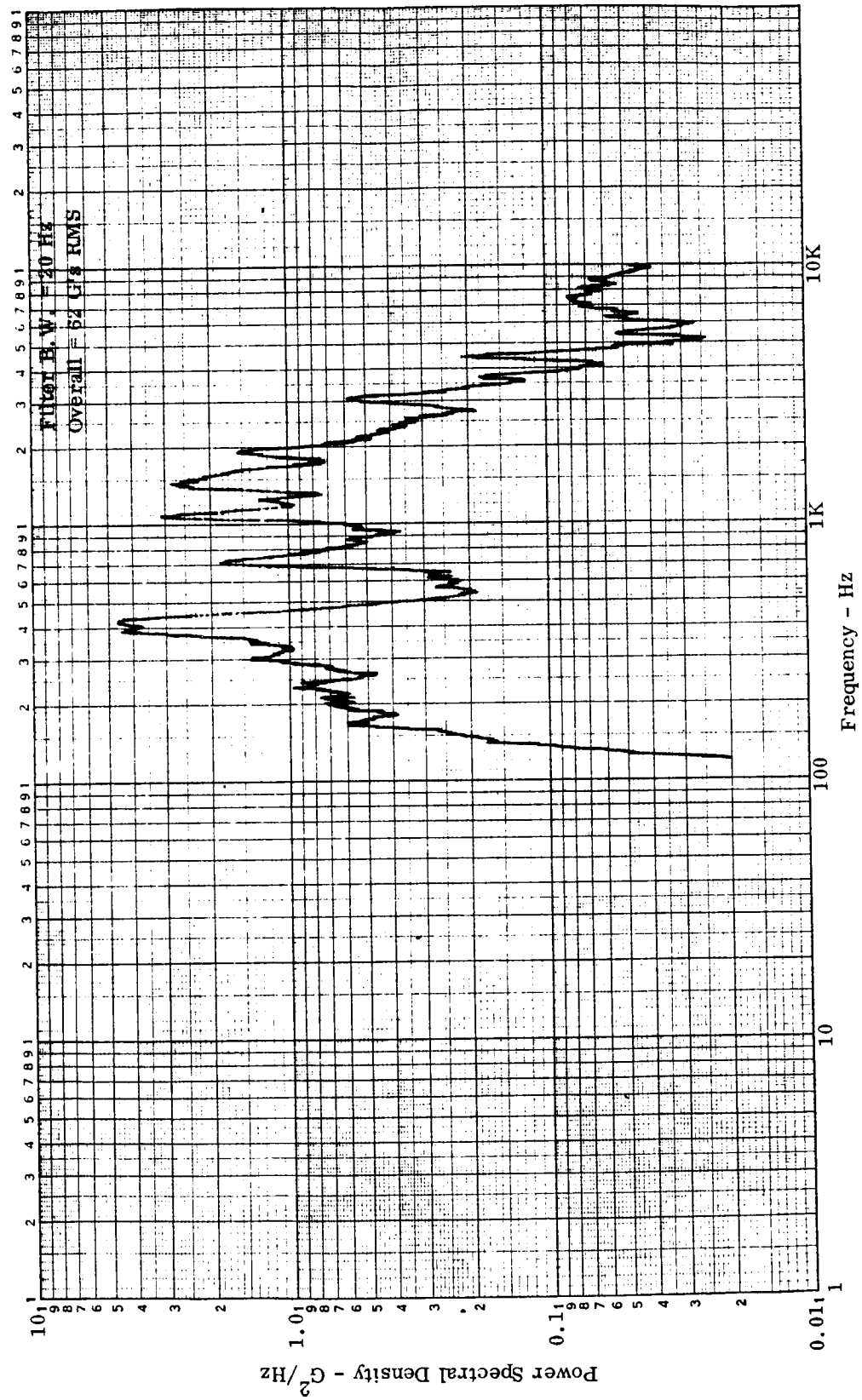


Figure E-17. Tee-Stiffened TPS, Accelerometer No. 3, 152 dB OASPL, Cycle No. 26

APPENDIX E — Continued

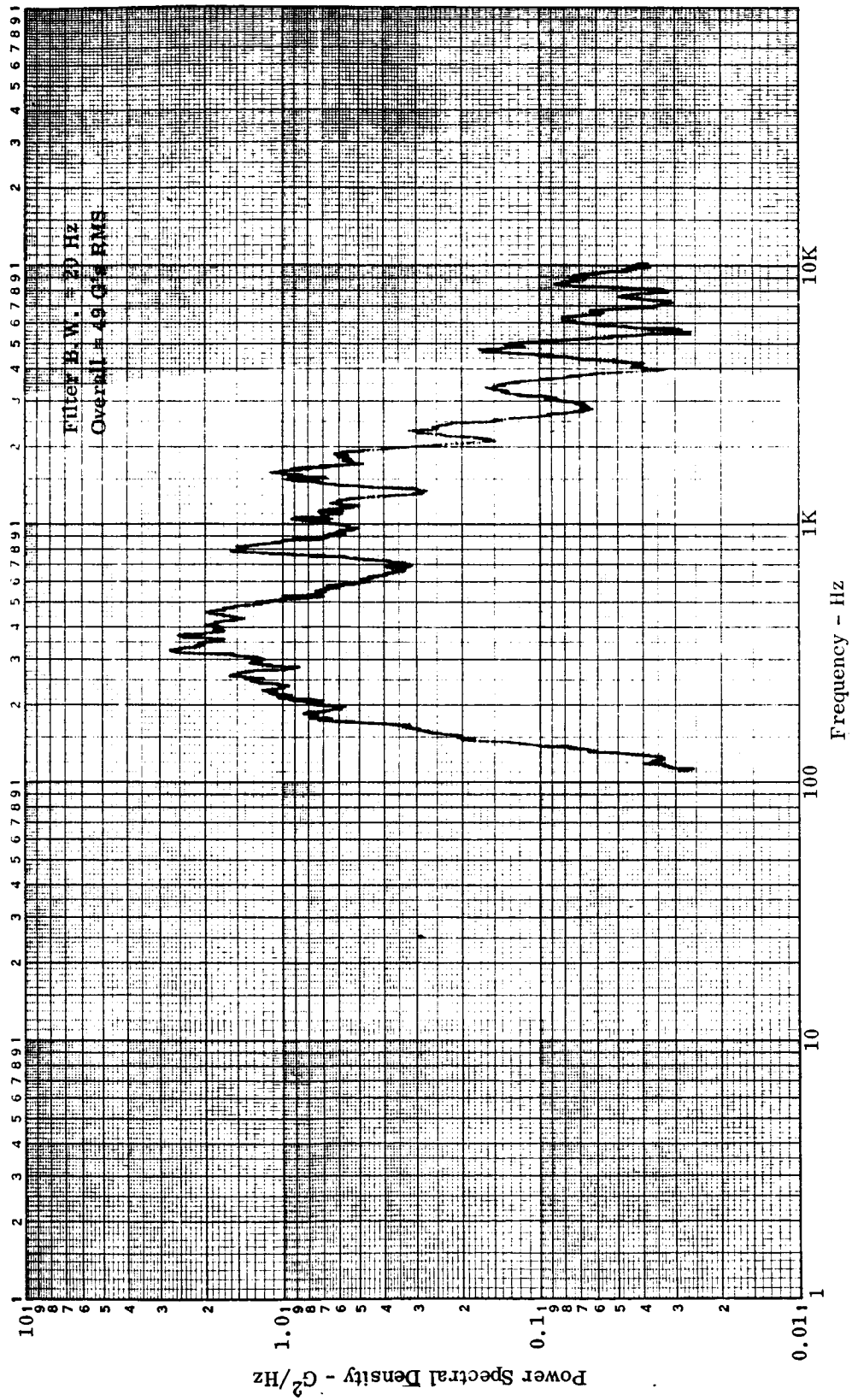


Figure E-18. Tee-Stiffened TPS, Accelerometer No. 6, 152 dB OASPL, Cycle No. 26

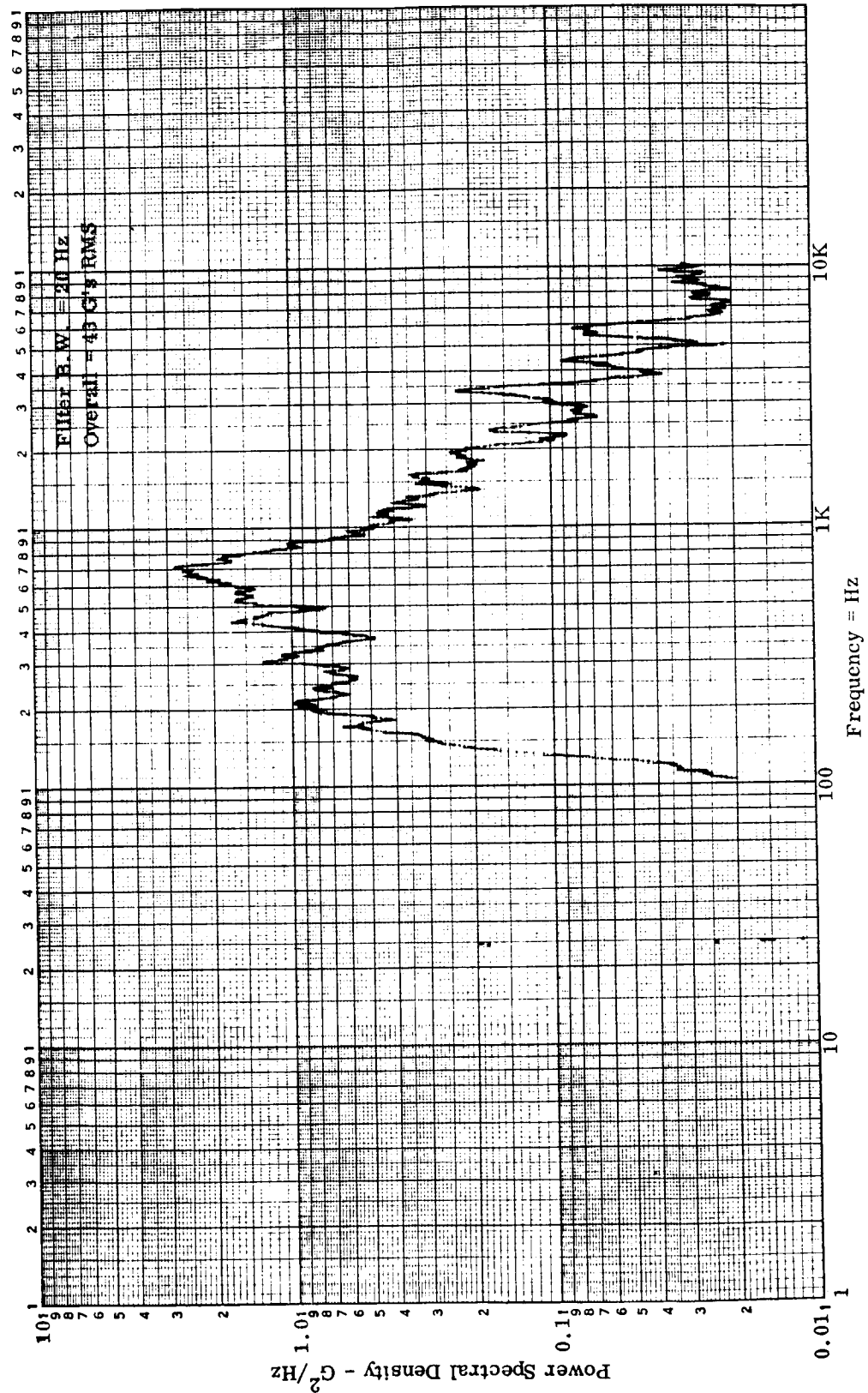


Figure E-19. Tee-Stiffened TPS, Accelerometer No. 2, 155 dB OASPL, Cycle No. 100

APPENDIX E — Continued

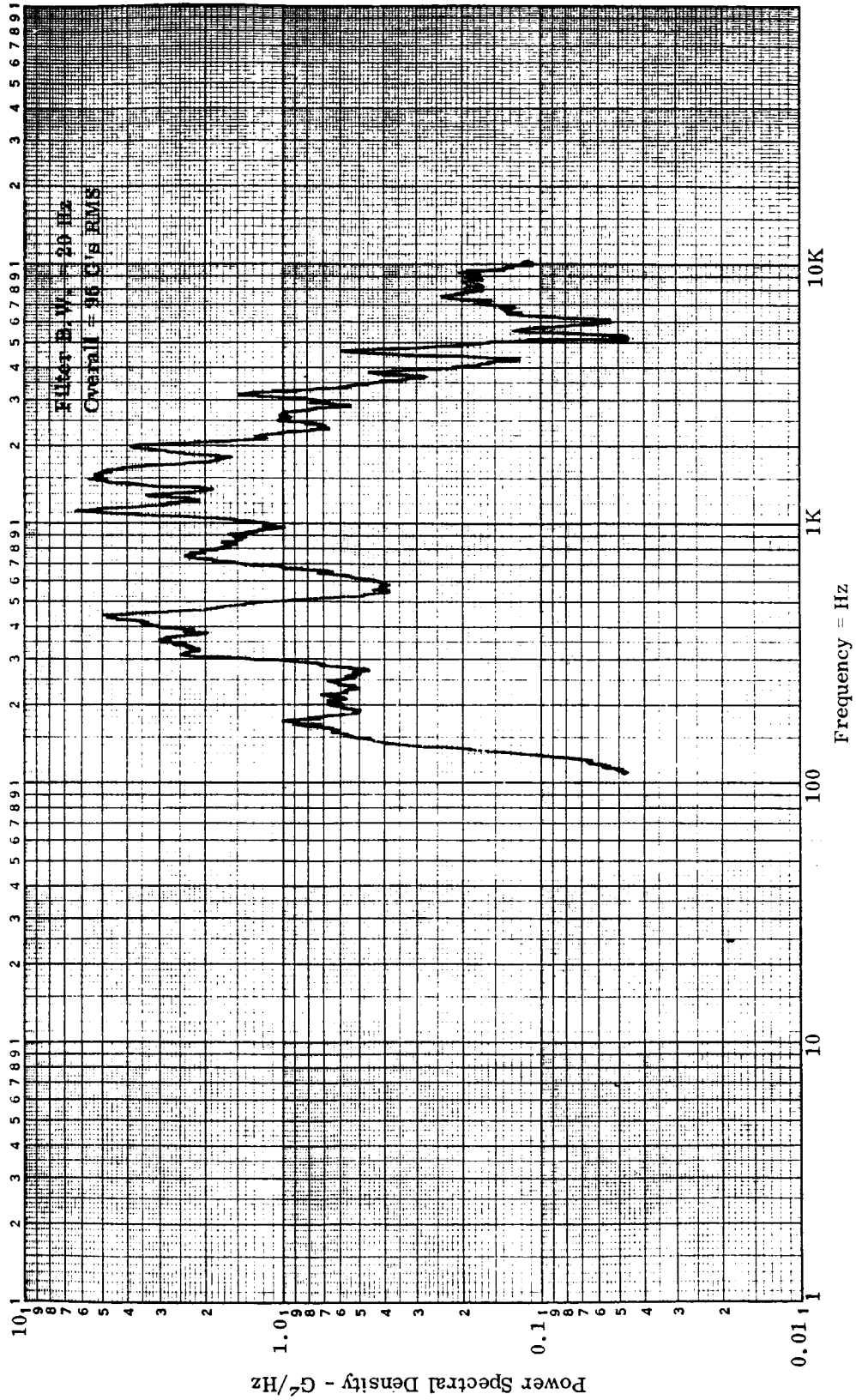


Figure E-20. Tee Stiffened TPS, Accelerometer No. 3, 155 dB OASPL, Cycle No. 100

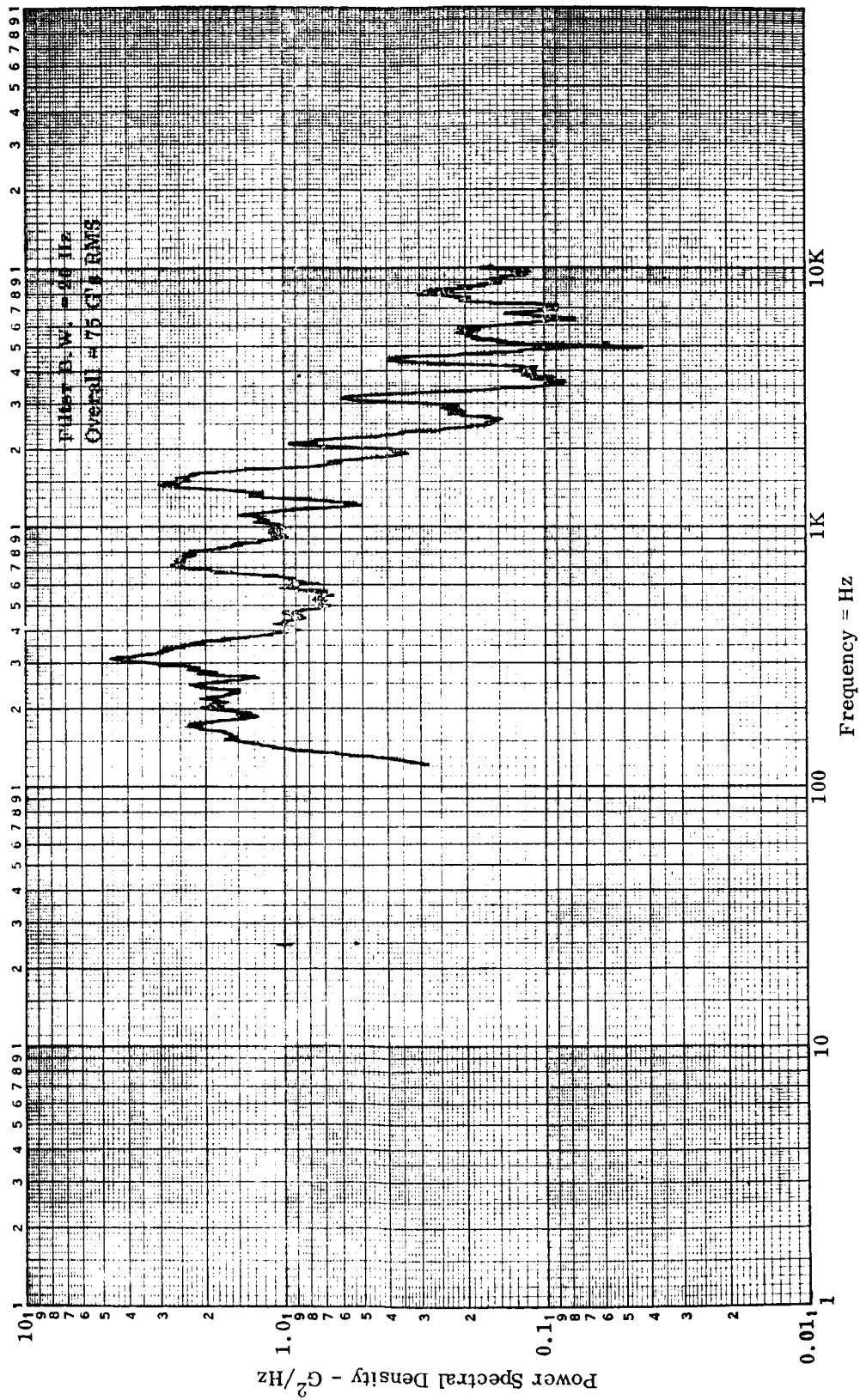


Figure E-21. Tee-Stiffened TPS, Accelerometer No. 6, 155 dB OASPL, Cycle No. 100

APPENDIX E — Continued

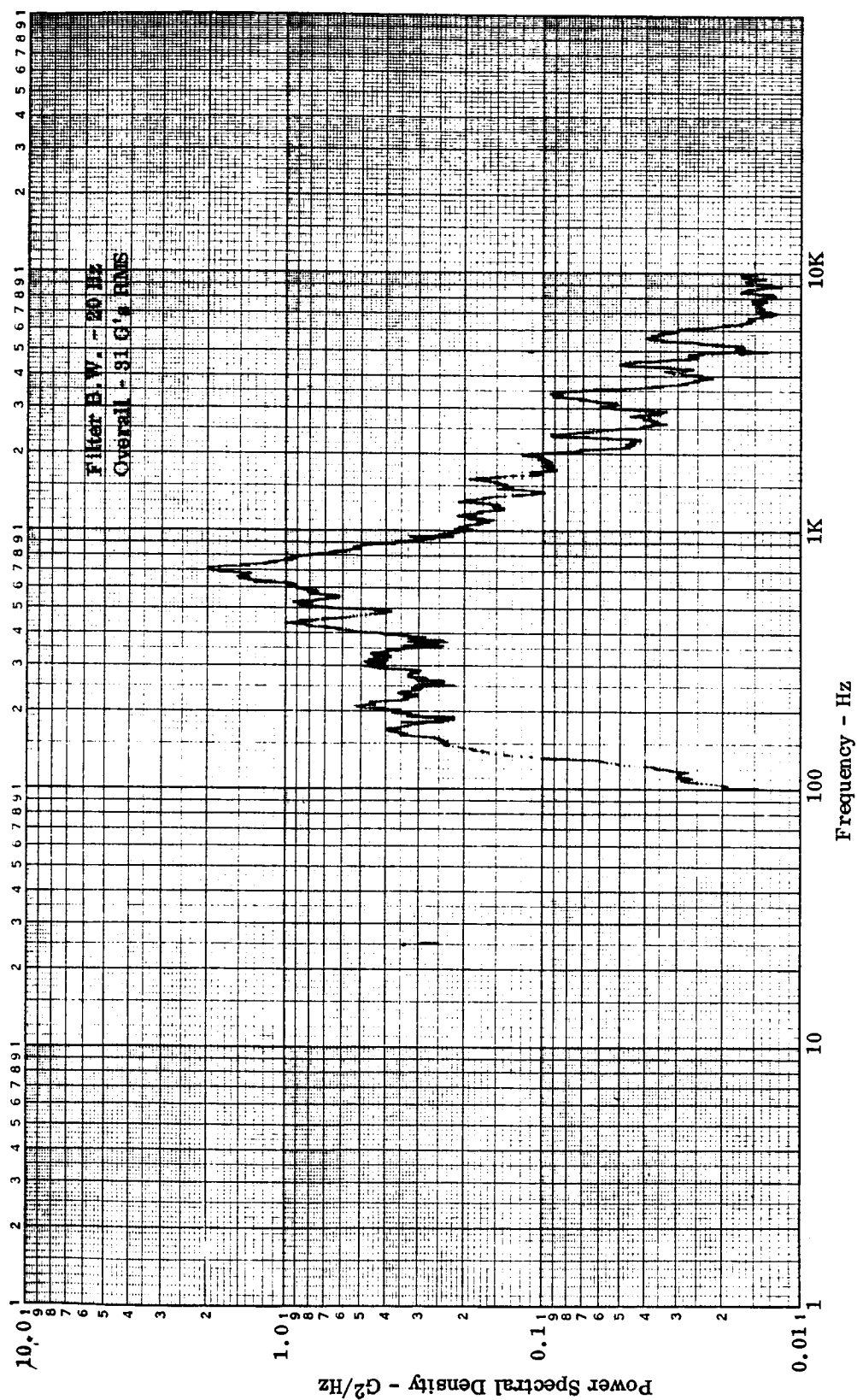


Figure E-22. Tee-Stiffened TPS, Accelerometer No. 2, 152 dB OASPL, Cycle No. 100

APPENDIX E — Continued

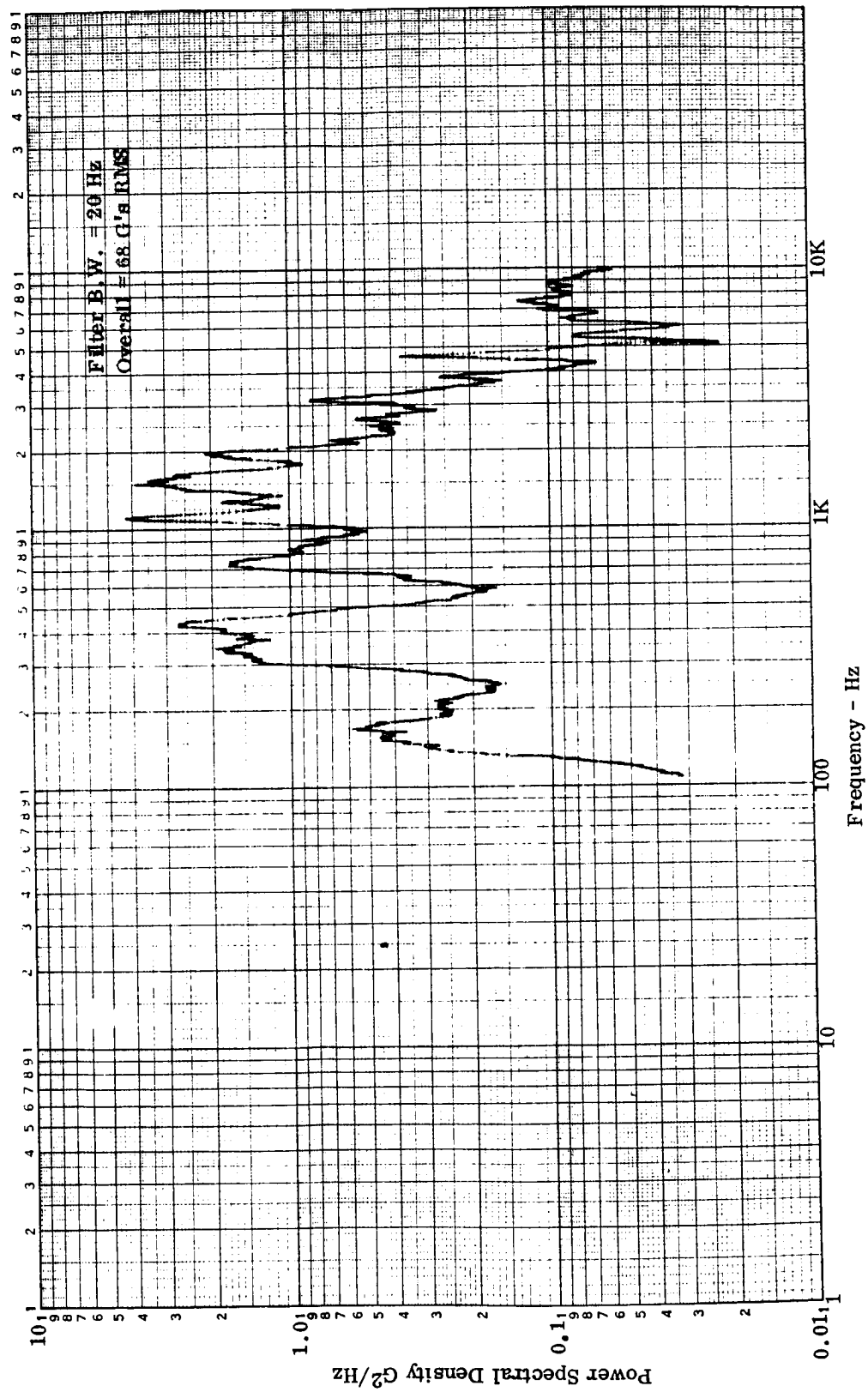


Figure E-23. Tee-Stiffened TPS, Accelerometer No. 3, 152 dB OASPL, Cycle No. 100

APPENDIX E — Continued

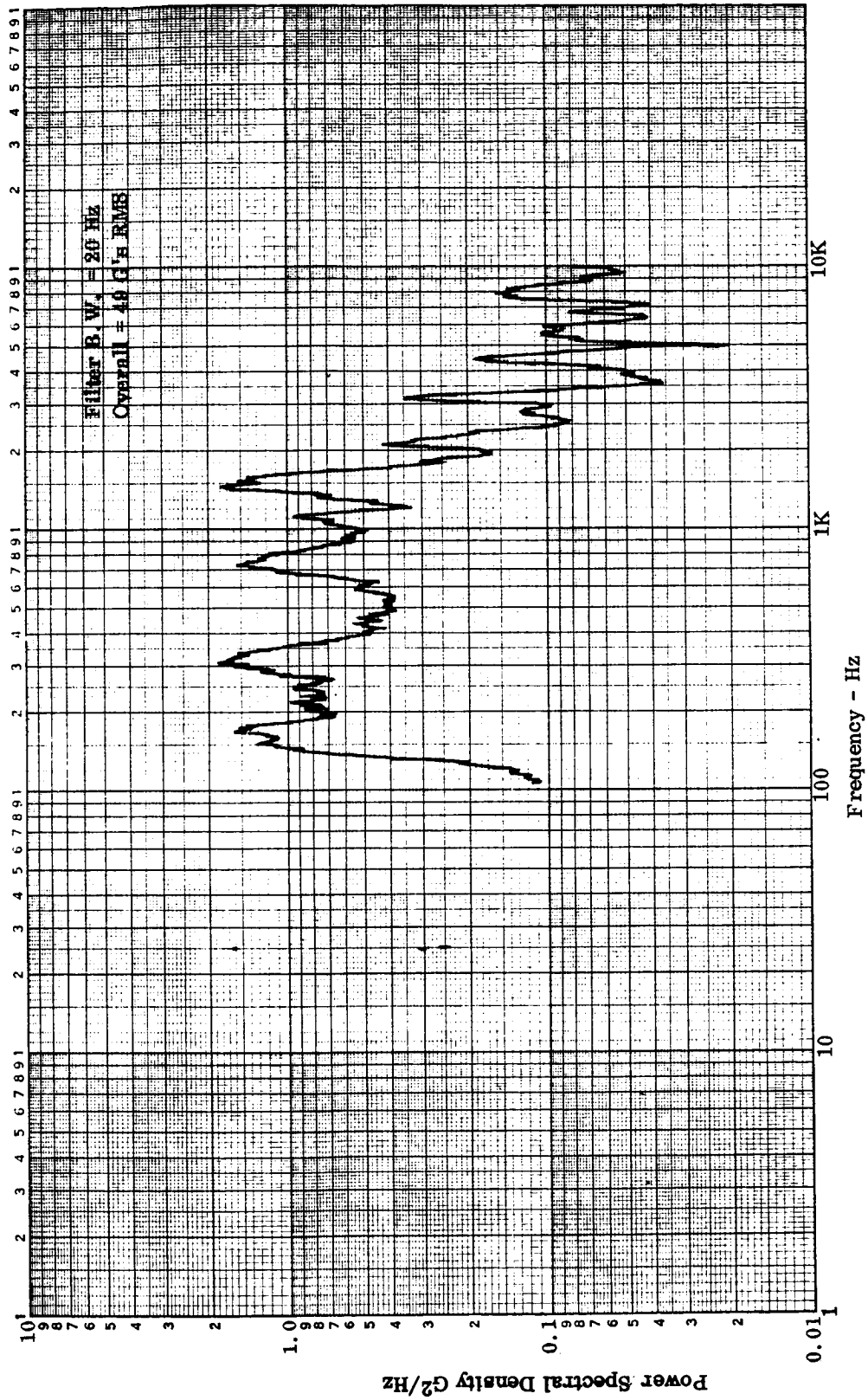


Figure E-24. Tee-Stiffened TPS, Accelerometer No. 6, 152 dB OASPL, Cycle No. 100

APPENDIX E — Continued

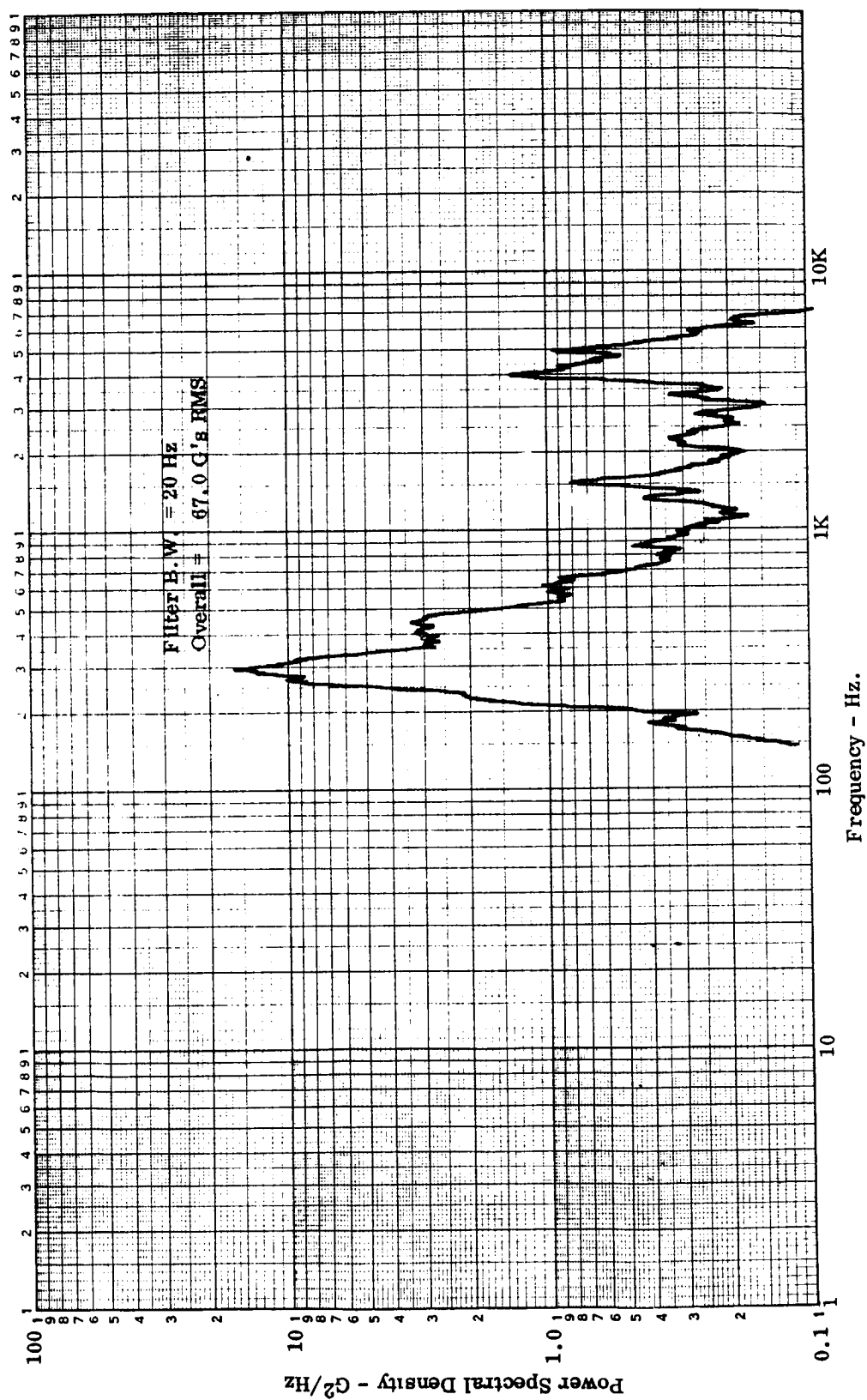


Figure E-25. Open Corrugation TPS, Accelerometer No. 2, 155 dB OASPL, Cycle No.1

APPENDIX E — Continued

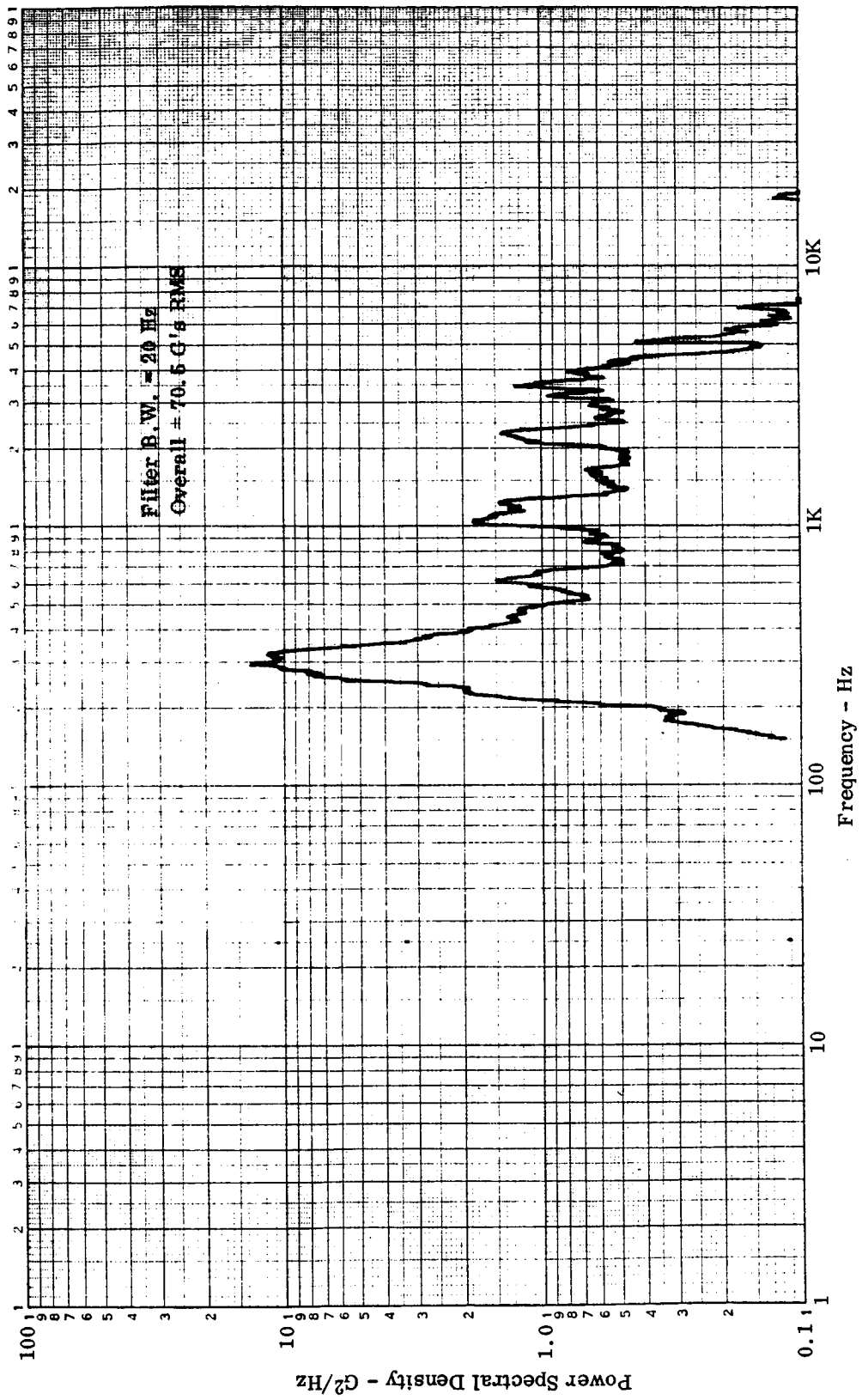


Figure E-26. Open Corrugation TPS, Accelerometer No. 3, 155 dB OASPL, Cycle No. 1

APPENDIX E — Continued

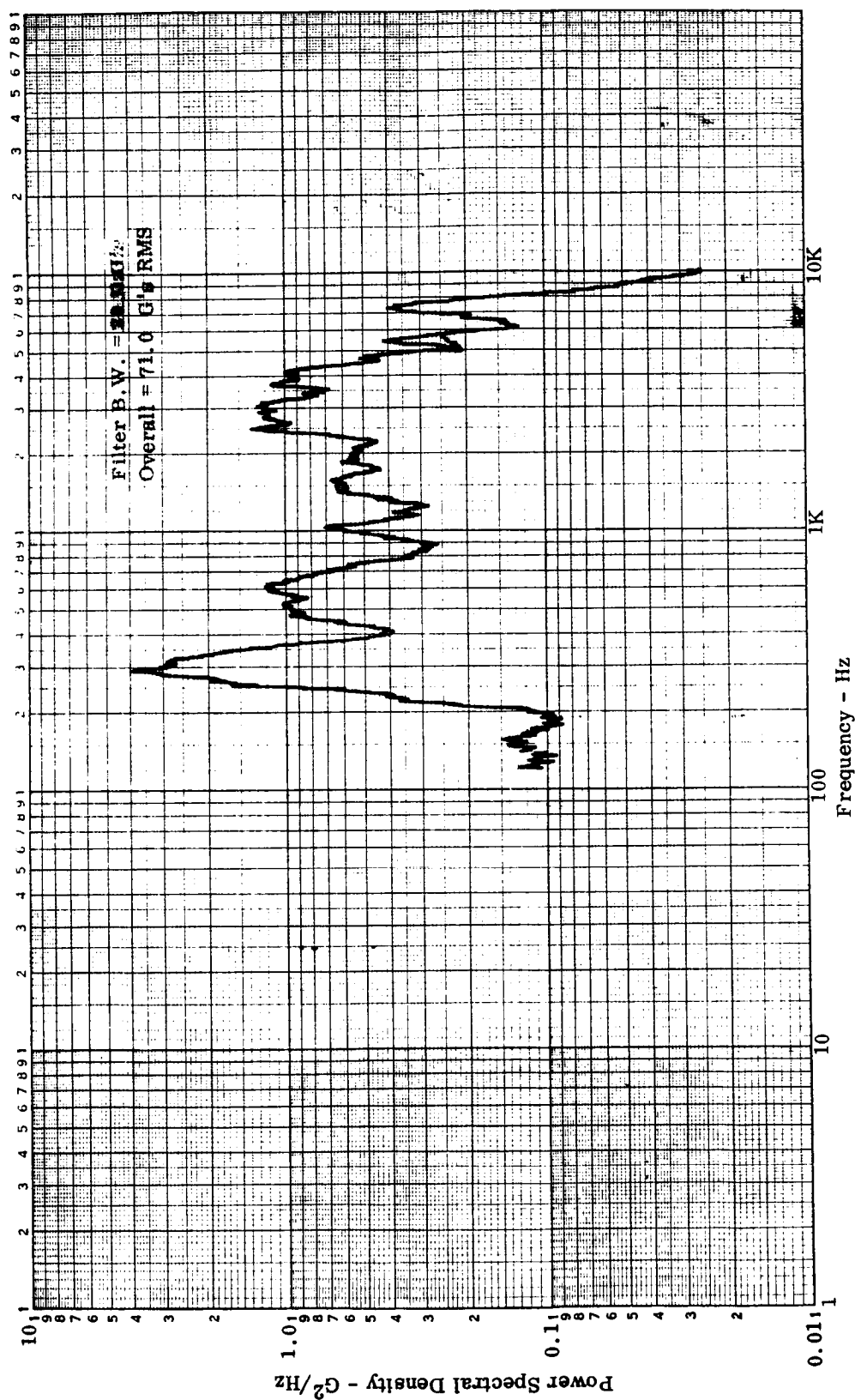


Figure E-27. Open Corrugation TPS, Accelerometer No. 7, 155 dB OASPL, Cycle No. 1

APPENDIX E — Continued

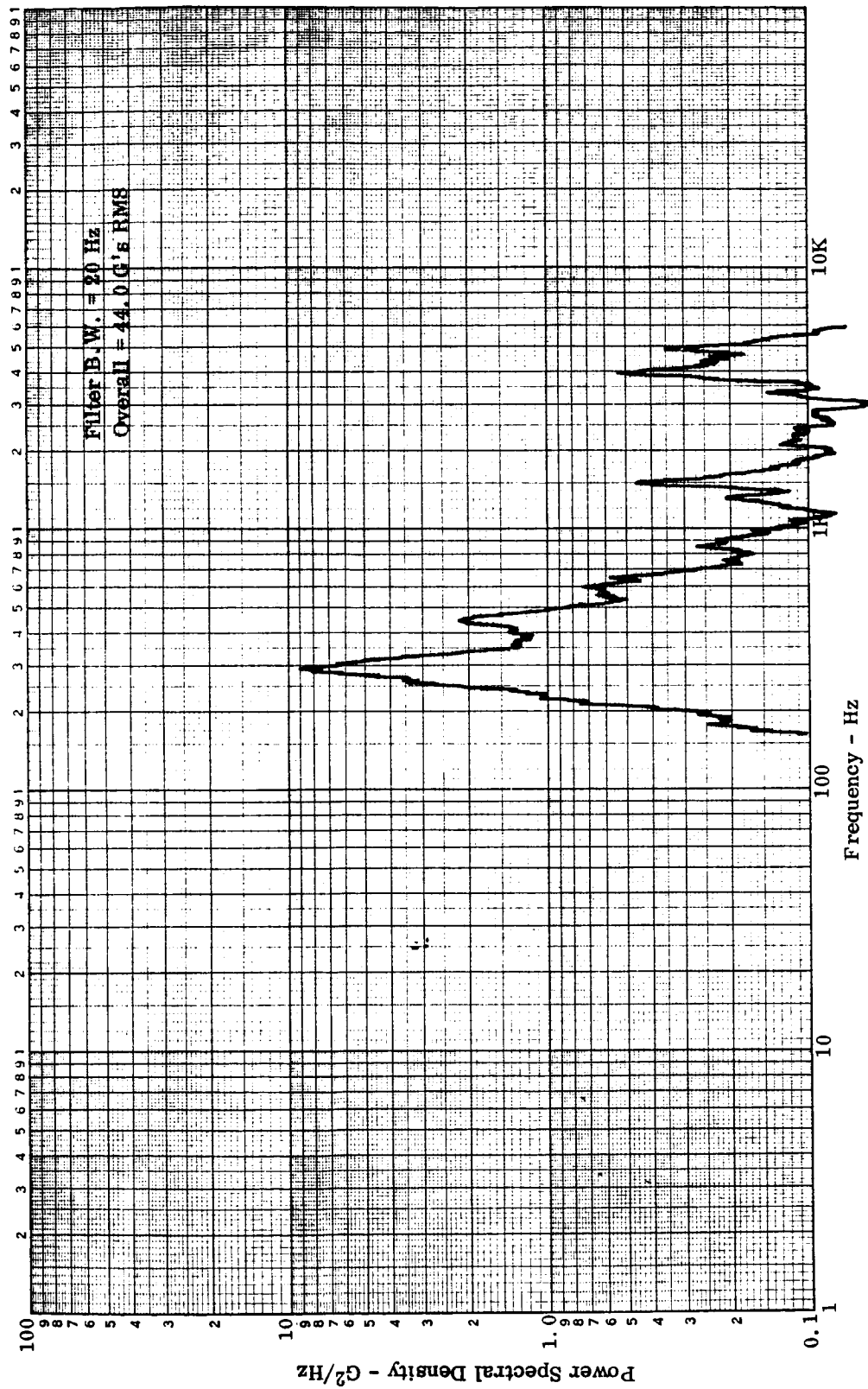


Figure E-28. Open Corrugation TPS, Accelerometer No. 2, 152 dB OASPL, Cycle No. 1

APPENDIX E — Continued

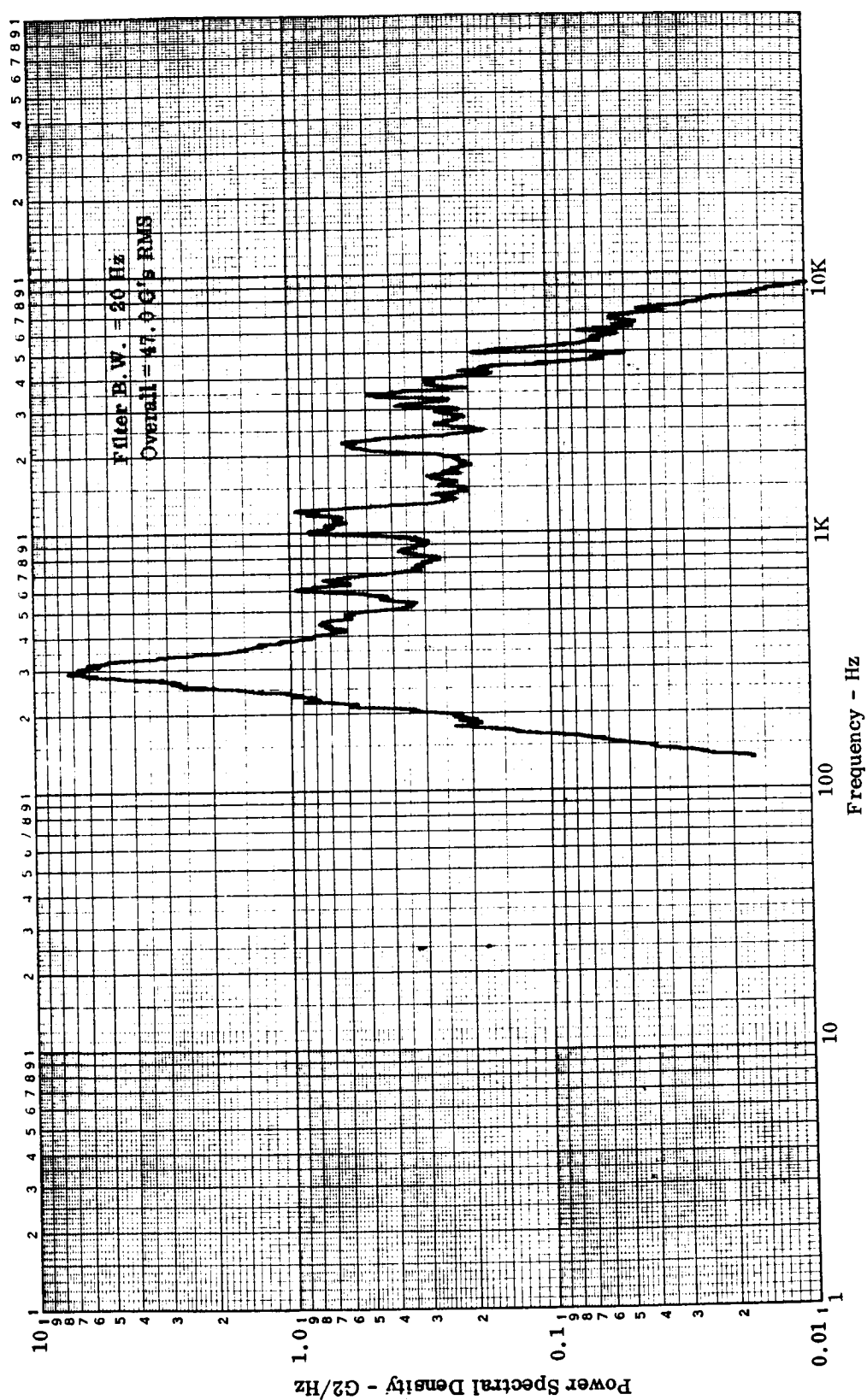


Figure E-29. Open Corrugation TPS, Accelerometer No. 3, 152 dB, OASPL, Cycle No. 1

APPENDIX E — Continued

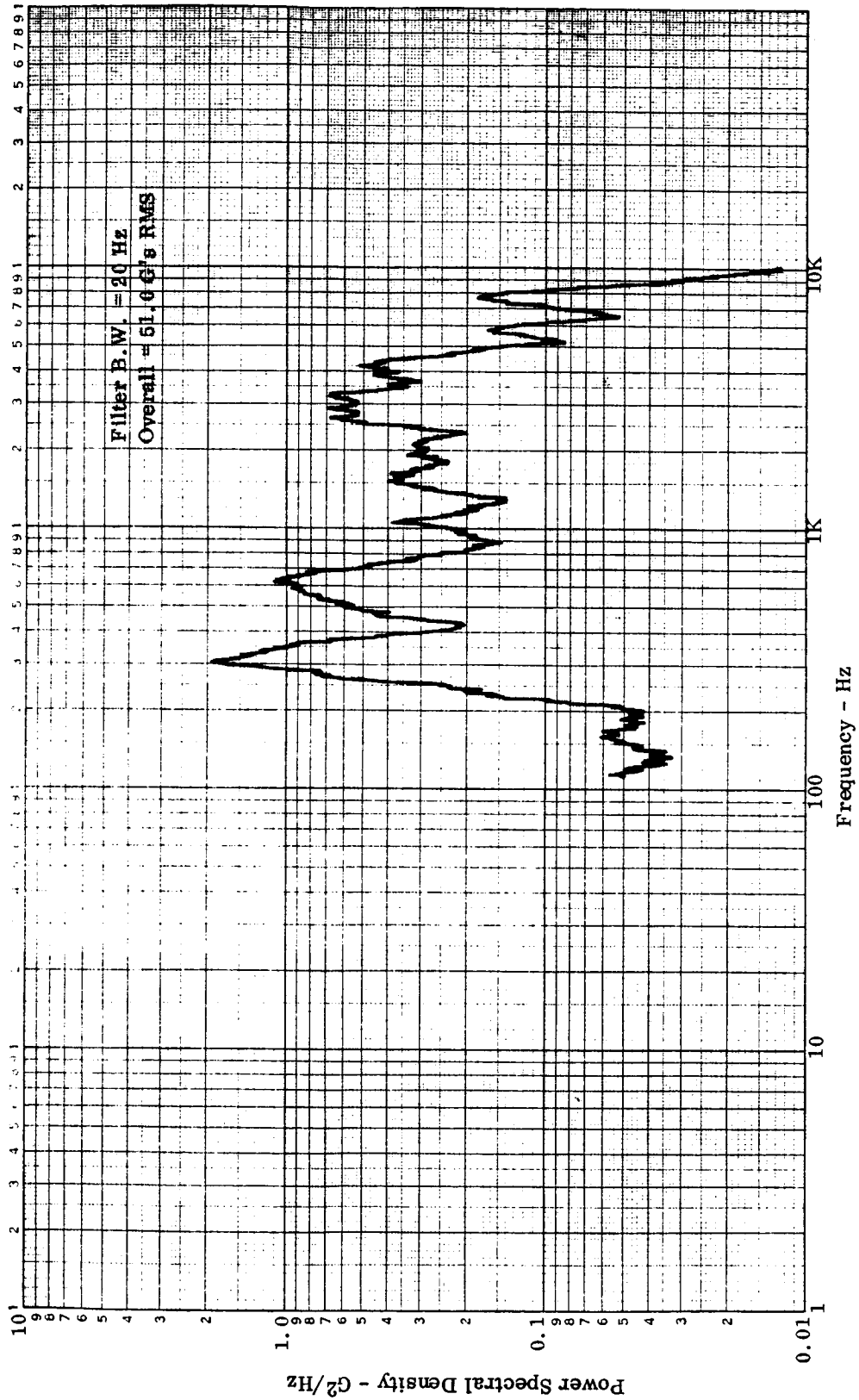


Figure E-30. Open Corrugation TPS, Accelerometer No. 7, 152 dB, OASPL, Cycle No. 1

APPENDIX E — Continued

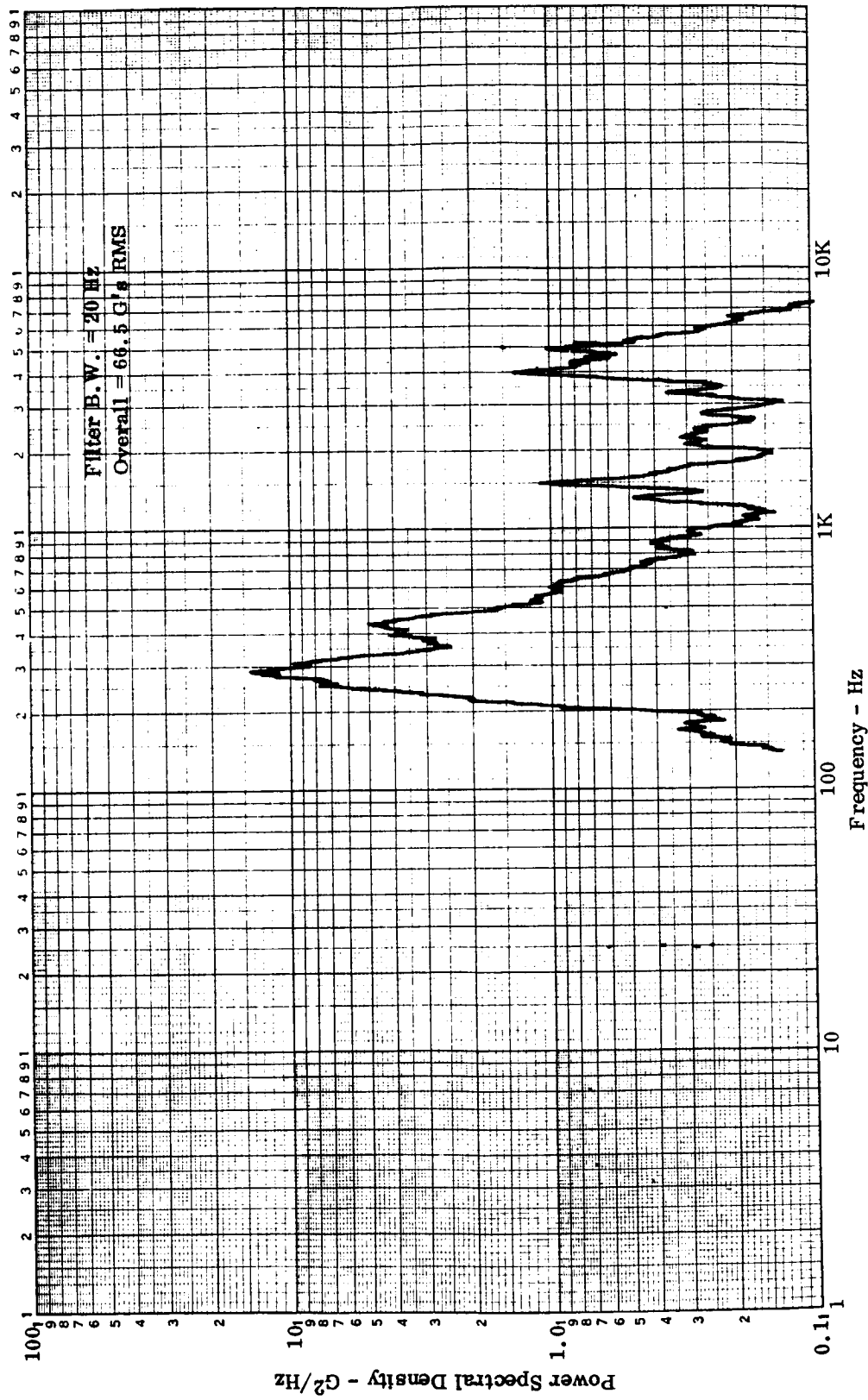


Figure E-31. Open Corrugation TPS, Accelerometer No. 2, 155 dB OASPL, Cycle No. 25

APPENDIX E — Continued

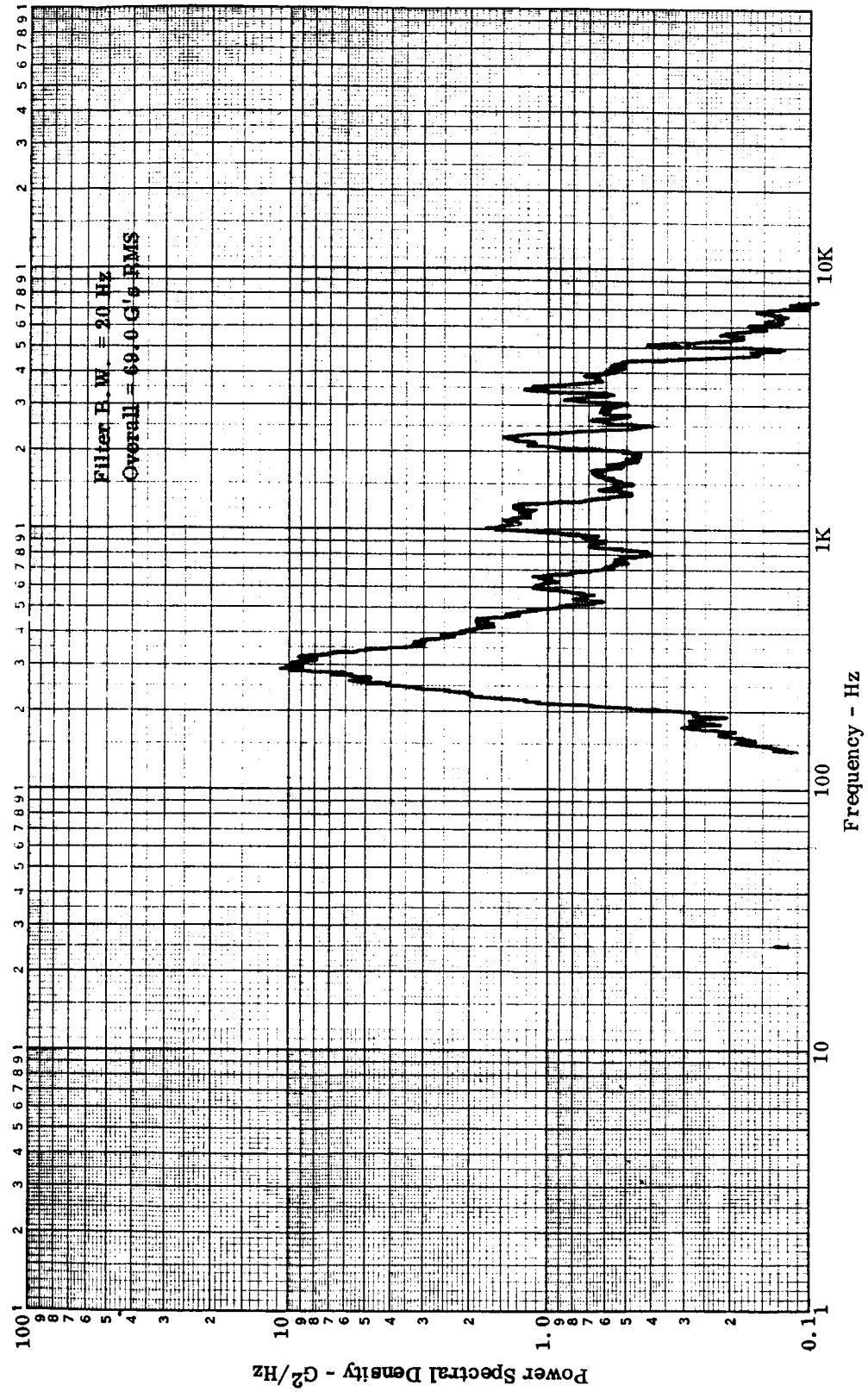


Figure E-32. Open Corrugation TPS, Accelerometer No. 3, 155 dB OASPL, Cycle No. 25

APPENDIX E — Continued

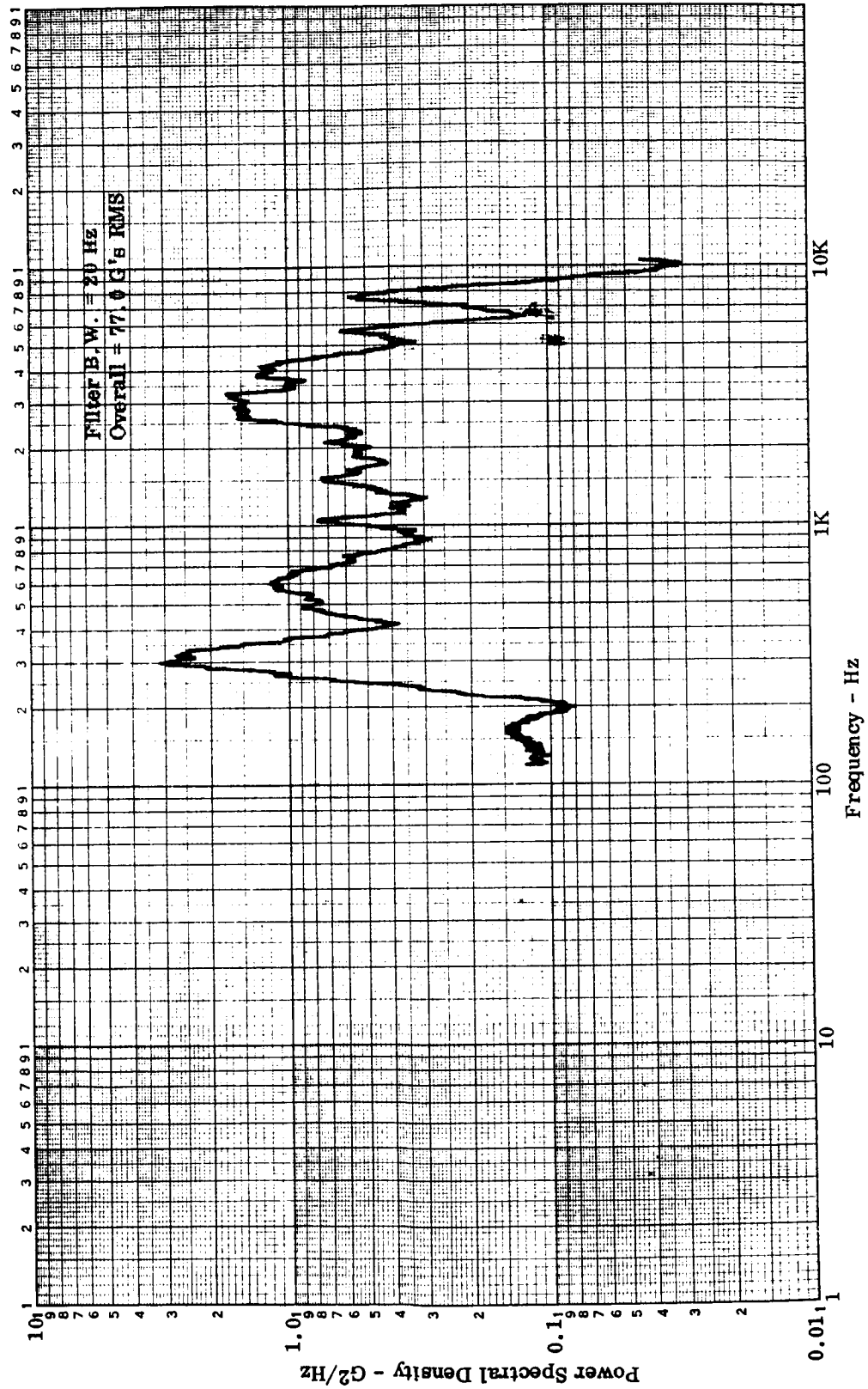


Figure E-33. Open Corrugation TPS, Accelerometer No. 7, 155 dB OASPL, Cycle No. 25

APPENDIX E — Continued

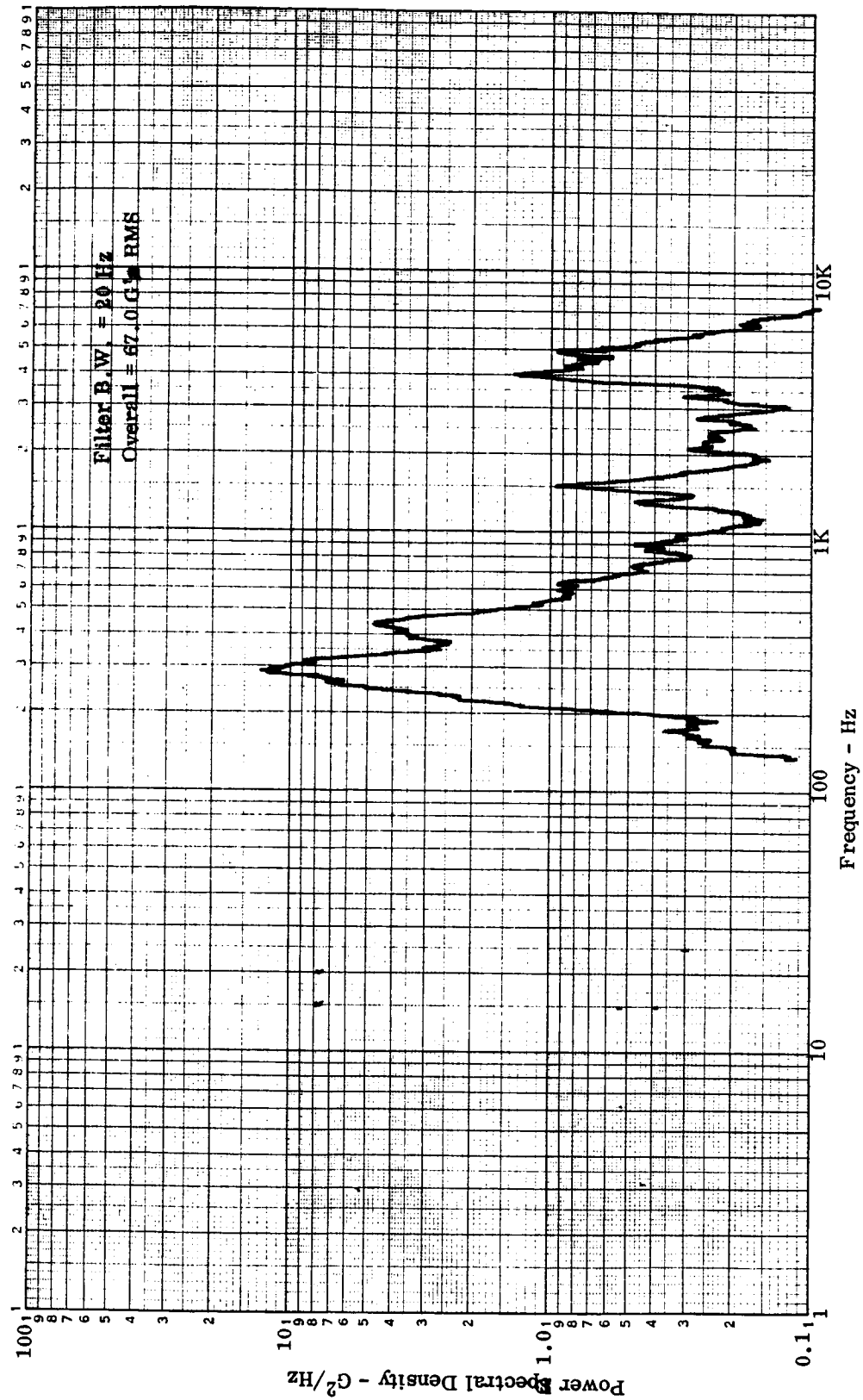


Figure E-34. Open Corrugation TPS, Accelerometer No. 2, 152 dB OASPL, Cycle No. 25

APPENDIX E — Continued

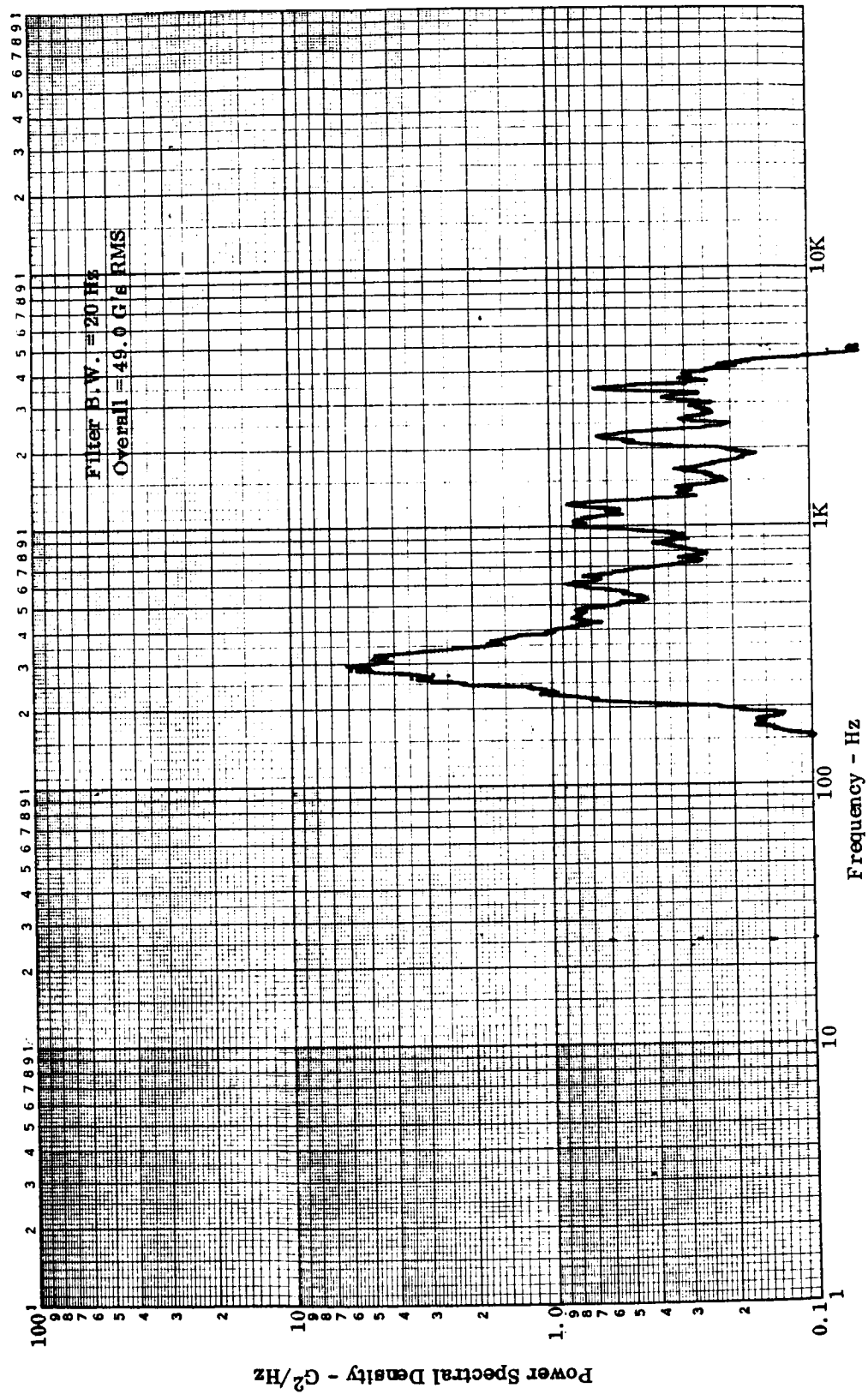


Figure E-35. Open Corrugation TPS, Accelerometer No. 3, 152 dB OASPL, Cycle No. 25

APPENDIX E — Continued

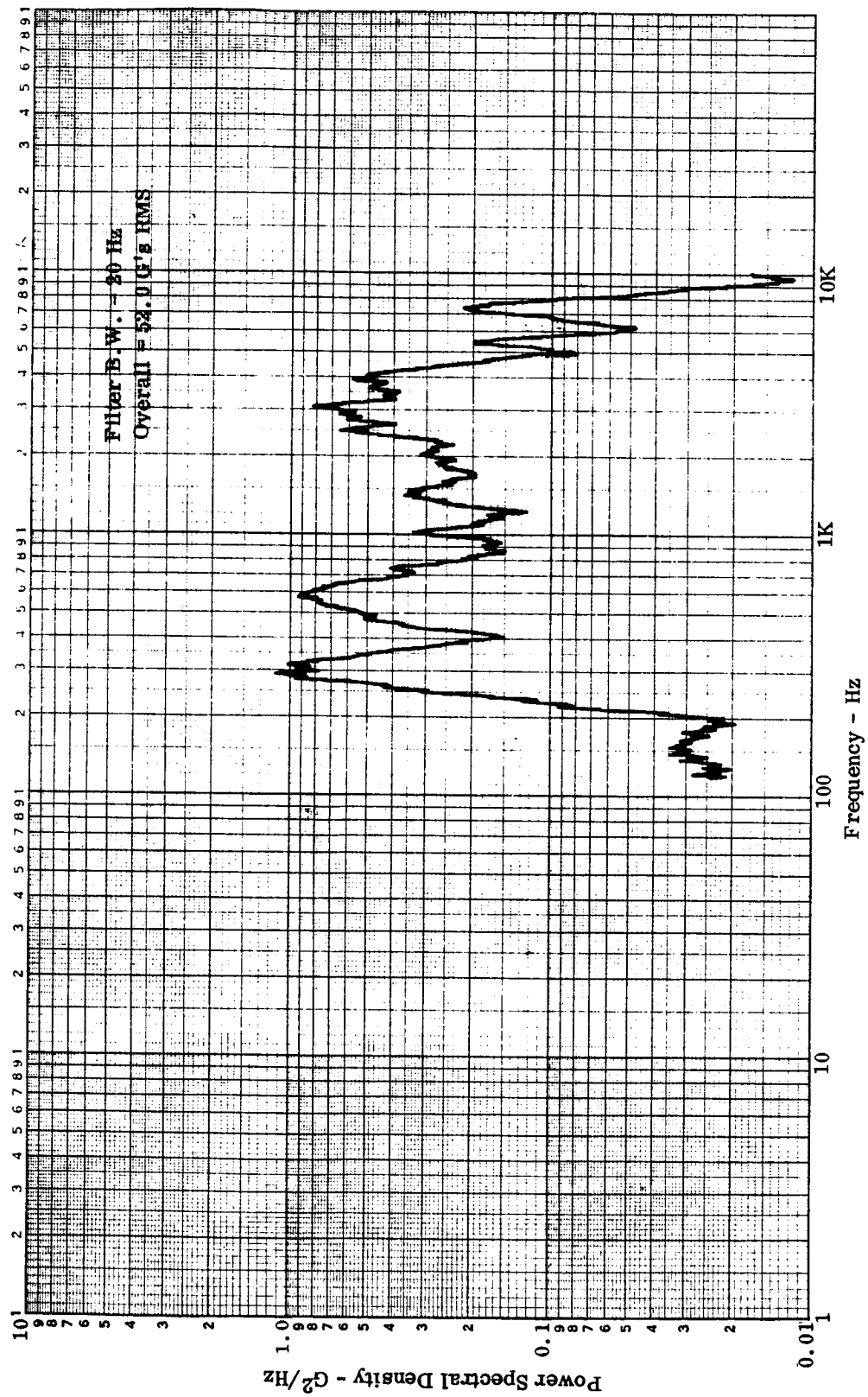


Figure E-36. Open Corrugation TPS, Accelerometer No. 7, 152 dB OASPL, Cycle No. 25

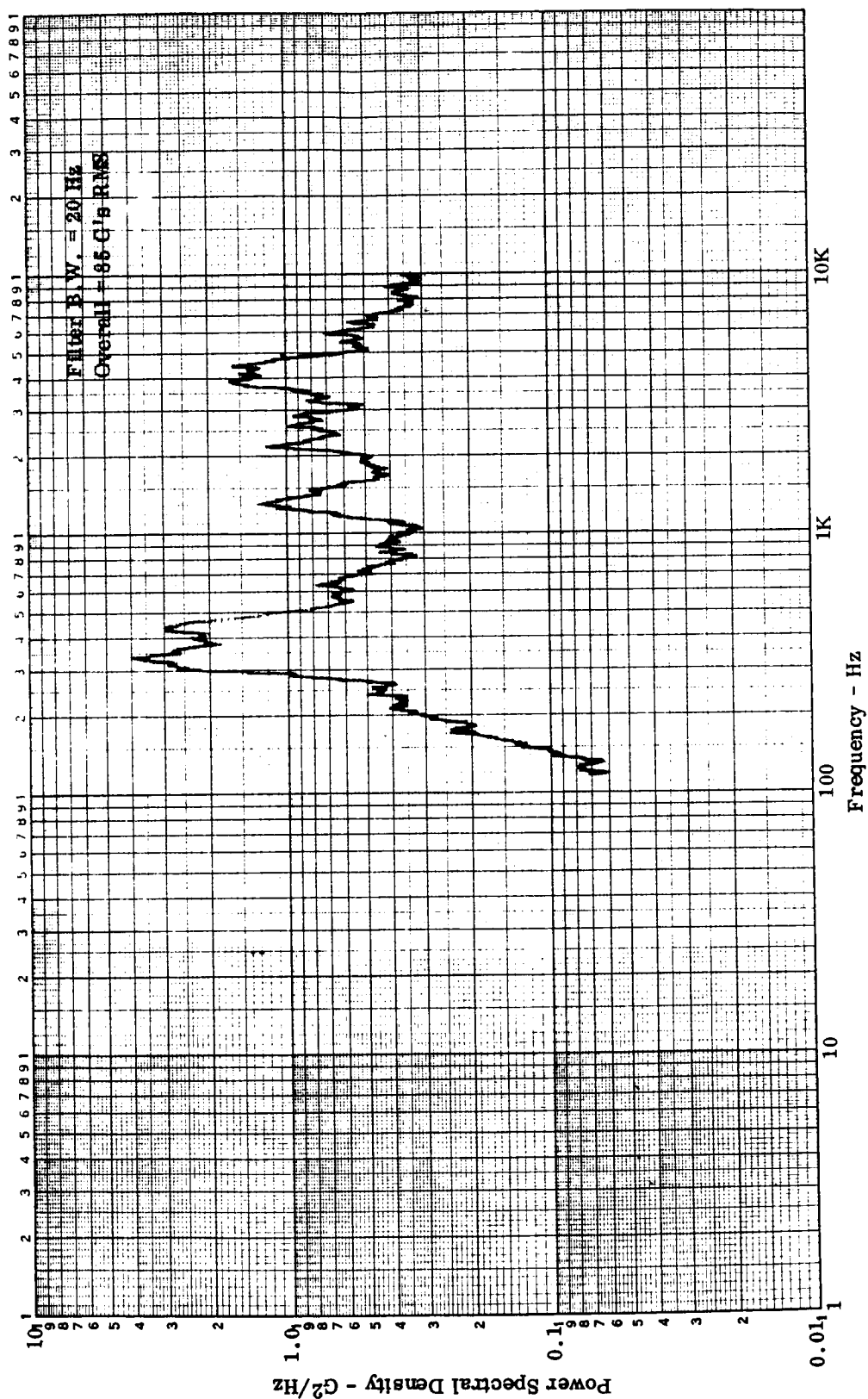


Figure E-37. Open Corrugation TPS, Accelerometer No. 2, 155 dB OASPL, Cycle No. 26

APPENDIX E — Continued

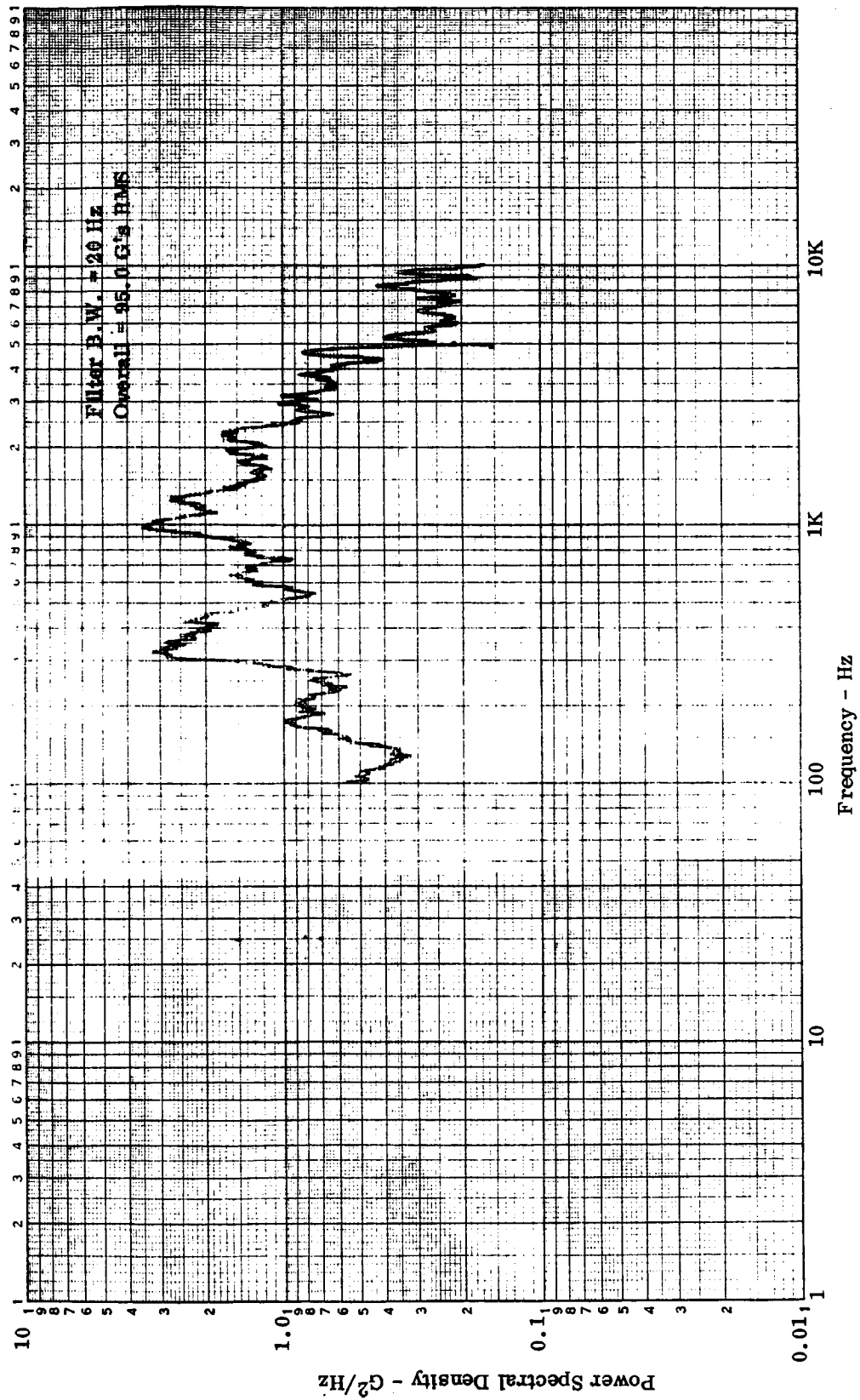


Figure E-38. Open Corrugation TPS, Accelerometer No. 3, 155 dB OASPL, Cycle No. 26

APPENDIX E — Continued

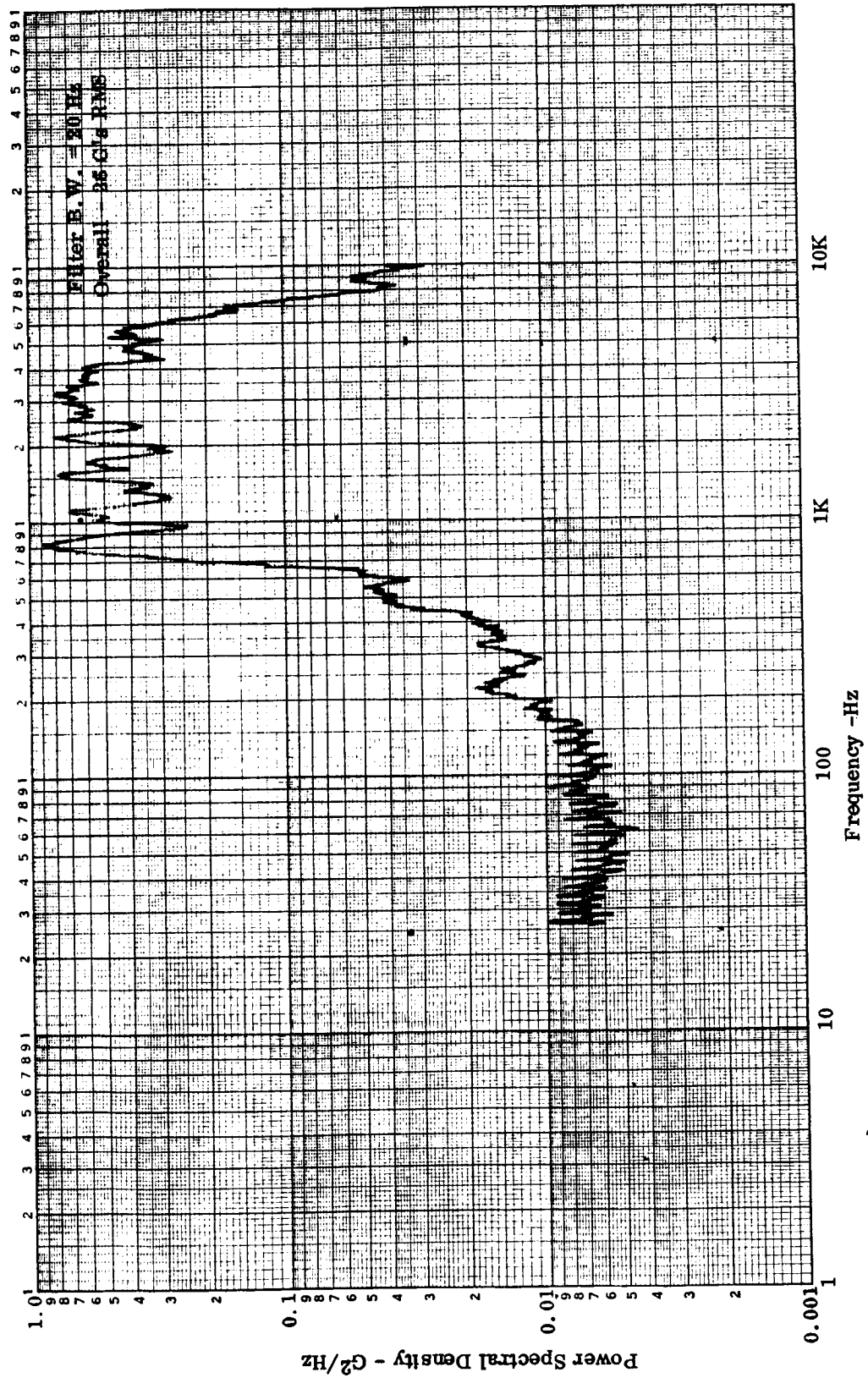


Figure E-39. Open Corrugation TPS, Accelerometer No. 7, 155 dB OASPL, Cycle No. 26

APPENDIX E — Continued

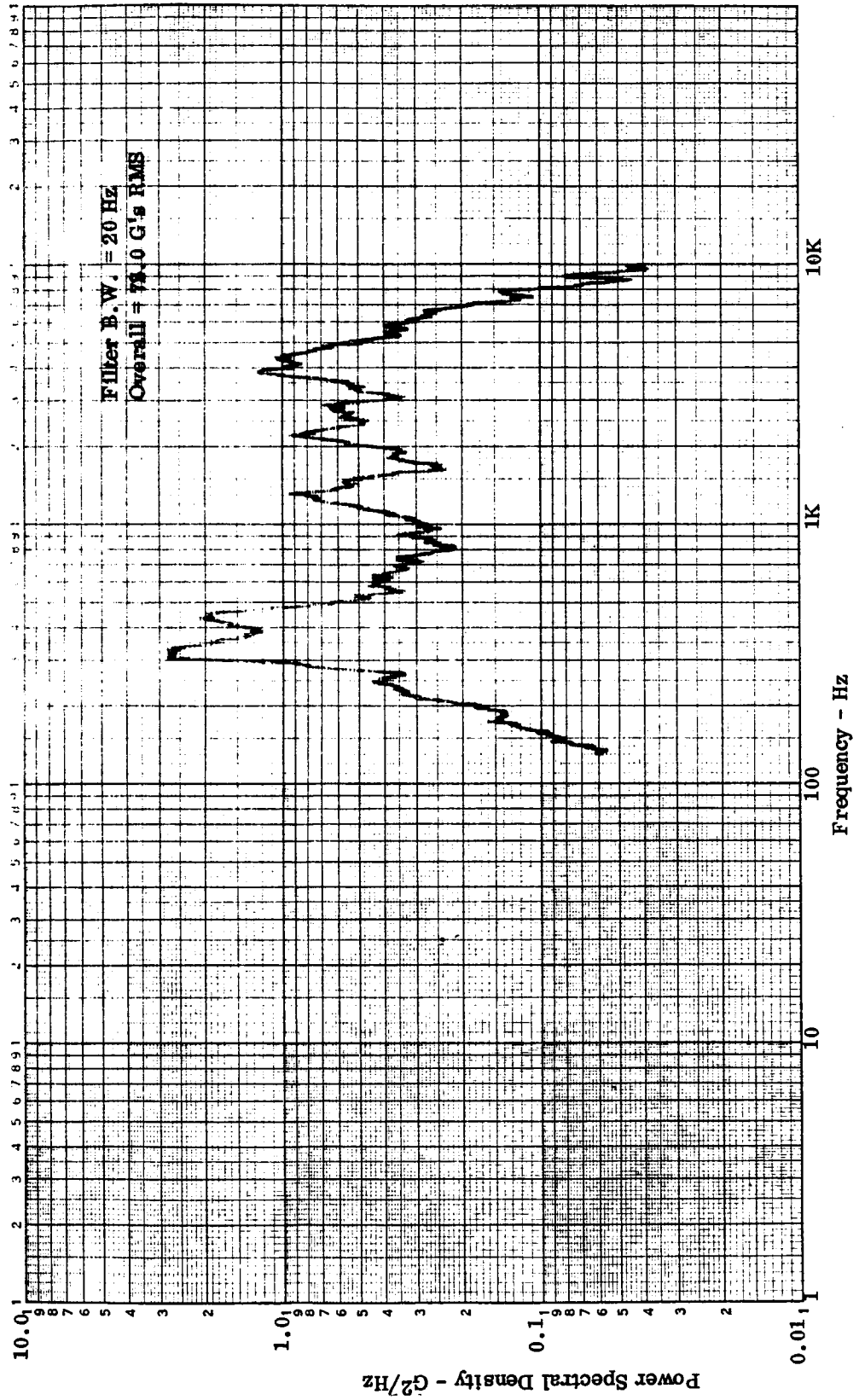


Figure E-40. Open Corrugation TPS, Accelerometer No. 2, 152 dB OASPL, Cycle No. 26

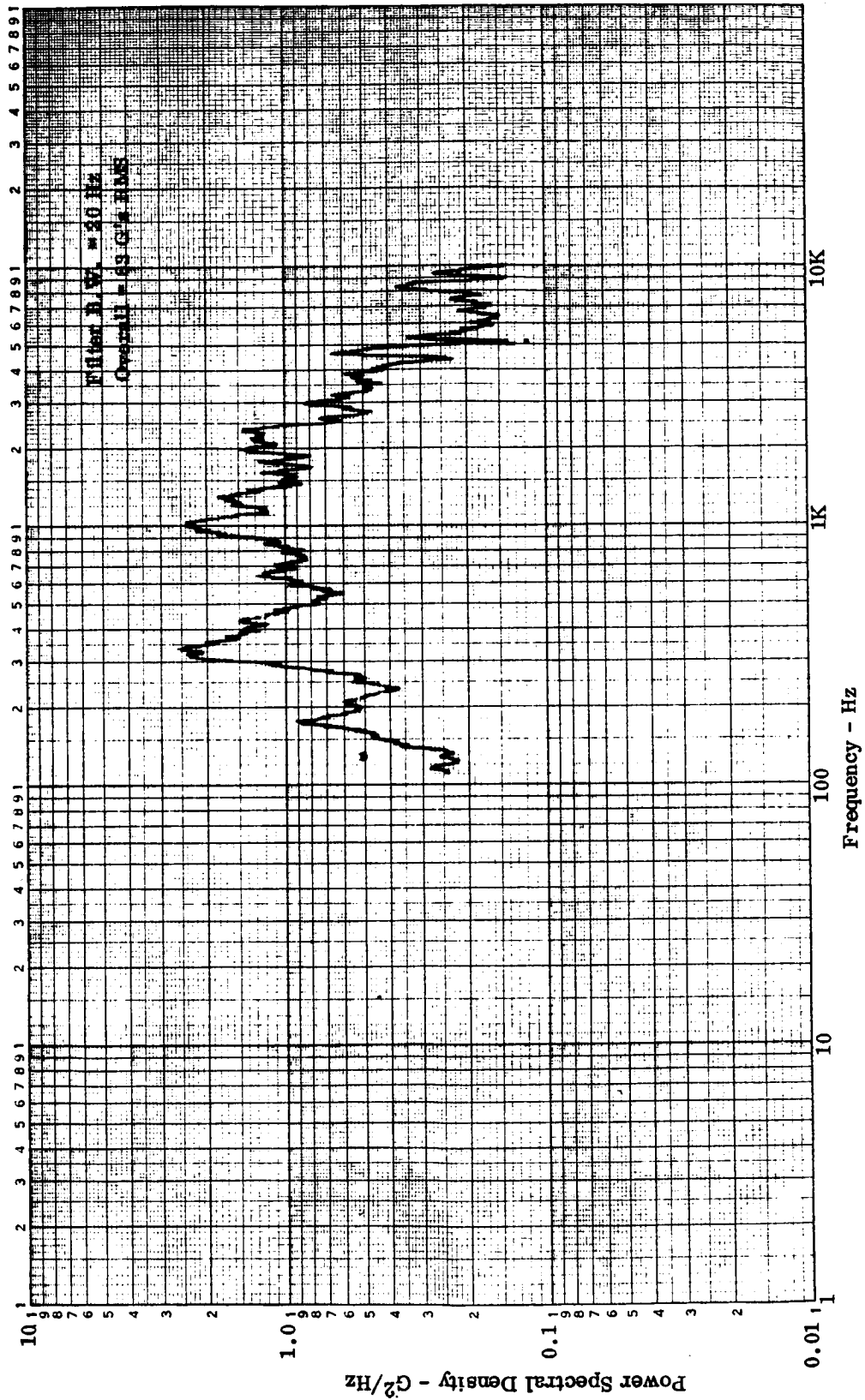


Figure E-41. Open Corrugation TPS, Accelerometer No. 3, 152 dB OASPL, Cycle No. 26

APPENDIX E — Continued

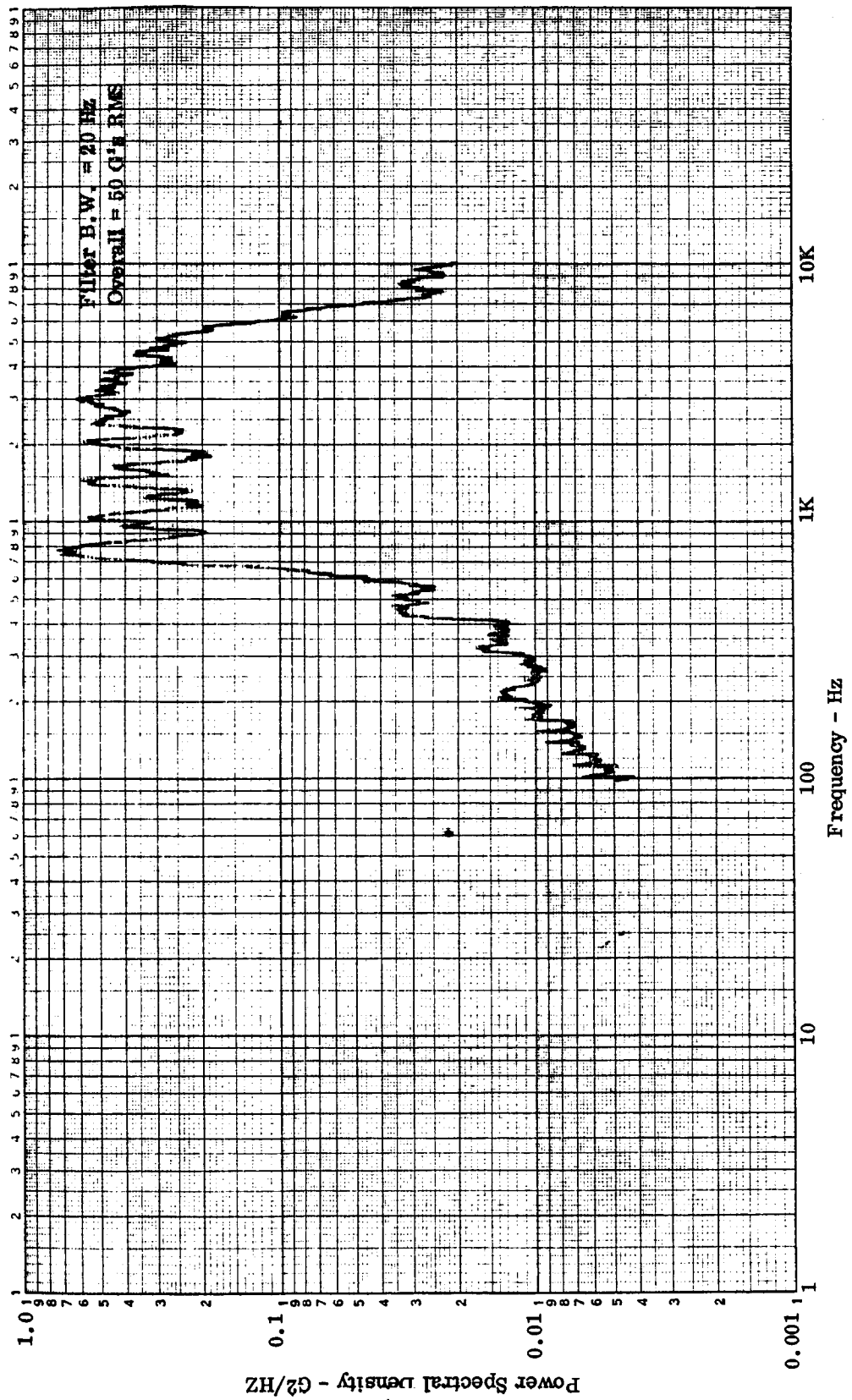


Figure E-42. Open Corrugation TFS, Accelerometer No. 7, 152 dB OASPL, Cycle No. 26

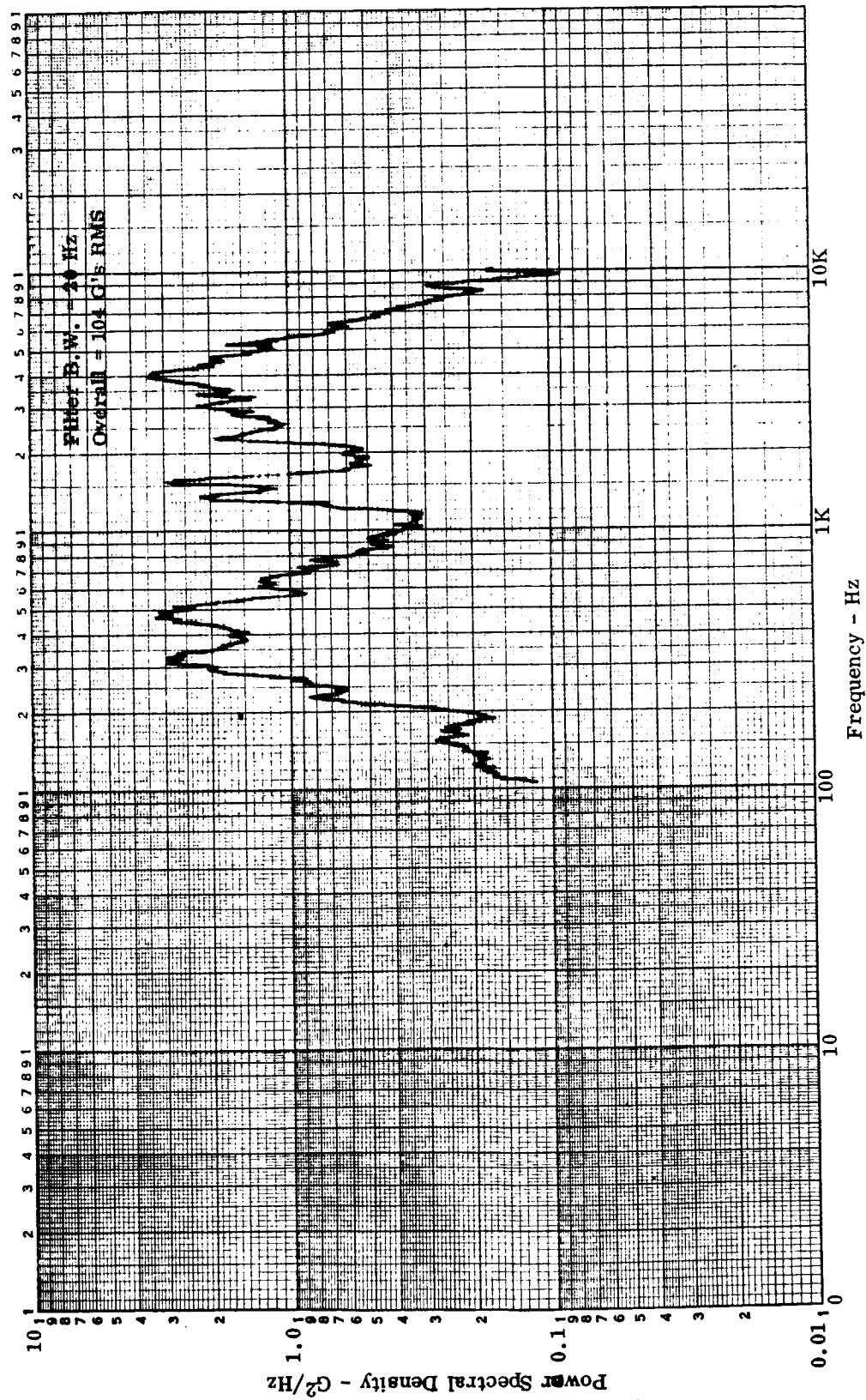


Figure E-43. Open Corrugation TPS, Accelerometer No. 2, 155 dB OASPL, Cycle No. 100

APPENDIX E — Continued

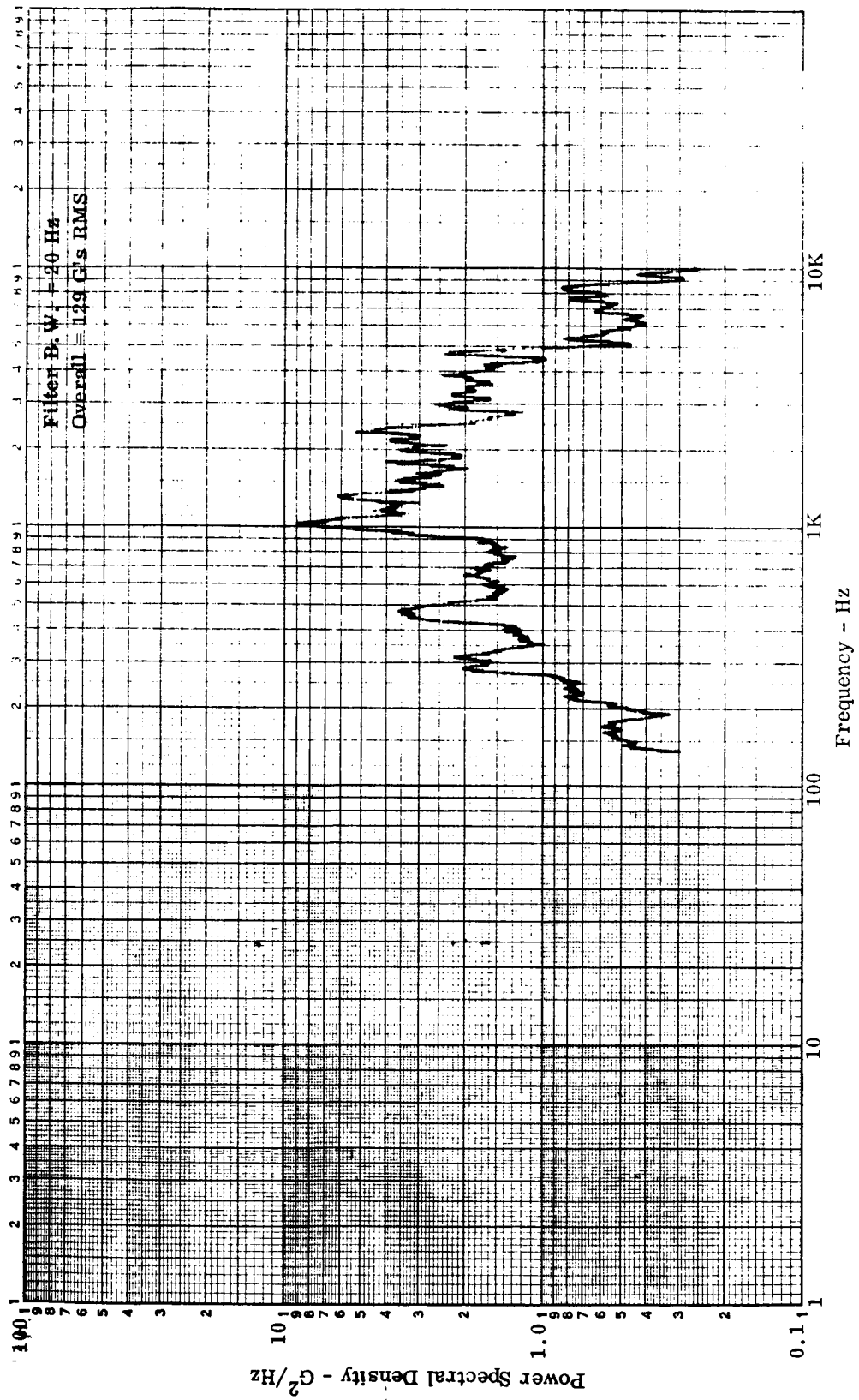


Figure E-44. Open Corrugation TPS, Accelerometer No. 3, 155 dB OASPL, Cycle No. 100

APPENDIX E — Continued

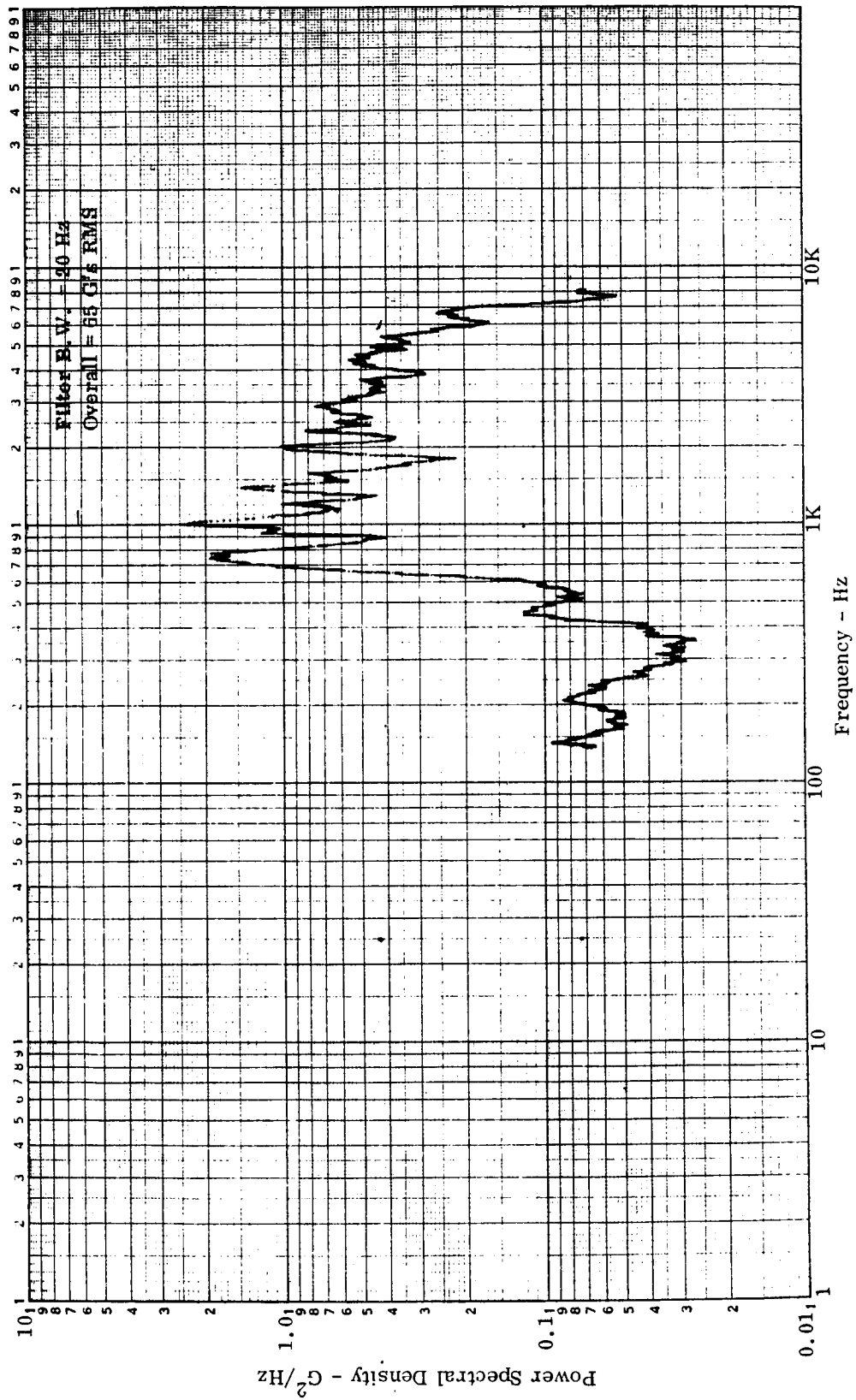


Figure E-45. Open Corrugation TPS, Accelerometer No. 7, 155 dB OASPL, Cycle No. 100

APPENDIX E — Continued

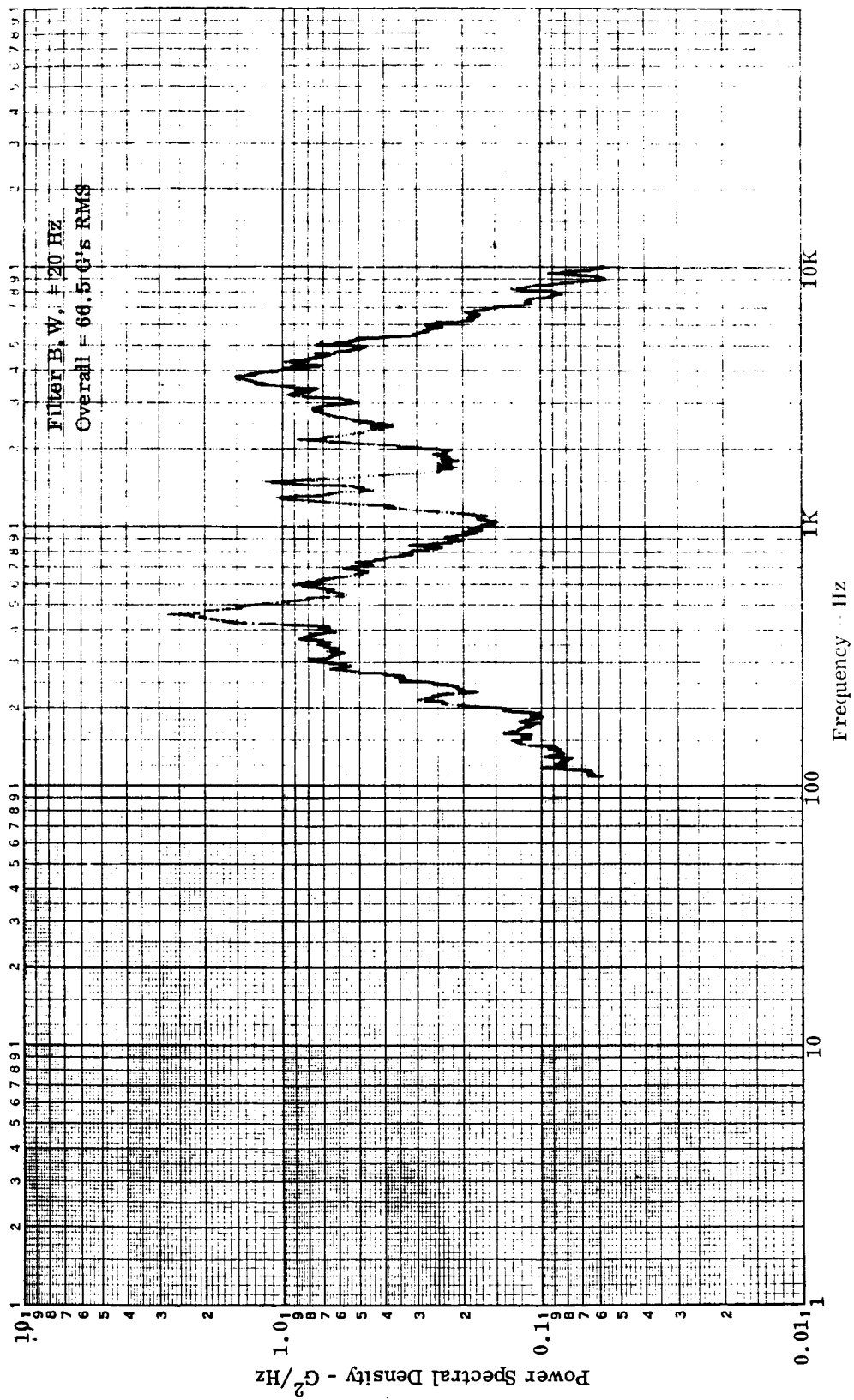


Figure E-46. Open Corrugation TPS, Accelerometer No. 2, 152 dB, OASPL, Cycle No. 100

APPENDIX E — Continued

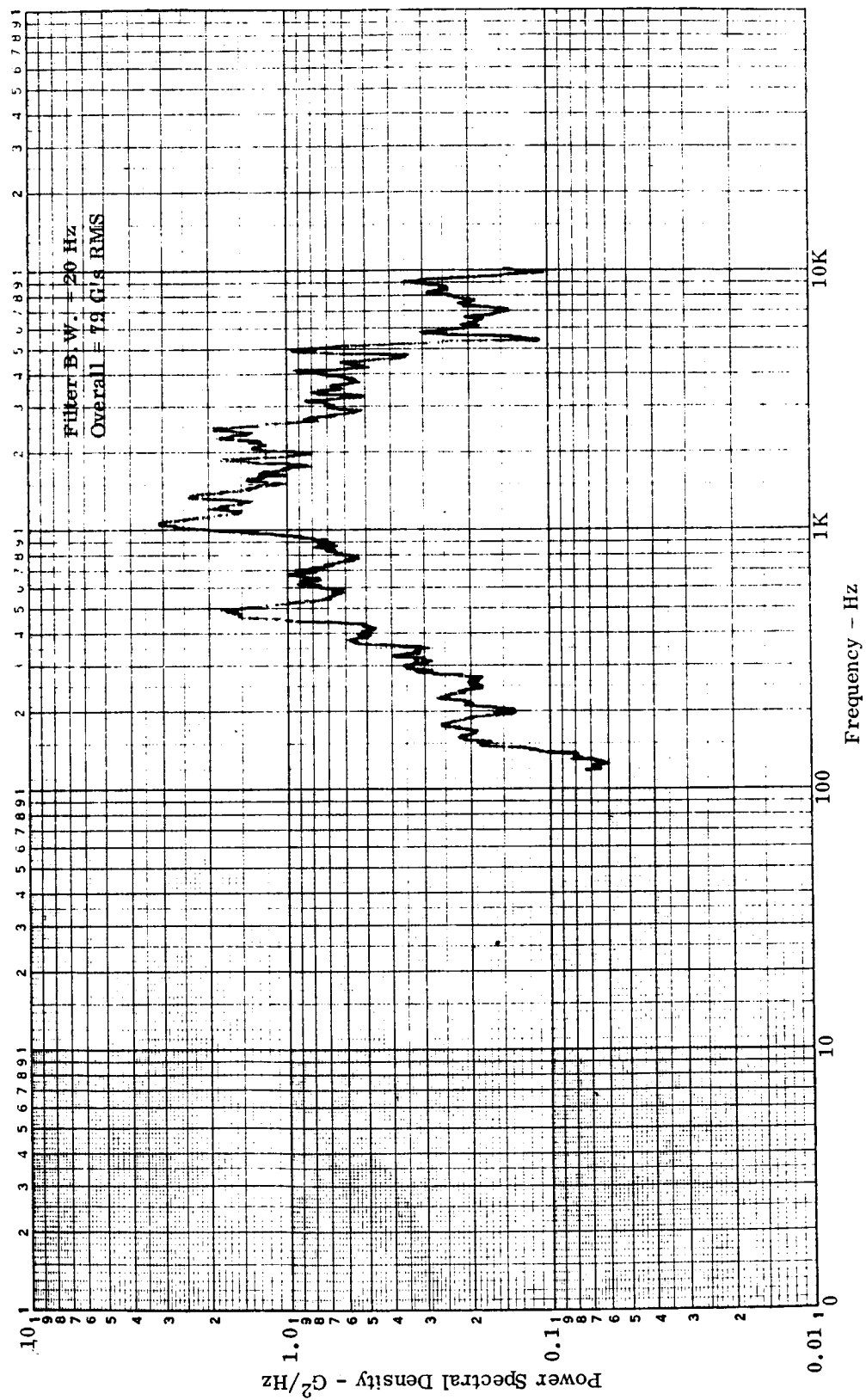


Figure E-47. Open Corrugation TPS, Accelerometer No. 3, 152 dB, OASPL, Cycle No. 100

APPENDIX E — Concluded

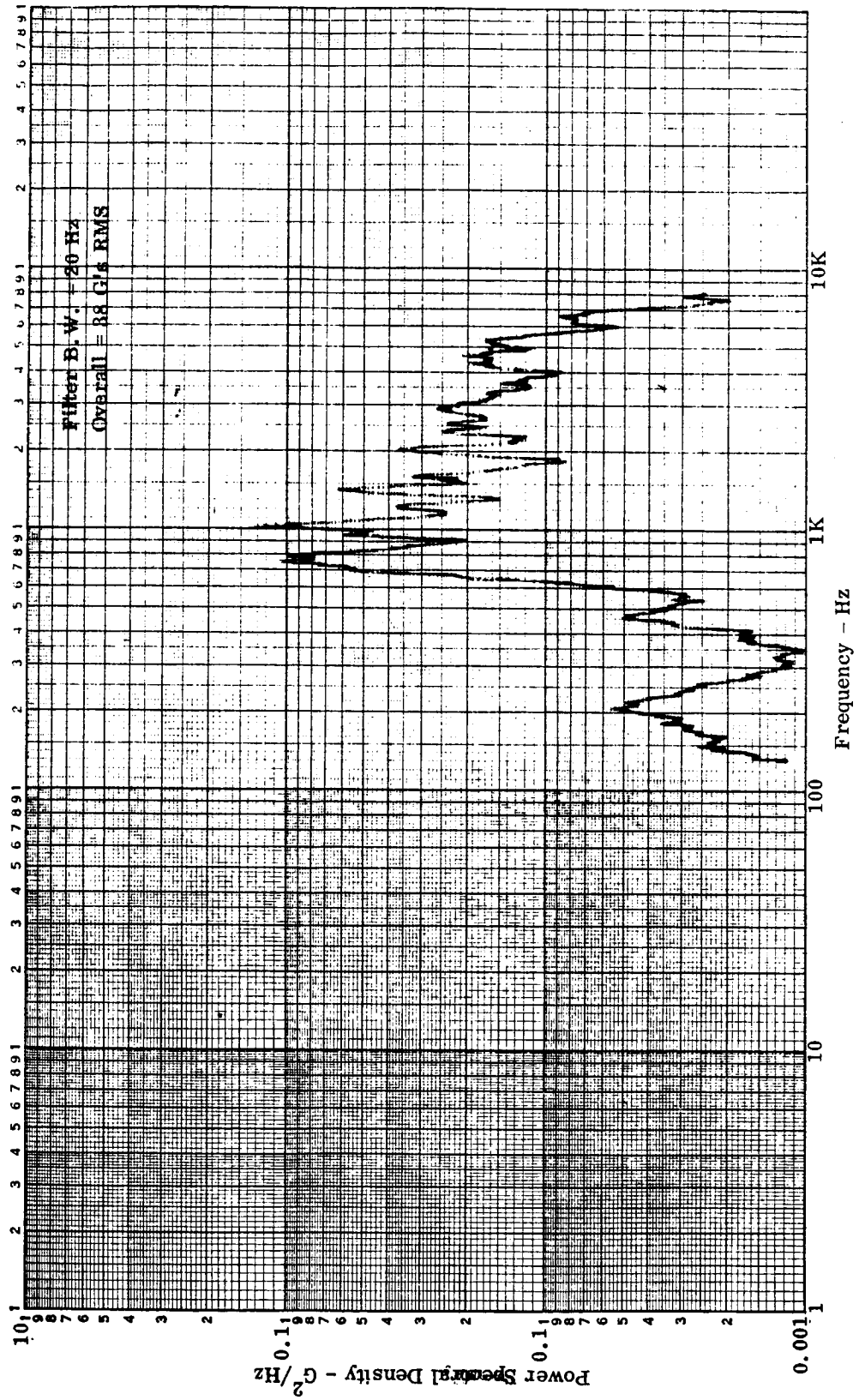


Figure E-48. Open Corrugation TPS, Accelerometer No. 7, 152 dB OASPL, Cycle No. 100

PRECEDING PAGE BLANK NOT FILMED

REFERENCES

1. Stein, B. A., Rummler, D. R., and Jackson, L. R., Refractory Metal Heat Shield Technology for Space Shuttle, presented at NASA Space Shuttle Technology Conference, Lewis Research Center, Cleveland, Ohio, 15-17 July 1970.
2. Gross, E. W., Sheet and Strip-Specification for Columbium Alloy Plate, General Dynamics Convair Division Specification 0.00947, March, 1969.
3. Black, W. E., et al, Evaluation of Coated Columbium Alloy Heat Shields for Space Shuttle Thermal Protection System Application, Volume I, NASA CR-112119, June 1972.
4. Convair Research Summary CRS-5, Convair Aerospace division of General Dynamics, 1970.
5. Cole, J. N., von Gierke, H.E., et al, Noise Radiation from Fourteen Types of Rockets in the 1,000 to 130,000 Pounds Thrust Range, WADC TR 57-354, Dec. 1957.
6. Franken, P. A., and Kerwin, E. M., Methods of Space Vehicle Noise Prediction, WADC TR 58-343, vol. II, November 1958.
7. Getline, G. L., Space Shuttle Booster Acoustic Environments, Convair Aerospace Division Report 76-549-4-151/AD-71-28, May 26, 1971.
8. Coe, C. F., and Rechtien, R. D., Scaling and Spatial Correlation of Surface Pressure Fluctuations in Separated Flow at Supersonic Mach Numbers, AIAA Structural Dynamics and Aeroelasticity Specialists Conference, New Orleans, April 1969.
9. Ailman, C. N., On Predicting Fluctuating Pressure at a Wall Beneath Turbulent Boundary Layer, NASA vol. 41, no. 6, p. 1583, June 1967.
10. Robertson, J. E., Characteristics of the Static and Fluctuating Pressure Environments Induced by Three Dimensional Protuberances at Transonic Mach Numbers, Wiley Labs Report WR 69-3, June 1969.
11. Lowson, M. V., Prediction of Boundary Layer Pressure Fluctuations, AFFDL-TR-67-167, April 1968.
12. Bier, D. A., A Review of Flight and Wind Tunnel Measurements of Boundary Layer Pressure Fluctuations and Induced Structural Response, NASA CR-626, October 1966.

REFERENCES (continued)

13. Anon., NASA/ARC 6 by 6 Wind Tunnel Data on Faget 1% Space Shuttle Model (Preliminary Data).
14. Anon., Test No. 99 — NASA ARC 3.5 feet HWT, August 1970.
15. Anon., Test No. 509 — NASA ARC 6 by 6 SSWT, Sept. 1970.
16. Palcheff, G. L., and Gaumer, G. R., Structural Thermal Protection System Criteria, Memo MRS-71 MDAC-East, March 28, 1967.
17. Anon., Material Properties for Columbium Alloy Cb-752 (Preliminary), North American Rockwell Space Division, 08.10.01.01, 1 October 1969.
18. Anon., Material Properties for Columbium Alloy C-129Y (Preliminary), North American Rockwell Space Division, 08.11.01.01, 10 November 1969.
19. Fitzgerald, B., Fused Slurry Silicide Coatings for Columbium Alloy Reentry Heat Shields, McDonnell Douglas Astronautics Company-East, Contract NAS 3-14307 Sixth Quarterly Technical Progress Narrative, 30 January 1972.
20. Pettyjohn, R. R., Thermal Insulations for High Temperature Heat Shield Applications, GDC-ERR-1431, Convair Division of General Dynamics, December 1969.
21. Cross, R. I., and Black, W. E., Optimization of Insulation and Mechanical Supports for Hypersonic and Entry Vehicles, AFML-TR-66-614, AF Contract AF33(615)-1672, AFML, Wright Patterson Air Force Base, April 1967.
22. Anon., TD NiCr, A Dispersion Strengthened Alloy, Fansteel, Inc., Metals Division, Bulletin TD-007-2, 1968.
23. Smithells, C. J., Metals Reference Book, Vol. II, Third Edition, Butterworth Inc., Washington D. C., 1962.
24. Hertz, J., and Knowls, D., Survey of Thermal Properties of Selected Materials, ZZL-65-008, Convair Aerospace Division of General Dynamics, 15 February 1965.
25. Touns, K. A., A General Computer Program for the Determination of Radiant-Interchange Configurations Factors, Technical Note ASD-TN-61-101, March 1963.

REFERENCES (continued)

26. O'Neill, R. F., et al, Shadowed View Factors Program 3523, Convair Aerospace Division of General Dynamics.
27. Winiarski, L. D., et al, Computer Program to Evaluate Radiation Exchange Factors for Grey, Diffuse Surfaces (Script F), DDB64-003, Convair Aerospace Division of General Dynamics, 10 April 1967.
28. Switzky, H., Forray, M. J., and Newman, M., Thermo-Structural Analysis Manual, WADD-TR-60-517, Volume 1, Section 4, August 1962.
29. Timoshenko, S. P., and Gere, J. M., Theory of Elastic Stability, Second Edition, Article 2.13, McGraw-Hill Book Co., Inc., 1961.
30. Structures Manual, NASA MSFC, 1961.
31. Bohon, H. L., Anderson, M. S., and Heard, W. L., Flutter Design of Stiffened-Skin Panels for Hypersonic Aircraft, NASA TN D-5555, December 1969.
32. Lemley, C. E., Design Criteria for the Prediction of Panel Flutter, AFFDL-TR-67-140, August 1968.
33. Gaspers, P. A. Jr., and Redd, B., A Theoretical Analysis of the Flutter of Orthotropic Panels Exposed to a High Supersonic Stream of Arbitrary Direction, NASA TN D-3551, August 1966.
34. McGowan, P. R., et al, Structural Design for Acoustic Fatigue, ASD-TDR-63-820, 1963.
35. Johnson, R. Jr., and Kilpatrick, D. H., Dispersion Strengthened Metal Structural Development, AFFDL-TR-68-130, Part I, July 1968.
36. Black, W. E., Space Shuttle Vehicle High-Temperature Load-Carrying Structure and Radiative Thermal Protection, GDC-ERR-1497, Convair Aerospace Division of General Dynamics, June 1970.
37. Beck, E., and Schwartzberg, F., Determination of Mechanical and Thermo-physical Properties of Refractory Metals, AFML-TR-65-247, July 1965.
38. Chubb, D. L., Fully Ionized Quasi-one Dimensional Magnetic Nozzle Flow, NASA-TM-X-52925, January 1971.

REFERENCES (concluded)

39. Lipson, C., and Juvinall, R. C., Handbook of Stress and Strength, Figures 20 through 24, The MacMillan Co., 1963.
40. Furman, J. H., Modification to Detail Test Requirements for Acoustic/Thermal Environmental Tests on Prototype No. 1 Thermal Protective Systems (TPS) Panels, Memorandum S&E-ASTN-AAD-70-62, NASA MSFC S&E-ASTN-AAD-71-3, January 13, 1971.
41. Anon., Space Shuttle Phase B Final Report, Volume II, Book 3, North American Rockwell Space Division Report SD 71-114-2, 25 June 1971.
42. Hugill, D. B., and Gaiennie, B., Quartz Lamp Radiant Heat Brazing of Large Refractory Metal Honeycomb Sandwich Panels, AFML-TR-64-352, November 1964.
43. Freedman, A. H., and Mikus, E. B., Brazing of Columbium D36 Honeycomb Structures, Supplement to the Welding Journal, September 1964.
44. Freedman, A. H., and Mikus, E. B., High Remelt Temperature Brazing of Columbium Honeycomb Structures, Supplement to the Welding Journal, June 1966.
45. Culp, J. D., Field Repair of Coated Columbium Thermal Protection Systems (TPS), McDonnell Douglas Astronautics Co. -East Report MDC E0681, Contract NAS8-26121, 15 September 1972.
46. Richardson, A. J., Meteoroid Analysis Results for Space Shuttle Orbiter (SSVO), North American Rockwell Space Division Letter Report SD&S 70-63, 19 Aug. 1970.
47. Cour-Palais, B. G., Meteoroid Environment Model 1969 (Near Earth to Lunar Surface), NASA MSC Report SP8013, March 1969.
48. Richardson, A. J., and McHugh, A. H., Hypervelocity Impact Penetration Equation for Metal by Multiple Regression Analysis, North American Rockwell Space Division Report STR 153, March 1966.
49. Richardson, A. J., and Sanders, J. P., Discrete Particle Penetration Mechanics Based on Debris Particles of Two Materials, North American Rockwell Space Division Report SD70-463, October 1971.
50. Bartlett, E. S., et al, Degradation on Reuse of Radiative-Thermal-Protection-System Materials for the Space Shuttle, Battelle Columbus Laboratories Report No. DCN 1-1-50-13647 (1F), Contract No. NAS8-26205, October 25, 1972.
51. DeLacy, T. J., and Anderson, R. T., Nondestructive Testing of Refractory Coatings - Problems and Solutions, Presented at the Refractory Composites Working Group, Seattle, Washington, 13-15 October 1969.